

Mark VERSCHUREN

An integrated 3D approach to clay tectonic deformation

and the development of a new 3D surface modelling method

Een integrale 3D benadering van kleitektonische vervormingen

en de ontwikkeling van een nieuwe 3D
oppervlaktemodelleringsmethode

1992

Proefschrift ingediend bij de
Faculteit van de Wetenschappen van de
Universiteit Gent voor het verkrijgen van de graad van
Doctor in de Wetenschappen (Groep Aard- en Delfstofkunde)

Promotor: Prof. Dr. R. Maréchal

Co-promotor: Dr. J.P. Henriët

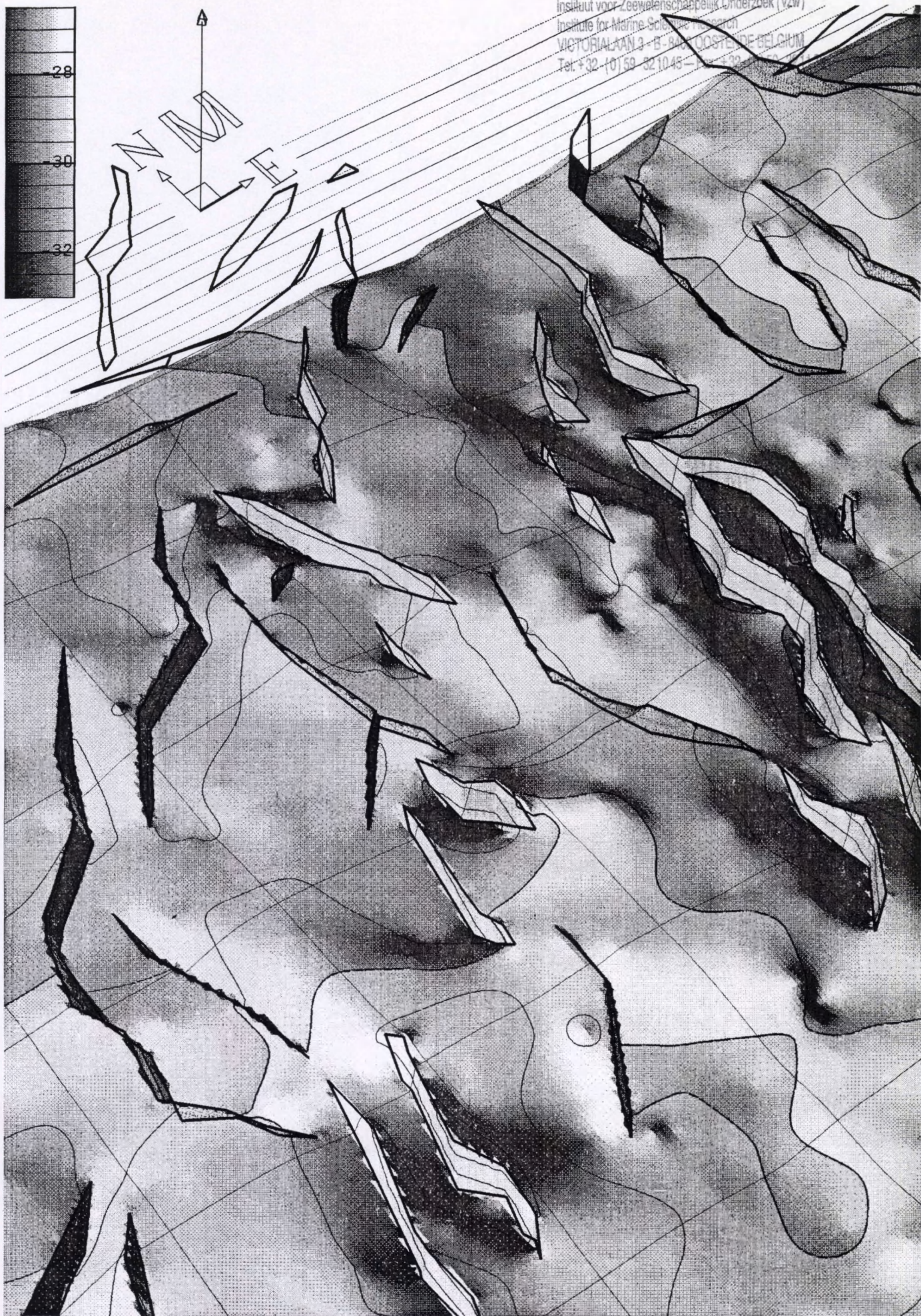
IZWO

Instituut voor Zeewetenschappelijk Onderzoek (vzw)

Institute for Marine Scientific Research

VICTORIAAN 3 - B-840 OOSTENDE-BELGIUM

Tel: +32 (0)59 821045 - Fax: +32 (0)59 821046



Clay tectonic deformation in North Hinder area, modelled with Geofox on a dense network of sparker seismic sections. Contour interval 0.5 m; grid line spacing 250 m; vertical exaggeration x50. Versaplot (black&white) hardcopy.

VLIZ (vzw)
VLAAMS INSTITUUT VOOR DE ZEE
FLANDERS MARINE INSTITUTE
Oostende - Belgium

An integrated 3D approach to clay tectonic deformation

and the development of a new 3D surface modelling method

Een integrale 3D benadering van kleitektonische vervormingen

en de ontwikkeling van een nieuwe 3D
oppervlaktemodelleringsmethode

Proefschrift ingediend bij de Faculteit van de Wetenschappen
van de Universiteit Gent voor het verkrijgen van de
graad van Doctor in de Wetenschappen
(Groep Aard- en Delfstofkunde)

Promotor : Prof. Dr. R. MARECHAL
Co-promotor : Dr. J.P. HENRIET

1992

Table of Contents

Acknowledgements.....	vi
Samenvatting.....	1
1. Clay diagenetic deformation in Palaeogene clays	12
1.1. Introduction	12
1.2. Soft-sediment deformation.....	20
1.3. Geologic setting.....	25
1.4. Clay tectonics	27
1.4.1. Seismic evidence for Ieper/London clay deformation styles.....	27
1.4.2. Land evidence.....	32
1.4.3. Microfractures.....	36
1.4.4. Working hypotheses.....	39
1.5. Clay diapirism.....	43
1.6. Methodology	45
2. High resolution (pseudo-) 3D seismics	48
2.1. 3D or pseudo-3D seismics and scale	48
2.1.1. Pseudo-3D reflection seismics and spatial aliasing.....	53
2.1.2. 3D reflection seismics	56
2.2. Positioning systems	58
2.2.1. Hydro-acoustic Positioning Systems.....	60
2.2.1.1. Ultra-short Baseline Systems.....	60
2.2.1.2. Short Baseline Systems.....	61
2.2.1.3. Long Baseline Systems.....	62
2.2.2. Rediopositioning	62
2.2.2.1. Range-range Method	62
2.2.2.2. Pseudo-range Method	64
2.2.3. Differential GPS.....	65
2.2.4. Laser Auto-tracking	66
2.2.5. Practice	66
2.3. Seismic acquisition system.....	68
2.3.1. Seismic sources.....	68
2.3.2. Receiver arrays.....	70
2.3.3. SEISCAT	71
2.3.3.1. Platform.....	71
2.3.3.2. System.....	72
2.3.3.3. Navigation.....	72
2.3.3.4. Positioning.....	74
2.4. Surveys.....	75
2.4.1. Pseudo-3D acquisition	75
2.4.1.1. Large scale network: North Hinder sag fault.....	75
2.4.1.2. Medium scale network: clay tectonic deformations.....	77
2.4.2. 3D acquisition.....	79
2.4.2.1. Bin size dimensioning in a true 3D approach.....	81
2.4.2.2. Scheldt test site.....	82

2.5.	Seismic interpretation.....	84
2.5.1.	Scheldt clay diapir.....	84
2.5.2.	North Hinder clay tectonics	85
2.5.3.	North Hinder sag fault	87
3.	3D surface modelling method	90
3.1.	Introduction	90
3.2.	Problem analysis.....	92
3.2.1.	Data distribution and redundancy.....	92
3.2.2.	Mis-ties.....	93
3.2.3.	Horizon modelling	95
3.2.4.	Fault modelling	96
3.2.5.	Inherent hard- and software limitations.....	98
3.3.	Existing software methods.....	99
3.4.	Hardware platform	102
3.5.	Data preparation.....	103
3.5.1.	Efficient manual digitization of curves	103
3.5.1.1.	Introduction	103
3.5.1.2.	Digitization and its limitations	104
3.5.1.3.	Efficient manual digitization of curves	105
3.5.1.4.	Measuring digitization precision	106
3.5.1.5.	Experimental results	108
3.5.2.	Data reduction.....	111
3.5.2.1.	Review	112
3.5.2.2.	Local maximum distance algorithm	113
3.5.2.3.	Experimental results	117
3.5.3.	Conversion.....	118
3.6.	A new 3D surface modelling method.....	119
3.7.	Geofox	120
3.7.1.	Introduction	120
3.7.2.	Software platform	122
3.7.3.	Program structure	124
3.7.4.	Input.....	126
3.7.5.	Data reduction.....	127
3.7.6.	Modelling by triangulation.....	130
3.7.6.1.	Automatic Delauney triangulation	130
3.7.6.2.	Mis-tie correction.....	137
3.7.6.3.	Fault correlation.....	137
3.7.6.4.	Fault tip, branch and intersection modelling	141
3.7.7.	Gridding.....	143
3.7.7.1.	Initialization	151
3.7.7.2.	Smoothing with splines in least tension	151
3.7.7.3.	Smoothing with splines in variable tension.....	160
3.7.7.4.	Optimizations	167
3.7.8.	Stratigraphic functions	167
3.7.9.	Solid shaded 3D visualization.....	172
3.7.9.1.	The quest for visual realism.....	172
3.7.9.2.	Perspective.....	176
3.7.9.3.	Solid surfaces through hidden surface removal	177
3.7.9.4.	Colour and line contours emphasize and quantify relief	179
3.7.9.5.	Smooth shading, except for selected discontinuities.....	180
3.7.9.6.	Stereopsis.....	181
3.7.9.7.	Hardcopy facilities	181
3.7.10.	Geofox applications and a word of caution.....	188
4.	New geological evidence.....	194
4.1.	Structural surface models.....	194
4.1.1.	North Hinder sag fault	194
4.1.2.	North Hinder clay tectonic faulting.....	198
4.1.3.	Scheldt diapir.....	201

4.2.	Outcrop evidence of clay tectonics	209
4.2.1.	Structures in outcrop	209
4.2.1.1.	Outcrops	209
4.2.1.2.	Techniques	212
4.2.1.3.	Major faults, Marke	224
4.2.1.4.	Intersecting faults, Marke	226
4.2.1.5.	Listric splay, Marke	229
4.2.1.6.	Connection structure, Marke	229
4.2.1.7.	Termination splays, Marke	229
4.2.1.8.	Folded faults, Marke	234
4.2.1.9.	Horses, Marke	237
4.2.1.10.	Major faults, Zonnebeke	242
4.2.1.11.	Slickensides and microfaults in Marke, Zonnebeke and Mol	244
4.2.1.12.	Clastic dykes, Marke and Zonnebeke	247
4.2.1.13.	Faults in Egem Member, Meulebeke	249
4.2.2.	Palaeostress analysis	252
4.2.2.1.	Stress inversion method	253
4.2.2.2.	Palaeostress information, Marke	254
4.2.3.	'Reverse' faults	259
4.2.4.	Quaternary reactivation	261
4.2.5.	Clay tectonic faults and slumping	264
4.2.6.	Permeability issues	265
4.3.	Microscopic and analytical evidence	268
4.3.1.	Grain size and clay-mineralogical composition	268
4.3.2.	Chemical composition	269
4.3.3.	Microfossil	274
4.3.4.	CT scans	274
4.3.5.	Thin sections	277
5.	Conclusions	290
5.1.	Conclusions proper	290
5.2.	A new synthesis	295
5.3.	General conclusions	298
	Addendum : Geofox manual	300
0.	Preparation of data for Geofox (RCMG Seismostrat only)	301
1.	Getting_Started	302
2.	Geofox tutorial	305
3.	Editing data files	312
4.	File formats	312
5.	Frame->	313
6.	Grids	314
7.	Legend	323
8.	Mode_cycle	328
9.	Mouse	331
10.	Move_points+triangles	332
11.	Print_Screen	333
12.	Scale	333
13.	Screen	334
14.	Shortcuts	337
15.	Shot_data	338
16.	Stop_it	339
17.	Triangles	339
18.	XYZ_lines	344
19.	XYZ_points	346
	References	348
	Index	357

Acknowledgements

While I finally draw a line under this thesis work, I would first of all like to thank my promotor, Prof. R. MARECHAL, who during his last five years as director of the Laboratorium voor Aardkunde not only gave me the opportunity to do my research there, but also stimulated me to do field work, with which many questions were answered and new ones raised.

I am also obliged to Prof. W. DE BREUCK, Dean of the Faculty of Sciences, Universiteit Gent, for presiding my jury and giving me the permission to write this thesis in English.

I am indebted to the Belgian NATIONAL FUND FOR SCIENTIFIC RESEARCH (NFWO) for assigning me a grant as Research Assistant (Aspirant) and the financial support with it.

Further, I wish to express my respect and deep gratitude to :

Dr. M. DE BATIST on whose geological work the present one builds;

E. MAES who provided a C version of and some critical enhancements to the Versaplot library, thus enabling black&white hardcopies of Geofox images;

W. VERSTEEG for his geophysical know-how and seismic data processing;

E. VAN HEUVERSWYN for developing new seismic acquisition hardware and helping me to sift the manufacturer's information about positioning systems;

other (past and present) staff of the RENARD CENTRE OF MARINE GEOLOGY, personnel of the LABORATORIUM VOOR AARDKUNDE and students for varied help, comments and a generally great time together;

R. JONKHEERE for his sound insight in statistical and other maths;

F. MEES and D. DE DECKER for suggesting appropriate analyses of samples and for mineralogical interpretation of thin sections;

Dr. J. DE CONINCK for the invaluable micropalaeontological dating with which upward fluid transport along clay tectonic faults was proven;

Dr. S. GEETS and Mrs. N. SELEN for granulometric, clay mineralogical and chemical analyses;

Prof. G. STOOPS for suggesting accepted soil thin section description practice in the micromorphological description of my samples and for the permission to use his microscope;

P. MESTDAGH for making the high quality thin sections and H. BOURDIN for his assistance in making microphotographs;

Prof. M. KUNNEN and Dr. H. LAUWERS (Radiology lab, University Hospital, Gent) for the CT scans and Dr. P. JACOBS (RCMG, Lithostratigraphy Unit) for preparing the opportunity and for his interest in this fine technique;

the staff of the BEHEERSEENHEID VAN HET MATHEMATISCH MODEL VAN DE NOORDZEE EN HET SCHELDE-ESTUARIUM (BMM, Oostende, Belgium) and the crew of *RV Belgica* for their effort to keep the acquisition on track;

the companies CORAMIC TERCA ("Marke Steenbakkerij NV" and "Steenbakkerij van Zonnebeke NV") and "Steenbakkerij OSTYN" (Meulebeke) for the permission to conduct my field work in their clay quarries;

Dr. F. MOSTAERT (Ministerie van de Vlaamse Gemeenschap, Bestuur Natuurlijke Rijkdommen en Energie) for accurate topographic data of the Marke clay pit, used to reconstruct one of the faults there in detail;

Dr. S. VANDYCKE, who shared her enthusiasm with me to do field work on faults "dans le mou" in Flanders, and expertly did the numerical stress inversion;

Prof. D. LEYTHAEUSER (now at Universität Köln), Dr. R. SCHAEFER, Dr. R. DI PRIMIO and Dr. R. LITKE (all at Forschungszentrum KFA-Jülich, Germany) for their precise organogeochemical analyses, the permission to use their Rolls Royce optical microscope, and their expertise in the interpretation of such data;

Dr. U. BAYER (KFA, Jülich), Dr. A. HEATH (Fault Analysis Group, Liverpool) and Dr. MARTIN HELLER (ETH, Zürich) for some very stimulating discussions;

Prof. R. PFLUG (Geologisches Institut, Freiburg), Danny PHILLIPS (Stratamodel, Houston), Prof. D. LEYTHAEUSER (Universität Köln) and Dr. J. WATTERSON (Fault Analysis Group, Liverpool) for their whole-hearted interest and for giving me opportunities to present Geofox and other parts of my research;

all Geofox users (8 at present), who had to endure quite a few system crashes before the program was made sufficiently fool proof, for suggesting or inspiring enhancements;

Mrs. M. BOGAERT for the marvellous pen drawings and my brother JO for last minute help with the umpteen figures;

and my parents for instilling a sense of beauty and accuracy, concurrent analysis and integration, and 3D mental visualization.

Last but far from least I wish to thank Dr. J.P. HENRIET, my co-promotor and currently director at IFREMER, Département Géosciences Marines, Brest, France. With never-ending energy, he set up a dynamic team (the RENARD CENTRE OF MARINE GEOLOGY, Universiteit Gent) with good equipment and an even better spirit and thus exposed me to up-to-date geologic tools and concepts. I am also obliged to him for saddling me with a complex problem, a mixture of many diverse challenges and startling geology in our own back garden, and for his confidence in my approach and hard-to-bridle creativity, however odd, futile or "not serious" it may have seemed to some at one time, and his trust in my curiosity and other talents, into whatever discipline they have taken me.

I very much liked doing this and hope that some of this enthusiasm lives on through this thesis and compensates for the support of all these people.

Samenvatting

1. Inleiding

In deze thesis introduceren we eerst de eigenaardige intraformationele vervorming van de klei van Ieper/London langs de zuidelijke rand van de Noordzee, en de werkhypothese, in 1988 door Henriët *et al.* voorgesteld, om deze vervormingen te verklaren. Om deze werkhypothese te testen, was het nodig om verder te gaan dan de 2D seismische methode waarmee tot nog toe de meest relevante waarnemingen waren gedaan (§2). Met een nieuwe computergesteunde oppervlaktemodelleringsmethode (§3) werd de overvloed aan seismische gegevens tot een samenhangend geheel verwerkt (§4). Verder werden gedetailleerde veldopnamen (§5) en laboratoriumanalyses (§6) verricht met als doel specifieke vragen die uit de eerste hypothese werden afgeleid te beantwoorden. Met de nieuwe gegevens en inzichten wordt de werkhypothese opnieuw geëvalueerd en afgesloten met enkele besluiten (§7).

Vanuit struktuurgeologisch oogpunt lijkt het studiegebied weinig interessant (fig. 1.1). Het gebied valt grotendeels samen met het ontsluitingsgebied van de klei van Ieper/London (de Formatie van Kortrijk (Maréchal, 1992; fig. 1.2)), die hier tijdens de hoge zeespiegelstand in het Ieperiaan (zo'n 50 miljoen jaar geleden) in de Zuidelijke Baai van de Noordzee en in het huidige zuidwest Vlaanderen is afgezet en meestal een dikte van meer dan 100 m bereikt. De Ieperiaanklei ligt tussen de fluvio-lagunaire zanden en kleien van het Thanetiaan onderaan en Ieperiaanzand erboven. Deze Paleogene afzettingen hellen ongeveer één graad naar het NNE, zijn nooit dieper dan enkele honderden meters begraven geworden en liggen bovenop het Massief van London/Brabant, dat bekend staat omwille van zijn relatieve stabiliteit gedurende de laatste 400 miljoen jaar. Dit is niet meteen een gebied om structurele komplikaties te verwachten.

En toch, zeer detailrijke seismische onderzoeken door het Renard Centre of Marine Geology hebben niet alleen toegelaten de Tertiaire afzettingen nauwkeurig in kaart te brengen (De Batist, 1989) maar brachten ook een bijzonder type van vervorming in niet verharde sedimenten, meer bepaald in de klei van Ieper aan het licht. Seismiek is een echografische techniek waarin met geluidswaarschuwingen een beeld van de ondergrond kan worden gevormd. Het sparkerprofiel

in fig. 1.8 bijvoorbeeld, werd dicht bij de Belgische kust opgenomen en toont in de klei van Ieper golvende vervormingen en breuken die de Thanetiaanzanden eronder ongemoeid hebben gelaten. Op andere profielen (fig. 1.11) verdwijnen deze breuken ook naar boven toe en verstoren slechts hier en daar de bovenliggende zanden. De oorzaak van deze verstoring ligt dus niet in regionale, tektonische spanningen, maar moet worden gezocht in de afzettings- en begravingsgeschiedenis van de klei zelf. Het profiel in fig. 1.9 toont kleine normale breuken dicht naast elkaar. De spronghoogte bedraagt hier tussen de 1 en 10 m. Deze regionale vervorming van onverharde klei is zo spectaculair dat we sinds haar ontdekking van 'kleitektoniek' spreken, om ze te onderscheiden van de decimeter grote barsten waarlangs deze klei in onsluiting (in kleigroeven e.d.) uit elkaar valt. Verscheidene auteurs (vanaf Moorkens & Brabb, 1968) hebben in kleigroeves ook breuken waargenomen die goed met die op de seismische profielen kunnen worden vergeleken.

Een genetisch model werd voorgesteld om deze en andere waarnemingen te verklaren (Henriet *et al.*, 1988; fig. 1.17). Tijdens haar afzetting drukte de klei zich waarschijnlijk normaal onder zijn eigen gewicht samen, waardoor de dichtere klei onderaan wateruitpersing naar beneden toe uitsloot. Toen de afzetting van klei werd afgelost door die van zand, kon uit de top van de dikke kleiige laag waarschijnlijk sneller poriënwater uitgeperst worden dan uit het middelste gedeelte. Dit kon dan leiden tot onderkompaktie en een tijdelijke dichtheidsinversie in het middelste gedeelte. Het water tussen de kleideeltjes ging meer en meer van het bovenliggende sedimentgewicht dragen en de klei kan op deze geringe diepten van enkele honderden meter de vloeigrens bereikt hebben. Zo ontstond een Rayleigh-Taylor instabiliteit van zwaarder viskeus materiaal bovenop lichter viskeus materiaal. Het grensvlak begon, net als bij water op olie, spontaan te golven (Ramberg, 1972). Opstulpingen kunnen in het normaal gekompakteerde dak van de ondergekompakteerde laag gegroeid zijn tot het begaf langs breuken. Het overvloedige poriënwater kan dan omhooggespoten zijn langs de spleten en breuken, waarbij zetting optrad van het centrale gedeelte en ineenstorting van het dak.

Deze werkhypothese was controversieel omdat ze in de ondiepe onderkompaktie-situatie viskeus gedrag impliceerde in klei, terwijl klei zich normaal alleen plastisch gedraagt. Breuken in plastische klei zijn niet zo speciaal. Maltman (1987) heeft experimenteel aangetoond dat plastische kleien, zelfs met een zeer groot watergehalte, door mikroskopische breukjes vervormd worden. Als de vervormingssnelheid voldoende groot is, kunnen deze breukjes met elkaar verbonden

worden en als een makroskopische breuk zichtbaar worden, net zoals de 'kleitektonische' breuken.

Om de werkhypothese te testen, moesten we nagaan of er enig ruimtelijk verband bestond tussen de breuken en de golvende vervorming, of de verantwoordelijke spanning alleen gebonden was aan de zwaartekracht, en of langs de breuken aanwijzingen voor opwaartse beweging van vloeistoffen en voor een snelle ineenstorting konden worden gevonden. Enkele waarnemingen konden ook verklaard worden door intraformationele afglijdingen (Allan, 1982; Crans *et al.*, 1980), maar een afglijding naar het afzettingscentrum toe hield in dat een overwegende WNW-ESE strekking zouden moeten voorkomen.

2. 3D en pseudo-3D seismische acquisitie en interpretatie

Met tweedimensionele (2D) seismiek kunnen plaats en schijnbare helling van breuken en plooien aan het licht worden gebracht, maar niet hun strekking, of hoe ze verlopen van profiel tot profiel. Duurdere driedimensionele (3D) seismiek lost dat probleem wel helemaal op (Brown, 1986; Dalley *et al.*, 1989), maar een rechthoekig netwerk van 2D profielen kan ook al de drie-dimensionele samenhang bepalen van lineaire structuren die minstens twee maaswijdten lang zijn (fig. 2.5). Zulke breuken kunnen gekorreleerd worden tussen de breuksneden op de profielen. Met een goede keuze van de maaswijdte kan dus een 'pseudo-3D' bedekking worden verkregen. Hoe dan ook, een breuk die korter is dan tweemaal de maaswijdte kan ten gevolge van een ruimtelijke onbepaaldheid ('aliasing') geïnterpreteerd worden als deel van een langer breukspoor. Fig. 2.12 toont het eerste deel van een pseudo-3D netwerk met een lijnspaciëring van 50 m over een kleitektonisch gebroken gebied in de Noord Hinder zone, tezamen met het geïnterpreteerde breukenpatroon. Over dit laatste bestonden twijfels, omdat dit netwerk unidirektioneel was en leemten bevatte nadat de opnames werden onderbroken wegens slecht weer. Breuken die min of meer evenwijdig verlopen met de overwegende profielrichting konden moeilijk gekorreleerd of zelfs gemist worden.

Een andere toepassing van pseudo-3D seismiek werd uitgevoerd op de Schelde bij Antwerpen. Omdat de situatie er zich toe leende, werden daar ook echte 3D opnames gemaakt met zeer hoge resolutie. In 1982 nam het RCMG er een netwerk van 'Uniboom'-profielen op, op de plaats van een geplande metrotunnel. Sommige profielen toonden een kleine kleidiapier in Rupeliaan klei. Het analoge éénkanaalsprofiel in fig. 1.19 toont een diapier met een schijnbare diameter van ongeveer 60 m. De reflektoren buigen omhoog met een verticale amplitude van

enkele decimeters op een diepte van 50 m, toenemend tot enkele meters op een diepte van ongeveer 25 m. Hogere seismische horizonten zijn doorbroken. Bijkomende kruisende profielen bedekten de diapier voldoende dicht om de vervorming gedetailleerd in kaart (fig. 4.9) te brengen met Geofox, het oppervlakte-modelleringsprogramma dat verderop nog uitvoerig aan bod komt. Een inzakking tot 0,5 m diep omringt de opwelling op de middelste horizont. De diepste horizont op een diepte van 40 m onder de rivierbedding is nauwelijks vervormd. De superpositie van diapier en Scheldegeul is opmerkelijk. Het kan betekenen dat de oorsprong van de diapier ligt in differentiële dekompactie onder de geul, misschien in combinatie met expanderend gas (Hovland & Judd, 1988).

In 1990 werd tijdens een tweede meetcampagne een echt 3D opnameprogramma uitgevoerd, gedimensioneerd naar het pseudo-3D model (Henriet *et al.*, 1992). Het 'SEISCAT' opnamesysteem (fig. 2.9) bestond uit een stel van 12 speciaal gebouwde microstreamers, parallel gesleept. De streamers en de seismische bron (een 'Uniboom' of een kleine 'watergun') werden achter een verbrede Hobiecat catamaran gesleept. De afstand tussen de streamers bedroeg 1 m en dat was ook de afstand tussen de twee hydrofoongroepen in elk van de streamers. Elk schot leverde dus 24 seismische sporen op, in een 5.5 m brede band langs de raaien. Het succes van 3D seismiek op water hangt af van een betrouwbare dynamische positionering. Omdat voor dit 3D onderzoek een sorteerrooster met mazen van slechts $1 \times 1 \text{ m}^2$ werd vooropgesteld, moest een dynamische precisie van enkele decimeters worden bereikt. In dit geval werd hiervoor gebruik gemaakt van een zelf-volgende laser-afstandsmetende theodoliet, opgesteld op de oever. Onophoudelijk volgde die een kroon van prisma's op de mast van SEISCAT. Plaats-koördinaten nauwkeurig tot op enkele cm werden naar het opnameschip overgeseind en meteen in de seismische bestanden op magneetband geschreven. De horizontale koördinaten van bron en ontvangers waren daardoor gekend tot op enkel dm, en tijdsverschuivingen te wijten aan het getij konden worden weggerekend. Fig. 4.10 toont de bedekkingsgraad over de meetsector. Met Geofox werd voor elk schotpunt 24 Common Mid Points gegenereerd en gesorteerd in een regelmatig rooster met mazen van $1 \times 1 \text{ m}^2$. Een SW-NE geöriënteerde sektor waarbinnen de seismische gegevens werden gesorteerd en opgeteld, werd gemiddeld meer dan 10 maal bedekt. De resulterende horizontale tijdsekties in fig. 4.11 werden onder de meest vervormde horizonten genomen. Ze volgen elkaar op om de 0.25 ms. Rode en gele kleuren staan voor positieve uitwijkingen, groen en blauw voor negatieve. Dankzij de samenhang van de gegevens tussen deze mazen van $1 \times 1 \text{ m}^2$ kan de diapier gemakkelijk worden afgelijnd.

Met de SEISCAT methode hebben we aangetoond dat het mogelijk is de ganse seismische 3D methode om te schalen naar de wereld van heel kleine vervormingen en geo-technisch onderzoek. Anderzijds blijft de pseudo-3D methode met hoge resolutie een goedkoper en dikwijls voldoende alternatief voor andere, b.v. academische doeleinden.

3. Een nieuwe 3D oppervlaktemodelleringsmethode

De meeste seismische onderzoeken aan het RCMG zijn van nature 2D of pseudo-3D. Hard- en software middelen ontbraken om het dichte stelsel van klei-tektonische breuken te karteren, met verantwoorde hoogtelijnen op zowel de zeer zacht golvende reflektoren als op de breuktrappen. Daarom werd 'Geofox' ontwikkeld, op een klein werkstation type SUN 386, zonder enige beschikbare 3D grafische bibliotheek of hardware.

Geofox is een geologisch/geografisch geöriënteerd computerprogramma dat toelaat natuurlijke en synthetische oppervlakken te modelleren en te visualizeren op alle SUN-werkstations (naast de PC het belangrijkste type computer in de geologische exploratiewereld). Die modellering gebeurt interactief, d.w.z. men ziet meteen wat men doet (Foley *et al.*, 1990).

De gegevens bestaan meestal uit gedigitaliseerde interpretaties van seismische reflektiehorizonten en bestaande contourkaarten. Modellering van zulke lijngegevens omvat de kwantitatieve bepaling van het gehele oppervlak, waarvan deze lijngegevens enkel de doorsneden zijn. Een natuurlijk geologisch/geografisch oppervlak is meestal grotendeels glad op enkele scherpe hoeken en schuine kanten na. De meeste programma's uit de industriële sfeer ondersteunen de manuele karteertechnieken en verplichten daarom tot een voorafgaandelijke interpretatie en scheiding van het oppervlak in de samenstellende gladde gedeelten enerzijds en de scherpe kanten (breuken, kliffen,...) anderzijds. Hierdoor wordt geen enkel van de vele fouten die bij een volledig manuele kartering van natuurlijke oppervlakte-diskontinuiteiten kunnen optreden, vermeden (fig. 3.1). Geofox daarentegen ondersteunt op een interactieve en kwantitatieve wijze het lastige interpretatieproces van schuine tot zeer steile oppervlakediskontinuiteiten zoals normale breukenstelsels, kraterranden en kliffen, zandgolven en bergkammen, op basis van een stel doorsneden. Op een voor de gebruiker zeer eenvoudige manier kan één continu oppervlak worden gekonstrueerd dat stuks-gewijs glad is, *tezamen* met tal van eventueel zich vertakkende en kruisende scherpe randen.

Daartoe werd een totaal nieuwe 3D oppervlaktemodelleringsmethode uitgewerkt bestaande uit drie elk op zich nieuwe technieken, die werden gekombineerd met gesofistikeerde 3D visualisatiemogelijkheden (Verschuren, 1992). Deze laatste steunen niet op dure 3D hardware of 3D grafische subroutine-bibliotheken, maar werden in het programma zelf geïmplementeerd, waardoor het programma zonder grote vertaal-inspanningen ook op andere computers zou kunnen worden overgebracht, PC's inclusief.

De gegevensdichtheid langs de ingevoerde lijnen en de hoeveelheid lijnen is meestal zodanig groot, dat interactieve modellering enkel mogelijk wordt indien men enkel die gegevens gebruikt die op de schaal van het model relevant zijn. Een eerste kerntechniek van Geofox laat toe deze meest interessante punten snel, objectief en automatisch maar gekontroleerd, te selecteren (fig. 3.17). Hierdoor stijgt niet alleen de modelleringsproduktiviteit met een faktor vijf tot tien, maar ook de opslag- en reken efficiëntie.

Een tweede kerntechniek bestaat uit het interactief aanbrengen van veranderingen in een automatische, geometrisch optimale maar geologisch meestal niet verantwoorde triangulatie van de geselecteerde punten (fig. 3.20; 3.26a). Een triangulatie legt een ruimtelijk verband tussen de punten, en daarmee ook tussen de structuren die ze beschrijven langs de gedigitaliseerde lijnen. Door een verandering van de verbanden of korrelaties tussen deze structuren (fig. 3.26b-d), en door toevoeging van een zeer beperkt aantal steunpunten (fig. 3.27-28), kan een bepaalde geologische interpretatie in het triangulair model worden ingevoerd. Dit interpretatieproces gebeurt interactief, waarbij door lineaire interpolatie vlakke driehoeken tussen de punten worden weergegeven met contourkleuren en -lijnen, en een schaduwberekening aan het model bijkomend reliëf toevoegt. De kleinste onnauwkeurigheden komen hierdoor meteen letterlijk aan het licht.

Een derde kerntechniek laat toe de hoekige triangulatie eenvoudig om te zetten in een rechthoekig en fijn rooster dat stuksgewijs glad is, met scherpe kanten daar waar de interpretator die in de triangulatie heeft aangeduid. Hiervoor werd een nieuw gridding algoritme ontwikkeld dat een oppervlak 'met variable spanning' interpoleert tussen de gegevens. Het grootste deel van het oppervlak gaat daardoor met een minimale spanning en dus glad door de punten (en niet eronder of erboven zoals dat met andere interpolatietechnieken gebeurt), terwijl het gedeelte in de buurt van de scherpe randen geleidelijk wordt strak getrokken aan die randen (fig. 3.41, 3.43d). Het idee achter deze benadering is totaal nieuw. De implementatie ervan in Geofox heeft zijn doeltreffendheid reeds uitvoerig

bewezen in zowel zeer ingewikkelde als eenvoudige modellen. Een stapel van dergelijke roosters kan in een realistische 3D projectie met schaduwberekening worden bekeken, waardoor niet alleen de kleinste details en overblijvende fouten in het geheel van één oppervlak aan het licht komen, maar ook de ruimtelijke verbanden tussen verschillende lagen onderling.

Een 'model' staat bij dit alles dan niet voor een mooi-ogend hersenspinsel, maar voor een konkrete, kwantitatieve, drie-dimensionele weergave van de werkelijkheid, gesteund op niets anders dan gegevens en een koherente interpretatie ervan. Dat de Geofox-modellen daarenboven ook nog door iedereen als mooi worden bestempeld doet niets af van hun intrinsieke kwaliteiten. Het spreekt vanzelf dat de modellen niet beter kunnen zijn dan de gegevens en de kennis die de interpretator heeft van de plaatselijk geologie en van de mogelijkheden van het modelleerprogramma.

Om de modellen tenslotte ook zwart op wit op papier te krijgen, werd een nieuwe plot-techniek ontwikkeld voor perspectief tekeningen op hoge-resolutie zwart/wit printers, waardoor zowel subtiele schaduw nuances als interval'kleuren' kunnen worden weergegeven (bijv. fig. 3.54-3.59).

De bronkode van Geofox bestaat 20000 lijnen (09/'91; dit is 400 blz. voor een dertigtal bestanden) in de programmeertaal 'C', en maakt gebruik van de 'SunView' graphical user interface (vergelijkbaar met MS Windows op PC of die van een Macintosh).

4. Strukturele modellen

Met fig. 4.4-4.7 knopen we opnieuw aan bij kleitektoniek. Dit oppervlaktemodel van een reflektor in fig. 2.14 bedekt een sektor met kruiselingse bedekking (fig. 2.13). De zachte golvingen in fig. 2.14 blijken langwerpige opwellingen en inzakkingen te zijn, waarbij de breuken graben-achtig geordend zijn op de toppen en horst-achtig in de inzakkingen. De roosterlijnen geprojecteerd om de 500 m en het kleurenhoogte-interval van 1 m geven een idee van de schaal. Dit model ondersteunt de hypothese van een gravitationele instorting van de welvingen. De ruimtelijke samenhang en haar interpretatie leidden tot een rekonstruktie van de golvingen op één van de seismische profielen (fig. 4.8). Het patroon van relatieve verplaatsingen van de blokken langs dit profiel bevestigde inderdaad dat blokken op de toppen van de antiklinalen het meest inzakten.

De N strekking van de breuken in fig. 4.5 valt samen met die van een dichtbijge tektonische normale breuk in de sokkel (fig. 4.2) en suggereert een tektonische invloed (maar niet een tektonische oorsprong) van E-W gerichte rek in de sokkel, mogelijks tijdens het vroege Oligoceen (Bergerat, 1987). Intraformationele afglijding of groeibreuken kunnen worden uitgesloten als interpretatie.

5. Veldwaarnemingen

De seismische waarnemingen werden ondersteund met heel wat nieuw veldwerk. Een enkele keer ziet de Koekelberg kleiput in Marke (bij Kortrijk) er uit zoals in fig. 1.13. Deze wand is ongeveer 20 m hoog vertikaal en helt 30°. Deze gekromde breuken met een spronghoogte tot enkele m zijn geheel vergelijkbaar met degene die op de seismische profielen te zien zijn. Meestal zijn de breuken heel moeilijk of zelfs helemaal niet zichtbaar, tenzij de gladde wand zorgvuldig wordt proper gemaakt met een vlijmscherpe spade (fig. 4.18 & 4.22).

Geplooid breuken zoals die in fig. 4.31-33 wijzen op een eerst hoge vervormingssnelheid, met sterk waterverzadigde kleien die zich op een broze manier gedragen (Maltman, 1987). Nadien vertraagde de vervormingssnelheid, met een plastische vervorming tijdens de verdere kompaktie. Terminale breukvertakkingen in een lemige laag (fig. 4.30) bevestigen dat kleitektonische breuken doorheen de kleiige formatie kunnen optreden. Deze tekening toont ook een tweede generatie van kleinere breuken die door de breukvertakkingen van de eerste heen snijden. In de kleigroeve te Marke werden systematisch ware helling, strekking en striatiërichting gemeten van alle echte breuken (met slickensides, fig. 4.39-42). Fig. 4.53 tot 4.55 geven deze gegevens grafisch weer. Breuken van de oudste generatie hebben min of meer willekeurige strekkingen en normale verschuivingsrichtingen, terwijl de transversale breuken van de tweede generatie in gekonjugeerde richtingen oplijnen. Een numerieke spanningsinversie (Angelier, 1989, 1990) bracht aan het licht dat het oudste spanningsveld bijna zuiver verticale samendrukking was. Een zwakke indicatie voor E-W rekspanning werd als onbetrouwbaar beschouwd, maar komt toevallig wel goed overeen met die in de Noord Hinder zone en een fase van rek die een groot deel van het Europese kontinent tijdens het Rupeliaan beïnvloedde (Bergerat, 1987). De tweede generatie van breuken kan in verband worden gebracht met een fase van Mioceen Alpijnse SW-NE samendrukking.

In een zone waar twee breuken elkaar snijden (fig. 4.26-27) waren nog enkele bijzonderheden te zien. De spronghoogte langs één van de grote breuken vermindert

snel naar beneden toe, te wijten aan een horizontale breuk die zich in een listrische vertakking van de grote breuk afsplitst. In de zone van de kruising zelf zijn tamelijk veel breuken afgelijnd met zwart breukleem, gestrieerd door de relatieve verschuivingen langs het breukvlak (fig. 4.45-46). Het minste wat op basis van deze structurele veldwaarnemingen kan worden gezegd is dat de kleitektonische breuken een ijl maar kompleks netwerk van breuken en aders vormen en verscheidene grootte-orden overspannen. In de zone van de snijdende breuken resulteerde de frakturatie ook in cm dikke klastische aders, gevuld met het zwarte breukleem. Uit de manier waarop klastische aders en breuken elkaar snijden en uit de latere vervorming kon worden afgeleid dat de aders tot de vroegste verstoringsfase behoren. Waarschijnlijk waren breuken met een zwarte breukleem eerst klastische aders, waarlangs glijding werd vergemakkelijkt.

Waarnemingen in Zonnebeke (bij Ieper) wijzen aan dat sommige kleitektonische breuken nog tijdens het Kwartair gereactiveerd werden (fig. 4.58-59).

Ongestoorde, geöriënteerde doosmonsters van breukleem en klastische aders werden geïmpregneerd, versneden en geslepen tot slijpplaatjes. Andere monsters werden aan allerhande analyses onderworpen.

6. Labo-analyses van breukleem

Op de site van monsternamen in de kleiput Koekelberg te Marke bleek geen verschil in samenstelling tussen het breukleem en de klei ernaast. Beide zijn siltige kleien en grotendeels samengesteld uit smektiëten (zwellende kleien) en illiet. Hun totaal gehalte aan organisch koolstof en MnO is gelijk en zeer gering, en kan de zwarte kleur van het breukleem niet verklaren. Gelijke hoeveelheden Fe sluiten ook aanrijking van mikrokristallijn pyriet uit, alhoewel enkele plaatselijke opeenhopingen van pyriet werden aangetroffen langs de klastische aders.

Bij geringe vergroting blijkt het breukleem in de klastische aders een breccie van gedeeltelijk geoxideerde kleiige aggregaten te zijn. De hoekige klast in fig. 4.68 vertoont interne parallele banden die vroege verschuiving langs een breuk suggereren, gevolgd door verkruimeling en snel transport. De gepyritiseerde sponsspicae zijn soms geöriënteerd in een vloeitekstuur. Langs de breuken zijn de klasten afgerond en de kleideeltjes evenwijdig geöriënteerd (fig. 4.69). De oorzaak van de zwarte kleur bleek uiteindelijk te liggen in de oxidatie van Fe tot Fe(O,OH) binnen de kleiige aggregaten. Bij de sterkste optische vergroting in opvallend licht ziet dat eruit als oranje vlekjes (fig. 4.74-75).

Het breukleem uit een klastische ader en de klei ernaast werd met mikrofossielen gedateerd. De dinoflagellaten in het breukleem komen van tussen de 30 en 50 m onder het stratigrafisch niveau van de klei naast de ader. Het breukleem in dit monster bevat ook gepyritiseerde diatomeeën (fig. 4.72), en die zijn alleen zo overvloedig aanwezig aan de basis van de klei van Ieper/London. Een gedeelte van dit breukleem is met andere woorden ongeveer 80 m omhoog gespoten.

7. Besluiten

We kunnen nu terug komen bij onze werkhypothese en stellen dat we uitvoerige nieuwe aanwijzingen hebben gevonden voor een gravitationele ineenstorting van golvingen te wijten aan een Rayleigh-Taylor instabiliteit, met snel vloeistof-transport langs klastische aders die zich gedeeltelijk tot normale breuken ontwikkelden. Dit bevestigt het voorgestelde vervormingsmechanisme. De vervorming werd waarschijnlijk wel tektonisch aan de gang gebracht ('ge-triggered') door een vroeg Oligocene E-W rek, dus later dan oorspronkelijk voorgesteld. Nadat de kleiige formatie normaal gekompakteerd was, werd ze ook nog verstoord door een waarschijnlijk Miocene SW-NE samendrukking.

Hieruit kan men besluiten dat dikke, kleiige afzetting op een kontinentaal plat in een tektonisch rustige omgeving geheel gebroken en gefractureerd kunnen zijn bij een geringe begraving. Langs deze breuken en barsten kan poriënwater uit ondergekompakteerde delen omhoog gespoten zijn.

Geofox implementeert een nieuwe, interactieve, hybride triangulatie-gridding oppervlaktemodelleringsmethode, en neemt heel wat vervelend werk weg uit de kartering van normaal gebroken oppervlakten, gedigitaliseerd langs seismische profielen en hoogtelijnen.

Een geïntegreerde 3D benadering over verschillende grootte-orden en geologische disciplines heen, was effectief.

1. Clay diagenetic deformation in Palaeogene clays

1.1. Introduction

"If we want to understand a history, we should not reduce it to the underlying regularities or to a chaos of random events. On the contrary, we should try to simultaneously understand relations and events." (translated from Prigogine & Stengers, 1989, p.58)

In this thesis we will try to unravel and understand the history of two layers of clay, one deposited during Ypresian times, between 54 and 50 million years ago and another during Rupelian times, between 35 and 30 million years ago. These were both periods of global sea-level highstand, during which sea-level is estimated to have been about 200 m higher than today (Haq *et al.*, 1987). The epicontinental sea flooding the NW part of the European block at those times was deeper and larger than today's North Sea, resulting in long periods of clayey sedimentation in the Belgian outcrop area.

The setting for the post-deposition history seems rather dull (fig. 1.1): the London/Brabant High onto which the Tertiary and late Cretaceous sediments were deposited is known for its stability during the last 400 million years. The only noteworthy activity since the Ypresian consisted of a subsidence to a few hundred metres and then a Quaternary inversion that tilted the Tertiary strata in the southern North Sea 1° to the NNE and exposed them to erosion. Ypresian and Rupelian clays that outcrop in Belgium, northern France, the southern North Sea and the London Basin are still unlithified and subhorizontally bedded between layers of sand and other clays.

The history of these Tertiary sediments therefore did not appear to be any more complex than a bit of compaction, slight tilting and erosion, until the mid 1970s. That was when the Renard Centre of Marine Geology, under the impulse of J.P. Henriët, started to acquire high-resolution seismic profiles in the Belgian sector of the North Sea. Primarily focused on regional geological mapping, harbour-

development projects and elaborating the seismostratigraphy of the outcropping Tertiary strata, these surveys eventually yielded a high-density grid of more than 15000 km of lines shot both in the single- and multichannel mode with a variety of seismic sources over a relatively thin but complete Palaeogene sequence, closely tying the classical Belgian Tertiary basin to its type localities (Ieper (Ypres), the Rupel, etc. (fig. 1.2)).

These profiles also revealed a most peculiar pattern of deformations, confined to the Palaeogene clays. Within the entire outcrop zone of the Ypresian clay, largely consisting of lithologically undifferentiated clays, the parallel bedding proved to be deformed by *intraformational* block faulting (figs. 1.6-1.11) that does not affect the Palaeocene basement and fades out in the overlying Ypresian sands. Small-scale deformation of unlithified sediments, also known as soft-sediment deformation, has been observed widely (§1.2), but argillaceous unlithified sediments were not "supposed to be" faulted on this scale at such shallow levels of burial and in such a tectonically quiet setting (§1.3). The faults throw up to 10 m and are spaced a few m to several hundreds of m apart. Detecting such faults in the relatively homogeneous clay mass is not straightforward and requires ideal sea state conditions and adequate seismic source selection and tuning (Henriet *et al.*, 1982). The best images have hitherto been obtained with multi-electrode sparkers, fired at relatively low energy levels. Systematic analyses by Heldens (1983) and De Batist (1989) revealed that the pattern of tilting and undulation of reflectors within the blocks varies widely both laterally and throughout the clayey sequence.

The marine observations triggered a search for such features on land, which soon proved that well-developed faults with comparable dimensions and spacing could also be observed in several clay quarries. Such faults on clay walls often elude observation due to the relatively uniform nature of the clays, but some had already been noted in detailed stratigraphic studies (§1.4.2) where their significance however had either been overlooked or had been attributed to very local basement-induced deformation or Quaternary effects. They therefore did not attract lasting interest, until Van Vaerenbergh (1987) systematically inventoried these and new observations. It can now safely be stated that intraformational faults are widespread both in the marine and land outcrop zone of the London/Ieper clay, a tectonically barely affected area, and that their origin should therefore be sought in the burial and compaction history of the clays. In other words, they are thought to be diagenetic features, involving little or no regional tectonic stresses. However, the deformation is so impressive that it has been termed *clay tectonics*

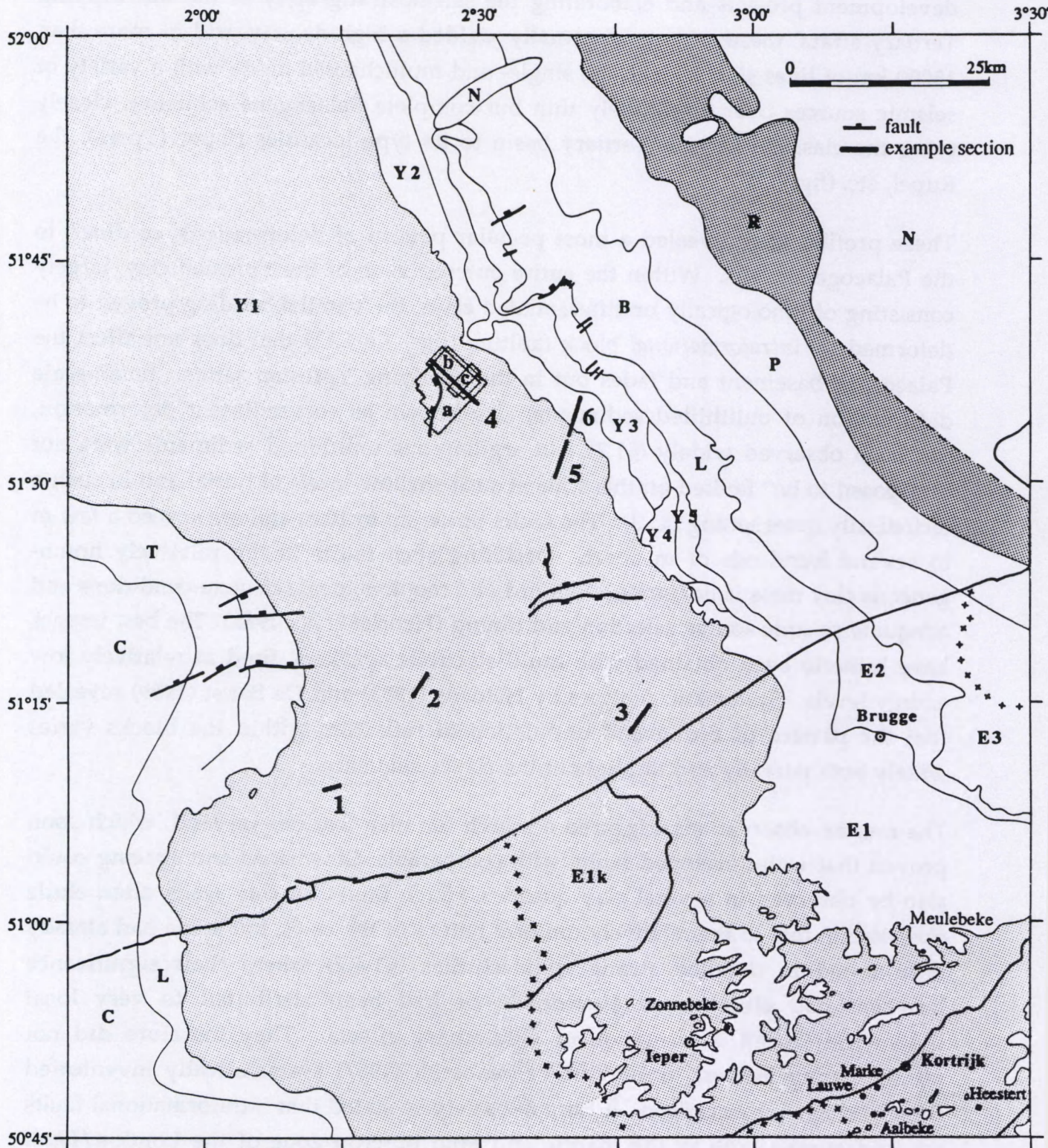
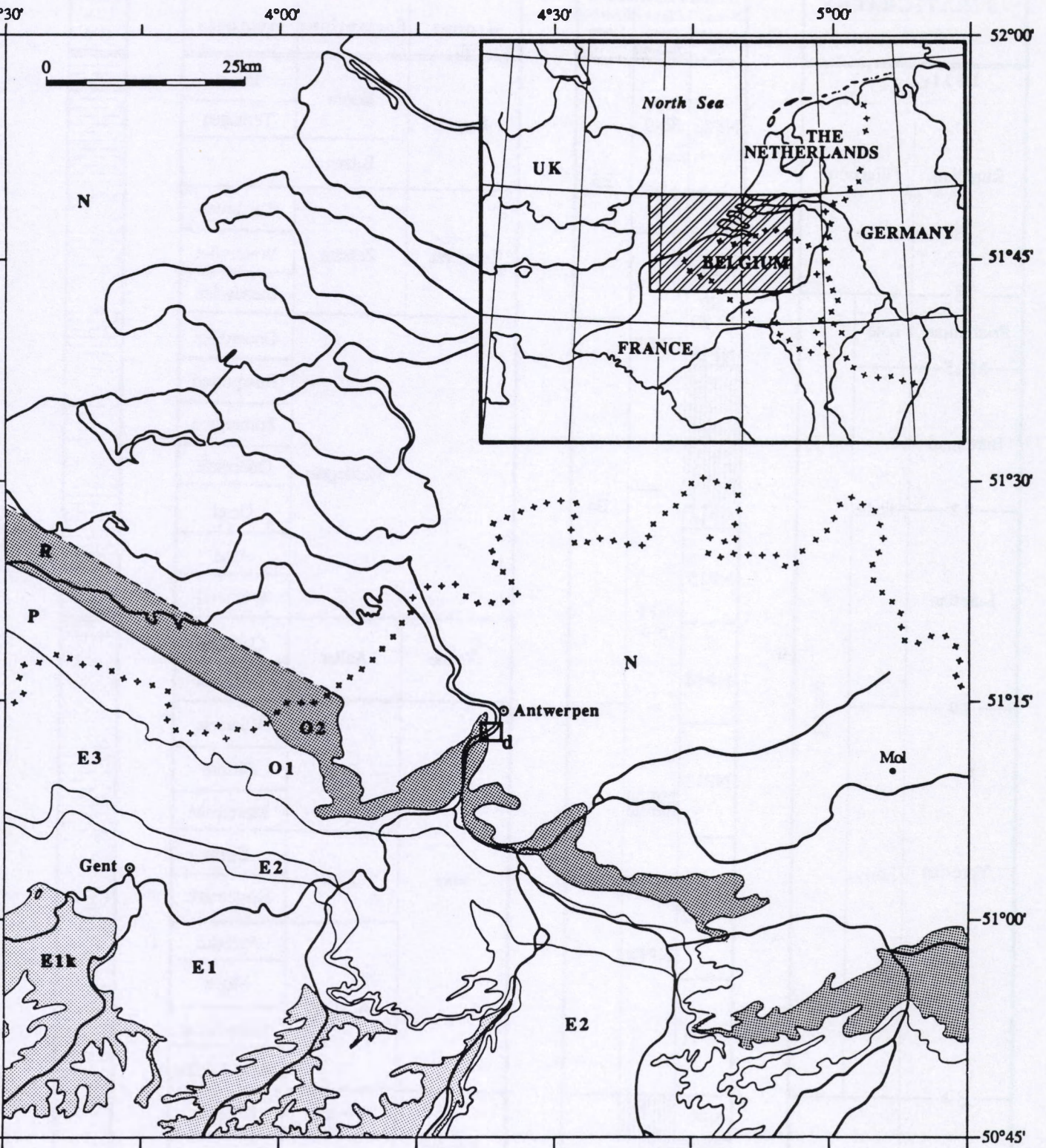


Fig. 1.1. Geological map of study area, with emphasis on outcrop area of Ypresian and Rupelian clay. Marine part and seismostratigraphic sequence notation after De Batist (1989); land part and lithostratigraphic sequence notation after Maréchal (1992). C = Cretaceous Formations; L = T = Landen Group; E1k = Y1 = Kortrijk Formation (Ieper clay, light grey); E1 = Tielt & Gent Formations; Y2=Merelbeke Member & Egem Member; Y3-Y5=Vlierzele Member; E2 = L = Zenne Group; E3 = B = Maldegem Formation; O1 = P = Zelzate Formation; O2 = R = Rupel Group (dark grey); N = Neogene



Formations. For seismic section 1, see Fig. 1.6; for section 2, see Fig. 1.7; for section 3, see Fig. 1.8; for section 4, see Fig. 1.9; for section 5, see Fig. 1.10; for section 6, see Fig. 1.11. Sectors a-d were covered with dense seismic networks, and d also with a 3D seismic survey. For sector a, see Fig. 2.11 & 4.3; for sector b, see Fig. 2.12; for sector c, see Fig. 2.13 & 4.5; for sector d, see Fig. 1.17, 4.9 & 4.11. Outcrops mentioned in text are also indicated.

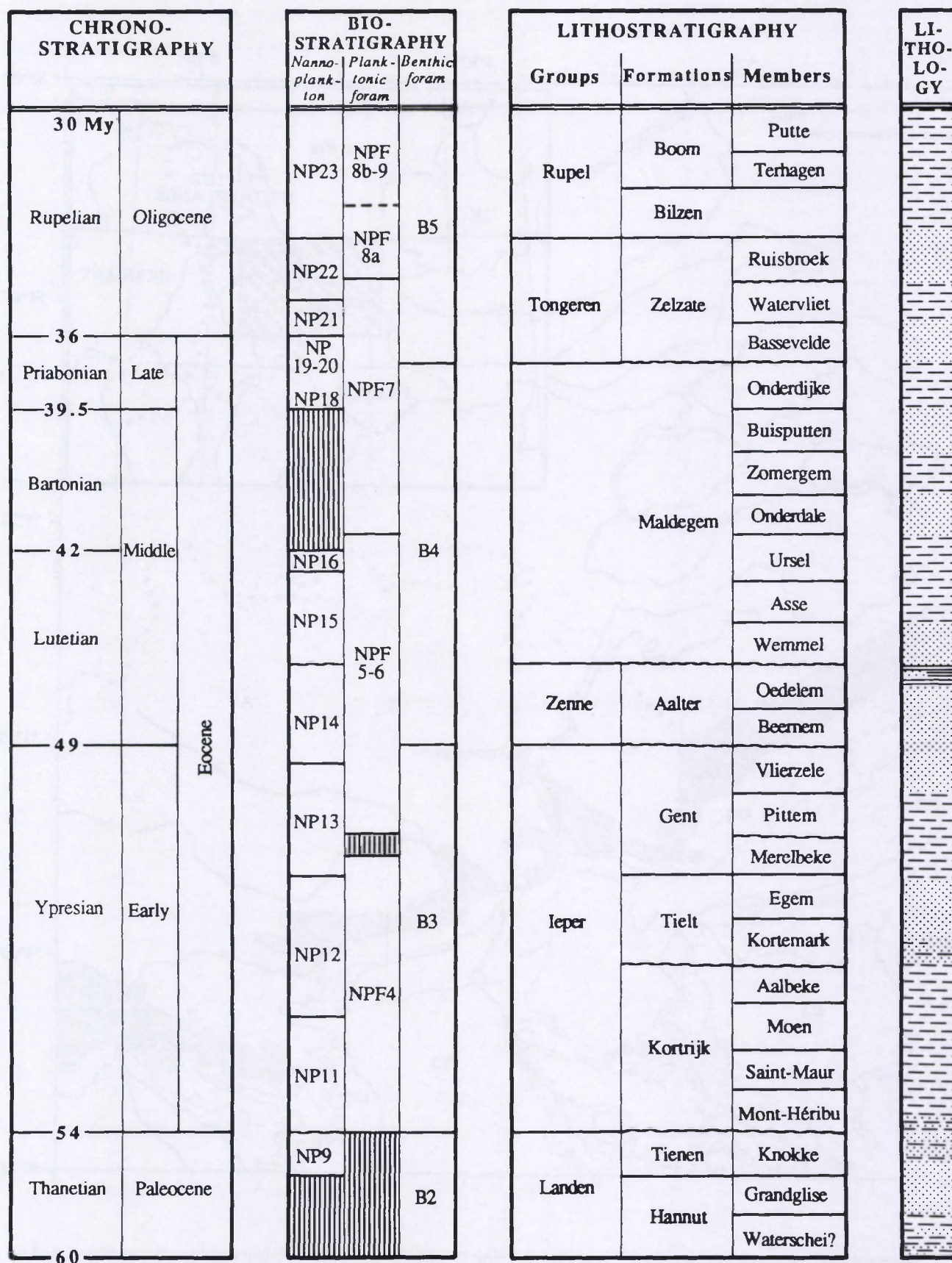
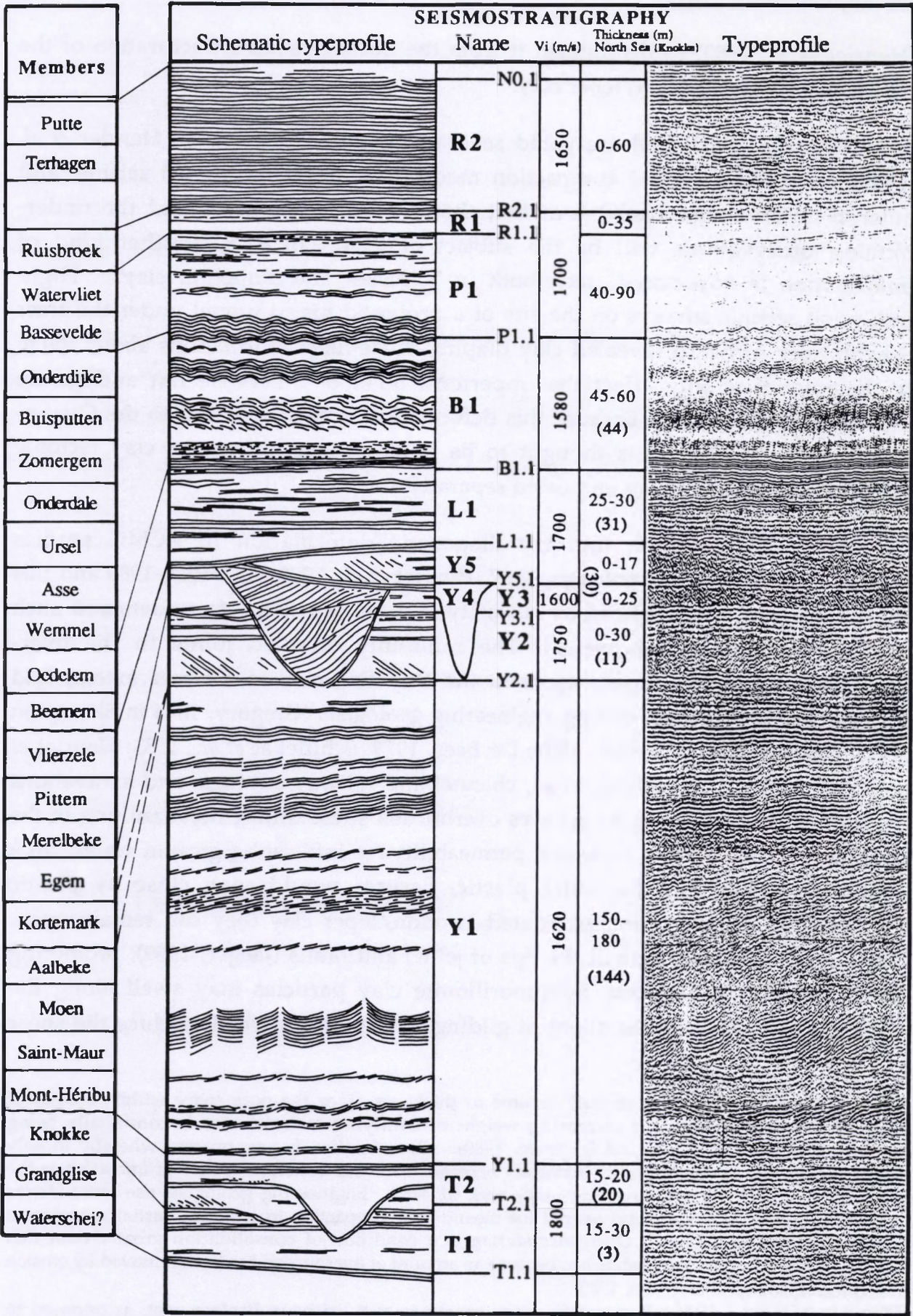


Fig. 1.2. Stratigraphical column of study area. Chronostratigraphy after Haq *et al.* (1987); biostratigraphy after Steurbaut (1988) & Vinken (1988); schematic lithology after Vinken (1988) (dots = sand; dashes = clay; lines = sandstone); lithostratigraphy after Maréchal (1992);



seismostratigraphy and schematic type section after De Batist (1989). Y1 may include the Kortemark Member, which is clayey under the North Sea (De Batist, pers. comm.).

(Henriet *et al.*, 1982) to distinguish it from the decimetre-scale fracturation of the overconsolidated¹ London/Ieper clay.

After Heldens (1983) had evaluated several possible explanations, Henriet *et al.* (1989) proposed a special compaction model to account for all 2D seismic and outcrop observations available at that time. These hypotheses and the underpinning observations will be the subject of §1.4. In §1.5, another kind of deformation is introduced, seen both in Ypresian and Rupelian clays. High-resolution seismic surveys on the site of a proposed metro tunnel under the river Scheldt near Antwerp revealed clay diapirs, dome-like deformations about 100 m in diameter that only affect the uppermost 50 m of otherwise flat and gently dipping Rupelian beds. Because this deformation is clearly bound to the Quaternary erosion surface, it is thought to be much younger than the clay tectonic features, and will therefore be treated separately.

The continued attention for clay diagenetic deformation in RCMG studies (Heldens, 1983; Van Vaerenbergh, 1987, Henriet *et al.*, 1988; De Batist, 1989 and this thesis) was not only inspired by curiosity and the aspiration to understand such odd and complex phenomena. The randomly oriented joints in the overconsolidated London/Ieper clay (and the Rupelian clay to a lesser extent) had already attracted interest among engineering geologists (Gregory, 1844 in Skempton *et al.*, 1969; Fookes & Parrish, 1969; De Beer, 1979; Schittekat *et al.*, 1983; Henriet *et al.*, 1986; §4.2.5). Tunnelling, road, channel and railway cuttings, and excavations for foundations and quarries relieve overburden stress differently, resulting in the opening of joints and an increased permeability for infiltrating ground water. In a clay that is less stiff, i.e. more plastic, fissures would soon close by plastic deformation. In the overconsolidated London/Ieper clay they can remain open. Stress tends to concentrate at the tips of joints and faults (Jaeger, 1969), promoting their growth. In addition, montmorillonite clay particles may swell along the fissures² and lubricate the slightest gliding. Both effects greatly reduce the shear

¹*Compaction* is the reduction in bulk volume or thickness of, or the pore space within, a body of sediments in response to the increasing weight of overlying material that is continually being deposited (American Geological Institute, 1980). *Consolidation* is any process whereby loosely aggregated, soft, or liquid earth materials become firm and coherent rock. *Lithification* is the consolidation of sediments to sedimentary rock (*ibidem*). Engineering geologists use *consolidation* when they mean *compaction* and restrict the meaning of *compaction* to *artificial*, partial compaction (Lambe & Whitman, 1969). *Overconsolidation* is a condition of consolidation greater than that normal for the existing overburden, e.g. because an amount of overburden has been removed by erosion (American Geological Institute, 1980).

²A *fissure* is an open joint. Both are *fractures*, breaks in rock without displacement, as opposed to *faults* (American Geological Institute, 1980). Engineering geologists use *fissures* to indicate the small joints in the London clay (e.g. Fookes & Parrish, 1969).

strength¹ of the clay mass, and slopes start to glide and slump along listric faults. Large construction works have thus been severely hampered by slumping (Skempton & La Rochelle, 1965; De Beer, 1979). Some of the larger clay diagenetic faults in the Zonnebeke quarry (Belgium) were found to have been reactivated as recently as the late Quaternary (§4.2.4), suggesting that the faults are still potential planes of failure as well (Henriet *et al.*, 1982).

Palaeogene clays are currently evaluated as potential underground storage sites for nuclear waste (for example, in the Mol underground laboratory (fig. 1.1)) or for liquefied natural gas. The evident concern in such cases is that the fractures could develop into preferential fluid migration paths under long-term thermal stresses.

Similar concern was expressed for highly toxic waste disposal in abandoned clay pits².

In petroleum geology (Henriet *et al.*, 1991), argillaceous petroleum source rocks often show evidence of fracturing, which is considered to be an important factor for the primary migration of hydrocarbons. Several authors consider overpressuring of the enclosed pore fluids at great burial depths (3000-4000 m according to Tissot & Welte, 1984) as a major factor for the generation of microfractures. Argillaceous potential source rocks³, having perhaps already undergone general fracturing *at shallow depths* may have reached the depths required for oil generation in a pre-fractured state. This would have a bearing on the timing of the onset of primary migration, perhaps starting earlier than generally thought.

Because the special compaction model proposed by Henriet *et al.* (1988) was based only on *qualitative* descriptions of the deformations along (*two-dimensional*) seismic and outcrop sections, it was also daring and in need of more, and different data. The complexity of the phenomenon called for a multi-disciplinary methodology (§1.6), bringing together new *quantitative* and *three-dimensional* seismic and outcrop observations of the clay diagenetic faults, and the microscopic analysis and grain size, clay mineralogical, (organo-)chemical and microfossil composition of any fault gouge that was hoped to be discovered along the faults. Along the way

¹*Shear strength* is the internal resistance of a body to shear stress, typically including a frictional part and a part independent of friction called cohesion (American Geological Institute, 1980)

²We will argue (§4.2.6) that the larger faults are just as unlikely to be open fractures along the flat bottom of dump sites as the microfractures (§1.4.3). Moreover, the gouge along the clay tectonic faults is clayey and likely to have equally low permeability. Therefore, if the microfractures did not pose a permeability problem until now (through artificial drainage and other safety measures), the rarer and entirely intraformational faults will not do so either.

³The London/leper clay, with a organic C content of only around 0.4% is not a potential source rock for hydrocarbons (Tissot & Welte, 1984), but many source-rock formations (>0.5%OC) *are* argillaceous.

and from scratch, a new interactive 3-D modelling program (a combination of new methods and old) for complex faulted horizons was developed on rather limited hardware, in order to interpret, model and visualize the clay diagenetic faults as they cut seismic reflectors. All of this to address the many questions that will be raised in the rest of this introductory chapter.

As this text without lengthy introductions attempts to be accessible and informative to an audience of geologists, geotechnical engineers and geological software developers, quite a few definitions will be found in the text and in footnotes. An Index keeps track of most of them.

1.2. Soft-sediment deformation

In their introduction, Jones & Preston (1987) distinguish two types of deformation of primary sedimentary structures : that which postdates lithification and that which predates it. The former is the subject of rock mechanics and 'hard-rock' structural geology, while the latter, also known as soft-sediment deformation and often dismissed by structural geologists (not a mention of it in Ramsay & Huber, 1987), has long been studied by sedimentologists (reviewed by Allan (1982)) and in soil mechanics, a field primarily developed by geotechnical engineers (Lambe & Whitman, 1969; Atkinson & Bransby, 1978). According to Maltman (1982), the essential difference between pre- and post-lithification deformation is in the *deformation mechanisms*, i.e. mechanisms the operation of which enables deformation to take place. Water-rich sediment, in contrast to sedimentary rock, deforms predominantly by grain boundary sliding. Building on the work of Allan (1982), Owen (1987) proposed the most comprehensive genetic classification so far (fig. 1.3). He tried to classify soft-sediment deformation according to *deformation mechanism* and *driving force system*, i.e. the physical system responsible for the stresses driving the deformation.

For sediments behaving as a cohesive material during deformation, the *yield strength*¹ may either be *exceeded* by applying a sufficient amount of stress, or it may be *reduced* to a level below the magnitude of stresses acting on it. A reduction in yield strength can be brought about through an increase in temperature, application of a stress over a long period of time, causing creep, an increase in the moisture content of clay-rich sediments or an increase in the pore fluid pressure,

¹*Yield strength* = *yield stress* = the differential stress at which a material begins to undergo permanent deformation (American Geological Institute, 1980)

Kinematics	Characteristics		discontinuities - faulting in muds and sands	cohesive materials - muds	cohesionless materials - sands			
					coherent lamination	disrupted lamination	shear dislocation	
	DEFORMATION MECHANISM DRIVING FORCE SYSTEM		BRITTLE FAILURE	COHESIVE FLOW	COHESIONLESS FLOW		INTER- GRANULAR SHEAR	
					LIQUEFACTION	FLUIDIZATION		
H + V	GRAVITATIONAL BODY FORCE		soft- sediment faults	CL (2b)	complex RF CL (2c)			
V	UNEQUAL CONFINING LOAD			loaded ripples (1)		sand volcanoes clastic dykes		
V	GRAVITATIONALLY UNSTABLE DENSITY GRADIENT	continuous		CL (2d)	CL (3f)			
		within a single layer			dish structure (3b)			
		2- layer		load casts (1)				
				not pierced	cryoturbation	passive deformation		
		multi- layer		pseudonodules (1)				
				pierced	clay diapirs			
H	SHEAR STRESS	tangen- tial			heavy mineral contortions			
					ball-and-pillow (1)			
V		vertical						
H + V	OTHERS	physical		CL (2a)	simple RF			
		chemical					RF (McKee)	
		biological		CL (2c)		dish structure(3a) cusps and pillars		
				desiccation cracks rain prints				
				concretions crystal growth				
				bioturbation			burrow collapse	

Fig. 1.3. Classification of soft-sediment deformation, with an emphasis on deformation in sands (from Owen, 1987). This is a simplified form of a more rigorous scheme, in which it is more difficult to situate actual types of deformation, for lack of confidence in the identification of deformation mechanisms. H = horizontal displacements; V = vertical displacements; CL = convolute laminations; RF = recumbent folds.

causing a reduction in the shear strength of the material. The result is brittle failure or ductile deformation. In the case of an increase in the pore fluid pressure, such brittle failure is known as hydrofracturing¹.

Still according to Owen's classification (1987), a second group of deformation mechanisms enables a normally solid-like substance of significant yield strength to

¹ In *hydraulic fracturing* or *hydrofracturing*, pore fluid pressure temporarily overcomes the tensile strength of the clay and pushed aside the clay walls against the action of total stress, giving rise to fissures that close to joints when pore pressure drops again (Mandl & Harkness, 1987). Before this process was recognized to occur naturally Price (1966), artificial hydrofracturing had long been used in the petroleum industry to increase the permeability of reservoir rocks (American Geological Institute, 1980).

behave temporarily in a liquid-like manner and deform as a viscous fluid, or as a plastic substance of negligible yield strength. A general term for such changes of state is *liquidization* (Allen, 1982). Liquidized sediment is capable of deforming in response to stresses which would be too weak to induce deformation of the sediment in its normal, solid-like state. Owen distinguishes four types of liquidization : thixotropy, sensitivity, liquefaction and fluidization. *Thixotropic* and *sensitive* material temporarily loses its strength when disturbed or shaken. This is due to a change in the packing of platy particles from a loose, flocculated structure to one in which they are dispersed in the pore fluid. Thixotropic material regains strength as the flocculated structure reforms. Sensitive material, such as 'quick clay', remains liquidized after shaking, until a sufficient amount of pore fluid is lost. *Liquefaction* is a loss of strength related to an increase in pore fluid pressure. In liquefaction, the weight of the overburden is transferred from particle contacts to the pore fluid. Particles become temporarily dispersed in the pore fluid, the strength of the system is virtually reduced to zero, and it behaves as a viscous fluid. Liquefaction is a time-dependent loss of strength occurring within a closed system, with no net loss nor gain of pore fluid relative to the metastable situation near the critical void ratio immediately prior to liquefaction. *Fluidization* occurs in an open system of cohesionless granular material, requiring a continuous flow of fluid through the sediment. It describes a condition of minimum fluidization velocity in which the upward component of fluid drag equals or exceeds the downward-acting particle weight. While liquefaction affects the sediment pervasively, fluidization tends to be channelled, like in clastic intrusions and mud volcanoes.

Several characteristics of deformed sediments can be used to identify deformation mechanisms, including the lithology, whether deformation is pervasive or localized, the style of deformation and how well lamination was preserved. Deformation of liquefied sediment, essentially as a viscous fluid, does not necessarily destroy lamination, on account of the small grain separations involved (Owen, 1987). This is the main reason why it is often difficult to recognize one deformation mechanism or another, or indeed, a combination of them. Because thixotropy and sensitivity depend only on a *trigger*, i.e. a geological agent causing disturbance, they are even harder to recognize in the style of deformation, and thought to be rarer than liquefaction and fluidization. Owen therefore did not include thixotropy and sensitivity in his working classification (fig. 1.3).

Several deformation mechanisms are initiated by the action of a trigger, although this is unlikely to influence the deformation further. Seismic shaking represents

perhaps the most readily available and regionally extensive trigger, but others include breaking waves, groundwater movements, rapid sediment deposition and pressure fluctuations associated with storm waves, flood surges or flow separation.

Under most circumstances, the action of a deformation mechanism alone will cause little or no deformation. A further condition is that an effective stress must act while the deformation mechanism operates (Owen, 1987). In a saturated porous material, the effective stress is defined as the total stress minus pore pressure. The stress may drive the deformation continuously, but only while the deformation mechanism operates is it effective in causing deformation. The style and orientation of a deformation structure depends on the initial sediment geometry and certain characteristics of the deformation mechanism, but it is mainly determined by the orientations of the deforming stresses. Relatively few driving force systems are likely to operate in unlithified sediments. Allan (1982) and Owen (1987) list gravitational body force, unevenly distributed confining load, a gravitationally unstable density gradient and vertical and tangential shear stresses.

A *gravitational body force* acts vertically downwards on all sloping surfaces. If it exceeds the shear strength of the sediment, it drives various types of slides (internal stratification substantially undisturbed), slumps (considerable disturbance of internal stratification, with overfolding) and sediment gravity flows (Allan, 1982). An *unevenly distributed confining load* exists where a sediment surface possesses relief or where one sediment layer of variable thickness is deposited or rests (after erosion) on another. A *gravitationally unstable density gradient* exists where relatively dense sediment rests on top of relatively less dense sediment. Upon liquidization such a system is unstable, representing a *Rayleigh-Taylor instability* (Ramberg, 1972; Turcotte & Schubert, 1982). Even an initially planar interface between the layers of contrasting density deforms into a series of anticlines and synclines, representing various types of load structure and convolute laminations. The characteristics of the deformed structure are controlled by several variables, including viscosity contrast between the layers, the number of layers involved, whether or not the denser layers become pierced, and whether both layers or just the lower become liquidized (Allan, 1982). Sources of density variation include variations in material density (e.g. quartz on pumice sands), grain size, degree of saturation and nature of the pore-filling medium (e.g. water on gas). An unstable density gradient may also be continuous within a single layer.

Shear stresses acting within or at the surface of the sediment may induce deformation as well. Tangential shear in the sedimentary environment is available from the drag of water currents, debris flow, glaciers or debris carried in a current. Displacements related to tangential shear are parallel to bedding. Examples include overturned cross-bedding and some convolute laminations. Pedersen (1987) describes thrust folding and faulting in Quaternary sediments in front of a prograding ice-sheet. Vertical shear can be associated with fluid drag during fluidization. Resulting vertical displacements may form pipe- or cusplike water-escape structures.

Tectonic stresses may induce impressive folds and faults in unlithified sediments as well as in hard rocks (Brodzikowski, 1987). Maltman (1977, 1982, 1987) has shown experimentally that water-rich argillaceous sediments do not deform by pervasive homogeneous flow, as has sometimes been conjectured in the past, but by intense slippage within very narrow, discrete zones of shear. These shear zones enable large total strains to be accomplished while leaving the bulk of the material undisturbed. Macroscopically, the zones are slickensided planes. Under the microscope the zones are seen to result from pronounced particle reorientation into sub-parallelism with the zone margins, presumably by slippage at the grain scale. In specimens with 15% water content, the shear zones lack cohesion and are analogous to shear fractures in brittle rocks. Between approximately 15-45% water content the same overall geometry persists, but the shear zones maintain cohesion. At greater water contents, up to at least 60%, the clay sediments are extremely weak and although they may appear to be undergoing pervasive (ductile) flow, microscopic examination reveals that even here arrays of short, narrow zones of concentrated displacement are being generated, taking up the bulk of macroscopic deformation. In all testing modes, the shear zones become more numerous and more closely-spaced as water content increases and strain rates or confining pressures decrease.

Whereas the American Geological Institute (1980) defines plastic deformation as permanent deformation of the shape or volume of a substance, without rupture, Mandl (1988) recognized that macroscopic plasticity may be perfectly compatible with brittle deformation on a microscale. The experiments of Maltman (1987) have shown that plastic clays deform through concentrated shear also on the macroscopic scale.

1.3. Geologic setting

The study area (fig. 1.1) is situated on the SW margin of the Meso-Cenozoic North Sea Basin, and covers the Southern Bight of the North Sea and Flanders, the northern part of Belgium. The Belgian Basin, the Belgian part of the North Sea Basin, has been studied and mapped in great stratigraphic detail since the late 1900s. Figure 1.2 resumes the geological history from the Palaeocene to the Rupelian, which was mainly determined by eustatic sea-level changes (De Batist, 1989) and by the Palaeozoic London/Brabant High underneath this area, that is known to be stable since the late Palaeozoic (Ziegler, 1982). The London/Brabant High was flooded only from the late Cretaceous onwards and deposition in the Channel Basin, a SW extension of the North Sea Basin, occurred throughout the Palaeocene, Eocene and Rupelian, apart from hiatuses that have been correlated with lowstands in global sea-level (De Batist, 1989). While the Cretaceous highstand resulted in the deposition of chalks, the early Cenozoic deposition was dominated by marine clays and coastal sands, except for a sandy continental phase during the late Thanetian.

With its thickness of 144 m in the Knokke well near the Belgian coast (Laga & Vandenberghe, 1989) and 150-180 m in the North Sea area (De Batist, 1989), the Ypresian Kortrijk Formation¹ is certainly the most dominant deposit in this area. While the formation is sufficiently heterogeneous (with silty and even some sandy intercalations) in Belgian outcrops to distinguish three members, it is an undifferentiated clayey complex in the southern North Sea area, a testimony of somewhat more basinward position and deeper shelf environment in the Channel Basin. The clayey Rupelian Boom Formation reaches a thickness of 60 m in this area (De Batist, 1989). Van Vaerenbergh (1987) measured the compactional flattening of *Turritella* in the Koekelberg clay pit (Marke, Belgium). He inferred that the original thickness of the Ieper clay was 1.45 larger than today's (a compaction ratio of 70%) and noted that this should be regarded as a minimum estimate, because the clay matrix may have undergone some compaction before the shells started to flatten. Present day porosity for both clays varies between 43-51% (De Beer, 1979; Schittekat *et al.*, 1983). The estimated original 260 m of Ieper clay was deposited in 5 My, implying a moderate average deposition rate of 5 cm/1000 y. Van Vaerenbergh's compaction ratio estimate implies an original porosity of $n + (145 - 100) / 145 = 61\text{--}66\%$, reasonable figures compatible with moderate clay deposition. Overburden for the Ieper clay in the southern North Sea outcrop area is

¹Kortrijk Formation is the new name for the Ieper Clay (Maréchal, 1992). The Ypresian or Ieper clay will be taken to include the Kortrijk Formation and the clayey-silty Kortemark Member (fig. 1.2).

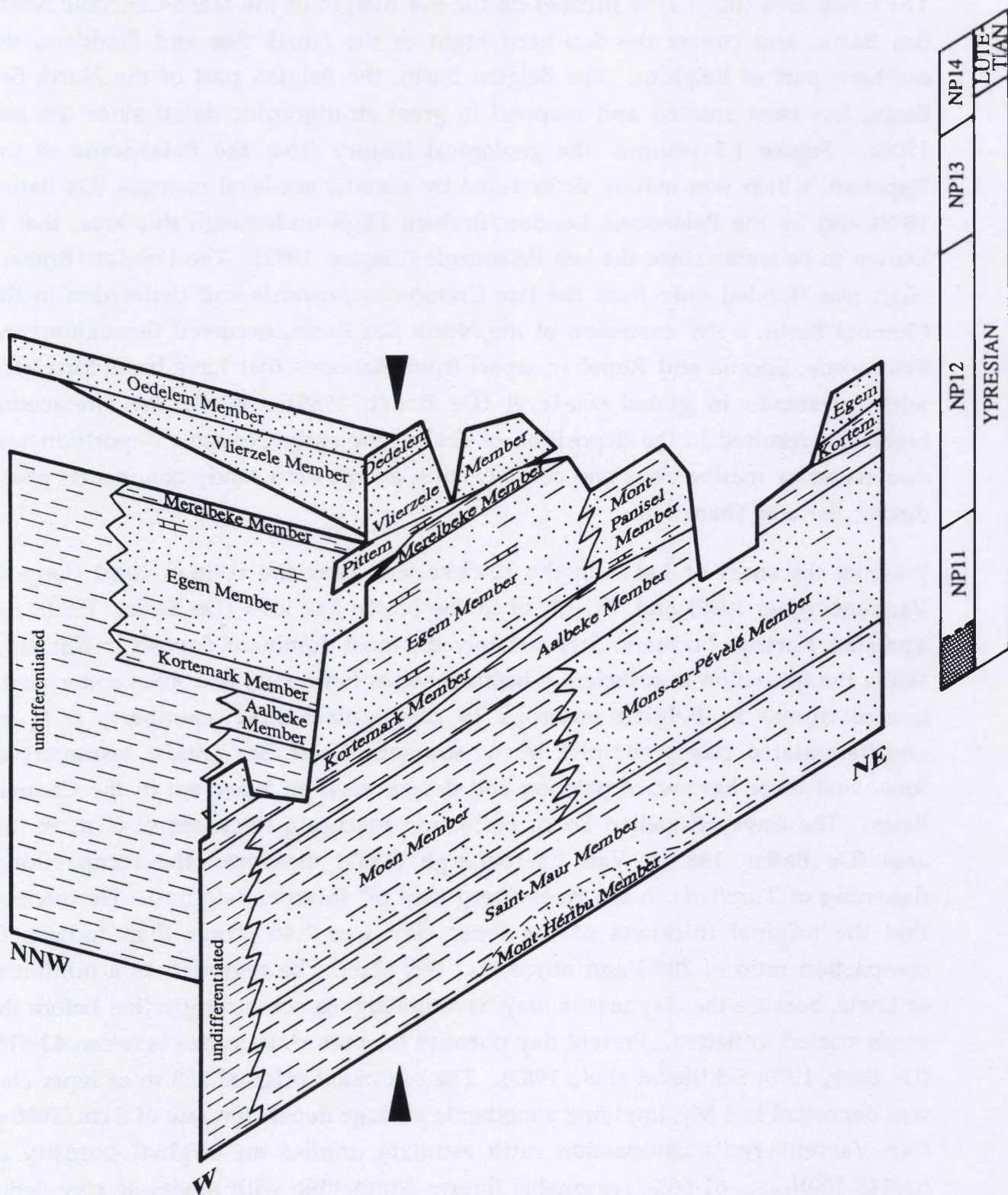


Fig. 1.4. Lithostratigraphic framework of study area (after Steurbaut & Nolf (1986), De Batist (1989) and Maréchal (1992)).

estimated to have been 100-300 m of Eocene to Rupelian deposits (or whatever remained after middle Oligocene erosion; De Batist, 1989) and an estimated extra 90 m of Neogene deposits over the Boom Clay outcrop area (Schittekat *et al.*, 1983).

The position and lateral facies changes of these clayey formations within the stratigraphic framework of the Belgian Basin are shown in fig. 1.4.

Based mainly on seismostratigraphic evidence, De Batist (1989) detected three mild tectonic deformation phases in this area, one near the Cretaceous-Palaeocene boundary (resulting in a small angular unconformity), during the late Lutetian (resulting in a large hiatus) and near the Eocene-Oligocene boundary. The main inversion of the Channel Basin took place during the late Oligocene - early Miocene (Ziegler, 1982). The Artois axis, more or less coincident with the old southern margin of the London/Brabant High, rose several hundred of metres, pronounced the erosional effect of the post-Rupelian sea-level drop and halted sedimentation in the area until the early Pliocene (De Batist, 1989). The Palaeocene to Oligocene strata now dip about 1° NE except in some local basement induced faults and folds with amplitudes of up to 140 m (fig. 1.5). The latter have been interpreted by Henriët & De Batist (1989) as drag folds caused by a sinistral strike-slip movement along a conjectured NE trending basement fault. This interpretation would fit the N-S compression that affected most of the West European plate during the late Eocene Africa-Eurasia collision (Bergerat, 1987). The same author also found widespread evidence of the Oligocene E-W extension that created the West European rift, but its influence seems to be restricted to the rift zone, the rest of the West European plate being subjected to continued N-S compression during the Oligocene. However, a N-S oriented, concave normal fault in the North Hinder deformation zone (De Batist, 1989) may be a basement fault reactivated by E-W extension. On land in Belgium, no tectonic deformation of the Cenozoic cover has been reported.

1.4. Clay tectonics

1.4.1. Seismic evidence for Ieper/London Clay deformation styles

A few examples of clay tectonic deformations on multi-electrode sparker profiles are shown on figs 1.6-1.11. These sections, which are located in the general outcrop or subcrop area of the London or Ieper Clay in the Southern North Sea (fig. 1.1),

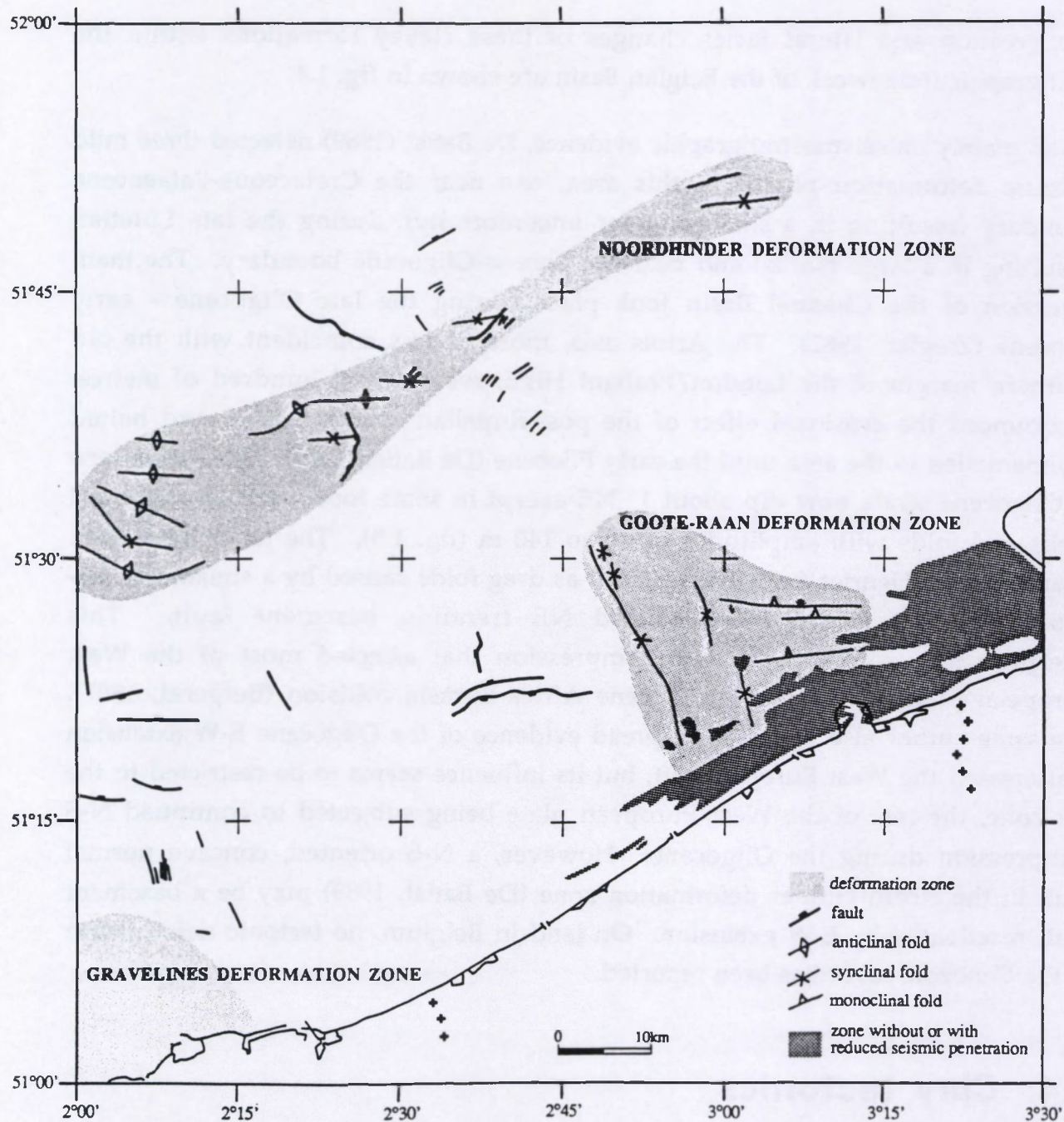


Fig. 1.5. Map of tectonic structures in Cenozoic deposits (after De Batist, 1989).

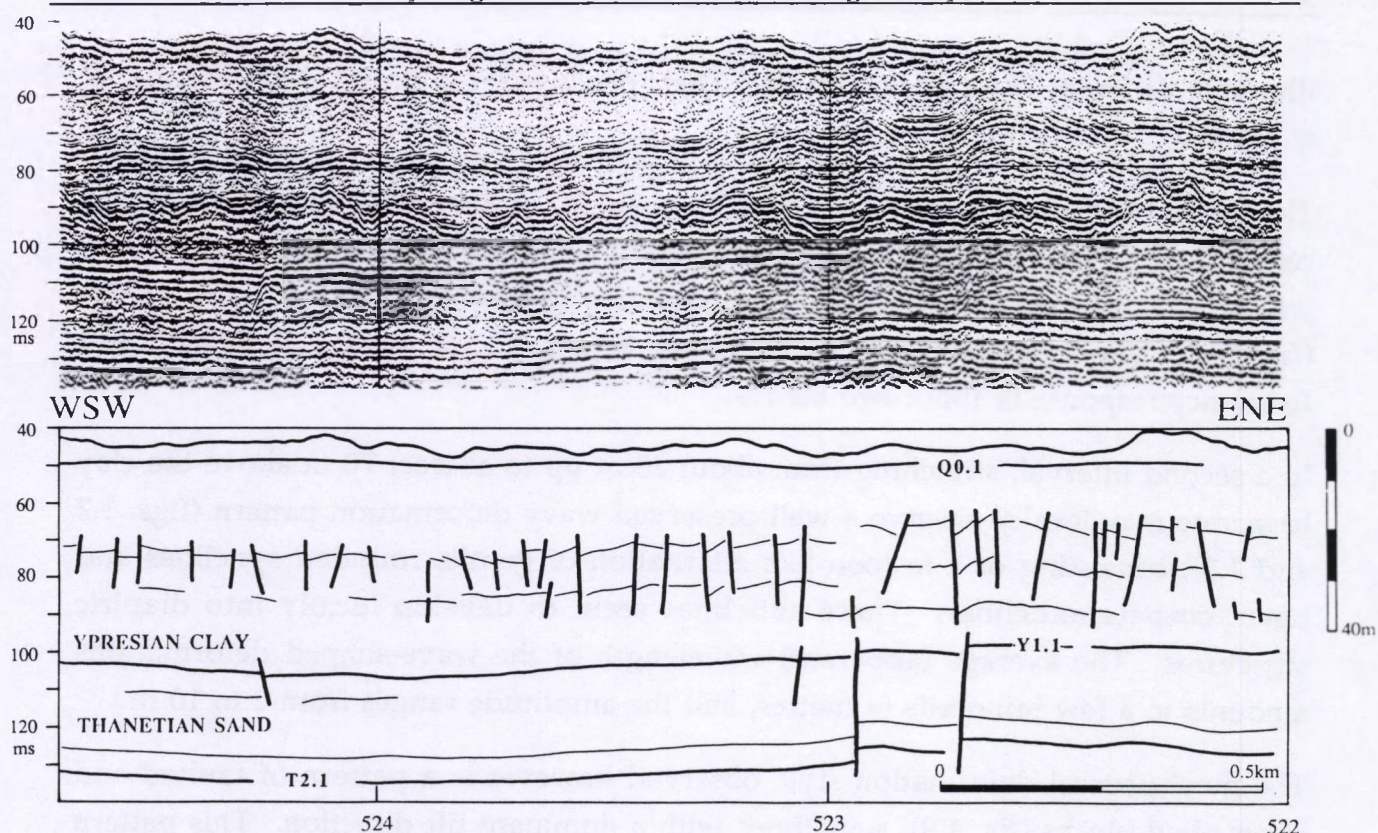


Fig. 1.6. Faulted and tilted blocks in the basal interval of the Ieper Clay (fig. 1.1, section 1, multi-electrode sparker, 300 J). The wavy reflector at about 90 ms is the first sea-bed multiple. (after De Batist, 1989)

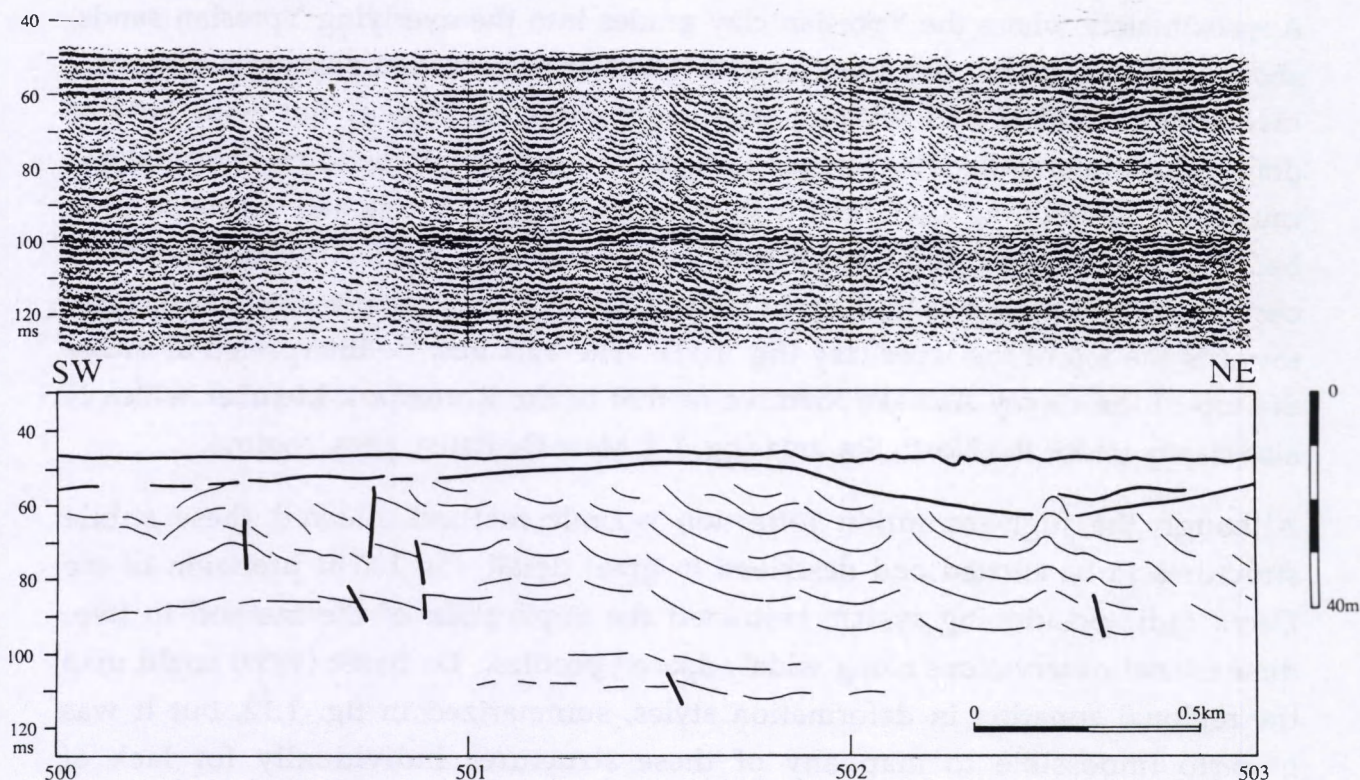


Fig. 1.7. Wavy deformation pattern in the Ieper Clay (fig. 1.1, section 2, multi-electrode sparker, 300 J). The flat reflector at about 100 ms is the first sea-bed multiple. On the right, the base of a palaeovalley is pierced by a diapiric clay ridge, probably the consequence of a Quaternary reactivation of a pre-existing deformation. (after De Batist, 1989)

illustrate different deformation styles. Their description is drawn from Henri \acute{e} t *et al.* (1988).

The lower interval of the Ieper clay, up to about 25 m above the undisturbed basal reflector of the clay, is generally characterized by a dense pattern of block faulting, with tilted and arched blocks and apparently randomly dipping fault planes (fig. 1.6). The average throw at the level of a reflector with a discrete high-frequency response is about two metres.

In a second interval, stretching from about 25 m up to at least 70 m above the clay base, one may locally observe a well preserved wavy deformation pattern (figs. 1.7 and 1.8), consisting of a festoon-like alternation of gentle, rounded synclines and open, cusped anticlines. These anticlines seem to develop locally into diapiric structures. The average (apparent) wavelength of the wave-shaped deformations amounts to a few hundreds of metres, and the amplitude ranges from 2 to 10 m.

The most general deformation style observed however is a pattern of faulted and often tilted blocks (fig. 1.9), sometimes with a dominant tilt direction. This pattern has the largest distribution in the deformed zones of the Ieper clay in the Southern North Sea.

Approximately where the Ypresian clay grades into the overlying Ypresian sands, about 140 m above the clay base, another peculiar deformation pattern is observed, involving faulted blocks without noticeable block movement but with inverse drag features along the fault planes. Indeed, in contrast with bedding deformations caused by normal drag associated with block faulting, the tilting and down-warping bedding terminations point away from each other (fig. 1.10). The deformations observed on seismograms in the roof zone of the Ieper clay progressively fade away towards the top of the Ieper clay (fig. 1.11). The Y2.1 may be interpreted as either the top of the clayey Aalbeke Member or that of the Kortemark Member which is also clayey under the North Sea area (fig. 1.2; Marc De Batist, pers. comm.).

Although the high-resolution reflection seismic method allowed these subtle structures to be elicited and described in great detail, the 100 m precision of the Decca radio-positioning system restricted the application of the method to two-dimensional observations along widely spaced profiles. De Batist (1989) could map the regional zonation in deformation styles, summarized in fig. 1.12, but it was hitherto impossible to map any of these structures individually for lack of positioning precision. Their orientation relative to known basement faults or any other clue to tectonic influence on clay diagenetic faulting therefore remained uncharted.

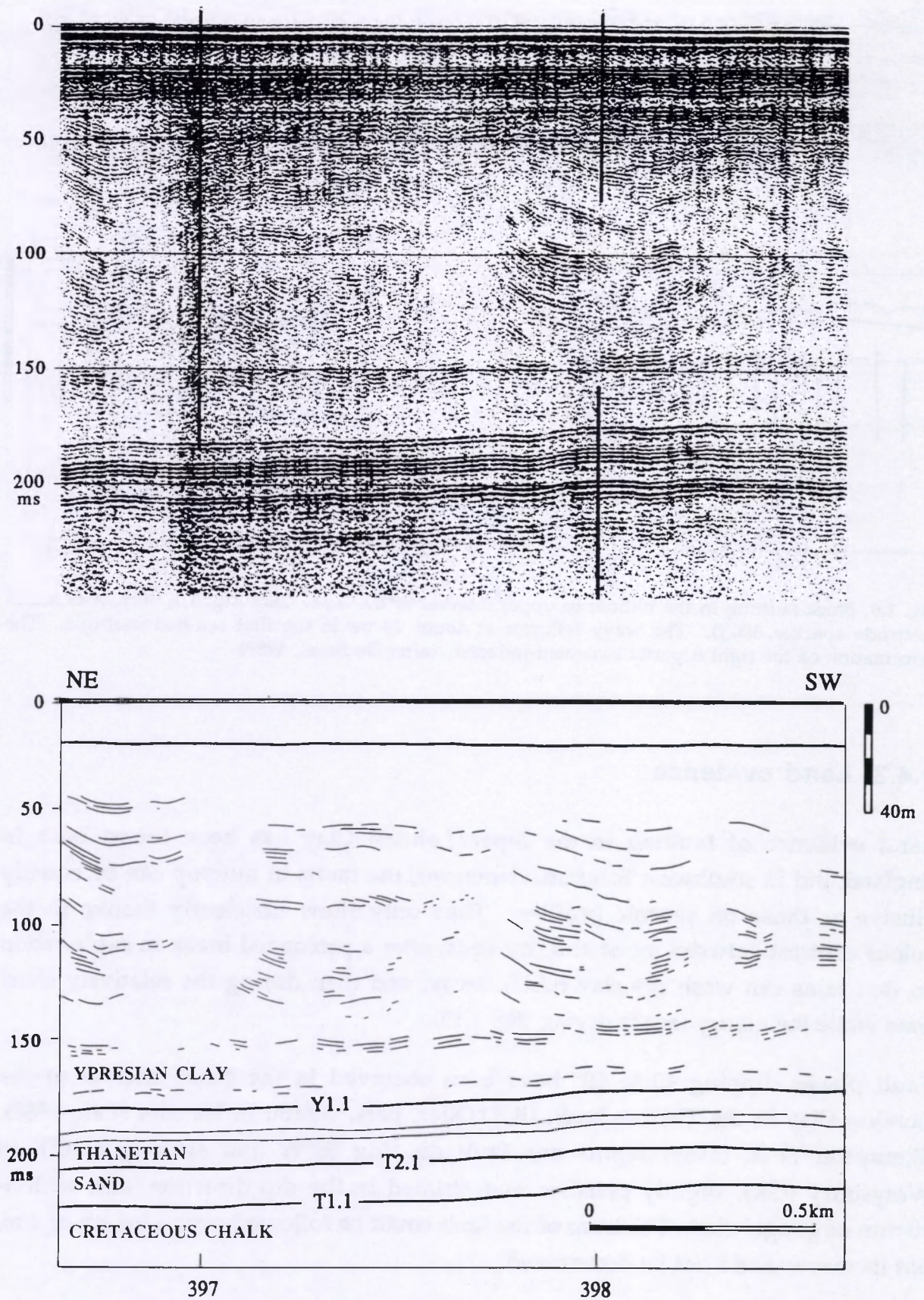


Fig. 1.8. Wavy deformation pattern in the Ieper Clay in a nearshore profile (fig. 1.1, section 3, multi-electrode sparker, 1000 J). (after De Batist, 1989)

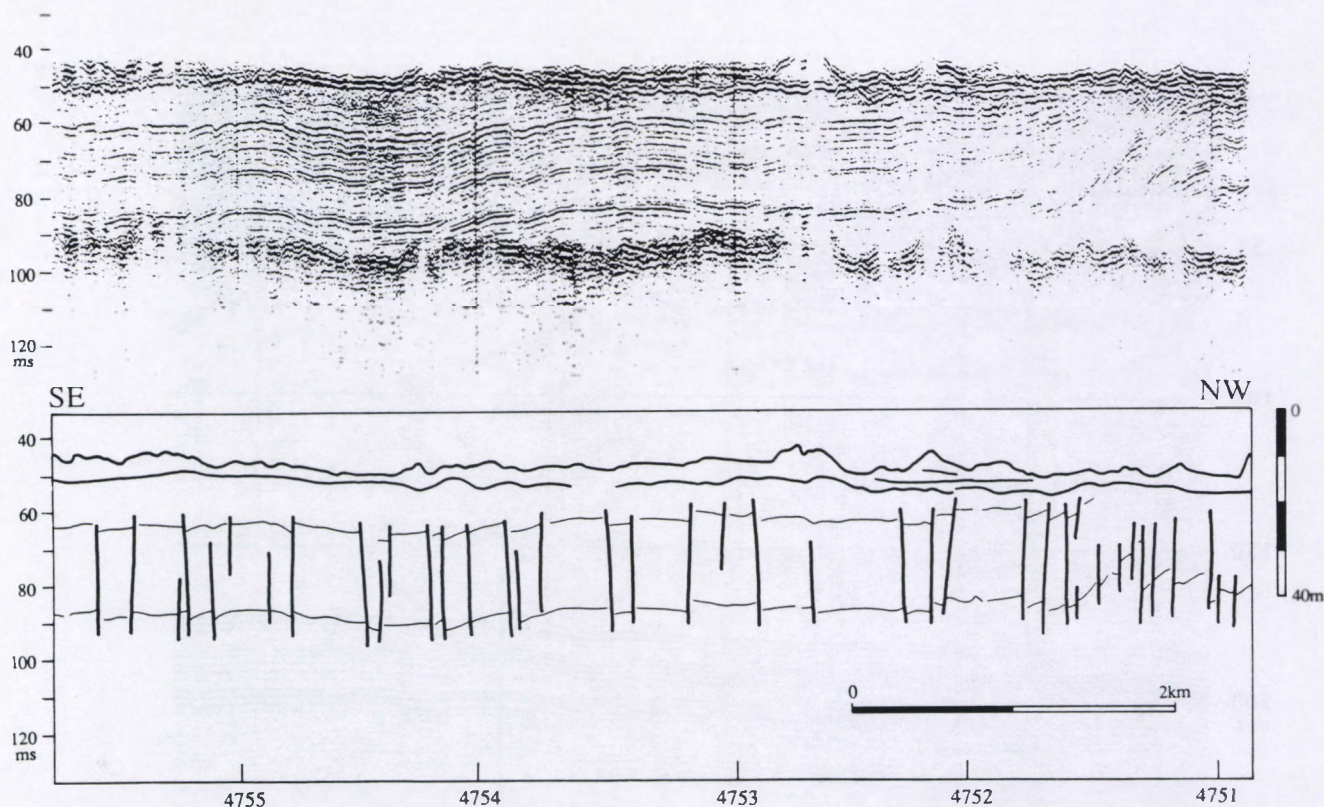


Fig. 1.9. Block-faulting in the middle to upper interval of the Ieper Clay (fig. 1.1, section 4, multi-electrode sparker, 300 J). The wavy reflector at about 90 ms is the first sea-bed multiple. The deformation on the right is partly basement-induced. (after De Batist, 1989)

1.4.2. Land evidence

Land evidence of faulting in the Ieper/London Clay has been found both in England and in southwest Belgium. However, the faults in outcrop can be equally elusive as those on seismic profiles. They only show up clearly thanks to the colour contrast between moist and dry beds, after a prolonged break in exploitation so that rains can wash the clay rubble away, and then during the relatively short time while the quarry face is drying (fig. 1.13).

Fault planes dipping 40 to 60° have been observed in the basal interval of the London Clay in the Thames basin (B. D'Olier, pers. comm. in Henriët *et al.*, 1988). Skempton *et al.* (1969) report one fault dipping 55°W and striking N10°E in Wraysbury (UK), slightly polished and striated in the dip direction, and with 5-10 mm of gouge¹ clay. The trace of the fault could be followed over a length of 4 m, but its throw could not be determined.

¹Gouge is a thin layer of soft, earthy fault-comminuted material along the wall of a vein or fault (American Geological Institute, 1980).

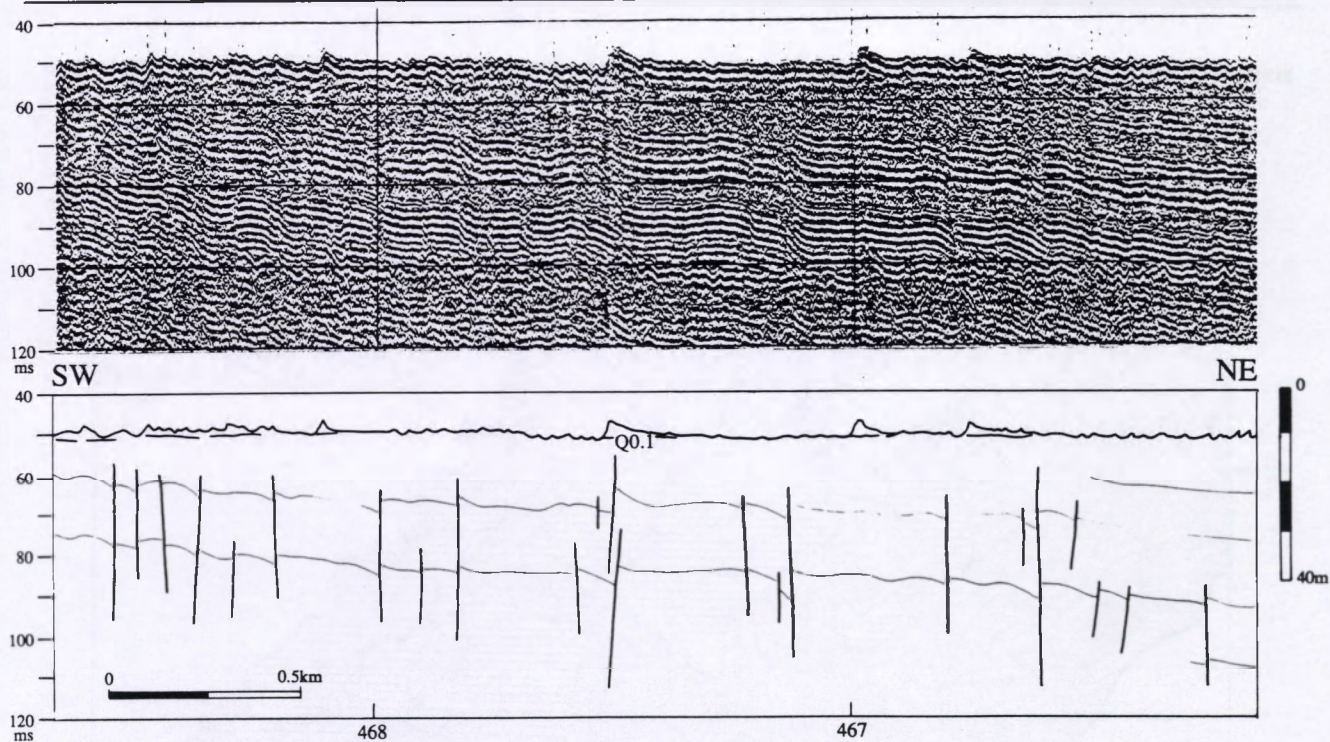


Fig. 1.10. Block-faulting near the top of the Ieper Clay (fig. 1.1, section 5, multi-electrode sparker, 300 J). The wavy reflector at about 90 ms is the first sea-bed multiple. Tilting and downwarping segments associated with each fault point away from each other. (from Henri \acute{e} t *et al.*, 1988)

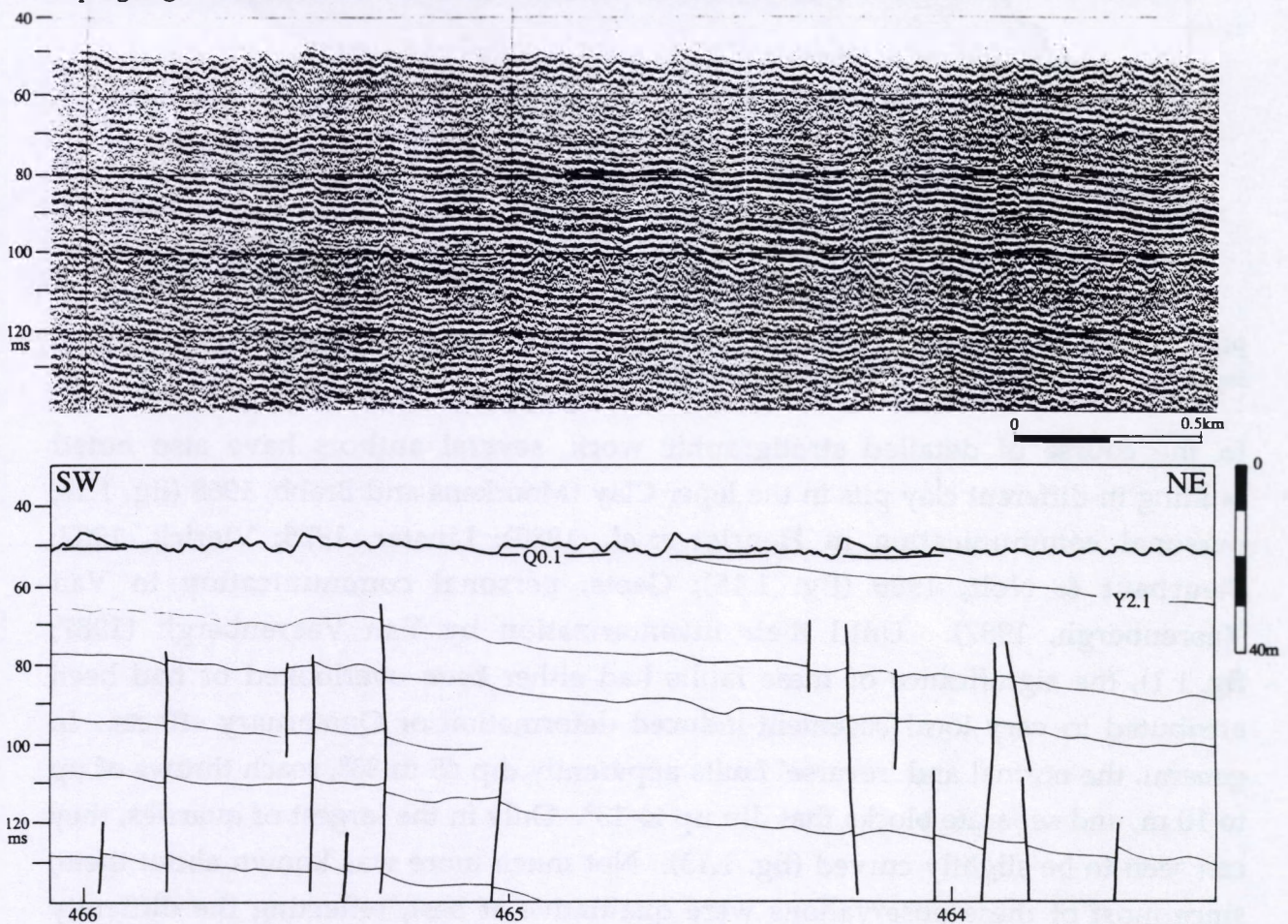


Fig. 1.11. Block-faulting dying out towards the top of the Ieper Clay (fig. 1.1, section 6 (continues to the right (NE) of the section in fig. 1.10), multi-electrode sparker, 300 J). The wavy reflector at about 90 ms is the first sea-bed multiple.

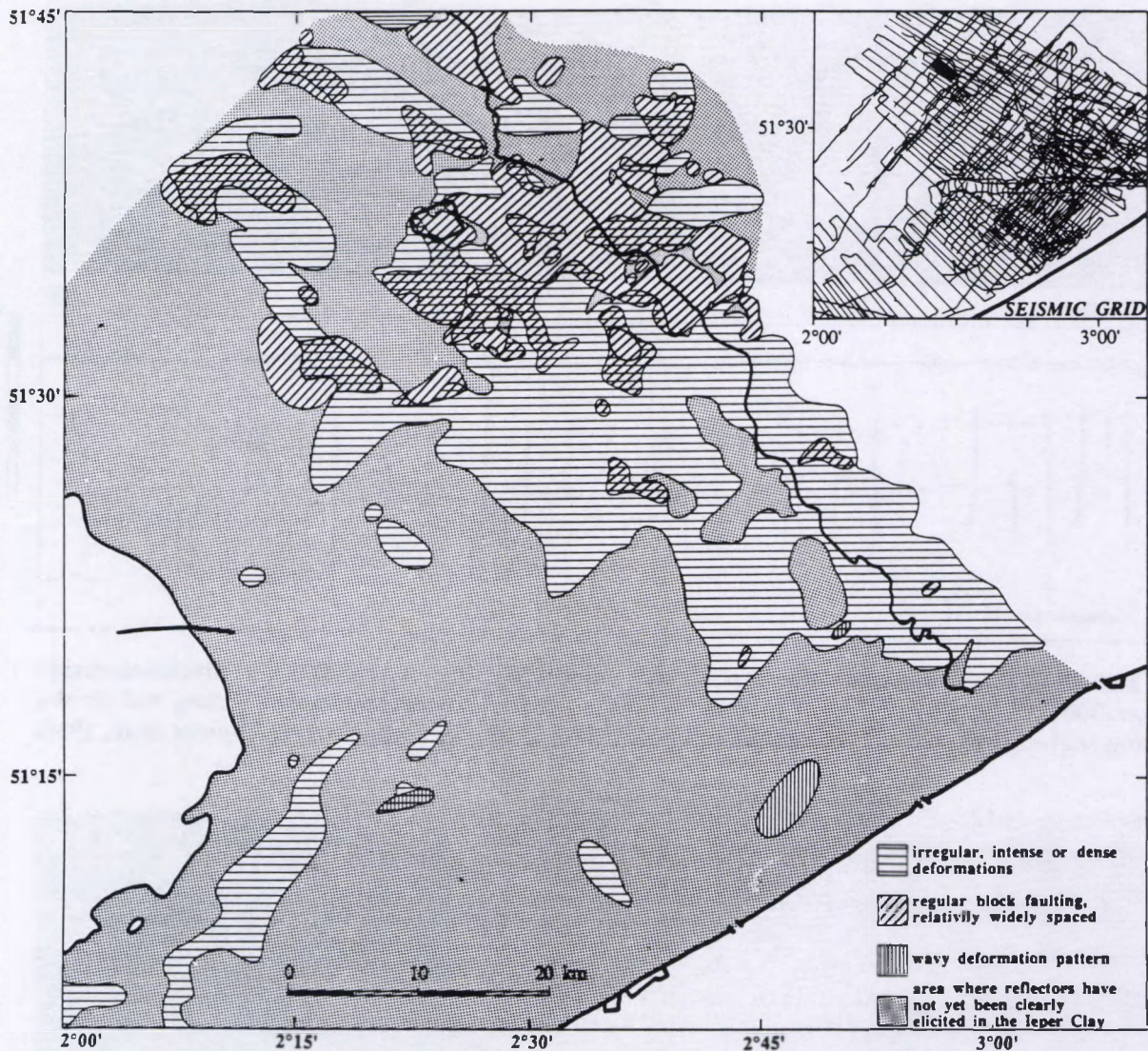


Fig. 1.12. Survey grid and regional zonation of deformation styles in the offshore extension of the Ieper Clay (from Henriët *et al.* (1991) after De Batist (1989)).

In the course of detailed stratigraphic work, several authors have also noted faulting in different clay pits in the Ieper Clay (Moorkens and Brabb, 1968 (fig. 1.14, personal communication in Henriët *et al.*, 1988); Linster, 1975; Vlerick, 1982; Steurbaut & Nolf, 1986 (fig. 1.15); Geets, personal communication in Van Vaerenbergh, 1987). Until their inventarization by Van Vaerenbergh (1987; fig. 1.1), the significance of these faults had either been overlooked or had been attributed to very local basement-induced deformation or Quaternary effects. In general, the normal and 'reverse' faults apparently dip 45 to 80°, reach throws of up to 10 m, and separate blocks that dip up to 13°. Only in the largest of quarries, they can be seen to be slightly curved (fig. 1.13). Not much more was known about them, since most of these observations were qualitative at best, reflecting the difficulty with which the faults, only sometimes visible from a distance, can be pinpointed

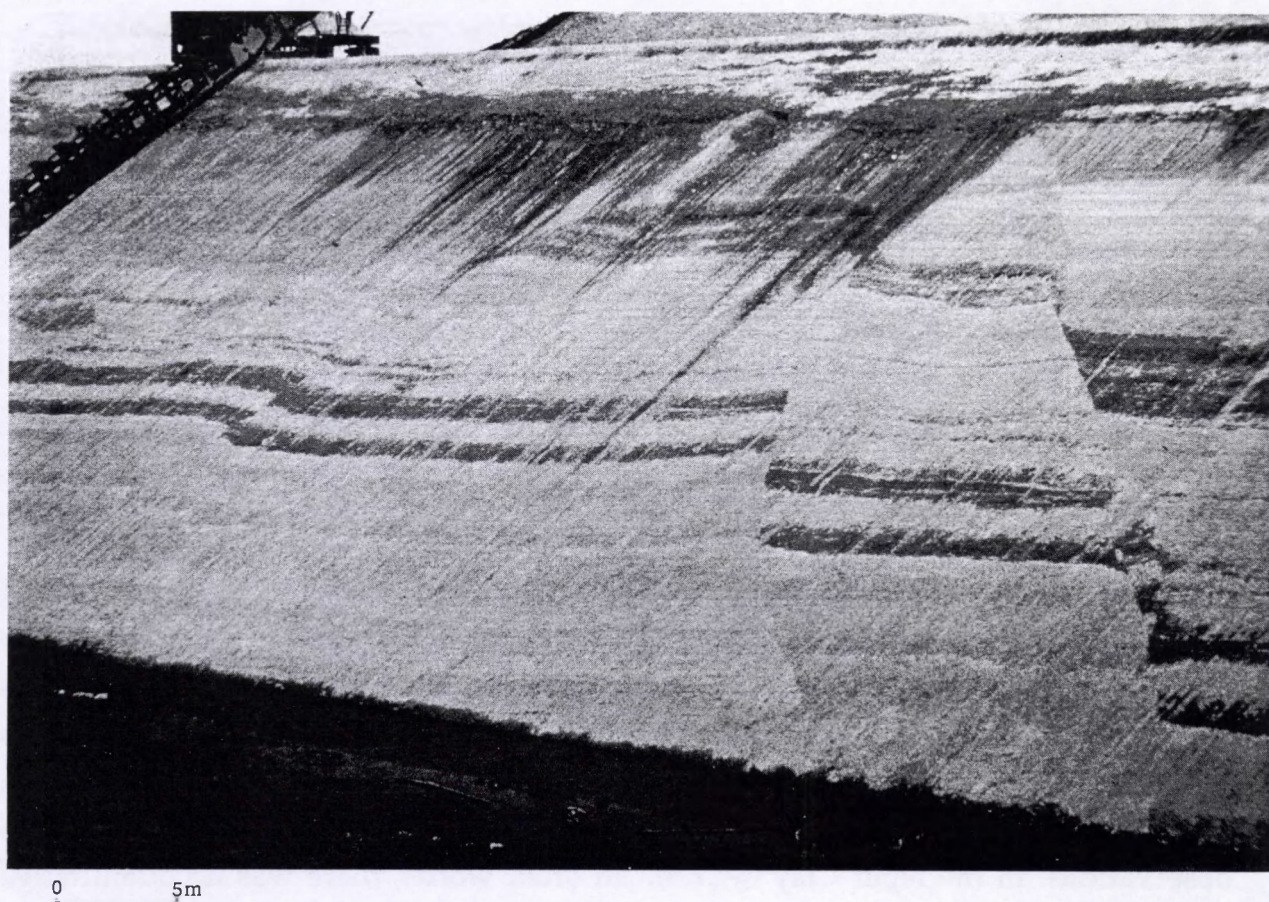


Fig. 1.13. Faulting in Ieper clay, Koekelberg clay pit, Marke, Belgium. Note the apparently 'reverse' fault at the left accompanying normal faults. The striations are due to extraction practices. (photograph by the author, 25.07.87).

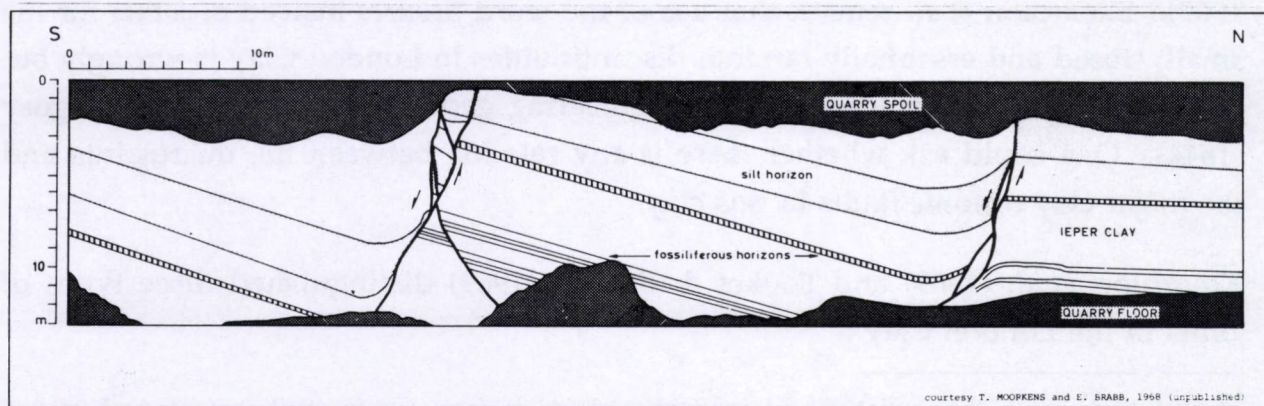


Fig. 1.14. Faulted blocks in Ieper clay, CBML clay pit, Lauwe, Belgium (after Moorkens & Brabb in Henriët *et al.*, 1988).

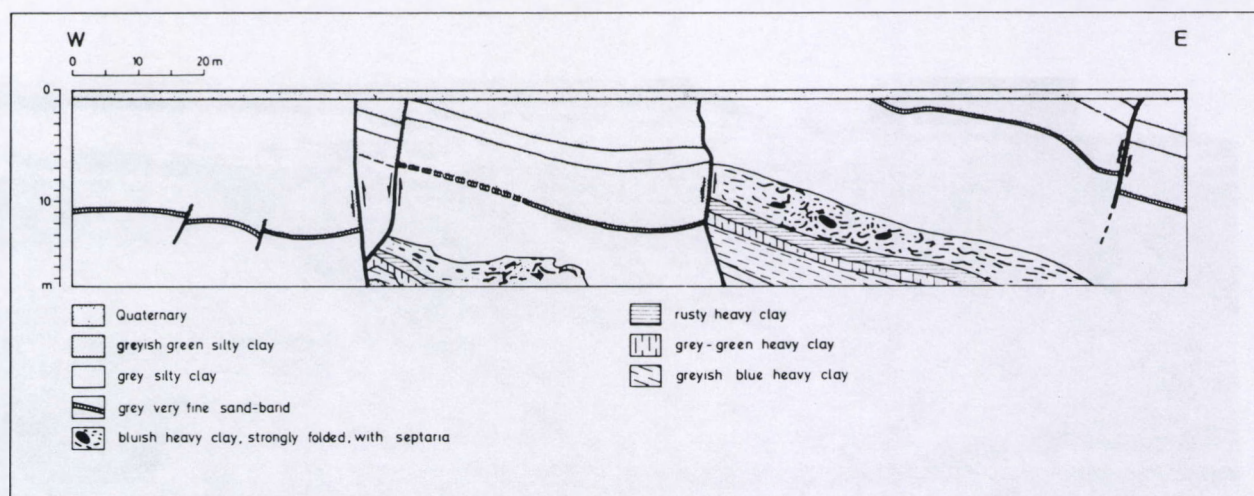


Fig. 1.15. Normal and 'reverse' faulting in Van Biervliet clay pit, Zonnebeke, Belgium (after Steurbaut & Nolf, 1986).

on the quarry slopes and measured. Moorkens & Brabb and Van Vaerenbergh did report fault planes with *slickensides*¹, but only Van Vaerenbergh actually tried to measure one, with doubtful results. Because the exploitation face of these clay pits slopes 30° to 50°, the apparent dips, directions and throws of the faults, as well as the apparent distances between them can be misleading. Normal faults may even appear to be reverse, as is most probably the case with all such outcrop 'observations' in the Ieper Clay (§4.2.3). In other words, there was no quantitative hold on the true three-dimensional orientation of clay tectonic faults, neither on seismic profiles, nor in outcrop, to give the clue to the driving force mechanism.

1.4.3. Microfractures

The microfractures in the overconsolidated London/Ieper Clay have been studied extensively by engineering geologists (Skempton *et al.*, 1969; Fookes & Parrish, 1969). Skempton *et al.* remark that use of the word *fissures* instead of *joints* for the small, closed and essentially random discontinuities in London Clay is wrongly but strongly established practice among engineering geologists, and cite a.o. Gregory (1844). One could ask whether there is any relation between the microjoints and the major clay tectonic faults in this clay.

Skempton *et al.* (1969) and Fookes & Parrish (1969) distinguished three types of joints in the London Clay :

¹A *slickenside* is a highly polished and smoothly striated surface, due to displacements and friction along a fracture (American Geological Institute, 1980). A *stria* or *striation* is one of multiple scratches or minute lines, generally parallel, inscribed on a rock surface by a geologic agent moving along, i.e. glaciers, streams or faulting (after American Geological Institute (1980) and Ramsay & Huber (1987)).

1. joints more or less parallel to bedding, with a gently undulating surface having a somewhat rough or bumpy texture;
2. large joints, 0.3-1.2 m high and up to 6 m long, perpendicular to bedding (dipping less than 3° in most of the studied outcrops) and with preferred and orthogonal orientations. Typically their surface is plane with a matt texture;
3. small planar or conchoidal joints ('fissures'), rarely more than 15 cm in size, with random orientations but generally dipping steeply (80-90°), and with a matt surface texture.

A minority of the latter category (5-15% depending on location) show slickensides and while these authors recognize this evidence of relative displacement by shear, they fail to classify these 'joints' (or "fissures") as microfaults. Only Fookes & Parrish (1969) suspected a different origin. In one of the locations they have studied, the Isle of Wight monocline, the London clay dips 85°. The evident tectonic stresses involved have indeed induced some preferential orientation of joints in the London clay, more or less coinciding with the orientations of joints in the adjoining Chalk. Their generalization, as to relate the microfracturing of the London clay to basement-induced tectonics, seems to be invalidated because microfracturing without preferential orientation is also observed in the London and Ieper clay where no significant tectonic deformation is known.

Ward *et al.* (1965) noted that joints in the London clay along a vertical shaft at Ashford Common, Middlesex, were more widely spaced and larger with depth below the current surface. The spacing of the joints varied from around 4 cm at 10 m depth to about 30-60 cm at 42 m depth¹. Water content increased towards the surface. This trend prevailed also in three other, widely separated places to depths of 10 m (Skempton *et al.*, 1969). Terzaghi (1961, in Skempton & Larochelle, 1965) asserted that removal of overburden by erosion resulted in considerable increases in water content, causing vertical expansion of the clay by amounts varying from about 5% at a depth of 15 m to a least 10% near the surface. Weathering may also cause the clay to swell superficially. Skempton (1964) and Fookes & Parrish (1969) suggested that such expansion may have caused some of the microfracturing. Under the periglacial conditions of Quaternary glaciations, clays may have been crumbled also by segregation ice down to depths of 10 m (Pissart, 1987). This is the maximum thickness of the Brown London clay, the weathered equivalent of the

¹"The increase in the spacing of the fissures was clearly shown by the way the men loaded the skips. At the upper level they loaded the clay with hand shovels, but at lower levels they lifted the large lumps in two hands and pitched them into the skips." (Ward *et al.*, 1965)

London Clay, in the London Basin (Skempton & La Rochelle, 1965; Fookes & Parrish, 1965). In Belgium, the weathered and intensely jointed zone rarely extends deeper than 4 m. It appears that the formation and development of some of the joints is related to extension by unloading and near the surface possibly also to cryogenic segregation and weathering.

However, microjointing of the Ieper/London clay may also be a result of overpressures in the pore fluid through the process of natural hydrofracturing (Henriet *et al.*, 1988). The required pore fluid overpressures will be explained in the section below. Because most of the joints are fairly planar and therefore hardly deformed by later compaction, general hydrofracturing (producing most of the joints) would have occurred only *after* the major clay tectonic deformation and compaction stage.

On the other hand, the slickensided and irregularly undulating microfaults with random orientations may still be related to an earlier gravitational collapse phase. Guiraud & Séguret (1987) described similar slickensided microfaults with curved divergent striae in the inverted Soria Basin (northern Spain). The microfaults there, whose length range from a few centimetres to a few metres, define a characteristic wedgy-sheared geometry and form bi-pyramidal cone-shaped slices with axes of the cones perpendicular to tilted bedding planes. They fit together perfectly with the load casts and rounded troughs and necks of water escape structures which are located at the limits of the neighbouring sandstone layers (fig. 1.16). The unequivocal geometrical relation between these two types of deformation lead Guiraud and Séguret to conclude that microfaults in clays and water escape load marks in coarse-grained sandstones are genetically related. Such

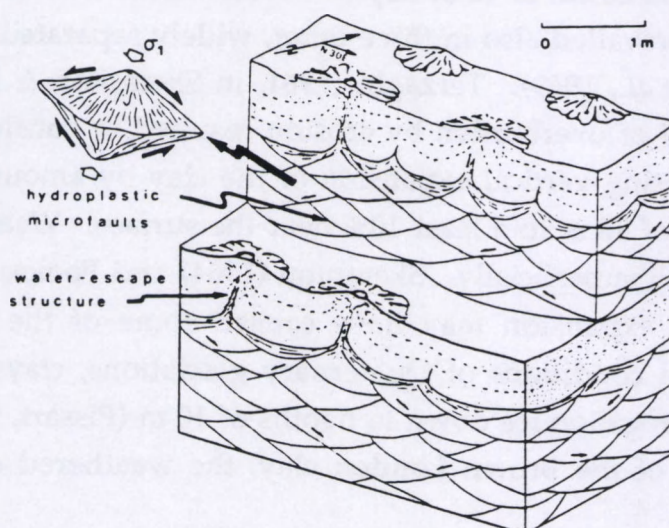


Fig. 1.16. Water escape structures in sandstones and microfaults in clayey siltstones of the Soria Basin (from Guiraud & Séguret, 1987).

a relation implies that these microfaults were penecontemporaneous¹ with the deposition of the overlying sands. In the London/Ieper clay on the other hand, the sparse microfaults do not add up to bi-pyramidal cone-shaped slices. Penecontemporaneous water escape structures of the scale of those in the Soria Basin have not been found within the formation, let alone any indication of a similar relation, and the clay tectonic (macro-)faults seen in outcrop are so large that they cut the silty horizons in which the escape structures would be expected. In conclusion, despite the similarity of individual slickensided microfaults in the Soria Basin clays and the Ieper/London clay, there are striking differences that suggest later-than-penecontemporaneous faulting in the Ieper/London clays.

The brecciation in the upper part of the Ieper clay in the Knokke well, described by Vandenberghe *et al.* (1990), together with clastic dykes filled with a black gouge (not described but evident in their photographs) is similar but more pronounced than that described in §4.2.1.12. These phenomena are probably related to clay tectonics.

1.4.4. Working hypotheses

A number of hypotheses have been advanced by Henriët *et al.* (1982, 1988) to explain the deformation described above. These and other hypotheses will be presented here in the perspective of known soft-sediment deformation mechanisms and driving force systems (Owen, 1987; §1.2).

Regional tectonic stresses can be ruled out as causing the *presence* of almost purely intraformational faults and folds, but their possible influence on the *orientation* of the structures can only be revealed or refuted by a 3D approach. Hydrofracturing may account for some of the microjoints, but cannot in itself produce the observed faults displacements and convolute bedding.

Most of the pervasive deformation was therefore and most probably caused by liquefaction of large sections of the clayey formation. Conditions for liquefaction can easily be found in its likely early burial history. The Ypresian clays were probably deposited as loose, high-porosity, water-logged muds (fig. 1.17a). As sedimentation progressed and the thickness of the clay deposits increased, pore space gradually decreased through the expulsion of pore water. Pore water

¹Penecontemporaneous faulting = a deformation occurring in soft rock, soon after the deposition of the strata involved, and caused by gravitational sliding or slump (American Geological Institute, 1980).

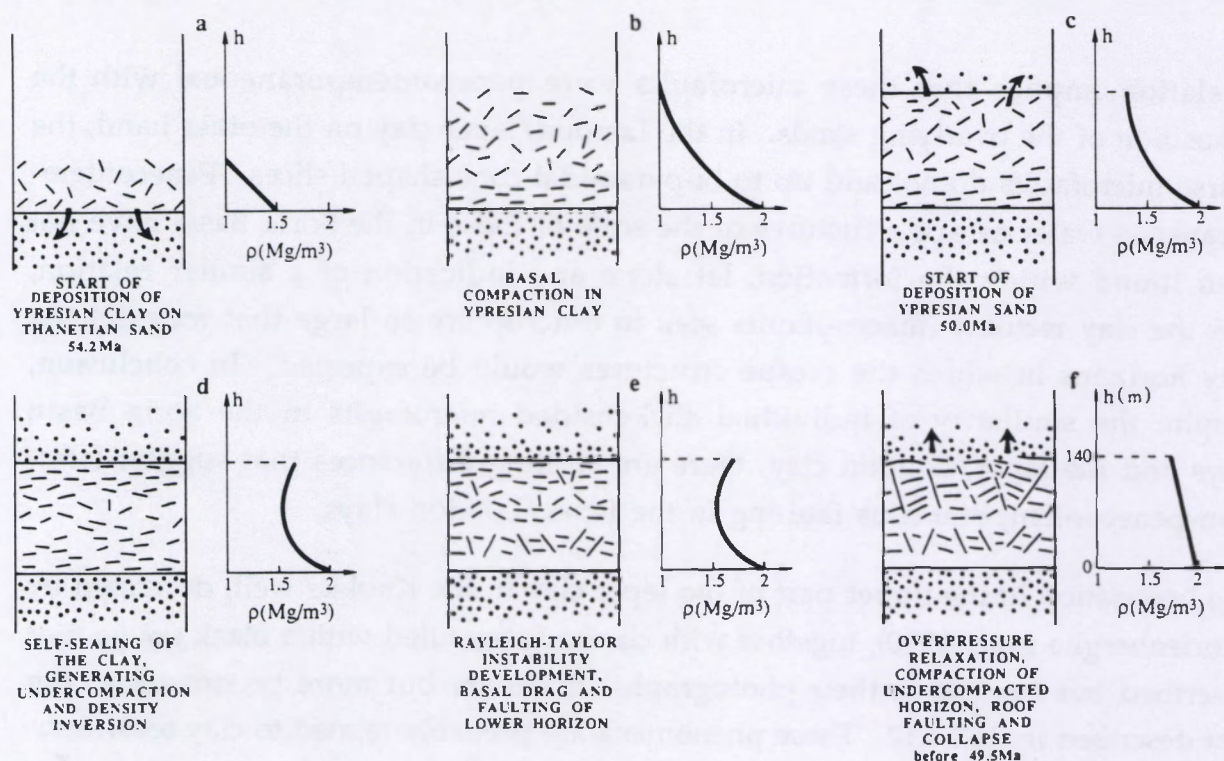


Fig. 1.17. Working hypothesis to explain the deformation in the Ypresian Clay. Arrows indicate dewatering direction. The graphs give density/depth variations of the clay. (after Henriët *et al.*, 1988)

drainage was probably greatest near the base, due to overburden weight tending to reduce pore space most there and to the presence of a permeable sand substratum (Thanet sands in U.K., sands of the Landen Group in Belgium) which may have provided an easy escape path for the water expelled from the basal layers of the clay. The relatively quickly drained basal clay beds could thereby experience a faster rate of compaction, soon building a permeability barrier which gradually impeded the further basal drainage of the clay beds¹. The increased compaction near the clay base will have resulted in a density increase, as shown in a schematic way on fig. 1.17b.

Clay sedimentation ceased and gave way to the deposition of Ypresian fine grained and dense sands. One might consequently imagine that a similar sealing phenomenon occurred at the top of the Ieper clay sequence. Fast drainage through the permeable sand cover could have induced a compaction from the top down, in addition to the compaction from the bottom up (figs. 1.17c and d).

¹Ulf Bayer (pers. comm.) pointed to a flaw in this part of our working hypothesis. Pore fluid flows only under the influence of an applied pressure gradient towards sites with a lower pressure. Downward pressure gradients may exist under overpressure conditions, but this is most unlikely while the clay is still being deposited. A normal compaction gradient as in fig. 1.17b, with pore fluids leaving the lower reaches of the formation upwards under continuous clayey deposition, may already provide sufficient downward sealing of a thick clayey formation. The basic message of this part of our working hypothesis therefore remains the same.

As a result, the clay may have sealed itself. Such a situation has two related consequences:

1. As soon as drainage was impeded in some part of the clay body, continued sedimentation meant that the locked pore water became overpressured. Overpressures by delayed compaction are very common in thick, buried clayey sequences (Fertl, 1976; Magara, 1978). The resulting decrease in effective normal stress acting on the interparticle contacts decreased the shear strength of the sediment, and at the shallow depths involved here perhaps even down to the point of liquefaction;
2. As water has a low compressibility, the sealed part of the clay will have remained undercompacted for a time and had a lower density than its overburden of compacted clays and sands (fig. 1.17d). This density inversion is gravitationally unstable.

At this point, shallow overpressuring provides both a deformation mechanism (1.) and a driving force system (2.). Jointly, they may be regarded as main agents in the development of clay tectonic deformations like those observed in the Ypresian clay, and especially of the clay waves. The gravitational instability probably acted as the motor, which drove the sediment flow, while the overpressurized pore water acted as a lubricant, decreasing the shear resistance at the level of the grain contacts.

The wave shape observed fits a model of deformation of an interface between two viscous fluids with different densities and viscosities, with the denser fluid resting on the lighter one. Such a model is known in fluid dynamics as a Rayleigh-Taylor instability (§1.2). It predicts that the interface between a high-density upper layer and an underlying layer with lower density (and possibly lower viscosity) develops a sinusoidal instability that may evolve into a pattern of regularly spaced upwellings of the lower-density fluid into the denser layer. This is also possible (Owen, 1985) in the case of a probably continuous density profile in the shallowly buried but undercompacted Ypresian clay (fig. 1.17e).

Overpressure in shallow horizons is however intrinsically transitory. It has its origin in the delayed compaction of a clay body and disappears when conditions of hydrostatic pressure in the pore fluid are restored, either by slow seepage or by fracturing of the permeability barriers. The fracturing of the compacted and hence more brittle clay beds above the main undercompacted horizon could have taken place both by progressive hydrofracturing and by local fault developments, induced by the buoyant force of the upwelling clay wave crests. The hydrofracturing of the

relatively recently compacted clay beds must apparently not have been a major problem, even at the moderate overpressure levels expected here.

As pore pressure relaxed, the upper, brittle horizons underwent faulting and tilting while progressively sagging into the initially undercompacted horizon and thus destroying the initial wave shape (fig. 1.17f). As Owen (1987) has shown experimentally, liquefied sediments can be macroscopically faulted upon gravitational collapse, especially when the strain rates are sufficiently high (Maltman, 1987). The relict wave shapes observed at a few places on the Belgian continental shelf have probably been 'frozen' by local regimes of pore water relaxation (faster, slower ?) which differed from those governing the compaction over the major part of the continental shelf. Faults caused by a gravitational collapse of growing anticlines are expected to show orientations and sag directions closely related with the anticlines. The randomly oriented microfaults fit with a hypothesis of entirely vertical gravitational collapse. This working hypothesis predicted that we should be able to find evidence of faulting in a very early stage of compaction, when the clays were still plastic, and of upward fluid ejection along the fault planes.

Two more driving force systems should be dealt with here : gravitational body force and unevenly distributed confining load. Gravity sliding can occur as well in overpressurized argillaceous sediments deposited on very gentle slopes ($<3^\circ$). The resulting *growth faults* (the theory of which was firmly established in Crans *et al.* (1980) and Crans & Mandl (1980)) strike parallel with the sloping surface and induce such typical characteristics on the sagging block as 'roll-over' anticlines and thickening of layers towards the growth faults. No such features can be identified conclusively on any of the seismic or outcrop sections. Because the present 1° NNE dip is likely to be the largest that the Paleogene beds have experienced since their deposition in this marginal part of the North Sea Basin, 3D analysis should reveal a dominant NW-SE strike. If not, this driving force should be ruled out altogether.

Henriet *et al.* (1982) also considered the effect of differential loading by advancing glacial ice or by prograding wedges in the overlying Ypresian and Lutetian sequences. The first effect can be ruled out because it is difficult to conceive how an advancing ice sheet (if one ever came this far S, which is generally doubted) could have induced the quasi-stratigraphically bounded zonation of deformation patterns observed in the dipping section of the Ieper clay. The second effect can be neglected because it would be expected to cause undulations that affect the top of the clayey formation and die out downwards (Allan, 1982) and not die out both upwards and downwards, as observed. The explanation of Vandenberghe *et al.*

(1990) for the marked brecciation of the Ieper clay in the Knokke well by Quaternary erosion and hence differential unloading in the Channel, is utterly unlikely, considering the depth of 150-180 m at which it was observed.

1.5. Clay diapirism

Laga (1966) described diapiric deformation in the Rupelian Boom Formation Clay, exposed in the trench wall of a nearby railway tunnel being constructed under the river Scheldt in Antwerp, Belgium. Some septaria had been dragged vertically upwards by the formation of the diapir. Wartel (1980) discovered two other clay diapirs nearby on O.R.E. subbottom profiles acquired on the Scheldt, but his profiles did not allow this deformation to be described in detail. In the course of a detailed seismic and geotechnical survey of another tunnel site, Henriët and Heldens (reported in Hemerijckx *et al.* (1983) and Henriët *et al.* (1986)) acquired a network of analogue single-channel profiles across one of them (figs. 1.18-19). The seismic source was an EG&G Uniboom fired at 300 J, yielding a resolution close to 0.5 m in the Rupelian (Boom) Clay beds. All data were recorded on a very high resolution recorder (the EG&G model 255 engineering seismic recorder).

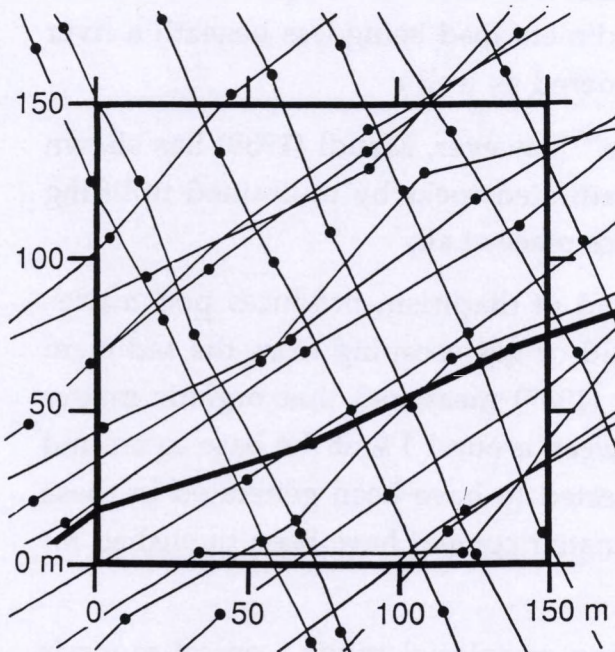


Fig. 1.18. Network of Uniboom profiles over clay diapir sector on the river Scheldt. Thick track line indicates position of profile in Fig. 1.19.

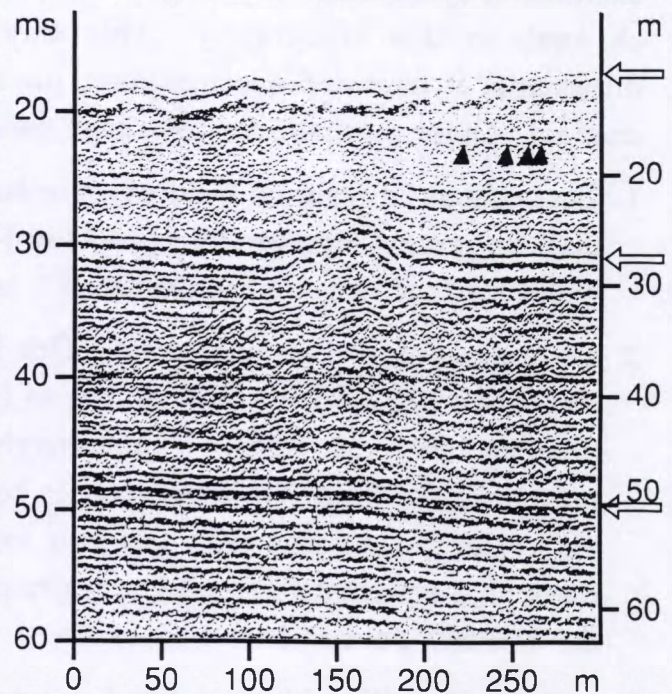


Fig. 1.19. Uniboom profile across clay diapir in Rupelian clay. Reflectors modelled in fig. 4.9 are indicated by arrows. Notice diffraction hyperbolae (triangles) on calcareous concretions along some of the reflectors.

The profile in fig. 1.19 shows the diapir with an apparent diameter of some 60 m. The reflectors bulge upwards with a vertical amplitude increasing from a few decimetres at 50 m depth, to a few metres at about 25 m depth. Higher horizons are pierced. The lowest horizons on most time sections do not appear to be significantly deformed below the diapir, so that the velocity pull-up effect (due to locally higher P wave velocities) can safely be ruled out. Actually if any velocity effect would be anticipated, the expansion of Rupelian clay in the diapir might be expected to result in locally lower P wave velocities and a velocity pull-down of reflectors below the diapir, rather than a velocity pull-up.

Henriet *et al.* (1988) also noted clay diapirism on high-resolution profiles in the Ieper clay (fig. 1.7), apparently due to a reactivation of clay tectonic upward flow anticlines by Quaternary channel erosion. London clay diapirs piercing into Quaternary sediments in buried scour hollows along buried channels, a possible analogy for the phenomenon observed in fig. 1.7, have been described in numerous outcrops in the London region (Berry, 1979). D'Olier (in Henriet *et al.*, 1982) gave an example of a London clay diapir, affecting a sequence of Pleistocene sands and gravels through faulting.

All of these diapirs are closely related with the post-Tertiary erosion surface, which excludes a syndimentary origin. Most of them more or less coincide with the channels in this topography. This may indicate that the diapirs are due to differential erosion and decompaction, the sediment load being less beneath a river channel. Other mechanisms have been considered as well :

1. local release of residual fluid overpressure. However, Mandl (1988) has shown that, in general, overpressuring of fluid-saturated rocks by undrained uplifting will remain of very modest degree, if it takes place at all;
2. gas expansion due to unloading. This kind of diapirism produces pockmarks, crater-like holes on the surface due to fluid or gas escaping from the sediment (Hovland & Judd, 1988). Vandenberghe (1987) measured that organic matter content in the Boom Formation varies between around 1% at the base to around 4% at the top, so that some gas may expected to have been generated in these clays. No systematic analyses of organic matter content have been published for the Kortrijk Formation;
3. peripheral uplift of beds around a growing periglacial pingo, conical mounds with a thickening ice core. While pingos may also be an alternative explanation for the hollows in the London area (Berry, 1979) and for superficial uplifting, they cannot account for the deeper deformation seen in fig. 1.19 (Pissart, 1987).

The deformation visible in network of 2D boomer profiles was mapped only crudely at first (Hemerijckx *et al.*, 1983). It was felt that a 3D surface modelling exercise with these pseudo-3D data (§2.1) would illuminate the deformation more accurately and hence also its origin. The Scheldt diapir would also become the focus of high-resolution 3D seismic acquisition, in the hope of revealing more internal detail.

1.6. Methodology

This study of clay tectonic deformation has thus (§1.4.4) been guided by one ruling hypothesis involving a build-up of undercompaction and consequently a density inversion as a result of self-sealing of the compacting clay body (Henriet *et al.*, 1988). This working hypothesis accounted for most of the two-dimensional observations of clay tectonic faults and large scale convoluted bedding (§1.4.1-3), but the possible influence of regional tectonic stress(es) could not be ruled out before the orientation and pattern of clay tectonic faults and undulations were known quantitatively and three-dimensionally. Similarly, understanding of clay diapirism (§1.5) in the Scheldt area might also benefit from a three-dimensional modelling exercise. Furthermore, quite a few phenomena (“inverse drag”, “reverse” faults in juxtaposition with normal faults,...) could not be interpreted conclusively. Finally, secondary hypotheses deduced from our ruling hypothesis (purely gravitational and sudden collapse of undercompacted clay, fluid ejection along the faults,...) needed to be tested (Schumm, 1991) with more and better outcrop and microscopic observations.

In order to understand clay tectonic deformation and its tectonic setting in a quantitative and three-dimensional way, Chapter 2 goes beyond 2D reflection seismics, and explores the possibilities and the limitations of high resolution 2D, pseudo-3D and 3D reflection seismic acquisition. Depending on the scale of the deformations, a choice has to be made between true 3D coverage or one with a dense network of 2D profiles. Data density in turn sets minimum requirements for the positioning system. The appropriate source/receiver configuration is also determined by the scale of the studied structures. These choices will be illustrated by a number of seismic surveys that were specifically designed to acquire coherent data sets of tectonic and clay diagenetic deformations at various scales.

Since the work of De Batist (1989), interpretation of the mostly parallel reflectors in the Belgian Basin was never much of a problem. The real challenge was to

correlate the fault intersections across a seismic network in a more or less unambiguous way, and to create a reliable, quantitative 3D model of both a complex fault system and the affected reflectors. To that end, we developed an interactive 3D surface modelling software package from scratch, on an entry-level (PC-like) workstation. In Chapter 3, the new fault/reflector modelling technique is introduced as well as some of the numerous original algorithms that are part of it. The implementation and integration of these new concepts into the graphically interactive program is also described.

Chapter 4 bundles all new geological evidence. With the pseudo-3D seismic data acquisition and modelling methods of the two preceding chapters, quantitative 3D models of tectonic and clay diagenetic structures have been produced. Their analysis in §4.1 addresses the questions about the shape and orientation of faults and undulations, the possible influence of tectonic stresses on clay tectonics in the Belgian North Sea sector, and the actual shape of the Scheldt diapir. This analysis leads to implications related to the origin and process of clay tectonic deformations.

'Hard' additional outcrop evidence is the subject of §4.2. With a new method to cut flawless faces in the stiff and jointed Ieper clay, it became possible for the first time to reliably put ones fingers on the most minute clay tectonic faults and primary sedimentary structures. Through systematic measurements of dip, strike and striae and a stress inversion method, palaeostress regimes were reconstructed for the Marke area (Belgium), illuminating the (absence of) influence of regional stress on clay tectonic deformation.

In the course of this field work in the Marke and Zonnebeke clay pits (Belgium), a black gouge was discovered along both faults and veins. Undisturbed and oriented box samples have been analysed in microscopic thin sections and with X-ray Computer Tomography. Together with new biostratigraphic, granulometric, mineralogical and geochemical analyses, the gouge has become a clue to fluid ejection and displacements along early clay tectonic veins and faults (§4.3).

A thread running through most of this thesis ensues from our continuous search for 3D coherence in the description of structures over six orders of magnitude, going from the scale of high-resolution seismics, over outcrop measurements to the scale of microscopic observations. Hence the title of this thesis. However, the results of directed biostratigraphic, mineralogical and geochemical analyses have also stressed the importance of an interdisciplinary methodology in providing a deeper understanding of the complex history of clay diagenetic deformation.

2. High resolution (pseudo-) 3D seismics

In order to understand clay tectonic deformations and its tectonic setting in a quantitative and three-dimensional way, we go beyond 2D reflection seismics in this chapter, and explore the possibilities and the limitations of high resolution 3D reflection seismic *acquisition*. Depending on the scale of the deformations, a choice has to be made between true 3D coverage or one with a dense network of 2D profiles (§2.1). Data density in turn sets minimum requirements for the positioning system (§2.2). The appropriate source/receiver configuration is also determined by the scale of the studied structures (§2.3). These choices will be illustrated by a number of seismic surveys that were specifically designed to acquire coherent data sets at various scales (§2.4).

The *seismic interpretation* (§2.5) of the mostly parallel reflectors in the Tertiary strata in the Southern Bight of the North Sea was never much of a problem and is only briefly discussed.

2.1. 3D or pseudo-3D seismics and scale

The basic technique of reflection seismics (Sheriff & Geldart, 1982) consists of generating a seismic pulse with an acoustic source, and measuring the arrival times of reflections from seismostratigraphic interfaces. At sea, such pulses can be produced at a regular interval along a ship's track. The result is a continuous (2D) profile that looks like a geological cross section of the subsurface. 3D seismic reflection methods produce data distributed throughout an area rather than linearly. Subsurface structure can thus be reconstructed directly at every node of a uniform grid, rather than having to be tentatively correlated and interpolated between profiles. Complex stratigraphic features such as a meandering channel (fig. 2.1) or subtle structures such as weak flexures or a network of small faults (fig. 2.2) that may be all but impossible to interpret or correlate on 2D profiles, stand out clearly on horizontal or other synthetic sections through the 3D data block. In addition to adequate area coverage, dipping reflectors can be more reliably restored to their true position, albeit with extensive computer processing. Safar (1985) and Brown (1986) stressed also the remarkably improved resolution of 3D over 2D seismics (§2.1.2).

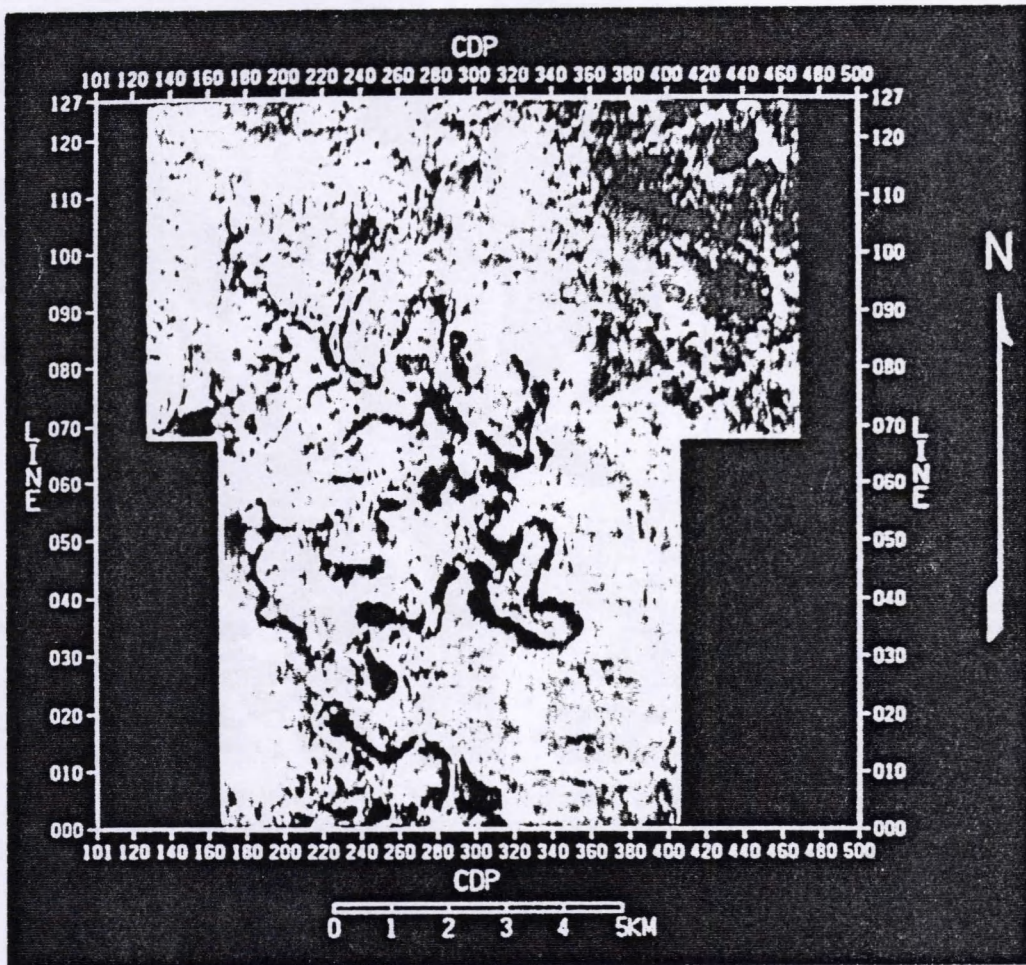


Fig. 2.1. Meander pattern of a Pliocene river, Gulf of Thailand. This is a time slice, or horizontal section through the 3D seismic data volume, at 196 ms. The smallest detail measures 33x100m. From Brown, Dahm & Graebner (1981).

3D seismic acquisition has first been developed on land (Walton, 1972), because of the ease with which source and receiver positions can be measured precisely enough to ensure proper 3D processing. The most common source-receiver arrangement is the 'block' layout (Sheriff & Geldart, 1982; fig. 2.3). Since 1977, 3D seismic data volumes have also been acquired at sea (Brown *et al.*, 1981). Until quite recently, acquisition consisted of shooting a number of closely adjacent multi-channel 2D lines. 3D processing techniques were used to merge all the data into a 3D volume in the computer. Only since the late 1980s, areal spreads of two or three streamers, towed from one or two ships sailing in parallel, have resulted in true 3D marine seismics (fig. 2.4). It requires both multi(up to 960)channel digital technology and a combination of dynamic positioning systems. In addition, a mix of acquisition methods has allowed integrated 3D land, shallow water, deep channel, and marine acquisition (Bukovics & Nooteboom, 1990). Early on, 3D seismics was

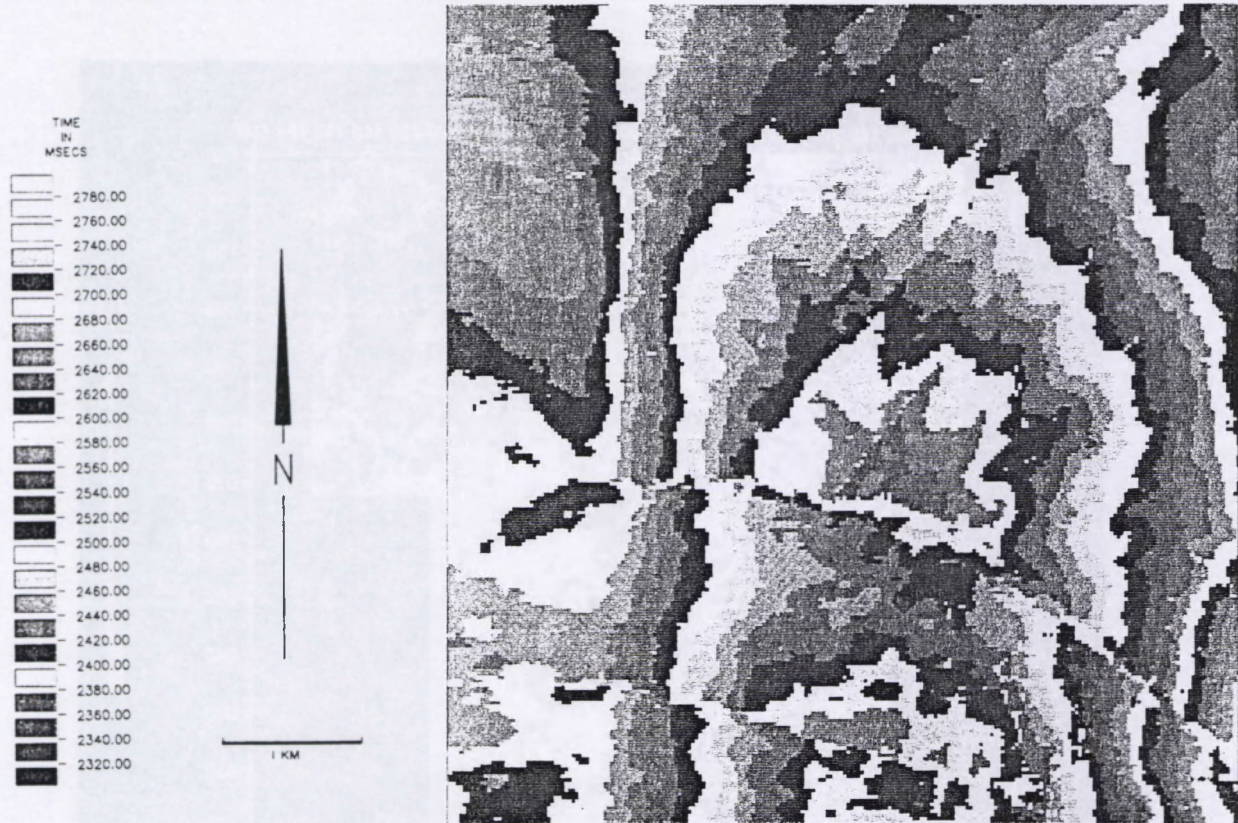


Fig. 2.2a. Time contour map of a reflector affected by a faulted anticline, North Sea Basin. To produce this map, the 3D data was tracked automatically along one reflection between each of the 220x380 grid nodes. The reflector sits between 2.7 and 2.3s; contour interval is 20ms; the smallest detail measures 25x25m. From Dalley *et al.* (1989).

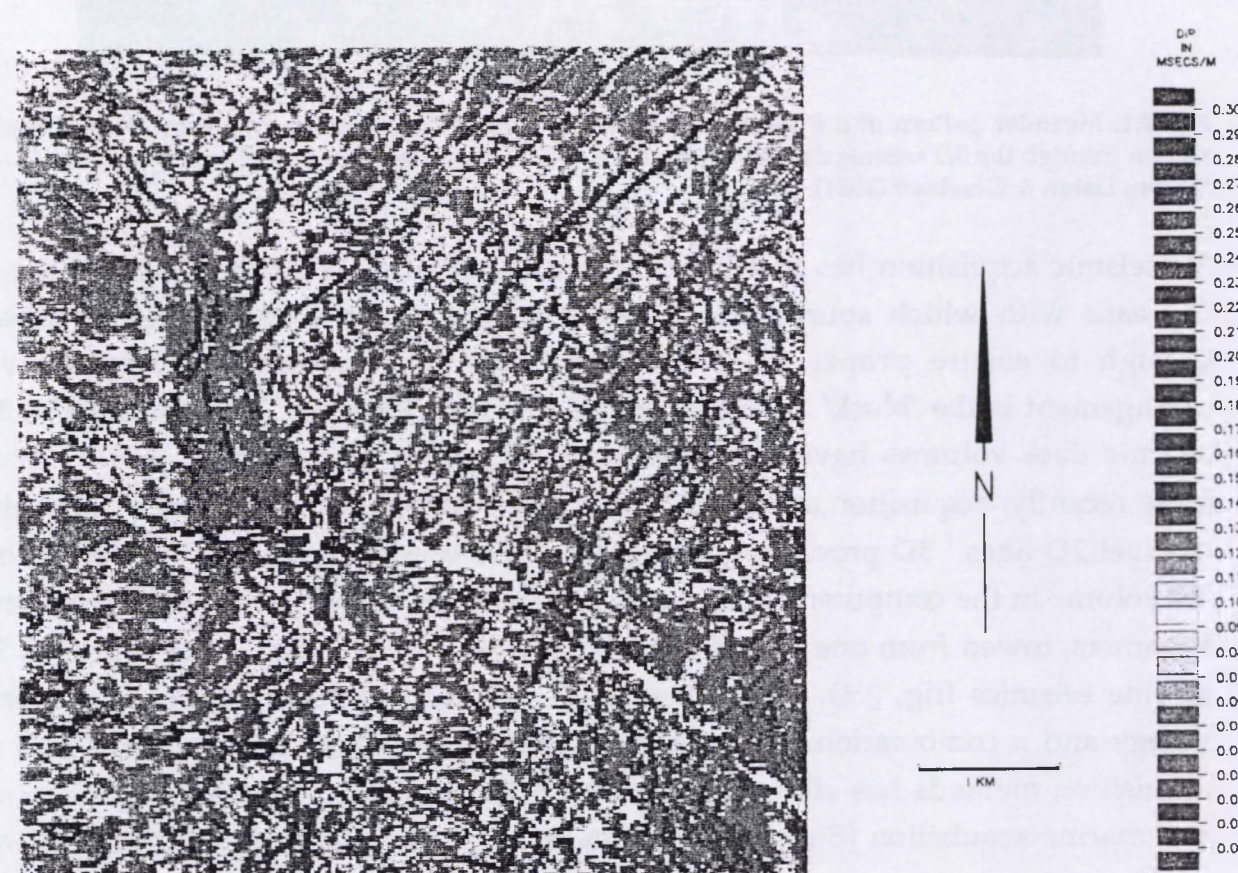


Fig. 2.2b. Dip map of the same reflector as in fig. 2.2a. Dips were calculated at each node of the grid by combination of gradients over two neighbours in each of the four directions. Darkest shade indicates steepest dip. Faults having throws of as little as 4ms two way time can still be interpreted. While fig. 2.2a. shows only the trend of these small faults, their precise location and en-échelon arrangement becomes clear on this map. White areas along the large E-W faults are without information. From Dalley *et al.* (1989).

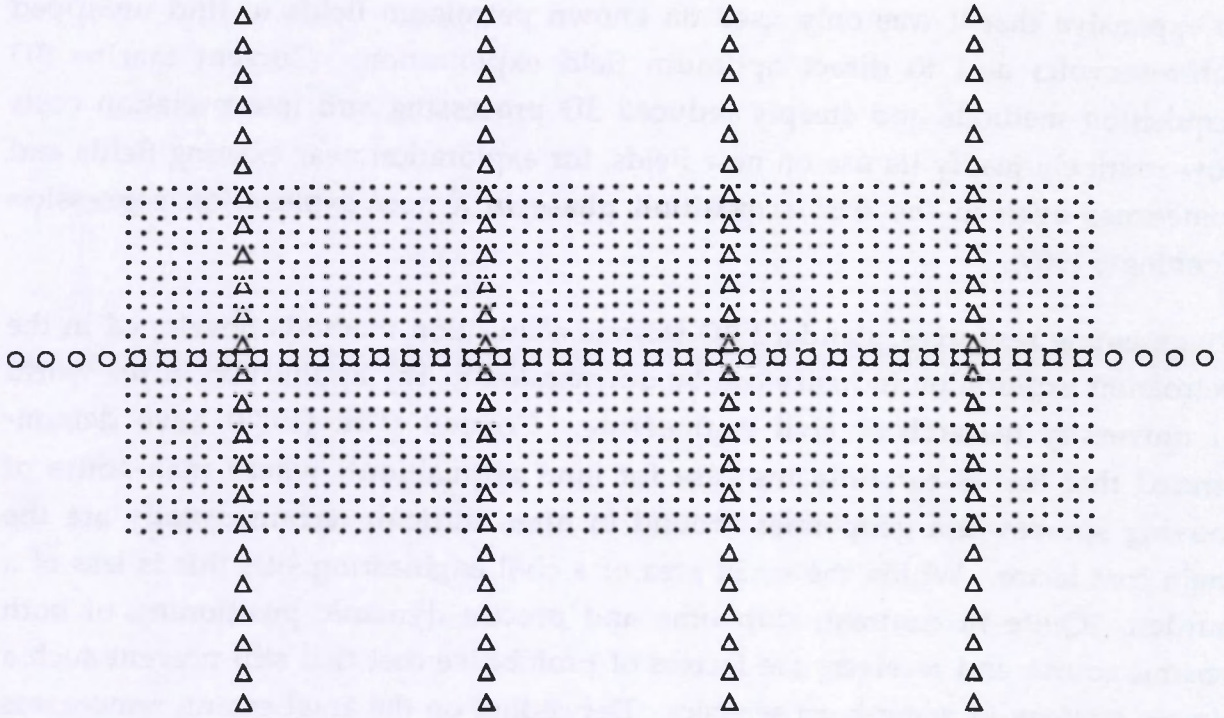


Fig. 2.3. "Block" layout for land 3D seismic acquisition. One line of geophone group centres (triangles) perpendicular to a line of sourcepoint locations (circles) result in data on Common Mid Points (dots) distributed on a regular grid. In petroleum exploration, four to eight geophone lines may be recording simultaneously. Sourcepoint interval and geophone group interval amount to 50-100m. In high resolution seismics they are only 2-10m apart. Modified from Sheriff & Geldart (1982) after Bukovics & Nooteboom (1990).

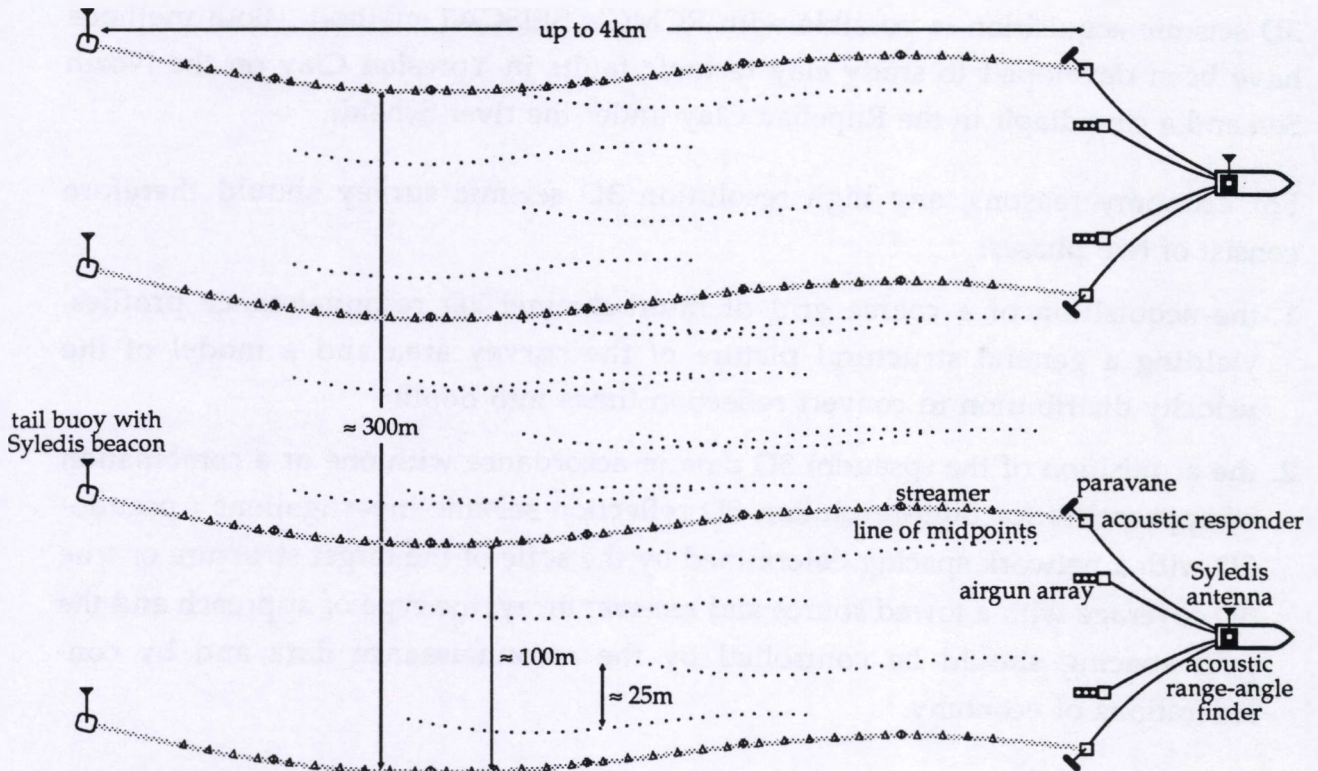


Fig. 2.4. Schematic layout in state-of-the-art marine 3D seismic acquisition. Two boats tow two airgun arrays and two streamers each. Streamers with 96 to 480 hydrophone groups (triangles) each, are pulled to the side of the ship's track by paravanes. Sources are popped sequentially, resulting in the simultaneous acquisition of 12 lines of midpoints (dots). Source and streamer head positions are measured relative to the boat with an acoustic range-angle finder. Streamer shape is determined with magnetic compasses (Φ s) along the streamer, in combination with the shape of the ship's track. Syledis beacons provide absolute positions of the vessels and the streamer tails. Modified from Sheriff & Geldart (1982) after Manin *et al.* (1988) and Bukovics & Nooteboom (1990).

so expensive that it was only used on known petroleum fields to find untapped sub-reservoirs and to direct optimum field exploitation. Current marine 3D acquisition methods and steeply reduced 3D processing and interpretation costs now routinely justify its use on new fields, for exploration near existing fields and sometimes even in the first acquisition phase in a new exploration concession (Jennings, 1989).

Given ample resources, standard 3D seismic acquisition methods developed in the petroleum exploration industry can be downscaled to any application in the world of university research or civil engineering. Corsmit *et al.* (1988) have demonstrated that this is certainly the case for land acquisition¹, where man-hours of moving sources and geophones around in often difficult terrain usually are the main cost factor. Within the small area of a civil engineering site, this is less of a burden. Quite in contrast, ship time and precise dynamic positioning of both seismic source and receivers are factors of prohibitive cost that still prevent such a simple strategy in water-born seismics. Depending on the areal extent, remoteness and required detail, we will argue that the most cost efficient solutions entail the substitution of a true 3D approach with a pseudo-3D one, one with an appropriately dense network of 2D profiles, in combination with computer aided 3D modelling. However, we will also demonstrate that water-born high resolution 3D seismic acquisition is possible with RCMG's SEISCAT method. Both methods have been developed to study clay tectonic faults in Ypresian Clay on the North Sea and a clay diapir in the Rupelian Clay under the river Scheldt.

For economy reasons, any high resolution 3D seismic survey should therefore consist of two phases:

1. the acquisition of a coarse grid of multi-channel 2D reconnaissance profiles, yielding a general structural picture of the survey area and a model of the velocity distribution to convert reflection times into depth;
2. the acquisition of the (pseudo) 3D data in accordance with one or a combination of approaches for high-resolution 3D reflection seismic investigations : pseudo-3D with a network spacing determined by the scale of the target structure or true 3D coverage with a towed source and receiver array; the type of approach and the grid spacing should be controlled by the reconnaissance data and by considerations of economy.

¹A prerequisite for high resolution land seismics is that source and geophones can be placed below the water table or in at least semi-consolidated material, ensuring sufficient ground coupling for the transmission of high frequencies.

2.1.1. Pseudo-3D reflection seismics and spatial aliasing

With a pseudo-3D survey, one aims to elucidate the 3D nature of geological structures with a dense network of 2D profiles. The network density should be entirely determined by the scale of the target structures :

a network of perpendicularly intersecting profiles with a constant maze width can only unambiguously reveal linear structures with a length and spacing of at least twice the maze width. Information on smaller or denser features may be spatially aliased, that is, small faults may appear as part of larger ones (fig. 2.5).

This is a fundamental limit to any discrete sampling method. 'Spatial aliasing' is well known with a different meaning and definition in seismology, the theory of seismic wave sampling (e.g. Sheriff & Geldart, 1982). 'Spatial aliasing' is also an important phenomenon in the interpretation and correlation of structures on continuous reflection seismic profiles, but the expression is frequently used in this field (e.g. Tearpock & Bischke, 1991) without a proper understanding, for lack of a formal definition such as the one given above. Brede & Thomas (1986) and Freeman *et al.* (1990) loosely described it for a unidirectional network of parallel profiles, apparently unaware that even the longest fault traces can not be pinpointed if they run more or less parallel to and between the profiles. Worse, Brede & Thomas (1986) discard the cross-secting control they actually have¹. Concerning the interpretation of isolated faults with a relatively small throw, O'Brien (1988) noted that "the thorny question remains as to which faults should be excluded from the map. There is no objective solution to this conundrum; the prevailing company or manager's preference is the main arbiter, although a set of guide-lines could be formulated." As such guide-lines have not been published yet, our definition may provide an objective one.

Pseudo-3D surveys are the obvious choice when the target structures have considerable lateral extension (e.g. faults, buried erosion scarps, the internal structure of a sandbank) and when cost-effectiveness is of major concern. If the maze width of a 2D network is chosen on the basis of reconnaissance profiles, so that the network will reveal most of the linear structures more or less unambiguously, it can rightly be named a pseudo-3D network. Such a network can

¹These authors only use dip sections and discard strike sections for they "tend to be confused because of a large amount of sideswipe" (which 2D migration cannot remove). The LANDMARK (Brede & Thomas, 1986) and FAPS (Freeman *et al.*, 1990) interactive fault mapping computer systems are evaluated in §3.3.

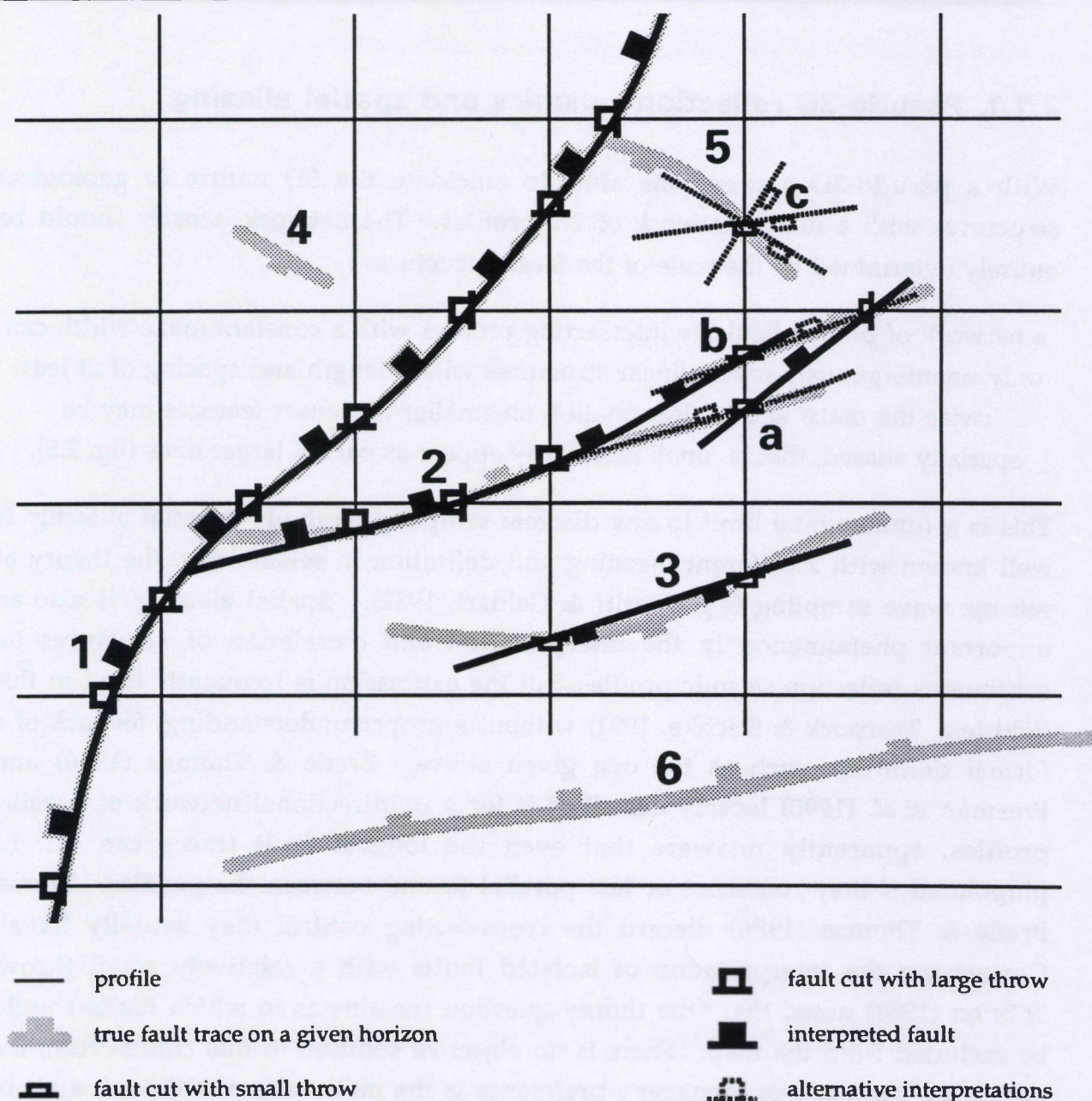


Fig. 2.5. Spatial aliasing in a pseudo 3D seismic network. The network consists of two perpendicular sets of parallel seismic profiles. A given horizon on the profiles intersects faults at fault cuts. The fault strike cannot be measured on a 2D profile. The interpretation of faults therefore comes down to the correlation of fault cuts guided by two rules of thumb. First, tectonic faults are generally quite straight, and secondly, the displacement along a fault trace varies only gradually, or at least systematically from one seismic line to the next (Barnett *et al.*, 1987). A large fault (1) crosses a number of profiles and is therefore easy to correlate. Fault 2 is also quite obvious, apart from its termination to the right. Either fault cut a or b may be the true continuation of fault 2: they have equal throw in the same direction, and both cuts line up with the rest of fault 2. The smaller fault through b may therefore incorrectly appear as, or *alias* part of a big fault. In general, a network of perpendicularly intersecting profiles with a constant maze width can only unambiguously reveal linear structures with a length and spacing of at least twice the maze width (this is an expression of the sampling theorem in a geostructural context). This network for instance still discloses fault 3, but not faults 4 and 5. Fault 4 is too small, does not cross any of the profiles and is therefore not detected in this survey. Fault cut c cannot be correlated to any other, so that it may be regarded as structural "noise", and not be used to trace a fault. With additional information on the fault cut positions and throws on other horizons above or below the horizon considered here, some of these ambiguities might still be resolved (Freeman *et al.*, 1990). The long fault 6 does not intersect any of the profiles. It would therefore be invisible in a unidirectional survey and only appear as a monocline.

yield a coherent 3D structural model containing about as much information as would have been extracted from true 3D acquisition, but at a far lower cost. Standard 2D acquisition methods can then be combined with efficient processing, interpretation and structural modelling.

Two disclaimers should be added to the above assertions. A pseudo-3D survey cannot reveal the exact location of singular points, such as fault tips or fault intersections. Moreover, true 3D acquisition and processing are irreplaceable in the presence of dips larger than about 5° and close folds (Sheriff & Geldart, 1982). Fortunately, the post-Palaeozoic cover rarely dips that steeply in the Southern Bight of the North Sea.

For example, detectable clay tectonic faults in the North Hinder area are 50-500 m (or 300 m on average) apart along earlier NW/SE seismic profiles, and they are believed to have hectometric or larger lengths. A network with a line spacing of 50 m should therefore suffice. The precision of standard absolute positioning systems with land based stations¹ is sufficient to ensure both proper navigation along the network, and reliable positions of the source-receiver tow. Dips are very small. The steepest apparent dip in fig. 2.10 for instance, amounts to no more than 3° , and that is a value for the 'highly' tilted blocks in the deformation zone at the right of that figure, where a reliable identification of reflections around the network is not possible anyway. Basically, acquisition can be carried out in the sole analog mode if necessary, as a structural model can be constructed by surface fitting on digitized interpreted reflectors. However, digital acquisition and processing has become commonplace as a tool for signal/noise improvement, leading to better interpretations, and for the geophysical analysis of subsurface rock mechanical properties.

As the field of pseudo-3D applications covers the whole near-shore environment with conventional land-based positioning systems (§2.2.2) and also the more remote off-shore environment where positioning could take place with GPS (§2.2.3) in the future, it is of particular significance for research in small scale geology and the geotechnical sector. We will reveal its potential through the study of clay diagenetic deformation at various scales.

Throughout this chapter, three scales of structures and seismic operations will be distinguished, each entailing specific acquisition strategies and positioning requirements. A 'large scale' survey concentrates only on structures that have an exten-

¹ Trisponder and Syledis systems have an accuracy of 3-5 m nearshore (on the North Sea up to some 50 km from the coastline).

sion measured in kilometres, such as a sag fault in the North Hinder zone. 'Medium scale' structures, such as clay tectonic faults, have hectometric dimensions and separation, while decametric features, e.g. the Scheldt clay diapir, are studied in a 'small scale' operation. Evidently, 'scale' here only applies to the dimensions of the investigated structures, and not to the cost or complexity of the operations. At each of these scales, 'high-resolution' seismics should not be confounded with subbottom profiling. 'High-resolution' will be taken to indicate peak source energy at frequencies between 200 and 2000 Hz, with a penetration ranging between 1 s and 100 ms respectively. It is also known as 'shallow' or 'profiling' seismics (Sheriff & Geldart, 1982). With such frequency contents, two reflectors that are between 2.5 and 0.5 m apart can still be distinguished.

2.1.2. 3D reflection seismics

In principle, pseudo-3D seismic methods also apply to remote off-shore surveys, where the grid spacing is larger than the order of magnitude of the dominant seismic wavelength. When the grid spacing comes in the range of the dominant seismic wavelength, we enter the domain of true 3D practice, where interpolation and surface fitting on selected horizons can be replaced by binning and true 3D data block processing and interpretation. This however requires full digital multi-channel data acquisition. In addition, as the data volume of a 3D seismic survey is an order of magnitude larger than that of a pseudo-3D network, its complete structural interpretation is not possible without the support of powerful graphical computers and sophisticated interpretation software.

The precise positioning of source and receiver is of paramount importance in any venture into high-resolution 3D work, and forms a point of major attention in this chapter. It is not only of importance for building correct CMP gathers, but also for observing adequate sampling densities. Quite formally, seismic processing can only be done precisely for the full frequency content, if at least four sample points are available per Fresnel zone at the maximum frequency (Newman, 1989). The (first) Fresnel zone (Sheriff & Geldart, 1982) is that part of a reflector which most of the reflected energy comes from. It is held to be a measure of the horizontal resolution of reflection seismics¹. The Fresnel zone can be calculated with

¹i.e. of unmigrated profiles or 3D data. With Kirchhoff migration, the lateral resolution Δx can become (Safar, 1985) $\Delta x \approx 1.4\lambda z_f / (2N\Delta x_s)$, in which $2N$ is the number of receivers and Δx_s their spacing, and z_f is the 'focal length' of the synthetic focussed array. z_f and consequently Δx can be chosen arbitrarily, and is only limited by the cost of computing and the accuracy of the applied velocity distribution.

$$R_1 = 1/2 V \sqrt{t/f}$$

where R_1 is the radius of the first Fresnel zone, f the frequency, V the average velocity and t the arrival time. For example, if $V_{min} = 1600$ m/s (a common value for clayey seabed sediments), $t = 40$ ms (a depth of about 30 m, common in the Belgian sector of the North Sea) and $f = 400$ Hz, then $R_1 = 8$ m. This strictly means that a sample spacing of 2 m should be required for imaging the sea-floor precisely in 3D practice. *A fortiori*, dynamic positioning of both source and receivers should be even more precise. This little exercise crudely states the major problem in high-resolution 3D. We will either have to observe this criterion - in this case we will talk of 3D seismic practice *s.s.* - or to ignore it and to have recourse to the acceptable surrogate practice of pseudo 3D, or simply 2D practice used for building 3D models.

In the case of towed arrays, the major problem is how to achieve the proper bin density, i.e. with bin sizes of for instance 6 m. Achieving an in-line reflection point spacing of 6 m is not a major problem with high-resolution seismic sources towed at a reasonably low speed: at a towing speed of three knots, this spacing is achieved with a shooting interval of 4 s, a shot frequency which can easily be sustained in high-resolution practice with a sparker or 0.25 l watergun.

The major problem is to achieve a similar cross-line density. Different solutions based on existing practice have been taken into consideration:

1. streamer feathering by sailing across a current (if any): is not significant with the short streamers, required for keeping offsets small in shallow work;
2. sailing parallel tracks at the required distance: a difficult navigational problem and heavily ship-time consuming;
3. dual or multiple streamer towing: practicable but generally requires a vessel specially fitted with towing booms and the associated hardware;
4. dual or multiple sources in a transverse array, sequentially fired: requires booms or paravanes; as sources are towed closer to the vessel, a wide lateral offset is more difficult to achieve;
5. multiple streamer towing with two laterally offset guns, which would broaden the width of the coverage: attractive but cumulates the operational problems of the two aforementioned approaches.
6. single or multiple streamer towing from two vessels, sailing next to each other at a fixed distance, with one or two sources.

The first two options are considered technically or economically not feasible for high-resolution true 3D practice. The other options are technically practicable if the hardware requirements are fulfilled, which is not that obvious in geotechnical surveys where often non-standard seismic vessels have to be used. Dual vessel operations (option 6) however may be excluded due to propeller noise effects.

Another possible approach involves an array of single- or multichannel streamers, towed behind a single source bearing vessel. The streamers would necessarily be very closely spaced, with an interval in the metre range. Because this approach looked attractive for small scale surveys, it was fully and successfully developed into the SEISCAT acquisition system with a 12 streamer array (§2.3.3), and tested on the small clay diapir under the river Scheldt. SEISCAT relies on a shore-based laser-ranging theodolite for precise dynamic positioning. Any high-resolution 3D survey to be carried out far away from land stations however entails the use of an acoustic relative positioning system with local beacons on the sea bottom.

2.2. Positioning systems

Each site and geostructural problem not only requires a different methodological approach but also a specific positioning strategy. Considering the critical role of positioning in (pseudo) 3D practice and the importance of the selection of a positioning approach which is not only adapted to the structural scale of local geology and required detail, but also to the site characteristics and economical constraints, a number of positioning system types have been reviewed from the latest manufacturers brochures and manuals. A discussion of this analysis is resumed below.

Three main groups of positioning methods can be taken into consideration for high-resolution 3D work, on the basis of the carrier wave they use. Systems like the TRISPONDER, SYLEDIS and GPS essentially rely on 100 MHz - 10 GHz radio waves, auto-tracking laser-ranging devices rely on infrared light, while hydro-acoustic methods use sound waves. Their basic features are discussed below and are also resumed in an itemized table (fig. 2.6). Selection criteria are not only the scale of operation or the level of required structural detail, but also site conditions such as distance to shore and water depth.

positioning systems	method	position information	precision / range	homogeneity	update interval	land station	subsurface positioning	duration of setup, calibration and recovery	integrated with acquisition
hydroacoustic + ultra-short baseline (pinger mode)	acoustic	multiple targets x,y,z (depth sensor)	$\pm 2\%$ / ~water-depth	low	1-2 s	no	deep	hours	yes
hydroacoustic + long baseline (transponder mode)	acoustic	multiple targets x,y,z	$\pm 1\%$ / ~baseline	medium	10 s	no	shallow + deep	1-2 days	yes
Trisponder & Micro-Fix	range-range, ~10 GHz	range, range or x,y	3-10m / horizon	low	10-1 s	yes (2-3 beacons)	no	hours	yes (not if range only)
Syledis (*)	pseudo-range, ~100MHz	x,y	2-6m / North Sea	high	1 s	strictly, yes, but installed	no	minutes	yes
differential GPS	satellite, ~ 1 GHz	x,y,z	5-10m / global	high	10 s (expected)	yes (1 reference)	no	minutes (if standard)	yes
laser tracking	IR laser theodolite	x,y,z	0.02-0.1m / 1-5km	high	0.4 - 0.1 s	yes	no	hours	yes

Fig. 2.6. Overview of marine, high precision, dynamic positioning systems.

(*) characteristics as installed and used by RCMG on R.V. Belgica.

2.2.1. Hydro-acoustic Positioning Systems

For precise underwater positioning of e.g. a (deep-towed) seismic source-receiver array, there is no alternative to acoustic methods.

Hydro-acoustic positioning systems are generally discussed in terms of the length of their baseline, which can either be 'long', 'short' or 'ultra-short'. The baseline is a line between two reference beacons. Short baseline and ultra-short baseline systems utilize shipboard hydrophone arrays to determine the underwater transponder (see below) positions relative to the vessel position. Long baseline systems operate in the opposite mode where a single shipboard transducer communicates to a fixed subsurface transponder array and tracks moving subsurface transponders relative to these beacons.

In general, static positioning precision improves and range increases proportionally with the baseline length (cfr. stereoscopic vision). However, system set-up and calibration of large baseline systems tend to become more complex and time consuming as well. For static or semi-static measurements, these systems generally have a sufficiently high precision of 1 m or less within their range of hundreds to thousands of metres. Due to the relatively slow propagation of sound in water however, their dynamic precision is rather poor.

Another weak point of acoustic methods is their sensitivity to local sound velocity variations. In fact, the distribution of this parameter along the trajectories needs to be known precisely, especially for deep water and long baseline applications. The resolution of acoustic positioning is also determined by the sound wavelength used: the shorter the wavelength, the better the resolution, but also the lower the immunity to noise and attenuation.

In contrast with all other methods, most of the available hydro-acoustic systems allow simultaneous tracking of multiple subsurface targets. In some high resolution 3D applications advantage might be taken of this capability, with a combination of hydro-acoustic and other positioning methods.

2.2.1.1. Ultra-short Baseline Systems

The acoustic transmitter-receiver elements are housed in a single, compact transducer unit or 'interrogator'. The elements are arranged at the vertices of an equilateral triangle. Each element is spaced less than half a wavelength from each of the other elements in the array. When a sound wave impinges upon the array,

the phase differences between the elements in the array provide the information required to calculate a three-dimensional vector from the array to the sound source.

Three types of sound sources are used : pingers, transponders and responders.

A *pinger* emits a sound pulse at a predetermined rate. The interrogator receives the pulse, so that bearing, inclination and range can be determined. The precision of an ultra-short baseline system in pinger mode is good for deep targets at a horizontal range of less than twice the depth, but it degrades rapidly for more shallow targets. The advantage of using a pinger mode is its dynamic performance, since the three-dimensional position vector is calculated independently from travel time.

Transponders only emit a pulse when a signal from the interrogator reaches them. *Responders* are activated with an electric signal through cable connections. Acoustic ultra-short baseline positioning in transponder mode offers good static precision in any direction, but this asset degrades in dynamic positioning. The most advanced systems can simultaneously track multiple responders/transponders. Recent technology introduced an auto-tracking narrow beam instead of a fixed wide beam interrogator. Such a system has a high precision in any direction and water depth, together with a good dynamic response due to adequate software handling of dynamic shifts and multipath signals in shallow water. However, it needs to be built into the hull of the ship and is therefore not available for research purposes. Some petroleum exploration companies already use such systems to track the head of streamers and seismic source arrays up to several hundred metres behind the vessel, supplementing streamer compass data and tail buoy positions.

The main advantage of ultra-short baseline systems in general is their compactness and ease of calibration and deployment.

2.2.1.2. Short Baseline Systems

In a short baseline system, three hydrophones are attached on the hull of the vessel, thus forming a fixed triangle with sides in the 10 m range. Positions are calculated in accordance with the same principles as in ultra-short baseline systems, but the stretch and precision prove to be better. However, installation and calibration of the hydrophone array are so time-consuming that short baseline

positioning should be considered only if the array can be a more or less permanent part of the ship.

2.2.1.3. Long Baseline Systems

In a long baseline system, a large triangular array of at least three separate and recoverable seabottom beacons needs to be installed on the site of interest. Deployment, calibration and recovery of these baselines alone can thus take days, the major drawback of these systems. The employed frequency band can be in the 100 kHz instead of the 10 kHz range, thus yielding a theoretically higher precision than the short baseline systems.

In a typical application, the seismic source would be equipped with a ruggedized selective HF hydrophone. Mini-responders could be built in in the streamer(s). Simultaneous tracking of these targets together with the reference baseline beacons could then be carried out by broadcasting a pulse from the interrogator, which would also receive the answers sent by the responders at different frequency bands.

Static positioning in this procedure can be remarkably precise, with errors in the cm range. Dynamically, the precision easily degrades to 1 m or more due to the long distances involved. In order to correct for local velocity variations, prior sound velocity logging is advisable, for the baseline is situated at the base of the water column and again, the trajectories involved tend to be relatively long. Dynamic response tends to be rather slow for the same reasons.

2.2.2. Radiopositioning

Radiopositioning systems provide 2D coordinates of mobile stations through UHF communication with fixed beacons. These are all 'line-of-sight' systems that cannot work beyond the horizon. Basically, these systems operate in either of two main modes (fig. 2.7).

2.2.2.1. Range-range Method

In range-range mode, the mobile interrogates two or more transponder beacons. These devices emit a signal upon receipt of the interrogating signal, comprising a sync (a time stamp) and a code (identifying the beacon). The elapsed time intervals are converted to ranges. Iso-range lines are circles that only intersect perpendicularly on semi-circular arcs connecting the beacons. These arcs define zones of highest precision. Away from the arcs however, precision quickly degrades.

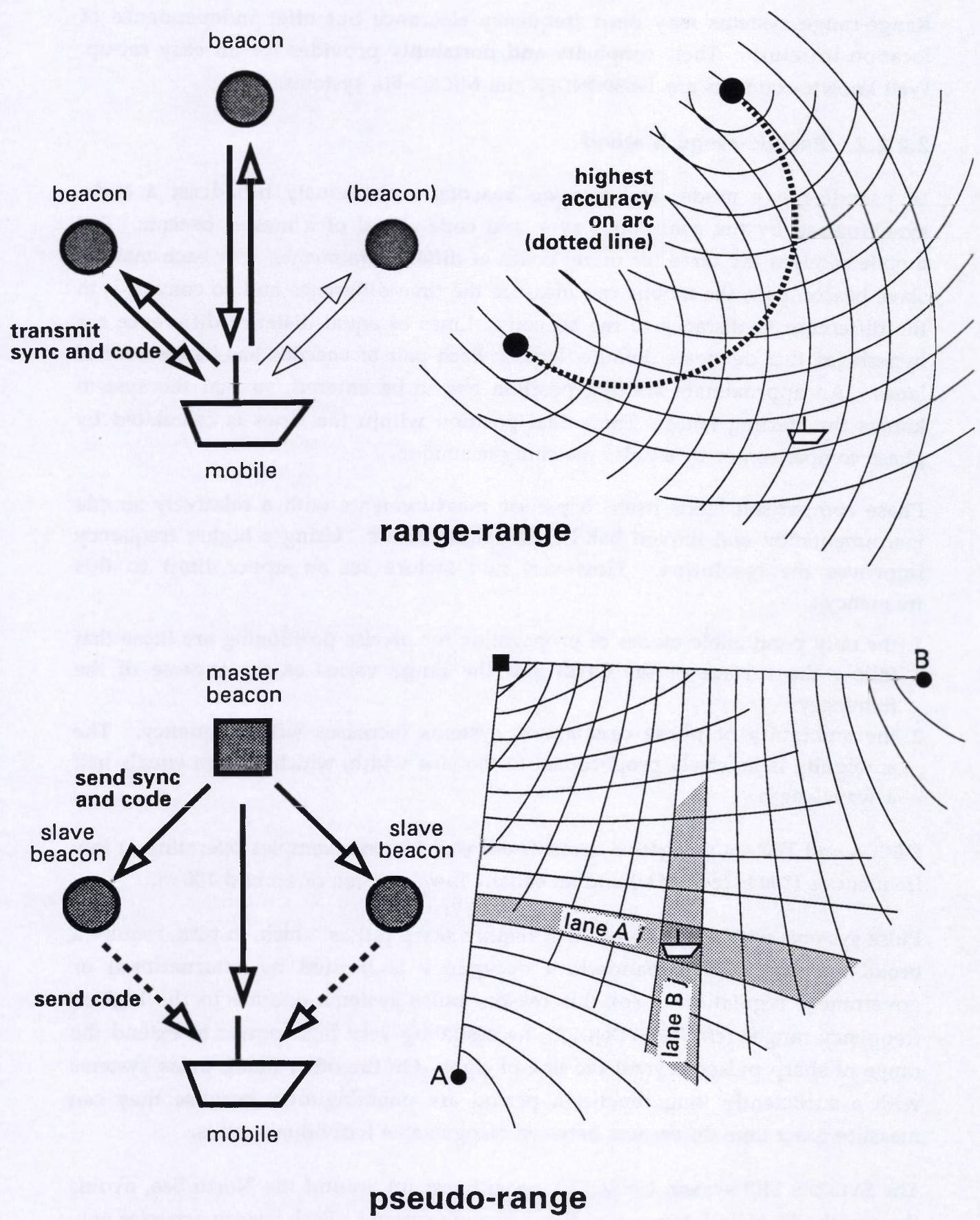


Fig. 2.7. Main radiopositioning methods.

Range-range systems may need frequency clearance but offer independence of location in return. Their simplicity and portability provides for an easy set-up. Well known examples are TRISPONDER and MICRO-FIX systems.

2.2.2.2. Pseudo-range Method

In pseudo-range mode, at least two beacons continuously broadcast a code, synchronised by the continuous sync and code signal of a master beacon. The mobile receives the three (or more) codes at different moments. For each master-slave beacon pair, the mobile can measure the time difference and so convert it to the difference in distance to the beacons. Lines of equal distance difference are hyperbolae that delineate definite 'lanes'. Each pair of beacons has its own set of lanes. An approximate starting position has to be entered, so that the system knows the starting lanes. The actual position within the lanes is calculated by phase comparison or by a pulse matching technique.

Phase comparison lends itself to precise measurements with a relatively simple instrumentation and limited bandwidth requirements. Using a higher frequency improves the resolution. However, two factors set an upper limit to this frequency :

1. the only permissible modes of propagation for precise positioning are those that follow the surface of the Earth and the range varies as the inverse of the frequency;
2. the ambiguity of phase comparison systems increases with frequency. The ambiguity is inversely proportional to the lane width, which in turn equals half a wavelength.

DECCA and TORAN navigation systems are well known examples operating at low frequencies (100 kHz-1 MHz) and an equally low precision of around 100 m.

Pulse systems with a good resolution require sharp pulses which, in turn, require a broad spectrum. The bandwidth occupancy is limited by international or government regulations. For this reason, pulse systems operate in the highest frequency ranges (cfr. TRISPONDER), necessitating very high power to extend the range of sharp pulses beyond the line of sight. On the other hand, pulse systems with a sufficiently long repetition period are unambiguous, because they can measure exact time differences between recognizable individual pulses.

The SYLEDIS SR3 system (SERCEL), recently set up around the North Sea, avoids the drawbacks of both types of radiopositioning systems. Each beacon occupies only a narrow (2 MHz) frequency band in the 406 to 448 MHz range. The signal is

constructed by modulation of the carrier with a repetitive sequence of 127 pseudo-random elements, 66.66 microseconds long. The auto-correlation of the pseudo-random sequence is -1 over the whole signal except at lag zero where it is +127, thus effectively yielding a sharp pulse. This pulse compression strongly increases the amount of energy available for each measurement and extends the range well beyond the line of sight for moderate peak powers.

The lane width of SYLEDIS is equal to half the modulation period, multiplied with the velocity of light, or 10 km. The ambiguity is therefore equivalent with DECCA, but its precision is far better (2-6 m), even with its high update rate. The system has been successfully integrated in the RCMG marine seismic digital acquisition system, and relied upon several times already for pseudo-3D purposes.

2.2.3. Differential GPS

The NAVSTAR Global Positioning System is a satellite navigation system designed and being deployed by the US Department of Defence. In 1990, 12 high orbit satellites allowed 24-hour two-dimensional global positioning with a dynamic precision of 20-40 m. The full constellation of 24 satellites will allow global three-dimensional dynamic positioning by 1992. Each of these satellites broadcasts a digital signal every 10 s. Direct measurement of pseudo-ranges to at least four satellites is required to solve for four unknowns, namely the 3D coordinates of the receiver and its clock error. The US DoD intends to restrict most civilian users through so-called 'Selective Availability' to an instantaneous positioning capability of 100 m.

With differential GPS, fixed groundstations 1000-2000 km apart may relay instantaneous corrections through geo-stationary communication satellites to GPS receivers. Thus, a dynamic precision of 3-10 m is expected to be attainable, even under SA. The satellite signal consists of two accessible carrier frequencies at 1575.42 MHz and 1227.60 MHz, which allow also carrier frequency phase measurements with dm to cm dynamic precisions. However, current technology can resolve carrier phase ambiguities with postprocessing only.

By 1992-93, when the complete GPS satellite network and GLONASS, its Soviet equivalent, will be operational, receivers costing \$5-10K are expected to revolutionize all positioning methods. This technological evolution clearly deserves further attention regarding world-wide application of position sensitive 3D seismic surveying.

2.2.4. Laser Auto-tracking

Laser auto-tracking is the only currently available positioning technology able to deliver dm to cm precisions in combination with sub-second update intervals. It can do so within 5 km distance of a shore based tripod onto which the laser auto-tracking apparatus is mounted. After the device has been manually pointed to the reflective prism crown on the target, it can remain electronically locked onto the target, even when the latter moves at speeds of 4 m/s at a distance of 100 m ($2^\circ/\text{s}$) or takes a turn. The actual range of the infra-red GaAs laser is limited by laser power, visibility and the number of prisms used. In the vicinity of a geodetic reference point, absolute 3D coordinates may be directly measured, and telemetrically transmitted in real time to the control vehicle or vessel.

2.2.5. Practice

For the study of clay tectonic deformations, an area just north of the North Hinder Bank was selected (§2.4.1). The best positioning capacities offered in this area are those of the SYLEDIS chain of beacons, based on the Belgian coast. At the considered range (more than 50 km), the positioning *precision* amounts to some 3-6 m. This precision only refers to the absolute position of the Syledis antenna on top of the vessel's bridge. The position *accuracies* of the source (if towed far astern) and especially of the receivers, towed in a streamer, are necessarily larger than the 3 m precision. Even with a relatively short streamer, such as the streamer with an active section of 100 m and a tow lead of 50 to 100 m used by RCMG, feathering due to a cross current can yield absolute positioning errors of the tail group larger than 20 m. Such numbers are clearly unacceptable for true 3D acquisition, especially in high-resolution work focussing on shallow targets.

The hydrocarbon exploration industry coping with this problem does not only enjoy a larger tolerance thanks to the larger minimal wavelengths, but also pins its faith to a wide range of auxiliary devices, such as acoustic range-angle devices, magnetic compasses spaced along the streamer at regular intervals, angular observations of a prism or a radar reflector on a tail buoy or absolute positioning of the tail buoy, for instance using SYLEDIS beacons (e.g. Manin *et al.*, 1988; fig. 2.4). Hydro-acoustic relative positioning of the source and the streamer head and tail may be workable in some high-resolution surveys. Magnetic compasses need to be built into the streamer. Tail buoys should be avoided as they form a potential

source of high-frequent towing noise, especially in swell conditions. They also would impede the proper functioning of the depth levellers.

Therefore, unless one of these auxiliary positioning devices is available, only pseudo-3D surveys can be carried out at open sea. Such a procedure was applied at the North Hinder site, where two grids of parallel lines with a nominal spacing of 50 and 500 m respectively were sailed, in order to test the potential of the pseudo-3D method on medium and large scale structures. True 3D water-borne seismic acquisition was attempted at the smallest scale, with an ATLAS POLARTRACK laser auto-tracking positioning system, fully integrated in the SEISCAT acquisition system (§2.3.3). The latter approach is only possible for local work close to the coast or a riverside.

Aside from the strict positioning problem, attention has also to be paid to the *navigation* problem, and more precisely the vessels capacity of tracking parallel lines as regularly as possible. Irregular line tracking leaves parts of a 3D survey without data coverage, and the sound interpretation of a pseudo-3D network demands a more or less equal line spacing (§2.1.1). Navigational regularity not only depends on the helmsman's skill but also on the available positioning auxiliaries and environmental factors (tidal currents, wind, swell).

Lastly, accuracy in dynamic positioning is also a matter of *synchronization*. For digital acquisition, this is not so much of problem, since the current antenna position is written to tape simultaneously with the seismic data. At RCMG, most interpretation of data acquired with *RV Belgica* is still served with analog recordings of the first channel signal (in multi-channel acquisition). The absolute position of a structural feature on analog profiles depends on its position relative to *fix lines*, i.e. vertical lines at (ideally) regular intervals. On most RCMG surveys, the clock of the digital acquisition unit is different from the clock that drives the positioning. If the latter clock is late by a constant 10 s, and the vessels velocity is 2 m/s, the erroneous but constant offset of 20 m can be taken into account during the conversion of digitizer coordinates to world coordinates (§3.5.3). If both clocks drift away from each other, the error becomes less predictable. The drift between two 'real time' clocks can amount to several seconds over a week. A more serious problem resided in the way fix positions were taken until recently. On the R.V. *Belgica*, positions are shown on a monitor that refreshes navigation information every 15 or 20 s, with a drift of several seconds every hour. On this monitor, the time is shown rounded to whole minutes. The first screen that showed the right time was therefore erroneously assumed to be refreshed at the exact interval, and it

was at that moment that the fix line was written on the analog recording. Actually, fix lines were from 1 s up to 15 or 20 s late, relative to the coordinates written to file by ODAS¹. Such a synchronization error introduced supplementary positioning errors of up to 30 or 40 m. The relative offset between two adjacent profiles sailed in opposite directions could even be twice as large, severely distorting the interpretation of linear structures intersected by several consecutive profiles. It was only during the interpretation and correlation of clay tectonic faults on the first part of a pseudo-3D network that these serious errors showed up. They had gone unnoticed during all previous mapping based on widely spaced 2D networks. This experience made painfully clear that pseudo-3D seismics relies on exact synchronization as much as on the best possible precision of the positioning system.

2.3. Seismic acquisition system

The entire RCMG seismic acquisition, processing and interpretation system is depicted in fig. 2.8. Seismic sources and receivers may vary from survey to survey and are therefore described in some more detail below.

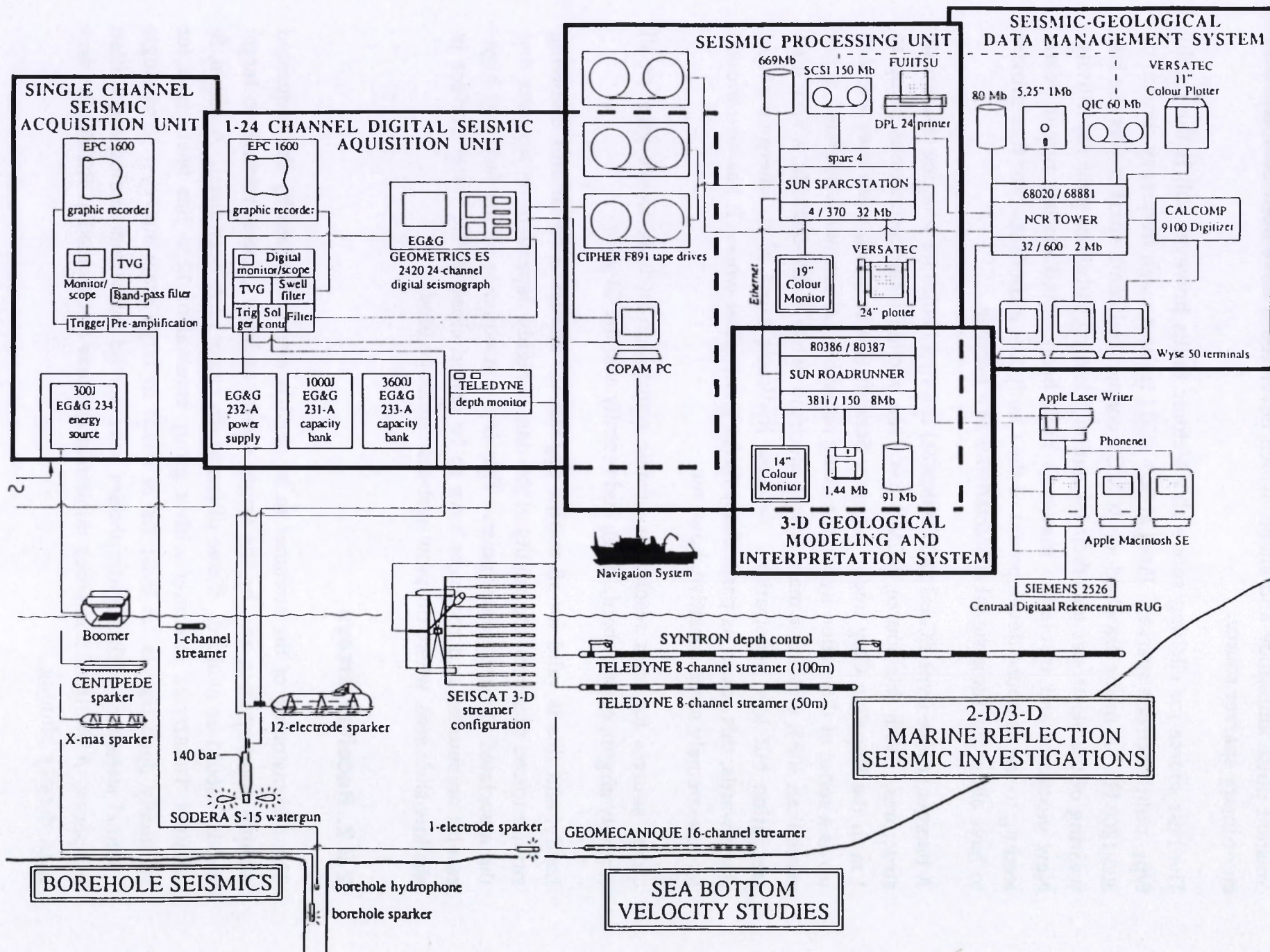
2.3.1. Seismic sources

The mean frequency content of the seismic sources determines both the smallest reflector interval that can be distinguished (§2.1.1), and the sample point spacing in truly orthodox 3D practice (§2.1.2). The preferred source for large scale high resolution structural studies is the 0.25 l SODERA watergun, with high pulse repetitivity. When towed at a depth of about 1.5 m, it has a mean frequency content of 100-700 Hz and a penetration of some 500 m.

A 0.25 l SODERA watergun can also be equipped with a special two-slit mouthpiece and directly suspended below a fender. The small immersion depth of only about 20 cm below the water surface results in constructive interference for the high-frequency peak of the watergun pulse with its 'ghost' reflection on the water surface, while low-frequency energy is lowered by destructive interference. The profiles thus acquired on small scale survey sites (see fig. 2.14) displayed the same structural detail as the multi-electrode sparker profiles, but with a virtually

¹Oceanographic Data Acquisition System, a real time data acquisition system developed for the collection of oceanographic, meteorological and hydrographic data aboard the oceanographic vessel *Belgica*.

Fig. 2.8. RCMG's high resolution 2D-3D seismic acquisition, processing, interpretation and modelling system.



constant pulse amplitude and shape, which never could have been obtained with an ordinary sparker source.

The best source for eliciting subtle clay tectonic faults however still is the comb-type multi-electrode sparker. Fired at 300-1000 J it has a mean frequency content of 300-1200 Hz. A major drawback of RCMG's commercial comb sparker was the fast wearing of the electrodes and their insulation, yielding pulses of poor repetitivity. New electrode and insulation materials have been tested during recent years, leading to the in-house development of the Centipede, a comb sparker that proved to have about the same signal characteristics as a boomer.

A boomer source (type EG&G 230 UNIBOOM) is a first choice for imaging small scale structures. With this source, RCMG has even elicited large concretions of up to 1 m in the Rupelian Clay under the river Scheldt (see further), where they showed up as a series of diffraction hyperbola along reflectors. A boomer is operated at not more than 300 J, yielding a main power spectrum between 200-5000 Hz, a very high resolution but low penetration. Because it directs most of its energy straight downwards, this source is particularly fit for short offset work. It has also proved to be extremely swell sensitive, however.

Other sources for high resolution seismic acquisition include sleeve gun, small capacity airgun, etc. (Trabant, 1984), and recently also the GI-gun.

Lastly, and this is valid for all marine approaches discussed so far and involving surface towed receivers, the quality of the data is highly dependent on sea state and the associated environmental noise. This is a consequence of the fact that high-resolution sources and receivers have to be towed close to the water surface in shallow shelf seas, where deeptow systems cannot be used.

2.3.2. Receiver arrays

The dimensioning of the streamer to be used is also controlled by the requested sample point spacing and by the target depth, as large offsets (relative to target depth) should be avoided. Three different streamers have been used. A 100 m, 8-channel TELEDYNE streamer with a group interval of 12 m has been used for relatively deep targets (at least 100 m deep) in large scale surveys. 6 m single channel streamers with 8 hydrophones have served numerous analog acquisition purposes. A swath of numerous ministreamers was constructed at RCMG for very high density binning.

2.3.3. SEISCAT

2.3.3.1. Platform

The shape of the clay diapir under the river Scheldt was already roughly known on the basis of a network of Uniboom profiles. Within the framework of a CEC sponsored project, RCMG developed the SEISCAT system to test the feasibility of very high resolution 3D seismic acquisition (Henriet *et al.*, 1992), and simultaneously to see whether such true 3D seismic acquisition could improve our knowledge of the internal structure of this clay diapir.

Water borne 3D seismics is a complex operation involving the installation of a generator, seismic sources and streamers, a full multichannel digital acquisition system, a positioning system and a compressor in case of watergun deployment. With some difficulties, all of this equipment can fit on a vessel as small as the *Parel II*, a 3x10 m survey boat of the local river authorities (Antwerpse Zeediensten) that was used for a seismic survey on the Scheldt river and canals, commissioned by the Ministry of Economic Affairs, Belgian Geological Survey. However, two practical limitations placed additional constraints on the design of a high-resolution 3D seismic acquisition system. Highly precise 3D positioning control on both source and receivers was only thought possible with a laser auto-tracking theodolite. Such a system cannot be used at open sea, because it requires a fixed position for set-up (§2.2.4). For the clay diapir, the Scheldt river banks were sufficiently nearby. The second limitation was the size of the Belgian oceanographic vessel *RV Belgica*, which impeded the approach involving systematic cross sailing over the river in front of a stationary receiver array. Instead, an array of parallelly towed ministreamers was designed, so that a high reflection point density and a small bin size could be achieved over the test site by sailing tracks parallel to the axis of the river bed.

RCMG's digital acquisition system is capable of running at 1 shot per second, which yields at a towing speed of 2 knots (1 m/s) a longitudinal reflection point spacing of 1 m, or, with dual channel streamers and 1 m group interval, only 0.5 m. The same point spacing can be achieved in the transverse direction with an array of parallelly towed receivers spaced 1 m.

2.3.3.2. System

The SEISCAT system (fig. 2.9) has been constructed around a modified Hobie Cat catamaran. The frame had a width of 8 m between the two floats, which were 6 m long. Two extension beams of 1.5 m length yielded a total tow width of 11 m, allowing a tow of 12 dual channel ministreamers at 1 m interval. A broader towing frame would probably not have been accepted by the *RV Belgica* and the Scheldt navigation authorities. However, broader towing frames are technically possible and may be more appropriate in other applications.

The connection between the floats consisted of Hobie Cat masts and tension cables. A mast 2 m high was mounted on one of the cross beams for carrying a reflector prism, that was automatically followed by an on-shore laser auto-tracking positioning system.

The seismic source was towed under the frame, close to the mast and the reflector prism. Two sources were used : a standard Uniboom source and a modified 0.25 l watergun with the two-slit mouthpiece, directly suspended under a fender.

The array of streamers was towed at a short offset behind the source, in order to get an optimal response of the shallowmost structures.

In view of the 3D acquisition, RCMG's EG&G model 2420 seismograph had been expanded to 24 channels. This system is capable of running at 1 shot per second, which yields at a towing speed of 2 knots (1 m/s) a longitudinal reflection point spacing of 1 m, or, with dual channel streamers and 1 m group interval, only 0.5 m. The same point spacing is achieved in the transverse direction with the streamer spacing of 1 m.

2.3.3.3. Navigation

The acquisition of a dense in-line coverage of reflection points (nominally at 0.5 m intervals) with the given source repetition rates, required a relatively low vessel speed relative to ground. On a river with high current velocities like the river Scheldt, this could only be achieved by sailing tracks against the current.

Turning the 45 m long vessel towing the SEISCAT frame after each profile was thought too difficult. It was consequently decided not to turn the *RV Belgica* until the current itself had reversed, but rather to make efficient use of the strong tidal current velocities: the *Belgica* sailed one track against the current with the

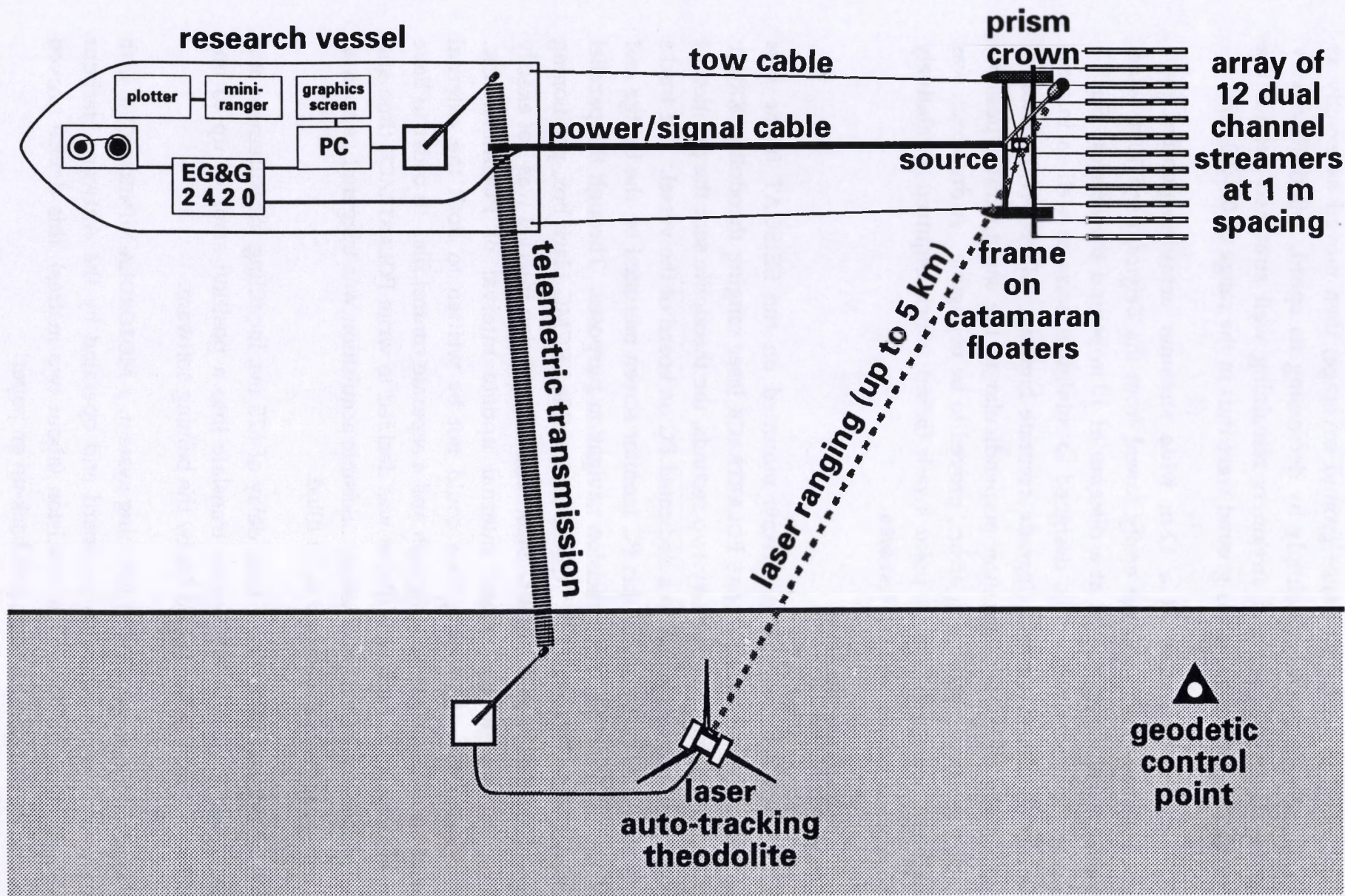


Fig. 2.9. SEISCAT, a system for high-resolution 3D seismic acquisition

necessary speed to achieve a dense ground coverage, then moved as exactly as possible to the next track and, simply by decreasing its speed, sailed effectively backwards, all towed gear and streamers remaining well stretched behind the vessel. Absolute velocities versus ground were thus in the range of 0.5-2.0 m/s.

The SEISCAT configuration of a 12 m wide streamer array suspended by a broadened catamaran frame, was easily towed from the *Belgica*, itself 10 m wide. The SEISCAT frame was towed at a distance of 10 m behind the *Belgica*. Such a source-receiver configuration was designed to minimize noise as well as internal relative movements that might degrade accurate binning. Moreover, rotation of the frame away from its orientation perpendicular to the sailing track, possibly introducing streamer positioning errors, proved to be negligible. A drawback was the relatively narrow reflection point swath (5.5m) which required a relatively large number of passes over the test area.

2.3.3.4. Positioning

The cylindrical set of reflector prisms mounted on the SEISCAT frame was automatically tracked by an ATLAS POLARTRACK laser ranging theodolite (KRUPP ATLAS ELEKTRONIK). About every two seconds, the theodolite sent the position of the prism crown by radio link to a dedicated PC on board of the vessel. The tracks were displayed in real time on this PC monitor screen mounted on the bridge and intensively used for the high-precision navigation purposes. Through the parallel printer port of the POLARTRACK PC and the modified RCMG black box, positioning data were transferred to the EG&G 2420. The transmission interval was not exactly constant due to the out-of-beat internal update interval of POLARTRACK. Unfortunately, the positioning data could not be written to both the external header of the EG&G-2420 seismograph and a separate control file. In order to have a complete header in each shot file, it was decided to write POLARTRACK time and 3D coordinates to the external header. Seismic acquisition was triggered as soon as the external header was detected to be filled.

The ATLAS POLARTRACK had a total delay of 675 ms, including measurement and transmission. Such a delay would translate into a position error of up to one metre if it were not compensated for by the binning software.

Apart from the laser-ranging positioning system, a MOTOROLA MINIRANGER with HP computer system was also on board and operated by the Antwerp Harbour Authorities. Despite its smaller precision (about two metres), this device proved very useful by providing a track plot back-up on paper.

2.4. Surveys

2.4.1. Pseudo-3D acquisition

De Batist (1989) has shown that clay tectonic deformation styles, as described on the basis of seismic reflection profiles, vary greatly within the outcrop zone of the Ypresian Formation in the Southern Bight of the North Sea (§1.4). One of the predominant styles consists of blocks with small relative vertical displacements (1-5 m), slightly folded or dipping in various directions, as in fig. 2.10. The profile in this figure was shot north of the North Hinder Bank, in the 'North Hinder zone' (fig. 1.1), which is interesting for several reasons. Some of the reflector endings show the puzzling 'inverse drag' (Henriet *et al.*, 1988; §1.4). Fault separation along SE-NW profiles amounts to a typical 300 m, within a range of 50-500 m. Smaller than average fault separations and larger than average throws can be seen where a large basement induced sag fault, part of the North Hinder deformation zone (De Batist, 1989), cuts through the Mesozoic and Cenozoic cover. Quaternary sand waves or banks are all but absent in this area, so that the analog profiles, free of velocity pull ups, can be directly interpreted and modelled.

A pseudo-3D seismic network in the North Hinder zone was designed to unveil the 3D nature of clay tectonic deformations, in conjunction with their possible sensitivity to tectonic stresses. The underlying sag fault therefore became the focus of a second, large scale network.

2.4.1.1. Large scale network: North Hinder sag fault

De Batist (1989) could track this fault's undulating fault trace over 8 km. The size of the sag fault structure justified a pseudo-3D approach with a profile spacing of 500 m. For this purpose, a grid of profiles has been shot during a 24 h fair weather period in the Belgica survey of 10-21 April 1989 (sector a in fig. 1.1; fig. 2.11). The seismic source used was SODERA's S15 watergun, towed 1.5 m below the water surface, and with a seismic penetration of about 1.0 s. The reflections have been detected with an 8-channel streamer having an active length of 100 m. The orientation of the grid and the sailing direction was severely constrained by the southeastern margin of the mid-Channel traffic separation system, in the vicinity of the North Hinder zone. Positioning and navigation has been carried out with

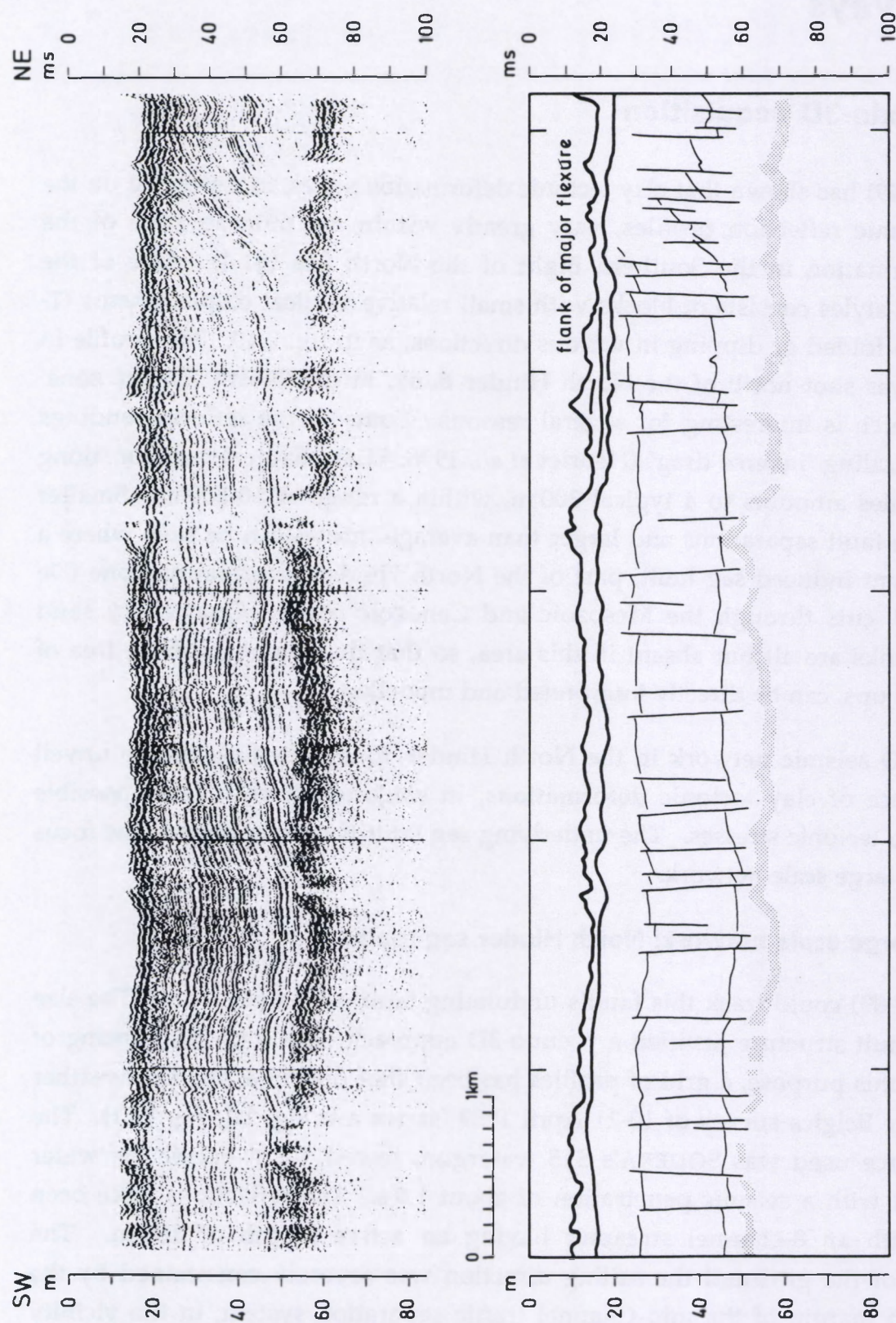


Fig. 2.10. Block faulting in the clayey Ieper Formation along a NW-SE profile in the North Hinder area. Notice "reversed drag" of reflector endings along some of the faults on the left, and more intense deformations on the right, induced by a major tectonic fault affecting the basement and all of the Tertiary cover (from Henri \acute{e} t *et al.*, 1988; see also fig. 2.11).

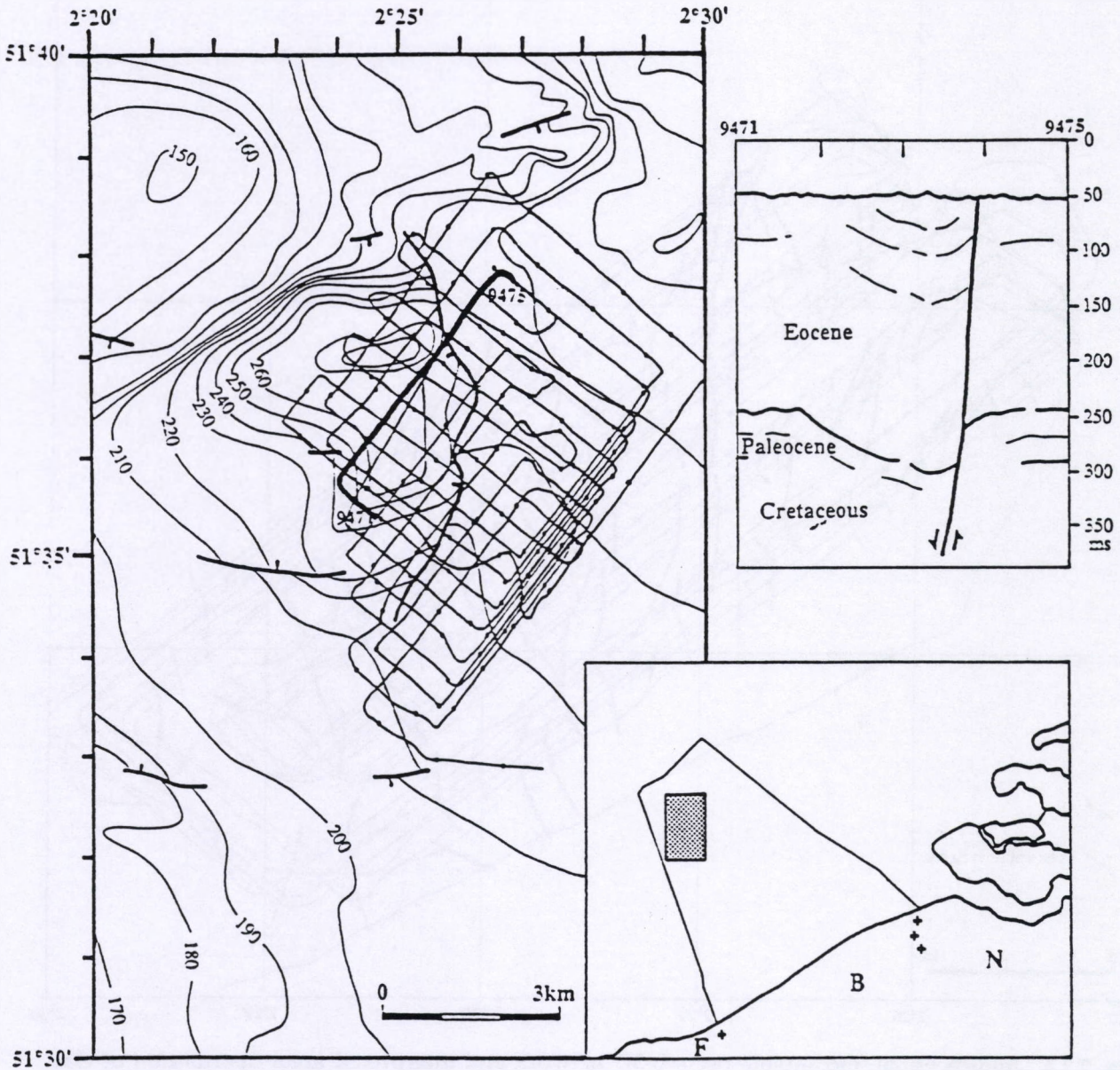


Fig. 2.11. Location of the sag fault in the North Hinder test area. Isobath map of the base of the Tertiary (after De Batist, 1989) with pseudo-3D structural reconnaissance grid. Interpreted line-drawing of a seismic section through the sag fault.

the SYLEDIS system, with positions directly written out in the extended header of each shot file. The claimed positioning precision in this area amounted to 3-6 m.

2.4.1.2. Medium scale network: clay tectonic deformations

The best seismic responses hitherto observed in the Ypresian Clay have been obtained with a multi-electrode sparker. The clay tectonic deformations in the North Hinder test area have been the subject of a detailed analysis with a dense

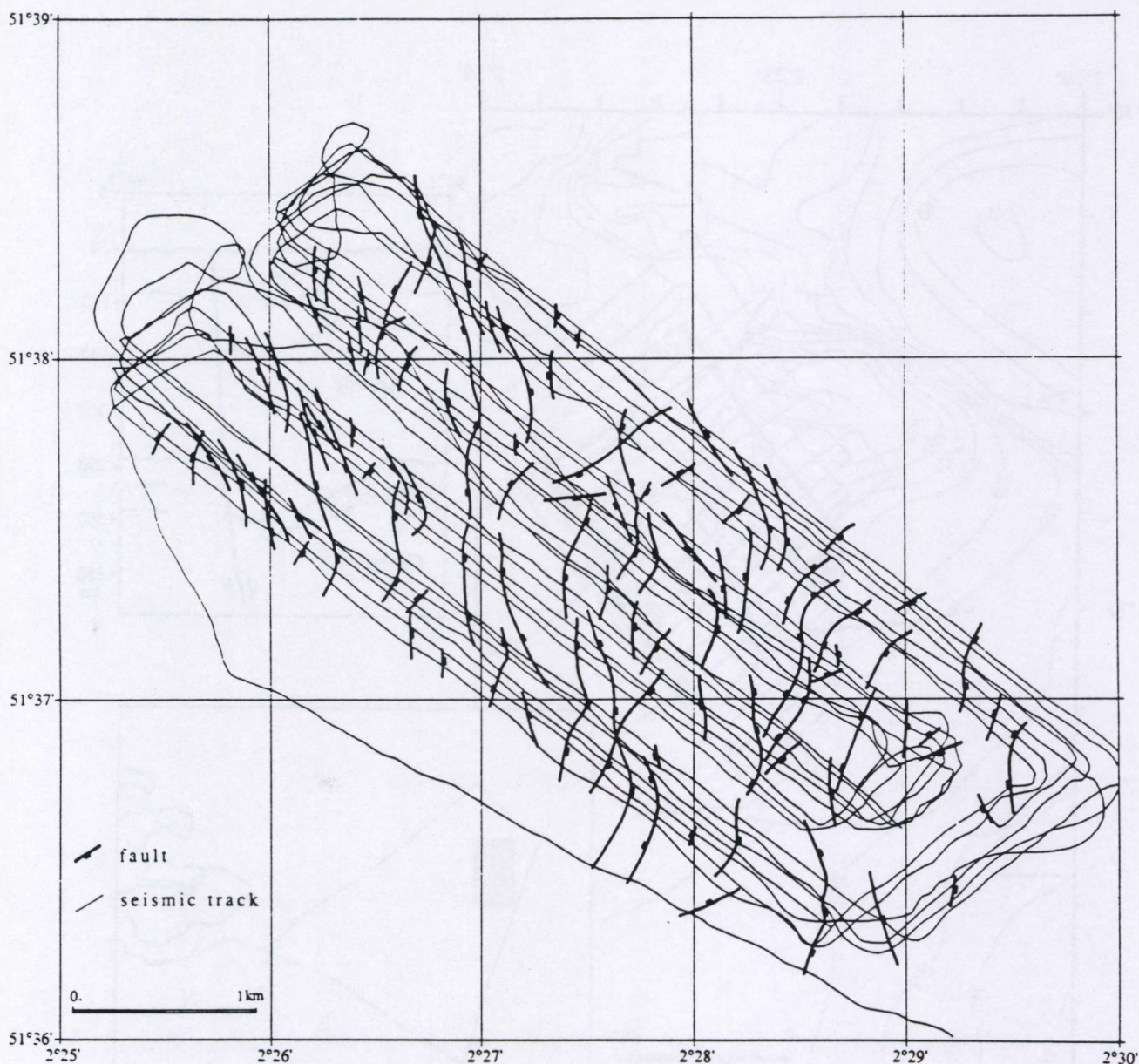


Fig. 2.12. Unidirectional, incomplete pseudo-3D network and interpreted areal distribution of clay tectonic faults in the North Hinder test area (1990).

grid of profiles in a limited area. In a summer 1989 survey, 28 single channel sparker profiles with an average spacing of 50 m have been recorded both in the analog and digital modes in little more than 24 h (sector b in fig. 1.1; fig. 2.12). The operations however had to be interrupted by the onset of adverse weather conditions after the acquisition of the 28 profiles.

During a second survey in June 1990, the above network has been completed with a set of longitudinal profiles and a tight perpendicular network of cross-sectioning profiles (sector c in fig. 1.1; fig. 2.13). Within the zone covered by perpendicular profiles, circular cross-correlation of faults around mazes of 50 m enabled the

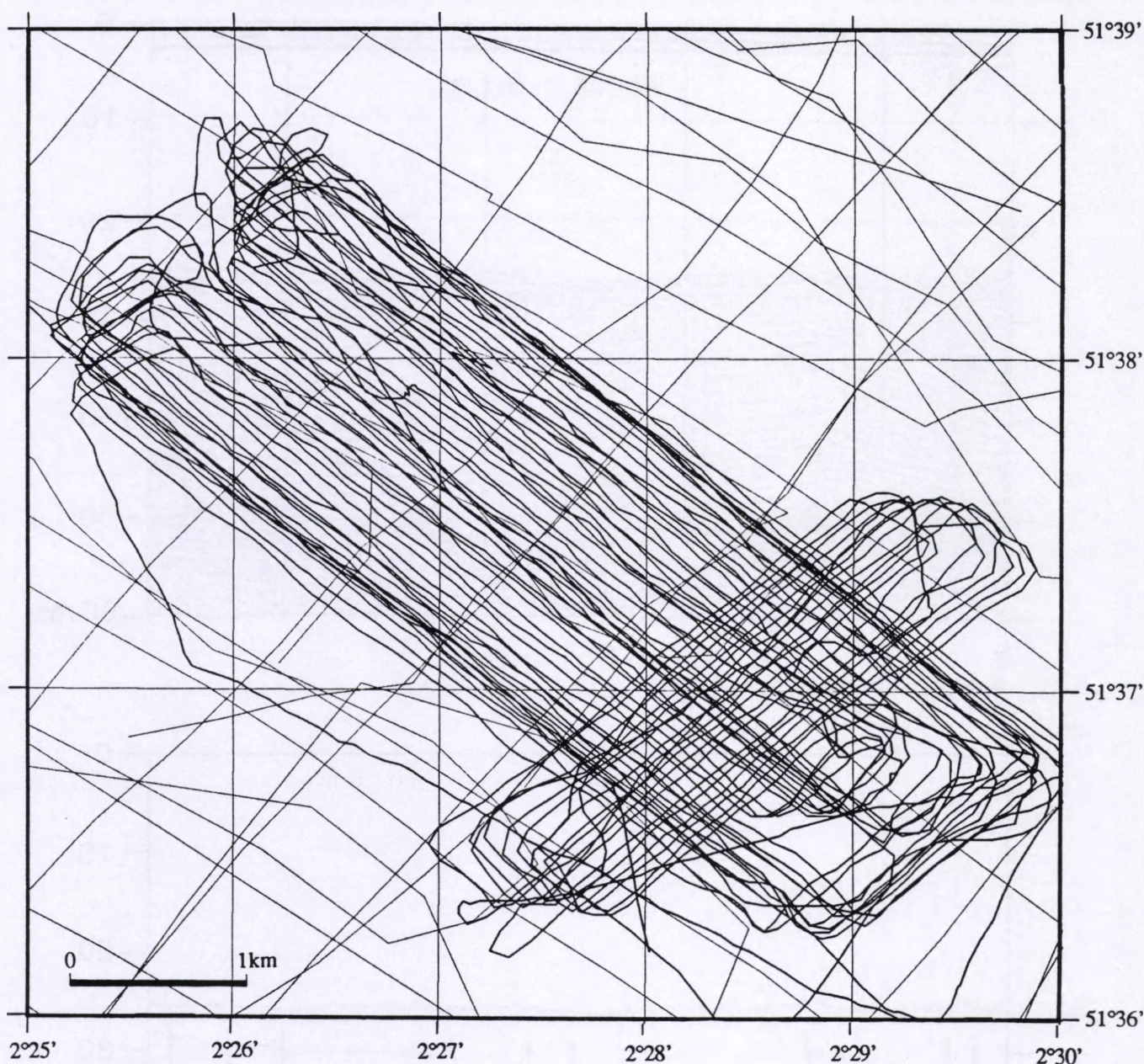


Fig. 2.13. Completed pseudo-3D network with a 50 m line spacing, in the North Hinder test area. 50 m line spacing and one Syledis position per minute. Note the differences with the earlier 2D seismic network (thin lines) : 1000 m line spacing and only one Decca position every 10 minutes.

clarification of several ambiguities in the mapping of small scale clay tectonic faulting, and allowed a detailed 3D interpretation of these structures (§4.2). The watergun source hitherto largely failed in imaging clay tectonic features. However, during the June '90 survey, the network has been completed with the S15 watergun, equipped with the two-slit mouthpiece (fig. 2.14).

2.4.2. 3D acquisition

Apart from the use of a SEISCAT or another acquisition system geared for high positioning precision, a choice of the final bin size affects the acquisition para-

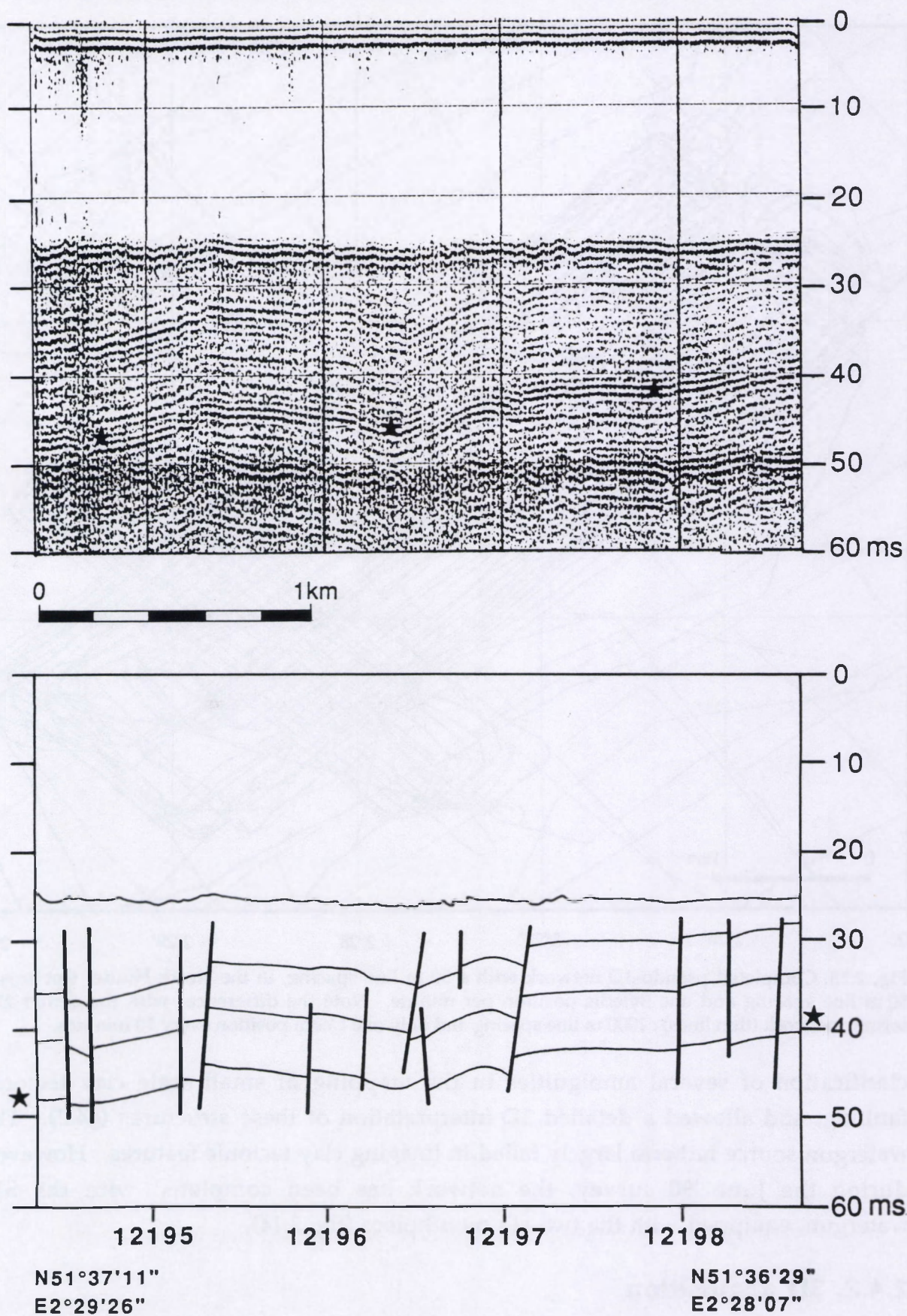


Fig. 2.14. Block faulting in the Ieper Formation along one of the NE-SW profiles of fig. 2.13. Reflector indicated with *, also recognizable on fig. 2.10, was used for modelling purposes (fig. 4.5 and 4.6). S15 watergun with modified mouthpiece.

meters and operations, and should therefore be well founded. Some of the constraints will be studied below, before the focus shifts to a report on the actual 3D acquisition on the river Scheldt.

2.4.2.1. Bin size dimensioning in a true 3D approach

Bin size lower boundary

A basic principle in 3D data acquisition is to care for short source-receiver offsets. If the angle of incidence exceeds the critical angle, refractions start to blur the reflection image. Offsets should in general not exceed twice the target depth.

In water depths of 75-100 m, where a hydro-acoustic positioning system would be used, the distance between an interrogator located near the source (vessel) and a tail responder on the streamer may consequently amount to some 200 m. Over a distance of 200 m, the rated Trackpoint positioning precision for instance is 3 m. It consequently does not make much sense in such circumstances to strive for a reflection point spacing and hence a bin size smaller than e.g. 6 m. Reflection points spaced 6 m form an adequate sampling of a first Fresnel zone of 24 m diameter (four sampling points). At a depth of some 100 m, such a Fresnel zone corresponds with a frequency of 520 Hz, according to

$$R_1 = 1/2 V \sqrt{t/f} \quad \text{or} \quad f = t/(2R_1/V)^2$$

where R_1 is the radius of the first Fresnel zone, f the frequency, V the average velocity (1500m/s) and t the arrival time (200m / 1500m/s). Somewhat higher frequencies could still adequately be sampled at depths below the sea floor, where the average velocity increases above 1500 m/s.

In more shallow waters where target depths are at about 50 m and where maximal source-receiver offsets hence amount to some 100 m, the shorter interrogator-responder distances entail a higher relative positioning precision, up to 1.5 m. Consequently, bin sizes could be downscaled to 3 m. A first Fresnel zone of 12 m diameter could adequately be sampled, corresponding to a frequency of 1040 Hz. Higher frequency sources could be used in these conditions.

In very shallow waters where the geological targets are at a depth of e.g. 25 m, it is in principle possible to work with maximal offsets of some 50 m. However, no significant further improvement of positioning precision should be expected from a hydro-acoustic positioning system. A bin size of 3 m and the use of the same sources would therefore be appropriate in these conditions as well. In such

shallow waters however, complications may be expected from the interference of multiple reflections.

On the river Scheldt, the most intensely deformed but still continuous reflector within the clay diapir is at a depth of about 20 m. With a shore based laser auto-tracking system and very short offsets (3-7 m), positioning precision was expected to be largely sufficient to allow a bin size of 1 m, which would moderately oversample a first Fresnel zone of 4 m for a signal frequency of around 1000 Hz.

Bin size upper boundary

There is evidently no reason to use minimal bin sizes when the structural grain which has to be resolved is many orders of magnitude larger than this bin size. For resolving fault patterns, one might advance that reflection point spacing may be an order of magnitude smaller than the mean distance between structural discontinuities of interest. The bin size may therefore often be larger than the lower boundary proposed above. If initial 2D profiling reveals faults at an average distance of 500 m for instance, a bin size of 12 to 25 m is more economical, without sacrificing relevant information. Instead of increasing bin sizes any further than that, a pseudo-3D approach is likely to be the better alternative for high resolution work.

2.4.2.2. Scheldt test site

In an early RCMG survey (1982) on the Scheldt river (sector d in fig. 1.1), a singular clay diapir structure had been identified and delineated with a pseudo-3D grid of UNIBOOM profiles (§1.5). This structure formed an ideal object for a test of 3D acquisition, as it would allow a comparison with pseudo-3D modelling.

The 3D acquisition over the Scheldt clay diapir was carried out with a bin size of 1 m, which not only helped in the accurate imaging of the diapiric deformation, but also opened the perspective of imaging the spatial distribution of larger concretions (up to one m in diameter) which are found in the clay horizons (fig. 1.19). A boomer source consequently was a first choice for such an imaging exercise, although a test has also been carried out with the specially fitted SODERA S15 watergun.

The fully integrated digital seismic acquisition and positioning system was up and running just one day after installation had begun. A KRUPP-ATLAS auto-tracking laser-ranging theodolite, installed on the riverside, constantly supplied SEISCAT

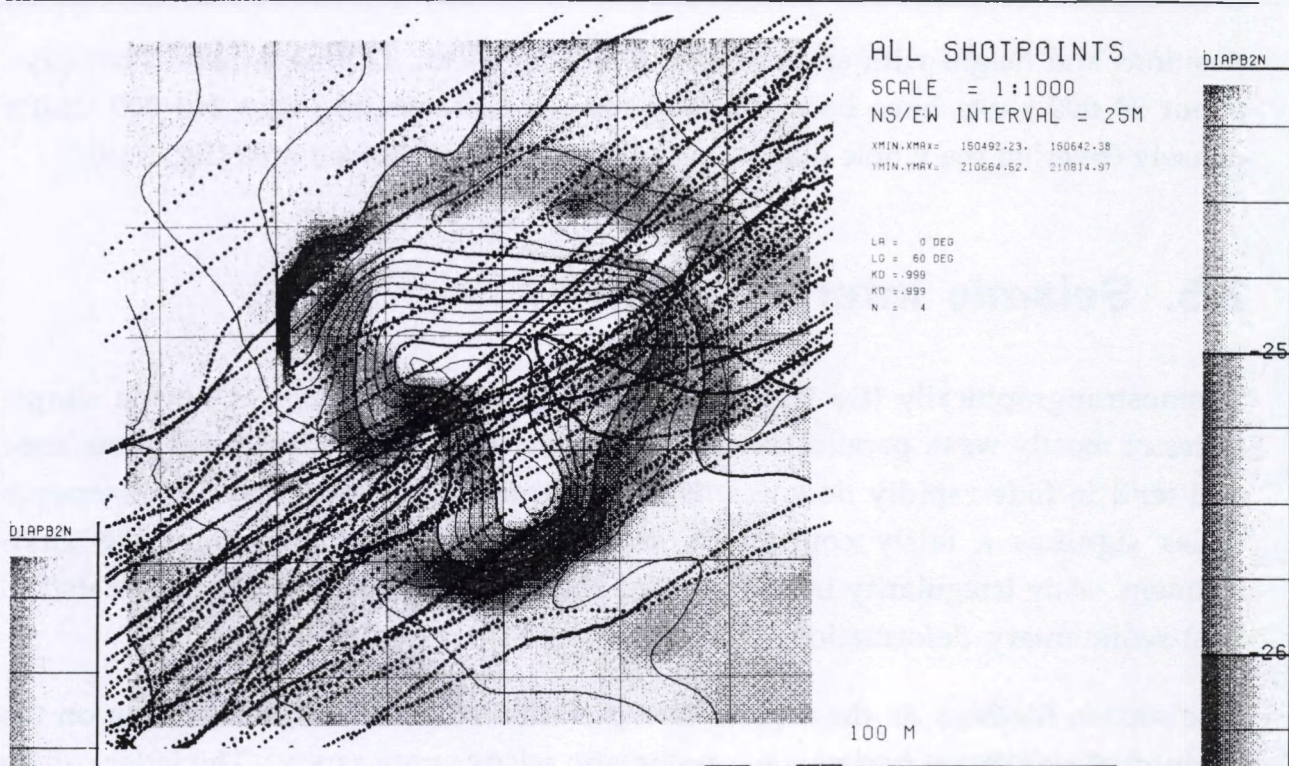


Fig. 2.15a

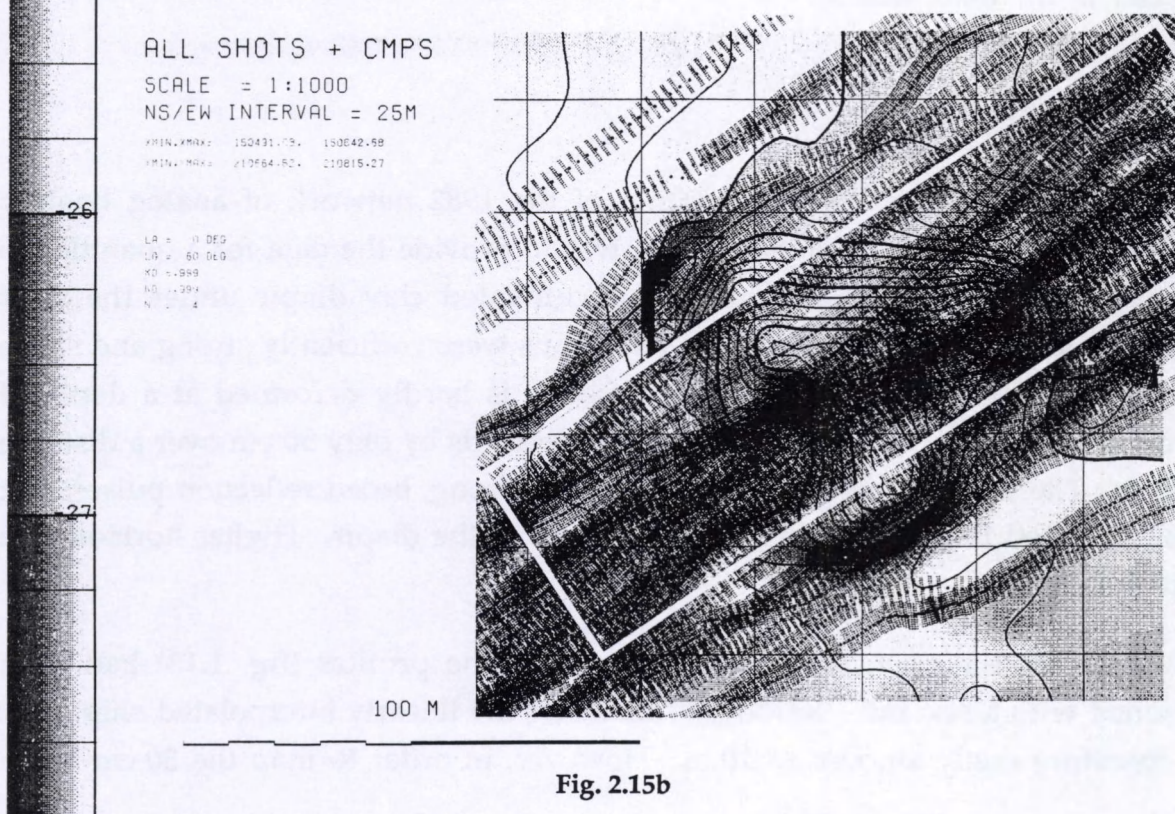


Fig. 2.15b

Fig. 2.15. (a) Map of shotpoints on top of a shaded bathymetric map of a clay diapir in the Rupelian clay, under the river Scheldt. Map is based on pseudo-3D data (fig. 1.17-18); grid line spacing is 25 m; colour interval is 1 m; contour interval is 0.25 m. (b) Idem as (a) plus common mid points (24 CMP's per shotpoint; see fig. 1.17 for a comparison with pseudo-3D coverage).

positions and height with an precision of at least 0.1 m. During a mere three days, about 20 000 shots have been digitally recorded, translating into 240 000 CMP's densely covering the whole diapir and an adjacent undisturbed area (fig. 2.15).

2.5. Seismic interpretation

Seismostratigraphically (De Batist, 1989), the Y1 and R2 sequences have a simple facies of mostly weak parallel reflectors, that are only observable in a shallow zone and tend to fade rapidly downwards (fig. 2.10 & 1.19). Their very homogeneous facies signifies a fairly continuous sedimentation in a shallow marine environment. Any irregularity in this parallel pattern can therefore safely be related to post-sedimentary deformation.

This section focusses on the seismic interpretation of structures, rather than on the position of significant horizons for systematic seismostratigraphy. The latter can be studied and mapped with sparse networks of seismic profiles. Only an appropriately dense pseudo-3D network (§2.1 and §2.4) can reveal the true spatial character of the deformation.

2.5.1. Scheldt clay diapir

The main purpose of a re-interpretation of the 1982 network of analog boomer profiles after the work of Heldens (1983), was to provide the data for a quantitative 3D model of the most prominent and documented clay diapir under the river Scheldt up to this moment. Only two reflections were sufficiently strong and sharp to serve this purpose (fig. 1.19). One reflector is hardly deformed at a depth of around 40 m below the river bed¹. It bulges upwards by only 50 cm over a distance of 100 m. The second reflector results in a very strong, broad reflection pulse², that can be followed through a more deformed part of the diapir. Higher horizons are completely pierced.

During the 1982 survey, reference points along the profiles (fig. 1.18) had been positioned with a sextant. Position errors along the linearly interpolated ship track may therefore easily amount to 10 m. However, in order to map the 30 cm bulge

¹at 1 m above septaria horizon S4(0) (Heldens, 1983), coincident with the top of the Terhagen Member of the Boom Formation, according to a lithostratigraphical section of Vandenberghe & Van Echelpoel (1987).

²coincident with septaria horizon S8(0) (Heldens, 1983; Vandenberghe & Van Echelpoel, 1987)

and equally subtle features on the higher horizon, it was necessary to calculate and map all depths with a precision of 10 cm. At the time of interpretation (1985), the only way to ensure such a high precision on the basis of approximately positioned boomer profiles acquired in a tidal environment, consisted of 1°) manually converting one reference profile to tide corrected depths, 2°) tying all other profiles at the level of the lower, least deformed reflector, and 3°) shifting the profiles laterally so that they also tied at the higher reflector.

One profile showed a small fault bordering a depressed zone around the diapir. Within the constraints of other nearby profiles, a few points were introduced to pin down the fault strike. The river bed data were evenly digitized from contours on a recent bathymetry map.

2.5.2. North Hinder clay tectonics

In a first approach to the earliest half of the network in the North Hinder zone (1989, §2.4.1.2), interpretation and correlation of the analog profiles was done the classical way, with paper and pencil. It provided the first coherent image of a complex clay tectonic fault system, as well as an assessment of problems that are met during such an exercise.

One relatively strong internal reflector was chosen because of its presence on all seismic profiles, no matter the quality, which was largely determined by the weather. Apart from faults that die out upwards or downwards within the depth of seismic penetration, this strong reflector is deformed in the same way as any of the other, parallel internal reflectors. Stratigraphically, it can only approximately be situated in the upper part of the Ypresian Clay (De Batist, 1989).

A first problem resided in the unidirectional nature of the first half 'network'. As explained in §2.1.1, faults that cut this direction under an oblique angle may either be difficult to correlate, or distort the interpretation of other faults. Correlation of fault cuts¹ was only possible after a complete characterization, describing the amount and direction of throw, the form of drape² at the reflector ends, and the shape of horizon segments. Fault throws as small as 0.5 ms two way time (at the vertical resolution of these sparker profiles; with an interval velocity of 1620 m/s

¹A *fault pick* is the interpreted intersection of a seismic profile with a fault plane. A *fault cut* on a profile is a part of a fault pick bounded by the upthrown and downthrown endings of the horizon mapped. (Brede & Thomas, 1986)

²as interpreted at that time. As will be shown in §4.2, true fault drags at the scale of high-resolution seismics are almost completely absent in this zone.

about 0.4 m) were taken into account. One method consisted in manually adding a colour code to the observed structures along the profiles and to plot these on a map. Faults were correlated over adjacent profiles by connecting similar colour patterns at fault scarps. Another problem introduced additional ambiguities.

Due to the specific way fix positions were taken on *RV Belgica* surveys until 1989, coordinates were recorded up to 15 s late, corresponding with an error of up to 30 m along the tracks. In widely spaced 2D networks that were primarily aimed at mapping seismostratigraphic units, such an error was never much of a problem. However, in the pseudo-3D network, fault positions could be up to 60 m out of order on neighbouring, parallel profiles, sailed in opposite directions at 50 m distance. Such an error led to interpretative ambiguities in fault correlation, as long as there were no control sections perpendicular to the already available profiles. The artificial notches that were thus introduced along fault traces were smoothed out manually.

The resulting map (fig. 2.12), based on the data of the first survey, showed a pattern of more or less parallel, rather straight faults, some of them lying en échelon, branching, or crossing each other. Faults with a throw of only a few metres and a length of hardly 200 m could still be mapped. The dominance of a certain fault orientation may have been caused either by an early local stress field related to the deformation of an underlying undercompacted horizon or by any contemporaneous regional stress field. It should however be mentioned that the general fault pattern interpreted here may also to a certain extent be biased by the unidirectional orientation of the seismic lines, which was necessitated by traffic lane regulations. For a more rigorous three-dimensional analysis of these patterns, the additional cross-sectioning lines needed to be incorporated as well.

The whole exercise took about a week but provided only one interpretation of the fault system (fig. 2.12), with no quantitative control. Contours, the hallmark of quantitative mapping, would have been much more time-consuming to draw on the affected reflector manually, for several reasons :

1. Tertiary strata dip only very gently towards the NNE, translating into a maximum height difference of only about 10 m over the entire 2x4 km survey sector;
2. Clay tectonic throws average only 2 m on seismic sections, and intra-block undulations are even slighter;
3. One would have to construct contours at 0.5 m interval or less in order to grasp the above-mentioned features, but that is, optimistically, near the precision of

marine sparker profiles. All kinds of factors may introduce systematic but erroneous height differences of 1 m or more between profiles. Extrapolation of contours towards the fault traces becomes a tedious and subjective exercise with dubious results in these circumstances.

In order to reach a 3D understanding of the relative clay tectonic block deformations and displacements and to replace a manually drawn, qualitative map of the fault pattern by a quantitative model of both a typical horizon and the system of fault scarps on the basis of a network comprising 20+40 seismic profiles with a total of about 1000 fault cuts, there was a clear need for the numerical assistance of a powerful software tool (§3).

2.5.3. North Hinder sag fault

For the interpretation of the North Hinder sag fault, six reflectors have been identified and interpreted on all digitally filtered and stacked¹ seismic profiles in the pseudo-3D network (fig. 2.16). They are sequence boundaries delineating lithologically distinct units.

The seabottom was digitized for time-depth conversion purposes only. The base of the Quaternary (Q0.1 reflector²) coincides on a 500 ms seismic profile almost entirely with the seabottom except for some local shallow gullies and under sand waves. It was digitized for isopach calculations and for use as a more or less featureless reference plane in 3D visualization.

Below Q0.1, all seismic sequences have been affected by the large complex sag fault. The remaining interpreted reference reflectors offer good continuity, but strong interference with seabottom multiples and internal multiples often makes them ambiguous to interpret.

The base of the Ypresian Y1 sequence (Y1.1) is defined as the base of a seismic sequence with weak parallel internal reflectors. The strong Y1.1 reflector laterally converges with internal reflectors of the underlying sequence.

¹Stacking is a step in seismic processing, in which seismic traces from several shots with different shotpoint and hydrophone group locations but with a common reflection mid point are summed to reduce noise. An accurate stack velocity function compensates for the later arrivals at larger offsets, so that the reflections of different traces line up horizontally, for maximum reinforcement during stacking. (Sheriff & Geldart, 1982)

²reflector names by De Batist (1989)

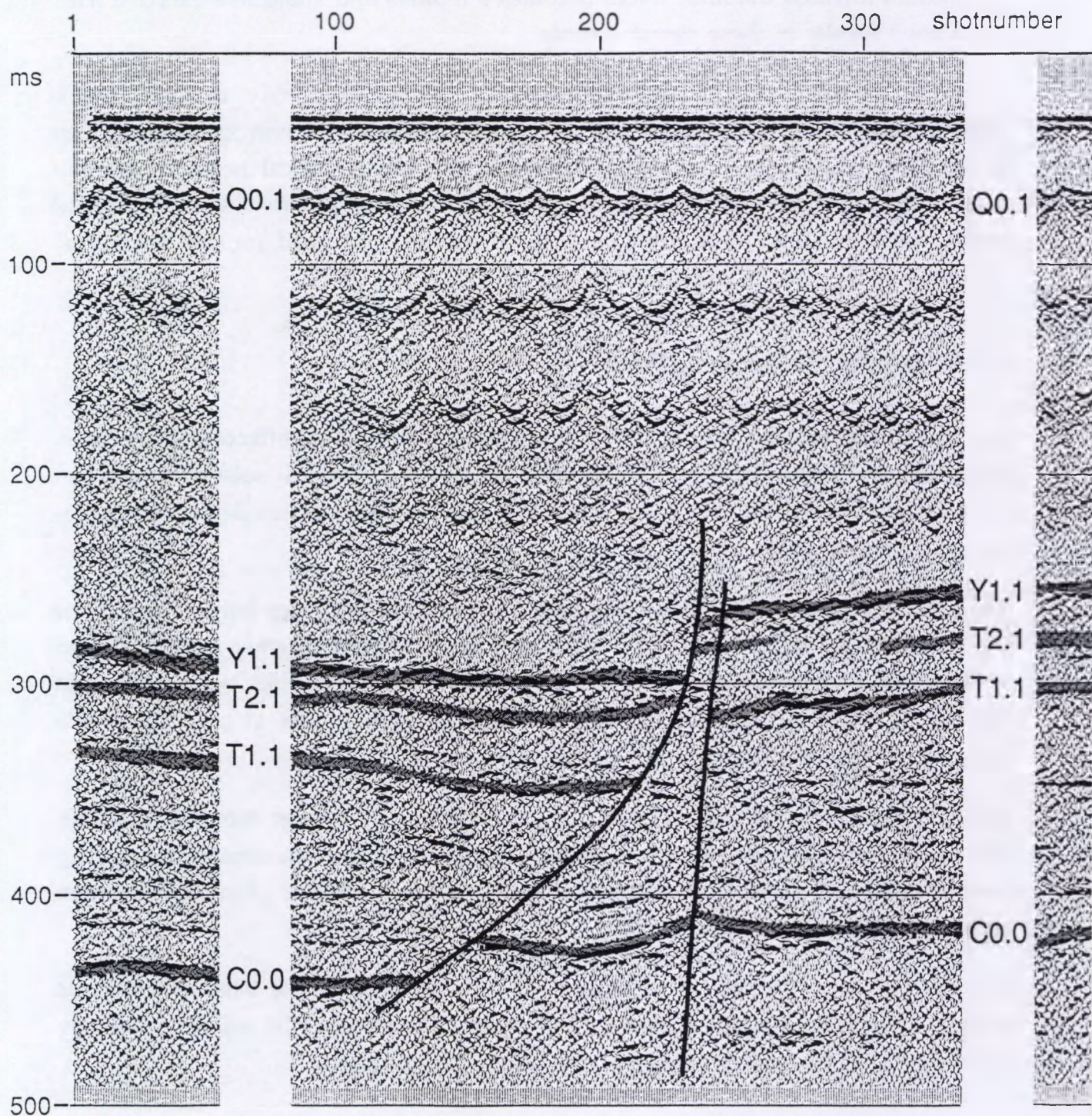


Fig. 2.16. Digitally filtered, stacked watergun profile, part of a pseudo 3D network in the North Hinder zone. All pre-Quaternary reflectors have been affected by a large composite normal fault.

The T2.1 reflector is defined as the base of a sequence with strong hummocky prograding or interfingering to parallel internal reflectors. This seismic sequence is equivalent with the 'continental' Thanetian.

The strong T1.1 reflector is the base of a seismic sequence with weak parallel internal reflectors, equivalent with the 'marine' Thanetian. Picking the right phase was often difficult, due to strong interference with a multiple of Y1.1.

Below T1.1, the weak parallel reflectors of the Cretaceous seismic sequence are almost completely masked by all kind of multiples. The C0.0 reflector, equivalent to the base of the Cretaceous or the top of the Paleozoic basement can be recognized as the lowermost continuous reflector with a strong first multiple.

3. 3D surface modelling method

3.1. Introduction

One of the main tasks of a geologist is to map structures below the surface of the earth. Unfortunately, the three-dimensional anatomy of sedimentary deposits and their internal architecture, and systems of folds and faults that constitute deformations of such primary structures, are all invisible to the naked eye. A three-dimensionally continuous image of the subsurface has to be *inferred* from isolated borehole data points and more or less dense networks of reflection seismic sections, to mention but the two most important sources of information. It is convenient to plot available data points or reflector lines pertaining to the same surface on a map and *contour* them. Jones *et al.* (1986) defined contouring as drawing lines of equal value through a set of data points so that a realistic surface is generated between observations. Several geometric as well as geologic rules govern the contouring process (see also Tearpock & Bischke, 1991), which leads to a *quantitative* interpretation of the available data. In a geologist's mind, a three-dimensional mental image of the subsurface gradually takes shape, guiding in turn the process of geological interpretation and contouring. However, this 3D mental image of a 3D reality is traditionally described with two-dimensional pictures, either horizontal projections (maps) or vertical cross sections.

Since the early 1960s, computer programs have been written and used to assist manual contouring. At first, they were very simple and could only produce rough first shots revealing the general trends with unnatural contours. Meanwhile, more sophisticated software has become popular because of the following advantages (after Jones *et al.*, 1986):

1. large data sets can be manipulated fast. Modern technology provides data prolifically, overwhelming manual practice. In the North Hinder sector of 2x4 km, a network of 60 seismic profiles with a total length of 200 km cut clay tectonic faults at about 1000 locations. 10000 data points along the network describe just one faulted reflector. Speed and efficiency is essential to test multiple correlation hypotheses or interpretations of this fault pattern;

2. existing maps can be digitized and combined with each other or merged with new data;
3. updates require much less effort;
4. contours maps are consistent and more objective. Manual contouring is laborious and prone to fatigue and inconsistencies. A host of interpolation algorithms¹ has been developed to suit various kinds of data with different amounts of uncertainty. These algorithms may each result in widely dissimilar maps, but the contours will at least be drawn consistently within one map.

Computer aided mapping still has its outspoken critics, however. For instance, Tucker (1988, p. 741) asserts that "Seismic contouring is a unique skill. The contour must express the variable nature of the seismic signal and its values and must combine these values into the varying structural styles of rock deformation. Contouring requires an intelligent analysis of the data being contoured. Contouring is often beyond the capability of the computer and must be hand-drawn. Contouring is not an easy task. [...] The laborious task of contouring has been alleviated by the computer. [...] However, all too often the maps do not depict the geology realistically. It is here that the computer-contoured map is often found wanting: it cannot incorporate the on-going thinking of the interpreter. The imaging concept is a strong argument for hand contouring. The interpreter can create in his mind a 3D image of an evolving structural interpretation, an image that becomes the limitless source of geologic concepts, not a suite of unnatural computer maps."

Several programs do offer interactive² modelling tools to incorporate geological interpretation and background information (such as regional stratigraphy, tectonic setting, ..) into the interpolated surface. Any geological interpretation that can thus be made numerically explicit with the aid of a computer, is honoured objectively. We agree with Tucker up to the point that it is in their interactive modelling capabilities that most programs, apart from a few very sophisticated and expensive ones, still leave much to desire. However, if the data cover a complex part of the subsurface with myriad faults and folds, such as clay tectonic ones, it is impossible for an interpreter to form a 3D image in his/her mind that is both a coherent overview and consistent in its details. It is here that advanced computer graphics can offer irreplaceable support and rather be a strong argument in favour of 3D

¹An *algorithm* is a sequence of rules that constitute a stepwise solution to a computational problem.

²A graphically *interactive* computer program produces immediate visual feedback on any action of the user, so that he or she can dynamically control a picture's content, instead of having to (re-)type a multitude of control parameters and wait for the result (after Foley & Van Dam, 1982).

surface modelling with the computer. We define *3D modelling*¹ here as a *process of integrated objective mapping, geological interpretation and 3D visual inspection*. We will demonstrate that if these three processes are thoughtfully integrated into an interactive computer program that provides immediate visual feedback, they do not only allow to map structural data that are next to impossible to hand-contour, but they do also most definitely become an exacting instrument to quantify an evolving geological image of the subsurface. It should be noticed that we do not regard 3D computer graphics merely as an eye-catching fancy after all the 'serious' work is finished, but as an integrated part of 3D surface modelling and mapping, and as one that helps to improve overall quality.

This chapter on 3D surface modelling techniques starts with an analysis of the mapping problems that we had to deal with (§3.2), which were partly well-known in the arena of geoscientific computing, and partly specific to the North Hinder data on clay tectonic faulting. After a review of existing commercial software (§3.3), and a description of the hardware platform available at RCMG (§3.4), we show how we implemented our own ideas on data preparation (§3.5). We formulate a new method for interactive 3D geological surface modelling in §3.6, and introduce its implementation, the Geofox program, in §3.7.

3.2. Problem analysis

3.2.1. Data distribution and redundancy

As the information density along 2D and pseudo-3D profiles (§2.1.1) is much higher than between them, special care needs to be taken to reduce data redundancy. This is especially true for crossing tracks, which is about the worst data pattern to handle with a computer (Sabin, 1986). Data redundancy is situated both at the level of data entry and that of modelling.

Computer programs require digital data. The interpreted reflection lines therefore have to be *digitized*, by moving a stylus over the lines while coordinates of points

¹We only deal with surface modelling here, and because we want to produce gridded surface models, the surfaces cannot have multiple elevations at the same horizontal positions. Reverse faults and recumbent folds therefore cannot be modelled with gridding programs without splitting the surfaces. Fried & Leonard (1990) give a more general definition, which includes also 3D modelling of geological attributes, such as porosity, throughout a *volume*. 3D modelling *sensu lato* is only possible with advanced 3D hardware.

along the lines are sent to the computer. After digitization, the originally more or less continuous curve is represented by a segmented curve that connects the points stored. Local detail is captured by a point's position relative to its neighbours. However, digitization and therefore also the coordinates of stored points have limited precision. Below the threshold of precision, local detail is not significant, and the points involved are therefore redundant for any later use. They should be filtered at the level of data entry, before they burden computer memory and increase processing time.

Jones *et al.* (1986) advise to use the minimum number of points possible to define geologic features. If a selection of the data points were just as informative at the scale of modelling as the whole set, modelling as well as calculations with and storage of the model would become more efficient. As far as interactive modelling is concerned, we will demonstrate that it can even make the difference between a manageable project and an intractably complex one. Furthermore, all surface interpolation methods produce better results when the data are distributed more evenly.

In conclusion, we need a filter that automatically and objectively selects significant points both at the level of data entry (§3.5.2) and that of modelling (§3.7.5)¹.

3.2.2. Mis-ties

Reliable geological surface models start with reliable data. Seismic reflection data are by no means exact and crystal clear to interpret, but only numerically exact data can be contoured with a computer directly. The first set of problems resides in the various imprecisions that are introduced during seismic acquisition, interpretation and digitization.

Vertical imprecisions are threefold². For a start, tidal amplitude has to be taken into account in marine high resolution acquisition. The theoretical correction

¹Increasingly, seismic horizons are digitized automatically, with the help of automatic tracking (horizon picking) programs. This is especially helpful in extracting all horizon information from 3D seismic data (Dalley *et al.*, 1989). In the latter case, horizons are entirely covered with data, and there is consequently no need for interpolation, and *a fortiori* little need for reducing data redundancy for modelling purposes. On the other hand, automatically picked horizons along 2D networks *do* pose the same data redundancy problems as have been sketched here.

²i.e. apart from imprecisions in the velocity function used to convert reflection times to depths (Parkes & Hatton, 1987). As explained in §2.1.1, time/depth conversion does not alter the structural interpretation of the North Hinder data, so it was not considered during 3D modelling. In this section's discussions, 1 ms Two Way Time is equivalent to about 0.8 m, at least for the first 100 ms. A depth converted 3D model is presented at the end (§4.2).

model applied to the North Sea data does not incorporate actual tidal measurements, and may therefore leave errors of up to several dm. More importantly, high resolution seismics is very sensitive to weather conditions, so that profile quality may vary widely even during one survey, such as the first half of the North Hinder sparker network. Picking the same reflection phase all along such a network is no sinecure. On good analog profiles, the right phase can be pinpointed to within a few tenths of a ms. If a wrong phase or simply a different reflector is picked across the numerous faults due to lower data quality, the error may locally amount to one or two ms. Thirdly, the process of digitization of high resolution profiles contributes up to a few extra tenths of a ms to the overall vertical imprecision.

Horizontal inaccuracies and imprecisions of (unmigrated) time-sections arise from digitization imprecisions and, more importantly, mispositioning. As explained in §2.2.5, position data storage was badly synchronized with the posting of 'fix lines' on seismic profiles of the first half of the North Hinder network. Fault positions could be anywhere between 0 and 60 m out of order on neighbouring, parallel profiles, sailed in opposite directions at 50 m distance. This not only lead to interpretative ambiguities during manual fault trace mapping (§2.5.2), but also to grave computer modelling problems. All of this first set of data points had to be shifted almost individually along the tracks. The reliably positioned second set could serve as a quantitative constraint. Even so, fault cuts that happen to be less than about 10 m apart on cross-secting profiles, may visibly jag the interpreted fault trace by as much as the Syledis precision of 3 m (§2.2.5). However, the Syledis precision compares favourably with the errors due to digitization and to off-track streamer feathering, both of which are estimated to be twice as large.

Theoretically, interpreted reflections must *tie*, i.e. have identical reflection times at profile intersections. Because of all the vertical and horizontal imprecisions specified above, this is rarely the case in a numerically exact sense. Hence, the digitized reflector data need to be corrected for *mis-ties*. Jones *et al.* (1986), Indelicato & Moore (1989) and Oliveros (1989) have described several more or less sophisticated mis-tie correction algorithms. Oliveros suggested to critically analyse the causes of mis-ties in a particular data set, before correcting them automatically with one single technique. He traced all mis-ties to five causes, and listed appropriate cures. 2D migrated seismic profiles show significant mis-ties if reflections originate out of the vertical plane. Partial map migration, for which he developed an algorithm, places 2D migrated seismic horizons in their correct 3D positions. Fortunately, dips in the North Hinder sector are so small that we can safely do without migration

(§2.1.1). Secondly, phase or time differences between different vintages of seismic data should be processed away with bulk time shifts of entire profiles. The remaining three causes for mis-ties, i.e. mispositioning of seismic data, digitization errors and 'static', vertical errors on the reference-level¹, are predominantly local problems, and should therefore be treated locally and in different ways. The latter four causes can easily be recognized in the analysis of the two preceding paragraphs. However, even if the North Hinder data were corrected for positioning, digitization and static errors, bulk time shifts would not be appropriate to compensate for phase differences, because they may vary across the myriad fault cuts.

In conclusion, mis-ties posed a serious problem that could not be treated in any automatic way. Fully controlled mis-tie corrections necessitates direct interaction with the position of individual or groups of data points along the profiles, supported by immediate quantitative and visual feedback of the effect on the surrounding surface. Affected contours should be adapted automatically at once.

3.2.3. Horizon modelling

Seismic horizons cut by clay tectonic faults undulate gently (fig. 2.10). Contours on the individual blocks should therefore be smooth and continuous up to the fault scarps. As the undulations' amplitude amounts to only a few ms, their significance would only become apparent from any coherence across the area. It was soon realized however, that the mis-ties were about as large as these subtle features, and that any remaining mis-tie would severely affect the shape of the latter. A reliably interpolated horizon model was therefore required to honour both the re-positioned data points and the shapes along the continuous seismic lines. If the shape of any contour line calculated with the model conflicted with the seismic information, the underlying data points and not the contour lines would need some further correction.

Since the dawn of computer contouring in the 1960s, ever different smooth surface interpolation algorithms have been published for a wide variety of purposes. Making an appropriate choice for our application proved to be a problem of its own.

¹a notion in land acquisition that is equivalent to incomplete correction for tidal variations during marine acquisition

3.2.4. Fault modelling

The requirement of a smooth surface contrasts strongly with that of contours that break at the upthrown and downthrown fault trace of clay tectonic normal faults. If it were possible to generate such contour lines automatically from our evolving quantitative 3D model, we would avoid a great many of the pitfalls associated with the manual mapping and contouring of horizons cut by a system of normal faults. Tearpock & Bischke (1991, pp. 292-334, 348-372) give a full account and treatment of the difficulties involved in manual practice. These authors are even trapped by a pitfall of their own design (fig. 3.1). Because of these difficulties and the drive to emulate manual techniques which are not necessarily correct, computer mapping of faulted horizons has traditionally approached fault traces¹ as something that is added to the horizon, instead of being part of it. Invariably (Jones *et al.*, 1986; Leonard, 1986; CEED Committee, 1986), geological modelling software requires the upthrown and downthrown fault traces, including bifurcations and crossings, to be interpreted manually and digitized separately, in order to constrain subsequent interpolation of horizon contours.

This has three major drawbacks. Firstly and most obviously, the software does not assist the interpreter to by-pass the pitfalls of manual fault trace interpretation. Secondly, the digitized interpretation may prove to be locally erroneous upon 3D inspection of the quantitative fault/horizon model, e.g. an improbable correlation of fault picks may show up as odd-looking deformation of the horizon, a fault gap² may be too wide or too narrow (fig. 3.1) and *bifurcation*³ and cross points may be placed incorrectly. Such errors can then only be mended by adjusting the fault traces, again without visual quantitative feedback, or even by entirely redigitizing the fault traces connecting badly correlated fault picks. A change of interpretation cannot be evaluated immediately, precluding truly interactive 3D modelling. Thirdly, too often the digitized fault traces largely consist of *control* points, i.e. points that are not part of the data. They are fake. Adding control points is not necessarily bad, however. They serve to quantify interpreted features that the pseudo-3D data simply cannot provide, e.g. interpreted singular points

¹*Fault traces* are the two lines on a structure map representing the intersection of a fault surface with the structure contoured surface in the upthrown and downthrown blocks (Tearpock & Bischke, 1991).

²*Fault gap* is defined as the horizontal distance between the upthrown and downthrown fault traces measured *perpendicular to the fault trace* as depicted on a completed structure contour map (Tearpock & Bischke, 1991).

³term used by Tearpock & Bischke (1991) instead of branch point (Ramsay & Huber, 1987).

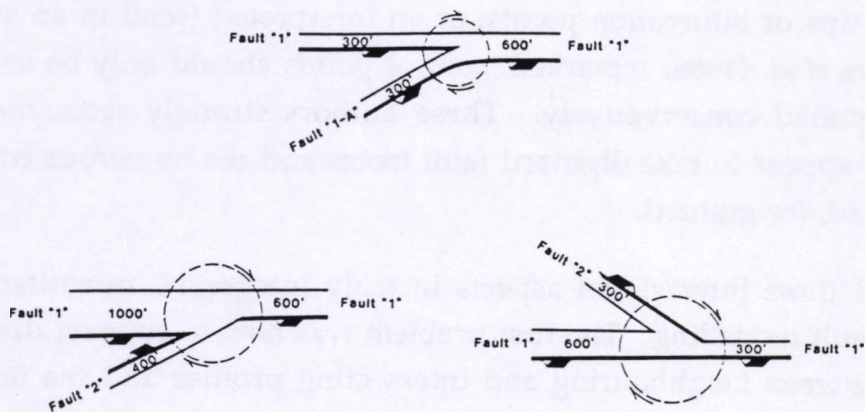


Fig. 3.1 a

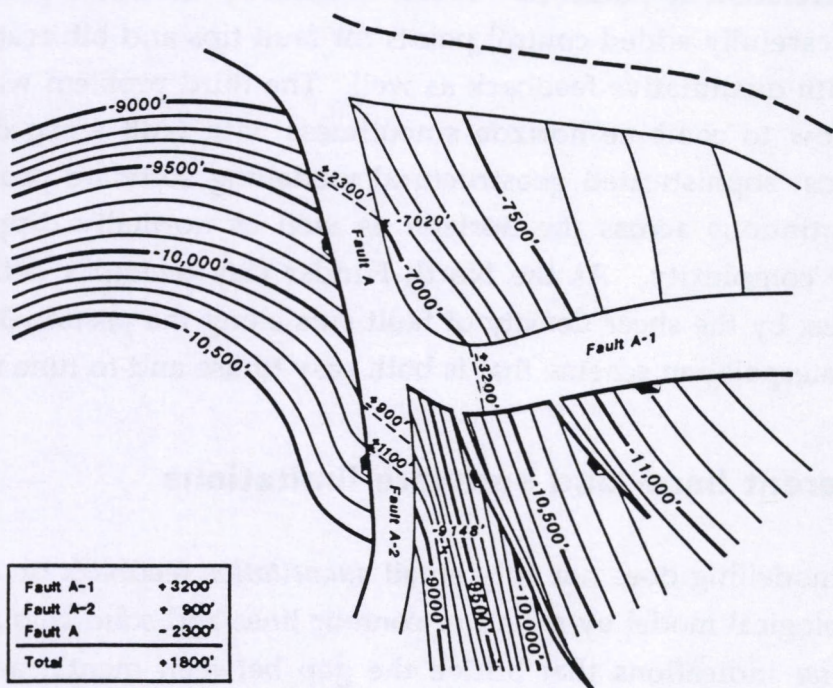


Fig. 3.1 b

Fig. 3.1. (a) Conservation of vertical separation at fault intersections (from Tearpock & Bischke, 1991). This property of intersecting fault means that the sum of vertical separations should equal zero at the point of intersection. This is checked by tracing a loop around the intersection and adding the vertical separations with an appropriate sign. Tearpock & Bischke (1991, p.333) give (b) as an example of a "mapping bust" in which the "failure to conserve the vertical separation around the intersection of Faults A-1 and A-2 is significant" (see table). It is, but then only because these authors do not take the height differences along the dipping horizon into account. Furthermore, it is easy to see that without explicit fault throw information or fault contours, vertical separations along a loop around an intersection will *always* cancel, no matter how well or badly the faulted horizon is contoured. The real errors reside in the width of the fault gaps and the position of a bifurcation : in order to conserve fault dip, the gap of Fault A-1 should be only half of that of Fault A, and the bifurcation point should be further North. These authors devote dozens of pages to the construction of proper fault gaps, but do not notice the error here. In addition, they never mention an elementary check on the correctness of fault traces, i.e. contouring the fault gaps together with the faulted horizon. Contours between the fault traces should make as much sense as those on the horizon (e.g. fig.3.28d).

such as fault tips or bifurcation points, or an interpreted trend in an area without data. As Jones *et al.* (1986) remarked, control points should only be used as a last resort and applied conservatively. These authors strongly recommend against their use, but appear to take digitized fault traces and the numerous control points thus introduced, for granted.

We discerned three interrelated aspects in truly integrated, quantitative horizon and normal fault modelling. The first problem was how to support direct fault cut correlation between neighbouring and intersecting profiles and the interpretation of bifurcating and intersecting faults, in such a way that only actual data points are used, and that any interpretation can easily be changed locally, in order to test multiple correlation hypotheses. When eventually the fault pattern would be established, carefully added control points for fault tips and bifurcations should be modelled with quantitative feedback as well. The third problem was one of interpolation : how to combine horizon smoothness with fault scarp discontinuities? Only the most sophisticated geostructural modelling software provides contours that are continuous across the horizon as well as normally dipping faults, no matter their complexity. As the North Hinder clay tectonics definitely rank as fairly complex by the sheer density of fault cuts along the pseudo-3D network, we needed an interpolation scheme that is both easy to use and to tune up.

3.2.5. Inherent hard- and software limitations

3D surface modelling does not only entail *quantitative* feedback on any interaction with the geological model by means of contour lines and solid colour intervals, but also *qualitative* indications that bridge the gap between mental and quantitative geological models.

3D projection puts the model into perspective, revealing the true spatial proportions of, and relations between, features on one surface, and also between a stack of surfaces. Because a computer does not 'know' which fragments of 3D projected surfaces are visible in front or hidden in the back, a part of the hard- or software has to deal with hidden line removal and hidden surface removal. Furthermore, computed illumination can throw a different light on the evolving model and may instantly elicit the smallest details and remaining flaws.

Such sophisticated graphics are still not standard on most computers. Geological modelling software that does offer this kind of feedback invariably comes at an extra price for the necessary hardware and graphics library auxiliaries. The 2D

interactive 'windows' environment on the entry-level SUN-386i workstation¹ at RCMG (§3.4) includes only the most basic 2D line- and polygon drawing routines. The manufacturers apparently considered this machine's memory and processing capacity too small to support a library of 3D graphics subroutines² such as PHIGS or GKS-3D (Foley *et al.*, 1990), and *a fortiori*, its capabilities too limited for any complex 3D surface modelling.

3.3. Existing software methods

During the 1980s, computer mapping has become widely practised in the exploration industry. The Comparison, Evaluation, Exhibition and Demonstration committee (1986) tested and evaluated no less than 21 computer mapping systems from 17 vendors who showed interest to participate. Green (1991) formulated helpful guide-lines to select among this multitude of complex software systems the most appropriate solution to geological problems.

Except for one company, all of these mapping systems use gridding techniques to interpolate a continuous surface between the discrete set of primary data points. *Gridding* uses the primary data points to generate a set of secondary, calculated points lying on a rectangular grid. It is therefore an indirect modelling technique (Banks, 1990), as opposed to *triangulation* techniques, which allow to incorporate and honour the data points directly into an irregular network representing the surface.

While the functionality of mapping systems has greatly increased since 1986, *gridding* remains central to most of them. Its popularity is derived from the following advantages:

1. storage efficiency, because only one grid value is stored for every grid node, without the horizontal coordinates. The horizontal coordinates of grid nodes are completely determined by that of the grid corners, the grid interval and the node's row and column index;

¹A *workstation* is a class of interactive computers that are generally more powerful than personal computers (PC's), in that they allow multi-processing (i.e. concurrent processing of several jobs) under a sophisticated operating system such as Unix. In general, they boast a fast central processor, a large main memory and hard disk, and a high-resolution colour monitor (typically 1000x800 *pixels* or addressable picture elements). Apart from the operating system, there is little difference between an entry-level (relatively cheap) workstation and a high-end (relatively powerful and expensive) PC.

²an isolated part of a computer program that can be used in other parts

2. regular grids are easy to do calculations with, such as thickness, intersections and volume between a pair of grids, reservoir simulations...;
3. 3D images are relatively easy to generate with efficient hidden surface removal and hidden line removal algorithms, and their evenly receding gridlines are easy to interpret spatially.

The requirement of smooth contours has lead to the development and commercial application of myriad interpolation algorithms (§3.7.7) that yield a continuous, smooth grid. Faults and other natural discontinuities therefore need to be handled in such a way, that the interpolation either uses only data points on the same fault block, or smooths across a fault by adding its throw to the data points on the adjacent block. Many variants of these two approaches have been implemented. Jones *et al.* (1986) give a general classification, and Zoraster & Ebisch (1990) is a recent example. However, they all require explicit descriptions of the upthrown and downthrown fault traces, together with the amount of throw along the entire fault system, *before* the gridding can start and the first contour map can be evaluated. The major disadvantages of this traditional horizon/fault mapping approach have been discussed in §3.2.4.

Triangulation of the data points has been applied in many different ways as well. Some commercial systems initialize grids with an automatic triangulation, and subsequently smooth out the triangular edges (§3.7.7.1). However, such a procedure does not make the most of a triangulation's advantages (Jones *et al.*, 1986; Banks, 1990):

1. contours can honour the data exactly, i.e. pass at the correct side of the data in all cases, without the ambiguities that arise from contouring a grid quadrilateral;
2. it is possible to handle multiple intersecting non-vertical faults (both normal and reverse) among multiple surfaces;
3. volumes can be calculated rigourously, even in fault wedge areas, albeit with some complications;

The only commercial system that is entirely based on triangles (Banks, 1990) was developed for isolated well-data. Faults are modelled with well penetration points, and horizons in restored blocks separated by the predefined fault system. Seismic data do not accommodate to such an approach. Sides (1990, 1992) described a comparable system and modelled complex orebodies affected by cross cutting faults. GO-CAD, originated by Prof. E. Mallet of the Ecole Nationale Supérieure de

Géologie in Nancy, is a more general and powerful package (e.g. Srivastava & Mallet, 1990)¹. While these recent non-commercial triangle-based systems allow for complex geological boundary representations, they now belong to only one genus in a growing family of true 3D spatial representation methods (Fried & Leonard, 1990), that indiscriminately rely on powerful 3D graphics hardware².

None of these mapping systems supports the difficult fault correlation process proper in an interactive way. Brede & Thomas (1986) remarked that "when fault aliasing³ is present, it is one of the most difficult problems in seismic interpretation". These authors developed the LANDMARK interactive fault modelling system with which fault picks can be correlated interactively and three-dimensionally into fault planes. The interactive system allows to quickly pose and test alternative interpretation hypotheses on the bases of geometric consistency across several seismic lines, and continuity of fault plane shape and slope. This approach to interactive fault interpretation would not be effective with the North Hinder clay tectonics data. The combination of limited seismic penetration and trace density results in very steep apparent fault dips that are difficult to interpret quantitatively. Furthermore, the LANDMARK system does not make the most of information on the shape of horizon segments, because horizons and faults are modelled separately. Precisely this kind of information is abundant in our data.

Recently, Freeman *et al.* (1990) and Lasseter (1990, 1992) described two prototype fault interpretation systems. While that of the first authors (FAPS) is an elaboration of the LANDMARK method that requires deep seismic penetration (not offered by the North Hinder profiles) to elicit and contour both lateral and significant vertical throw variations, the latter system (IREX) calls for high-performance 3D graphics capabilities.

All of these systems force the *a priori* distinction between horizon and fault system unto the interpretation process. We argue that this distinction is not necessarily relevant during the fault correlation stage, in which any change to the fault cut correlations automatically affects the faulted horizon, the deformations of which may be important clues to more probable fault correlations. Moreover, as we have argued in §3.2.4, the distinction leaves the pitfalls of manual contouring in the

¹The Freiburg University group (Klein *et al.*, 1989; Pflug *et al.*, 1990, 1992) models digitized geological maps and parallel interpreted sections, i.e. finished interpretations and not raw data, primarily for visualization purposes.

²The two leading commercial systems (STRATAMODEL's SGM (Denver & Phillips, 1990) and DYNAMIC GRAPHICS' IVM (Paradis & Belcher, 1990; Paradis, 1990)) even allow to model both complex stratigraphical frameworks and heterogenous volume properties.

³a form of spatial aliasing (see §2.1.1)

presence of faults wide open. These observations underpin the approach we have taken in the development of a new interactive 3D horizon/fault modelling method on an entry-level 2D workstation.

3.4. Hardware platform

In 1988, RCMG acquired a Unix workstation because of its educational value, its flexible interactive and multiprocessing capabilities (in 1988 not widespread on PC's), its possible support for large databases of interpreted seismic profiles and its high speed connection with a planned standard seismic processing system. The challenge taken in the framework of this thesis work therefore was to develop the relevant data preparation, management, interactive 3D surface modelling and visualization software from scratch on a computer as small as the SUN-386i, which is essentially a low-end 2D interactive graphics workstation. It is built around a 20 Mhz INTEL 80386 central processing unit, working in close connection with a 80387 floating point processor, featuring a modest throughput of 3 mips¹ and 0.5 mflops². Many of today's PC's incorporate the same processing pair. Compared with an average PC, it has an ample 8 Mb of main memory and a seemingly sizable 91 Mb hard disc. However, SunOS, a version of the Unix operating system for SUN workstations, shares with the SunView development libraries 70 Mb of disk space, leaving only 20 Mb for the user. The 14" (34 cm diagonal) colour graphics terminal with a 1024x768 pixel screen allows the simultaneous display of 256 colours, programmer definable from a palette of 16.777.216.

Other computer resources at RCMG (fig. 2.8) include an NCR Tower-32 mini-computer, coupled to a CALCOMP 9100 digitizer tablet for input of interpreted seismic profiles and existing maps. A standard seismic processing system ((Raytheon) Seismograph Services' PHOENIX VECTOR) was recently installed on a SUN-370. Our SunView based program can be started under OpenWindows, successor to SunView as the interactive operating system for SUN computers, and runs about five times faster on this medium-range workstation. Its SPARC processor performs 16 mips and 2.6 mflops, and it has a main memory of 32 Mb, a hard disk of 600 Mb and a 19" (48 cm) colour graphics terminal with a 1152x900 pixel screen. The two workstations are linked in a high-speed Ethernet network, so that both can access each other's data on hard disk, and make black and white

¹million instructions per second, a measure for general system performance

²million floating point operations per second, a measure for calculation performance

plots on a 24" (61 cm) VERSATEC electrostatic printer with a resolution of 200 dots/inch (79 dots/cm).

3.5. Data preparation

Data preparation consists of the entry of interpreted seismic profiles in a digital format into the computer, by means of digitization (§3.5.1), and the conversion of 2D digitizer device coordinates (in mm on the tablet) into 3D world coordinates (geographical position and depth, §3.5.3).

In §3.2.1, we have formulated the problem of redundancy at the level of data entry. On the one hand, at least some data redundancy is required to represent the generally gently undulating reflectors with segmented curves that are suitably smooth. On the other hand, digitized points that describe local detail below the precision of digitization are not significant, and should be filtered. This tangled problem leads to the following questions :

1. What are the factors that determine the precision of digitization?
2. How can this precision be measured?
3. Can we formulate a manual digitization procedure in terms of memory efficiency and of detail resolved, in the knowledge of this precision?
4. Which details are significant, or, what is a significant point?
5. How can redundant points be filtered?

The first three questions are addressed in §3.5.1, the latter two in §3.5.2.

3.5.1. Efficient manual digitization of curves

3.5.1.1. Introduction

Foley *et al.* (1990) define *digitization* as the manual conversion of a continuous curve into a segmented line connecting discrete points, by moving a digitizer stylus or cross-hair over the line while coordinates of points along the line are sent to the computer. Manual digitization¹ is a popular way of transforming a real world

¹A high-resolution scanner can perform automatic digitization. Appropriate software transforms the ensuing raster image into a vector format comparable with hand digitized lines. Auto-pick programs automatically track indicated horizons on digital seismic sections and also produce a large amount of points along the horizon.

curve into a computer graphical form. Quite often, the user picks a digitization method rather arbitrarily, aware or unaware of its limitations and accepting data redundancy. A study of how mere quantity and precision limit the usefulness of the digitized curve, will lead us to propose an efficient digitization method in terms of memory and processing efficiency and of detail resolved. At the same time we will illuminate the relation between the original curve and the digitized version.

Quite surprisingly, a systematic approach to this fundamental problem has not been described in the literature, except for Ward & Phillips (1987) who did so at the level of digitizer technology. Before the advent of cheap memory hardware, data efficiency requirements did lead to the development and use of data reduction methods (§3.5.2). On the other hand, manual digitization introduces operator dependent imprecisions that never have been quantified, but which we will show to be the truly limiting factor to the usefulness of digitized curves. In general, data reduction is applied without a proper understanding of these imprecisions.

3.5.1.2. Digitization and its limitations

Ideally, digitization as defined above should preserve all information, but like with any sampling process, data density and precision limit the usefulness of the digitized curve.

Several methods of digitization are available. In 'point mode', the user determines which points to select, and manually digitizes each of them separately. This method is very popular (Jones, 1986), since the operator has a sense of 'control' over what he or she is digitizing. A more or less horizontal and featureless reflector is digitized in point mode with the same sample interval as more rugged relief. But even small errors in picking the reflector lead to contours that wiggle between superfluous data points and that thereby suggest relief where there is none. Such meaningless contour wiggles are known as 'trivia' (Tucker, 1988) and usually need to be smoothed out manually. In addition to this problem, resolvable detail can be inadvertently skipped. Because of its non-objectivity and non-uniformity, we therefore recommend against digitizing curves in point mode.

Two 'continuous modes' allow the curve to be safely oversampled. In 'increment mode', a fixed, small distance interval has to be travelled, before a new point is stored. In 'line mode', sampling occurs after a fixed time interval. Digitization in increment mode produces curves made up of points at regular intervals. The distance increment should therefore be at least as small as the smallest detail of

interest. Because local detail of a curve is captured by the position of a digitized point relative to its neighbours, a *detail* can be defined (Asada & Brady, 1986) as a point where curvature changes significantly or reaches a maximum. Parts of the curve with constantly low curvature will yield a lot of superfluous points. In line mode, inevitable changes of digitizing speed lead to unequal spacing of points. It should be noted however that speed generally varies inversely with curve complexity, so that less points are produced where curvature varies rapidly. If as much detail is to be preserved as possible, either the distance increment should be very small or the sampling rate high, resulting either way in many superfluous data points idly occupying disk space and wasting processing time.

Three factors determine the smallest detail digitization can resolve. Firstly, the curve can be too complex at the smallest visible scale, so that any detail smaller than the resolution of the human visual system (about 0.05 mm at reading distance) is inevitably lost.

The resolution of digitizer tablets (0.025-0.1 mm after Ward & Phillips, 1987 and Hearn, 1987) is usually comparable to the resolution of the human eye. The accuracy however, can vary from high (0.1 mm) when a flat-bottomed puck with a cross-hair is used on a high quality tablet, to low with a stylus or light-pen (*ibidem*).

Thirdly, operators using a digitizer have a varying sense of accuracy and ability to concentrate, also depending on fatigue and the complexity of the curve, a smooth curve being easier to digitize. In addition, seismic reflections on analog profiles are not very sharp and not always easy to pinpoint. Hence, operator errors can be larger (on the order of 1 mm) than the resolution of the eye and of the digitizer. This imprecision is therefore the truly limiting factor of digitization quality and should be quantified, preferably for each digitizer session.

3.5.1.3. Efficient manual digitization of curves

An efficient digitization procedure in terms of detail resolved and memory economy therefore consists of several steps. Firstly, the operator should know his/her precision at digitizing a given type of curves. How can such a highly varying precision be measured easily and reliably? We will introduce our method in the following section. Then, one of the continuous modes should be used with either a distance or time interval small enough to ensure oversampling of the smallest detail of interest. Finally, any point holding detail smaller than the digitization accuracy should be filtered automatically, since such points do not hold actual information. Line simplification algorithms do this objectively (§3.5.2).

3.5.1.4. Measuring digitization precision

The error on the position of a digitized point can be defined as the distance between the point and the original curve. The digitization precision can then be regarded as the mean absolute error. This approach raises two questions : where exactly is the original curve and how to define and calculate the distance of a point to a (segmented) curve?

We define the distance of a point P to a complex curve as the length of the shortest line connecting both. For segmented curves, this is the distance to the closest segment. It should be noted that this is not the same as the smallest of all distances of P to the lines through all consecutive pairs of vertices. Instead, it is either the distance to the nearest vertex, or the smallest distance to a segment perpendicularly above or below P (fig. 3.2). The distance defined in this way is always positive, because it does not take into account that the points are either to the one side of the segmented curve or the other.

The exact location of the original curve can only be approximated by some kind of averaging between repeated digitizations. Such a procedure is not only likely to be computationally complex, but cumbersome for the operator as well. For the sake of an experiment however, we can measure the exact location of a simple curve, consisting of only a few straight line segments, by digitizing its vertices repeatedly in point mode, and by calculating an average position for each of the vertices. We then digitize the simple curve in line mode and calculate the digitization precision as the mean distance of all digitized points to the precisely situated segmented curve. Next, this precision is compared with a substitute that can be calculated routinely : the mean distance between two successive digitizations.

An algorithm to calculate the mean distance between two segmented curves can be formulated as follows :

1. Calculate and sum the distances of each point of the first segmented curve to the nearest segment or vertex of the second one;

that is to say, for each point $P1_i$ of the first curve :

- 1.1. Find the nearest point $P2_j$ on the second curve and the distance d_i to it;
- 1.2. For each segment $[P2_k, P2_l]$ of the second curve within a neighbourhood of $P2_j$; if $P1_i$ lies perpendicularly above the current segment then calculate the perpendicular distance to that segment and assign this distance to d_i if it is smaller;

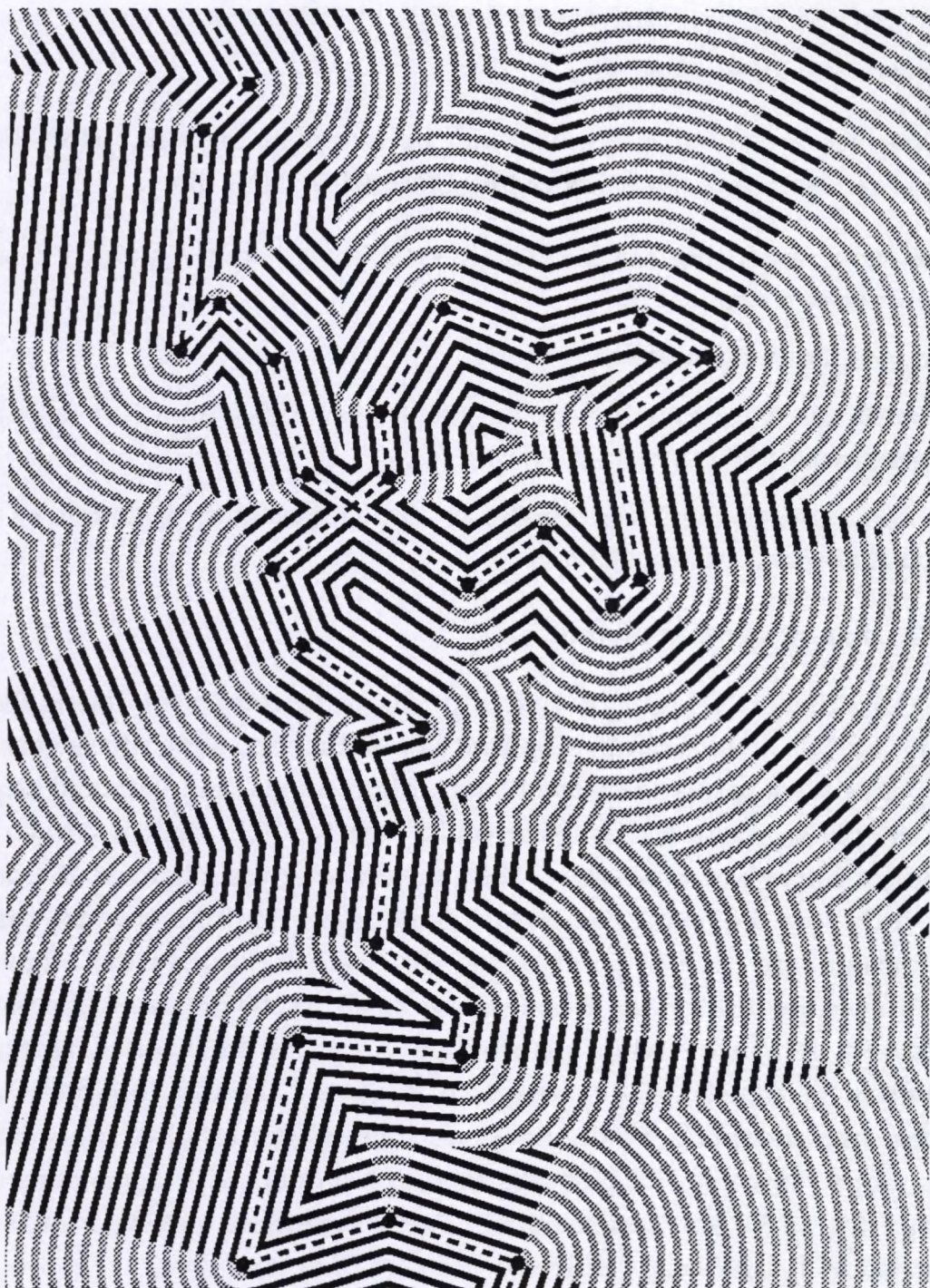


Fig. 3.2. Equidistance lines around a digitized curve. The digitized version of a continuous curve is a segmented curve (dashed) connecting a series of vertices (black dots). The distance between a point and a segmented curve is defined as the length of the shortest line connecting both. Points in the plane around the segmented curve are either closest to the vertices (grey/white zones), or to the segments (black/white zones).

2. Idem as 1., but with first and second curve interchanged;
3. Calculate the mean distance.

Since the nearest point or segment can be found in the neighbourhood of the previous segment, this algorithm can be executed in $O(N)$ time¹.

The following algorithm can be used to establish whether a point P lies perpendicularly above a segment S :

1. Calculate the slope m of S ;
2. Calculate the X -coordinate x of the intersection of S with a line through P and perpendicular to S (with slope $-1/m$);
3. If x lies between the X -coordinates of the endpoints of S , it follows that P is situated perpendicularly above S .

3.5.1.5. Experimental results

For the experiment, 20 regularly spaced points at the corners and along the sides of a $30 \times 40 \text{ cm}^2$ box were carefully digitized in point mode. Very precise positions for these points were calculated from 10 such digitizations, and gathered sequentially into a simple segmented curve that could pass for 'the original curve', being as close to the actual box as possible. Then, the drawing was digitized 15 times in line mode, each time producing 500 points on average. Fig. 3.3 shows the distribution A of distances of all 7500 points of all digitized versions to the original, while fig. 3.4 shows the distribution B of distances of all 105000 points of all possible pairs of digitized versions. While distribution A can be interpreted as that of the distribution of actual absolute errors, B is merely the distribution of distances between two independent digitizations. Both figures also show how these distributions compare with half a normal distribution with a standard deviation based on the 68.3% smallest samples. The distributions can be seen to be quite similar but still significantly different from a half-normal one.

¹If the algorithm were to search for the closest point by scanning the whole sequence of vertices, and not just the immediate neighbourhood of e.g. the first 10 vertices, its time requirement would increase to $O(N^2)$. The notation $O(N)$ is a measure of the efficiency of an algorithm and can be thought of as 'execution time linearly proportional to N ', in which N is the number of data. For example (Bentley, 1986), two algorithms that require resp. $(15N^2 + 100N)$ and $(N^2/2 - 10)$ calculation steps have $O(N^2)$ both. The notation reflects the fact that execution time is mainly determined by N , the number of data, and that an algorithm with e.g. $O(N^2)$ results in execution times that increase quadratically rather than linearly as with $O(N)$. See the preface in Sedgewick (1983) for a short discussion of the main types of $O()$ functions, and Knuth (1973) for a formal definition and algorithm analysis techniques. Bentley (1986) provides an intuitive and practical understanding of algorithm design and efficiency.

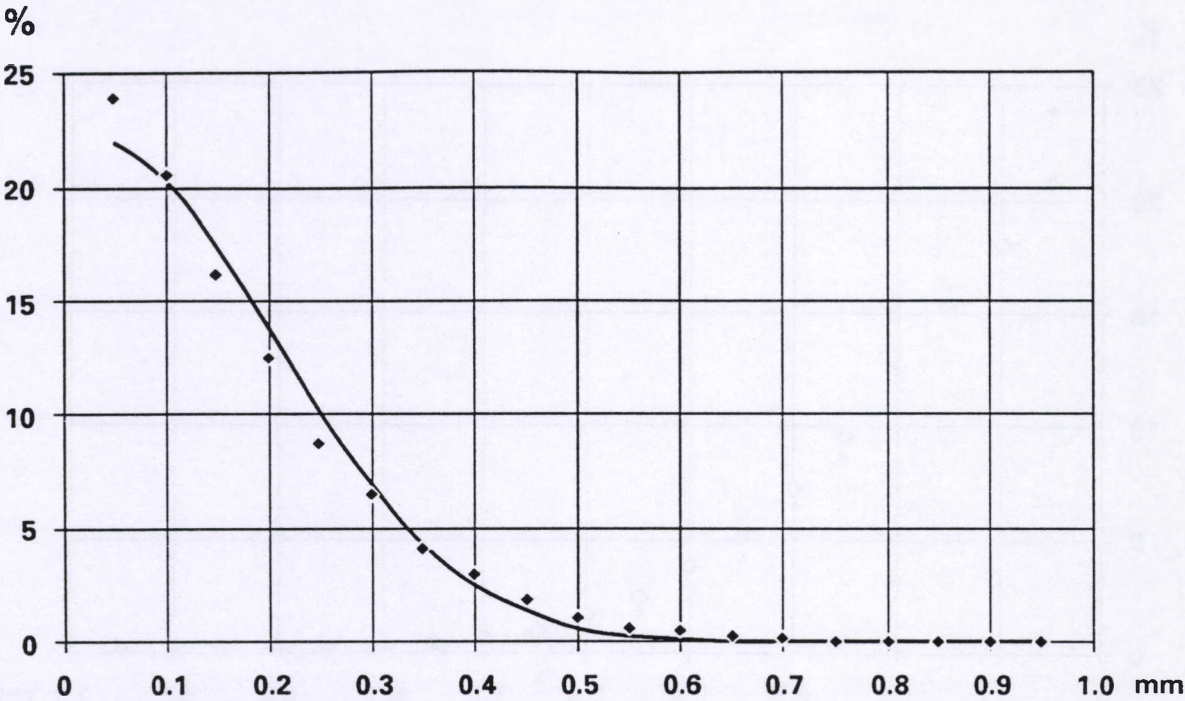


Fig. 3.3. Measuring the precision of manual digitization. Distribution (A) of distances between points digitized along the borders of a 30x40 cm box, and the "true" position of those borders (\diamond). This distribution corresponds with the distribution of *actual operator errors* on a digitized curve. Note the small but significant difference with half a normal distribution based on the 68.3% smallest distances (solid line).

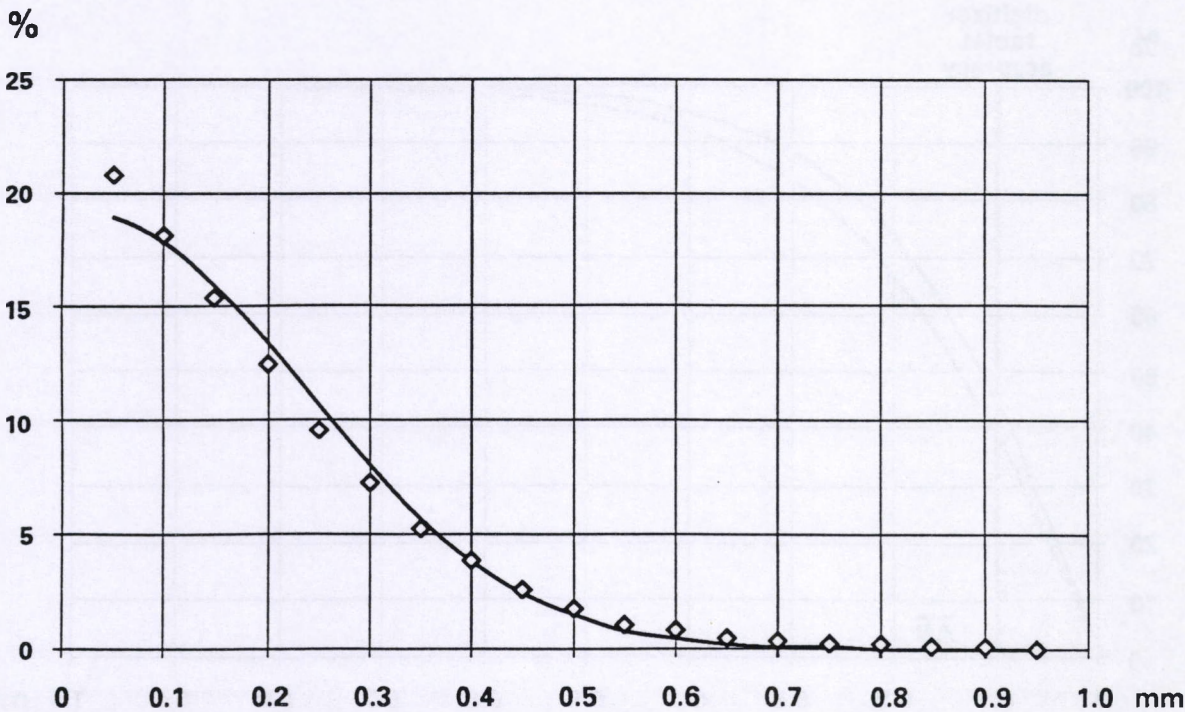


Fig. 3.4. For each pair of digitized versions of the 30x40 cm box, distances were calculated between one version and the points of the other. This is the distribution (B) of those distances (\diamond), which is also the distribution of the distances between any two independent digitizations. Note that the difference with a half-normal distribution (solid line) is completely similar to that in fig. 3.3.

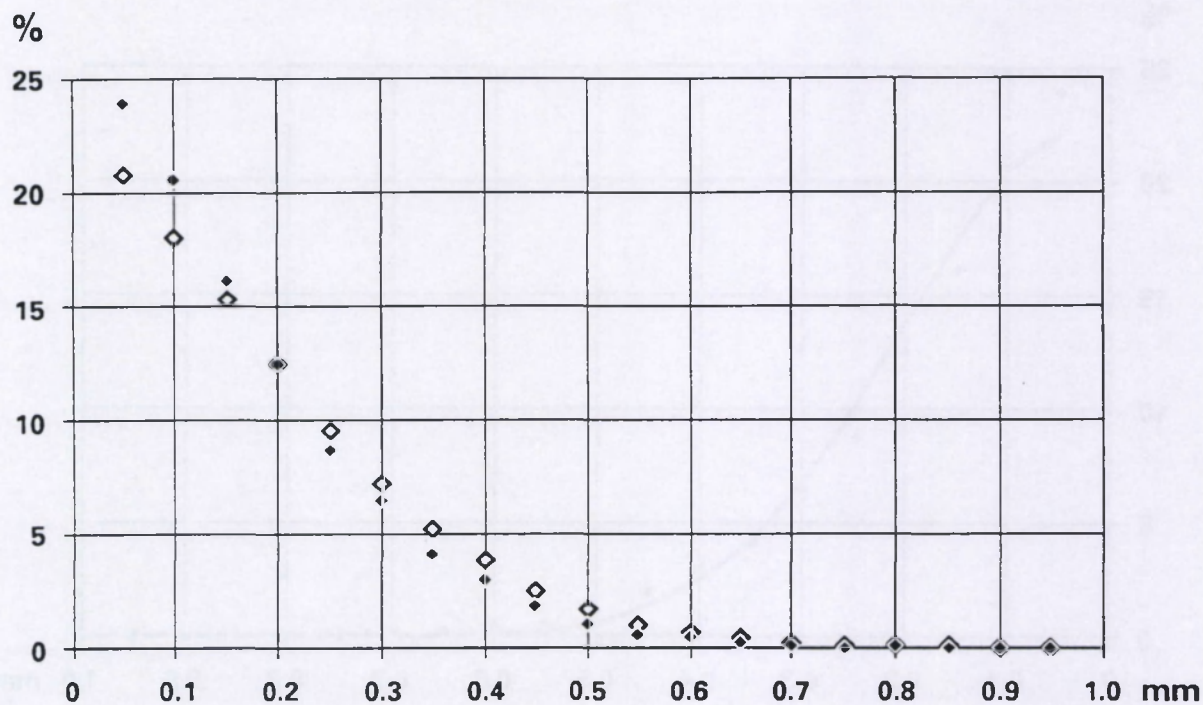


Fig. 3.5. A comparison of distribution A (◆) and B (◇).

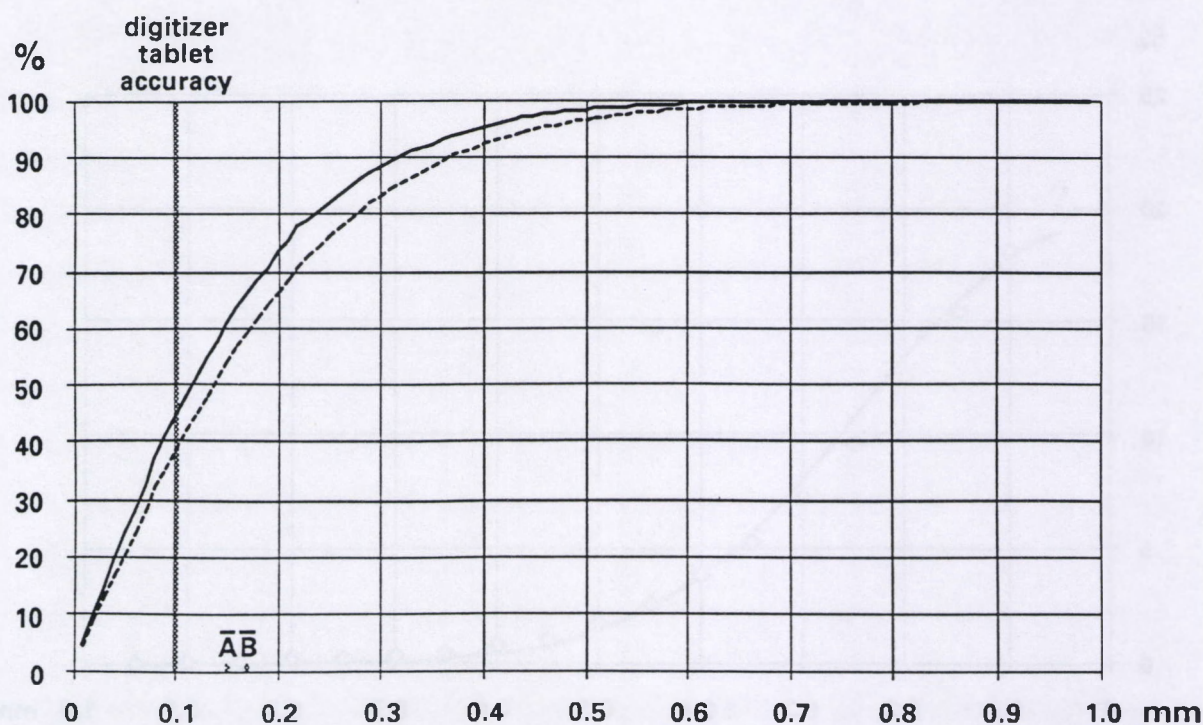


Fig. 3.6. Cumulative distributions A (solid line) and B (dashed). Means of both distributions can be read along the distance axis. For comparison, worst-case digitizer tablet accuracy is indicated on top. The mean of distribution B, which can be calculated routinely at the start of a session from two successive digitizations of a typical curve, can be seen to be a good measure of overall digitization precision.

Distributions A and B are compared with each other in fig. 3.5 and their corresponding cumulative distributions in fig. 3.6. It is clear that distributions A and B are not dissimilar. This experiment with a very simple curve resulted in a high precision of 0.15 mm. The mean distance in B was with its 0.17 mm only 1.15 times larger. The mean distance calculated from distribution B can therefore serve as a measure for the actual operator precision, that can be derived from A. A precision of 0.15 mm was still markedly worse than the 'worst-case' accuracy of 0.1 mm for the digitizer tablet concerned. The worst-case errors in this experiment were huge by comparison : on a total of 7500, 8 points were at a distance of between 0.8 and 0.95 mm from the actual box. These maximum distances were also found to vary widely from one digitization to another : on a total of 15 digitizations, the mean maximum distance was $0.72 \pm 0.15(\sigma)$ mm. For comparison, the mean maximum distance between a total of 120 pairs of digitizations was $0.88 \pm 0.15(\sigma)$ mm, 23% larger.

In conclusion, the precision of manual digitization depends on the operator, curve complexity and the quality of the digitizer tablet. The mean distance between two digitized versions of a sufficiently long part of a typical curve can be expected to be a stable and dependable measure of an operators digitization precision at a certain level of curve complexity. More complex curves result in simply wider distributions, with correspondingly larger means. Hence, this measure should and can be calculated routinely at the start of each digitizer session.

We developed a program on the NCR Tower-32, connected with the tablet, to do this automatically. After the operator has digitized the same typical curve twice in line mode, the precision of digitization is calculated as 1/1.15 times the mean distance between the two versions. An example is illustrated in fig. 3.7.

3.5.2. Data reduction

Having measured the precision of digitization (§3.5.1), we face the next two questions raised at the beginning of §3.5: what is the relation between an insignificant detail, an insignificant point and the measured precision, and how to filter insignificant and therefore redundant points away? The latter question is also known as the problem of curve simplification, for which dozens of algorithms have been published. Depending on the definition of a significant point, each of the resulting curve simplifications has different properties. Because the literature on the subject is rather voluminous, we focus only on the different types of

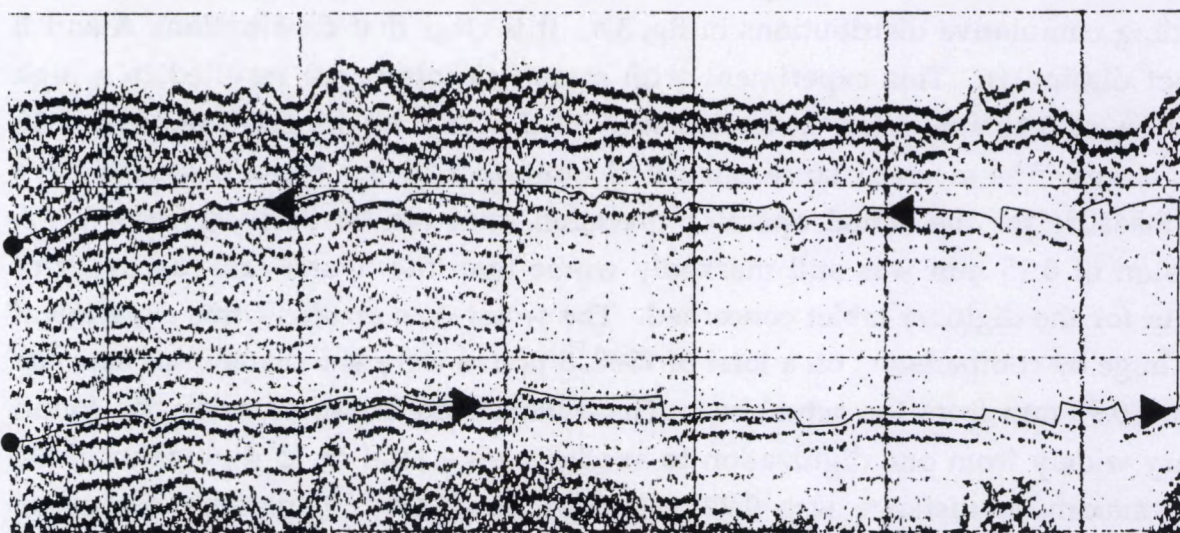


Fig. 3.7. Typical profile from North Hinder sparker network, used to gauge the precision of digitization. The indicated line with a total length of 50 cm was digitized twice in line mode, yielding resp. 550 and 440 points. The mean distance between these two digitizations was 0.185 mm, which is equivalent with a precision of 0.16 mm. The maximum distance was 0.81 mm.

approaches and a restricted number of examples (§3.5.2.1). We then introduce our own algorithm and show how it can be used to reduce data redundancy at the level of data entry (§3.5.2.2).

3.5.2.1. Review

Research on computational vision has lead to automatic silhouette recognition with curve representations ('finger prints') based on significant changes and extrema in curvature at multiple scales (Asada & Brady, 1986; Mokhtarian & Mackworth, 1986). While this approach to curve detail at multiple scales and curve simplification matches very well with human perception of curve characteristics, it is very complex computationally, and cannot be related to a distance based precision.

Curvature based curve representations not only consist of the positions of significant points but also of local tangent direction, curvature and change of curvature. All other methods of curve simplification store significant vertices only, chained together in a 'polygonal approximation' of the original curve.

One possibility is to characterize a detail as a change of curve tangent direction. Williams (1978) and Sklansky & Gonzales (1980) developed simple and efficient 'cone intersection' algorithms that select significant points on the basis of this definition. They add the constraint that the resulting curve should not deviate from the original beyond a given distance. While Williams (1978) was the only

author who included an ALGOL¹ description of his algorithm, making implementation in any programming language particularly easy, his approach was found to be incapable of locating the local extrema accurately. As the curve was scanned sequentially, the first point that lay outside a tangent cone was selected as a significant point. This criterion is sufficient to locate points where curve direction changes gently. Local peaks are often missed, because one of its immediate neighbours may be found to honour the requirement before the peak itself is tested. And when it is tested, it may not be significant relative to the 'peak' just selected.

The majority of published curve simplification algorithms use an explicit distance tolerance criterion in the selection or construction of significant points (Kurozomi & Davis, 1982; Cromley & Campbell, 1990). Some authors (e.g. Kurozomi & Davis, 1982) prefer to construct segments connected at new vertices instead of selecting points from the original curve. This alters curve shape, which is not acceptable in our case. Most other authors propose algorithms that select a subset of the vertices of the original curve. Among these, 'optimal' algorithms (e.g. Cromley & Campbell, 1990) minimize the number of retained segments under a combination of constraints, the maximum deviation criterion being one of them. Such optimal solutions come at a steep price of processing time and implementation complexity, but they may be visually indistinguishable from the solutions of a number of simple heuristic algorithms that are very fast ($O(N)$ time efficiency). The popular Douglas-Peucker algorithm (Douglas & Peucker, 1973) for example, recursively splits the original curve at the vertex most distant from a line connecting start and end point, the selected vertices becoming new local start and end points. Recursion halts when all intermediate vertices are within a certain distance of the selected curve. It is obvious however, that vertices selected at a global level in the early stages of recursive subdivision are not necessarily significant at a local level.

In conclusion of this short review, distance based polygonal approximation algorithms were found either to be simple, fast, but lacking in local optimization, or to be too complicated to implement in a program practical for our purposes.

3.5.2.2. Local maximum distance algorithm

An algorithm was developed, based on a simple but sufficiently effective concept of maximum local significance, and that scans the original segmented curve sequentially, so that it is also efficient in processing time.

¹ALGOL is a both a true programming language and a generic pseudo programming language used to describe algorithms in some detail. Such pseudo code can easily be translated into any real programming language, such as C, Pascal, Fortran, ..

Let P be the original segmented curve of $n > 1$ vertices $P = \{P(i); i=1, \dots, n\}$ and $P' = \{P'(i); i=1, \dots, m \leq n\}$ the polygonal approximation of P , with $P' \subset P$, so that the maximum distance between P and P' is d , the *weeding tolerance* (Douglas & Peucker, 1973).

The definition of a *significant* vertex as a local extremum at a maximum distance from a local scan segment, leads to the following simple local maximum distance algorithm (fig. 3.8):

1. Select $P(1)$ as $P'(1)$;
2. Construct a scan segment $S(ibegin, iend)$ connecting the point last selected $P(ibegin)$, which is currently last in P' , with the next scan segment end point $P(iend)$;
3. Scanning all points $\{P(i); ibegin < i < iend\}$, establish point $P(imax)$ with maximum distance d_{imax} to S ;
4. Point $P(imax)$ is significant and can become $P(imax) \in P' \Leftrightarrow d_{imax} > d$. If such a point is not found with the current $S(ibegin, iend)$, increase $iend$ and re-iterate from 2. until $i=n$;
5. Include $P(n)$ as $P'(m)$.

Because this is a purely sequential algorithm, it can be executed in $O(n)$ time. But when there are many redundant vertices, which is the case for curves of low complexity such as digitized reflectors, the re-iteration needed to find an endpoint of the scan segment that lies far enough to detect a local extremum may be rather time-consuming. Furthermore, the algorithm in this form is too conservative, as the distance between P and P' can never be larger than a fraction d . An allowable shortcut consists of taking $P(i) = P(iend) \Leftrightarrow D(ibegin, i) > k \cdot d$ where D is a distance function of the coordinates of $P(ibegin)$ and $P(i)$, and k an integer. In order not to miss significant points in the presence of narrow peaks, D should not be the Euclidean distance but the integrated path length between $P(ibegin)$ and $P(i)$. It is also clear that $k \geq 2$, since a point $P(i): D(ibegin, i) < 2d$ cannot be significant.

In order to make this simple and efficient algorithm more accessible for implementation in other applications, an ALGOL embodiment is given in fig. 3.9. As will be shown in §3.7.5, extension of this algorithm to filter spacefilling polygonal curves (e.g. seismic reflectors along a curved profile, during the modelling stage) is straightforward.

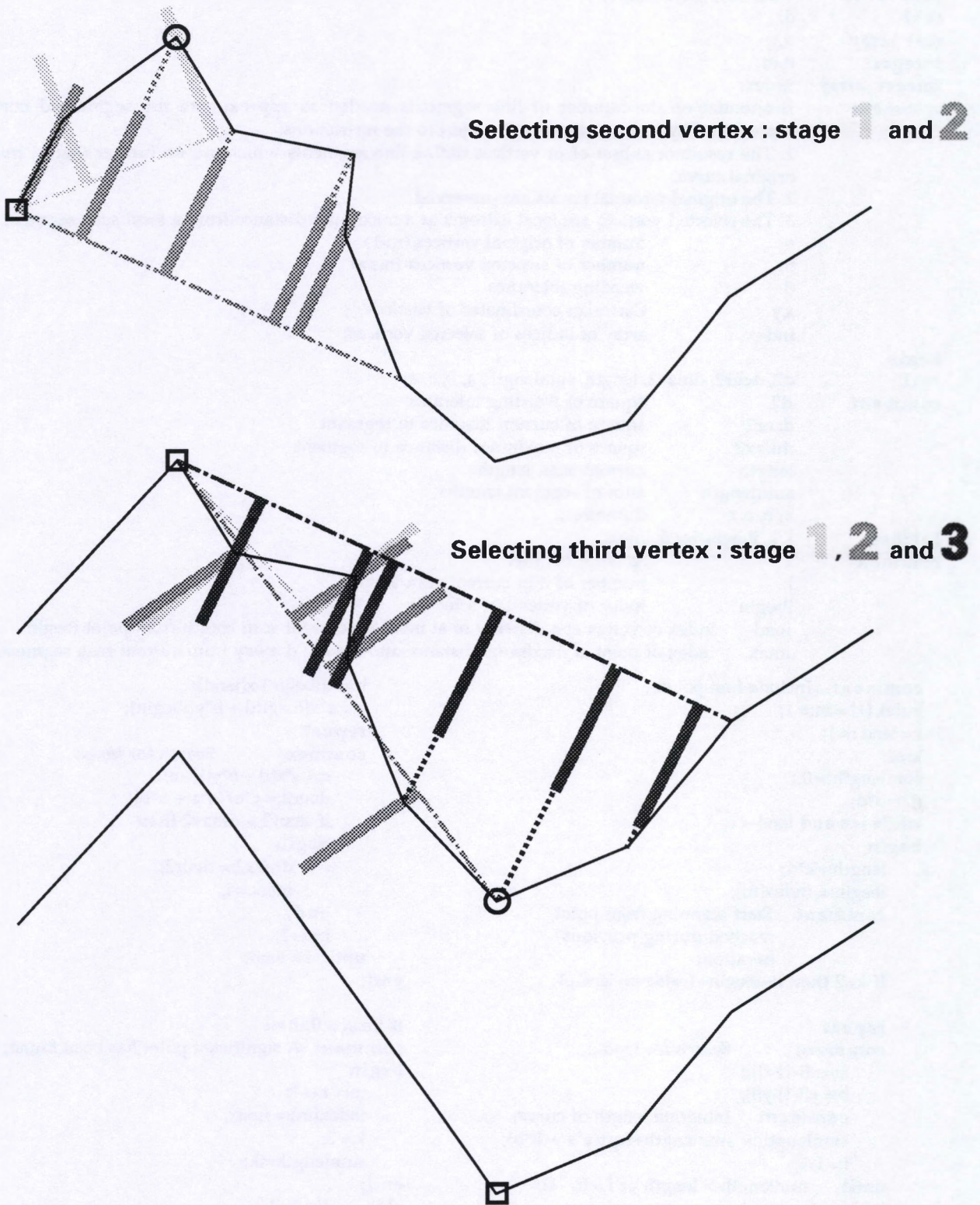


Fig. 3.8. Principle of a new polygonal approximation algorithm.

A polygonal approximation of a segmented curve (thin black solid) is found by selecting vertices that are local extrema at a maximum distance from a local scan segment, in such a way that the distance between the original and resulting polygonal curves is never larger than a given weeding tolerance. Starting at one of the ends (square in uppermost drawing), a local scan segment (thin dash-dotted) reaches in stages farther and farther along the polygonal curve. Each time, the distances to all of the intermediate points are calculated. As soon as the maximum distance is found to exceed the weeding tolerance (thick solid line), the corresponding vertex is considered to be locally significant (circle) and is selected as the next starting point.


```

procedure    filter (x,y,n,d,index,m);
real        d;
real array   x,y;
integer      n,m;
integer array index;
comment      Economize on the number of line segments needed to approximate the segmented curve
                represented by the n vertices (x,y) subject to the restrictions:
                1. The resultant subset of m vertices define line segments which are no further than d from
                original curve.
                2. The original terminal points are preserved.
                3. The selected vertices are local extrema at a maximum distance from a local scan segment.
                n          number of original vertices (n>1)
                m          number of selected vertices (m≤n)
                d          weeding tolerance
                x,y        Cartesian coordinates of vertices
                index      array of indices of selected vertices;

begin
real        d2, dcur2, dmax2, length, sumlength, a, b, c, e;
comment      d2          square of weeding tolerance
                dcur2      square of current distance to segment
                dmax2      square of maximum distance to segment
                length     current scan length
                sumlength  sum of segment lengths
                a, b, c, e  dummies;

integer      i, k, ibegin, iend, imax;
comment      i          general counter
                k          number of d in current scan length
                ibegin     index of vertex last selected
                iend       index of vertex at a distance of at most the current scan length from point ibegin
                imax       index of point at maximum distance and at least d away from current scan segment;

comment      Include first point;
index [1]:= m:= 1;
i:= iend := 1;
k:=2;
sumlength:= 0.;
d2:=d*d;
while i<n and iend < n
begin
    length:=k*d;
    ibegin:= index[m];
    comment      Start scanning from point
                reached during previous
                iteration;
    if k=2 then i:=ibegin+1 else i:= iend+1;

    repeat
    comment      Search for iend..;
        a:= x[i-1]-x[i];
        b:= y[i-1]-y[i];
        comment      Integrate length of curve;
        sumlength:= sumlength+sqrt(a*a + b*b);
        i:= i+1;
    until sumlength > length or i > (n - 1);
    iend:= i-1;
    i:= ibegin+1;
    dmax2:= d2;
    imax:= 0;
    if iend - ibegin > 1 then
        a:= y[iend]-y[ibegin];
        b:= x[ibegin]-x[iend];
        e:= a*x[ibegin] + b*y[ibegin];
        repeat
        comment      Search for imax;
            c:= a*x[i] + b*y[i] - e;
            dcur2:= c*c/(a*a + b*b);
            if dcur2 > dmax2 then
                begin
                    dmax2:= dcur2;
                    imax:= i;
                end;
            i:= i+1;
        until i = iend;
        end;

    if imax ≠ 0 then
        comment      A significant point has been found;
        begin
            m:= m+1;
            index[m]:= imax;
            k:= 2;
            sumlength=0.;
        end;
        else k:= k+1;
    end;
    comment      Include last point;
    m:= m+1;
    index[m]:= n;
end;

```

Fig. 3.9. ALGOL embodiment of local maximum distance algorithm to find a polygonal approximation of a segmented curve of (x, y) vertices.

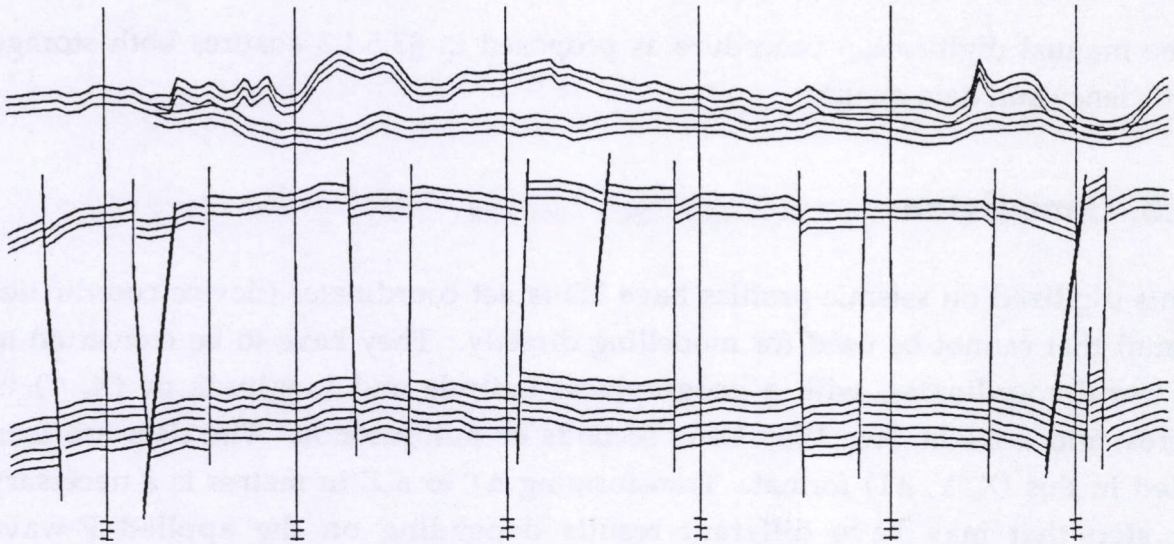


Fig. 3.10. Three versions of the interpreted linedrawing of the profile in fig. 3.7. The top line in each triad connects all 987 digitized points. Using automatic polygonal approximation with a weeding tolerance equal to the precision of digitization ($p = 0.16$ mm), only 380 or 39% of the digitized points were found to be significant. The middle line connects only these significant vertices. The lowermost line ensues from using a the weeding tolerance of $2p$, and connects only 280 or 28% of the digitized points.

3.5.2.3. Experimental results

We can now demonstrate the effectiveness of this algorithm as an integrated part of the efficient manual digitization of curves, as proposed in §3.5.1.3. Several reflectors in fig. 3.7 have been digitized and plotted in fig. 3.10 (top lines), together with simplified versions (middle and lowermost lines). Using automatic polygonal approximation with a weeding tolerance equal to the precision of digitization, measured as explained in fig. 3.7, only 40% of the digitized points have been identified as significant vertices. There was no noticeable loss of information when only these significant vertices were connected (middle lines). The lines actually gained some clarity as most of the digitization 'noise' was filtered away. In this survey, there was therefore no reason to store more than 40% of the points digitized in line mode. With a weeding tolerance of twice the precision, the algorithm worked as expected as well, but some visible and perhaps interesting details were filtered away along with truly insignificant vertices.

We conclude that :

1. our new curve simplification algorithm reliably and objectively removes insignificant vertices from a polygonal line, below any given level of detail;
2. polygonal approximation can be used to reduce data redundancy before permanent storage, without a loss of significant information;

3. the manual digitization procedure as proposed in §3.5.1.3 ensures both storage efficiency and data quality.

3.5.3. Conversion

Points digitized on seismic profiles have 2D tablet coordinates (device coordinates in mm) that cannot be used for modelling directly. They have to be converted to 3D world coordinates, with a geographical latitude and longitude or (X, Y) in metres, and a ΔT in Two Way Time seconds or milliseconds. The data are then stored in this (X, Y, ΔT) format. Transforming ΔT to a Z in metres is a necessary last step that may have different results depending on the applied P-wave velocity/depth function. In order to easily generate several time-depth converted models based on different velocity hypotheses, time-depth conversion has been incorporated in the interactive modelling program Geofox (§3.7.8).

The first conversion relies solely on regularly measured positions along the seismic tracks, the so-called *fixes*. These fixes are marked on the profiles with *fix lines* that are digitized together with the interpreted reflections and faults. Absolute positions of the interpreted data can then be interpolated between the known fix positions. This conversion has been programmed separately from the modelling software because it needs to be performed only once.

The program is based on the work of Van De Walle (1988), but makes the most of SunView's and OpenWindows' interactive file management capabilities in order to restrict user input to a minimum, while at the same time enabling the automatic conversion of all (filtered) digitizer files to profiles in world coordinates, and the creation of files that each contain all the data of an individual, named reflector, ready for input into the modelling program.

Geographical coordinates are converted to Cartesian coordinates with a Universal Transverse Mercator projection, with any arbitrary central meridian. In order to obtain the best possible (X, Y) precision for 3D surface modelling, positioning data available between the fix points are used as well. In addition, the offset between the source-receiver pair and the radio positioning antenna is taken into account by moving the data backwards relative to the vessel's heading along the curved track. These enhancements avoid position errors of up to 50 m in the case of the North Hinder seismic networks.

Lastly, optional time-depth conversion of profiles is provided with a simple velocity model, consisting of mean P-wave velocities in water and the substratum.

3.6. A new 3D surface modelling method

In §3.1, we envisaged 3D geological surface modelling as a process of integrated objective mapping, geological interpretation and 3D visual inspection. Tackling the problems with the North Hinder data enumerated in §3.2 asked for a modelling method based on *entirely new interactive functions* summarized by Verschuren (1992).

Firstly, the dense network of 20x40 profiles contains a large number of fault cuts, even by petroleum industry standards. Interaction with a computed surface that is modelled directly with the digitized data points can only become efficient if the modeller works only with data points that are relevant at the modelling scale. This calls for *interactive 3D curve simplification*, complementary to automatic 2D curve simplification at the level of data entry (§3.5.2).

Because the data contained both non-systematic mis-ties and positioning errors, data could be 'wrong' relative to the evolving interpretation. *Interactive data correction* therefore had to be an integrated part of modelling. If interpolated contours turn out to be suspect, the modeller should be able to move individual or groups of data points up or down, simply by selecting them and dragging them up or down, while contours are continuously updated, until the data are seen to be more in line with the neighbouring profiles. Gridding and automatic contouring in the presence of faults is usually so tedious and unreliable that suspect contours are corrected, rather than the imprecise data points themselves, leaving these corrections unrecorded in the database. It should also be possible to move selected points horizontally, to correct for positioning errors.

Any change in the correlation of fault cuts implicitly changes the faulted surface. We therefore envisaged to *interactively model surface discontinuities as part of a generally smooth surface*, not separately. Basically, this entailed a direct interaction with data points, their *known* connections (the 2D shape along a profile) or the correlation of fault cuts and other features, which are *interpreted* connections. The latter determine the 3D shape of a geological surface. A network of triangular connections between the data points is therefore the most logical data structure to interact with directly and to create the surface model efficiently.

The visualization of faulted surfaces in 3D is more tricky. Firstly, a surface needs to be constructed that does not smooth out every discontinuity. For most gridding

techniques, discontinuities such as faults are a mere nuisance. Again only direct interpolation on a pure triangulation can accurately preserve discontinuities, because it guarantees a perfect fit at the data points proper. Hidden surface removal on an irregular triangulation however is not very practical on a 2D workstation, because of the unpredictable ways triangles can overlap in projection. Moreover, projected triangles are hard to interpret three-dimensionally, since they lack perspective. Lastly, contours are not smooth but break at the edges of flat triangles. On the other hand, gridding offers perspective and straightforward hidden surface removal and has numerous other advantages as well (§3.3).

We wanted to combine the best of both worlds into a *hybrid triangulation/grid modelling method*. This required no less than a new gridding technique, with which a grid could directly inherit the shape of the underlying triangulation, together with interpreted discontinuities, but without the need for explicit digitization of scarp or fault traces.

Such powerful interactive and interpretative functions are a far cry from what is usually understood as 'interactive mapping' (Jones, 1986). In addition, all but the most powerful workstations lacked realistic 3D visualization to aid efficient model evaluation and spotting flaws. All too often, available 3D functionality merely satisfied an appetite for 'nice', qualitative pictures that catch the eye. We envisaged *3D visualization as an integrated part of the tool*, in order to provide both quantitative and qualitative feedback (§3.2.5).

3.7. Geofox

3.7.1. Introduction

We decided to collect all relevant data management, modelling and visualization software in a single application that would incorporate the SunView facilities (§3.7.2), and hence its 'user-friendly' interactive interface. The general flowchart of interaction with the program, named 'Geofox' after Prof. A.F. Renard, is outlined in fig. 3.11. The main phases of interaction comprise selected input, modelling and viewing. It should be noted however that the start-to-end character of the flowchart is only used for clarity of explanation, and therefore can hardly convey the freedom of combination and possibilities a user has. A Manual written to serve both as a tutorial and reference is available as on-line help (see Addendum).

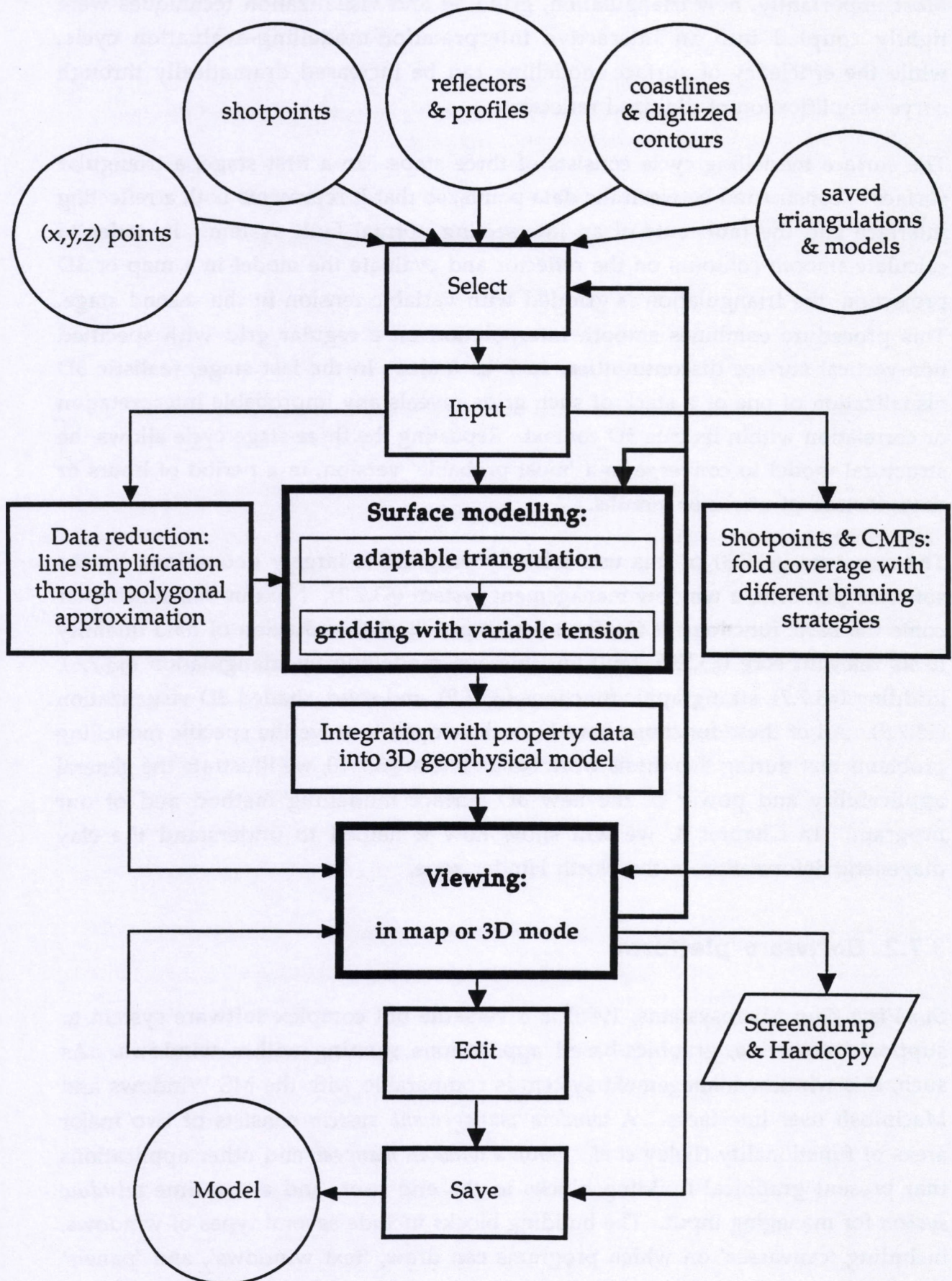


Fig. 3.11. Flowchart of modelling with Geofox. The main modelling loop consists of the steps in boldface.

Most importantly, new triangulation, gridding and visualization techniques were tightly coupled into an interactive interpretation-modelling-evaluation cycle, while the efficiency of surface modelling can be increased dramatically through curve simplification of digitized reflectors.

The surface modelling cycle consists of three steps. In a first stage, a triangular surface is constructed between the data points, so that it represents both a reflecting interface and the fault cuts of an intersecting normal fault system. In order to calculate smooth contours on the reflector and evaluate the model in a map or 3D projection, the triangulation is gridded with variable tension in the second stage. This procedure combines smooth interpolation on a regular grid with specified non-vertical surface discontinuities, such as faults. In the last stage, realistic 3D visualization of one or a stack of such grids reveals any improbable interpretation or correlation within its true 3D context. Repeating the three-stage cycle allows the structural model to converge to a 'most probable' version, in a period of hours or days, instead of weeks or months.

The structure (§3.7.3) of this user-friendly program is largely determined by the software platform, a window management system (§3.7.2). Next in this subchapter come the basic functions of Geofox : data input (§3.7.4), reduction of data quantity to its relevant core (§3.7.5), fault and horizon modelling by triangulation (§3.7.6), gridding (§3.7.7), stratigraphic functions (§3.7.8), and solid, shaded 3D visualization (§3.7.9). All of these functions have been developed to solve the specific modelling problems met during this thesis work (§3.2), but in §3.7.10, we illustrate the general applicability and power of the new 3D surface modelling method and of our program. In Chapter 4, we will show how it helped to understand the clay diagenetic deformation in the North Hinder zone.

3.7.2. Software platform

SunView (Sun Microsystems, 1988) is a versatile but complex software system to support interactive, graphics-based applications running within windows. As such, this window-management system is comparable with the MS Windows and Macintosh user interfaces. A *window management system* consists of two major areas of functionality (Foley *et al.*, 1990): a *window manager* and other applications that present graphical building blocks to the end user, and a run-time *window system* for managing input. The building blocks include several types of windows, including 'canvasses' on which programs can draw, 'text windows', and 'panels' containing items such as buttons, choice items, and digital sliders. Transient inter-

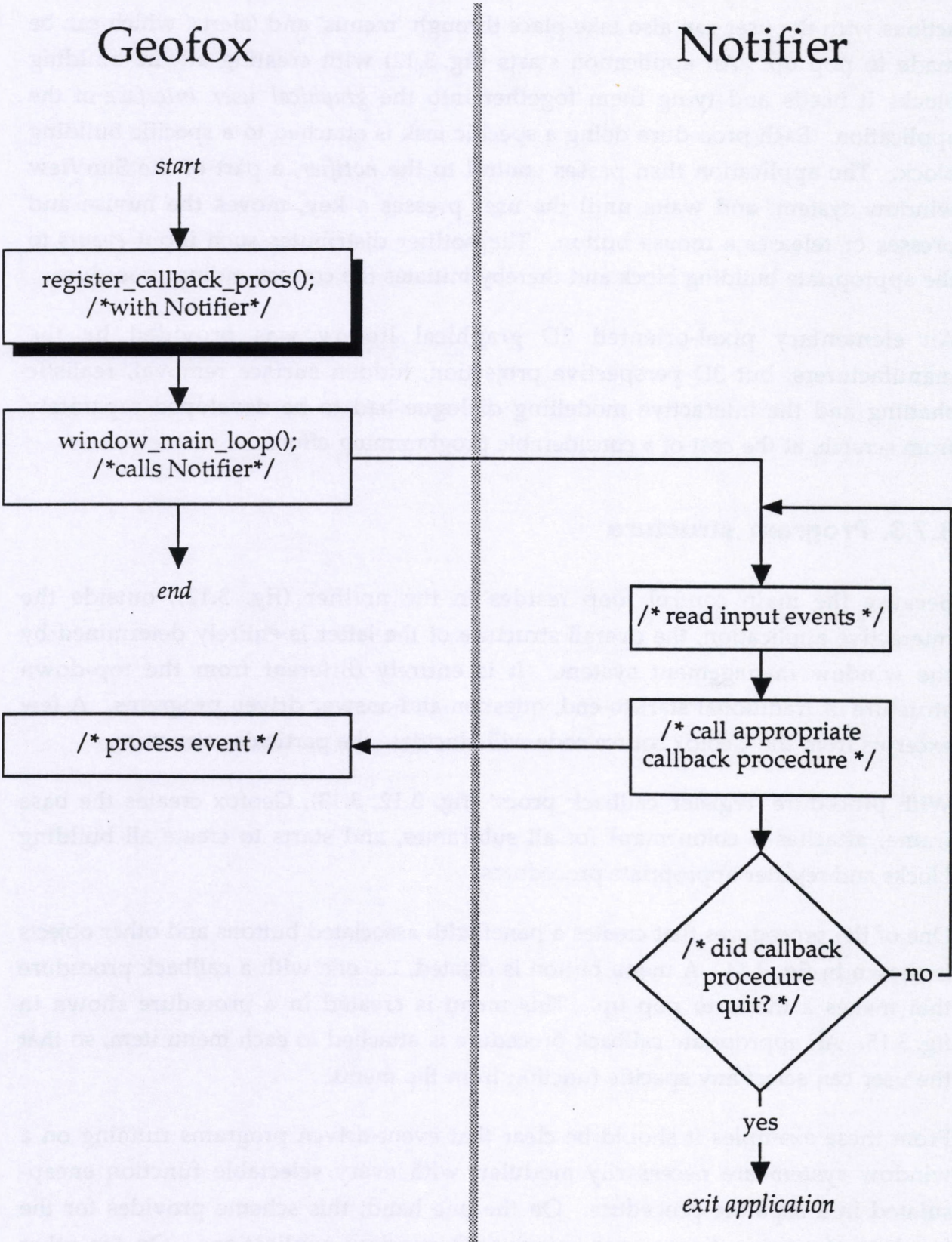


Fig. 3.12. Flow of control between notifier-based application (Geofox) and the notifier (a part of the window manager; after Sun Microsystems, 1988). The routine 'register_callback_procs' (box with shadow) creates all window objects and pulldown menus of the application's graphical user interface, and registers the respective callback procedures with the notifier. After 'window_main_loop' has

been called, the notifier takes over control and directs any *event* (a key has been pressed, the mouse has moved, a mouse button has been pressed or released,...) to the appropriate object and calls back this object's procedure in the application. The callback procedure then processes the event (or "interprets the intentions of the user") and starts the selected action.

actions with the user can also take place through 'menus' and 'alerts' which can be made to pop up. An application starts (fig. 3.12) with creating all the building blocks it needs and tying them together into the *graphical user interface* of the application. Each procedure doing a specific task is attached to a specific building block. The application then passes control to the *notifier*, a part of the SunView window system, and waits until the user presses a key, moves the mouse and presses or releases a mouse button. The notifier distributes such input *events* to the appropriate building block and thereby initiates the corresponding procedure.

An elementary pixel-oriented 2D graphical library was provided by the manufacturers, but 3D perspective projection, hidden surface removal, realistic shading and the interactive modelling dialogue had to be developed separately from scratch, at the cost of a considerable programming effort.

3.7.3. Program structure

Because the main control loop resides in the notifier (fig. 3.12), outside the interactive application, the overall structure of the latter is entirely determined by the window management system. It is entirely different from the top-down structure of traditional start-to-end, question-and-answer driven programs. A few excerpts from the Geofox source code will elucidate the particular structure.

With procedure 'register_callback_procs' (fig. 3.12, 3.13), Geofox creates the base frame, attaches a colourmap¹ for all subframes, and starts to create all building blocks and register appropriate procedures.

One of the procedures that creates a panel with associated buttons and other objects is shown in fig. 3.14. A menu button is created, i.e. one with a callback procedure that makes a menu to pop up. This menu is created in a procedure shown in fig. 3.15. An appropriate callback procedure is attached to each menu item, so that the user can select any specific function from the menu.

From these examples it should be clear that event-driven programs running on a window system are necessarily modular, with every selectable function encapsulated in a separate procedure. On the one hand, this scheme provides for the freedom of combination a user enjoys with window applications. On the other hand, it forces the programmer to ensure against erroneous combinations, which

¹a list of 256 (red, green, blue) intensity values between 0 and 255, which need to be specified by the program(mer).


```

register_callback_procs()
{
    frame = window_create(NULL, FRAME, 0);          /* create base frame*/
    frame_pw = (Pixwin *) window_get(frame, WIN_PIXWIN);
    set_lut_8x32();                                /* create colourmap for base frame */
    window_set(frame, FRAME_INHERIT_COLOR, TRUE); /* and all subframes */
    create_start_popup();
    create_menus();                                /* create all menus and attach callback procedures */
    create_mainpanel_popup();                       /* create main panel and attach callback procedures */
    create_ddpar_popup();                           :
    create_ddgridinterpol_popup();                  :
    create_ddgridview_popup();
    create_velocity_popup();
    create_legend_popup();
    create_shading_popup();
    create_canvas();
}

```

Fig. 3.13. Procedure 'register_callback_procs' (see fig. 3.12). Transient panels are created "on the fly" and are not included in this procedure. Procedures in boldface are expanded in figures 3.14 and 3.15.

```

create_mainpanel_popup() /* (IN PART) */
{
    /* creates main panel with mode_cycle and menu buttons; creates map panel as well */
    mainpanel_frame = window_create(frame, FRAME,
        WIN_SHOW, FALSE, FRAME_SHOW_SHADOW, FALSE, 0);
    mainpanel = window_create(mainpanel_frame, PANEL, 0);
    mode_cycle = panel_create_item(mainpanel, PANEL_CYCLE,
        PANEL_LABEL_X, ATTR_COL(0), PANEL_LABEL_Y, ATTR_ROW(0),
        PANEL_CHOICE_FONTS, screenbl4, screenbl4, 0,
        PANEL_CHOICE_STRINGS, "Map", "3D", 0, /* to switch between map and 3D mode */
        PANEL_NOTIFY_PROC, mode_notify_proc, 0);
    panel_create_item(mainpanel, PANEL_BUTTON,
        PANEL_LABEL_X, ATTR_COL(74), PANEL_LABEL_Y, ATTR_ROW(0),
        PANEL_LABEL_IMAGE, panel_button_image(mainpanel, "Triangles", 9, courbl6),
        PANEL_EVENT_PROC, triangles_event_proc, 0);
    /* (more buttons follow in this panel here) */
}

void triangles_event_proc(item, event)
Panel_item item; Event *event;
{
    /* if event is right button down, bring up the triangles_menu to allow selection */
    if (event_action(event) == MS_RIGHT && event_is_down(event))
        menu_show(triangles_menu, mainpanel, event, 0);
}

```

Fig. 3.14. Parts of procedure 'create_mainpanel_popup'. It creates the main panel together with a 'cycle' that allows to switch between map and 3D visualization, and a series of menu buttons, one of which is included in this excerpt. Its callback procedure (in boldface) makes the triangles_menu (underlined; fig. 3.15) to pop up, in order to allow the user to make a selection.

is pretty complicated in an application that can be in many different states, each of which may entail a different interpretation of a user's input. The user should also get a sufficient amount of unambiguous visual feedback, so that the application 'behaves' as intuitively expected. This in turn requires a careful user-computer dialogue design. Relevant design considerations have been expounded by Foley *et al.* (1990). A geologist using the program should have the impression that he/she is interacting with the data and his/her mental model of them in a graphical, geological language, not burdened by the bits and bytes that a computer scientist has put together into the geological problem solving tools (Peikert, 1969).


```

create_menus()      /* (IN PART) */
{
    triang_sign_menu = menu_create(MENU_STRINGS, "Depth", "Height", 0,
        MENU_NOTIFY_PROC, set_read_par, 0);      /* >-(1)-> */

    view_menu = menu_create(MENU_STRINGS, "All", "Visible", "Hidden", "Scarp", 0,
        MENU_NOTIFY_PROC, do_triview, 0);      /* >-(2)-> */

    triangles_menu = menu_create(
        MENU_ITEM, MENU_STRING_ITEM, "Read saved", 1, /* only active item now */
        MENU_PULLRIGHT, triang_sign_menu,      /* <-(1)-< pull-right here */
        MENU_ACTION_PROC, tthead_notify_proc,    MENU_INACTIVE, FALSE, 0,
        MENU_ITEM, MENU_STRING_ITEM, "Triangulate", 2,
        MENU_ACTION_PROC, trtriang_notify_proc,    MENU_INACTIVE, TRUE, 0,
        MENU_ITEM, MENU_STRING_ITEM, "Save", 3,
        MENU_ACTION_PROC, trsave_notify_proc,    MENU_INACTIVE, TRUE, 0,
        MENU_ITEM, MENU_STRING_ITEM, "View", 4,
        MENU_PULLRIGHT, view_menu,      /* <-(2)-< pull-right here */
        MENU_ACTION_PROC, triview_notify_proc,    MENU_INACTIVE, TRUE, 0,
        MENU_ITEM, MENU_STRING_ITEM, "Narrow...", 5,
        MENU_ACTION_PROC, trnarrow_notify_proc,    MENU_INACTIVE, TRUE, 0,
        MENU_ITEM, MENU_STRING_ITEM, "Make all visible", 6,
        MENU_ACTION_PROC, trallvis_notify_proc,    MENU_INACTIVE, TRUE, 0,
        MENU_ITEM, MENU_STRING_ITEM, "Set Edit ON", 7,
        MENU_GEN_PROC, tdel_toggle_proc, /* may change text of this item */
        MENU_ACTION_PROC, trchange_notify_proc,    MENU_INACTIVE, TRUE, 0,
        MENU_ITEM, MENU_STRING_ITEM, "Set VertexAdd ON", 8,
        MENU_GEN_PROC, tvadd_toggle_proc, /* may change text of this item */
        MENU_ACTION_PROC, tvadd_notify_proc,    MENU_INACTIVE, TRUE, 0,
        MENU_ITEM, MENU_STRING_ITEM, "Contour solid", 9,
        MENU_ACTION_PROC, trcont_notify_proc,    MENU_INACTIVE, TRUE, 0,
        MENU_ITEM, MENU_STRING_ITEM, "Contour lines", 10,
        MENU_ACTION_PROC, trcontl_notify_proc,    MENU_INACTIVE, TRUE, 0,
        0);
    /* many menus follow here */
}

```

Fig. 3.15. Parts of procedure 'create_menus'. It creates all menus and sub- or 'pull-right' menus (top). A callback procedure ('ACTION_PROC') is registered at each of these menu items. When Geofox is started, only the first item will allow the user to read a saved triangular surface model. The read procedure will activate the other items, so that they can be selected as well.

By September 1991, Geofox occupied about 20000 lines of C code (± 400 typewritten pages), all written since April 1989¹. The highly modular structure ensured continuous extensibility, with little risk of pervasive interference with the existing functionality.

3.7.4. Input

Geofox has been designed to read a wide variety of ASCII² data files, including :

1. raw 3D data points, e.g. irregularly distributed well data;

¹Apart from about 1000 lines of hidden line removal code, written originally in FORTRAN 66 (Verschuren, 1985). During 1986-87, this part was improved with ideas from Anderson (1982) on an NCR minicomputer, together with most of the data preparation (§3.5) software development.

²A universal data format that can be written and read by all types of computer.

2. individual seismic horizons interpreted along a seismic network;
3. entire profiles, including topography, main and internal reflectors, fault picks;
3. background lines, such as coastlines and digitized contours;
4. previously saved triangular models, in order to avoid time consuming re-triangulation and re-editing of large data sets. A saved triangulation effectively stores the evolving interpretation together with the data and their connectivity;
5. shot points (for coverage control).

The file formats are described in the Geofox Manual (see Addendum). Either all or an areal selection of data can be read from specified files. The scale is automatically adapted to the selected sector or chosen to fit all the data on the screen. The map scales are exact on the screen and on hardcopy.

At this point, it is appropriate to explain how the data are stored in Geofox. All 3D data points, either isolated or connected into lines, are stored in one array of Geopoints, a data structure with (X,Y,Z) coordinates and two codes, one to indicate whether that point is visible or not, and another to characterize the point as isolated, the start or end of a line, or as significant or not at the current weeding tolerance. A mixture of any number¹ of points and lines can thus be stored in a very simple but versatile way, both internally and in files.

3.7.5. Data reduction

Firstly, the amount of detail along digitized reflectors, even when line simplification has removed 60% of the raw digitized points, may far exceed the scale of modelling, because small details cannot be correlated between profiles and therefore also cannot be extrapolated to the surface model.

Secondly, the dense network of 20x40 profiles in the North Hinder area contains a large number of fault cuts. Interaction with a computed surface that is modelled directly with the digitized data points can only become efficient if the modeller works only with data points that are relevant at the modelling scale. This is also true for lines digitized in point mode, or from digitally scan-converted or auto-picked lines (§3.5.1.1). Hence, both the irrelevance of small details and modelling efficiency call for *interactive* 3D curve simplification, complementary to automatic 2D curve simplification at the level of data entry (§3.5.2).

¹The required memory space is allocated dynamically and only limited by machine memory.

For this purpose, our local maximum distance algorithm for line simplification needed to be generalized to 3D. Instead of calculating the distance d of a point A to a line through two other points $[B,C]$ in-line like in fig. 3.9, d is calculated as a slightly more complicated function of three 3D points (A_x, A_y, A_z) , (B_x, B_y, B_z) and (C_x, C_y, C_z) . From Fig. 3.16, it is clear that the distance d is given by $d = |BA| \sin\theta$. Because $|BA \times BC| = |BA||BC| \sin\theta$, d is also given by

$$d = \frac{|BA \times BC|}{|BC|} = \frac{\begin{vmatrix} i & j & k \\ A_x - B_x & A_y - B_y & A_z - B_z \\ C_x - B_x & C_y - B_y & C_z - B_z \end{vmatrix}}{\sqrt{(C_x - B_x)^2 + (C_y - B_y)^2 + (C_z - B_z)^2}}$$

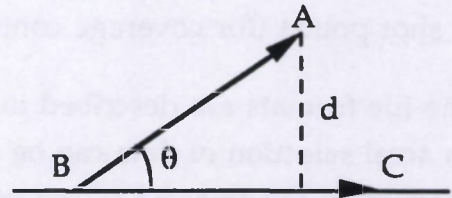


Fig. 3.16

Polygonal line simplification with our algorithm therefore became geometrically and computationally more complicated than with the 2D version, but it proved to be only marginally slower. Moreover, with Geofox both weeding tolerance and vertical exaggeration can be interactively controlled, so that at each moment data density can be adapted to user needs. Vertical exaggeration during line simplification is usually the same as that used for 3D surface modelling purposes. Depending on the weeding tolerance and line smoothness, continuously digitized lines can be reduced to less than 10%, without losing essential geological detail (fig. 3.17). Such a reduction dramatically speeds up drawing, triangulation and interactive modelling, as well as gridding.

In fig. 3.19, all data points on a clay tectonically affected horizon in the North Hinder zone have been triangulated (see further). Even with curve simplification at the level of data entry, the 9000 remaining data points result in triangles that are too small and too narrow to interact with comfortably. With Geofox the lines have been further simplified, in this case with a vertical weeding tolerance of 0.25 m, which corresponds at a vertical exaggeration of 25 times with a lateral weeding tolerance of 6.25 m. In other words, curves in the seismic track are 25 times less important at the modelling scale than the tiny vertical undulations in the Ypresian horizon. At this stage, about a 1000 fault cuts were waiting to be correlated between the tracks, with the complication of relatively large and irregular vertical and lateral mis-ties. Surface modelling time tends to increase quadratically with the number of data. Modelling with the ensuing 3000 points and 6000 less narrow triangles (fig. 3.21) was already much less of a headache.

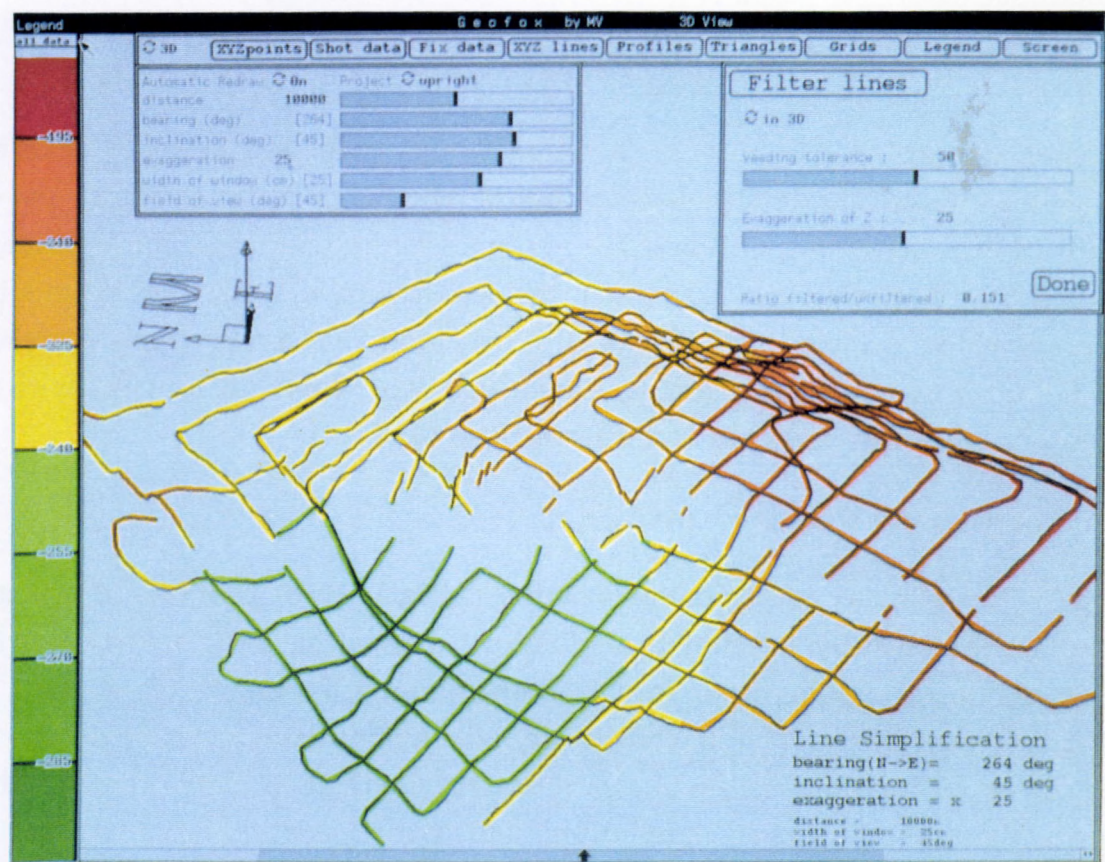


Fig. 3.17. Application of polygonal approximation to network of seismic lines on the basal Ypresian reflector in the North Hinder area. Points digitized along the seismic profiles are connected with thin black lines. Colour contoured lines connect only the essential points, which will be used for modelling purposes in a next stage. In this case, the data were thinned out by 85%, without any significant loss of information at the modelling scale and vertical exaggeration.

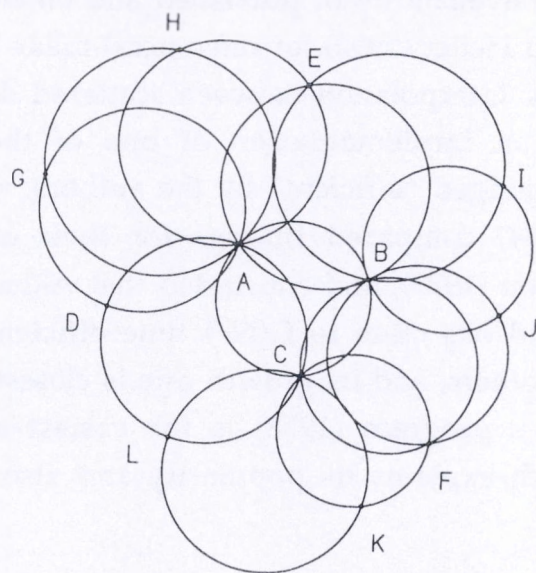


Fig. 3.18a

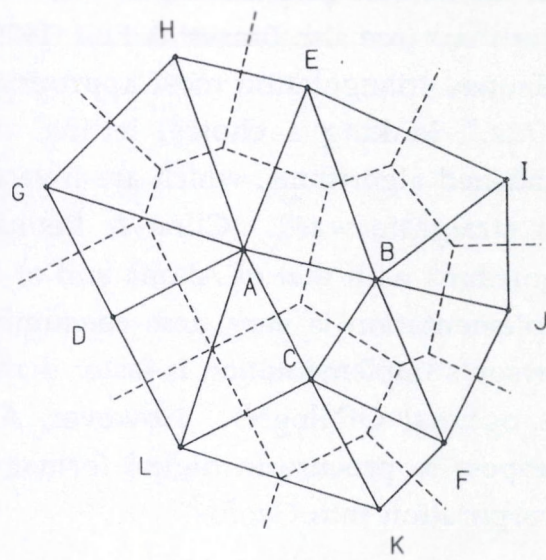


Fig. 3.18b

Fig. 3.18. (a) Natural neighbour circumcircles. Each data point is a natural neighbour of any data point with which it shares a circumcircle. The natural neighbours of A are B, C, D, E, G, H and L. (b) Delauney triangulation (solid lines) and Voronoi tessellation (dashed lines). The Voronoi polygons on the perimeter are not bounded completely. (From Watson & Philip, 1987)

3.7.6. Modelling by triangulation

In the first stage of the Geofox surface modelling cycle, a triangular surface is constructed between the data points, so that it represents both a horizon and the fault cuts of an intersecting normal fault system. An automatic Delaunay triangulation (§3.7.6.1) creates a surface between the data points that may reveal mis-ties. These are usually corrected first (§3.7.6.2). Then fault cuts are properly correlated (§3.7.6.3) into acceptable fault scarps, which get their finishing touches with the modelling of fault tips, branches and intersections (§3.7.6.4).

3.7.6.1. Automatic Delaunay triangulation

An automatic Delaunay triangulation routine (Akima, 1978) provides a means to generate a geometrically optimal triangulation, connecting only data points that are nearest natural neighbours. In a Delaunay triangulation, no data point lies inside the circumcircle of any other triangle, which simultaneously maximizes the interior angles of the triangles (fig. 3.18). It can also be defined (Sabin, 1986) with its geometric dual, the Voronoi tessellation, which for each data point gives the region closer to that data point than to any other. The unique Delaunay triangulation only joins data points whose region has a common frontier.

Watson and Philip (1984) evaluated Delaunay and other triangulations, and found that the nearest neighbour property and the availability of published and efficient algorithms (see also Brassel & Reif (1979) and Heller (1990) for references) made the Delaunay triangulation most appropriate for interpolation between scattered data points. Making a choice, letting alone an implementation of one of these published algorithms, which are invariably judged "efficient" by the authors, was not straightforward. Cline & Renka (1984) compared timings for their own algorithms with that of Akima and of Lawson (1977), and concluded that Akima's implementation is very time consuming and has close to $O(N^2)$ time efficiency. Lawson's implementation is faster than the others, and its growth rate is closest to the optimal $O(N \log N)$. However, Akima's program (1978) is the easiest and cheapest to procure in digital format, which explains its popularity and also its incorporation into Geofox.

The triangulation routines were originally written in FORTRAN (Akima, 1978), and were translated to C, for lack of a FORTRAN compiler on the SUN 386. The data structure of the triangulation is very simple. A unidimensional array (iwk)

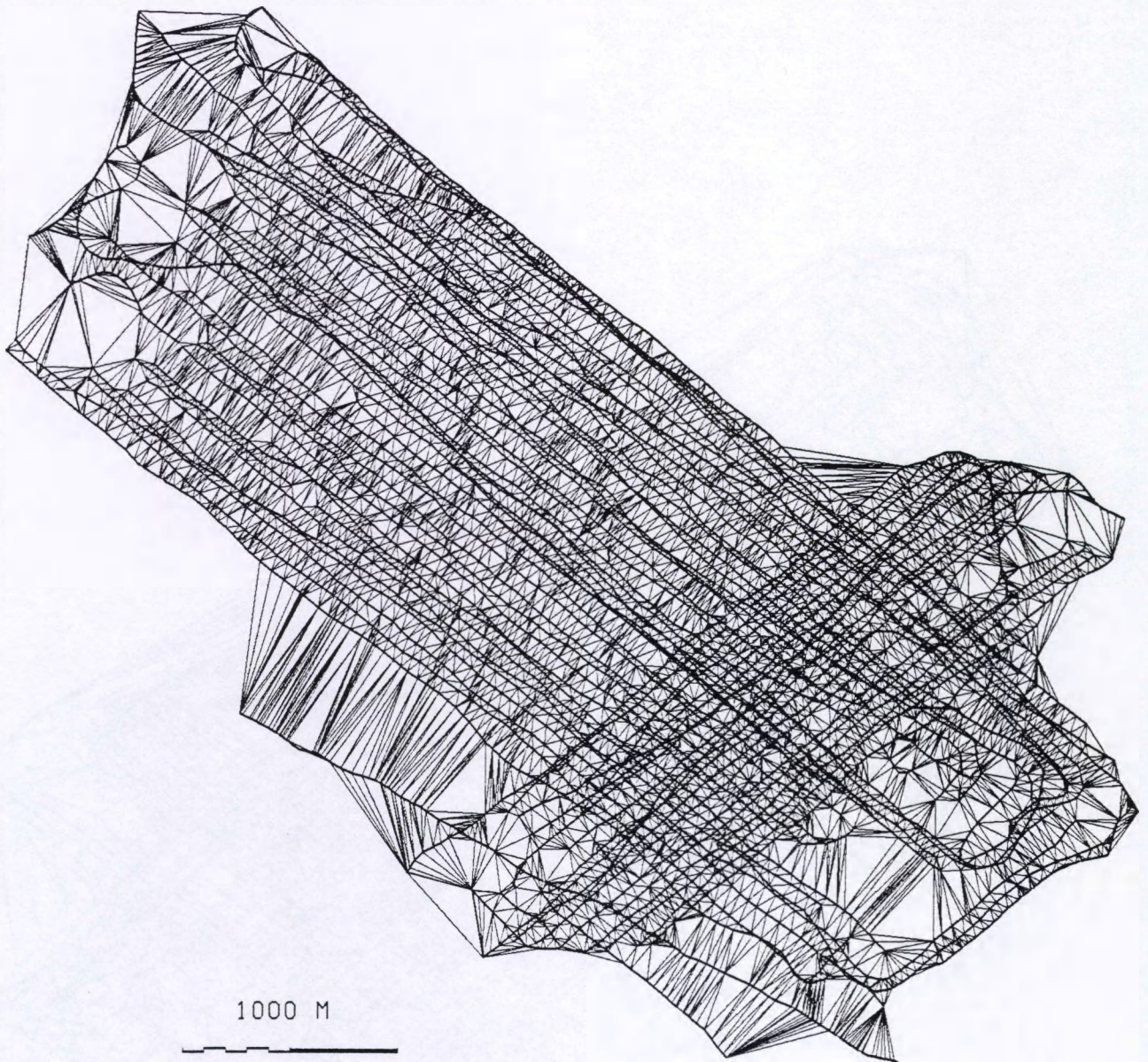


Fig. 3.19. Automatic Delauney triangulation of 9000 digitized data points along the North Hinder network. At this stage, about a 1000 fault cuts still need to be correlated explicitly.

stores triads of indices to another array of vertices. The triangular surface models are saved in files in the same manner. The number of triangles is twice the number of vertices minus the number of vertices along the boundary (Cline & Renka, 1984).

A number of modifications and additions to Akima's source code have been introduced in the Geofox implementation. The triangulation can be forced to

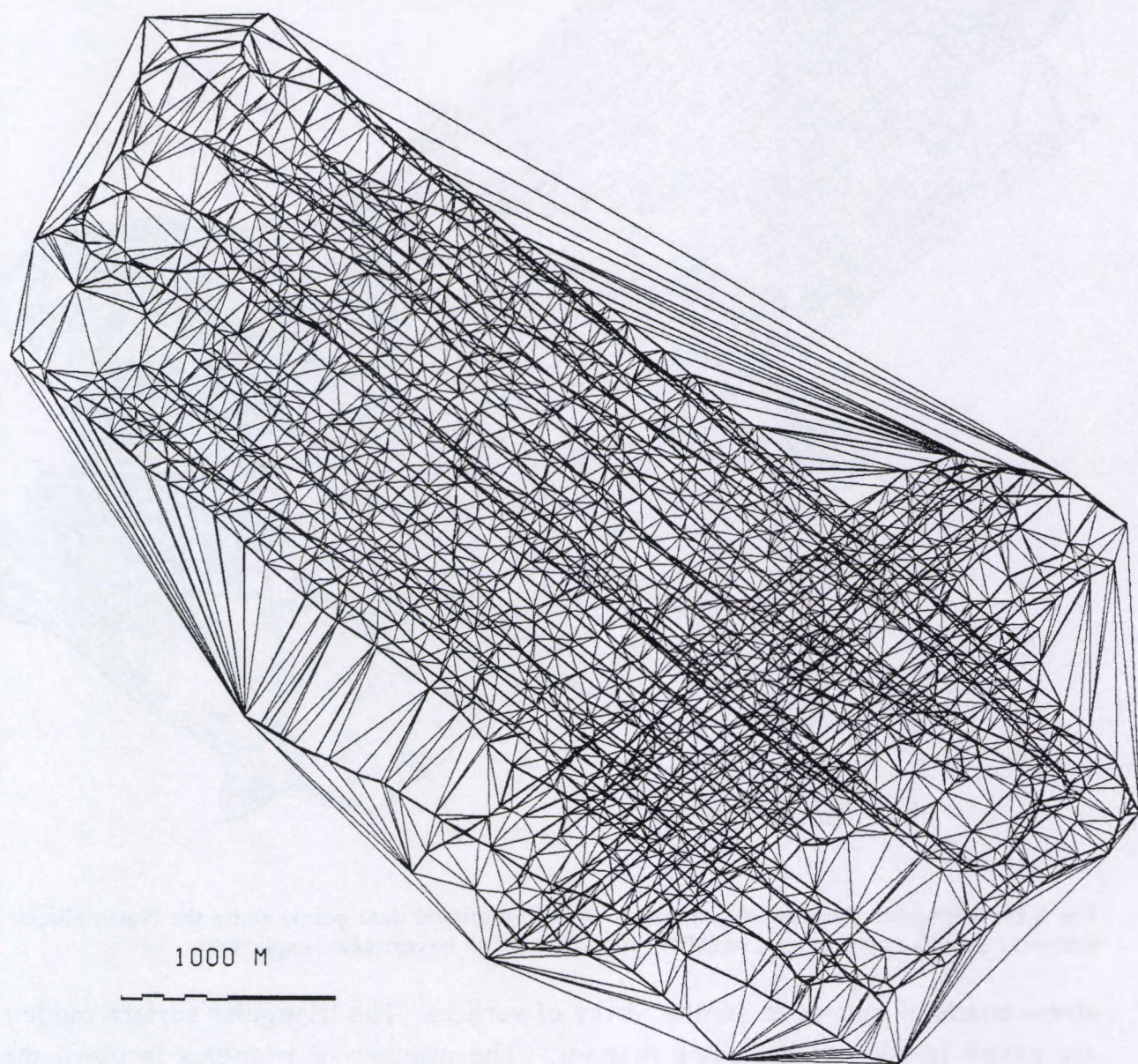


Fig. 3.20. Automatic Delaunay triangulation of only 3000 data points relevant at the modelling scale. Lateral curves of less than 6.25 m and vertical undulations of less than 0.25 m have not been considered here. Interactive mis-tie correction and modelling with only these 6000 less narrow triangles is already much more efficient than with all of them.

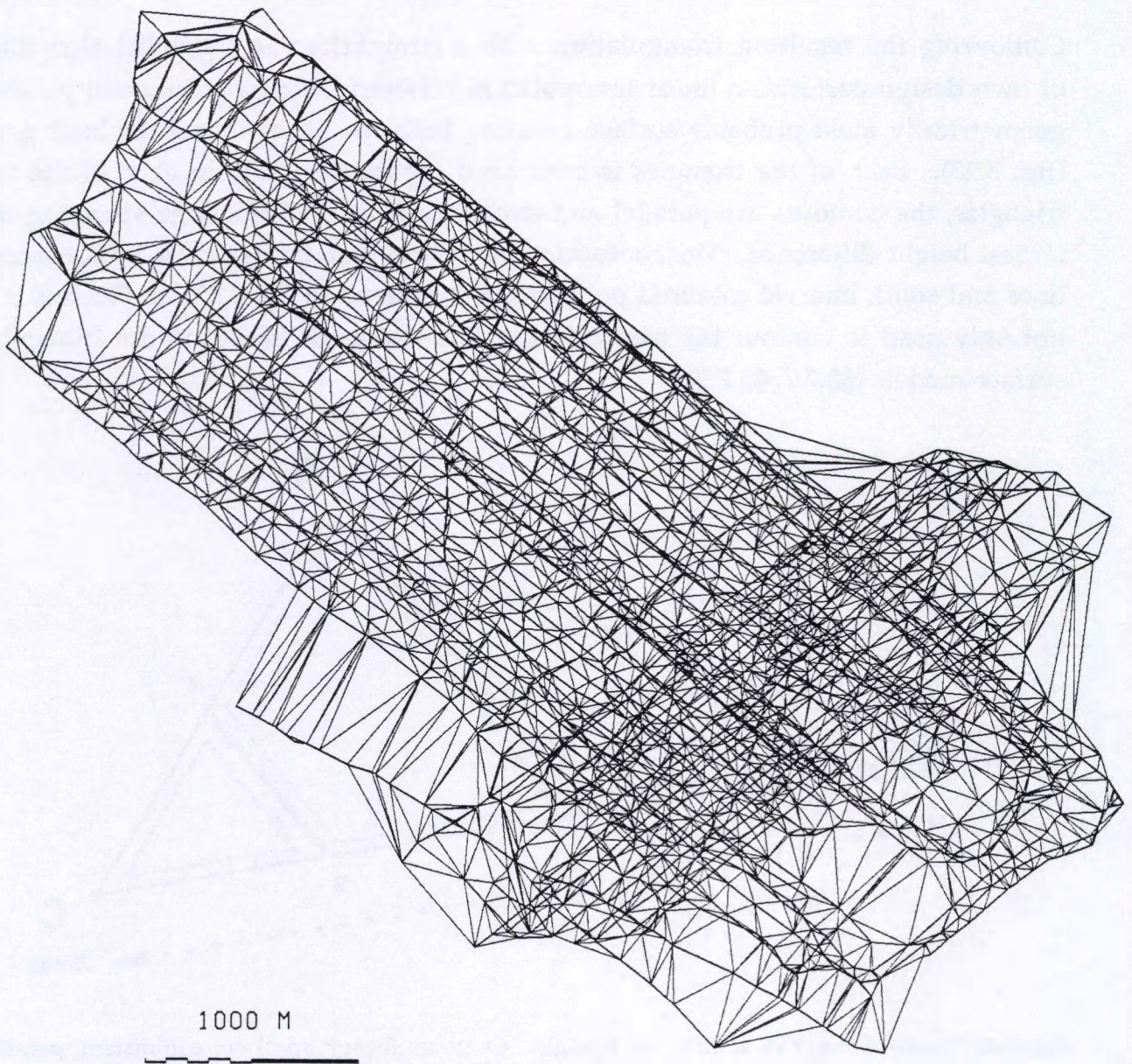


Fig. 3.21. Narrow triangles along the necessarily convex triangulation boundary (fig. 3.20) connect points that are too far apart to have any geologically meaningful relation. A Geofox function removes such border triangles automatically if they are narrower (a larger longest base to height ratio) than a user given limit. Internal narrow triangles are not removed.

honour the line coherence of data points along reflector lines (fig. 3.20). For creating surface models based on digitized contour maps, the triangulation can be changed automatically so that no triangle has three vertices on the same contour. Figure 3.20 also shows that along the necessarily convex boundary of the triangulation, data points form triangles far too extended to depict any realistic structural relation. A facility was added to delete such triangles automatically if they are narrower (a larger longest base to height ratio) than a user given limit (fig. 3.21). Internal narrow triangles are not removed, unless explicitly required.

Contouring the resulting triangulation with a straightforward, parallel algorithm of own design performs a linear interpolation between the data points and yields a geometrically most probable surface covering both the horizon and the fault gaps (fig. 3.23). Each of the triangles is contoured separately. Within each of the flat triangles, the contours are parallel and equidistant, and cut the edge spanning the largest height difference. The contouring algorithm that can generate both contour lines and solid, interval coloured polygons, is explained in fig. 3.22. In Geofox, it is not only used to contour the triangulation, but also grids based on the triangular surface models (§3.7.7, §3.7.9).

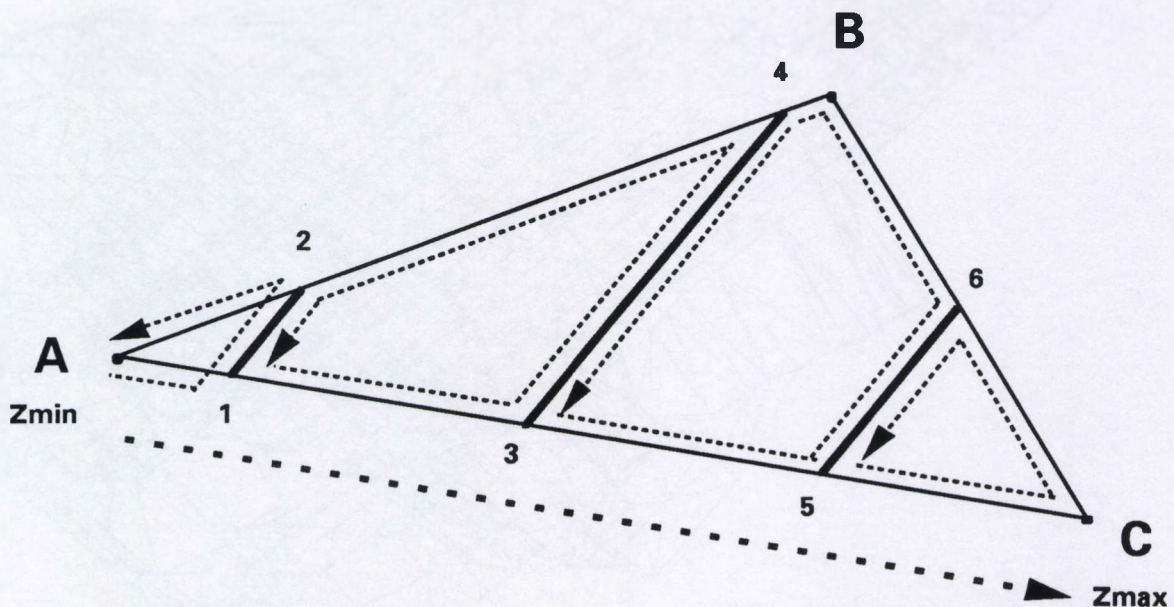


Fig. 3.22. Linear interpolation on a flat triangle. Contours (heavy lines) are equidistant, parallel and all cut edge spanning largest height difference. The latter observation underpins the following simple contouring algorithm. First, reorder the vertices from lowest (A) to highest (C), determine the number of contours passing AC. For all passing contour levels, starting with the lowest, interpolate the intercept points on AC and AB or BC, depending on whether B is higher or lower than the current contour level. For each contour level, draw a contour line and polygon between the intercept points and, for the polygons on the first and last interval, as well as the interval straddling the intermediate vertex, also the relevant vertices. E.g. contour lines in this triangle are drawn in order 12, 34 and 56, and interval polygons are generated in order A12A, 13421, 356B43 and 5C65.

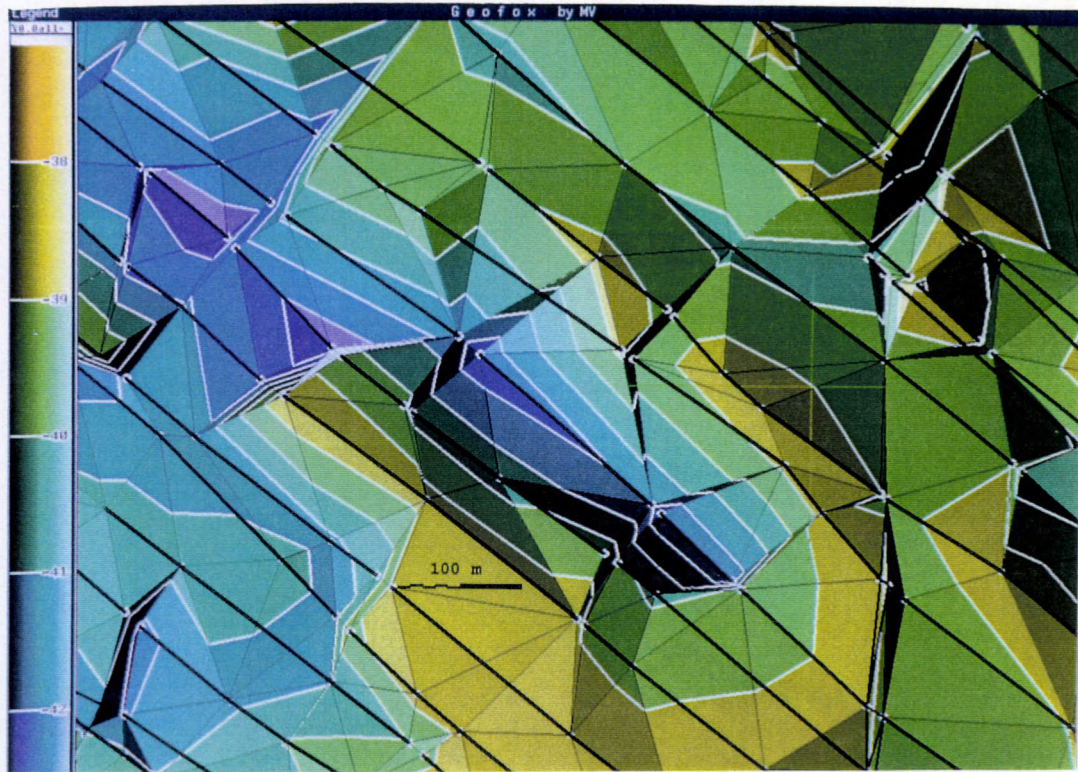


Fig. 3.23. Part of initial triangulation of data on faulted horizon. A linear interpolation between the data points results in mechanical contours that honour the data perfectly and cover both the horizon and the fault gaps (interruptions between heavy black horizon segments). Contour interval 1 m; illumination from left. Several non-systematic vertical mis-ties are evident from the contour patterns, emphasized by shading.

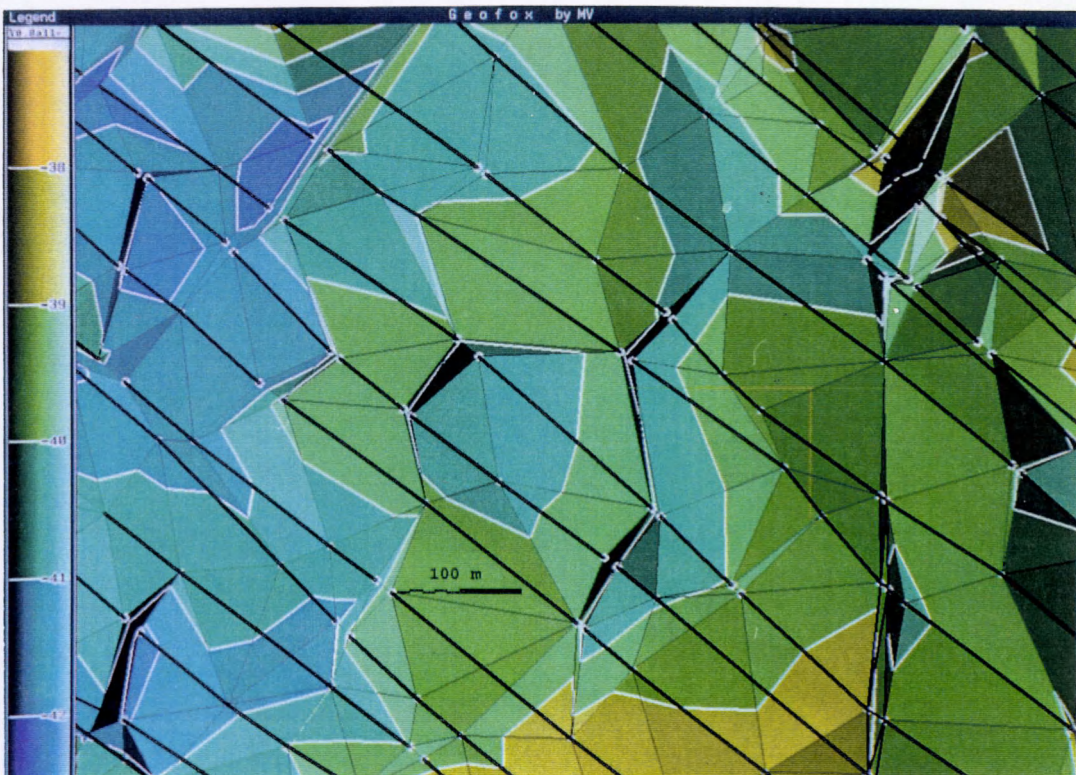


Fig. 3.24. Same area as in fig. 3.23, but with vertical mis-ties interactively corrected, so that the horizon segments are at more or less the same depth from section to section, while fault direction and segment shapes are more or less conserved. Horizontal mis-ties, in this case of up to 60 m in this unidirectional part of the survey, are almost impossible to correct without cross-sectioning control.

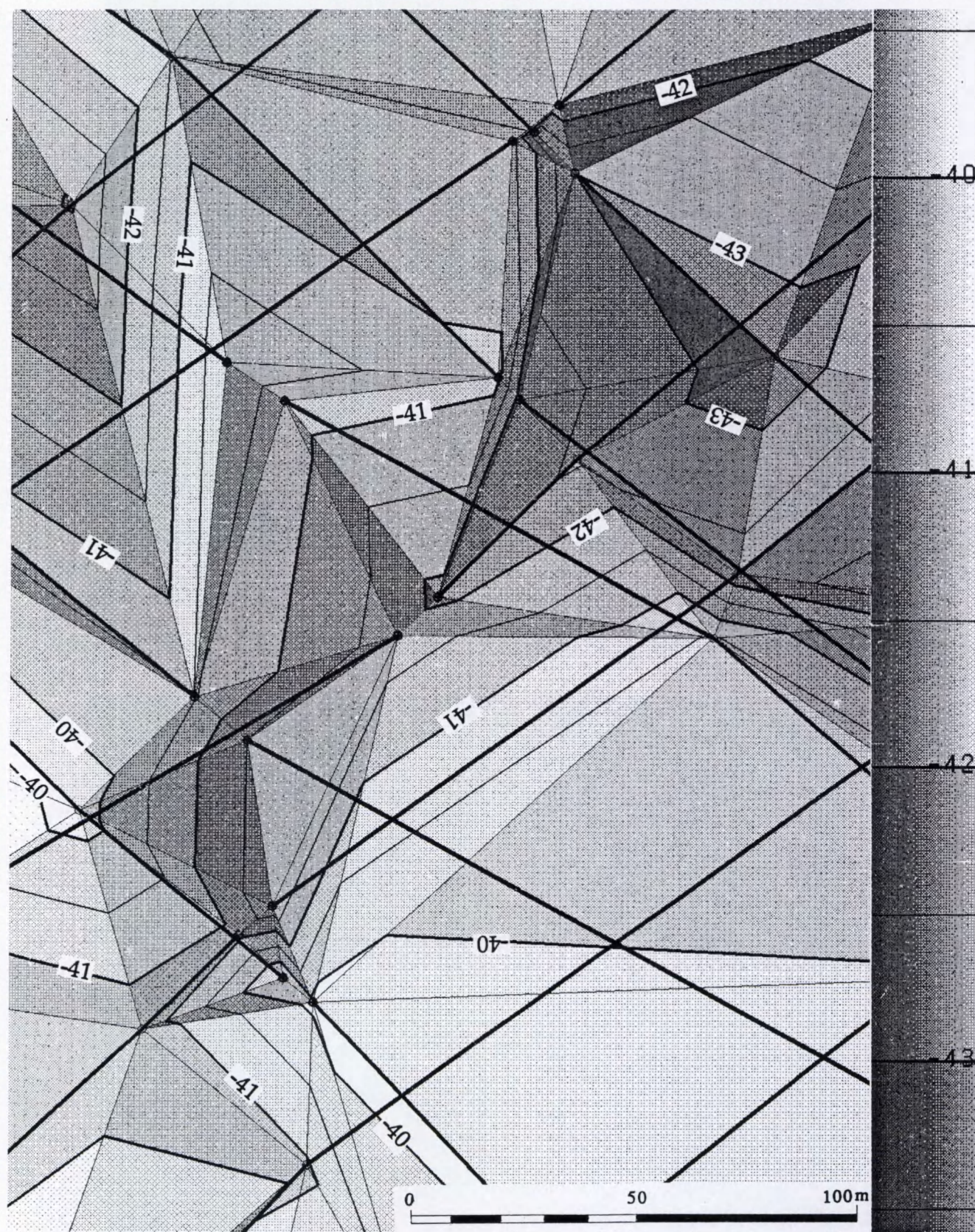


Fig. 3.25. Part of initial triangulation of data on faulted horizon, covered with perpendicular sections. All fault gaps in this area probably belong to the same fault, but they appear displaced by horizontal mis-ties of up to 60 m. Cross-sectioning control thus reveals both vertical and horizontal mis-ties. Because both are non-systematic, they need to be corrected interactively. Versatec hardcopy.

3.7.6.2. Mis-tie correction

Contouring the initial triangulation with a linear interpolation reveals vertical (fig. 3.23) as well as horizontal (fig. 3.25) errors in the 3D position of the data points. Shading emphasizes the anomalies. All kinds of factors introduce systematic but erroneous height differences and lateral offsets between profiles (§3.2.2). This leads to mis-ties in a network of two sets of intersecting profiles. During the first stage of modelling, these mis-ties can be corrected. Automatic vertical mis-tie removal would reduce the error on unreliable profiles, but would still lead to unacceptable linear anomalies. Therefore, a facility was added to move parts of profiles up or down *interactively*, in which the orientation of all connected triangles offers immediate visual and quantitative feedback. Notches along the trace of faults, due to timing and positioning errors along the seismic track, can be corrected with another facility that provides for accurately controlled shifts in the position of points along a profile. In fig. 3.24, vertical mis-ties have been corrected, so that the horizon segments are at more or less the same depth from section to section, while fault direction and segment shapes are more or less conserved. Horizontal mis-ties in this area are almost impossible to gauge, let alone correct, without cross-sectioning control.

Figure 3.25 shows another part of the initial triangulation covered with perpendicular sections. All fault gaps in this area probably belong to the same fault, but they appear displaced by horizontal mis-ties of up to 60 m. Cross-sectioning control thus reveals both vertical and horizontal mis-ties. In fig. 3.26a, all mis-ties have been corrected, so that the fault gaps line up better.

3.7.6.3. Fault correlation

The automatic triangulation and contouring sketched above is very much akin to mechanical contouring (Tearpock & Bischke, 1991) and honours all data points perfectly, but evidently fails to produce geologically most probable correlations of features between profiles. The objective linear interpolation between data points needs to be adapted to ones mental image of the surface, which may be more geological, but necessarily less objective. The automatic triangulation especially needs to be edited near the fault gaps and other surface discontinuities. This is done by swapping diagonal connections interactively, thereby effectively connecting points along fault traces. Figure 3.26 explains how the fault gaps in fig. 3.25 have been correlated.

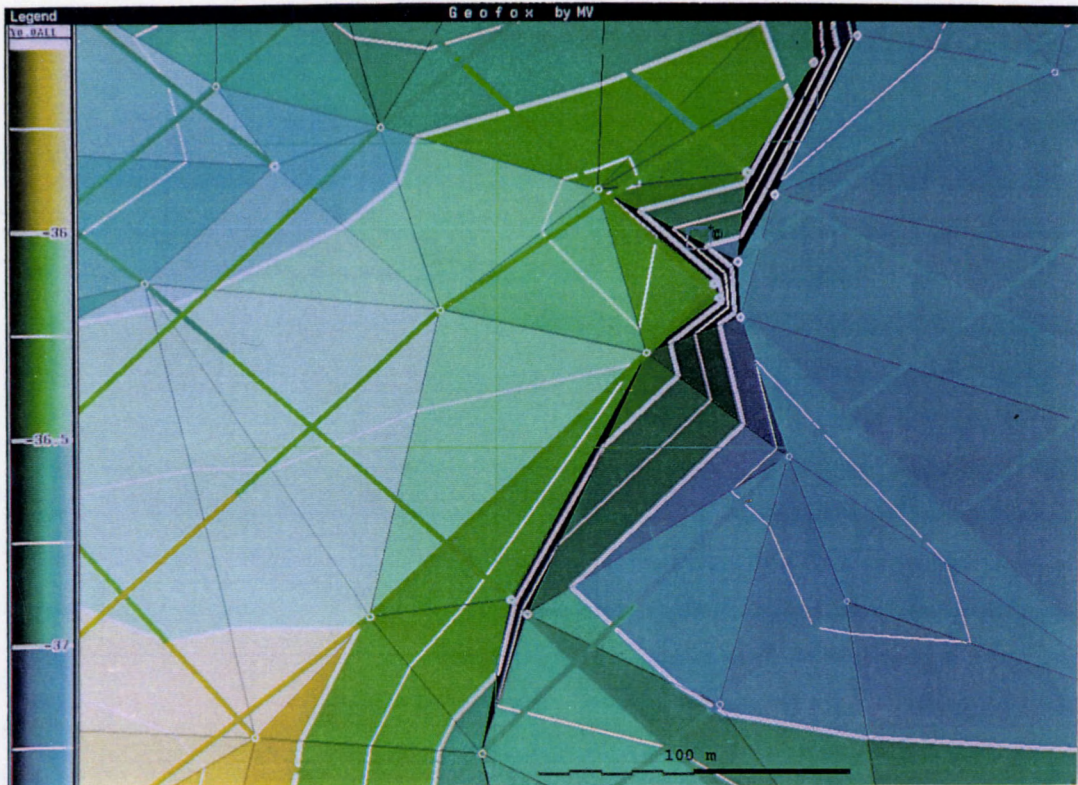


Fig. 3.26a. Same area as in fig. 3.25, but with all mis-ties interactively corrected, so that fault gaps (interruptions of coloured horizon segments) line up better. Two pairs of fault gaps that are close together (upper right) have been automatically correlated by the initial triangulation. A diagonal connection in between is selected by drawing a box across it.

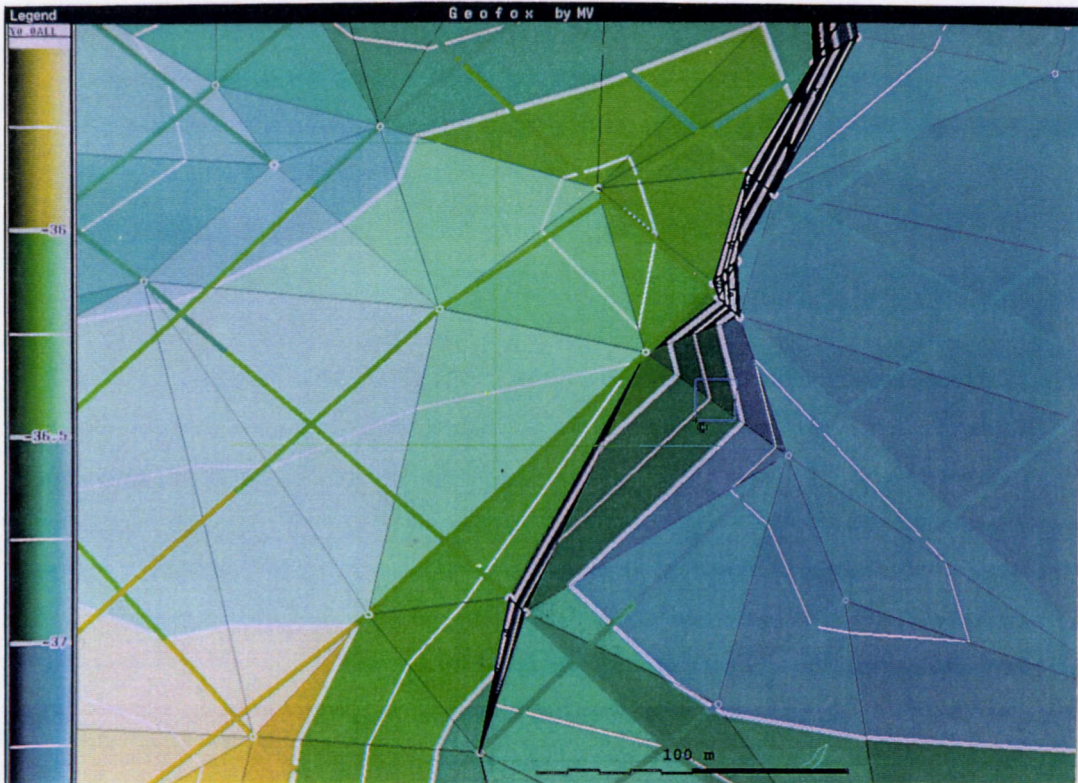


Fig. 3.26b. The diagonal connection selected in fig. 3.26a has been swapped, so that the upthrown fault trace is more complete. Triangles across the fault gaps are interactively identified as part of a fault scarp by clicking on them. They are redrawn with thicker edges. Another diagonal connection is selected, to complete the downthrown fault trace.

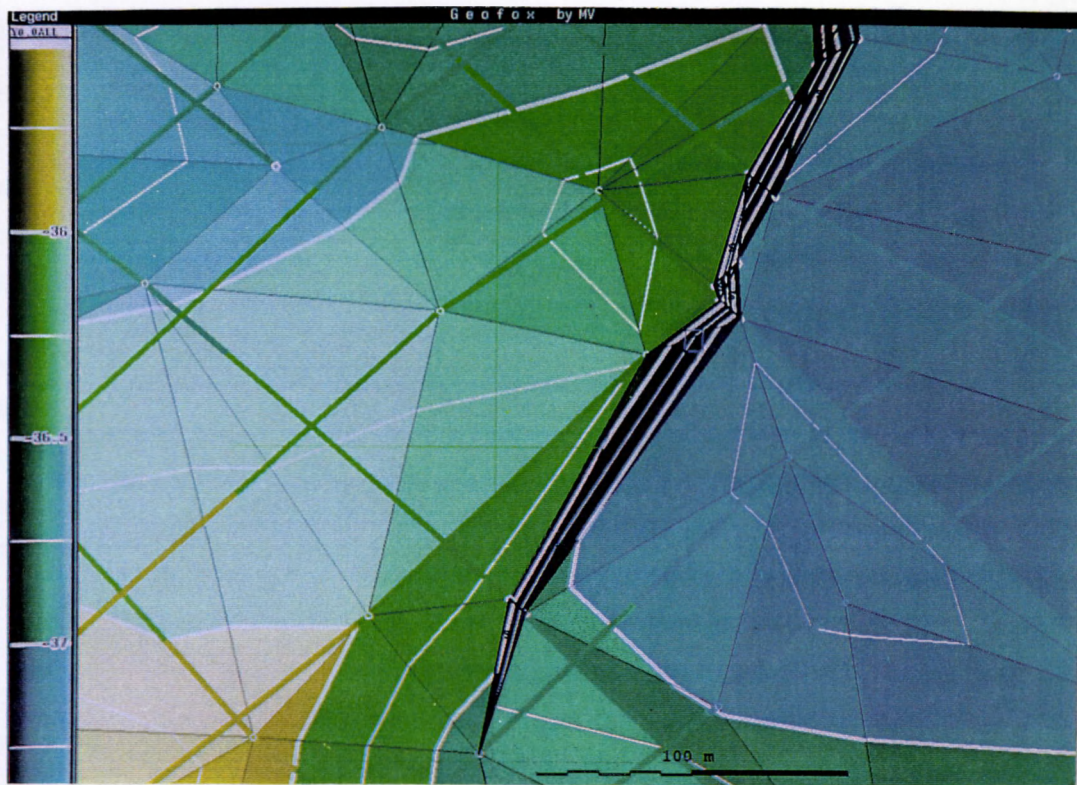


Fig. 3.26c. The downthrown fault trace is now complete. One more swap will complete the upthrown fault trace. Solid shaded (from left) and contoured (every 0.25 m) triangles are continuously updated during the process.



Fig. 3.26d. All fault gaps in this view are now correlated into one continuous fault scarp. Because this method uses only data points and the connections between them, alternative correlations can easily be tested. For the time being, the scarp ends on one of the sections, while it actually lies somewhere within the maze of adjacent and cross-secting horizon segments.

Geo-logic correlation of fault cuts has to observe some rules, such as those summed up by Barnett *et al.* (1987). Tectonic faults (as opposed to faults related to slumping) are generally quite straight, and secondly, the displacement along a fault trace varies only gradually, or at least systematically from one seismic line to the next. Spatial aliasing (§2.1.1) may be so severe that many alternative correlations need to be evaluated. Isolated fault gaps may remain uncorrelated to fault traces.

All along, contour lines and shaded colours are immediately updated, and only data points and their connections are manipulated, so that alternative correlation hypotheses can easily be tried out. The triangulation can only be adapted in a map view, but realistic shading provides 3D-like interactive feedback, emphasizing the quantitative information in the contours. During this surface modelling phase, relevant triangles are identified as fault triangles, or more generally, scarp triangles by clicking on them. Triangles can also be hidden in badly constrained areas of the surface. It is convenient to keep an eye on the actual line coherence along the profiles or contours (coloured lines in fig. 3.26). The triangulation can be saved at any moment in a file containing a list of indices to triads of vertices and a code for whether a triangle lies on a scarp, on the horizon, or is hidden, followed by the list of vertices, in the same format as given in §3.7.4. This is an important file, because it stores the triangular surface model, together with the horizon segments and all the interactive modelling work, for later use.

A number of improvements are left to be desired. The method may become more practical if the correlation of both up- and downthrown traces could be forced directly into triangulation instead of stepwise. This could be done with an algorithm given by Heller (1990). Smoothing the fault traces between the fault cut data with parametric cubic curves (Foley *et al.*, 1990) could result in smooth fault scarps, doing without the additional control points that are so popular among programmers, but that restrict the geologist's freedom to correlate. It would also be handy if a fault correlation on one horizon is automatically transferred to other horizons linked via the fault cuts¹.

¹This requires a relational database of horizon and fault segments. It could then be combined with the FAPS system (Freeman *et al.*, 1990) into a very powerful interactive and quantitative fault interpretation method for 2D seismic data. In contrast, the entire fault geometry could be extracted from 3D seismic data (such as those published by Dalley *et al.*, 1989) almost automatically. An algorithm is envisaged that would identify all voxels with very low local horizon continuity or with minimal correlation between adjacent gathers within a certain time window. The process could be seeded by manually interpreted fault cuts. Such an algorithm would actually do the reverse of auto-picking algorithms. The extracted voxels would then need to be thinned to fault planes with another algorithm. The fault geometry would need to be carefully checked for spurious effects, especially along the 3D data boundaries. Until now, faults in 3D data are still interpreted in the same way as in a dense perpendicular network of 2D profiles, which is too tedious.

Limited as the method presented here may seem relative to the above-mentioned ideas, the Geofox implementation does allow *interactive quantitative interpretation* of a horizon together with the intersecting fault system, based on seismic sections. Various geological interpretations can be easily tested in the triangular surface model, to the benefit of mapping quality.

3.7.6.4. Fault tip, branch and intersection modelling

The correlation of fault cuts is followed by the modelling of singularities such as fault tips and bifurcations. These cannot be revealed by 2D seismics. They are always situated somewhere within the mazes between the sections, while the triangulation connected only digitized data points until now. Modelling the singularities entails manually adding control points, a practice that should be shunned as much as possible (Jones *et al.*, 1986). However, it is common oil industry practice to interpret the presence and location of faults prior to mapping, and to digitize the fault traces in order to constrain subsequent gridding. We have argued against such practice (§3.2.4 and §3.3), but we can not do without control points to model otherwise ungeologically looking fault tips (fig. 3.26d, 3.27a) and bifurcations (fig. 3.28a).

With Geofox, control points can be added to the triangulation at any location. They are visually distinct from data points, so that they can be easily recognized as liable to other interpretations. The triangle into which a control point is added, is split into three coplanar triangles. The depth of a control point and the connections to it can then be changed just like for other vertices, to introduce any particular interpretation.

Modelling fault singularities with additional control points, a geologist should bear in mind some guide-lines based on considerations by Tearpock & Bischke (1991). For a *fault tip*, one control point is added within the maze into which the fault trace is thought to die (fig. 3.27). The control point should be in line with the rest of the fault trace, and located so that the fault loses throw towards its pinch out slightly more rapidly than between the neighbouring fault cuts. For a *fault bifurcation*, just two control points are carefully added between the sections on either side of either the up- or downthrown trace of the main fault (fig. 3.28). The contours on the main fault should be continuous across the bifurcation, and the amount of throw lost to the satellite should be compatible with the throw variations along the two faults in the neighbourhood of the intersection. Intersecting fault scarps can be modelled with four control points. They should form a parallelogram, and contours on the youngest fault scarp should be

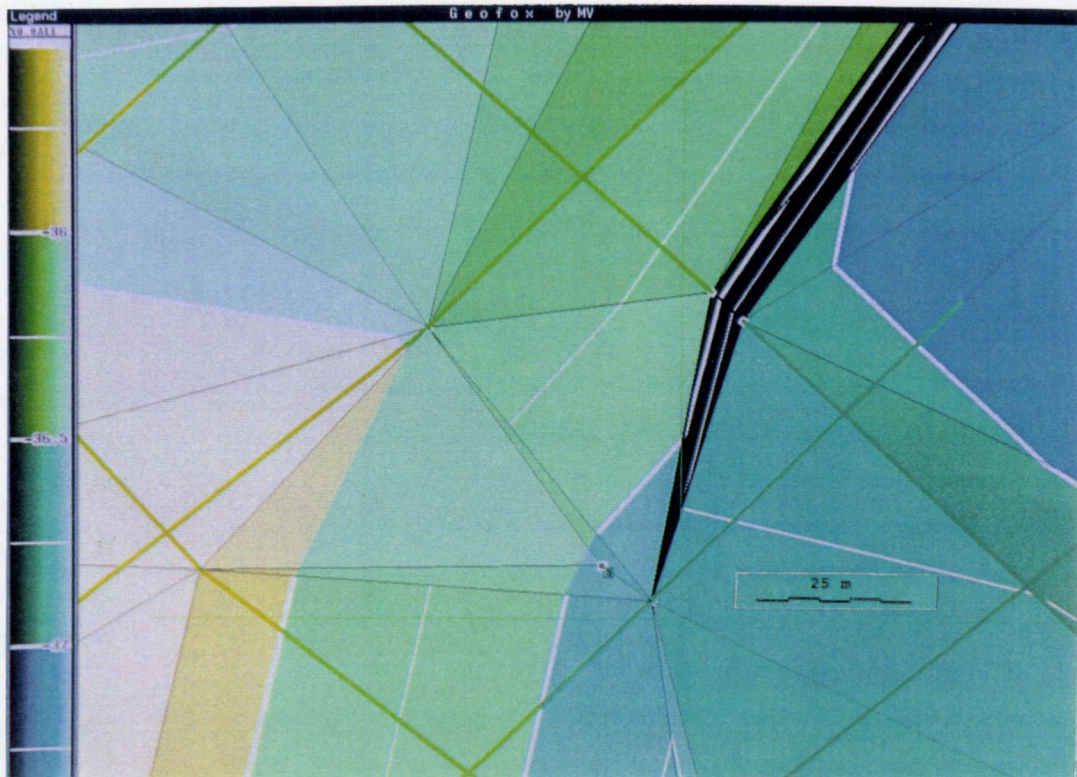


Fig. 3.27a. Modelling a fault tip. This is part of fig. 3.26d, showing how a fault pinches out exactly on a data point along a horizon segment, instead of within the maze between the sections. A control point (box) is added at the interpreted location of the fault tip, projected from the fault traces in the adjacent maze. The triangle into which the tip falls, is split into three coplanar triangles.

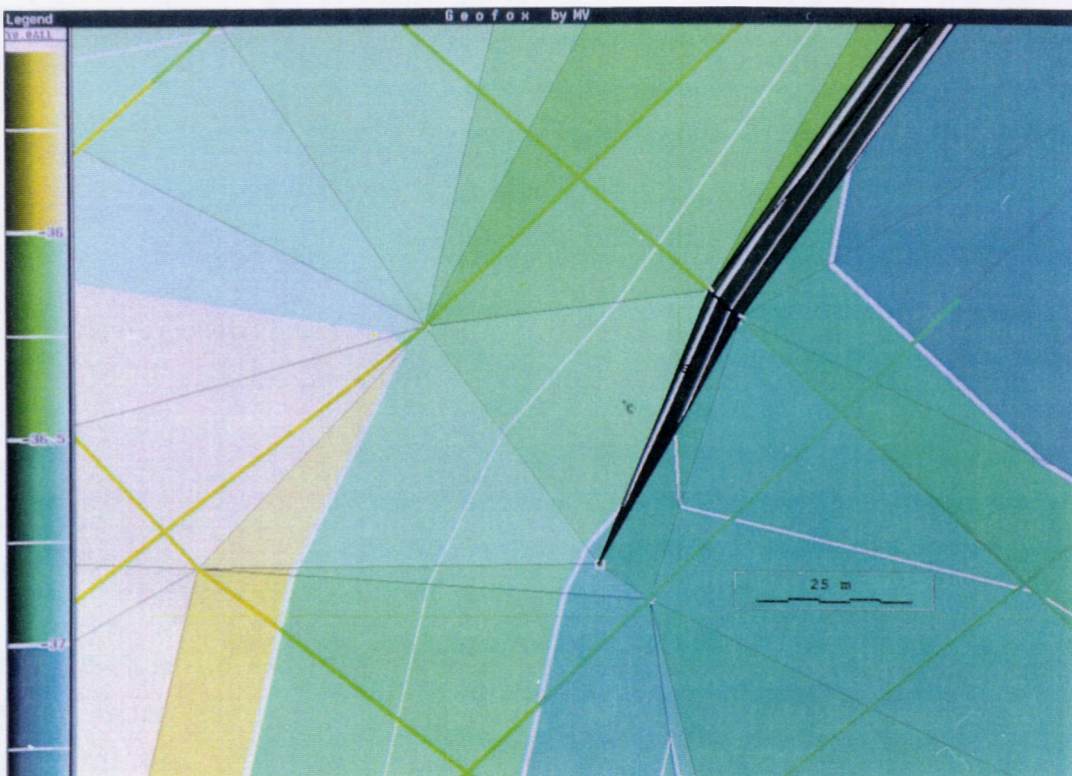


Fig. 3.27b. The connections within the maze have been changed so that the scarp pinches out on the interpreted fault tip. The altitude of the new vertex may also be adapted.

continuous across the intersection. The fault traces of both faults should be offset across the intersection, both horizontally and vertically. No intersecting faults have been modelled in the available data, but an intersection could look like fig. 3.29. Such considerations prove cumbersome to honour in manual contouring, and add up to so many pitfalls, some of which Tearpock & Bischke (1991) fell into themselves (fig. 3.1). In Geofox, continuous feedback with contour lines and solid colours on both the fault scarps and the faulted horizon highlights any geologically improbable situation and simultaneously allows to correct them easily.

Scarp triangles can be automatically grouped into entire fault traces, through the deletion of internal triangle edges (fig. 3.46). Such traces could be smoothed without the need for control points. It would also be convenient to be able to remove (control) points from the triangulation, e.g. with an algorithm given by Heller (1990).

In conclusion, with a very limited number of control points one can model fault tips (fig. 3.27b), normal (fig. 3.28d, 3.30b) and compensating (fig. 3.31) fault bifurcations, and intersections (fig. 3.29). Thus, several original interactive surface modelling tools have been implemented that allow to adapt the triangulation so that it more or less mirrors the geological model one has in mind. This mental model gradually takes shape as the geologist interacts with the data through the triangular model and the 3D views of *grids* derived from them.

3.7.7. Gridding

Contours are the hallmark of quantitative structural mapping (§3.1). Linear interpolation on the triangular surface model results in angular contours on a surface that honours the data points perfectly. On the other hand, such a surface grasps the shape of scarps and faulted horizons only roughly. Seismic horizons in the North Hinder area undulate gently, implying smooth contours. Apart from triangulation code, Akima (1978) provided subroutines to fit a smooth grid on the triangulation, so that first and second derivative are continuous at every data point. Not very useful for a faulted surface. Preusser (1984) incorporated Akima's program in his own, and used quintic polynomials to calculate a smooth surface. In addition, his program allows the user to change the tangents to the surface at every triangulation vertex. Contrary to the Akima program, this would have provided a way to honour surface discontinuities such as fault scarps. Unfortunately, it was not possible to make a working Fortran to C translation of his

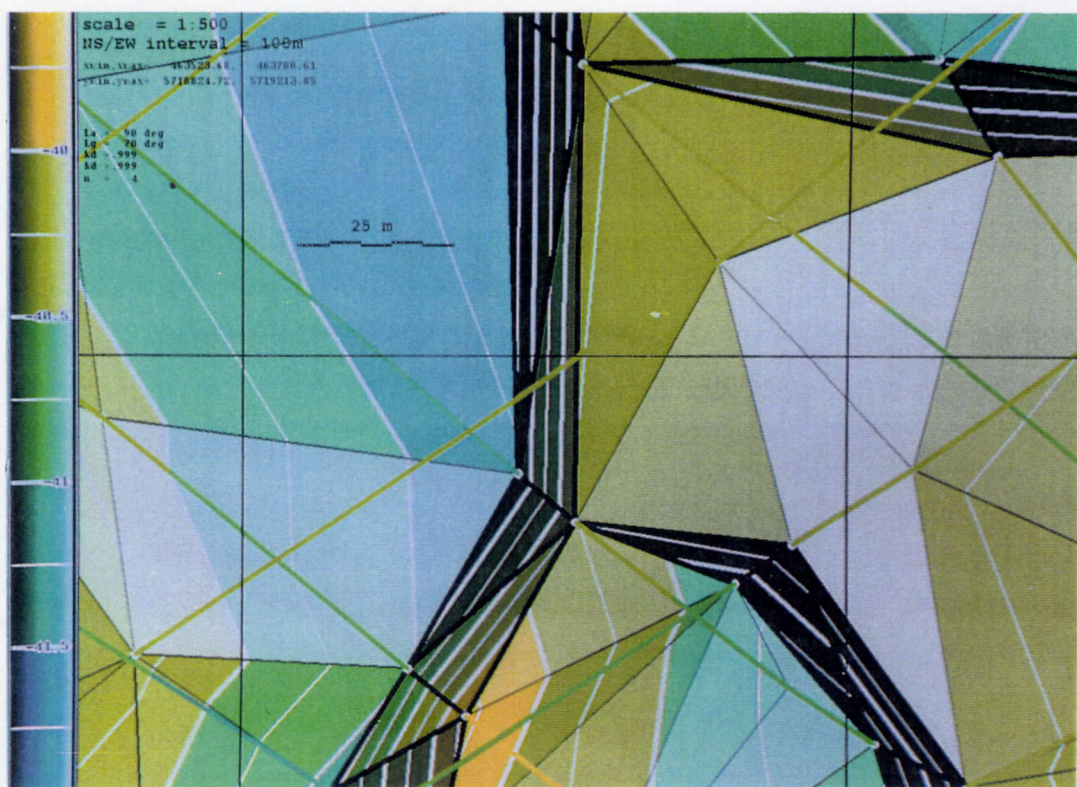


Fig. 3.28a. Fault bifurcations after correlation phase. While the correlations may be acceptable (fig. 3.30a), the bifurcation looks unnatural because the satellite fault joins the main fault necessarily on one data point, while the bifurcation is bound to be located somewhere between the sections. This calls for two manually added control points within the maze of intersecting profiles.

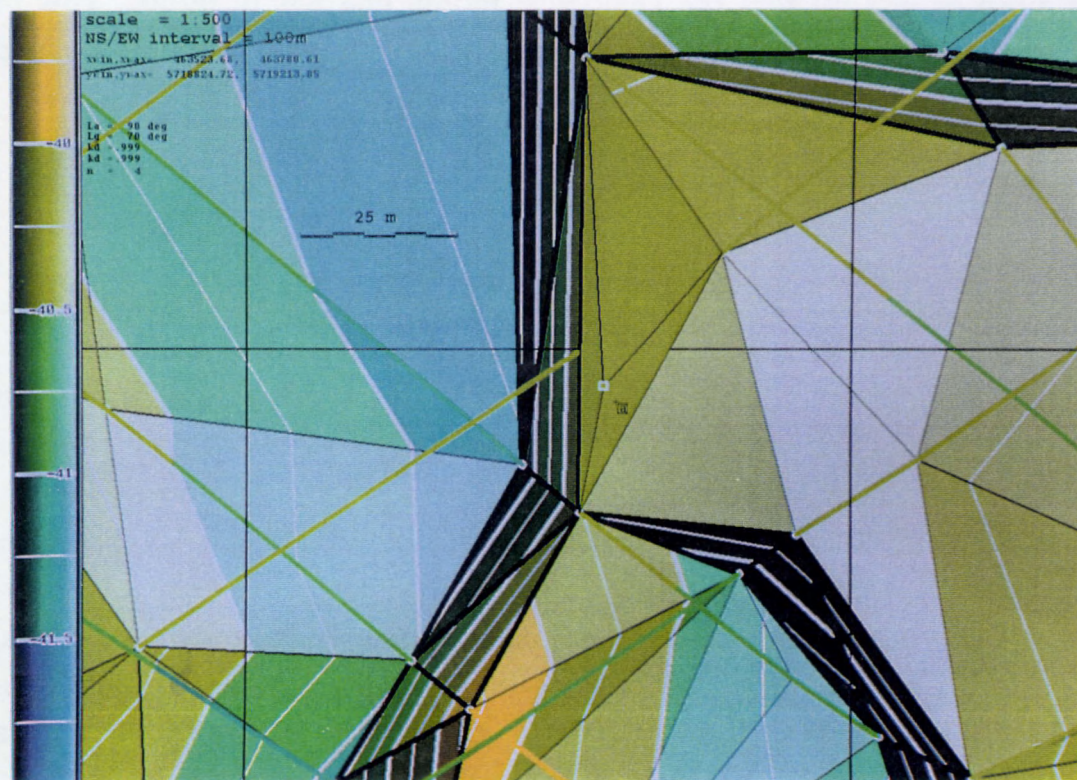


Fig. 3.28b. A control point is added to the right of the upthrown trace of the main NS fault, so that it lines up with the upthrown traces of both main and satellite fault. The low quality SW-NE profile running across two faults without revealing them, is ignored.

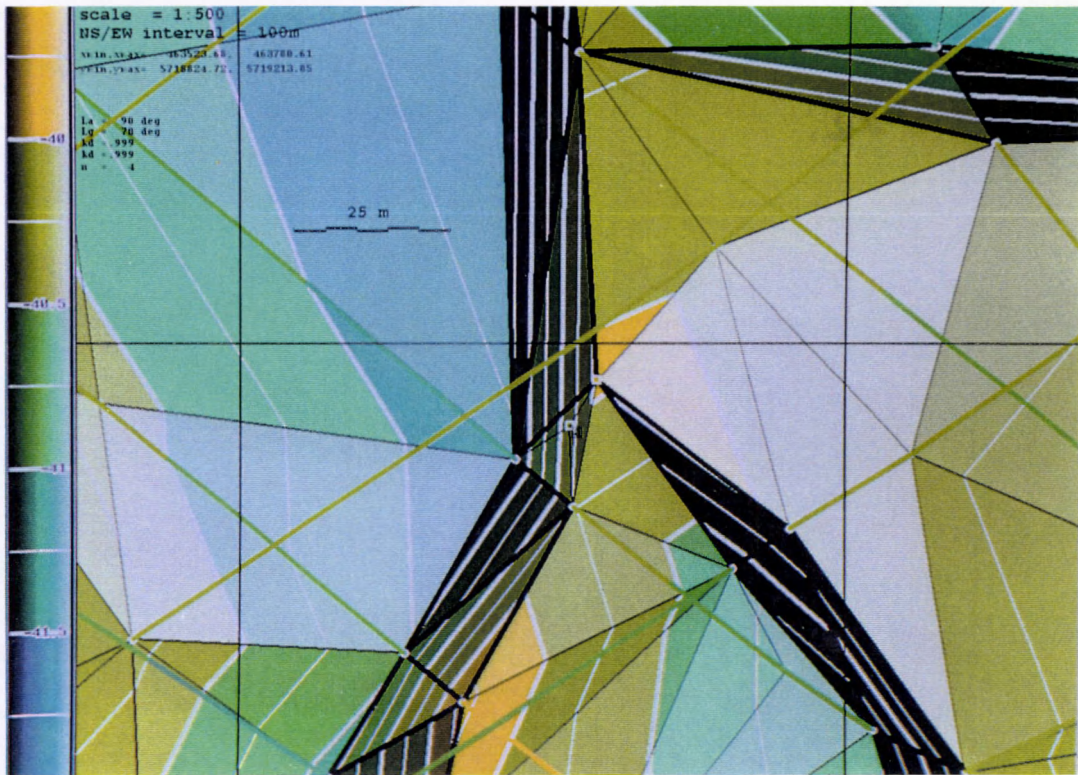


Fig. 3.28c. The triangulation has been changed so that the upthrown bifurcation point connects to both upthrown fault traces. The control point has been moved up a little to conserve the slope of the main fault across the bifurcation. A second control point has just been placed on the main scarp. Its position determines how much throw is taken away by the satellite.

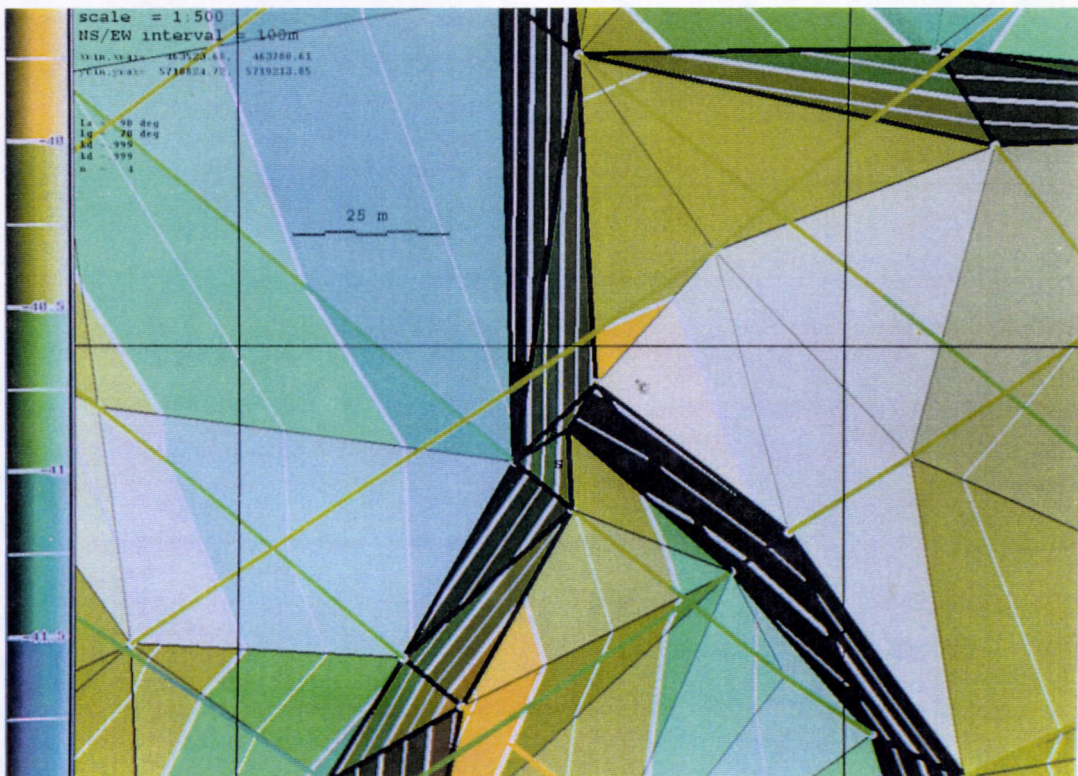


Fig. 3.28d. The triangulation is changed a second time to connect the new bifurcation point with the downthrown trace of the satellite fault and the upthrown trace of the main fault. Relevant triangles are indicated to be part of fault scarps (heavy black lines). Scarp slope can be seen to vary gradually along the "normally" branching faults. Compare with fig. 3.30b.

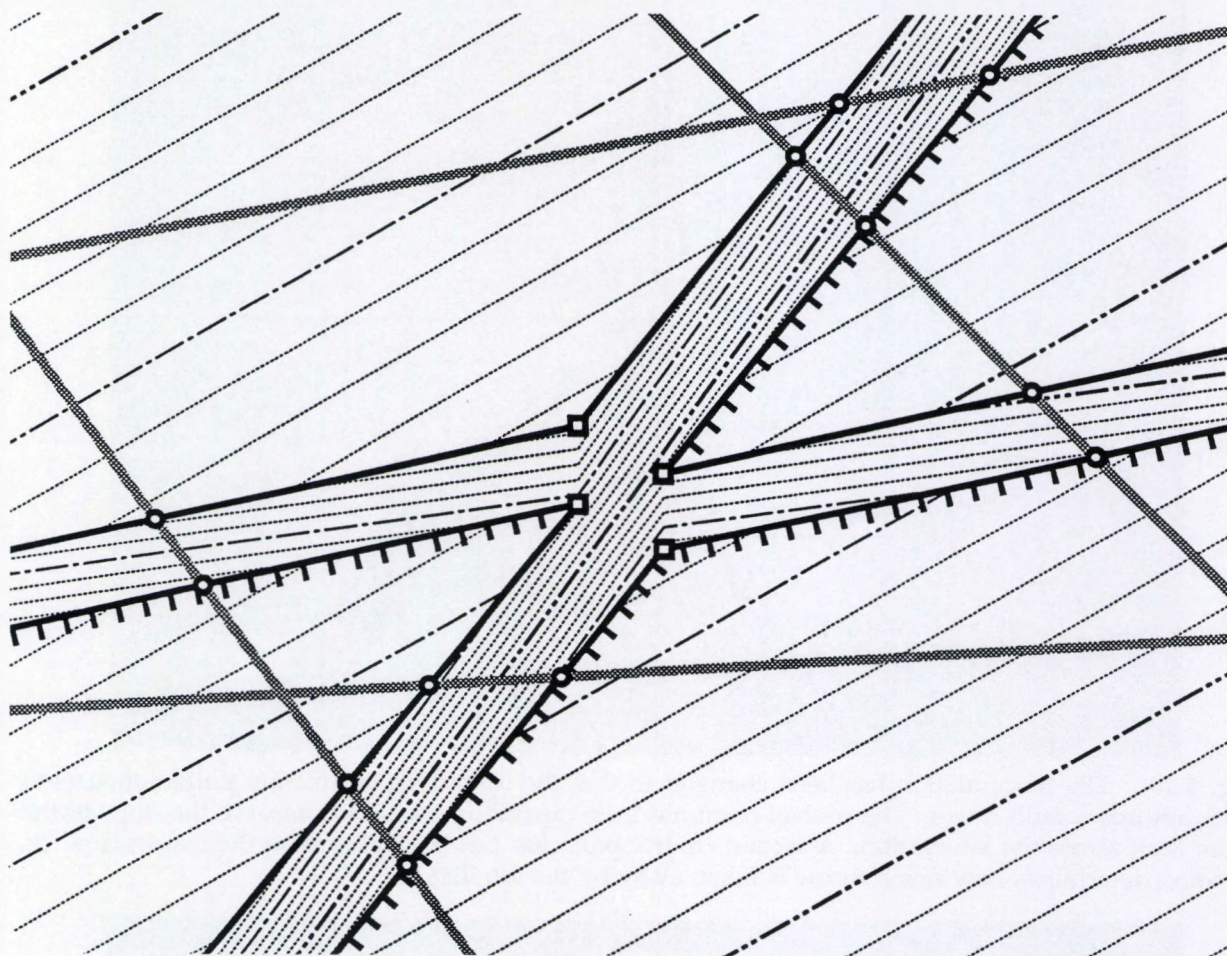


Fig. 3.29. Modelling intersecting faults (tickmarks on downthrown side). Four control points (boxes) are added, forming a parallelogram. One of the fault scarps, interpreted as the youngest, should remain continuous across the intersection. The traces of both faults should be offset on either side of the intersection. Section control in circles on grey seismic lines.

program. Anyhow, a triangulation is not easy to interpret spatially in a 3D projection, because it lacks regularity, as opposed to grids.

Myriad gridding techniques for smooth surface fitting exist, each with their own advantages and drawbacks. Jones *et al.* (1986, p.43-55) and El Abbass *et al.* (1990) provided reviews, and Maslyn (1987) even designed a small expert system to aid in selecting a gridding algorithm. In contrast with a triangulation, a perfect fit of a grid to irregularly spaced data points can not be fully warranted. Gridding always tends to remove information from the original data. Furthermore, the density of information along seismic profiles is higher than between them, and tightly constrains the shape of a reflector along the profiles. A statistical approach with kriging (Olea, 1975; Haas & Viallix, 1976) or adaptive fitting of a harmonic solution (Armitage, 1990) would not only smooth away the fault induced discontinuities, but also fail to honour the reflector data closely. Nevertheless, Pouzet (1980) shows

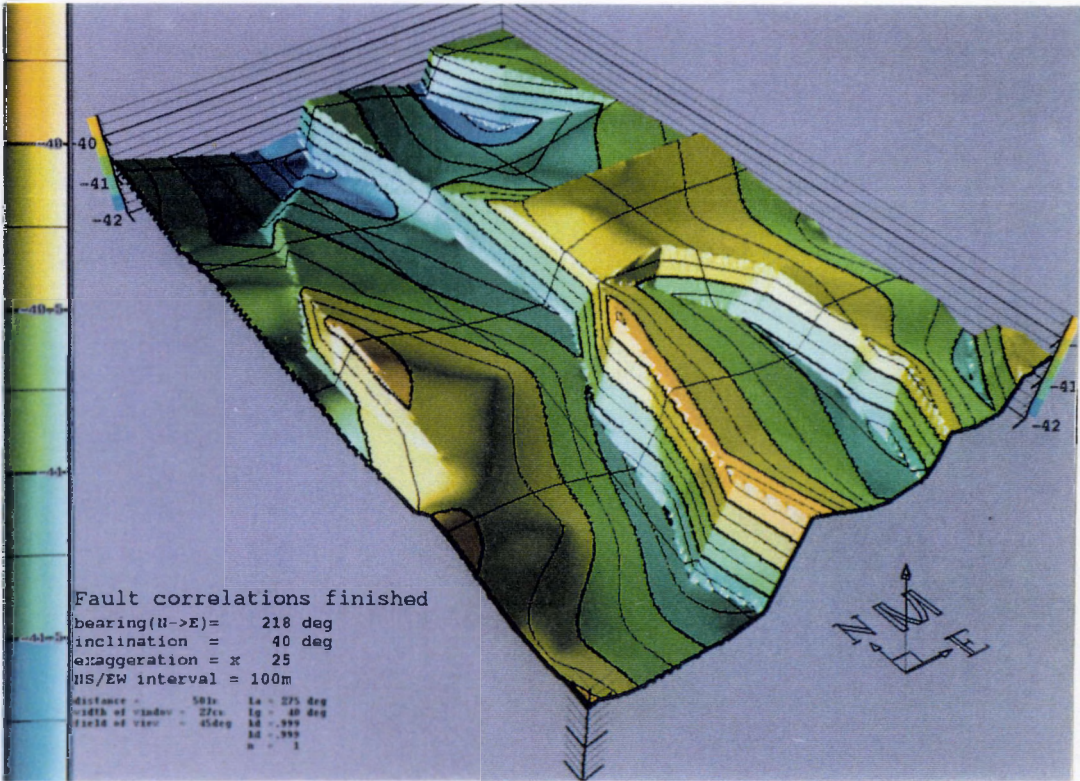


Fig. 3.30a. Gridded 3D view of normal fault bifurcation. The fault scarps look acceptably correlated, but they still lack explicit tips and bifurcation points. Compare with fig. 3.28a and notice smooth contours on horizon, breaking sharply at fault traces.

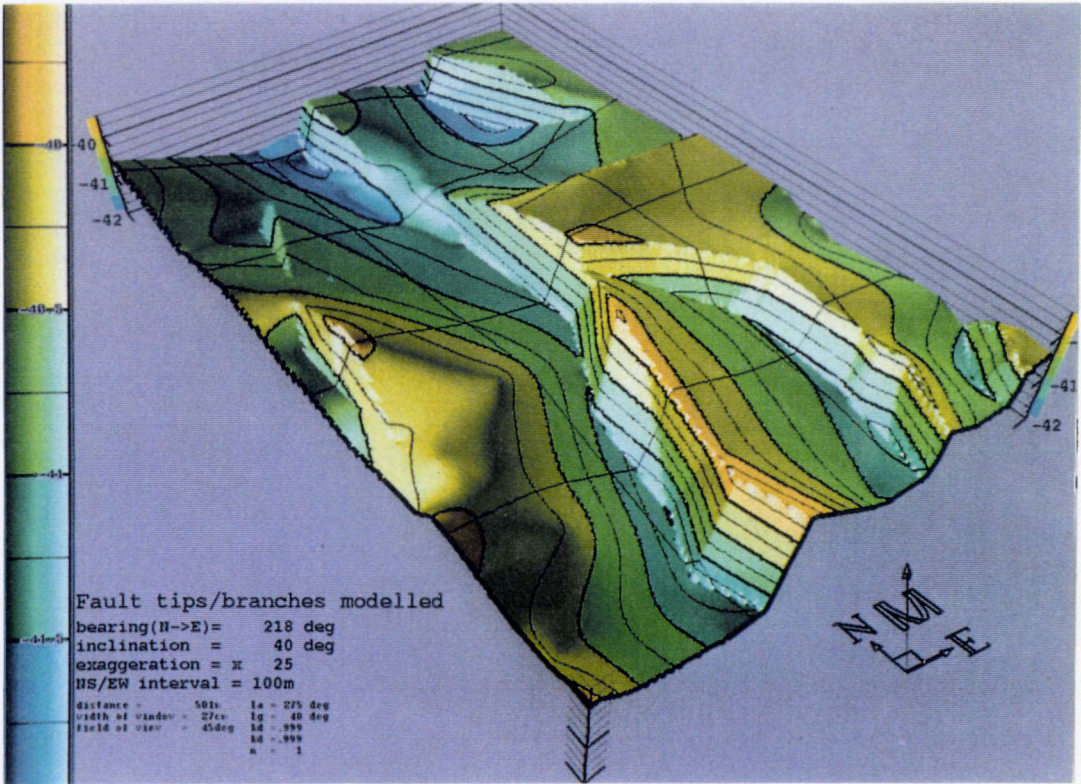


Fig. 3.30b. Same normal fault bifurcation after fault tip and bifurcation modelling. Compare with fig. 3.28d. Contour line interval 0.25 m, colour interval 0.5 m; gridlines projected every 100 m; vertical exaggeration x25; view from SW, illumination from W.

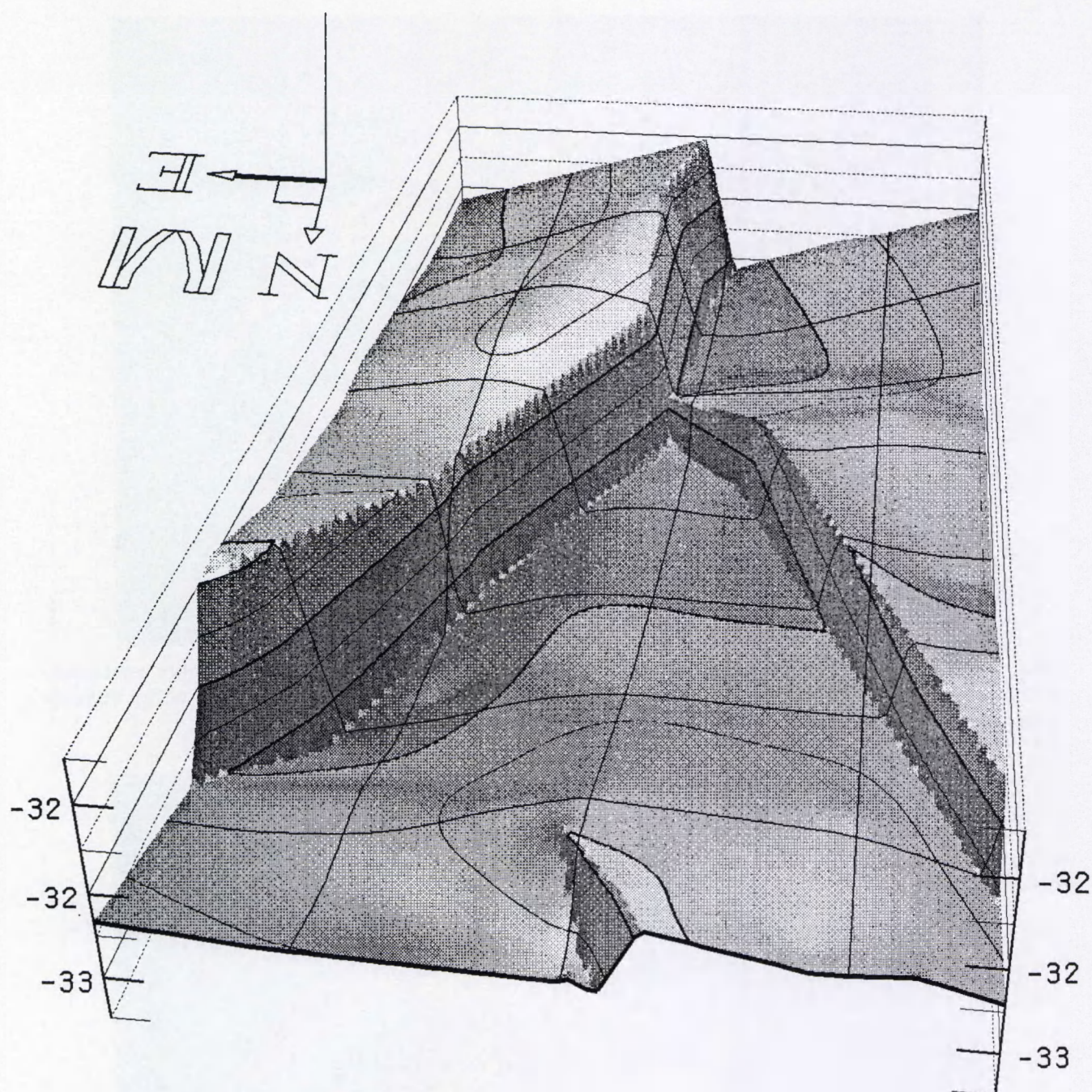


Fig. 3.31a. Gridded 3D view of a "compensating" fault bifurcation, where the angle between main and satellite fault on the intermediate block (upper right) is obtuse. Contour line interval 0.25 m, pseudo-colour interval 1 m; gridlines projected every 50 m; vertical exaggeration x50.

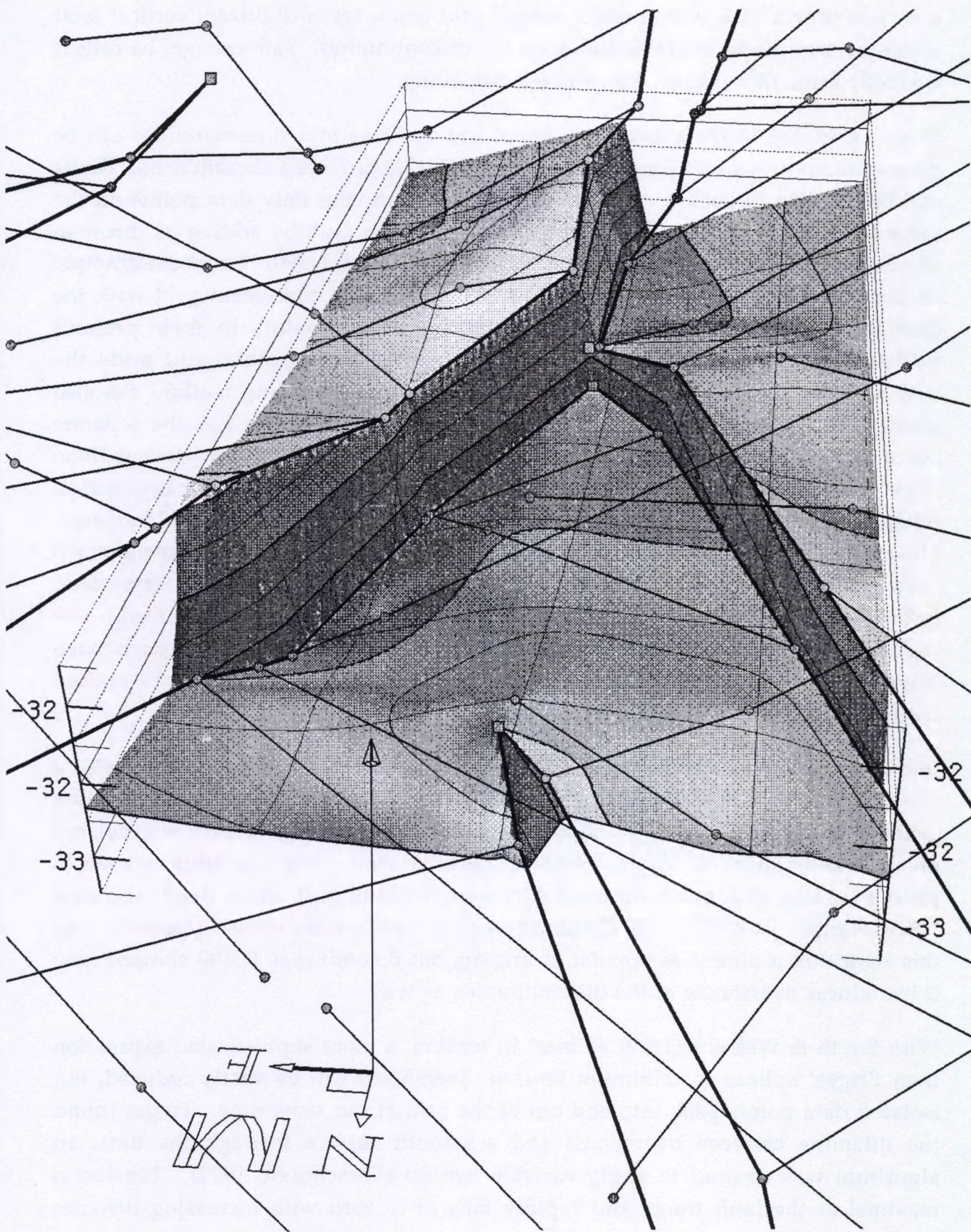


Fig. 3.31b. 3D view of same compensating fault bifurcation, with fault traces (heaviest lines), horizon segments (next heavy lines) connecting data points (circles). Notice control points (boxes) for a fault tip and a bifurcation. Black/white Versatec hardcopy.

a way to play a trick with a coarse kriged grid and a set of digitized, vertical fault traces, so that the contours do break on the discontinuities. Fair enough, he calls it aesthetic estimation rather than surface modelling.

Proper gridding in the presence of faults and other natural discontinuities can be done in many ways, and Jones *et al.* (1986, p.141-173) provide a classification. Faults can be handled in such a way that the interpolation uses only data points on the same fault block, or the gridding can smooth across a fault by adding its throw to the data points on the adjacent block. Zoraster & Ebisch (1990) is a recent example of the latter approach. Another method calculates a displacement grid with the fault trace and throw information, restores the data points to their prefault position with the displacement grid, grids the restored points, and adds the displacement grid again to introduce the fault. A last gridding method can also handle reverse faults, by gridding the fault location data as well as the separate parts of horizons. The grids are operated against one another to prevent them from projection across the fault planes. The latter two methods are impractical when there are many faults, dying out or branching within the gridded area. However, they all require explicit descriptions of the upthrown and downthrown fault traces, together with the amount of throw along the entire fault system, *before* the gridding can start and the first contour map can be evaluated. The major disadvantages of this traditional horizon/fault mapping approach have been discussed in §3.2.4. Our triangular modelling method offers a way around these disadvantages but no smooth contours so far.

In order to combine the interpreted features of the triangular surface model with a smooth grid that honours both the data points and the discontinuities, Geofox grids as follows. The grid is initialized with values that are linearly interpolated on the triangulation (§3.7.7.1). Next, an iterative smoothing algorithm is used to yield a surface with minimum total curvature, holding grid nodes fixed near data points (Briggs, 1974; §3.7.7.2). Contours on such a surface are naturally smooth, and this algorithm is almost as popular as kriging, but Bolondi *et al.* (1976) showed how it introduces overshoots at the discontinuities as well.

With Smith & Wessel's (1990) splines¹ in tension, a more sophisticated expression than Briggs' splines in minimum tension, overshoots can be vastly reduced, but isolated data points peak into and out of the grid at the same time. To get round the dilemma between overshoots and a smooth surface through the data, an algorithm was devised to apply variable tension (Verschuren, 1992). Tension is maximal at the fault traces and rapidly falls off to zero with increasing distance

¹A *spline* is a third degree polynomial that passes (in principle smoothly) through control points (Foley *et al.*, 1990).

(§3.7.7.3). The implementation includes some optimizations (§3.7.7.4) worth mentioning.

A Fortran version of Briggs' (1974) gridding algorithm, implemented on the NCR Tower-32, has been translated into the C programming language and incorporated into Geofox. There it was extended to splines in variable tension. Internally, grids are stored in arrays of Gridvalues (an interpolated Z-value, a code to indicate how it relates to the triangular surface model, and a code for the tension), while temporary grids (arrays of Geopoints) store projected/T-D converted/isopach grids. Dynamic memory allocation and indirect addressing of array elements allows to create and manipulate stacks of dense grids, only limited by computer memory.

3.7.7.1. Initialization

Parts of a grid can initially be made to coincide completely with the triangulation from the first modelling stage (fig. 3.32, 3.42a). Grid nodes that coincide with scarp triangles or data points are marked with special codes for subsequent smoothing. In order to preserve small discontinuities, the grid only needs to be sufficiently dense, typically a few hundreds of grid rows on a side for the complex models shown in this thesis.

The code at each grid node also indicates whether it was initialized with a visible triangle or not, so that the final maps can be automatically bounded by the polygonal boundary around the visible triangles. Areas with no data, e.g. because of truncation, can be indicated by hiding internal triangles that span the gap. This is much more practical than having to digitize the map boundary and holes explicitly, like in most gridding programs (Jones *et al.*, 1986, p.56).

Grid nodes not covered with visible triangles are initialized with a quadratically weighted average of three data points closest to a node (Jones *et al.*, 1986, p.48). Depending on the ratio of the areal data density to the mesh node density, a mesh node that almost coincides with a data point is initialized with the depth of that data point. If the data is not supposed to describe a surface with scarps, be it faults, cliffs or crater rims, there is no need for a triangulation. In that case, grid initialization is speeded up 16 times if a weighted average of the closest neighbours is only calculated every fourth node (fig. 3.33, 3.42b). A reasonable estimate for the rest of the surface is reached after only a few smoothing iterations (fig. 3.34, 3.42c).

3.7.7.2. Smoothing with splines in least tension

Whatever the initialization, subsequent smoothing iteratively reduces tension in the surface, so that the underlying triangulation does not show up as contour breaks, except at the interpreted scarps. The surface converges to splines in

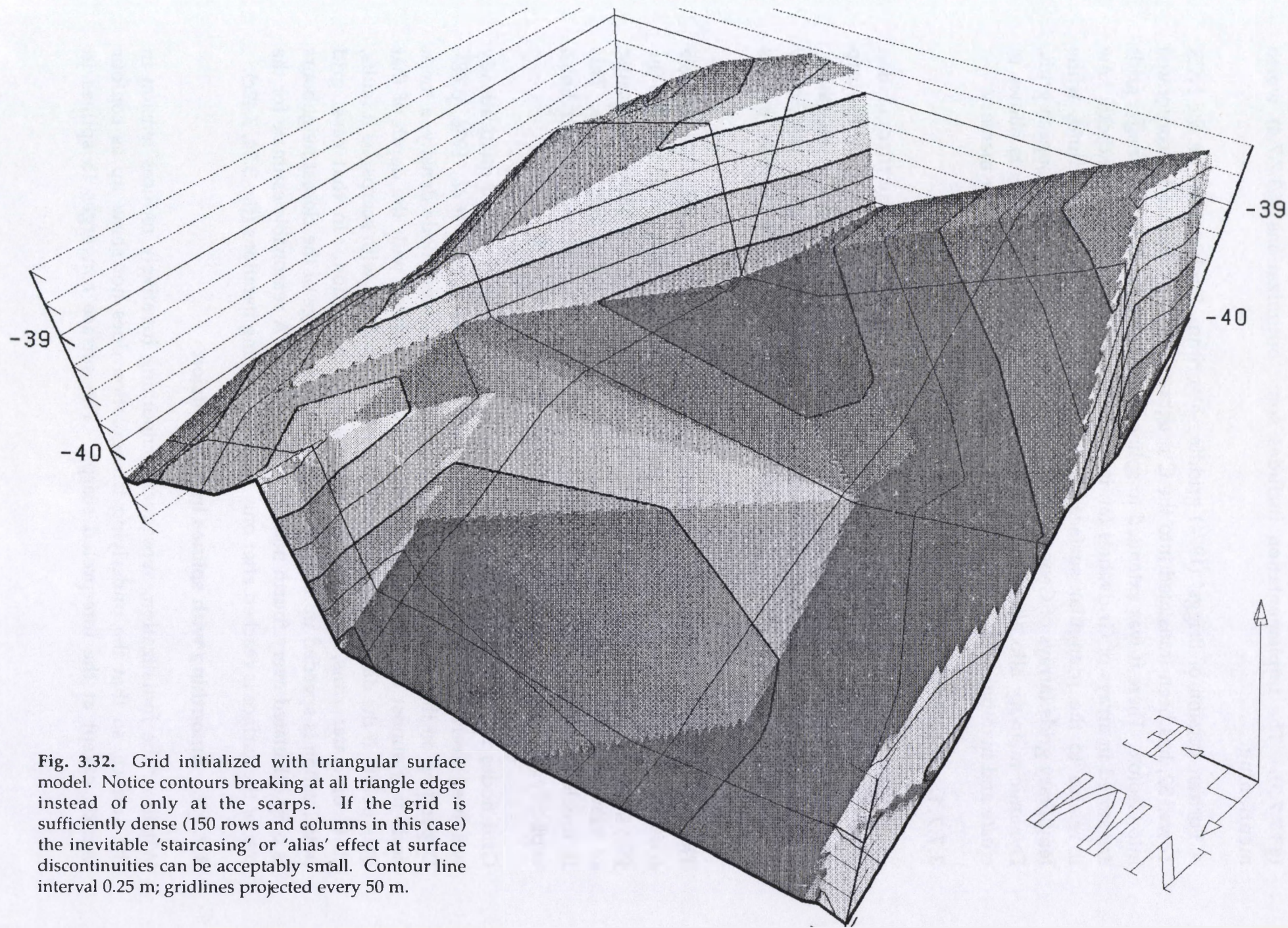


Fig. 3.32. Grid initialized with triangular surface model. Notice contours breaking at all triangle edges instead of only at the scarps. If the grid is sufficiently dense (150 rows and columns in this case) the inevitable 'staircasing' or 'alias' effect at surface discontinuities can be acceptably small. Contour line interval 0.25 m; gridlines projected every 50 m.

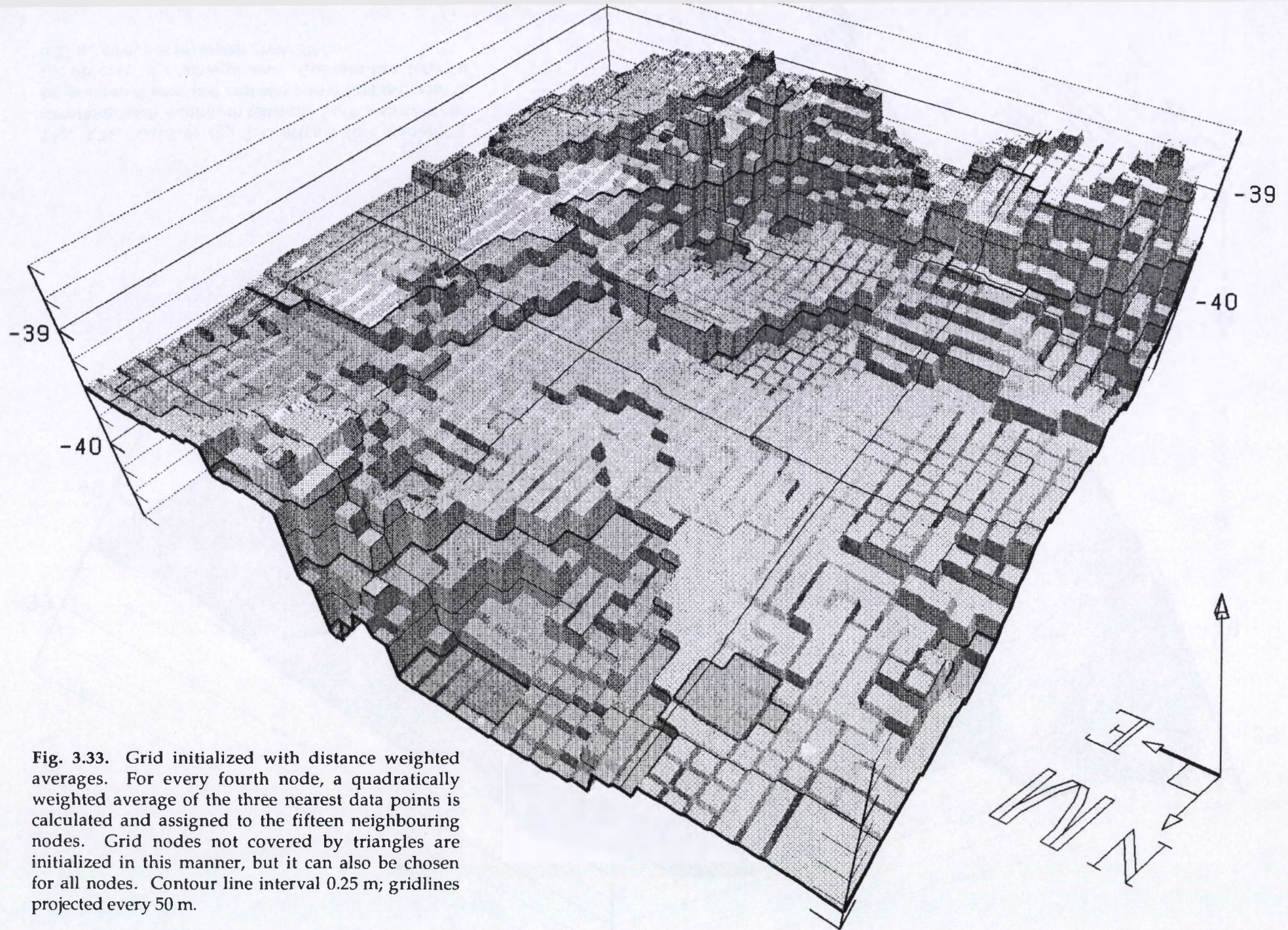


Fig. 3.33. Grid initialized with distance weighted averages. For every fourth node, a quadratically weighted average of the three nearest data points is calculated and assigned to the fifteen neighbouring nodes. Grid nodes not covered by triangles are initialized in this manner, but it can also be chosen for all nodes. Contour line interval 0.25 m; gridlines projected every 50 m.

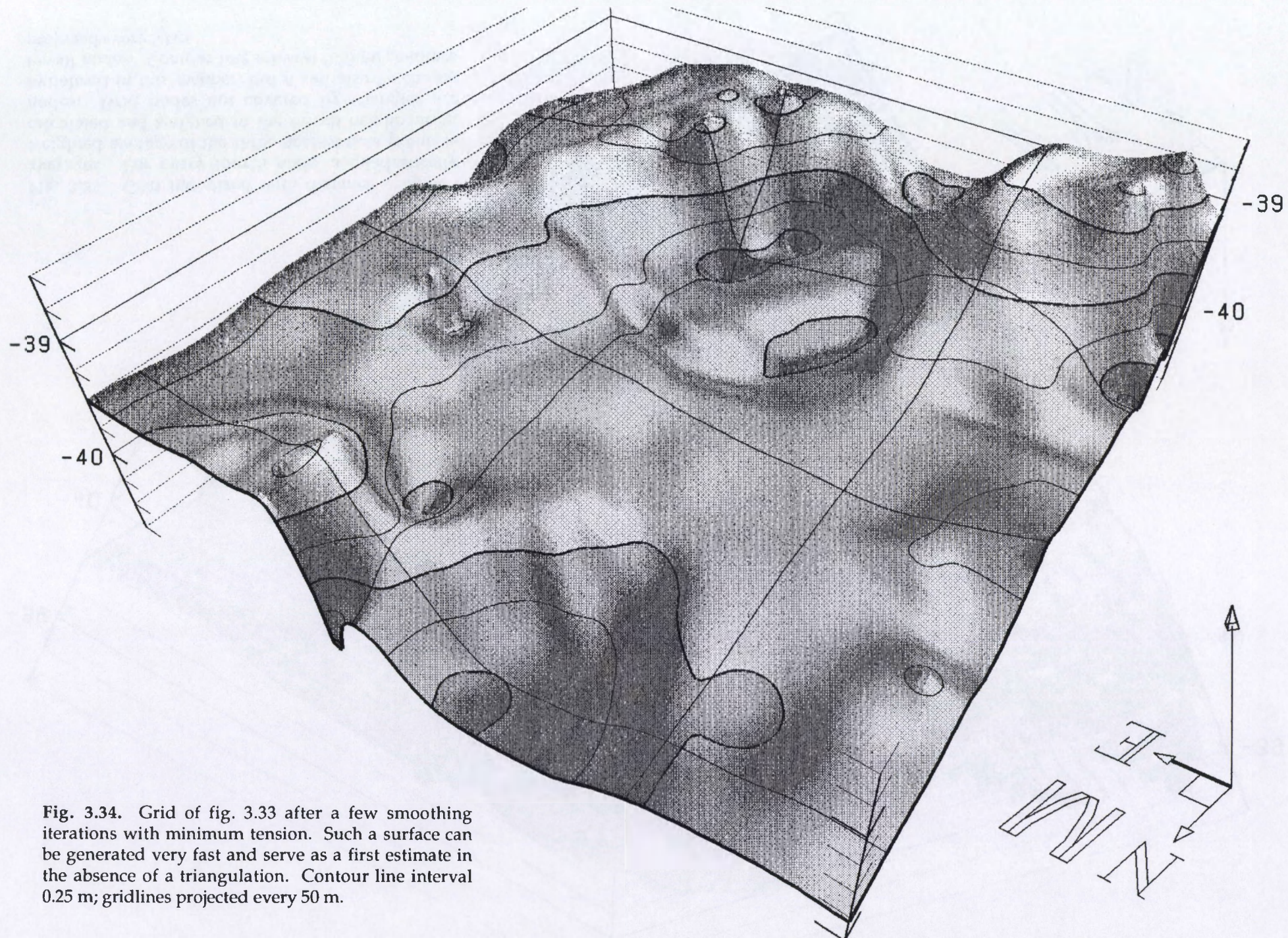


Fig. 3.34. Grid of fig. 3.33 after a few smoothing iterations with minimum tension. Such a surface can be generated very fast and serve as a first estimate in the absence of a triangulation. Contour line interval 0.25 m; gridlines projected every 50 m.

minimum tension between data nodes. The difference equation for a grid node $u_{i,j}$ away from the grid edges is (Briggs, 1974):

$$20 u_{i,j}^{m+1} - 8 (u_{i+1,j}^m + u_{i-1,j}^m + u_{i,j+1}^m + u_{i,j-1}^m) + 2 (u_{i+1,j+1}^m + u_{i+1,j-1}^m + u_{i-1,j+1}^m + u_{i-1,j-1}^m) + (u_{i+2,j}^m + u_{i-2,j}^m + u_{i,j+2}^m + u_{i,j-2}^m) = 0 \quad [\text{eq.1}]$$

in which a new value $u_{i,j}$ for a grid node at row i and column j in the $(m+1)^{\text{th}}$ iteration is determined with the grid values in a neighbourhood of twelve nodes (fig. 3.35) from the m^{th} iteration. The author also provided special difference equations for nodes along the edges of the grid.

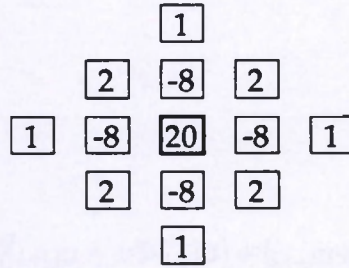


Fig. 3.35. Coefficients of difference equation (Briggs, 1974) for splines in minimum tension in a neighbourhood of twelve nodes.

The scope of Briggs' equation has been found to be insufficient to reduce tension completely in very dense grids, however. Successive grid refinement (§3.7.7.4) offers only part of the solution. If more than four nodes are skipped, the coarse subgrid smooths away too many details that need to be recalculated in a finer subgrid. The difference equation for the normal grid node away from the edges has therefore been extended to include 33 instead of 13 nodes. The deduction is rather involved, but it may be interesting to see how an iterative difference equation is deduced from a set of difference equations.

Just like Briggs, we want to minimize total tension and curvature C in a regular bivariate grid $u(x,y)_{i,j}$. Let local and total (squared) curvature be given respectively by

$$\frac{\partial^2 u}{\partial x^2} + \frac{\partial^2 u}{\partial y^2} \quad \text{and} \quad C(u) = \iint \left(\frac{\partial^2 u}{\partial x^2} + \frac{\partial^2 u}{\partial y^2} \right)^2 dx dy.$$

Total curvature can be rewritten as a sum of discrete curvatures $C_{i,j}$, a function of $u_{i,j}$ and neighbouring nodes:

$$C = \sum_i \sum_j C_{i,j}^2$$

Setting $\frac{\partial C}{\partial u_{i,j}} = 0$ to have minimal curvature and continuous second derivatives at all nodes i,j , we get

$$\begin{aligned}\frac{\partial C}{\partial u_{i,j}} &= \frac{\partial}{\partial u_{i,j}} \left[\sum_i \sum_j C_{i,j}^2 \right] \\ &= \sum_i \sum_j \frac{\partial C_{i,j}^2}{\partial u_{i,j}} \\ &= \sum_i \sum_j 2 C_{i,j} \frac{\partial C_{i,j}}{\partial u_{i,j}} = 0.\end{aligned}\quad [\text{eq.2}]$$

Now,

$$\begin{aligned}\frac{d^2 u}{dx^2} + \frac{d^2 u}{dy^2} &= \lim_{h \rightarrow 0} \frac{1}{h^2} [(u_{i-1,j} - 2u_{i,j} + u_{i+1,j}) + (u_{i,j-1} - 2u_{i,j} + u_{i,j+1})] \\ &= \lim_{h \rightarrow 0} \frac{1}{4h^2} [(u_{i-2,j} - 2u_{i,j} + u_{i+2,j}) + (u_{i,j-2} - 2u_{i,j} + u_{i,j+2})]\end{aligned}$$

so instead of having

$$C_{i,j} = \frac{1}{h^2} [u_{i-1,j} + u_{i+1,j} + u_{i,j-1} + u_{i,j+1} - 4u_{i,j}]$$

like Briggs (1974), we can just as well incorporate more nodes with

$$\begin{aligned}C_{i,j} &= \frac{1}{h^2} [u_{i-1,j} + u_{i+1,j} + u_{i,j-1} + u_{i,j+1} - 4u_{i,j}] + \frac{1}{4h^2} [u_{i-2,j} + u_{i+2,j} + u_{i,j-2} + u_{i,j+2} - 4u_{i,j}] \\ &= \frac{1}{4h^2} [4(u_{i-1,j} + u_{i+1,j} + u_{i,j-1} + u_{i,j+1} - 4u_{i,j}) + u_{i-2,j} + u_{i+2,j} + u_{i,j-2} + u_{i,j+2} - 4u_{i,j}] \\ &= \frac{1}{4h^2} [-20u_{i,j} + 4u_{i-1,j} + 4u_{i+1,j} + 4u_{i,j-1} + 4u_{i,j+1} + u_{i-2,j} + u_{i+2,j} + u_{i,j-2} + u_{i,j+2}].\end{aligned}$$

Instead of having to sum only the curvatures in the first five nodes of this equation into eq.2, we now have

$$\begin{aligned}0 &= \sum_i \sum_j C_{i,j} \frac{\partial C_{i,j}}{\partial u_{i,j}} = C_{i,j} \frac{\partial C_{i,j}}{\partial u_{i,j}} + C_{i-1,j} \frac{\partial C_{i-1,j}}{\partial u_{i-1,j}} + C_{i+1,j} \frac{\partial C_{i+1,j}}{\partial u_{i+1,j}} + C_{i,j-1} \frac{\partial C_{i,j-1}}{\partial u_{i,j-1}} + C_{i,j+1} \frac{\partial C_{i,j+1}}{\partial u_{i,j+1}} \\ &\quad + C_{i-2,j} \frac{\partial C_{i-2,j}}{\partial u_{i-2,j}} + C_{i+2,j} \frac{\partial C_{i+2,j}}{\partial u_{i+2,j}} + C_{i,j-2} \frac{\partial C_{i,j-2}}{\partial u_{i,j-2}} + C_{i,j+2} \frac{\partial C_{i,j+2}}{\partial u_{i,j+2}}\end{aligned}\quad [\text{eq.3}]$$

Partial derivatives to $u_{i,j}$ are zero in all other nodes, and so are their contributions to the sum in eq.1. Because $h \neq 0$, it can be omitted from eq.3. Taking (0,0) as another notation for $u_{i,j}$, and placing partial derivatives first, eq.3 becomes

$$\begin{aligned}
 & -20 [(-20) (0,0) +4 (1,0) +4 (-1,0) +4 (0,1) +4 (0,-1) + (2,0) + (-2,0) + (0,2) + (0,-2)] \\
 & +4 [(-20) (1,0) +4 (2,0) +4 (0,0) +4 (1,1) +4 (1,-1) + (3,0) + (-1,0) + (1,2) + (1,-2)] \\
 & +4 [(-20) (-1,0) +4 (0,0) +4 (-2,0) +4 (-1,1) +4 (-1,-1) + (1,0) + (-3,0) + (-1,2) + (-1,-2)] \\
 & +4 [(-20) (0,1) +4 (1,1) +4 (-1,1) +4 (0,2) +4 (0,0) + (2,1) + (-2,1) + (0,3) + (0,-1)] \\
 & +4 [(-20) (0,-1) +4 (1,-1) +4 (-1,-1) +4 (0,0) +4 (0,-2) + (2,-1) + (-2,-1) + (0,1) + (0,-3)] \\
 & +1 [(-20) (2,0) +4 (3,0) +4 (1,0) +4 (2,1) +4 (2,-1) + (4,0) + (0,0) + (2,2) + (2,-2)] \\
 & +1 [(-20) (-2,0) +4 (-1,0) +4 (-3,0) +4 (-2,1) +4 (-2,-1) + (0,0) + (-4,0) + (-2,2) + (-2,-2)] \\
 & +1 [(-20) (0,2) +4 (1,2) +4 (-1,2) +4 (0,3) +4 (0,1) + (2,2) + (-2,2) + (0,4) + (0,0)] \\
 & +1 [(-20) (0,-2) +4 (1,-2) +4 (-1,-2) +4 (0,-1) +4 (0,-3) + (2,-2) + (-2,-2) + (0,0) + (0,-4)]
 \end{aligned}$$

= 0 (hopefully).

Grouping and summing common coefficients, the difference equation to reduce tension and curvature in a regular grid, using a neighbourhood of 33 nodes becomes [eq.4]:

$$\begin{aligned}
 & 468u_{i,j}^{m+1} - 152(u_{i+1,j}^m + u_{i-1,j}^m + u_{i,j+1}^m + u_{i,j-1}^m) + 32(u_{i+1,j+1}^m + u_{i+1,j-1}^m + u_{i-1,j+1}^m + u_{i-1,j-1}^m) \\
 & - 24(u_{i+2,j}^m + u_{i-2,j}^m + u_{i,j+2}^m + u_{i,j-2}^m) + 8(u_{i+1,j+2}^m + u_{i+1,j-2}^m + u_{i-1,j+2}^m + u_{i-1,j-2}^m + u_{i+2,j+1}^m + u_{i+2,j-1}^m + u_{i-2,j+1}^m + u_{i-2,j-1}^m) \\
 & + 2(u_{i+2,j+2}^m + u_{i+2,j-2}^m + u_{i-2,j+2}^m + u_{i-2,j-2}^m) + 8(u_{i+3,j}^m + u_{i-3,j}^m + u_{i,j+3}^m + u_{i,j-3}^m) + u_{i+4,j}^m + u_{i-4,j}^m + u_{i,j+4}^m + u_{i,j-4}^m = 0.
 \end{aligned}$$

Fig. 3.36 shows how contributing coefficients and nodes are situated around $u_{i,j}$.

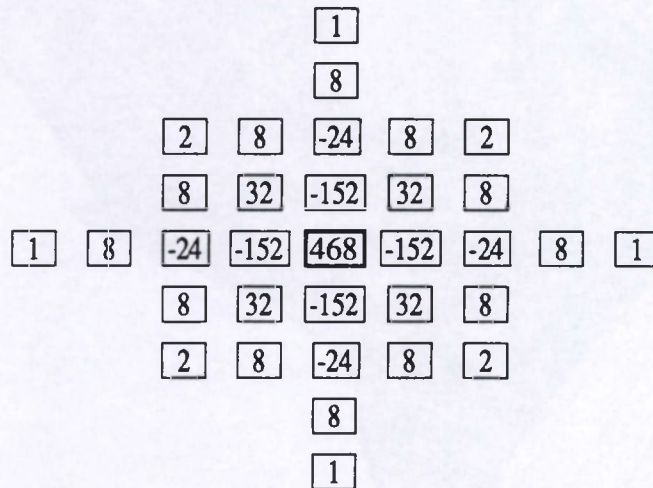


Fig. 3.36. Coefficients of difference equation (Verschuren, 1992) for splines in minimum tension in a neighbourhood of 32 nodes.

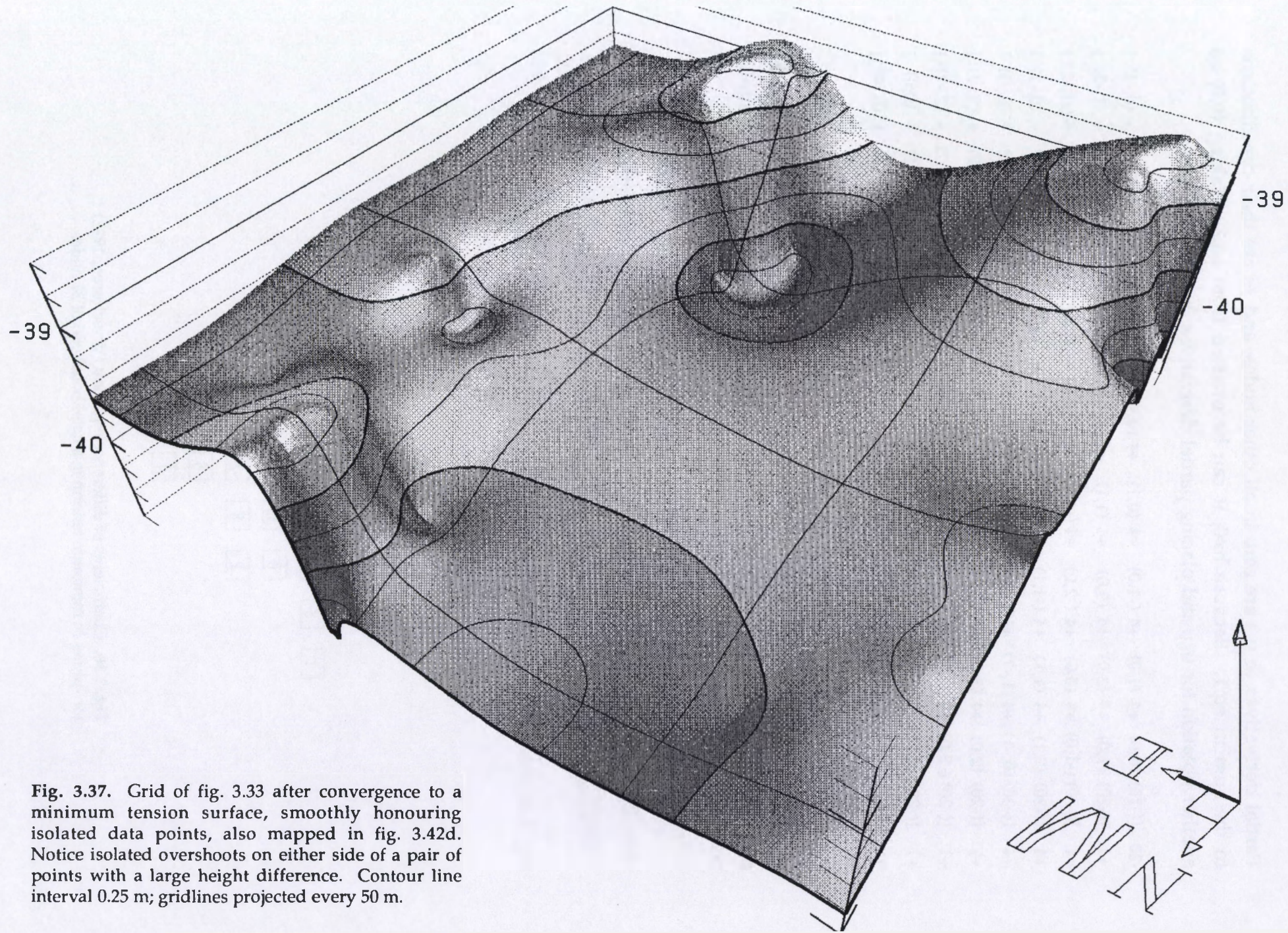


Fig. 3.37. Grid of fig. 3.33 after convergence to a minimum tension surface, smoothly honouring isolated data points, also mapped in fig. 3.42d. Notice isolated overshoots on either side of a pair of points with a large height difference. Contour line interval 0.25 m; gridlines projected every 50 m.

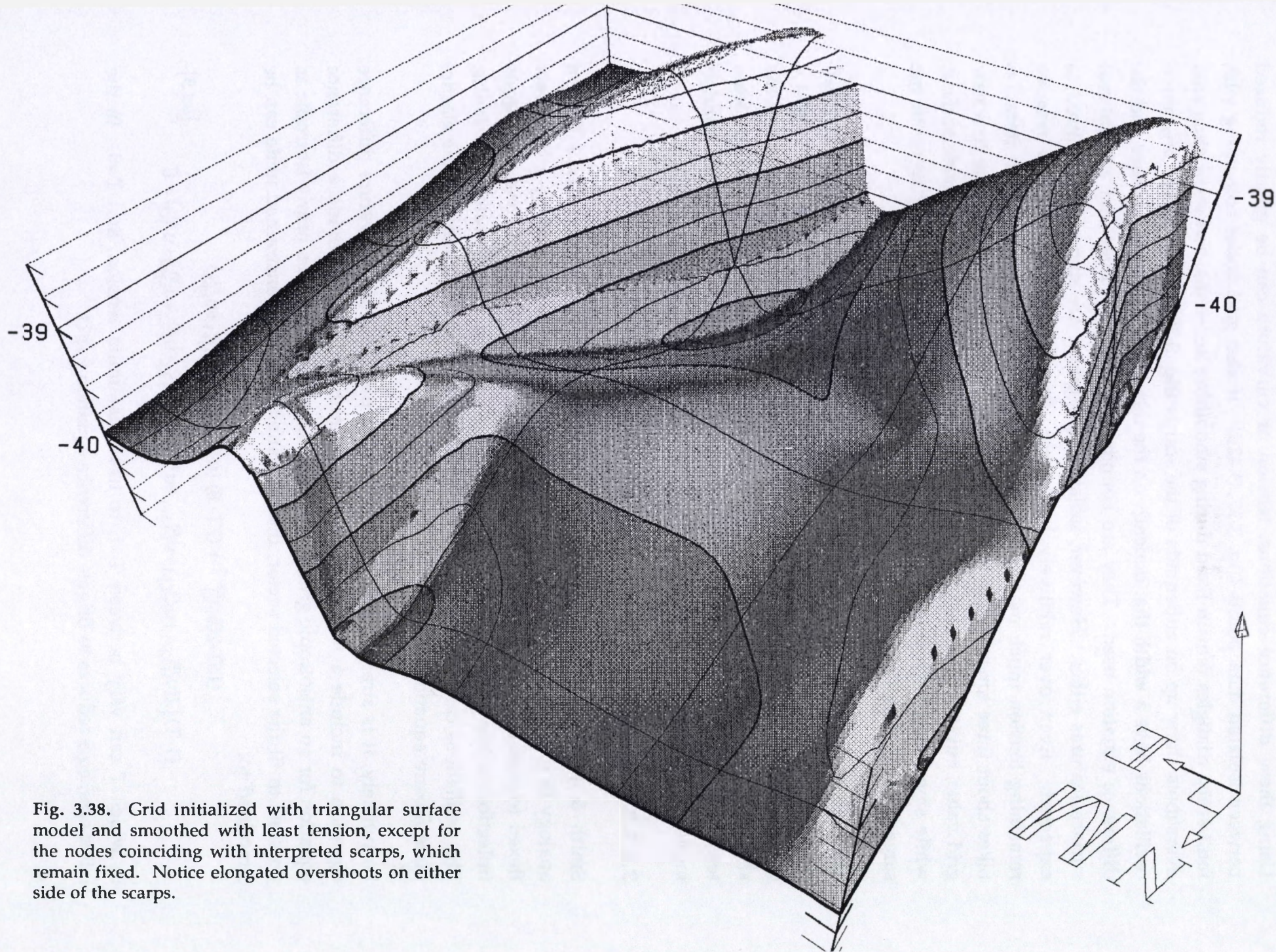


Fig. 3.38. Grid initialized with triangular surface model and smoothed with least tension, except for the nodes coinciding with interpreted scarps, which remain fixed. Notice elongated overshoots on either side of the scarps.

Using these difference equations, tension or curvature can be greatly reduced between isolated data points (fig. 3.37, 3.42d). If also grid nodes coinciding with fault scarp triangles remain fixed during smoothing iterations, awkward elongated overshoots show up on either side of the scarps (fig. 3.38, 3.43a). These unwanted oscillations have a width that depends on the number of smoothing passes and the difference equation used. They are bounded by inflection lines that are not real surface features either. However, isolated data points are smoothly honoured as expected. Even over relatively large grid distances, eq.4 proves to remove remaining tension much more effectively than Briggs' equations. Each iteration takes about three times longer because that much more nodes contribute to a new grid value, but it does not take many iterations to converge to an acceptable surface, while smoothing with Briggs' difference equation may take forever to reach the same level of smoothness.

The least tension approach can also be applied in the 3D modelling of geophysical parameters (Paradis, 1990). The actual distribution of data points may vary from a collection of wells, a network of profiles to a sparse 3D grid. An extension of the above difference equations to 3D would allow to calculate a 'most probable', least tension, homogeneous interpolation of parameter values in a dense 3D gridded model (Fried & Leonard, 1990).

3.7.7.3. Smoothing with splines in variable tension

Smith & Wessel (1990) remarked that the minimum-curvature surface has an analogy in elastic plate flexure. It approximates the shape adopted by a thin plate flexed to pass through the data points. Hence the large oscillations and extraneous inflection points which make it unsuitable for gridding in the presence of faults. The oscillations can be reduced or even eliminated by adding tension to the elastic-plate flexure equation.

Fortunately, it is straightforward to generalize the minimum-curvature difference equation to include a tension parameter. Smith & Wessel provide a difference equation for an anisotropic grid, but because Geofox grids are as nearly isotropic as possible to fit the selected sector, their equation for an unconstrained node can be simplified to:

$$(16T-20) u_{ij}^{m+1} + (7T-8) (u_{i+1,j}^m + u_{i-1,j}^m + u_{i,j+1}^m + u_{i,j-1}^m) + (1-T) [2(u_{i+1,j+1}^m + u_{i+1,j-1}^m + u_{i-1,j+1}^m + u_{i-1,j-1}^m) + u_{i+2,j}^m + u_{i-2,j}^m + u_{i,j+2}^m + u_{i,j-2}^m] = 0 \quad [\text{eq.5}]$$

in which T can vary between T=1, to have maximum tension, and T=0. In the latter case, eq.5 reduces to Briggs' difference equation (eq.1).

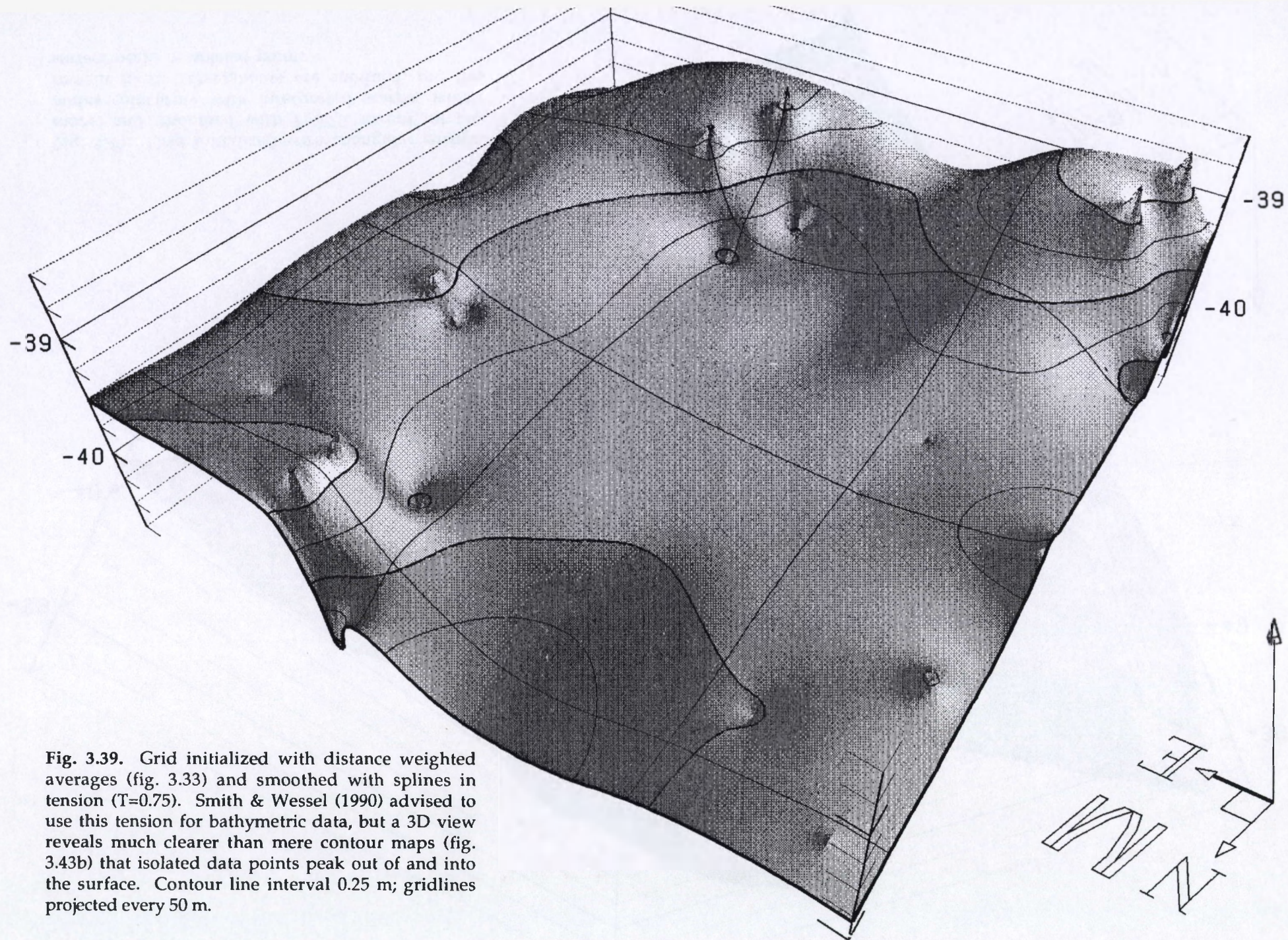


Fig. 3.39. Grid initialized with distance weighted averages (fig. 3.33) and smoothed with splines in tension ($T=0.75$). Smith & Wessel (1990) advised to use this tension for bathymetric data, but a 3D view reveals much clearer than mere contour maps (fig. 3.43b) that isolated data points peak out of and into the surface. Contour line interval 0.25 m; gridlines projected every 50 m.

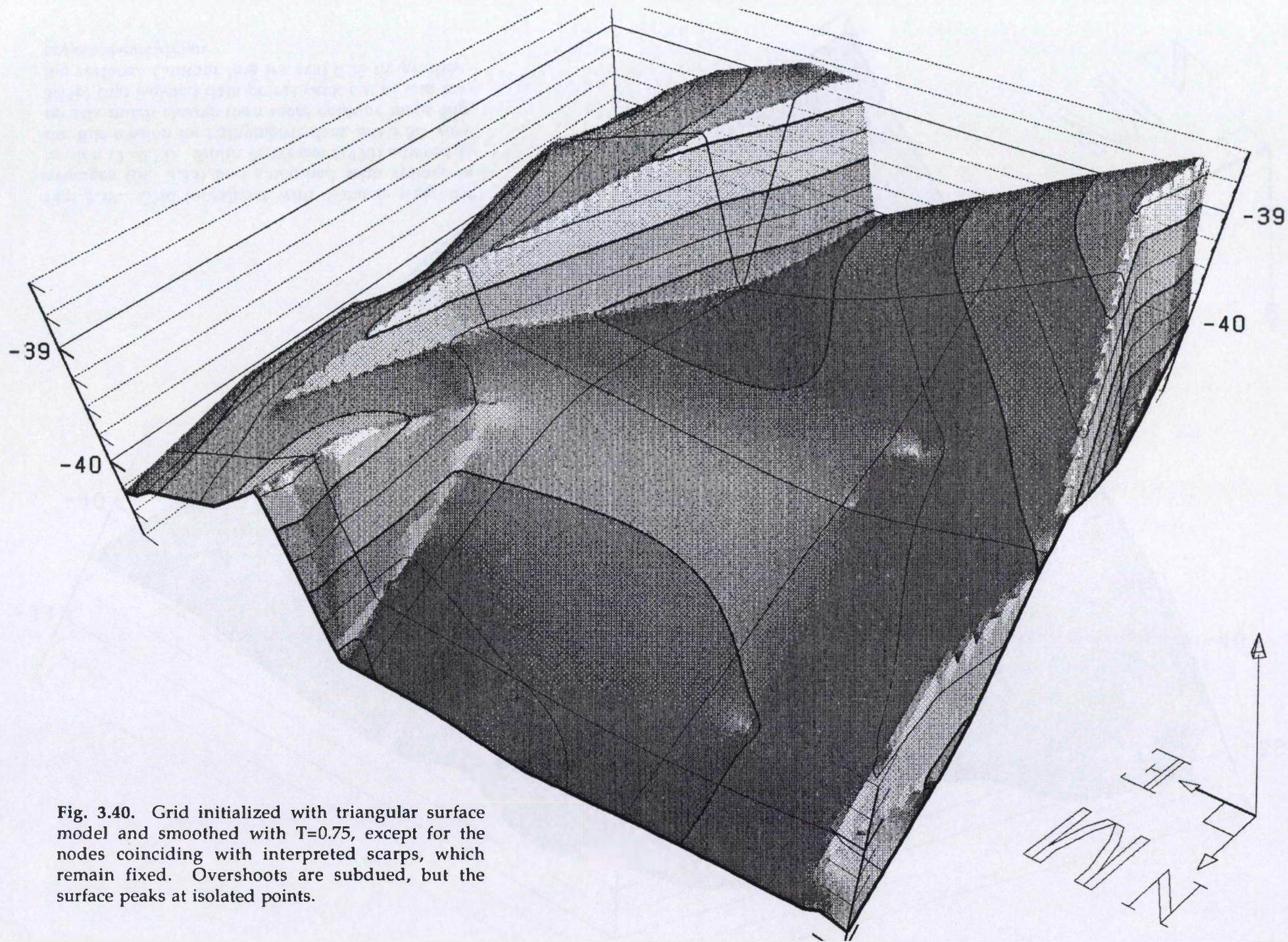


Fig. 3.40. Grid initialized with triangular surface model and smoothed with $T=0.75$, except for the nodes coinciding with interpreted scarps, which remain fixed. Overshoots are subdued, but the surface peaks at isolated points.

For bathymetric data, Smith & Wessel (1990) suggest to use a tension of $T=0.75$. Such a tension indeed does away with overshoots (fig. 3.39), but the surface peaks at the data points. The effect is hardly visible on a mere contour map (fig. 3.43b and examples given by Smith & Wessel), where contour lines look more acceptable than they are. Initializing the grid with the triangular surface model and holding grid nodes coinciding with scarps fixed just like in fig. 3.38, a homogeneous tension of 0.75 largely subdues the unwanted oscillations along the scarps (fig. 3.40, 3.43c) but isolated points peak into and out of the surface.

Faced with the dilemma between a smooth surface with overshoots and one that is discontinuous at the interpreted fault scarps as well as at the data points, Bolondi *et al.* (1976) devised a sophisticated smoothing algorithm that produces a surface similar to a kriged one: smooth but passing below high points and above low ones. We took the conceptually simple but more successful approach of applying a high tension at the scarps and a low one for most of the rest of the faulted horizon, and a *variable* tension in between. In a zone that should be as narrow as possible, tension should decrease gradually but rapidly with increasing distance from the scarps.

Devising an efficient and robust algorithm to calculate the right distance-dependent tension in the presence of myriad faults proved to be less than straightforward. In Geofox, a fixed neighbourhood around each grid node is scanned to sum the number of nodes covered by scarp triangles. Because the relation between nodes and triangulation has been stored during grid initialization, this algorithm has $O(\text{number of nodes})$ complexity, *independent* of the number and complexity of fault scarps. Tension is related to the ratio of that sum to the number of scanned nodes and to the tensions at and away from the scarps. Both tensions can be set by the user. The neighbourhood was chosen so as to have a tension varying both gradually (not too small) and rapidly (not too large) between the two tensions. The tension is stored at each node, so that it can be used during subsequent smoothing passes. To save memory, only one byte is used per node.

With maximal tension ($T=1$) at the scarps and minimal tension ($T=0$) away from them, isolated data points on the horizon can be smoothly honoured. At the same time, the maximal tension effectively ensures a linear surface interpolation at the scarps, and eliminates the problem of overshoots entirely (fig. 3.41, 3.43d). In this way, even complex faulted horizons can be modelled and contoured in a reliable and predictable way. The surface models in §3.7.10 and Chapter 4 serve as further demonstrations.

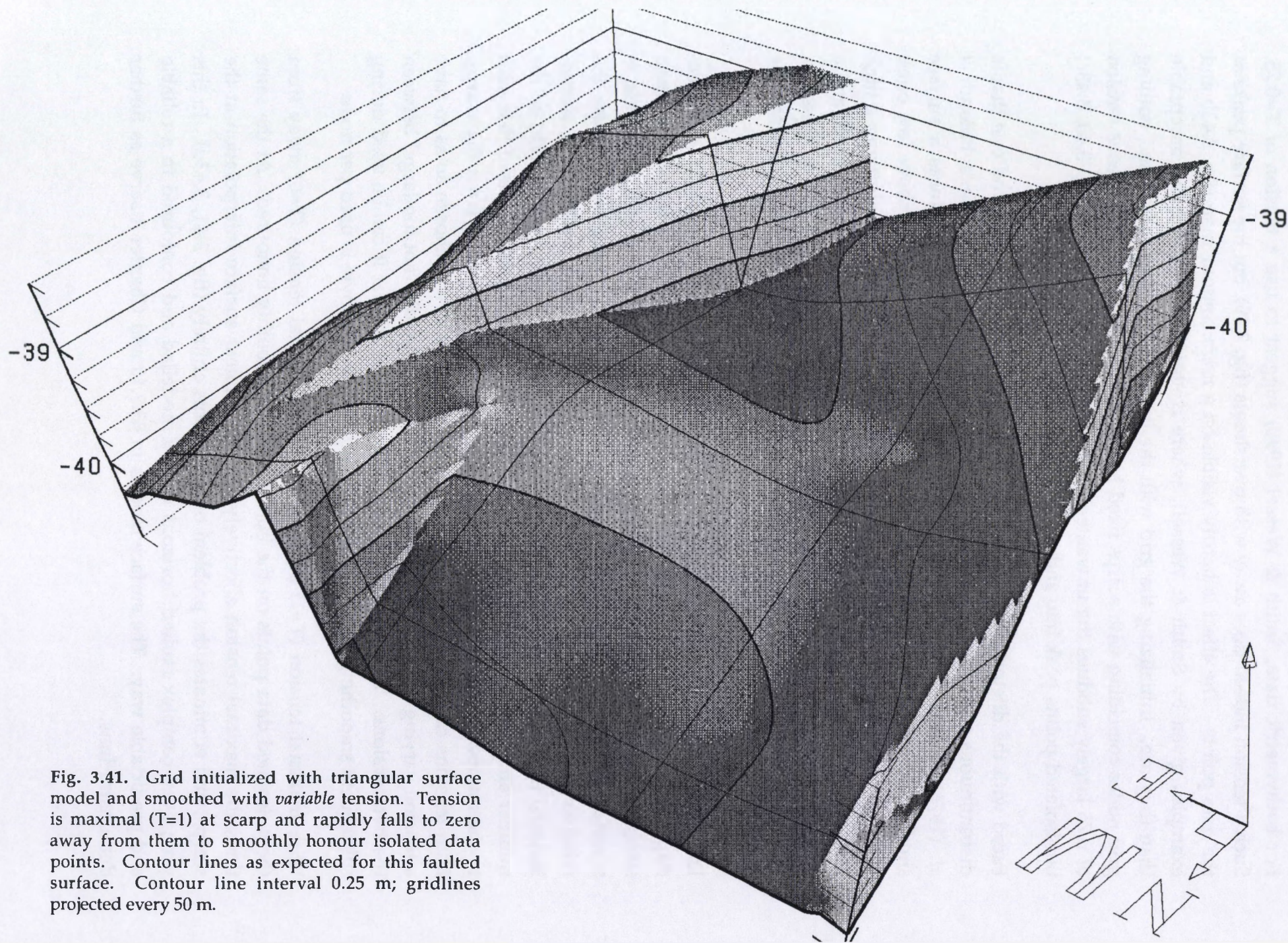


Fig. 3.41. Grid initialized with triangular surface model and smoothed with *variable* tension. Tension is maximal ($T=1$) at scarp and rapidly falls to zero away from them to smoothly honour isolated data points. Contour lines as expected for this faulted surface. Contour line interval 0.25 m; gridlines projected every 50 m.

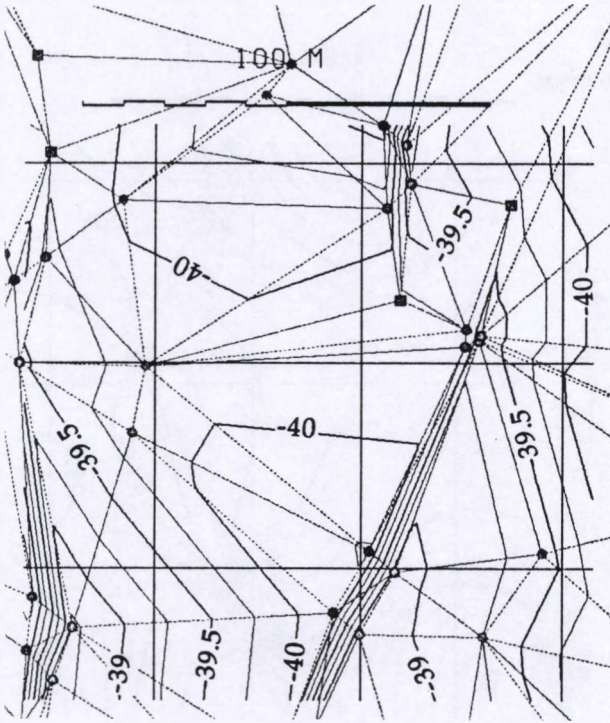


Fig. 3.42a. Grid initialized with triangular surface model. Notice contours breaking at all triangle edges (dashed lines). Contour line interval 0.25 m.

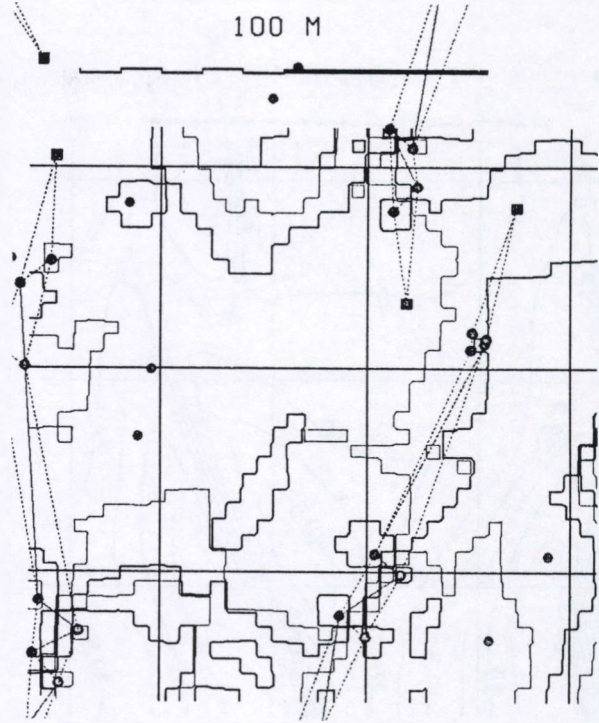


Fig. 3.42b. Grid initialized with distance weighted averages, without further smoothing. Circles are data points and boxes are control points. Contour line interval 0.25 m.

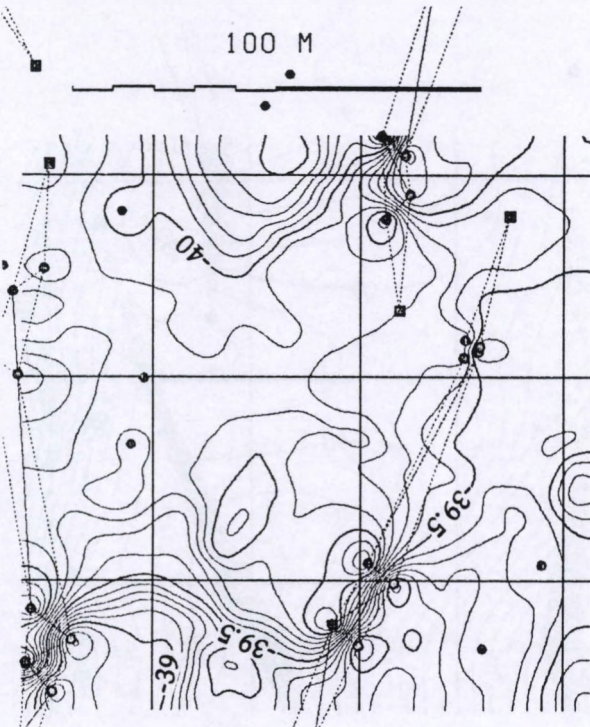


Fig. 3.42c. Grid of fig. 3.42b after a few smoothing iterations with minimum tension. Scarp triangles in dashed lines. Contour line interval 0.1 m.

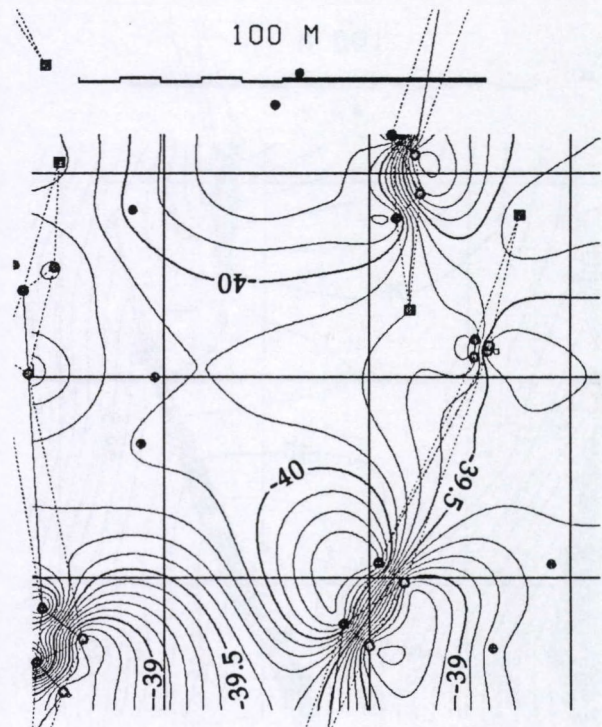


Fig. 3.42d. Grid of fig. 3.42c after convergence to a minimum tension surface. Notice isolated overshoots. Contour line interval 0.1 m.

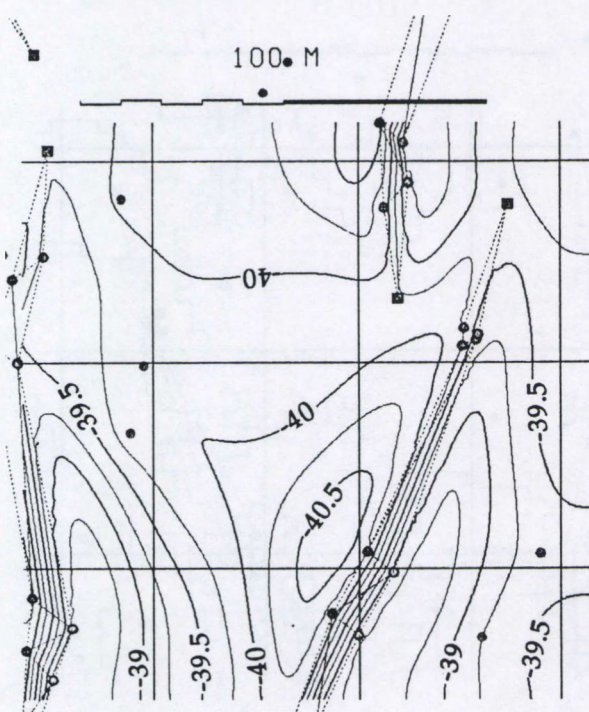


Fig. 3.43a. Grid initialized like in fig. 3.42a and smoothed to least tension, except for scarp nodes. Notice elongated overshoots on either side of the scarps. Contour line interval 0.25 m.

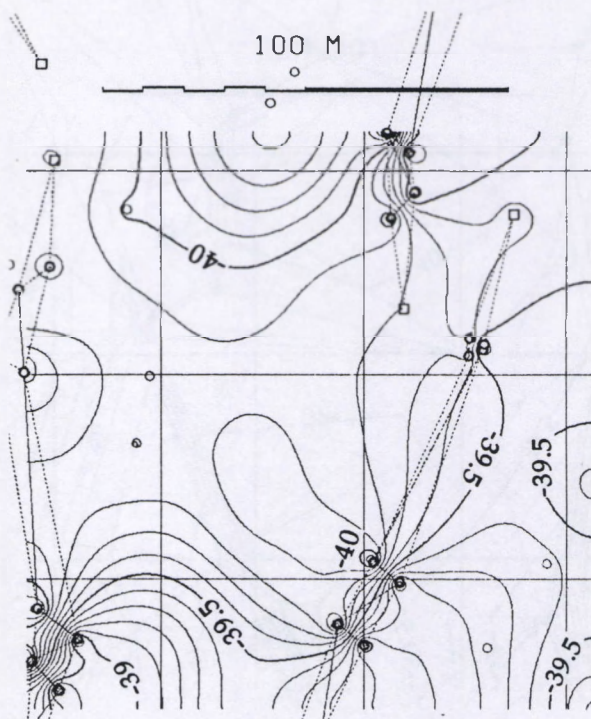


Fig. 3.43b. Grid of fig. 3.42b and smoothed to a tension of $T=0.75$ (Smith&Wessel, 1990). Contour lines look more acceptable than they are (fig. 3.39). Contour line interval 0.1 m.

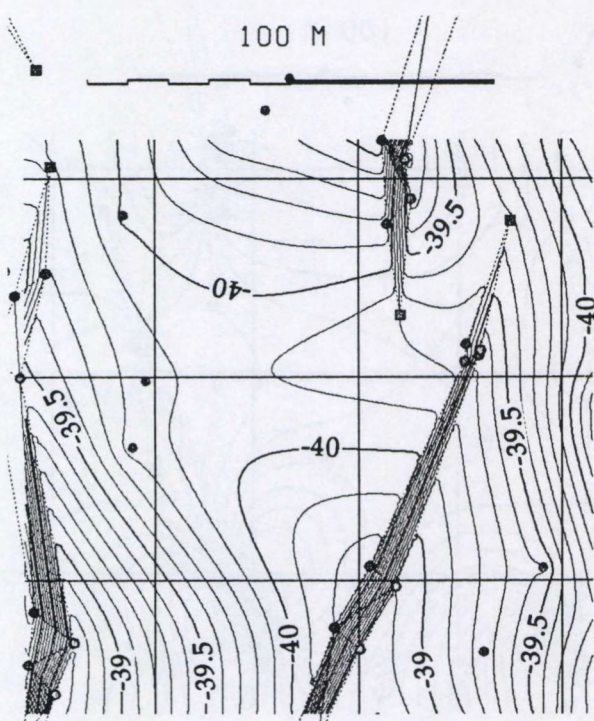


Fig. 3.43c. Grid initialized with triangular surface model and smoothed to a tension of $T=0.75$. Overshoots are subdued, but isolated data are misplaced. Contour line interval 0.1 m.

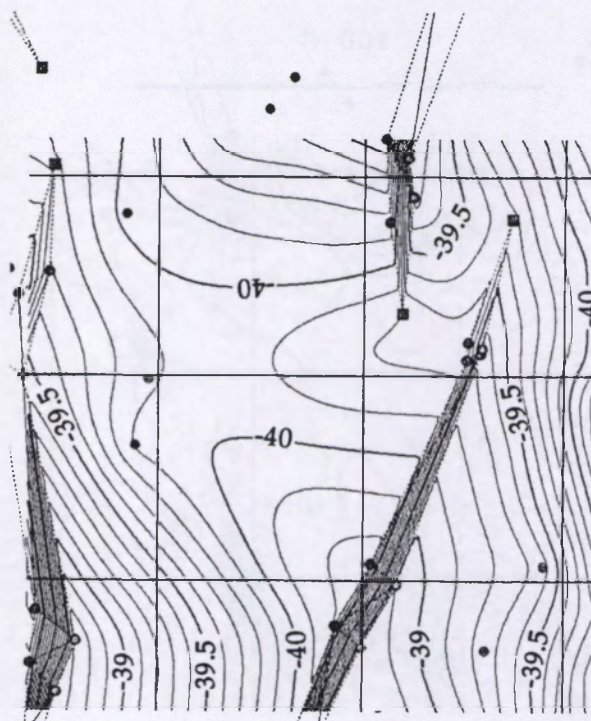


Fig. 3.43d. Grid initialized with triangular surface model and smoothed with variable tension. Contour lines as expected for this faulted surface. Contour line interval 0.1 m.

3.7.7.4. Optimizations

A number of optimizations that greatly improved gridding efficiency are worth mentioning here.

Grid initialization time with a triangular surface model can be linear in the number of triangles. For each triangle, find the gridnodes it covers and get a (linearly interpolated) value for each of them. This is arguably a better and faster estimate of the surface than distance weighted averages, which involves a lot of searching.

Because the linear interpolation on a triangulation is a very good estimate of the surface, gridding with variable tension around the scarps has also the advantage of being faster than both minimum and maximum tension smoothing applied homogeneously. When the grid is initialized with a triangulation, minimum tension smoothing takes a long time to converge to stable oscillations, while maximum tension smoothing takes a long time to converge to the tent-like surface peaking at the data points.

Through successive grid refinement (Smith & Wessel, 1990) the scope or 'smoothing effect' of the splines (the finite difference equations), is varied from large scale structures or trends between sparse 2D profiles, to small scale detail along profiles. With successive grid refinement disabled, a grid can smoothly honour the trends modelled in the triangulation without their being 'frozen' as scarps. Thus, the triangular trends can be smoothed to anything between fig. 3.32 and 3.41.

A convergence detection mechanism (*ibidem*) tests whether the largest changes between consecutive iterations are sufficiently relevant to justify continuation of calculations. The convergence detection limit can be selected by the user as a small to very small fraction of the height range of the grid.

In order to save memory, only one grid is used during the smoothing iterations. However, asymmetries arising from a unique grid traversing direction are avoided through regular reversals.

3.7.8. Stratigraphic functions

Geofox is also used by seismic stratigraphers at RCMG to map individual and series of sequence boundaries on the basis of seismic sections, from the internal stratigraphy of a sandbank of 5x15km and a depth of a few tens of m, to the architecture of a complex submarine fan in an area of 200x200km and a depth of several

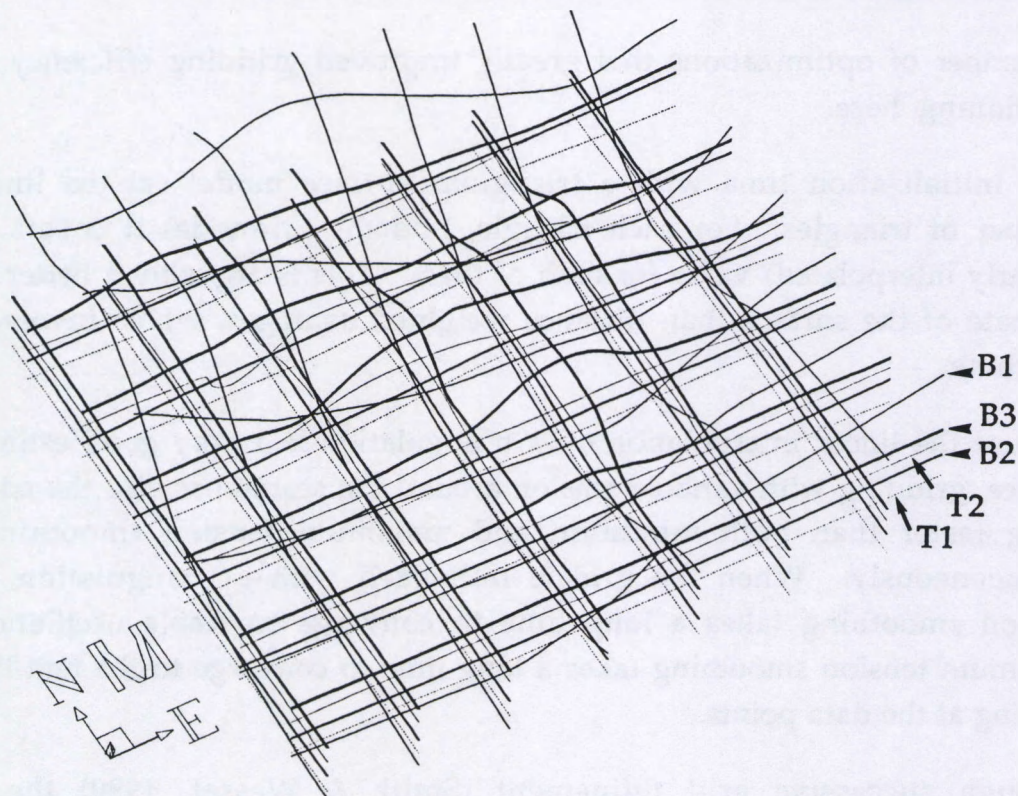


Fig. 3.44a. Grids calculated for five sequence boundaries (thickest is youngest) intersect one another because they are extrapolated beyond the respective data areas, covered by triangulations.

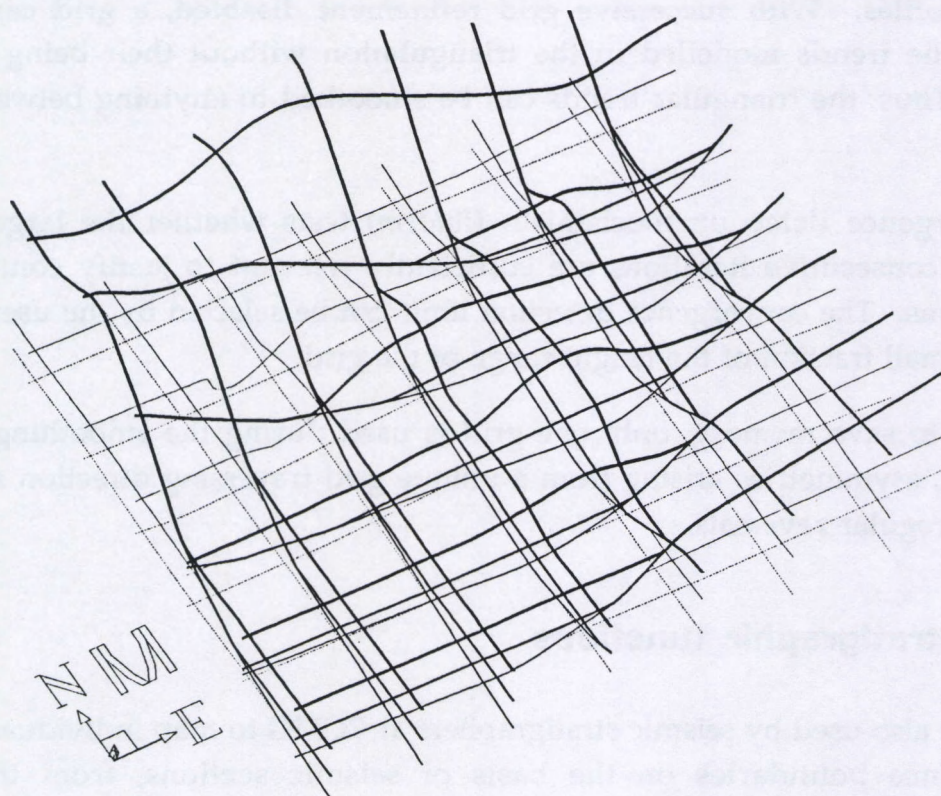


Fig. 3.44b. Same grids after stratigraphic framework builder algorithm automatically removed the extrapolations, so that the horizons are truncated or pinch out as expected (see also fig. 3.45).

thousands of m. Automatic isopach¹ maps in combination with the possibility to test alternative velocity hypotheses for Time/Depth conversion of reflection time maps, where therefore highly desirable extra's in the program.

For each of the sequence boundaries, digitized data points along the sections are filtered and triangulated. Faults or other scarps can be modelled. A list of triangular surface models can then be gridded with one command. Typically, the sequence boundaries are known in only part of the grid sector, because of horizon pinch out, truncation or simply lack of data. Each of the grid is extrapolated beyond its triangulation, i.e. beyond the area covered by data, to be fully determined. The grids therefore tend to intersect one another (fig. 3.44a), leading to meaningless isopach calculations with negative thicknesses, or non-zero thicknesses where a sequence bounded by two horizons pinches out on a third horizon (fig. 3.45a-c) or is truncated by yet another.

The problem is well known and its traditional solution (Jones *et al.*, 1986) is to specify stratigraphic relations explicitly with a table of codes. This table is used to build the *stratigraphic framework* in which the grids are made to coincide (with zero thicknesses in between) where the sequence is absent. Stratigraphic relations can be complex, and filling in the table of codes together with all the pair-wise grid operations can be just as complex.

In Geofox, the user only has to enter the names of the modelled sequence boundaries in stratigraphic order, from young to old, and the stratigraphic framework of grids can be built automatically after their inter/extrapolation. Grids pinch out or are truncated as geologically expected (fig. 3.44b), and isopachs make more sense as well (fig. 3.45d).

It was possible to devise an algorithm for these otherwise cumbersome operations, because the grids in Geofox not only store an interpolated value at each of the grid nodes, but also a code to indicate whether that node is covered by the modelled triangulation of the data or not. For each node, the stack of grids is scanned sequentially for pairs of grids with negative thickness in between, and either the upper undetermined grid node is brought down to the younger truncating grid, or the lower upwards to the older onlap surface (fig. 3.44).

Isopach grids can be calculated for any pair of interpolated grids, or between one grid and any arbitrary level. In the latter case, positive and negative differences can

¹In Geofox, isopach maps are regarded as synonymous with isochore maps, which is the correct name for thicknesses measured vertically instead of perpendicularly to bedding (AGI, 1980).

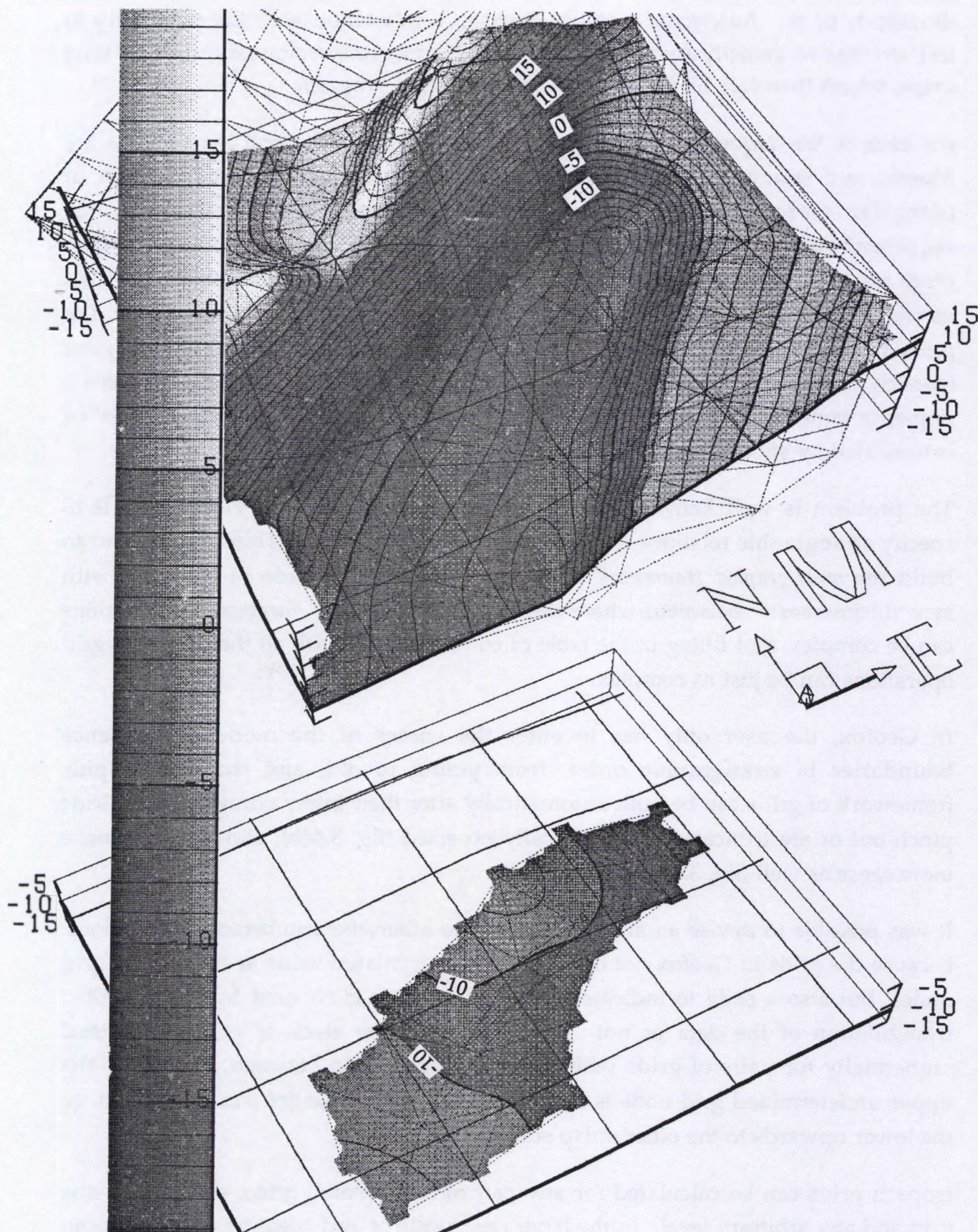


Fig. 3.45a (above). Grid B1 from fig. 3.44a, together with the triangulation with which it was initialized. Grid nodes not covered by the triangulation can be left away. Notice concave triangulation boundary. b (below). Grid B2 from fig. 3.44a, together with triangulation. This sequence boundary laps onto B1. Both gaps and overlaps are present between the two models.

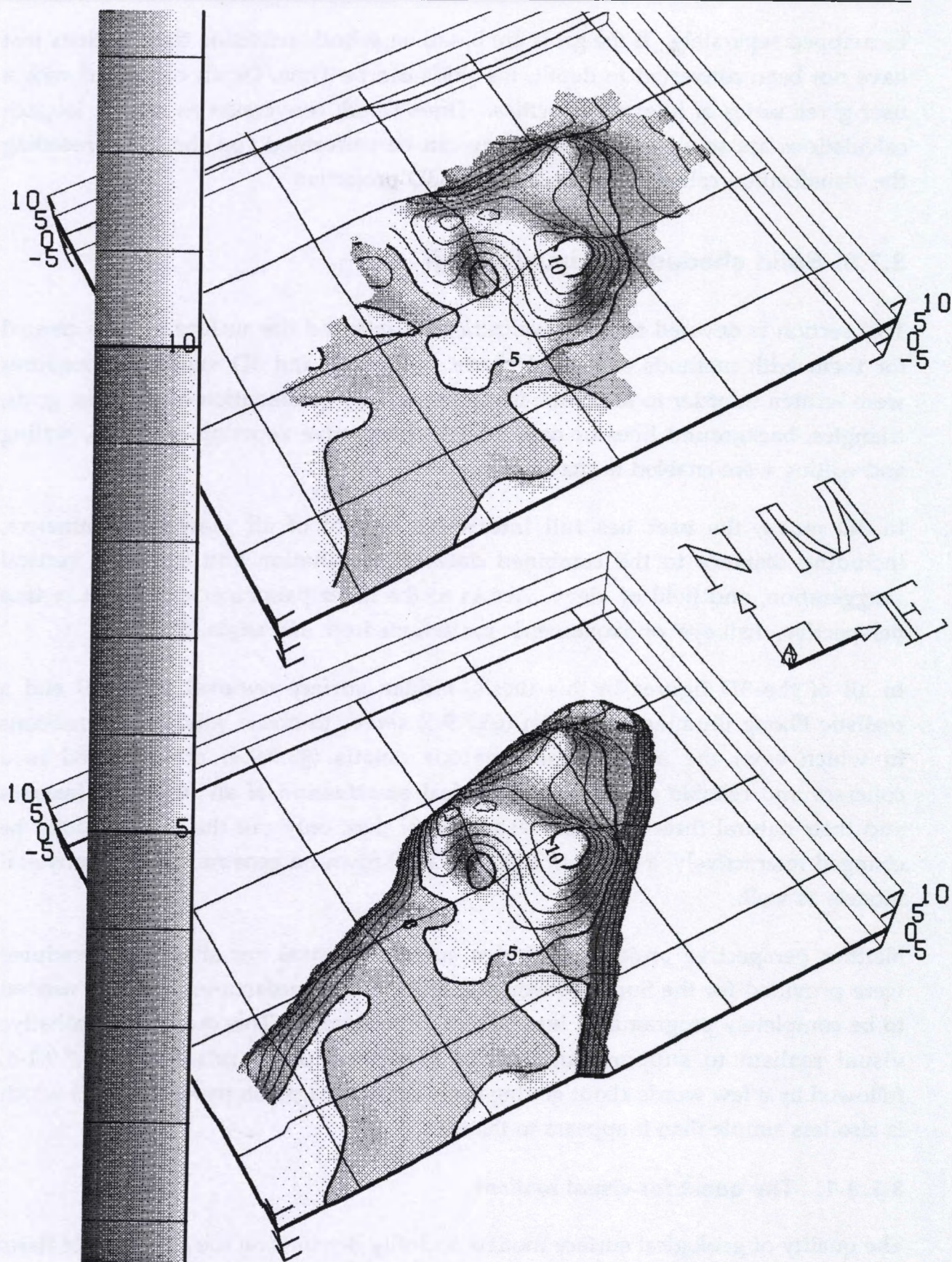


Fig. 3.45c (above). Thickness grid between grids B2 and B3 from fig. 3.44a. The area shown is that of B3. Due to extrapolation, the thicknesses do not thin out towards the onlap of sequence B23 onto B1. d (below). Same thickness grid, after application of the automatic framework builder (fig. 3.44b). Thickness of sequence B23 thins to zero as expected.

be mapped separately. If the grids are based on seismic reflection time sections that have not been converted to depth, the grids can be Time/Depth converted with a user given series of interval velocities. Time/Depth conversion as well as isopach calculations are so elementary that they can be performed "on the fly", preceding the visualization calculations for a map or 3D projection.

3.7.9. Solid shaded 3D visualization

This section is devoted to the *visualization* of data and the surface models created for them with methods explained above. Mapping and 3D viewing procedures were written in order to allow the inspection of any combination of surfaces, grids, triangles, background lines or data points. Interactive zooming, panning, scaling and editing were enabled in map mode.

In 3D mode, the user has full interactive control of all viewing parameters, including distance to the combined data set, inclination and azimuth, vertical exaggeration, and field of view. Access to the latter parameter can result in true perspective, 'fish eye' or axonometric projections from any angle (§3.7.9.2).

In all of the 3D figures in this thesis, hidden surface removal (§3.7.9.3) and a realistic Phong illumination model (§3.7.9.5) serves to create solid representations in which even the minutest sub-contour details (§3.7.9.4) are revealed in a coherent and reliable way, allowing critical examination of all structural features and their natural three-dimensional relations. Not only can the 3D viewpoint be changed interactively, a different light can be thrown on geostructural/geophysical models as well.

Neither perspective projection, hidden surface removal nor shading procedures were provided for the Sun 386i workstation by the manufacturers, so they needed to be completely programmed into Geofox from scratch. This quest for qualitative visual realism to support quantitative interpretation is related in §3.7.9.1-6, followed by a few words about getting these screen images on paper (§3.7.9.7) which is also less simple than it appears to the user.

3.7.9.1. The quest for visual realism

The quality of geological surface models critically depends on the detection of flaws and a spatial understanding of the structures involved. It was felt that high 3D visual realism would greatly improve both. The figures in this thesis should also make the point that solid, line contoured and above all realistically shaded surfaces

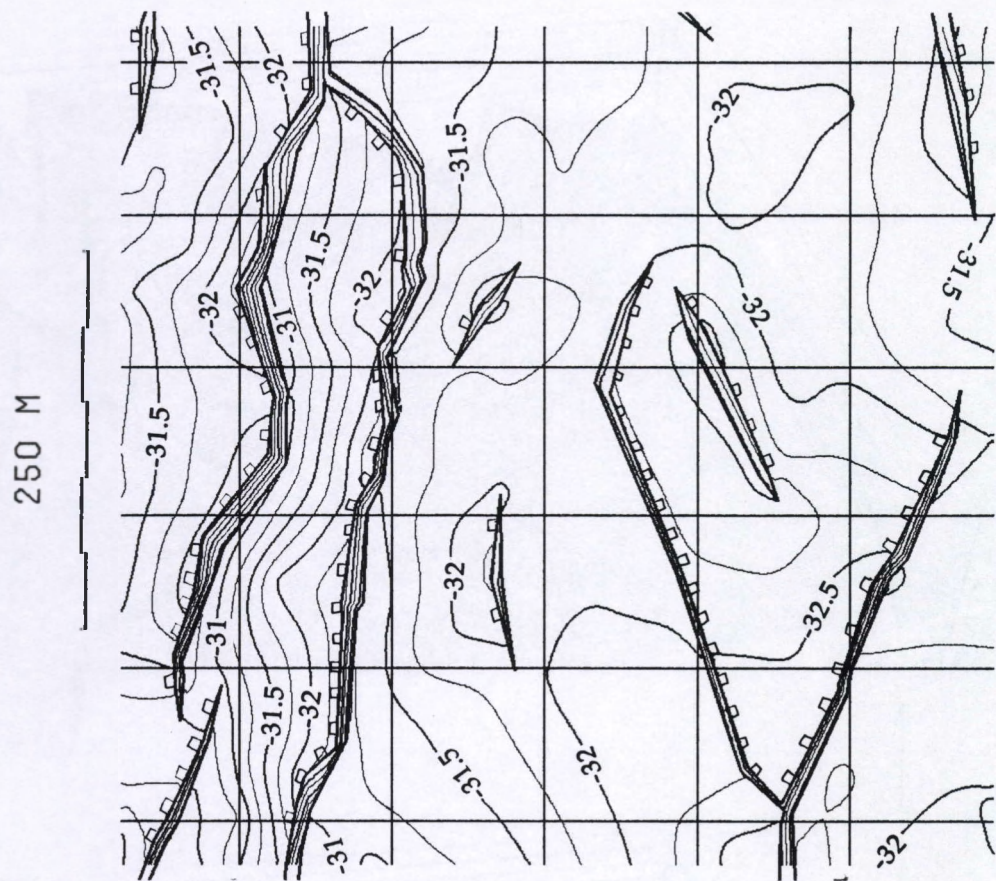


Fig. 3.46a. Line contoured map of horizon affected by clay tectonics. Fault traces in heavy black lines.

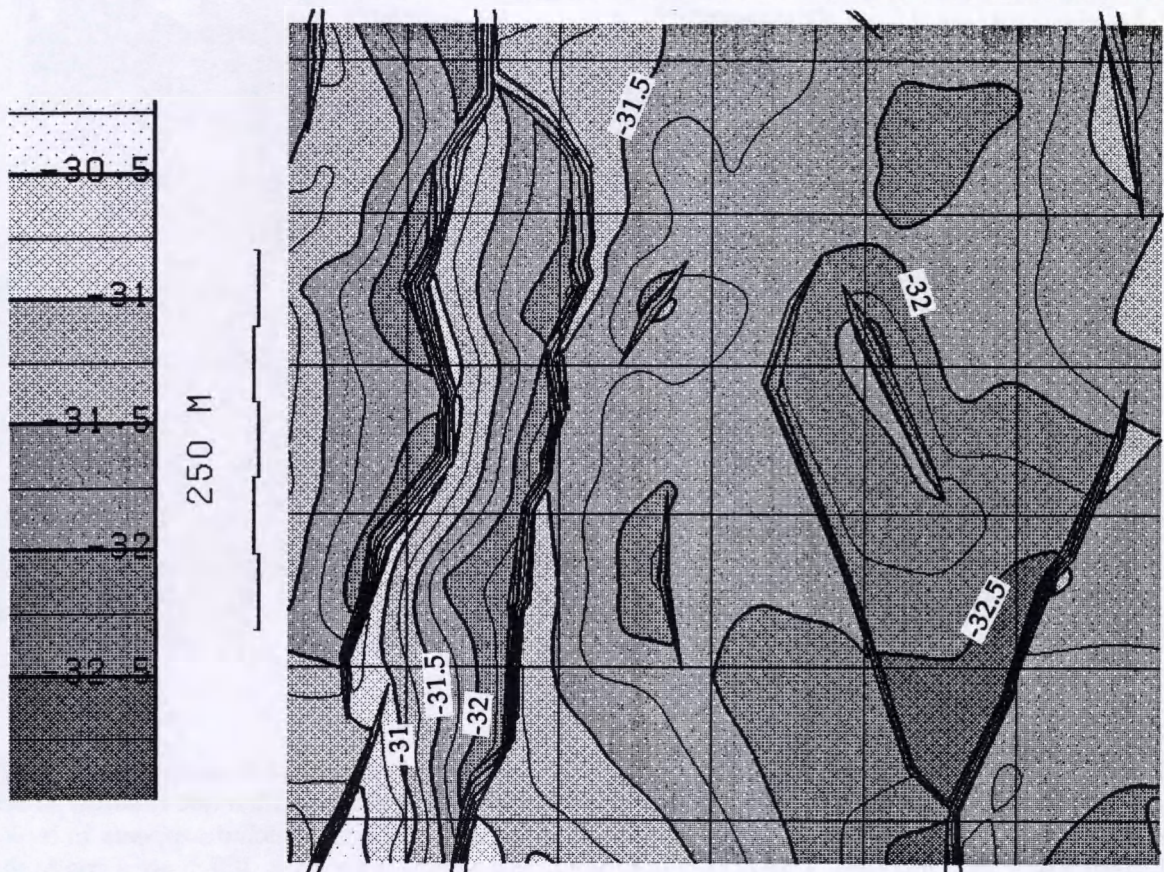


Fig. 3.46b. Solid contoured version of fig. 3.46a. Depth relations are visible at a glance.

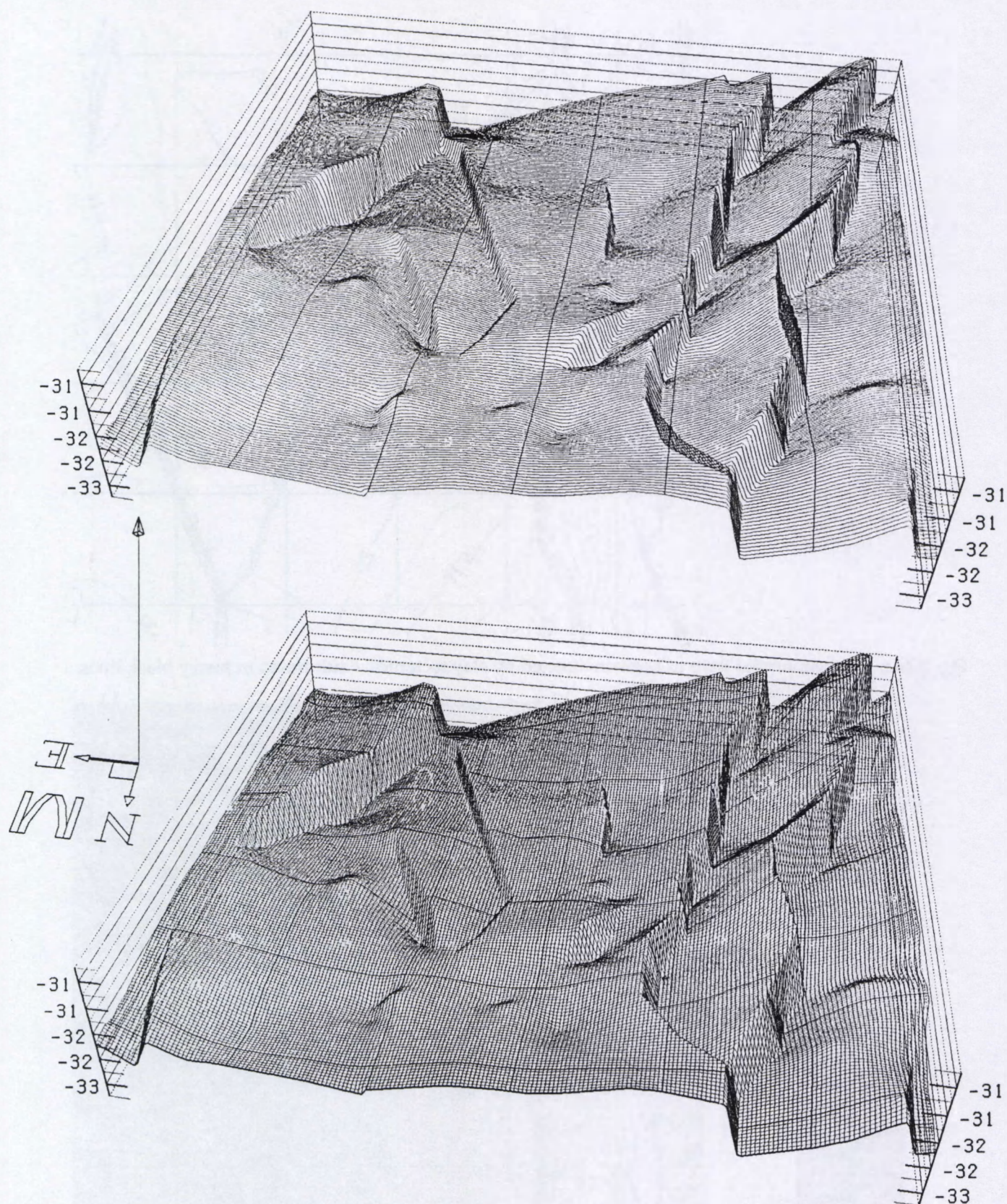


Fig. 3.47. Perspective projection of grid in fig. 3.46, with true perspective foreshortening. Faults and undulations stand out well in both, but **a** (above) was drawn without hidden line removal as opposed to **b** (below). Notice confusing effect at faults in W part of grid in **a**, which disappears in **b**. Vertical exaggeration x50; 'box ring' lines at 0.25 m interval; heavy grid lines every 100 m are a cue to distance and angle between features on the surface.

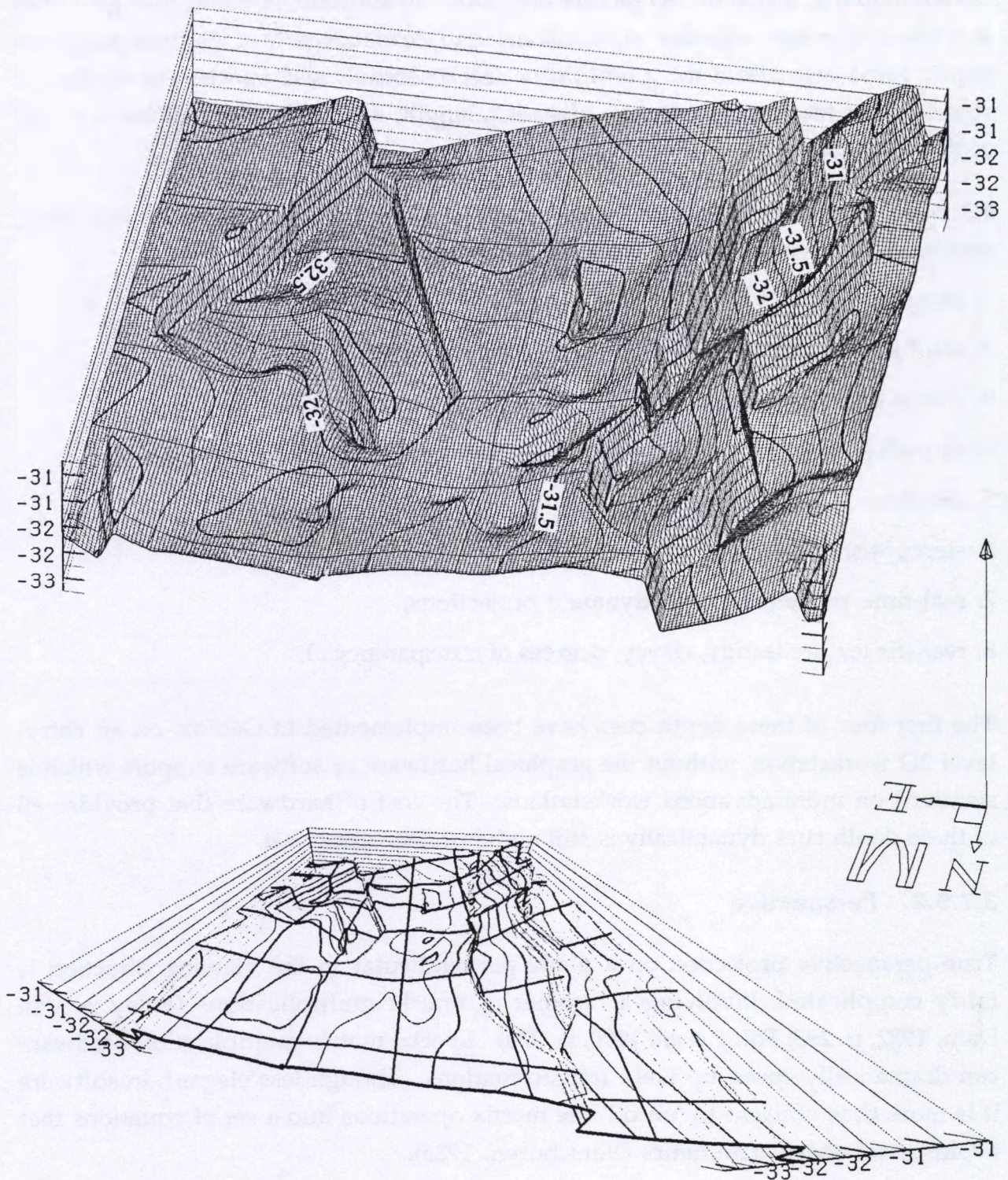


Fig. 3.48. Special projections of grid in fig. 3.46. Depending on view distance and angle of view, projection can be axonometric as in a (above), which can be useful for quantitative analysis, or exaggerated perspective ('fish eye' effect) as in b (below). 'Box ring' lines and contour lines at 0.25 m interval are quantitative height cues; heavy grid lines every 100 m are distance cues. Fish net drawings with hidden contour line removal, and with (a) or without (b) minor grid lines.

can more directly convey far more structural information than a classical line-drawn map (fig. 3.46a) or 3-D picture (fig. 3.47). In addition, N-S and E-W grid lines at known intervals together with colours and contours with a definite height or depth value also allow the *quantitative* interpretation and spatial correlation of structures in terms of orientation, distance, length, area and height difference. All of this in the same 'nice' 3D picture.

3D visual realism comes about when an image offers one or more of the following, mostly qualitative depth cues (Foley and Van Dam, 1982; Flynn, 1990):

1. perspective (§3.7.9.2);
2. solid surfaces through hidden surface removal (§3.7.9.3);
3. colour and line contours quantifying and emphasizing relief (§3.7.9.4);
4. smooth shading, except for selected discontinuities (§3.7.9.5);
5. shadows;
6. stereopsis;
7. real-time movement with dynamic projections;
8. realistic texture (sandy, clayey, degrees of transparency..).

The first four of these depth cues have been implemented in Geofox, on an entry-level 2D workstation, without the graphical hardware or software support which is standard on more advanced workstations. The cost of hardware that provides all of these depth cues dynamically is still high but decreasing fast.

3.7.9.2. Perspective

True perspective projection on a plane perpendicular to the viewing direction is fairly complicated, involving a number of matrix multiplications (Foley & Van Dam, 1982, p. 295; Foley *et al.*, 1990, p. 270). Special matrix multiplication hardware can dramatically speed up these transformations. Though less elegant, in software it is more time efficient to 'unroll' the matrix operations into a set of equations that avoid unnecessary arithmetics (Verschuren, 1985).

The realistic effect of perspective foreshortening distorts the exact shape and dimensions of projected objects (fig. 3.47). An axonometric projection may therefore sometimes be preferred to a perspective projection, so that distances can be measured along the principal axes and parallel lines do project as parallel lines (fig. 3.48a). In Geofox, this can be achieved by reducing the field of view to 1°, i.e. to

that of a moderately strong telescope, and increasing the viewing distance so that the objects of interest are within the field of view. On the other hand, a very large field of view, e.g. one of 170° , can result in an exaggerated 'fish eye' perspective (fig. 3.48b).

3D pictures of surfaces projected as fish nets (fig. 3.47-48) look rather poor compared with solid representations. However, they have the distinct advantage of conveying more realistic perspective, and hence, a more acute sense of fore- and background, than irregular solid surfaces (fig. 3.50) can. Therefore, Geofox offers the possibility to combine hidden surface removal with hidden line removal (fig. 3.51&53, see further). Properly selected grid lines, e.g. every 10 or 500 m, are drawn as N-S and E-W 'guide-lines' that visually emphasize true perspective foreshortening, while at the same time also allow the quantitative interpretation of a map or 3D image in terms of distance, length and area. They very conveniently serve as a graphic scale that is not affected by perspective projection, or enlargement and reduction for reproduction.

3.7.9.3. Solid surfaces through hidden surface removal

X-ray viewing all subsurface structures and interfaces may be a geologists' dream, but she/he would be confused by the vast and intricate network of innumerable surfaces crossing each other. Even on one surface this is an annoying effect (fig. 3.47a). Hidden surface algorithms tell a computer which parts of a 3D model are expected not to be seen. Graphical models therefore need to be decomposed into elementary surfaces that can be sorted in such a way that, depending on the viewpoint, the order in which they may hide each other is completely known in advance. Precisely this depth sort usually is a complex and time consuming procedure in the removal of hidden lines and surfaces.

A Fortran program for *hidden line removal* of a projected grid (Verschuren, 1985) was originally developed on a PDP-11 minicomputer, then improved on the NCR Tower-32 with ideas from Anderson (1982), and finally converted to C and built into Geofox (fig. 3.47b). Taking advantage of the predictable way grid mazes may hide each other, the grid mazes are drawn from the front of the grid to the back, always away from the viewpoint. Starting with the front row (or column, depending on the viewpoint), an upper and lower silhouette line keeps track of the growing outline, against which new line pieces are clipped. The algorithm needs to be fairly sophisticated to allow for all possible viewpoints, from below included. An extension with multiple silhouette lines allows a stack of mutually hiding grids to be handled properly as well (fig. 4.3 & 4.9).

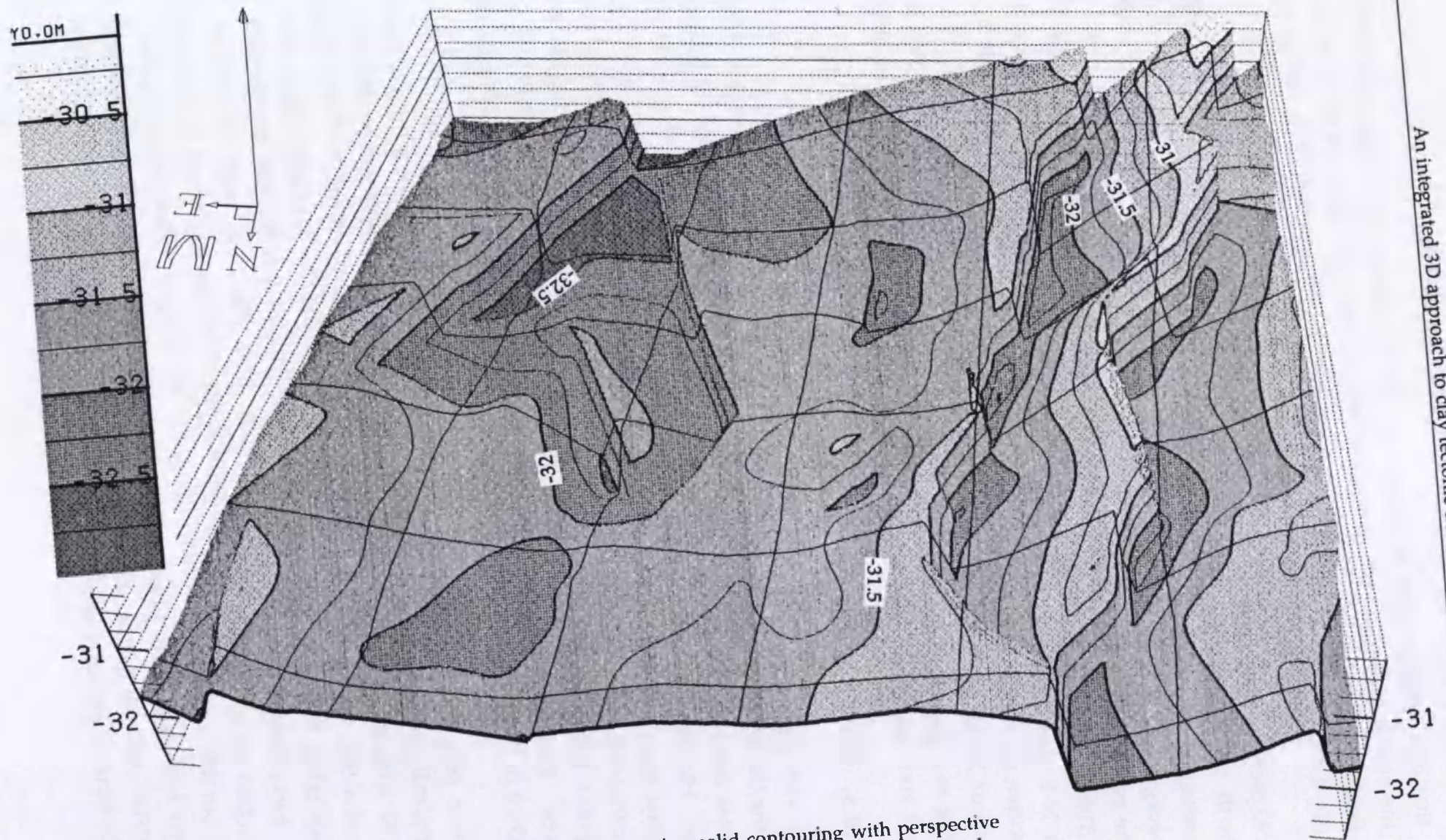


Fig. 3.49. Perspective projection of grid in fig. 3.46b. Combining solid contouring with perspective projection is less clear than the line contoured fish net representation in fig. 3.48a. The pseudo-shades on a fish net give valuable qualitative support to the quantitative information.

The fastest and most straightforward way to do *hidden surface removal* on regular grids is with a variant of the painter's algorithm (Harrington, 1983). Since the order in which the individual facets of a regular grid need to be drawn is completely predictable, a preceding depth sort is not required. When drawing rows of facets from the 'back' to the 'front', a facet is painted over by facets on the same line of sight but closer to the viewpoint (fig. 3.50). It was therefore possible to implement the painter's algorithm as a simplified inversion of the already programmed hidden line removal algorithm. The grid mazes are split along the diagonals into two or four triangles, contoured (§3.7.9.4), projected and drawn with a constant shade (§3.7.9.5). This algorithm implies also hidden contour line removal (fig. 3.48 & 3.51).

3.7.9.4. Colour and line contours emphasize and quantify relief

Contours are expected as an integral part of any map or 3D image of a geological model, because they allow the quantitative interpretation of depth or another parameter, rather than merely providing a qualitative impression. Solid colour or grey level contoured maps (fig. 3.46b & 3.52) are preferred to merely line contoured ones with numerous numbers in various orientations distributed along contour lines (fig. 3.46a), since colours or constant grey levels more directly reveal depth relations. The same observation holds for 3D representations of geological models. A colour scale has been created in Geofox for colour shading purposes, the colours of which have been carefully chosen in order to have a light saturated colour such as yellow for the highest level, a dark one (e.g. purple) for the deepest. With equal brightness steps in between, such a colour scale naturally emphasizes relative height.

In order to refine the contours and to avoid contouring ambiguities, each grid maze is divided into four triangles, their tops joining at the geometrical centre of the four grid nodes involved. Line contouring of such a composed surface, solid and line contoured with the algorithm explained in fig. 3.22, yields smoother contours, since these triangles approach hyperboloids between the grid nodes. The number of colour intervals is limited by the programmed colour scales (8 or 12 shaded colours, 200 constant colours, or 256 grey levels), but the number of line contours is only limited by cluttering. The contour interval may be any real number, and contour lines can be drawn heavier every so many intervals (fig. 3.46a & 3.48).

3.7.9.5. Smooth shading, except for selected discontinuities

With the aid of smooth or sudden variations in illumination, smooth shading renders a flat map as a tangible surface that vividly accentuates sub-contour details and structural discontinuities. A comparison of figures 3.46a, 3.46b and 3.52, should make the point. Again, the same observation holds in 3D representations (fig. 3.49 & 3.53). Smooth shading on regular grids consists of two elements:

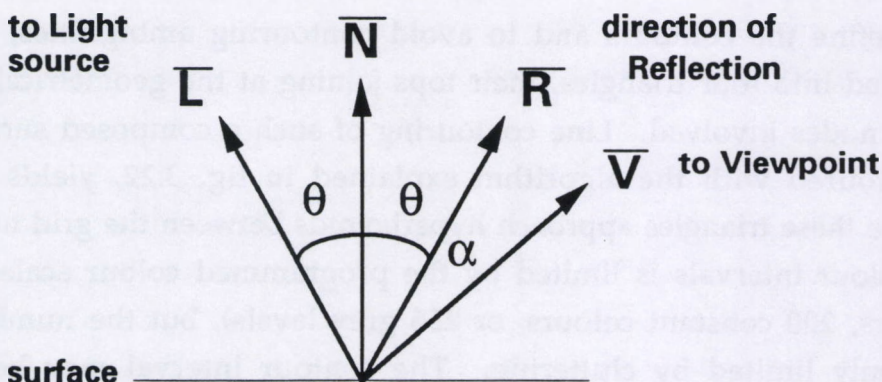
1. the calculation of a shade or intensity for each facet, depending mainly on its orientation relative to the viewpoint and the light source, and
2. the interpolation of a smooth sequence of shades across the triangle edges.

The latter is not only very time consuming for the complex structures encountered in this study, it also creates nothing more than an illusion of smoothness. Contours still need to be smoothed separately and the two surfaces may therefore not coincide. We have solved both problems by the calculation of grids that are sufficiently dense to be physically smooth for both shading and contours, with the interpolation procedures described above (§3.7.7).

The most realistic shading effects on textureless surfaces are produced with the Phong illumination model. This model is based on the following intensity equation (Foley & Van Dam, 1982):

$$I = I_a k_a + \frac{I_p}{r+k} [k_d (\vec{L} \cdot \vec{N}) + k_s (\vec{R} \cdot \vec{V})^n]$$

in which (see figure)



- I = intensity of light reflected by a flat surface;
 I_a = intensity of ambient light;
 k_a = reflection coefficient of the surface for ambient light;
 I_p = intensity of the point light source (direct light);

- r = distance from the viewpoint to the surface;
 k = distance from the light source to the surface;
 k_d = reflection coefficient of the surface for direct light;
 \vec{L} = vector from the surface to the point light source;
 \vec{N} = vector normal to the surface;
 k_s = reflection coefficient of the surface for specular light;
 \vec{R} = direction of specular reflection on the surface (i.e. \vec{L} mirrored around \vec{N});
 \vec{V} = vector from the surface to the viewpoint;
 n = power proportional to the surface smoothness (infinite for a perfect reflector).

Shading should not be confused with shadows cast by objects illuminated with point light sources. Shadow shapes depend on the relative position of light source(s) *and* objects. The latter are not taken into account by the above equation.

3.7.9.6. Stereopsis

Although it has not been implemented in Geofox yet, stereopsis can be achieved by the juxtaposition of images from slightly different bearings. A difference of 6-8° works fine, for it simulates stereopsis similar to that of looking at an object from a distance of about 0.5 m. Two types of stereo-pairs are used (Verschuren, 1985; Tucker, 1989; fig. 3.54a). The first and most common type is arranged to be viewed with uncrossed visual axes (fig. 3.54b). If the images are wider than the eye base, a stereoscope is required. The other type (fig. 3.54c), should be viewed with crossed visual axes. The right eye views the left member of the pair, and vice versa. In this manner, even large stereo-pairs can conveniently be viewed in three dimensions with naked eyes.

3.7.9.7. Hardcopy facilities

All the abovementioned visualization parameters can be set interactively. It does take some experimenting with

1. a 'slider' for the vertical exaggeration of surface relief,
2. three viewpoint position sliders (distance, bearing and inclination),
3. three light source position sliders and
4. six independent shading parameter sliders, in addition to
5. contour colour and line interval,
6. line thicknesses of contours and projected grid lines,
7. as well as the distance between the latter,

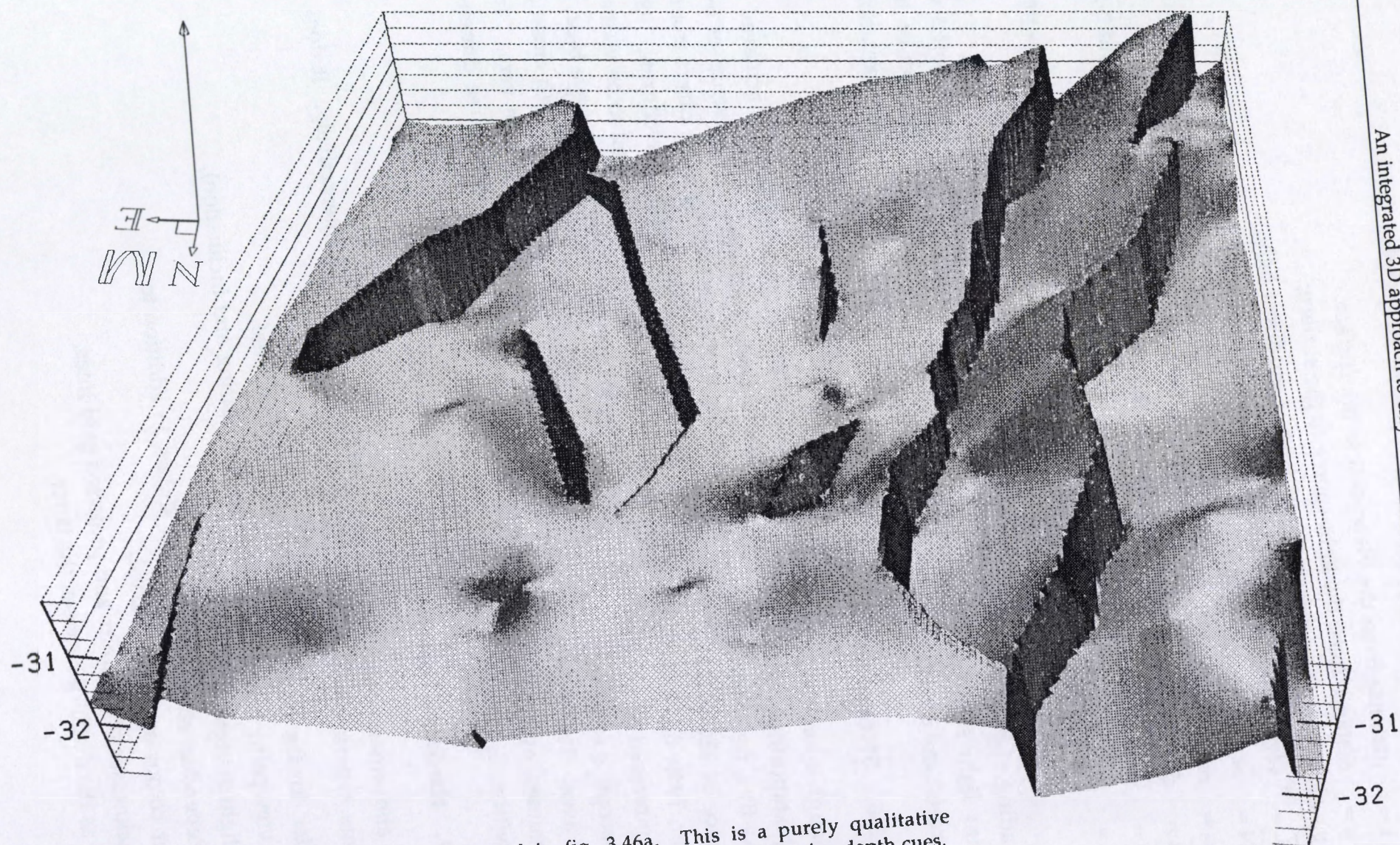


Fig. 3.50. Shaded perspective projection of grid in fig. 3.46a. This is a purely qualitative representation. Hidden surface removal and solid shading are the only two qualitative depth cues. Light source position opposite to viewpoint, enhancing contrast between horizon and fault scarps.

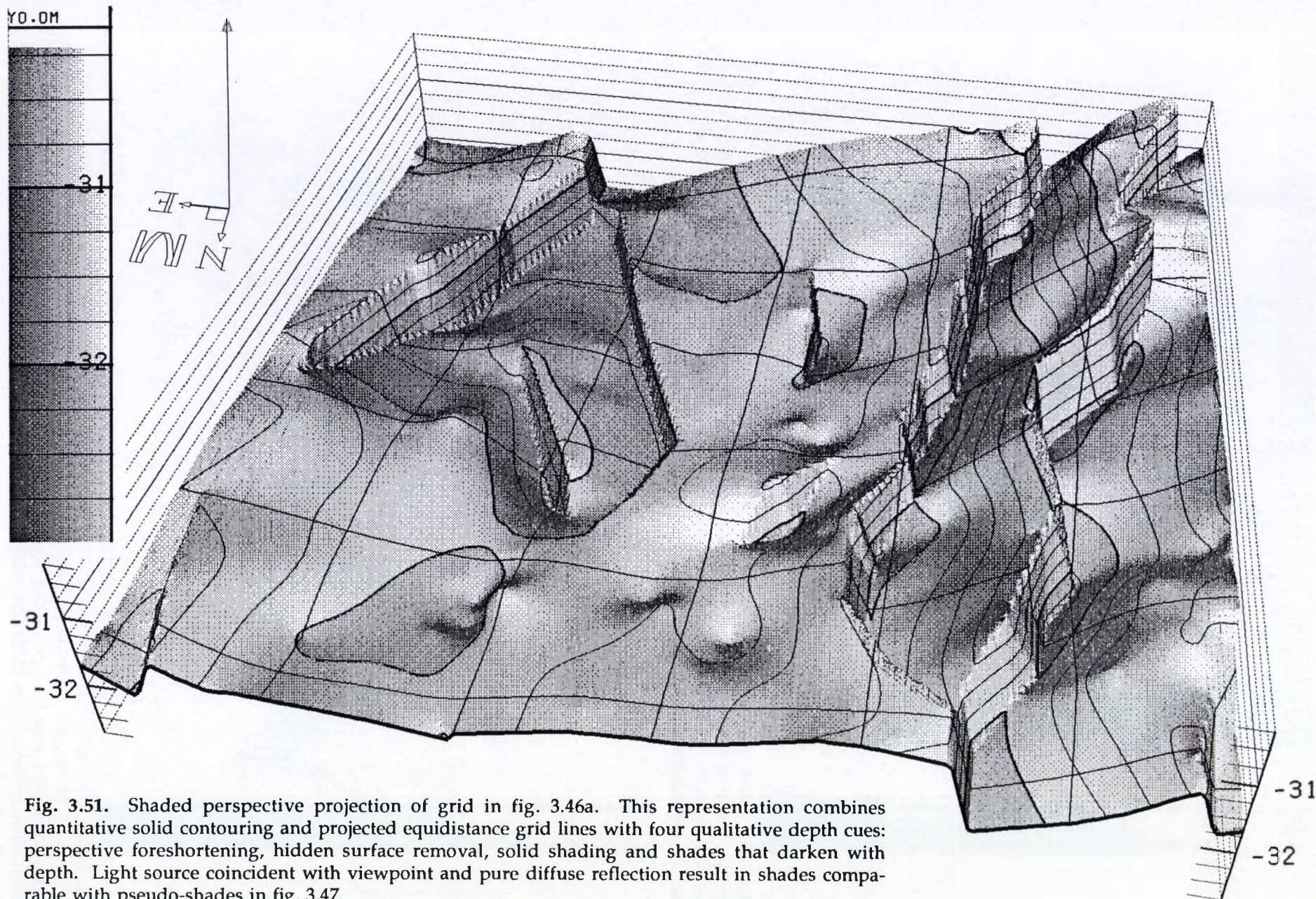


Fig. 3.51. Shaded perspective projection of grid in fig. 3.46a. This representation combines quantitative solid contouring and projected equidistance grid lines with four qualitative depth cues: perspective foreshortening, hidden surface removal, solid shading and shades that darken with depth. Light source coincident with viewpoint and pure diffuse reflection result in shades comparable with pseudo-shades in fig. 3.47.

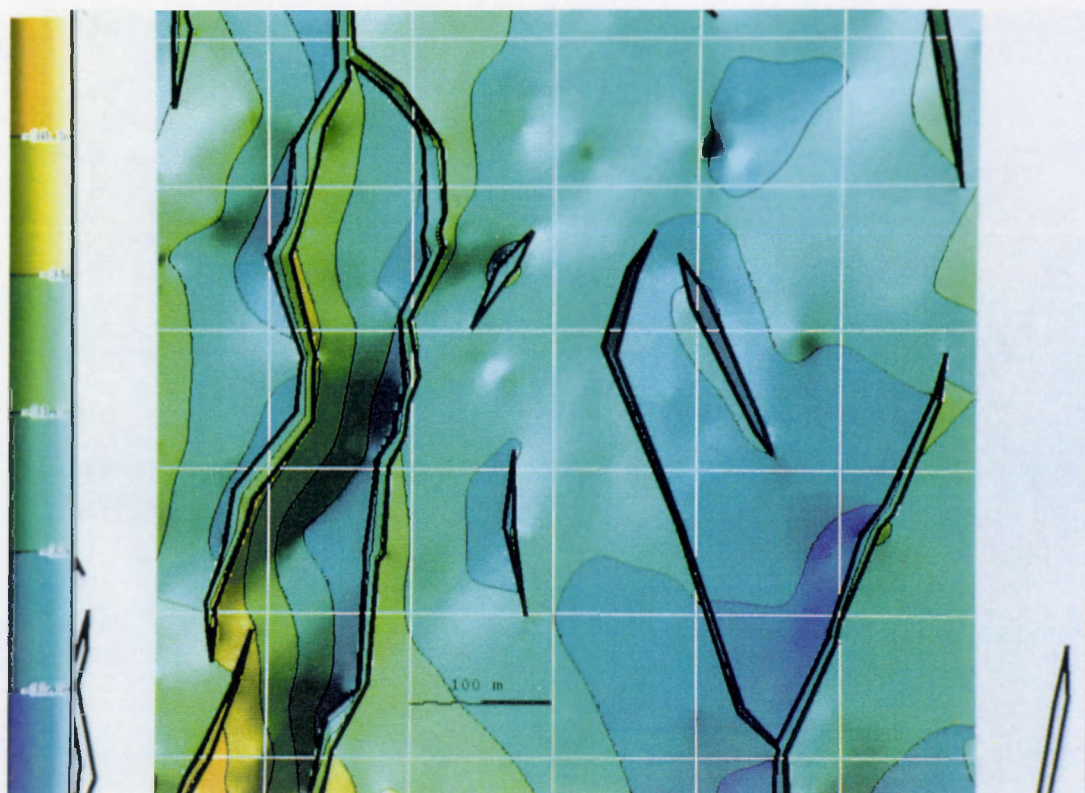


Fig. 3.52. Colour shaded map representation of grid in fig. 3.46a. Fault traces in heavy black lines. The light source has a NW bearing and an inclination of 45° , classical for shaded relief maps. Colours are notably easier to recognize than levels of grey (fig. 3.46b). Shading emphasizes relief and reveals sub-contour details. Colours delicately darken with depth.

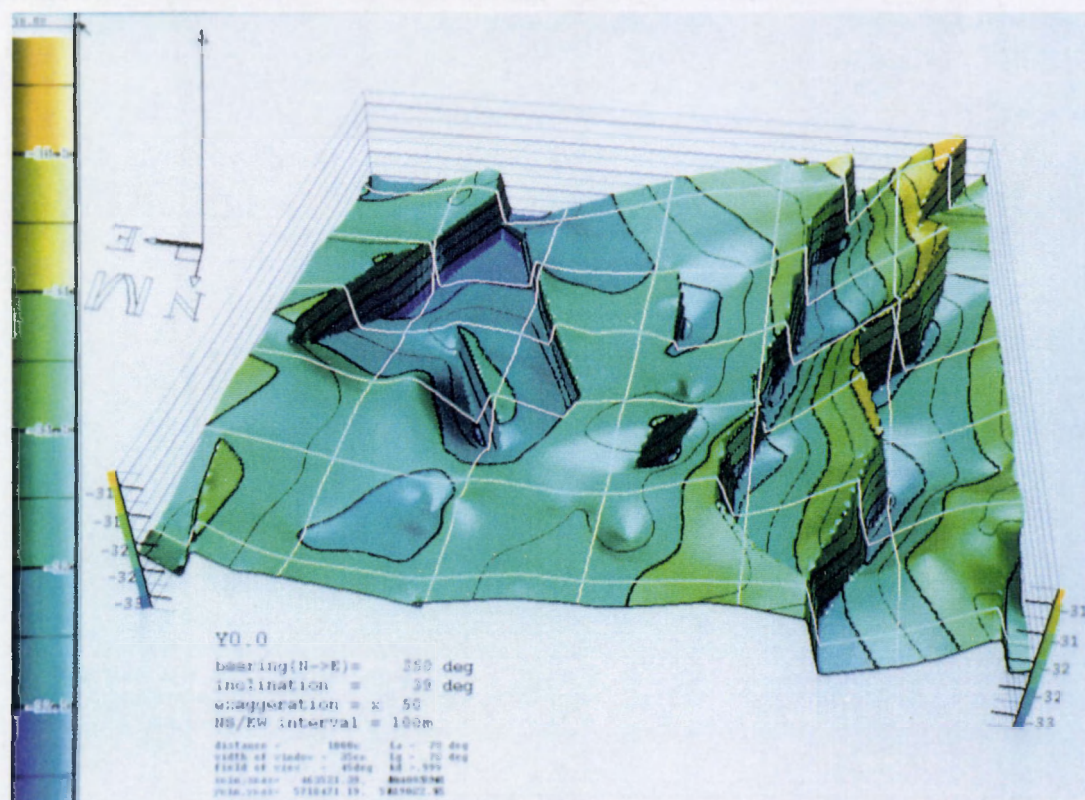


Fig. 3.53. Colour shaded 3D representation of grid in fig. 3.46a. Light source position opposite to that in fig. 3.51, to enhance contrast between horizon and fault scarps. Because colours are easier to distinguish than levels of grey, this figure has twice the number of colour intervals, and its quantitative information is more accessible than in fig. 3.51.

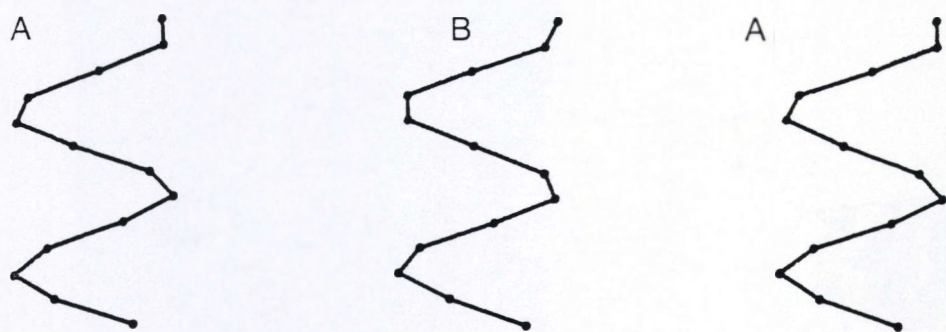


Fig. 3.54a. A stereo-triplet of a helical structure. Stereopsis of any two adjacent members yields two three-dimensional images with reversed depth and handedness. With crossed visual axes, the image on the right is right-handed, like a conventional screw thread. With uncrossed axes, it is left-handed. (From Tucker, 1989)

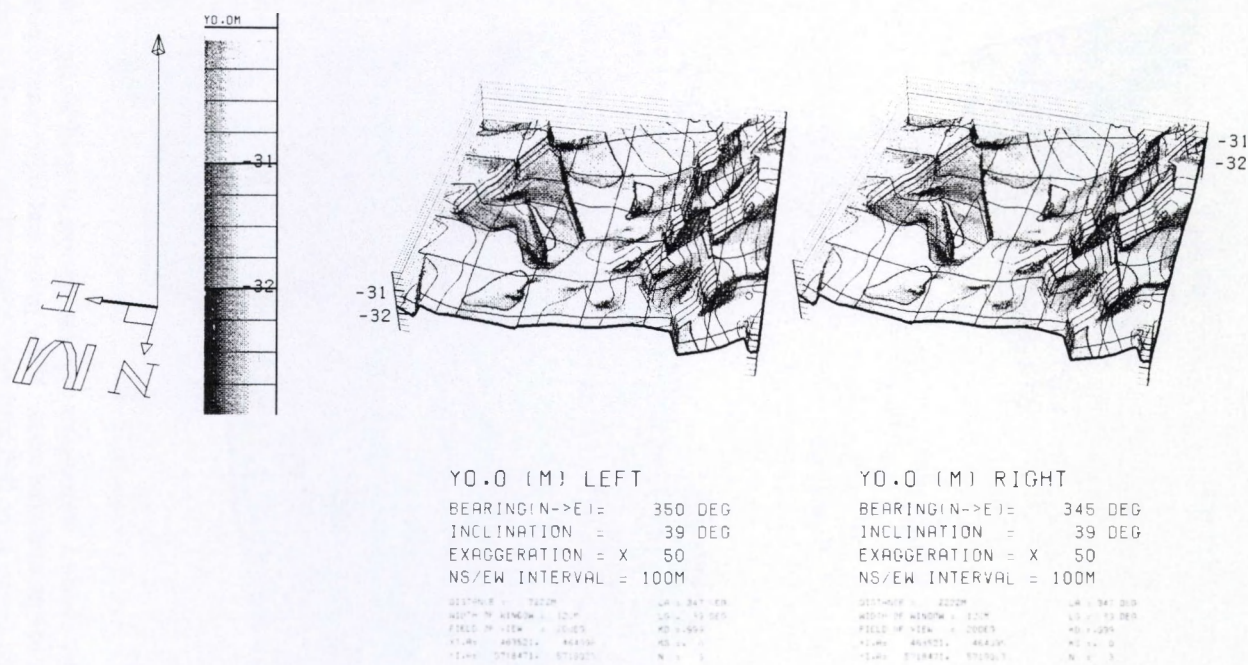


Fig. 3.54b. Greytone shaded stereo-pair representation of grid in fig. 3.46a. This stereo-pair has to be viewed with *uncrossed* visual axes, with the left eye viewing the left image and *vice versa*. View point and light source position 3° to the West of that in fig. 3.51. Viewpoints are separated by 5°.

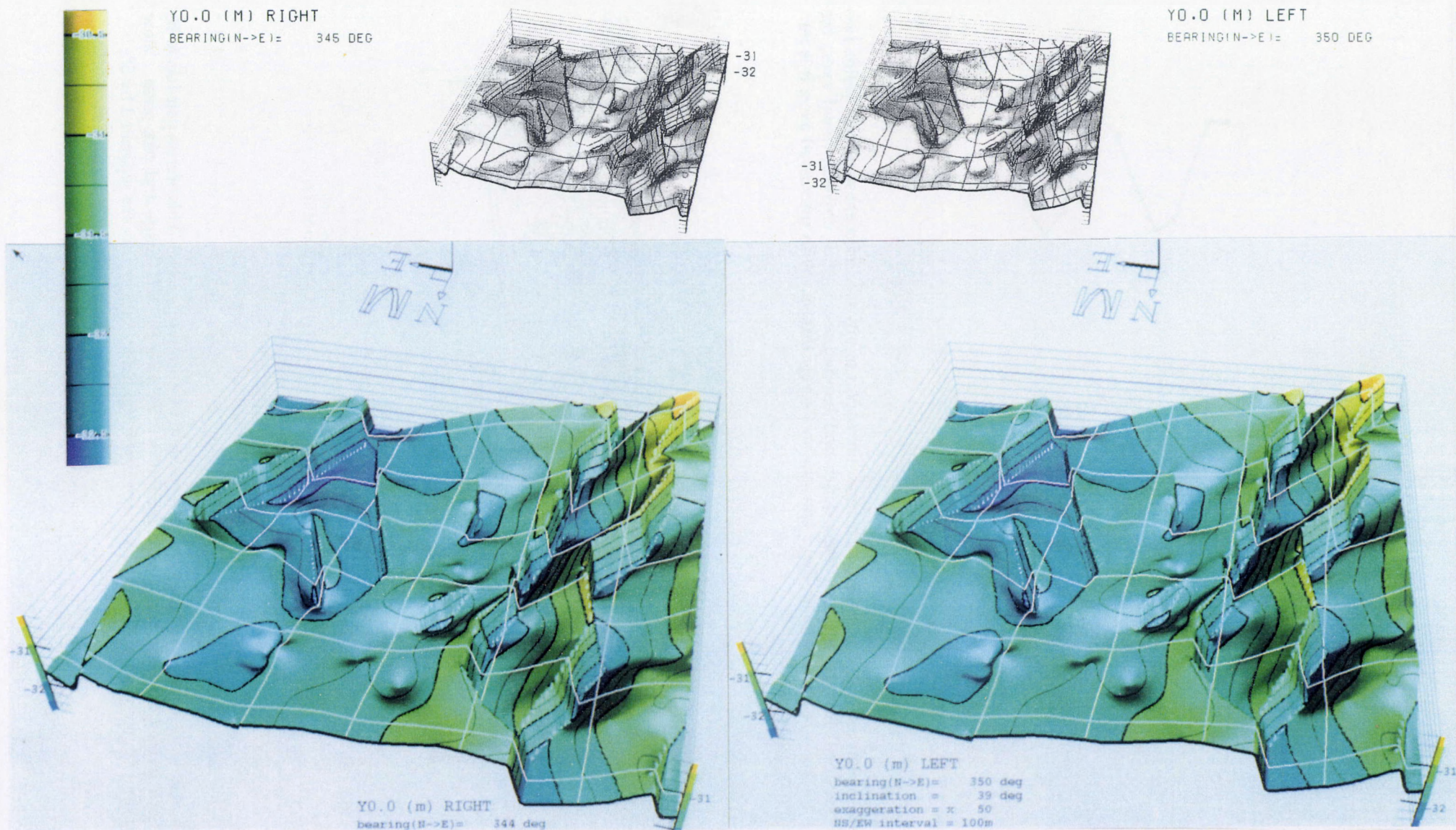


Fig. 3.54c. Colour shaded stereo-pair representation of grid in fig. 3.46a. This stereo-pair has to be viewed with *crossed* visual axes, with the left eye viewing the right image and *vice versa*. View point and light source position 3° to the West of that in fig. 3.51. Viewpoints are separated by 6° . A version of 3.54b for crossed visual axes (left and right image interchanged) is provided at the top.

in order to optimize the information content of a single map or 3D view of a geological model, but it can be worthwhile indeed, as the numerous examples in this thesis testify. But sophisticated 3D visualization on a computer screen is not enough. An invaluable asset has been the development of hardcopy¹ facilities, using at first a Versatec Spectrum colour electrostatic printer. It involved the not so straightforward reproduction of the user defined 256 RGB² colours on the workstation, with differently saturated CMY dot patterns on the Spectrum. Due to physical limitations of the printer and the inks, the quality of these hardcopies was never up to that of the actual on-screen images.

Another colour hardcopy facility was developed by building the workstation's screendump function into the program. Screen images can thus be saved in files. Series of images can then be consecutively re-loaded to the screen with a proper shellscript (a combination of a number of operating system commands), and be photographed. With proper precautions³, the quality of hardcopy photographs and slides can match that of the screen image.

Black&white hardcopies can be generated fast and cheaply (at least in reproduction) on a 24" 200 dpi Versatec electrostatic printer. Instead of redrawing on the screen, the elementary drawing instructions (drawing a line with a specified thickness, filling a projected polygon with a specified colour, ..) are translated into Versaplot subroutine calls. Colours and shades are carefully transformed into sensitively different grey dot patterns, based on 256 'ordered dithers' (Foley & Van Dam, 1982) of 16x16 dots (in dotpat.dat), and generated with a specially written program. After finishing the redraw, the Versaplot plot file is automatically rasterized and sent to the printer. Eric Maes of RCMG translated the whole standard Versaplot drawing and rasterization library from Fortran to C, so that it could be compiled and linked with Geofox. He also short-circuited the vector and polygon ordering phase during rasterization, so that Geofox vectors and polygons could be painted on paper in the same mutually obscuring order as on the screen.

¹a hardcopy is a copy of the screen image on paper, as faithful to scale and colour as possible.

²Colours specified by amounts of Red, Green and Blue, primary additive colours for colour computer and television monitors. Cyan, Magenta and Yellow are the subtractive primaries for colours composed of printer pigments on paper.

³Use a long focus objective (e.g. 100mm) to avoid curvature. Using a level, position the camera on a tripod so that it is exactly perpendicular to the middle of the screen, to avoid other distortions. For a 100 ASA emulsion, select an opening of 4.5 and a shutter speed of 1/4 s. Check against light bulbs or the sun reflecting on the screen. For photographs, do not darken the room entirely so that part of the monitor around the screen is framed together with the picture (otherwise, there is a risk that the negatives are not properly cut), apply a weak yellow filter and provide the lab with a correctly developed example (preferably the colourscale). The latter specific precautions are not necessary for slides.

3.7.10. Geofox applications and a word of caution

3D modelling of a single valued, smooth but partly discontinuous surface, honouring irregularly distributed data points, is a fairly general problem. It is often essential to be able to modify otherwise 'neutral' surface models so that they also honour a geological or other interpretation. All kinds of data and surface modelling problems can therefore be handled with Geofox. Figures 3.55-59 illustrate but a few of the many possible applications of our new 3D surface modelling method.

In addition, geophysical properties can be combined with a 3D structural model into an integrated multi-layer 3D geophysical model. The program was also used to visualize the distribution of common mid points (CMP's) over a regular grid (fig. 4.10) that can help to select a binning strategy for 3D seismic processing.

It is appropriate to add a word of caution here. The results of computer aided interpretation and mapping not only depend on the capabilities of the software, but on those of the interpreter as well. This is also true for Geofox. The user should be familiar with the data and possible errors or imprecisions (see §3.2), as well as with the available software procedures and their sensitivity to changes in control parameters. To cite Pflug (1992): "What is seen on the screen is only as good as the modelling effort that has been invested in developing the 3D geometric model, particularly if only sparse observations are available. [...] Also, the user should be aware that the development of a consistent 3D geometric model that fulfils expectations will require considerable time and effort."

With most mapping programs, automatic and 'neutral' contours can be generated effortless and in less than no time after data input. But to believe that *geologically meaningful* contours do not require a lot of effort to quantify, input and check the data, and to quantify and introduce an often vague and/or complex geologic interpretation into the surface model, is to believe in a myth. The reasons why it is still better to map with the help of a sufficiently powerful computer program than without it, have been presented in §3.1.

All of the 'bells and whistles' available in Geofox are fully described in on-line help as well as in the reference section of the Manual (see Addendum). The tutorial section of this Manual introduces new users to Geofox. This chapter should have provided some background information.

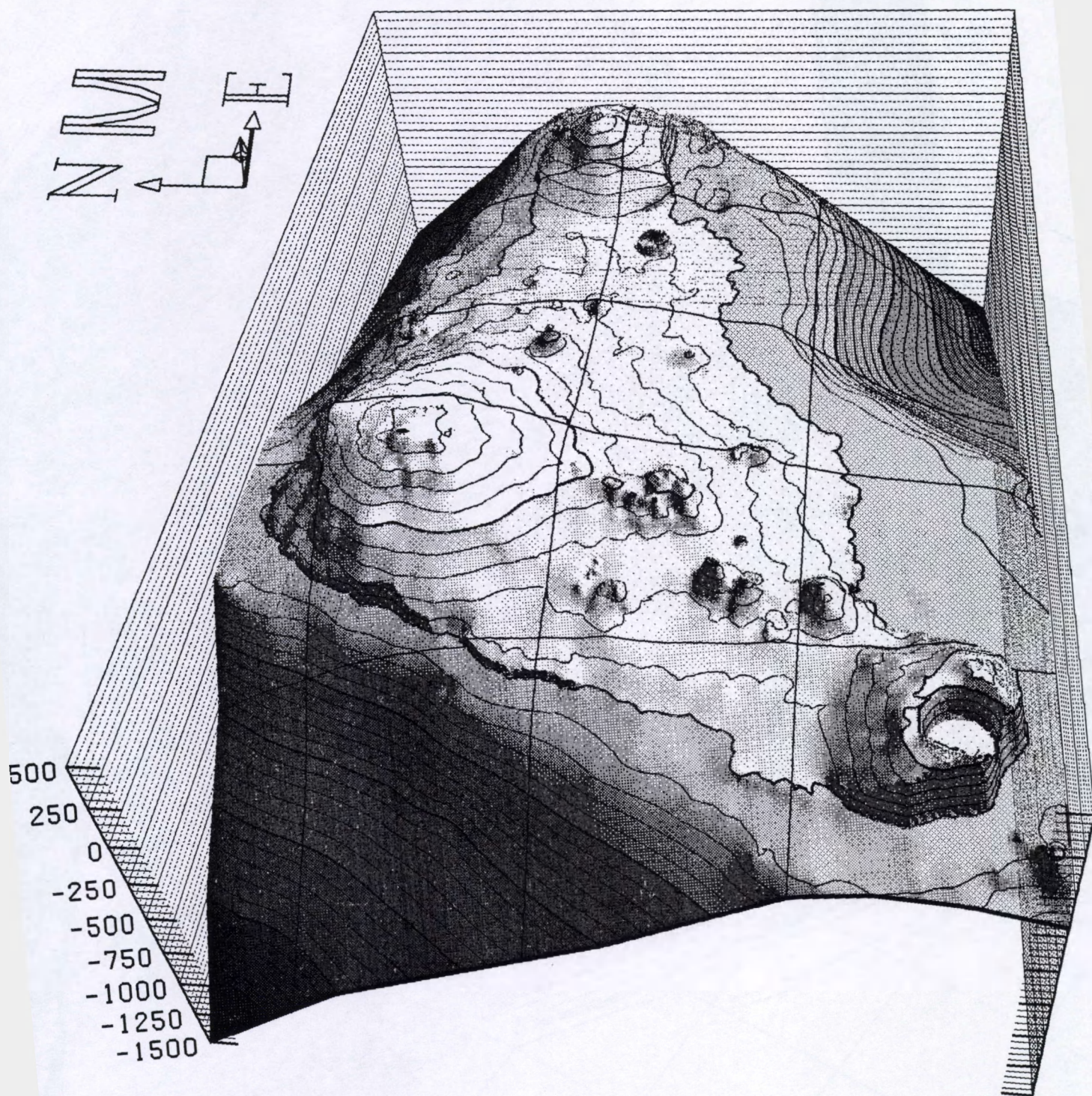


Fig. 3.55. Easter Island and bathymetry around it, based on digitized contours. Cliffs and craters modelled with scarp triangles. Grid line interval 5 km. (Courtesy Paul De Paepe, Gent, Belgium)

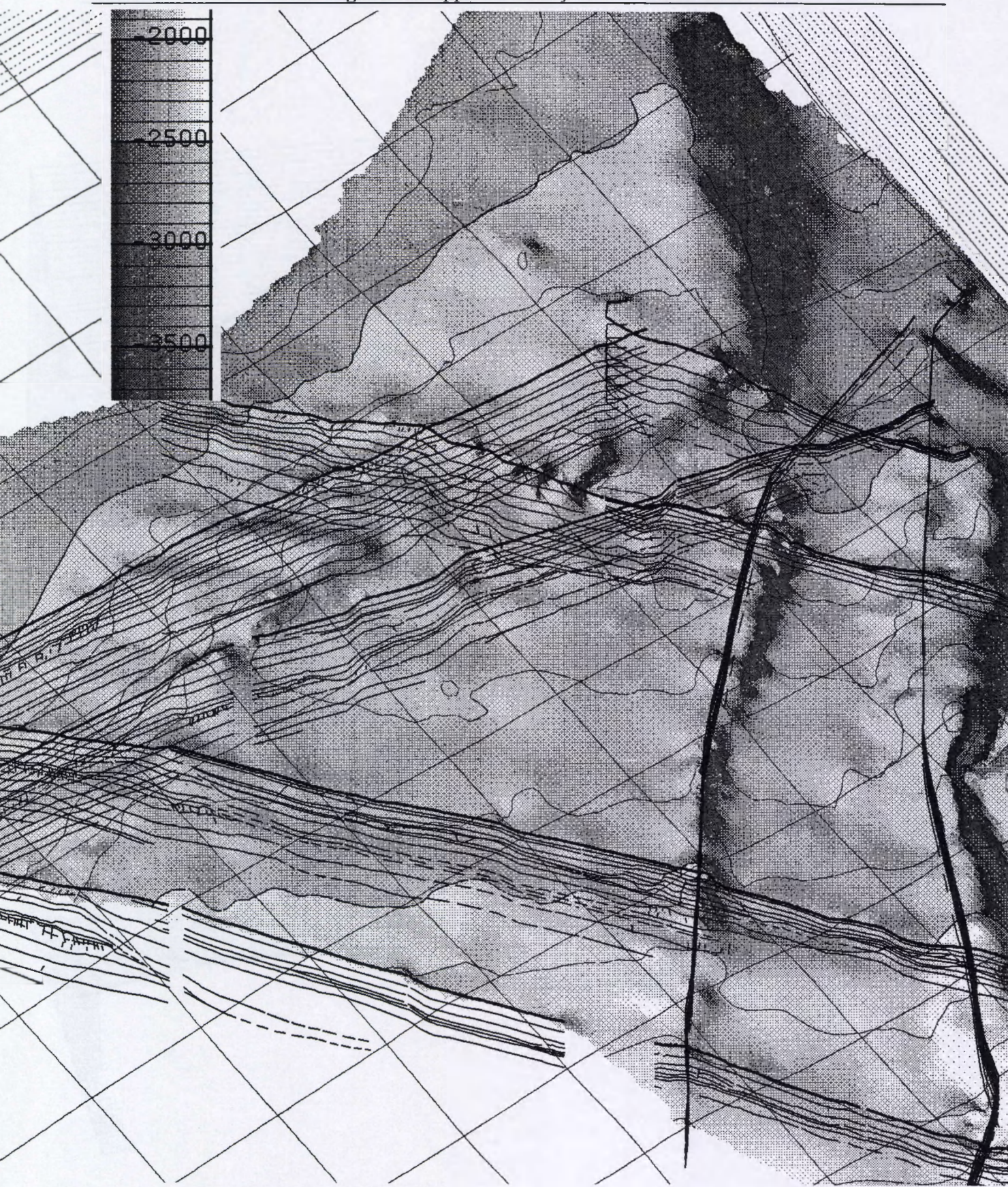


Fig. 3.56. Crary Fan in Weddell Sea, Antarctica. Topography (in m), largely based on digitized contours and extended with seismic sections, neatly shows levies and structural coherence with interpreted seismic sections. Axonometric projection conserves thickness along sections. UTM grid line interval 10 km. (Courtesy Bernard Dennielou, Brest, France)

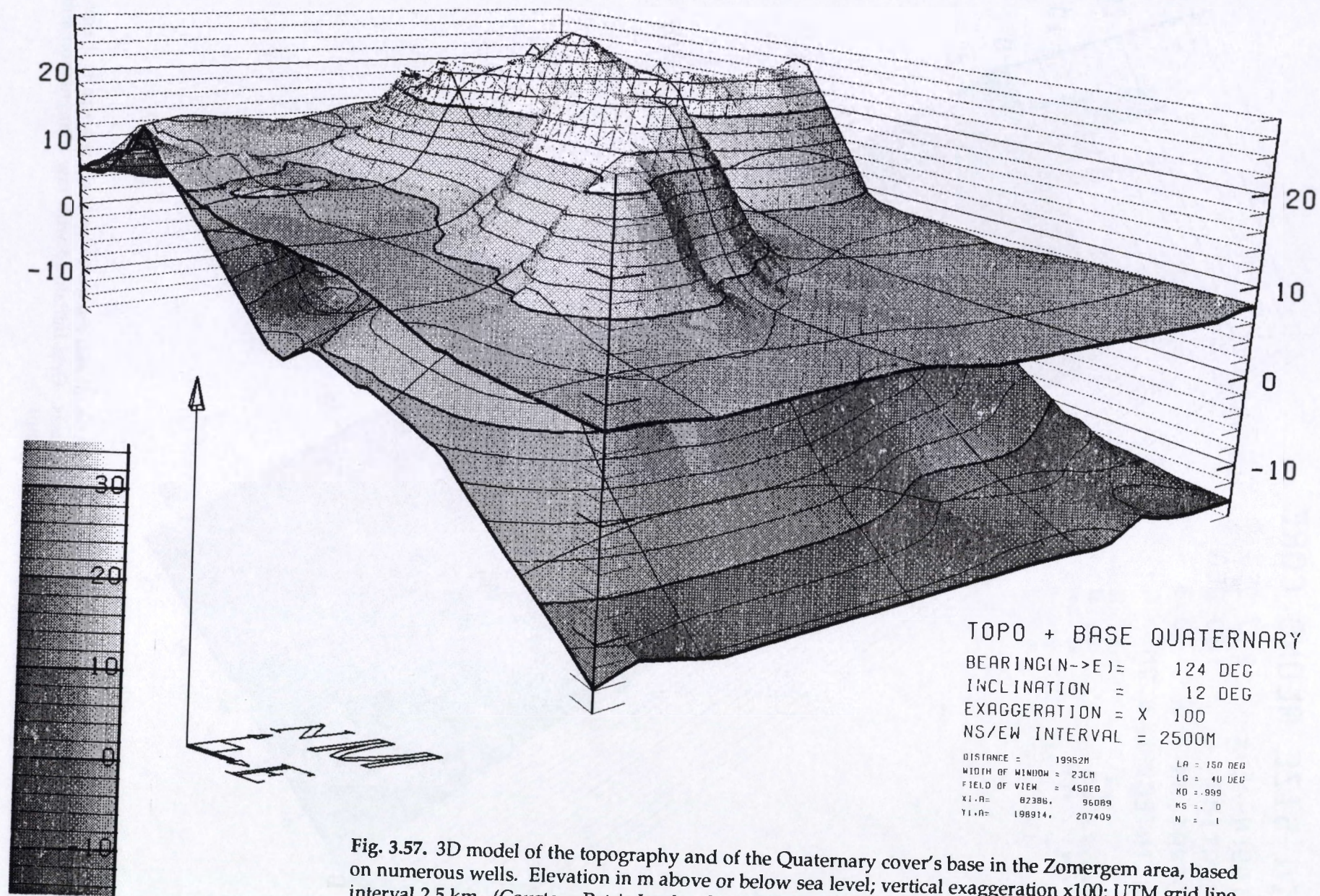


Fig. 3.57. 3D model of the topography and of the Quaternary cover's base in the Zomergem area, based on numerous wells. Elevation in m above or below sea level; vertical exaggeration x100; UTM grid line interval 2.5 km. (Courtesy Patric Jacobs, Gent, Belgium)

GRAIN SIZE ALONG CORE

BEARING(N->E)= 240 DEG
 INCLINATION = 60 DEG
 EXAGGERATION = X 0.3
 NS/EW INTERVAL = 2M

DISTANCE = 50M
 WIDTH OF WINDOW = 25CM
 FIELD OF VIEW = 45DEG
 XI,A= -36. -3
 YI,A= -1. 10

LA = 145 DEG
 LG = 28 DEG
 KO = .999
 KS = 0
 N = 1

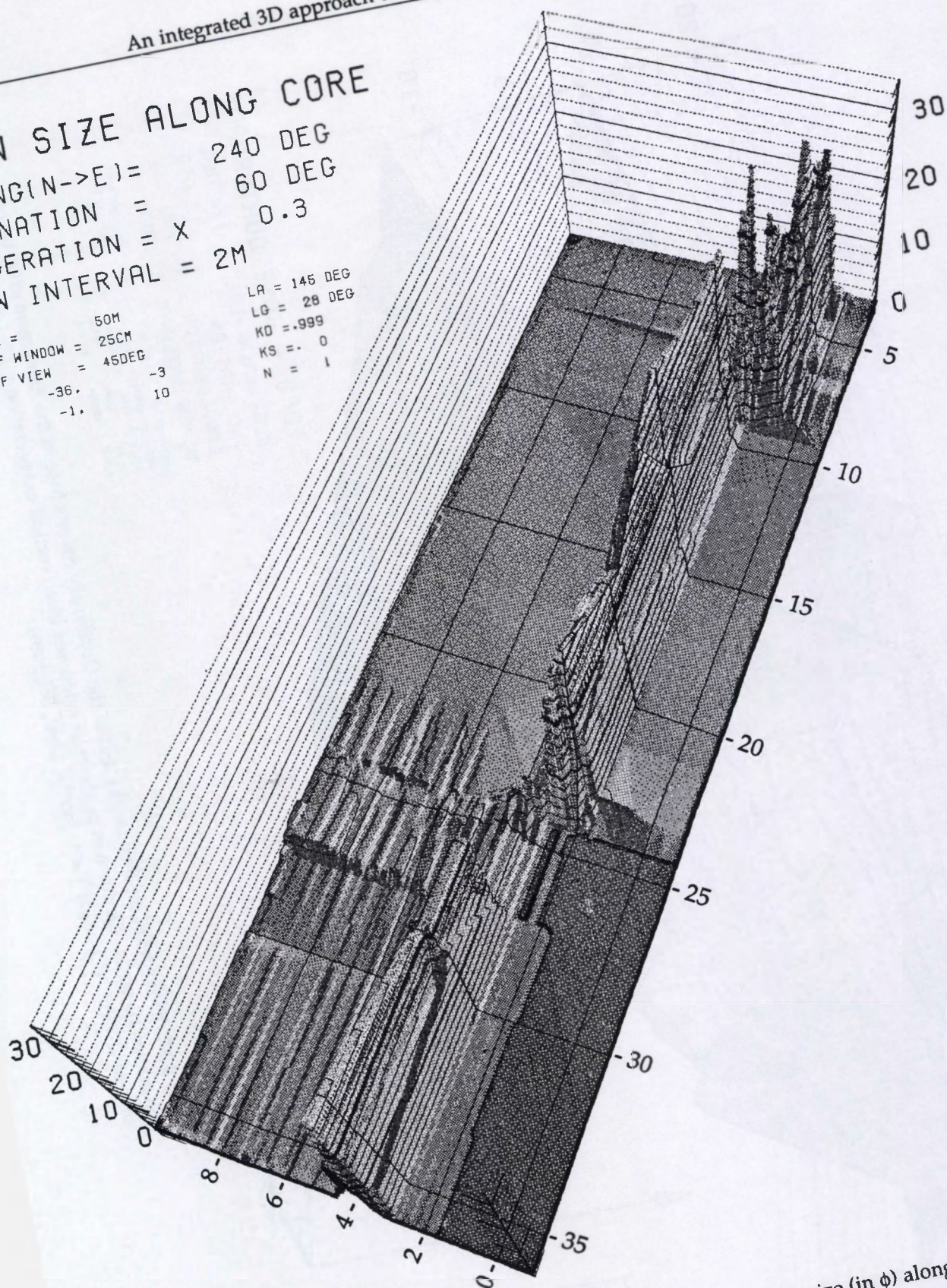


Fig. 3.58. 3D granulometric plot. Depth along core (in m) and grain size (in ϕ) along horizontal axes, frequency (in % per class of 0.25ϕ) along vertical axis. Grid initialized with raw triangulation and not smoothed. (Courtesy Erwin Sevens, Gent, Belgium)

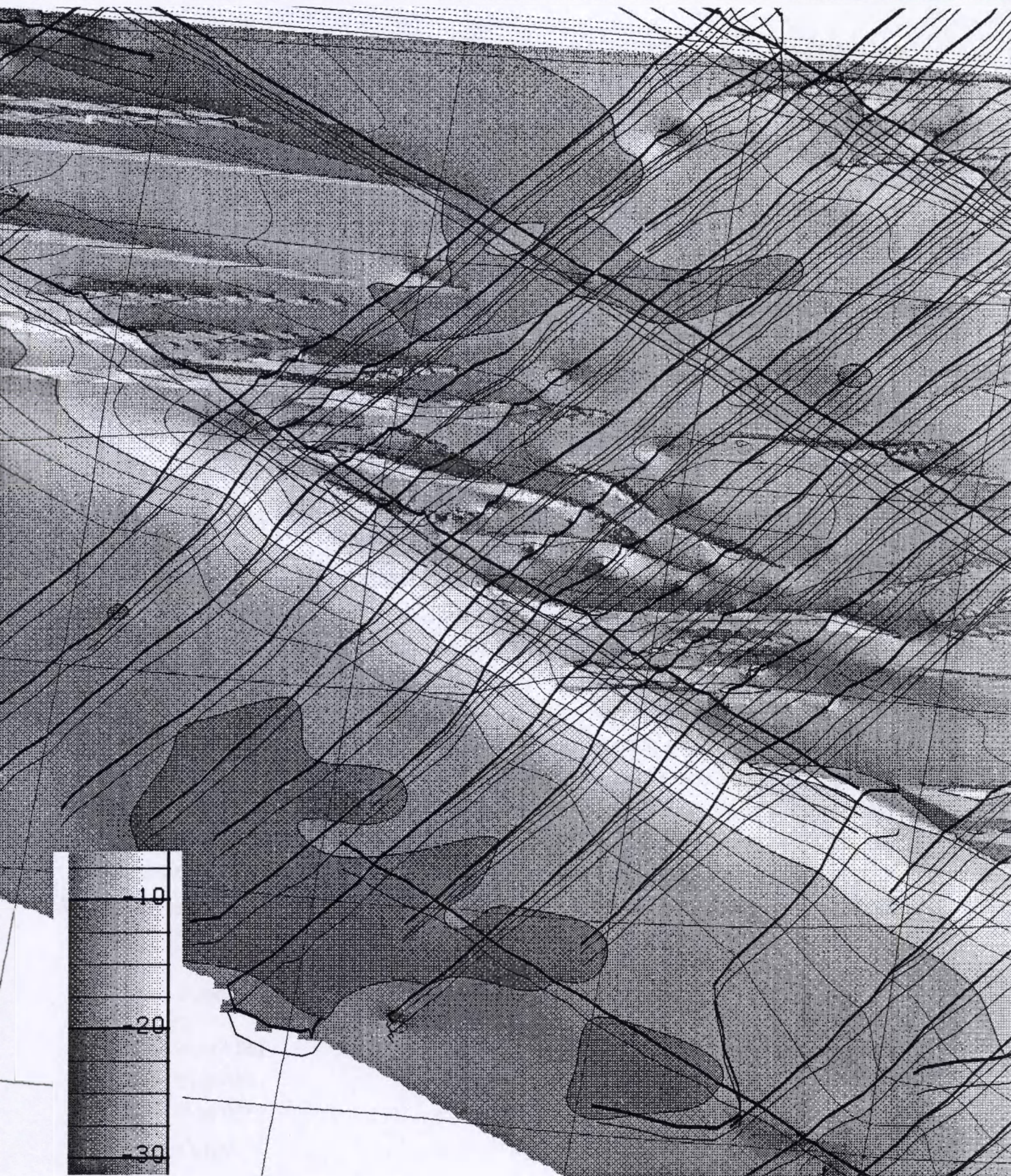


Fig. 3.59. Part of Middelkerke Bank, a sand bank in the Belgian North Sea sector. Heaviest line in projected sections is topography, others are Quaternary sequence boundaries defining the architecture of the sand bank. Sand waves on top of the bank were tentatively modelled with scarp triangles between sections. UTM grid line interval 1 km; depth in ms TWT. (Courtesy Alain Trentesaux, Lille, France)

4. New geological evidence

4.1. Structural surface models

In §2.5, we discussed the interpretation of 2D seismic data on three sites, i.e. for a clay diapir on the river Scheldt, for clay tectonic faulting in the North Hinder zone, and for a sag fault affecting the basement just to the W of the latter site. In this section, we briefly report how Geofox was used to interpret and model continuous surface models for these data. Next, an analysis of these models leads to implications for our working hypotheses.

4.1.1. North Hinder sag fault¹

Polygonal approximation reduced the number of data points to only 15%, without any significant loss of information at the modelling scale (figs. 3.17 & 4.1). Upon triangulation, vertical mis-ties appeared to be quite small on these digitally processed data of homogeneous quality. Due to the synchronization problem explained in §2.2.5, horizontal position errors were such that some fault gaps ended up on the wrong side of intersecting sections. These errors were corrected interactively until the triangular surface models for each of the horizons and interpolated smooth grids looked acceptable, like in fig. 4.2. In Geofox, a stack of such grids was converted to depth in m (fig. 4.3) with the following interval velocities, derived from a multi-channel stack velocity function and from previous refraction measurements and borehole velocity shooting (Vercoutere, 1987; De Batist, 1989; Wim Versteeg (RCMG), pers. comm.):

geological unit	interval velocity	previous data
Ypresian Y (Ieper or London clay)	1700 m/s	1620 m/s
Thanetian T2 (Landen sands)	1875 m/s	1850 m/s
Thanetian T1 (Landen sands)	2030 m/s	1850 m/s
Cretaceous	3200 m/s	3000 m/s
Palaeozoic	4000 m/s	n.n.

¹A *sag* or *fault sag* is a depression produced by downwarping of beds on the downthrown side of a fault (AGI, 1980). The associated normal fault will be called a *sag fault* here.

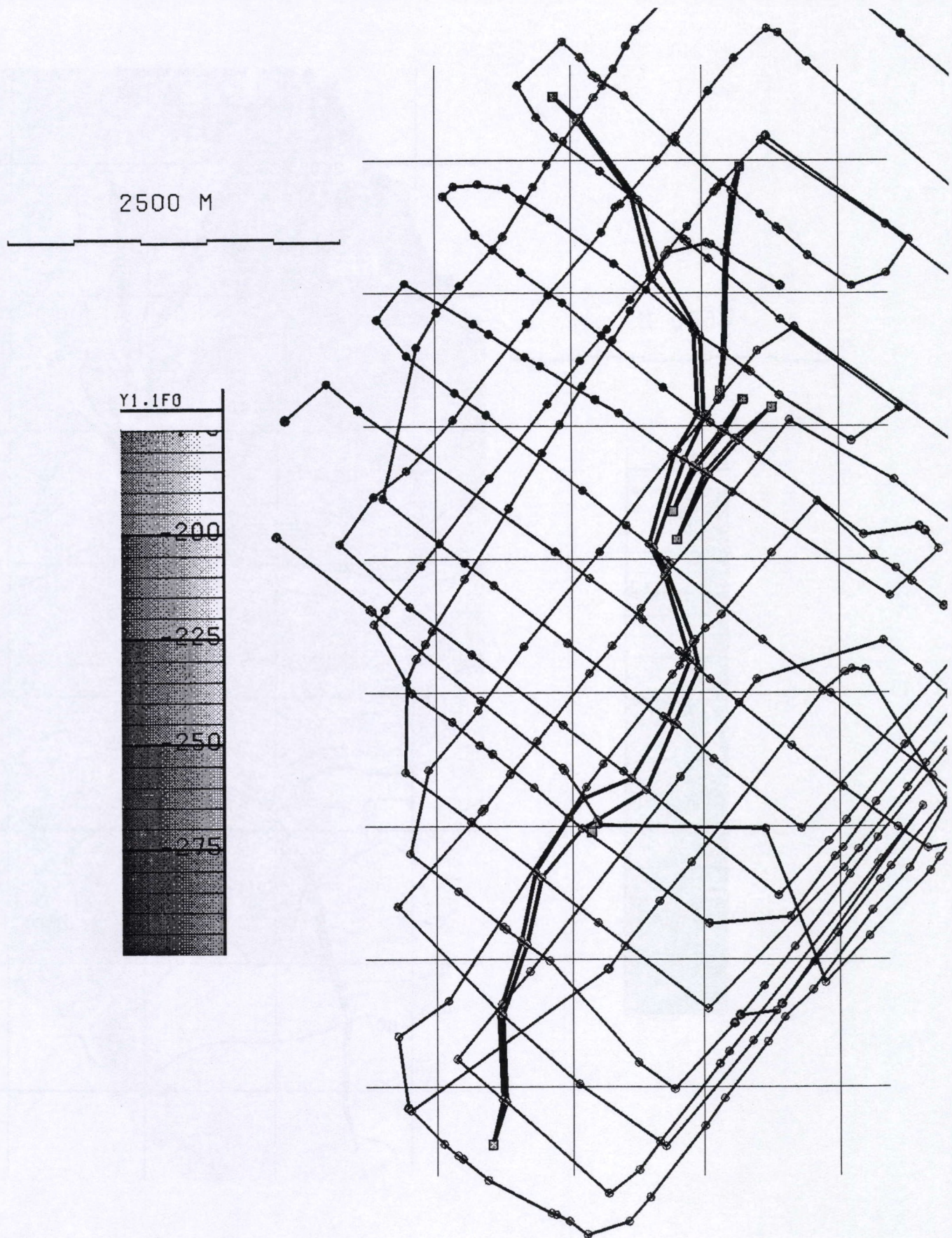


Fig. 4.1. Seismic network and grid sector over North Hinder sag fault. Compare with fig. 1.1 and 2.11 for location. Circles indicate selected points along reflector at base of Ieper Group (see also fig. 3.17). UTM projection; UTM grid lines every km; fault scarp traces in semi-heavy lines.

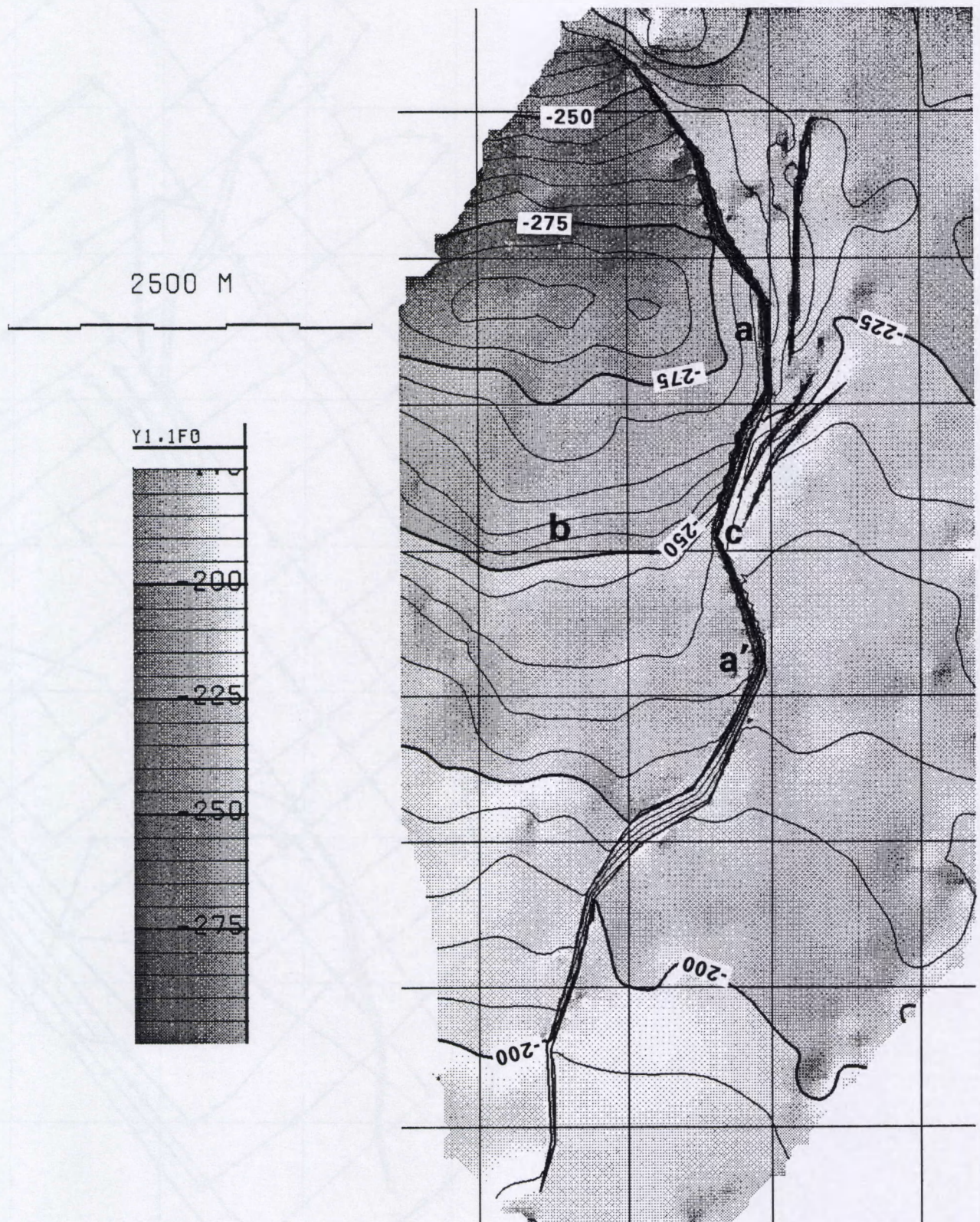


Fig. 4.2. North Hinder sag fault. Map of horizon at base of Ieper Group. UTM projection; depth in ms Two Way Time; grey level interval 25 ms, contour line interval 5 ms; grid lines every km; fault scarp traces in semi-heavy lines. The sag fault has two concave parts (a, a') and has together with the satellite faults an overall NS orientation. A central EW monocline (b) to the W of a corner point (c) can be seen to bound the deepest part of the sag.

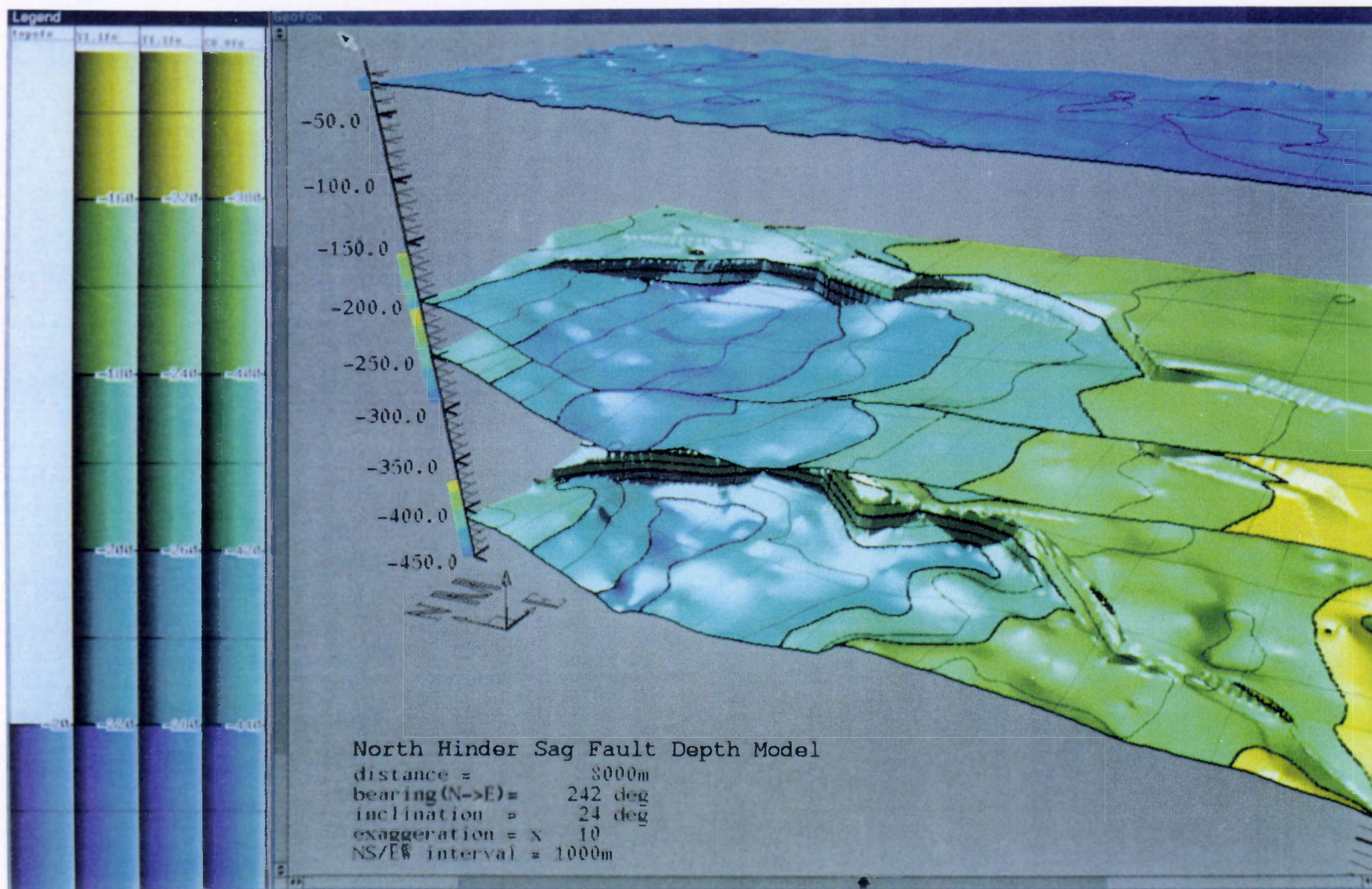


Fig. 4.3. Time-depth converted 3D structural model of North Hinder sag fault. Surfaces from top to bottom of stack: topography, base of Ieper Group, base of Landen Group and top of basement. The doubly concave normal fault has affected the basement as well as the Cretaceous and Cenozoic cover. Depth in m can be read along the vertical axes; colour interval 20 m, contour line interval 10 m; vertical exaggeration is x10.

The model and maps show satellite faults with the same NS orientation as the main sag fault. They are situated on the upthrown block of the northern part of the fault. More interesting is that the two concave parts (a-a' in fig. 4.2) of the fault trace combine with a monocline¹ (b), starting at the central corner point (c) and running West across the downthrown block, thus dividing it in two parts that may have sagged down more or less separately. The normal and doubly convex sag fault cuts through all of the Meso-Cenozoic cover, and does not change shape in the basement. This basement fault geometry is not compatible with a NE trending basement fault, conjectured by Henriët & De Batist (1989) to explain the North Hinder deformation as a result of deep seated strike-slip movement. We prefer to interpret the deformation as the result of E-W extension, possibly of Eo-Oligocene age (Bergerat, 1987; De Batist, 1989; §1.3).

4.1.2. North Hinder clay tectonic faulting

The strong internal reflector selected and interpreted in §2.5.2 (fig. 2.14) was digitized continuously, except for interruptions at interpreted fault cuts. The seabottom reflector was also digitized, but its very low topography virtually eliminated its use in time/depth conversion to compensate for velocity pull-ups.

The data were split into two parts, one consisting of the NW-SE sections (sector b in fig. 1.1), the other of the NE-SW sections (sector c). After conversion from digitizer coordinates to 3D world coordinates, the two sets were read into Geofox and triangulated separately. Vertical mis-ties, apparent from reflector lines that were consistently higher or lower than neighbouring ones, were corrected interactively. Next, polygonal approximation was used to select the most relevant 25% of all data points for interactive modelling. The two sets of sections have been merged, triangulated and systematically correlated from one side of the network towards the other (fig. 4.4). Doing so, parts of NW-SE sections that had been acquired during the Summer of 1989 were moved laterally along their track to correct for positioning errors of up to 30 m relative to the Summer 1990 sections, that were free of such errors. Remaining vertical mis-ties were corrected away as well.

Interpreted fault correlations were interactively introduced in the triangular surface model of horizon and fault system. Dense gridding and appropriate smoothing with our special variable tension algorithm produced the structural model (fig. 4.5) that could be evaluated in 3D projection (fig. 4.6-7). The three-stage

¹A *monocline* is a local steepening in an otherwise uniform gentle dip (AGI, 1980).

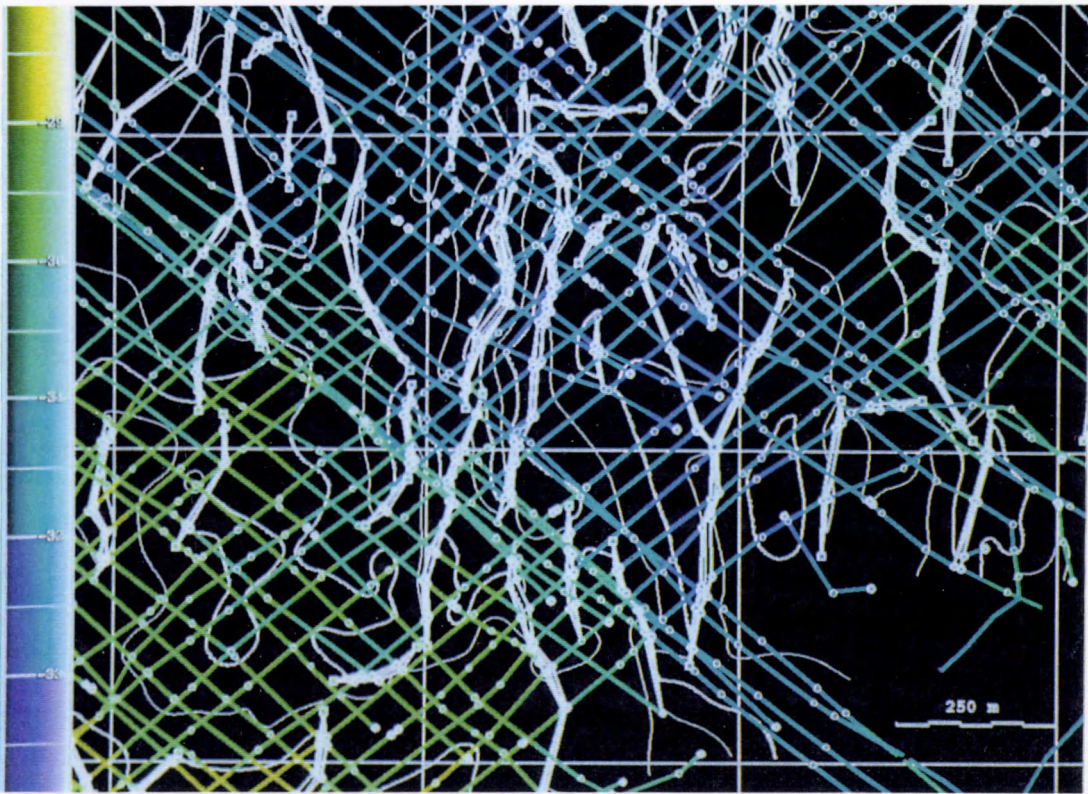


Fig. 4.4. North Hinder clay tectonic faulting. Coloured lines convey depth in m along the digitized reflector, indicated in fig. 2.14. UTM grid lines every 250 m; compare with fig. 1.1 and 2.13 for location. Fault traces in heavy white lines connect fault gaps along sections; squares are control points for fault tips and branches; circles show selected data points used for modelling (see fig. 3.20).



Fig. 4.5. Relief map of clay tectonic faulting in North Hinder zone (reflector indicated in fig. 2.13). Sector as in fig. 4.4; UTM grid lines every 500 m; colour interval 1 m, contour lines every 0.5 m. Fault traces in heavy black lines.

modelling cycle (edition of triangulation, gridding, 3D evaluation) was then repeated to correct remaining errors and try out different correlations of the fault traces. In a matter of days, the 3D structural model converged to a most probable version. After this fault correlation phase, the finishing touches consisted of modelling fault tips and branches.

Spatial aliasing was not severe because of the sufficiently dense section spacing. Short faults (less than 100 m fault trace on this horizon) that would cause most of the problems, have throws that can only barely be discerned on the sparker sections. They are interpreted on perhaps only one section, so that their strike remains unknown. These isolated, uncorrelated scarps show up as little bumps in the model, due to small minimum tension overshoots at the fault gap points.

Thus, the first quantitative 3D model of clay tectonic faulting (fig. 4.5-7), or indeed of any complex fault system of this scale and subtlety was produced with the Geofox program. Within the doubly covered sector of 40 NW-SE profiles intersecting 20 NE-SW profiles, fault traces less than 100 m apart and with a length of only 200 m were sufficiently well constrained to allow reliable correlations.

The model shows that the main northward direction of clay tectonic faults in the North Hinder zone is roughly parallel to the nearby sag fault that cuts the basement and all Tertiary strata. This confirms the fault trace trend that was mapped manually (fig. 2.12). Computer aided mapping of the enlarged database also revealed the detailed geometry of both faults and faulted horizon. The model shows a slight irregular undulation with an amplitude of 4 m and a wavelength of 2 km, superposed on the regional 1-2° NE dip. Clay tectonic faults are not very straight in a horizontal plan, and some are markedly concave towards the downthrown side. The faults can be seen to be arranged in a graben-like setting in the antiform domain and in a horst-like setting in the synform domain, while blocks on fold limbs dip towards the trough line.

This kind of deformation points to a purely vertical movement of material. Indeed, it is strong new evidence for brittle behaviour over fossilized partial convection cells that could be due to a Rayleigh-Taylor instability over under-compacted, overpressurized clays. In view of the general direction, the deformations may have been triggered tectonically.

Gravity sliding can be ruled out entirely as deformation driving force system, because that would imply intraformational slumping or growth faulting with a supposedly dominant NW-SE strike (§1.4.4).

The unexpected 3D coherence between clay tectonic faults and a subtle horizon geometry and its implications prompted us to go back to one of the seismic sections (fig. 2.10) and try to restore the horizons in their pre-fault position. The pattern of relative displacements of blocks along this section indeed revealed that blocks at the crest of anticlines sagged most (fig. 4.8). This exercise also de-mystified the 'inverse drag' (Henriet *et al.*, 1988; §1.4) as the result of a collapse of growing undulations along their limbs. It is not impossible however that part of the horizon deformation was concurrent with faulting.

In conclusion, 3D modelling of these mis-tie ridden sparker data with Geofox has enabled us to

1. map a complex normal fault system and subtle undulations with a density, throw and amplitude that were beyond the capabilities of manual contouring;
2. gain geological insight from the 3D surface model that made us weed between multiple hypotheses and look at 2D sections with new eyes.

4.1.3. Scheldt diapir

The data described in §2.5.1 have been used for building a 3D model of the diapir, which then could later be compared with the output of a more rigorous 3D seismic approach.

The reflectors modelled in fig. 4.9 are indicated in fig. 2.19. The triangulations of data points for the two subbottom reflectors were adapted to model the subtle dome on B.1 and the circular depression around the bulge on B.2. With splines of limited scope and without successive grid refinement (§3.7.7.4), the triangular surface models were only partly smoothed in order to honour modelled trends that were too subtle to 'freeze' as scarps. The digitized bathymetry contours were triangulated and automatically changed so that no triangle had three vertices on the same contour (§3.7.6.1), which would otherwise create small horizontal steps in the gridded surface model. The latter technique was also used for fig. 3.55 & 3.56.

In 3D projection and with solid shading (fig. 4.9), the clay diapir stands out clearly and a small fault at the NW can be seen to sharply cut the smooth surface. At the same time, the model can be quantitatively interpreted. A slight circular depression up to 0.5 m deep can be seen to surround the bulge on the more deformed horizon B.2, and is most pronounced E of the small fault. It was not

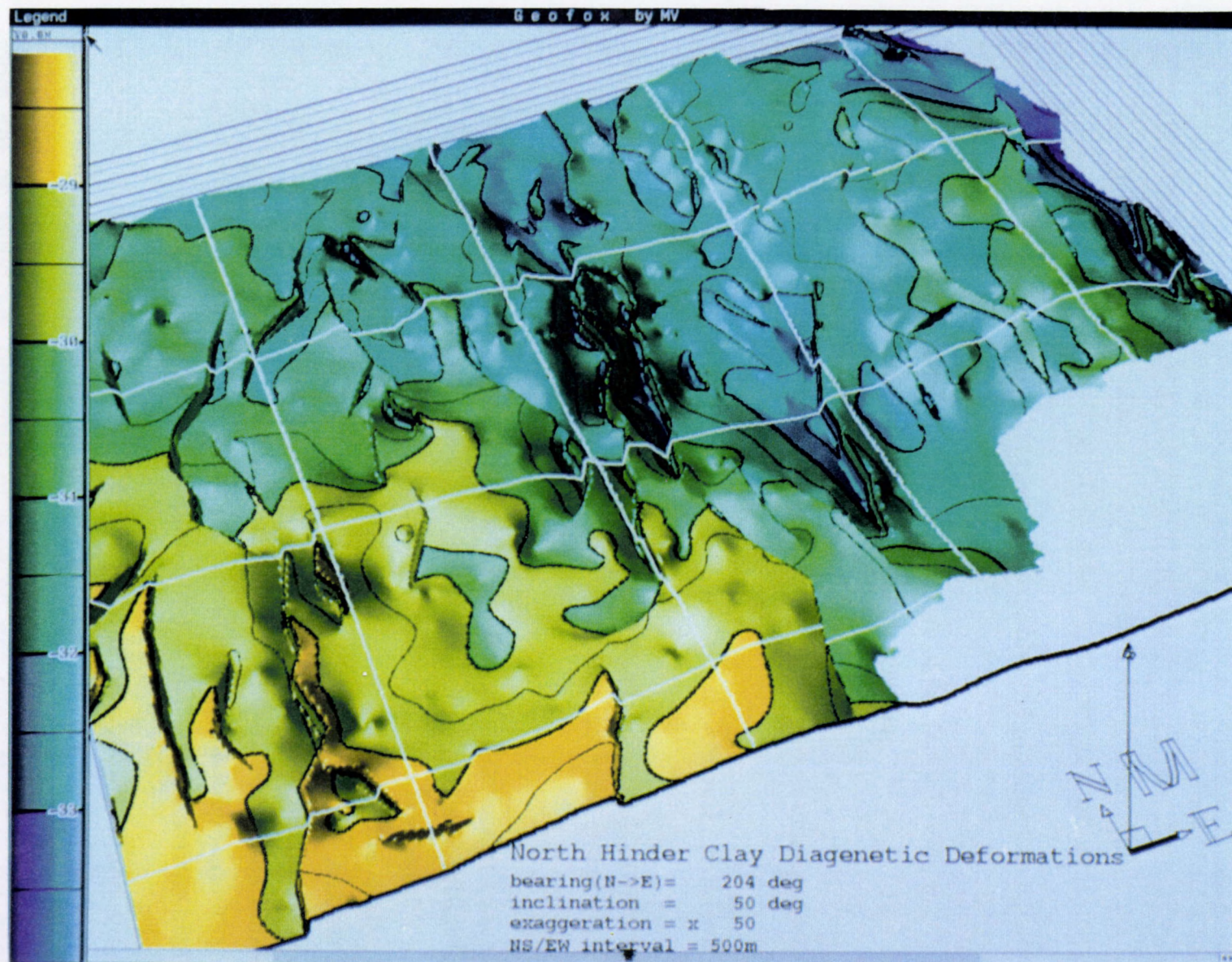


Fig. 4.6. Solid shaded 3D view on clay tectonic faulting in North Hinder zone, looking N (downdip). Same grid as in fig. 4.5; UTM grid lines every 500 m; depth in m; vertical exaggeration x50. Notice graben on anticline in lower left corner.

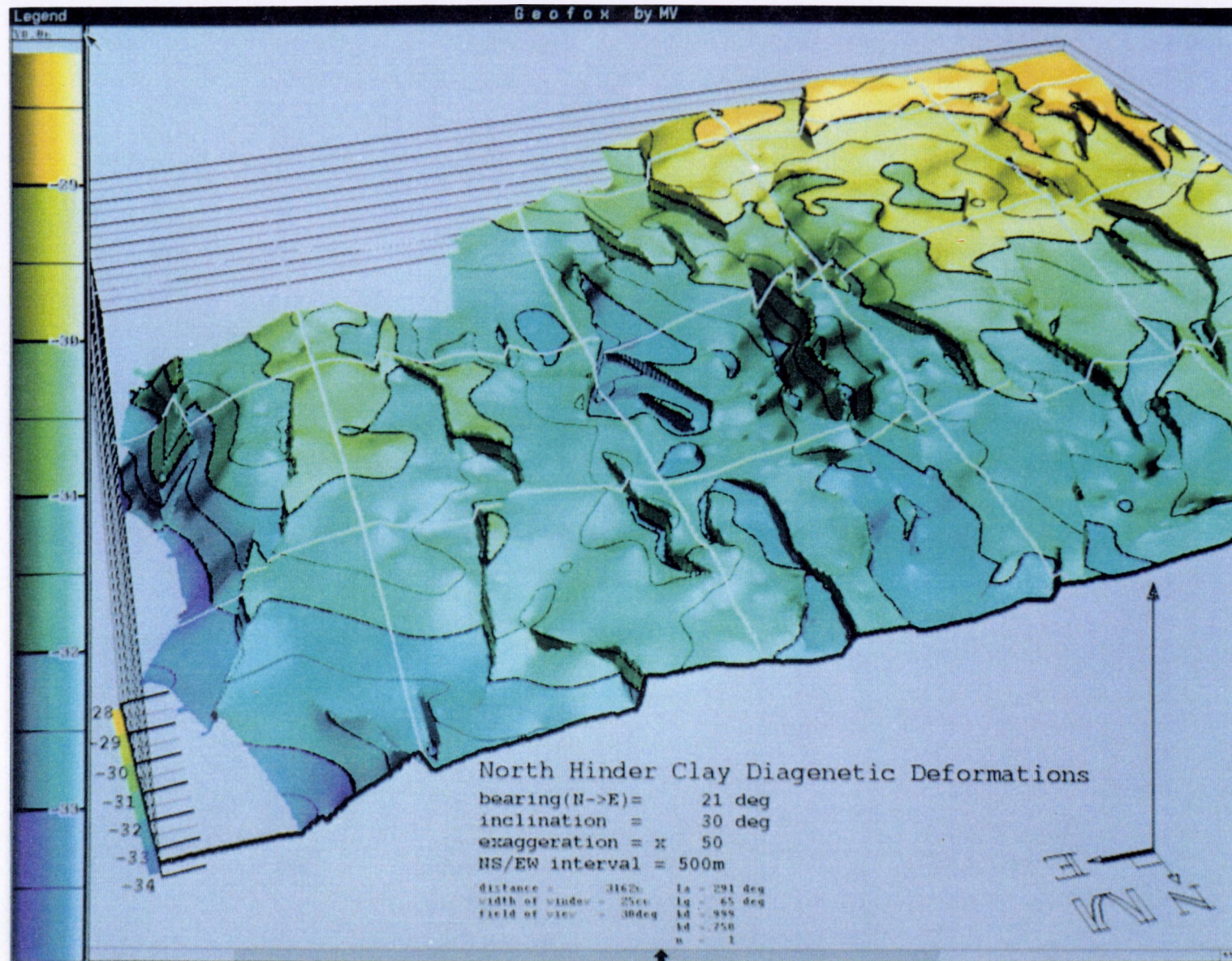


Fig. 4.7. Solid shaded 3D view on clay tectonic faulting in North Hinder zone, looking S (updip). Same grid as in fig. 4.5; UTM grid lines every 500 m; depth in m; vertical exaggeration x50. Notice horst in syncline in central front, and normal faults dipping towards the anticlines on either side of the depression.

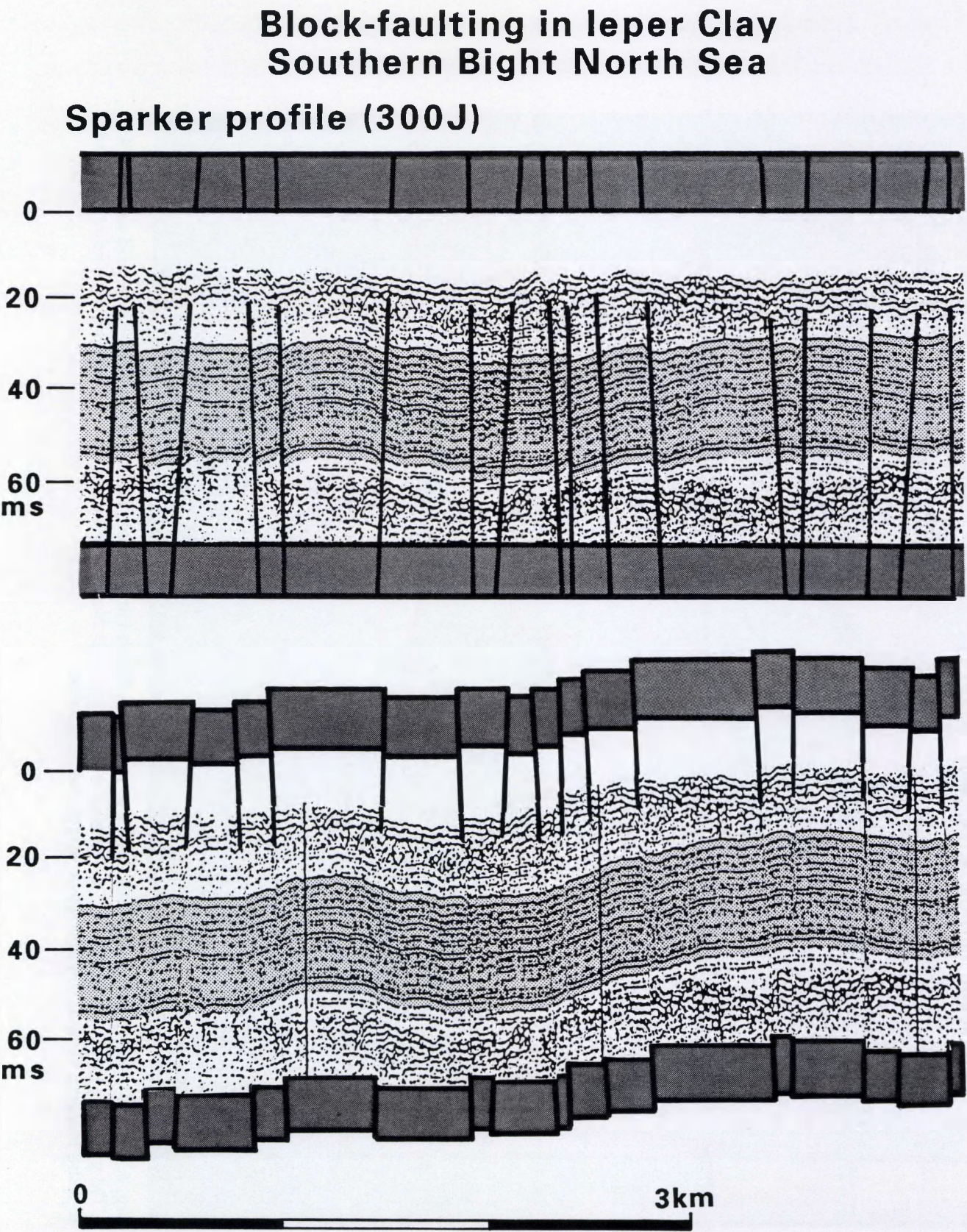


Fig. 4.8. Profile of fig. 2.10 (above) and a version in which the seismic horizons were restored to their pre-fault position. Blocks at the crest of anticlines sagged most. "Inverse drag" (fig. 2.10) is the result of a collapse of growing undulations along their limbs.

possible to follow the strong B.2 reflector through the central part of the diapir, which means that little is known about the internal structure of this diapir. The B.2 reflector was simply extrapolated above the -25 m contour. The deepest reflector in this model (B.1) is hardly deformed at a depth of about 40 m below the river bed. It domes less than 1 m, without a depression around it.

Whether it would be possible to improve this information by true 3D acquisition and processing remained a challenging question until the SEISCAT approach was applied (§2.3.3, §2.4.2.2). The digital processing of SEISCAT data was reported in Henriët *et al.* (1992). We only mention here that the boomer data, which covered the diapir more fully than the watergun data, were sorted and stacked in a regular grid of 1x1 m² bins within a NE/SW oriented sector of 50x180 m² (indicated in fig. 2.15b and 4.10). With Geofox it was possible to see that the boomer data covered the bins between 5 and 10 times on average within the final bin sector (fig. 4.10). The time slices in fig. 4.11 have been taken from 5 ms below the B.1 reflector. These synthetic horizontal seismic sections (compare with fig. 2.1) come from consecutively deeper horizons. They are separated by only 0.25 ms. Red and yellow colours stand for positive amplitudes, green and blue for negative ones. Thanks to the data coherence between the 1x1 m² bins, two structural features can be readily interpreted on these time slices. As you look deeper and deeper into the 3D set, concentric reflector patterns grow from the centre outwards at the base of the diapir. A slight dip towards the right (NE) can also be deduced from the asymmetric distribution of colours around the diapir, which corresponds to the general dip of the Tertiary strata in this area.

Time slices above those in fig. 4.11 were less and less coherent in the core of the clay diapir, just like the earlier analogue profiles, so that its internal structure remains unknown. The irregular dome interpreted from pseudo-3D data on reflector B.2 could not be confirmed. The very regular dome at the deeper level merely confirms the earlier 3D model.

It was already known from 2D seismic data that this kind of clay diapirism is closely related to the Tertiary-Quaternary unconformity (§1.5). In the 3D model, the superposition of Scheldt gully and diapir is remarkable, for it may indicate that the origin of the diapir resides in differential decompaction. Although two other clay diapirs are in the vicinity of the present Scheldt gully, and most scour hollows in the London clay are also within or close to Quaternary gullies (§1.5), we recognize with the qualifier “may” that coincidence does not equal causal relation.

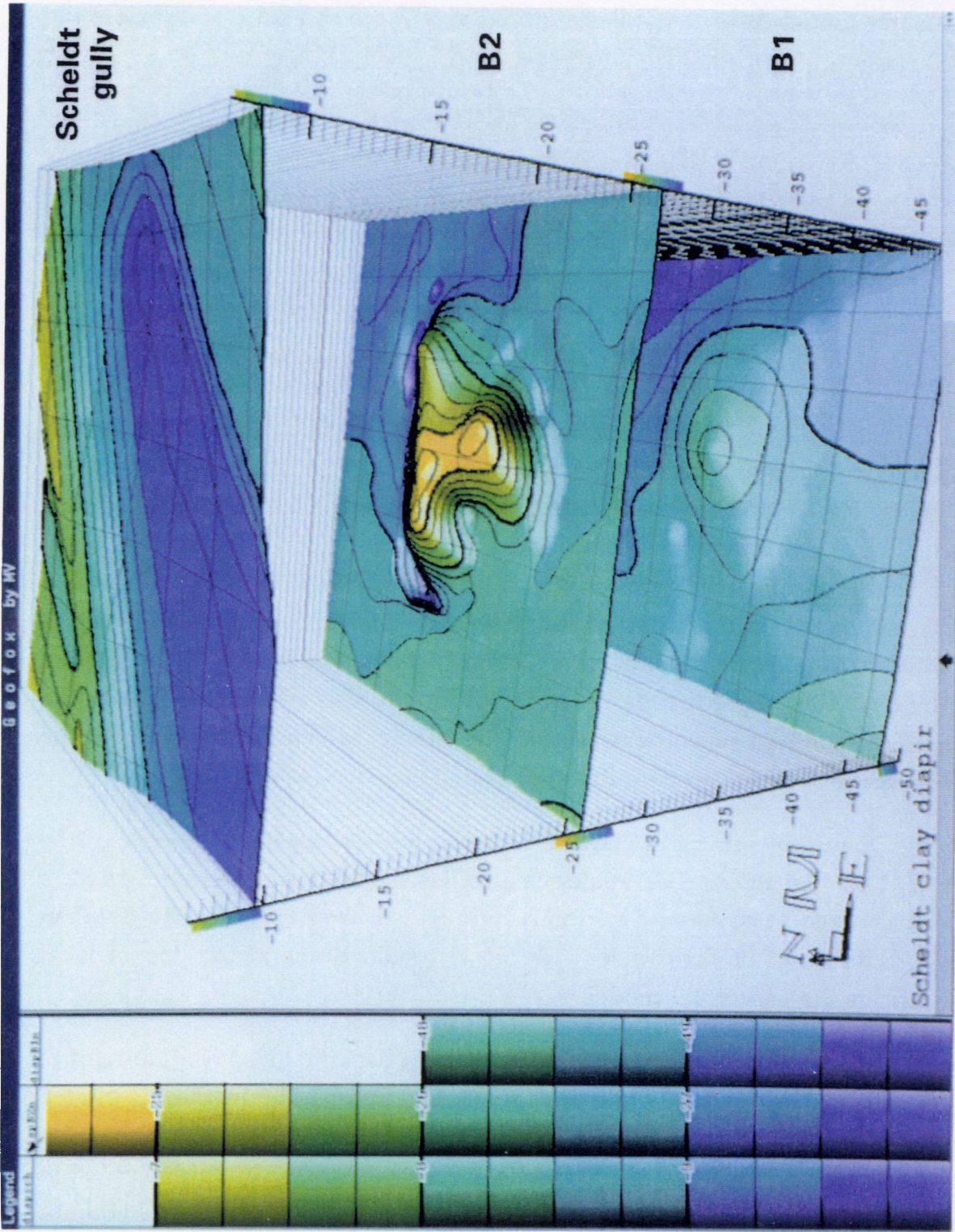


Fig. 4.9. Solid shaded quantitative 3D model for clay diapir under the river Scheldt. Sector as in fig. 1.18; reflectors as in fig. 1.19. Colour interval is 0.5 m; UTM grid lines every 25 m; vertical exaggeration is x10.

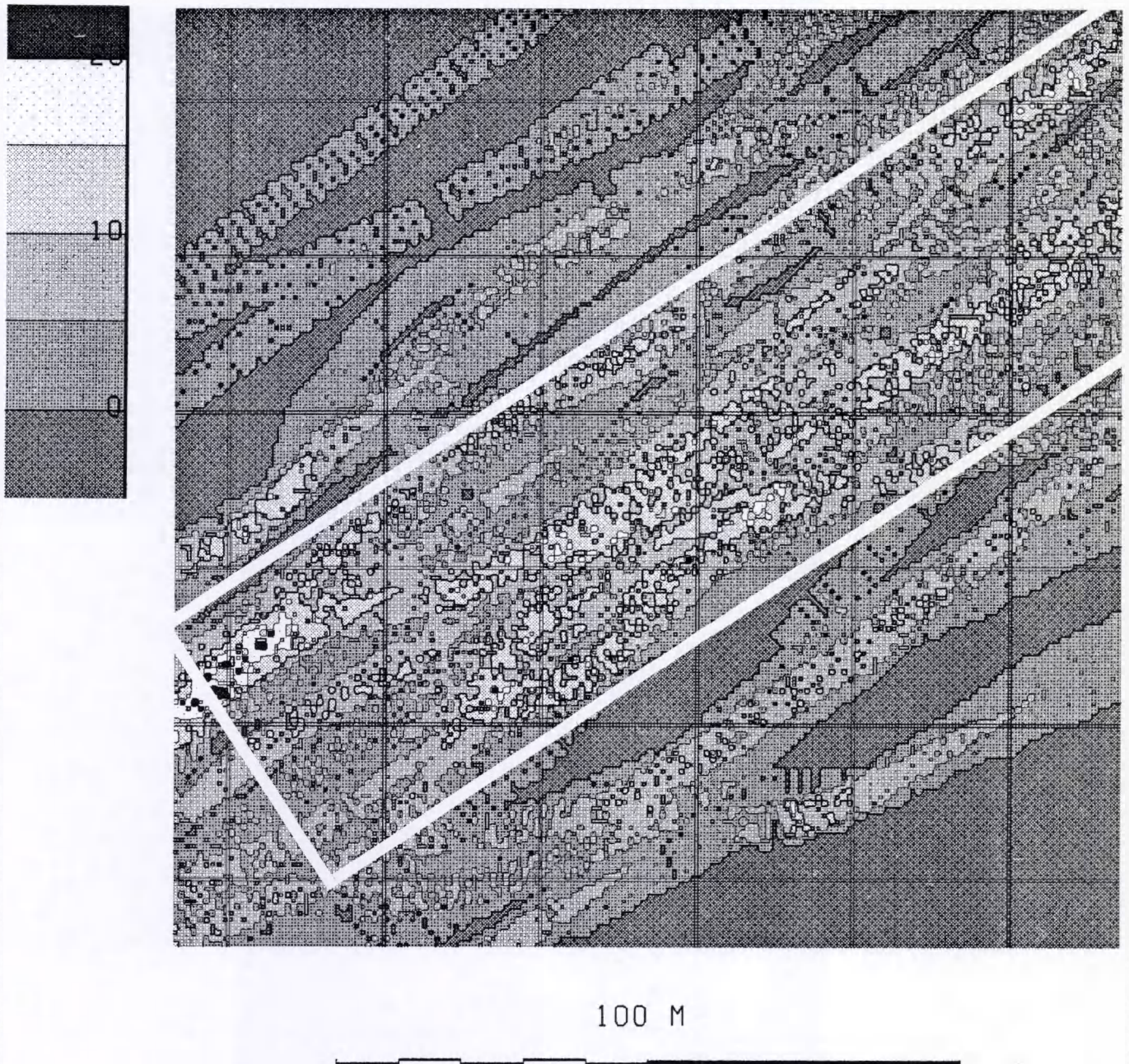


Fig. 4.10. CMP fold coverage chart for boomer data in the same area as covered by the model in fig. 4.9. Most of the bins in the final bin sector (white lines) are covered 5 times or more.

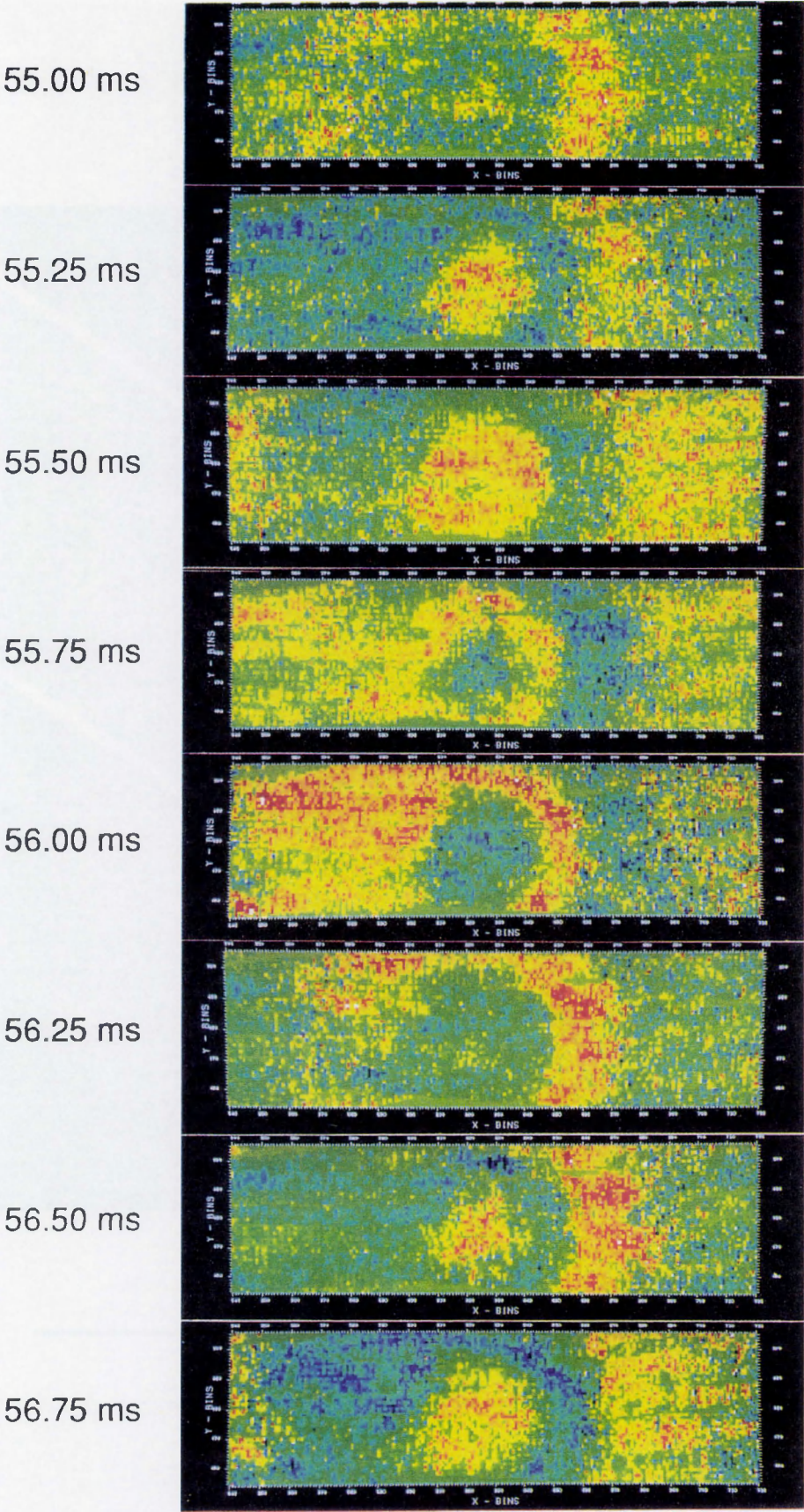


Fig. 4.11. Time slices with 0.25 ms (≈ 0.2 m) interval, showing concentric reflector patterns over clay diapir, and slight dip to the right (NE). Sector measures $50 \times 180 \text{ m}^2$ and is indicated with white lines in fig. 2.15 and 4.10; bin size is $1 \times 1 \text{ m}^2$.

4.2. Outcrop evidence of clay tectonics

Apart from a shallow Quaternary growth fault related to subaerial slumping (Van Vaerenbergh, 1987), no detailed land outcrop observations on the nature and styles of deformation within the Ypresian Formation existed. With new techniques (§4.2.1.2) developed during extensive field work in selected clay quarries (§4.2.1.1), we provide the first detailed descriptions of clay tectonic and other deformation on the scale of centimetres to tens of metres (§4.2.1.3-13). Because the faults also showed slickensides, numerous fault slip data were collected and subjected to a stress inversion method (§4.2.2.1) that produced valuable palaeostress information (§4.2.2.2). Throughout this section, we show how the observations illuminate the possible deformation mechanisms.

In this section, we also unmask the 'reverse' faults noted by several authors in juxtaposition with normal clay tectonic faults (§4.2.3), signal unmistakable Quaternary reactivation of clay tectonic faults (§4.2.4), argue against a link between clay tectonic faults and recent slumping along natural and artificial slopes (§4.2.5), and deal with permeability issues (§4.2.6).

4.2.1. Structures in outcrop

4.2.1.1. Outcrops

In our fieldwork, we focussed on three clay pits. Fig. 4.12 shows maps of the areas around the clay pits in Marke, Zonnebeke and Meulebeke (Belgium). These outcrops not only represent widely separated sites but also three superposed lithostratigraphic intervals. Fig. 4.13 brings together lithologic descriptions and biostratigraphic interpretations by Steurbaut (1986, 1987). The following remarks pertain to the lithostratigraphic interpretation of these sections:

1. Because the base of the Aalbeke Member is situated in a zone barren of calcareous nannoplankton, it can only be interpreted on lithologic criteria in the Marke clay pit. The problem is that the lithology of the underlying Moen Member varies between silty clay and clayey silt in this part of the basin (Steurbaut, 1986). The barren zone in the Marke clay pit corresponds to silty clay that rests on clayey silt. Steurbaut (1986, 1987) recognized the Aalbeke Member

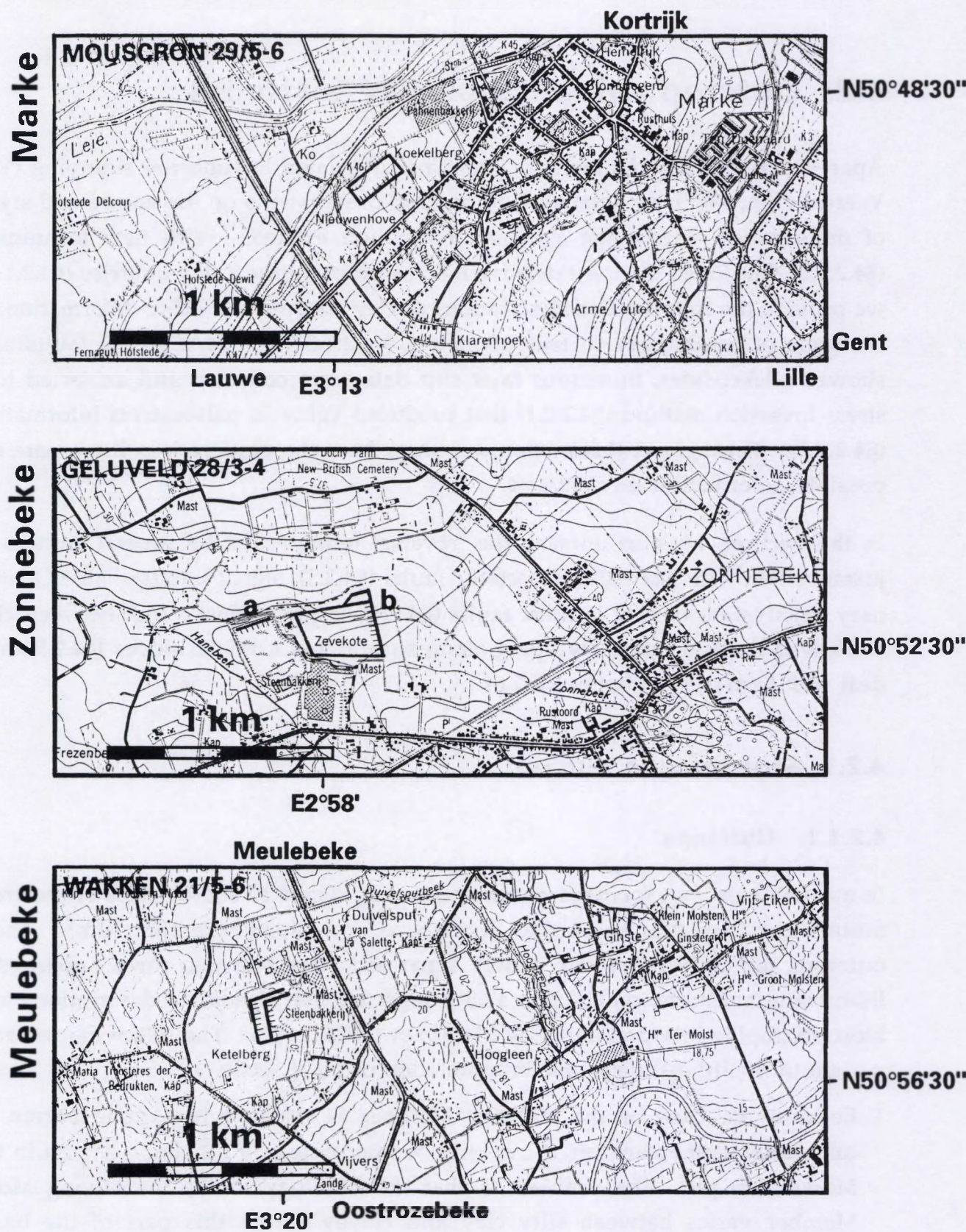


Fig. 4.12. Maps of outcrops locations studied in this chapter. For general location, see Fig. 1.1. (top) Koekelberg clay pit in Marke (near Kortrijk, Belgium). (middle) "Van Biervliet" clay pits in Zonnebeke (near Ypres, Belgium). Outcrop **a** described by Steurbaut (1986; fig. 1.15), outcrop **b** described in this chapter. (bottom) "Ostyn" clay pit in Meulebeke (Belgium). These are parts of topographic maps of scale 1:25000 (names in upper left corner; courtesy National Geographic Institute, Abdij ter Kameren 13, B-1050 BRUSSEL, Belgium; tel.: 02/648.52.82, fax : 02/646.25.18).

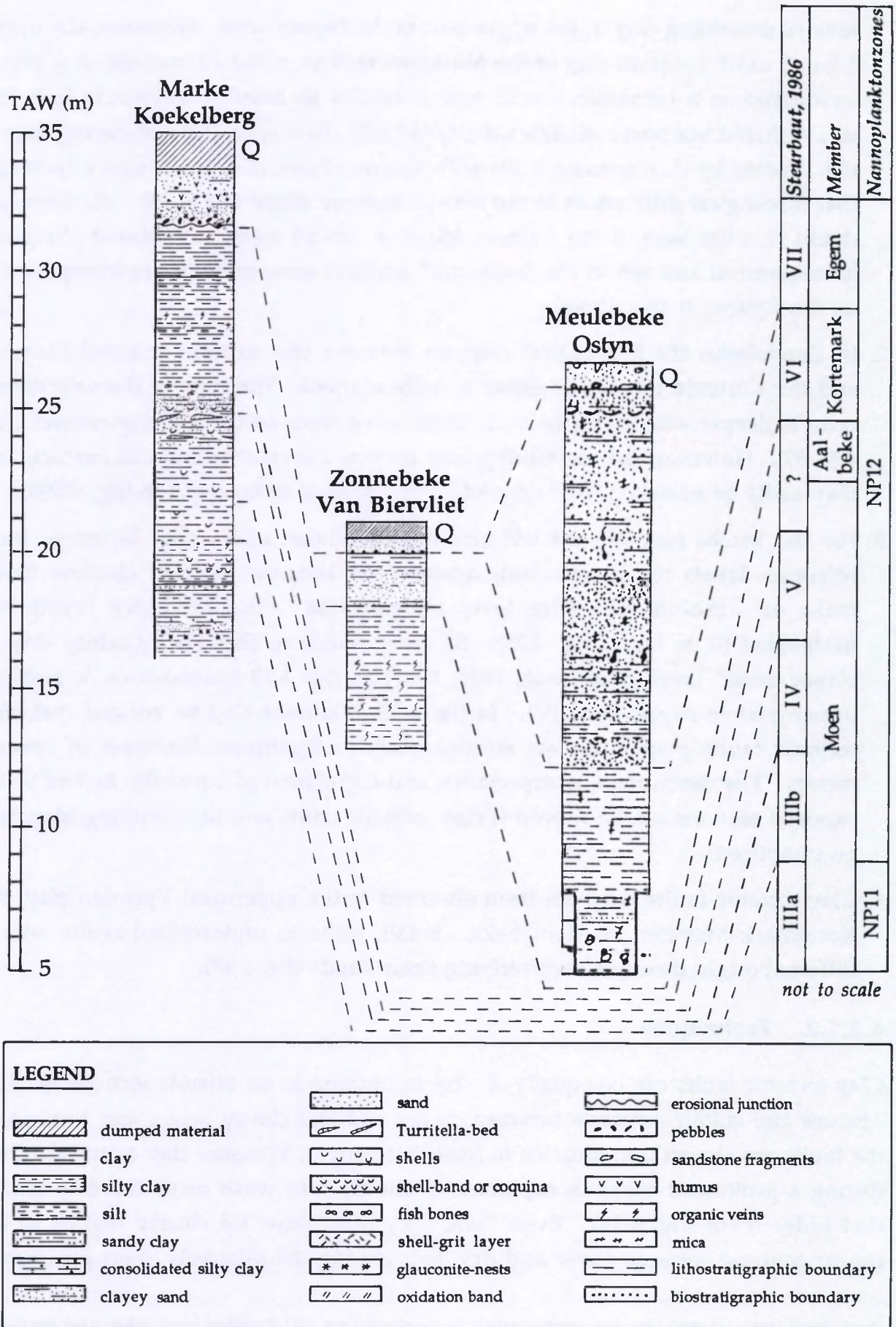


Fig. 4.13. Litho- and biostratigraphy of the studied quarries (after Steurbaut, 1986, 1987).

here as crumbling clay in the upper part of the barren zone. However, the upper 1.5 to 3 m of Ypresian clay in the Marke as well as in the Zonnebeke clay pits is weathered to a brownish colour and crumbles to smaller fragments than the unweathered but overconsolidated clay (§1.4.3). In Marke, the weathering base is not affected by clay tectonic faults with throws of several metres, which indicates that lithological differences in the barren zone are slight (fig. 4.15). We therefore doubt that the base of the Aalbeke Member can be safely pinpointed along the whole section and across the faults, and we have consequently not interpreted it on the figures in this thesis.

2. In Zonnebeke, the lithological contrast between the Aalbeke (clayey) Member and the Kortemark (silty) Member is quite marked. The base of the weathering zone is deeper where clay tectonic faults have lowered the silt-clay contact (fig. 4.58-59). However, the weathering base may be above or below this contact, and may easily be mistaken for it depending on the state of the outcrop (fig. 4.59b).
3. For the Marke clay pit, we will use the succession of six silty layers as local reference levels for all our fault descriptions because the clay tectonic faults make an absolute reference level meaningless. The reference layers are designated S1 to S6 on fig. 4.23c. S6 corresponds to the “shelly sandy clay to clayey sand” layer (Steurbaut, 1986, 1987) in fig. 4.13 (nanno-zone V and the upper part of nanno-zone IV). In fig. 4.23, it should also be noticed that clay tectonic faults may introduce stratigraphically significant hiatuses of several metres. The description, interpretation and correlation of boreholes and of badly exposed sections can be flawed if clay tectonic faults and the resulting hiatuses go unnoticed¹.
4. Clay tectonic faults have not been observed in the uppermost Ypresian clay, the Kortemark Member, in Meulebeke. Small, hitherto undescribed faults with a different origin do affect the overlying Egem sands (fig. 4.47).

4.2.1.2. Techniques

Clay tectonic faults can be equally elusive in outcrop as on seismic sections (§1.4.2). Texture and colour contrasts between clayey and less clayey layers and hence also the faults are almost unnoticeable in fresh outcrops in Ypresian clay quarries. Only during a prolonged break in exploitation can the rain wash away the clay rubble that hides them (fig. 4.14). Even then, they only show up clearly thanks to the colour contrast between moist and dry beds during the relatively short time while

¹Steurbaut (pers. comm.) is preparing a much more rigorous and detailed bio-, litho- and sequence stratigraphic description of this reference outcrop.



Fig. 4.14. Clay rubble that hides bedding and faults, partly washed away (Marke 25.07.87).



Fig. 4.15. While the clayey outcrop is drying, silts retain their grey tone. Clay, darker than silt when moist, dries to a much lighter grey colour. This colour contrast brings out bedding and faults (Marke 26.10.89).

the quarry face is drying. Clays, a shade darker than silts when wet, superficially dry to a markedly lighter grey, while capillary water in silts can initially keep up with evaporation and maintain the silts superficially moist and medium grey (fig. 4.15). If the silts dry out as well, colour contrasts between clays and silts become too small again for bed identification and fault disclosure. Even when faults are clearly visible from a distance, they may be hard to locate on the clay face, because contrast are blurred and overview is lost when walking around on a clayey outcrop sloping 30° to 40°.

For systematic observations, it was therefore necessary to develop a few new techniques with which the structures could be revealed and described in detail independent of outcrop conditions (fig. 4.16). Two sets of field work techniques are worth mentioning here: techniques to prepare large outcrops in soft sediments and with subtle structures for photography, judicious sampling and measurements, and techniques for faithful outcrop rendering.

Preparing large outcrops in soft sediments

Fig. 4.17 demonstrates the striking difference in clarity of interpretation between the clay face in an average condition and a part after clean up. Even then the clay face must be explicitly interpreted in the field, because the colour and texture contrasts remain too small to be interpreted on photographs. The overconsolidated Ypresian clay is too stiff and fractured for the outcrop to be cleaned up with anything else but a sharp spade. An ordinary spade (fig. 4.18a) however is sharpened on the back, which results in smearing of clay and clayey silts. This in turn blurs the image of sedimentological and structural details. Furthermore, a truly flat outcrop plane is not possible because the cutting edge is curved. Experience learned that the spade needed to be sharpened with the oblique edge on the front (fig. 4.18b), in order to cut razor-sharply through clay, without smearing. By grinding the spade edge on a lint sanding machine to a particular shape (fig. 4.18b), a slanting cut with the spade could be fairly flat, so that parallel cuts could overlap smoothly, resulting in a perfect outcrop plane showing the minutest details even in compact and seemingly homogeneous clay. Diffuse light such as in a shadow or in cloudy or misty weather, enhances the contrasts (fig. 4.34). Unfortunately, slide or photograph emulsions are not sufficiently sensitive to render the subtle colour and texture contrast visible in the field (fig. 4.19a). Faults (fig. 4.19b) and bedding (fig. 4.22) need to be explicitly interpreted before anything is photographed.

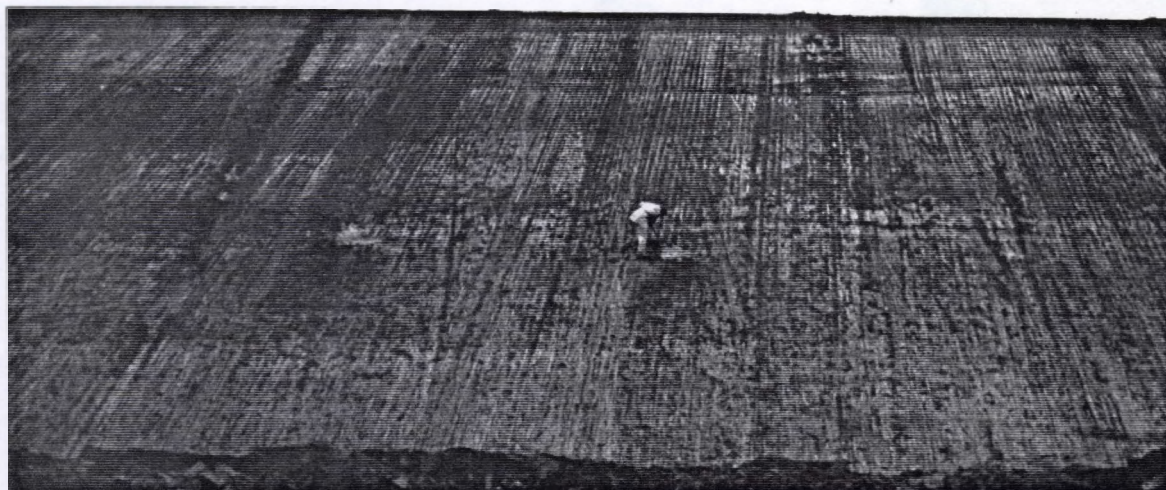


Fig. 4.16. The author in search of faults during a shower. The slippery clay face is almost homogeneous medium grey and covered with rubble. About a hundred fault and slip vector orientations were measured that day (photograph Sara Vandycke; Marke 19.10.90).



Fig. 4.17. Overview of fault with listric splay (fig. 4.27) on a shiny prepared part of the clay face, with measuring tape and folding meter (1+1m; see also fig. 4.22). From this viewpoint, faults are invisible around the prepared part, but they may be visible from a larger distance (Marke 11.09.90).

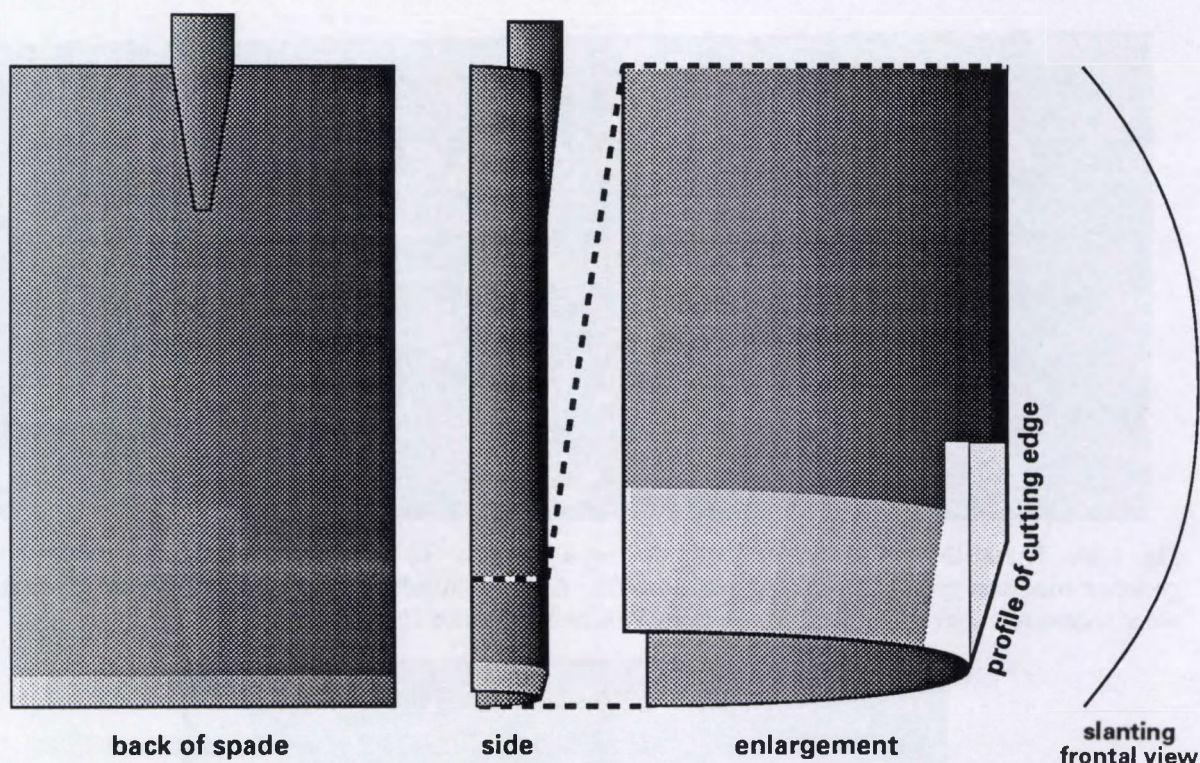


Fig. 4.18a. The oblique edge of an ordinary spade is on the *back*, resulting in the smearing of clay, which blurs the image of sedimentological and structural details. A truly flat outcrop plane is not possible because the cutting edge is curved.

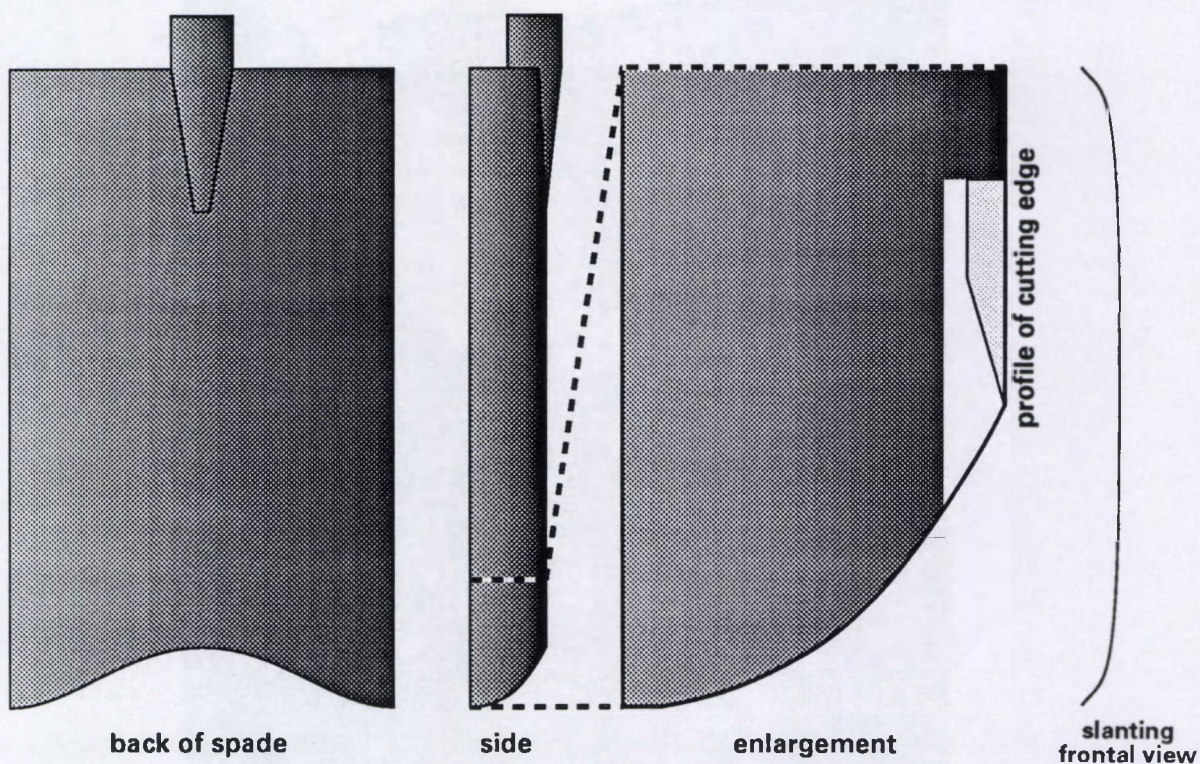


Fig. 4.18b. Same ordinary spade, but sharpened with a cutting edge appropriate for cleaning outcrops in clays. The oblique edge of the spade is on the *front*, cutting razor-sharp through clay, without smearing. A slanting cut with this spade is fairly flat (right). Cut with such a spade, the outcrop plane can show the minutest details even in compact and seemingly homogeneous clay.



Fig. 4.19a. Clay face cleaned up. Black gouge shows up in a photograph, but not the faults, because the colour and texture contrasts are too subtle (Marke 27.10.89).



Fig. 4.19b. *Idem* but with explicit indication of black clastic dykes, faulted by parallel shear faults that are only directly visible on a freshly cleaned outcrop (Marke 27.10.89).

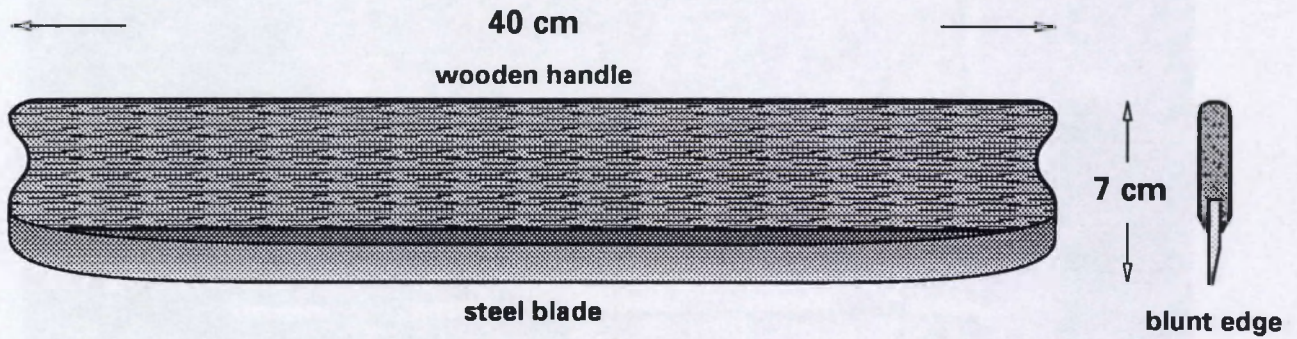


Fig. 4.20. Sand scraper, ideal for preparing large outcrops in sands and silts. A steel blade ($4 \times 30 \text{ mm}^2$) is fastened with a polyurethane or other waterproof glue in a groove in a $10 \times 50 \text{ mm}^2$ lath of wood with fine and straight graining (e.g. Doussié ('Afzelia') from Cameroun, 'Merbau' from SE Asia, Taxus, and oak, ash or elm; the latter deciduous trees should be sawn obliquely to the growth rings in order to avoid warping). A lint sanding machine was used to round off the handle and grind the blade. The blade corners were rounded off in order to have invisible overlaps while scraping. The blade was thinned on one side to a blunt square edge. If the edge were sharpened or rounded, it would be sensitive to indentations that result in stripes on the sand face.

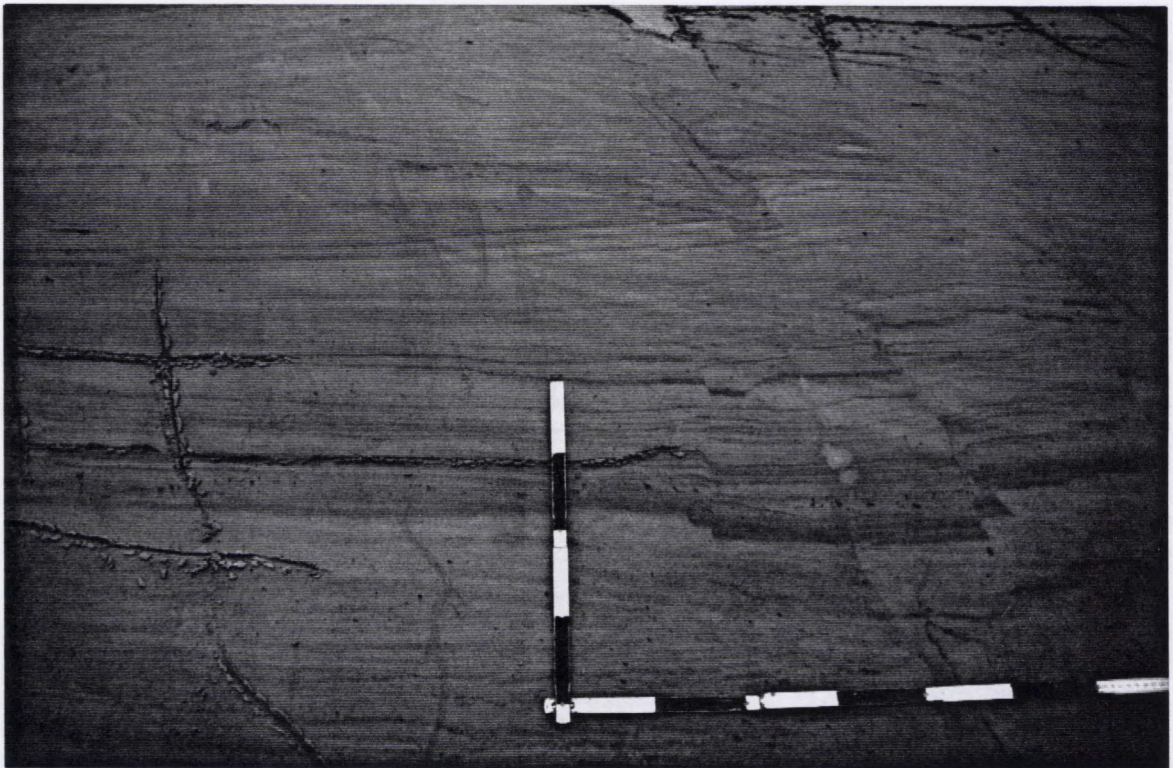


Fig. 4.21a. Outcrop of "homogeneous" fine sand in Egem Member. The face is cleaned up, revealing the smallest sedimentary structures and deformation in the field but still hardly so in a photograph. The darker bands are stained with (probably) Fe-oxides. They have nothing to do with bedding, but they are useful in delineating the faults (Meulebeke 09.02.89).

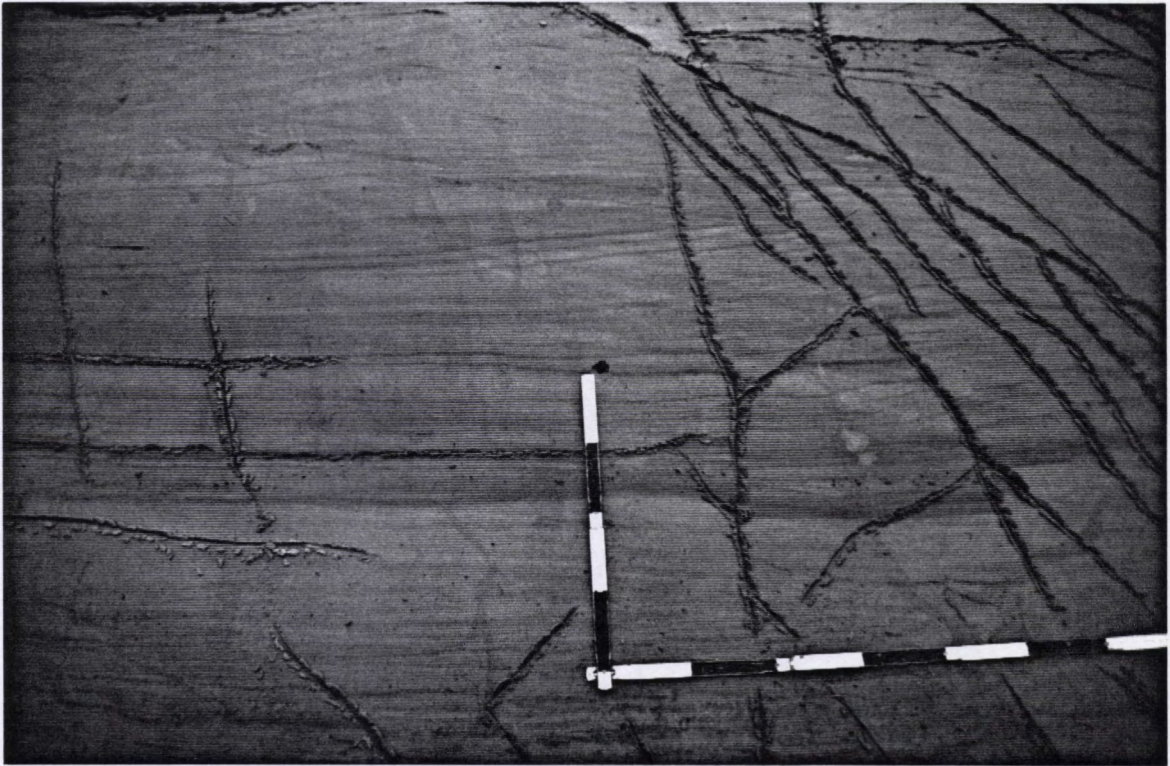


Fig. 4.21b. *Idem* with explicit indication of faults. Faults postdate staining (Meulebeke 09.02.89).



Fig. 4.21c. *Idem* with explicit interpretation of faults (heavy lines), trough cross-bedding (thin lines) and FeO (?) bands (dashes; Meulebeke 09.02.89).

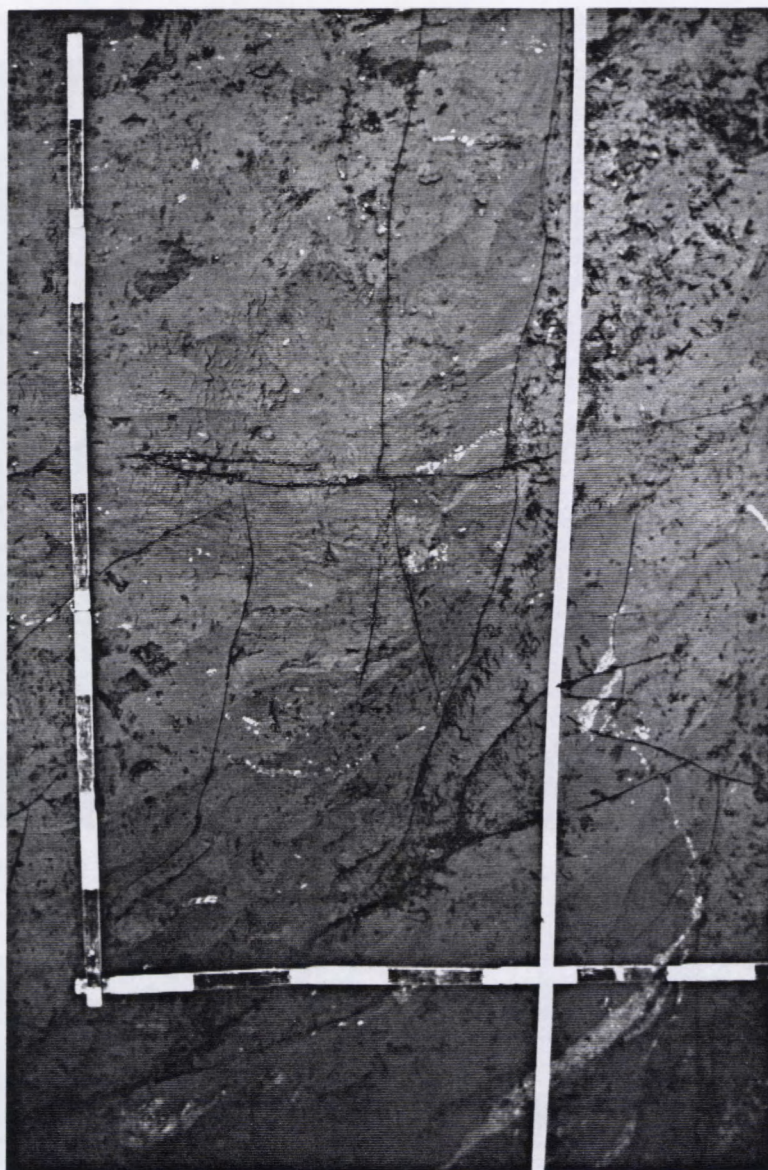


Fig. 4.22. One of the regular photographs for outcrop reconstruction (one of twenty-four for fig. 4.27), showing a listric splay (to the left) along a major fault (right half, top to bottom) that is distorted at the splay, and cut by later small shear faults. Photographed with a wide angle (28 mm) lens, perpendicularly to slope. The folding meter serves as scale, and the measuring tape indicates relative position of this part of the outcrop (Marke 11.09.90).

The same procedure goes for seemingly homogeneous and featureless fine sands, such as in the Ypresian Eggen Member cropping out in the Meulebeke clay pit. To prepare large outcrop surfaces to perfection, not a spade but a specially developed sand scraper turned out to be the most efficient tool. Its manufacture is explained in fig. 4.20. With such a sand scraper, hundreds of square metres of sandy outcrop have been cleaned and interpreted in the Meulebeke clay pit (fig. 4.47). After clean up (fig. 4.21a), faults were interpreted (fig. 4.21b) by tracing interruptions of bedding and of alteration patterns that apparently stained the sands before the faulting. Then the bedding was interpreted explicitly as well, in order to have a grasp on relative displacements (fig. 4.21c). A perfect outcrop plane was necessary to easily

distinguish trough cross-bedding from the more pronounced and banded alteration patterns that may be locally parallel with bedding in the small sets. Spring and autumn are the best periods to do such field work in sands. On summer days, the outcrop dries quickly, colour contrasts almost disappear and the prepared surface is blown away before large parts can be photographed.

Outcrop rendering

After preparation and interpretation, the outcrop was systematically photographed. Structural details such as those in fig. 4.22 only make sense as part of a larger picture. In order to accurately render the latter, the outcrop was photographed in parts, the slides were projected, the interpreted lines were copied, and the drawings were assembled to a complete picture of the outcrop. The outcrop parts were photographed as large as possible with a wide angle lens (28 mm), and perpendicularly to the slope. A folding meter arranged in a square angle with one horizontal limb (fig. 4.22) served to check against perspective distortion, which can be severe with a wide angle lens if the camera does not point perpendicularly to the outcrop plane. In addition, the meter was used to reduce the different slide drawings to the same scale. A measuring tape rolled out along the outcrop indicated the relative positions of the drawings. Fig. 4.22 is only one of the twenty-four that were needed to cover and render the structures in fig. 4.26. The latter figure alone has cost four days in the field to prepare, interpret, photograph, measure and sample, and as much time again to draw, assemble, redraw and finish.

In order to render an entire quarry face, it is photographed at regular intervals from along a line parallel to the face. We prefer to use a small telelens (105 mm) and relatively closely spaced photographs in order to restrict perspective distortion. In this manner, the Marke and Meulebeke clay faces have been followed for three years as they receded by exploitation. Thus, the eight sections documented for the Marke clay pit and the twelve sections through the Egem Member in Meulebeke, represented by about 250 slides, possibly could be put together for 3D reconstruction. However, this would require a lot of time and very powerful software to capture the data, do away with distortions, convert to 3D planes in world coordinates, assemble, and model the entire 3D fault network together with the stratification, which is also a complex and interesting affair in the case of the Meulebeke trough cross-bedding (3D facies analysis, palaeocurrents,...).

Koekelberg clay pit Marke, Belgium

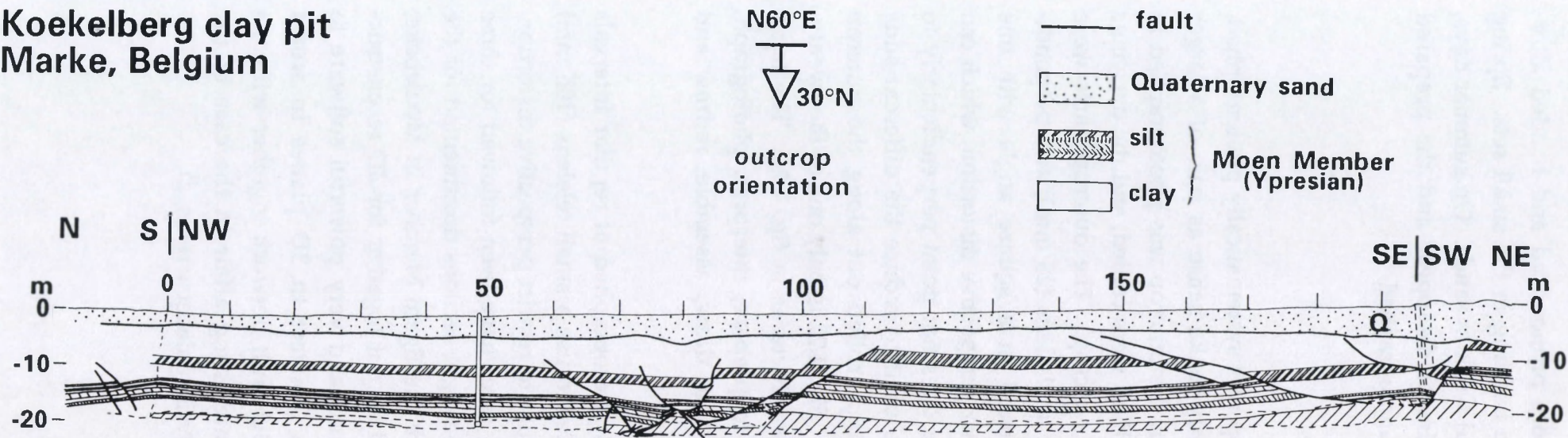
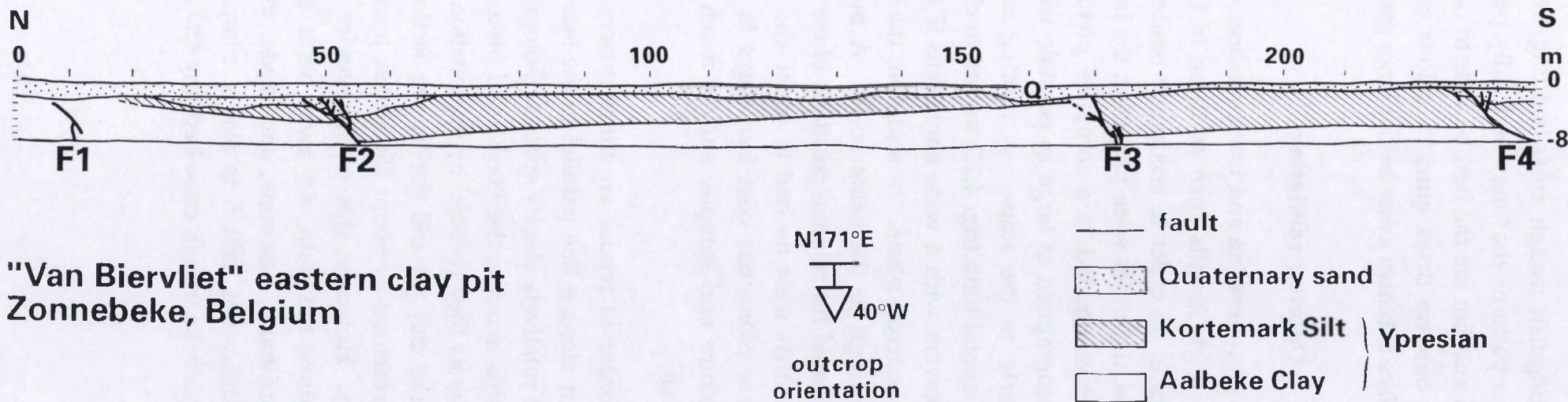


Fig. 4.23a. Overview Koekelberg clay pit in Marke (15.09.90).



"Van Biervliet" eastern clay pit Zonnebeke, Belgium

Fig. 4.23b. Overview "Van Biervliet" clay pit (E side) in Zonnebeke (20.05.91) on the same scale for comparison.

Koekelberg clay pit Marke, Belgium

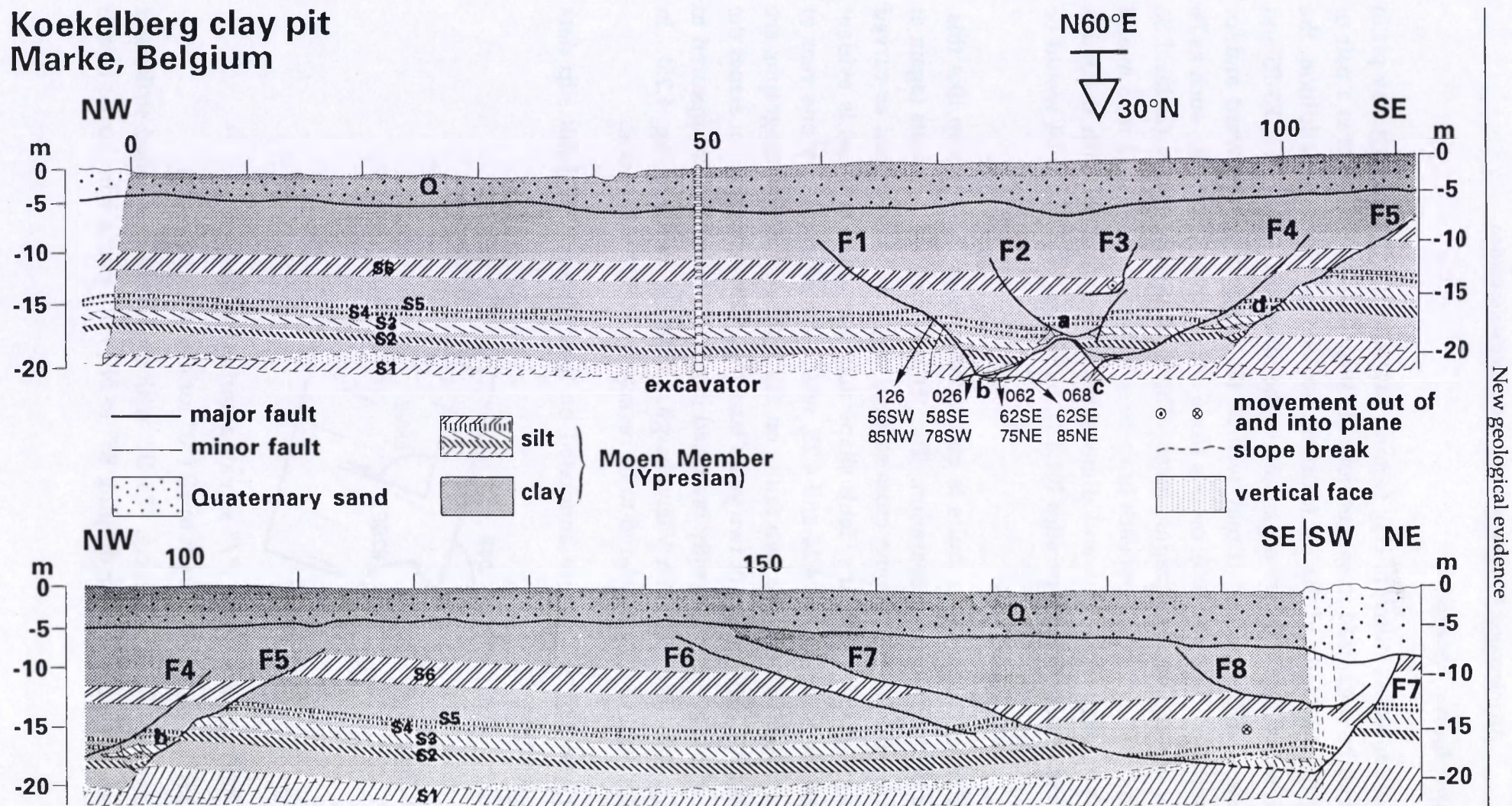


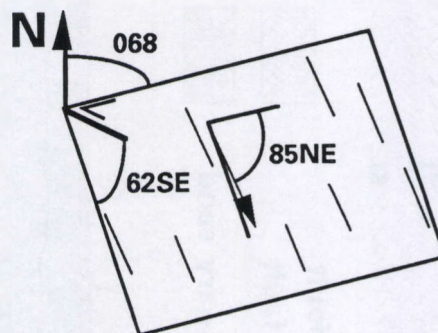
Fig. 4.23c. Enlargement of the two halves of fig. 4.23a, with designation of main faults and reference silty layers, used in subsequent figures. Three faults intersections were visible in this outcrop: **a** (F2/F3), **b** (F1/F3) and **c** (F2/F4). Intersection **a** is enlarged in fig. 4.26-27. **d** is a 'connection structure' between F4 and F5, enlarged in fig. 4.29. (Marke, 15.09.90)

4.2.1.3. Major faults, Marke

On the scale of the entire outcrop, clay tectonic faults in the Koekelberg clay pit in Marke appear to be organized in sets of normal faults (fig. 4.23). There is a pair of faults cutting the NW side of the pit (extreme left of fig. 4.23a). In addition, the faults enumerated in fig. 4.23c are organized in the following sets: F1-F2, F3-F5 and F6-F7, possibly related with F8. It may well be that these are downward and/or lateral (depending on how you look on this slope of 30°) en-echelon sets, such as F6 and F7 clearly are at this stratigraphic level. The total vertical throw (at level S6 and in this arbitrary section) across each of these sets amounts to resp. 2 m, 5 m and 3 m. Their apparent separations and dimensions are compatible with the faults seen on high-resolution seismic profiles (§1.4.1), but faults F1, F2 and F4 would be at the detection limit.

Any other information on these faults is only accessible on an outcrop like this, and then most of it only after preparation. The general shape of the faults (again at the scale of tens of m and in sloping cross-section) can best be described as curved around a straight trend. Laterally, fault shape may vary markedly, as is evident from a comparison between fig. 4.24 and 4.25, which are separated by one year of exploitation or about 10 m. The two faults on the right of these photographs are probably F1 and F2. The section of two years later (fig. 4.23c) shows them across the fault on the left (b), which apparently branched into F3-F5. Fault F1(?) appeared to be listric in fig. 4.24 (see also Van Vaerenbergh, 1987), but was not (fig. 4.25). In addition, the fault at (a) only appeared to be reverse from this view point.

Selected fault orientation data are annotated on the figures. Full fault slip data consist of (see figure) :



1. strike; e.g. "068" means N68°E ("/" signals a horizontal fault);
2. dip; e.g. "62SE" means a dip of 62° to SE ("0" for a horizontal fault);
3. dip of striae on the fault plane; e.g. "85NE" with the above-mentioned strike and dip values means a slip vector dipping 85° to NE on a plane with strike N68°E

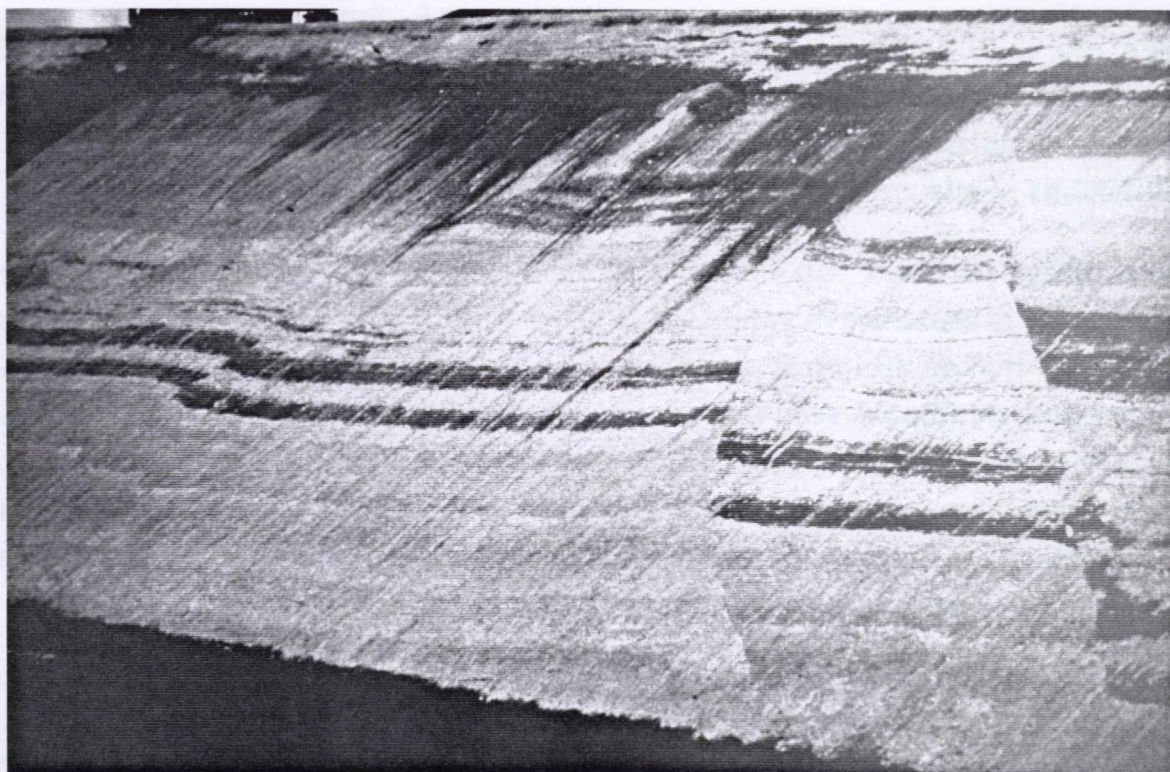


Fig. 4.24. Two curved normal faults, probably en-echelon and corresponding to F1 and F2. Notice rotated horse on F2, a "reverse" fault (a), and a large apparently normal fault (b). (Marke 25.07.87).



Fig. 4.25. Same view as in fig. 4.24, but one year later or about 10 m further SE. The twin faults have changed shape and a horse is now also visible on F1. The apparently low angle fault (left) intersects F1 at the top of the outcrop (Marke 01.06.88).

and dip 62°SE , with the vector direction given by normal/reverse, or sinistral/dextral block movement; “/” means no striae seen or measured; two values behind accolades indicate two sets of striae and therefore two successive directions of slip.

Given these fault and slip orientation data and the orientation of the outcrop slope, which is also always annotated in these figures, the reader is left to convince him/herself that an arbitrarily dipping outcrop plane should in no way be regarded as a vertical ‘textbook’ section perpendicular to the orientation of major faults, which happens to vary widely. Interpretation should proceed very carefully and on the basis of measurements and a study of the details (e.g. §4.2.1.4-8), lest a general drawing like fig. 4.23a remains more akin to an optical illusion than a representative depiction of reality (see also §4.2.3).

4.2.1.4. Intersecting faults, Marke

Fig. 4.26 focusses on fault F3. This fault bifurcates downward several times: once (a) into a listric *splay*¹ (next section), and twice (b and c) towards the intersection with F2.

The intersection itself, enlarged in fig. 4.27, is rather complex. One splay (a) joins the group of splays (d) into which F2 bifurcates towards its intersection with F4 (c in Fig. 4.23c). Another splay apparently curves up (b) towards F2, and is perhaps continuous with a splay of F2. Above the block of S1, F3 bifurcates again (towards c). F2 bifurcates several times downwards with one splay towards the left in this figure and a number of splays towards the intersection. They cut a thin *clastic dyke*² (e) filled with a black gouge. The clastic dykes are therefore older than the clay tectonic faults. Other clastic dykes can be seen around (f). Both clay tectonic faults and clastic dykes are deformed by a second generation of small strike slip faults (e). A host of connection splays and other minor faults are hard to interpret, because they bound fault blocks that are so small that this section, dipping only 30° , may show the lateral rather than the vertical extent and arrangement.

Other intersections that were studied in this outcrop (c and d in fig. 4.23c) look different but are just as complex. F2 and F4 also join through connection splays

¹A *splay* is a fault that asymptotically branches off from another fault (Ramsay & Huber, 1987; their nomenclature includes isolated, diverging, rejoining, connecting and termination splays).

²A *clastic dyke* is a cross-cutting tabular body of sedimentary material (Potter & Pettijohn, 1977). See further in §4.2.1.12 and §4.3.

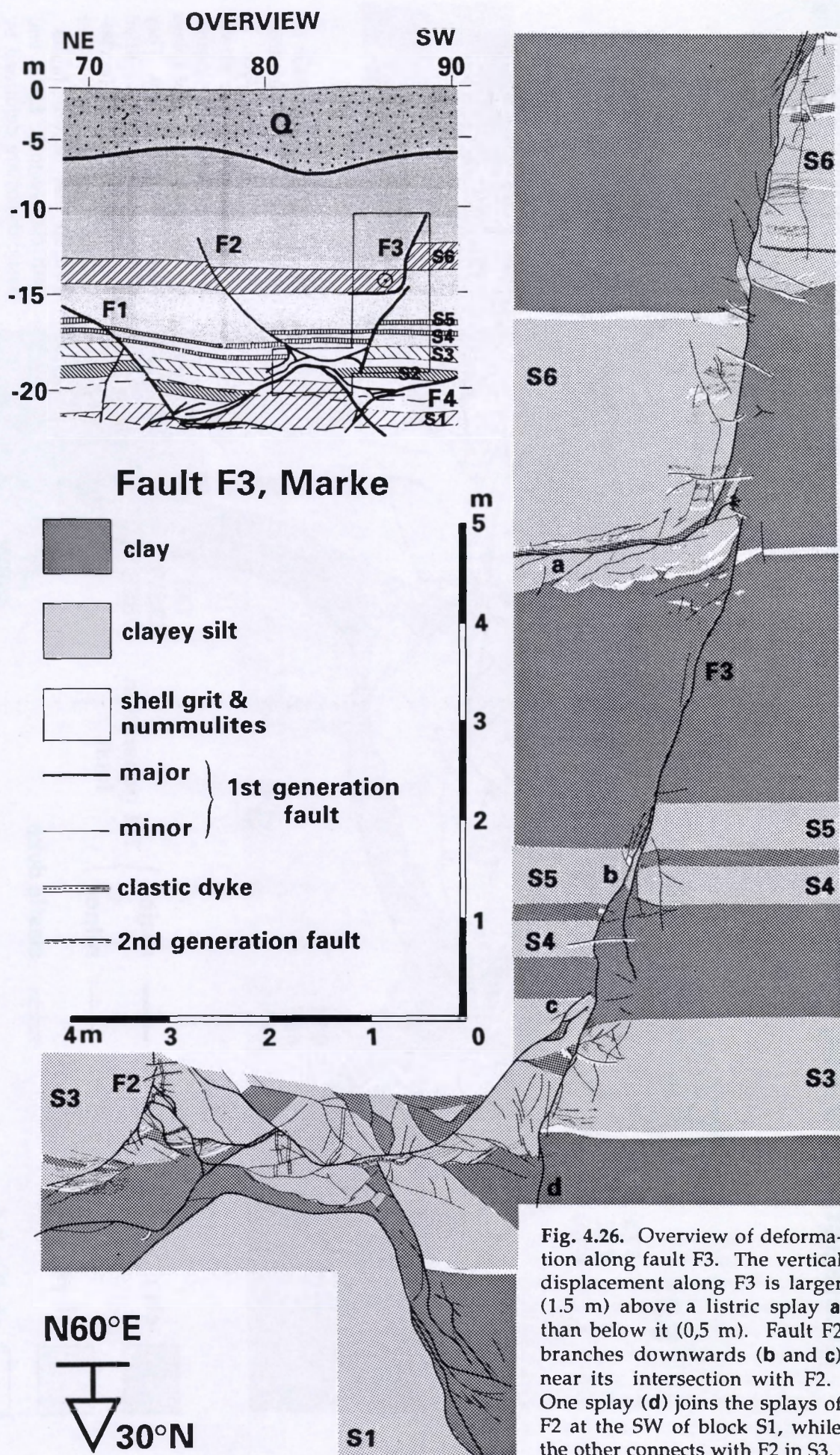


Fig. 4.26. Overview of deformation along fault F3. The vertical displacement along F3 is larger (1.5 m) above a listric splay **a** than below it (0.5 m). Fault F2 branches downwards (**b** and **c**) near its intersection with F2. One splay (**d**) joins the splays of F2 at the SW of block S1, while the other connects with F2 in S3.

Intersecting faults, Marke

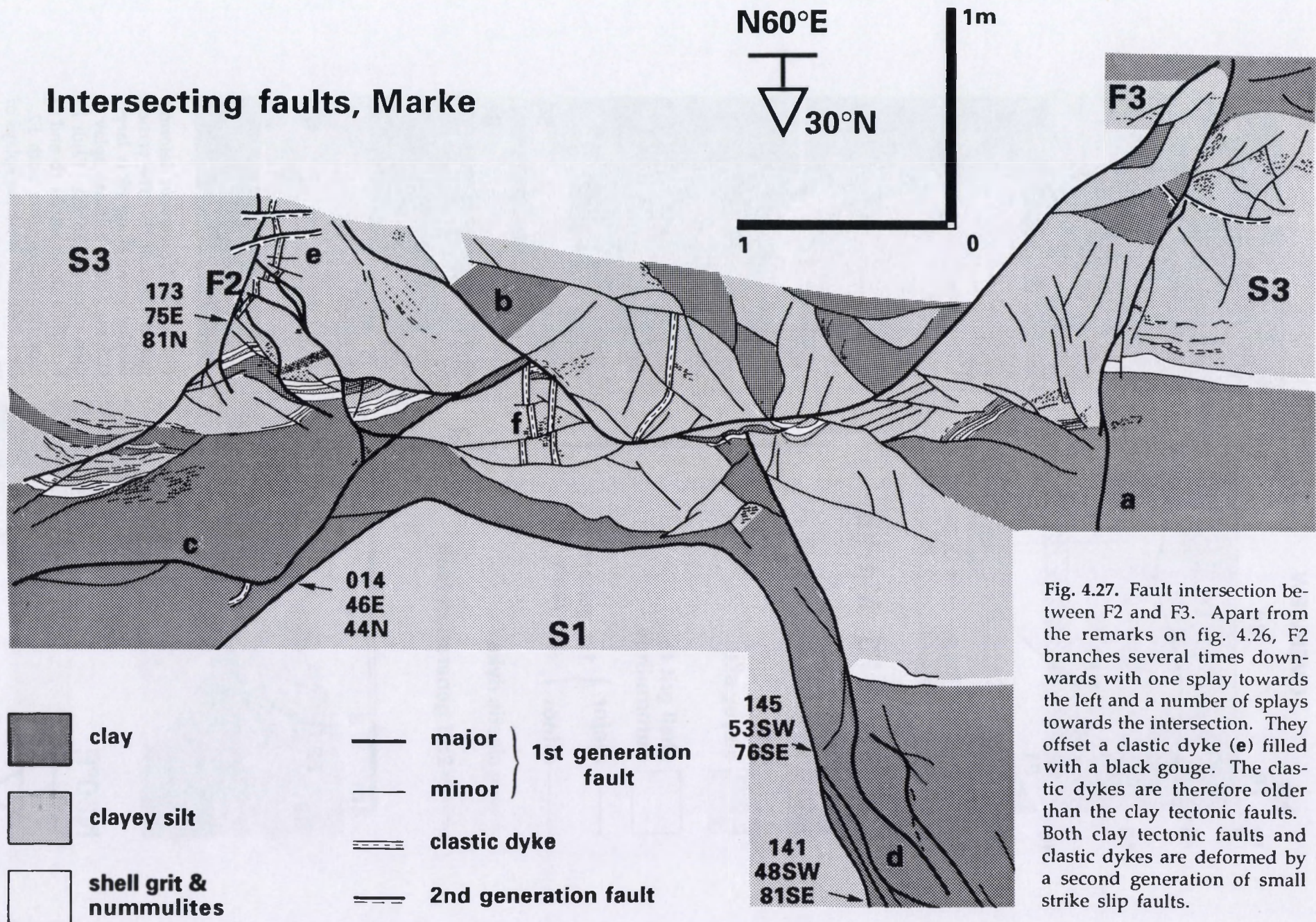


Fig. 4.27. Fault intersection between F2 and F3. Apart from the remarks on fig. 4.26, F2 branches several times downwards with one splay towards the left and a number of splays towards the intersection. They offset a clastic dyke (e) filled with a black gouge. The clastic dykes are therefore older than the clay tectonic faults. Both clay tectonic faults and clastic dykes are deformed by a second generation of small strike slip faults.

above their intersection (c). From the descriptions in §4.2.1.3 and in this section we can at least conclude that thick intervals of Ypresian clay are deformed along a sparse but complex network of major faults and myriad smaller ones that cluster around the major faults.

4.2.1.5. Listric splay, Marke

In fig. 4.26, vertical throw along F3 amounts to 1.5 m¹ at the level of S6, while it measures only about 0.25 m at the level of S4-S5. It was only after preparation that the isolated listric splay was noticed (fig. 4.22). Throw was “lost” along this splay.

The listric splay (fig. 4.28) developed into a horizontal fault in a clayey lamina (a). Two intersecting sets of weakly developed striae could be measured on the horizontal fault (b), signalling two slip directions. The zone around the branch point is deformed by second generation faults (c), but it can be ascertained that most of the throw along F3 at S6 was offset by displacement along the listric splay *after* S4 and S5 had been dislocated.

Another interesting feature in fig. 4.28 are the penecontemporaneous load casts (d) of the base of S6 (a lamina of shell grit) into the underlying clay.

4.2.1.6. Connection structure, Marke

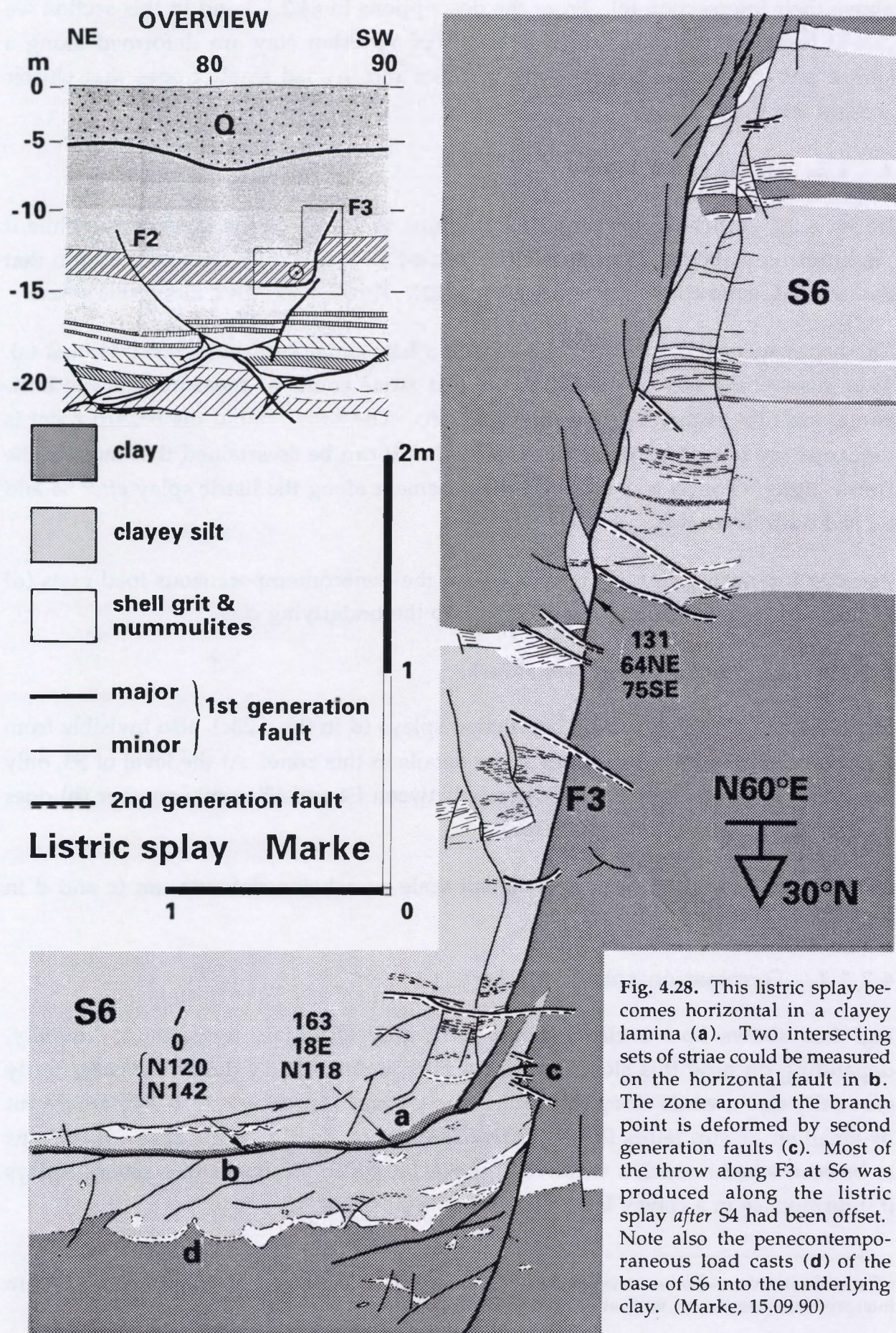
Faults F4 and F5 are linked by connection splays (d in fig. 4.23c), also invisible from a distance. Fig. 4.29 shows some of the details in this zone. At the level of S3, only one splay (a) probably connects directly between F4 and F5, while another (b) does so through several intermediate faults.

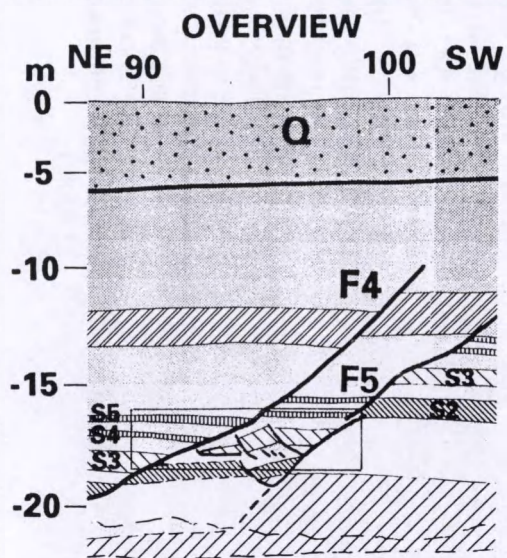
In addition, F4 and F5 both show small scale en-echelon deformation (c and d in fig. 4.29).

4.2.1.7. Termination splays, Marke

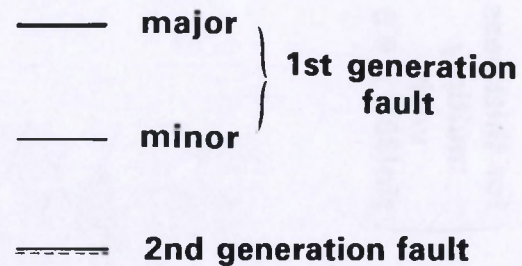
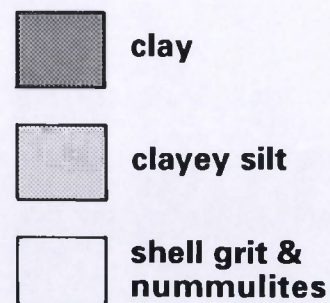
Fig. 4.30 shows how a clay tectonic fault may terminate upwards or laterally, depending on how this sloping outcrop is regarded. Fault throw increases fairly gradually downwards along this fault. The termination splays (a) in silty S6 are cut by small strike-slip faults (b) that affect S6 quite markedly in this zone. It remains to be seen whether such a (relatively) major fault also bifurcates into several splays if it terminates in a clayey layer rather than a silty one.

¹The scale in this and other detailed figures is measured on the outcrop plane, which dips 30°. To interpret thicknesses and vertical distances, multiply with $\sin(30^\circ) = 0.5$.





Connection structure Marke



6m

5

4

3

2

1

0

2 m

1

0

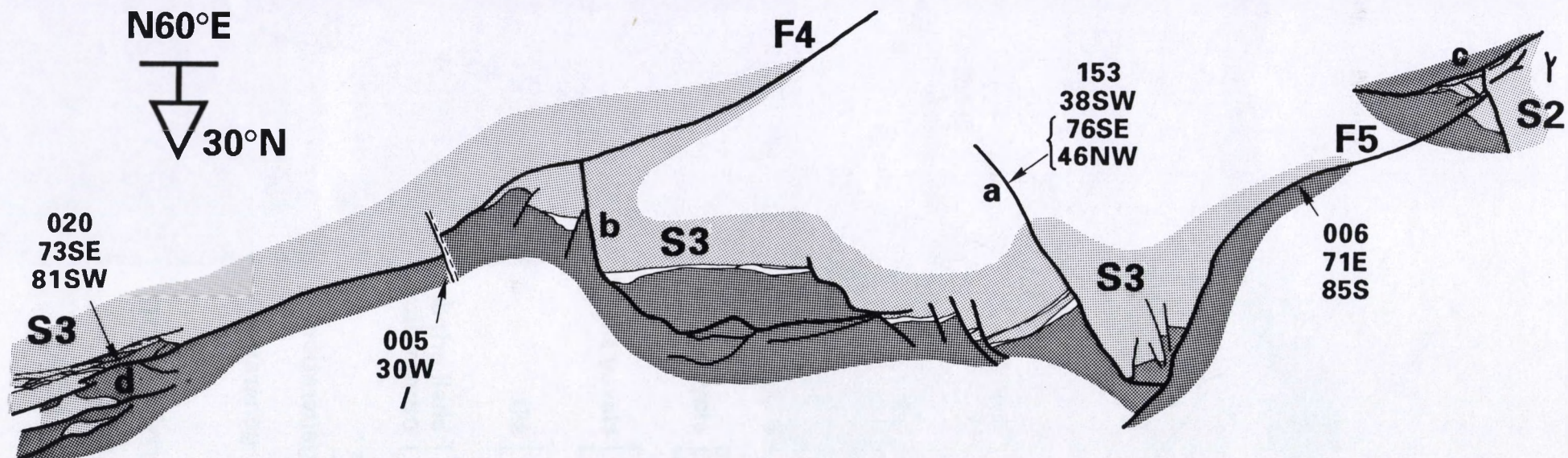


Fig. 4.29. Fault connection structure. Faults F4 and F5 are linked by connection splays. Only one splay (a) probably connects directly between F4 and F5, while another (b) does so through several intermediate faults. (Marke, 15.09.90)

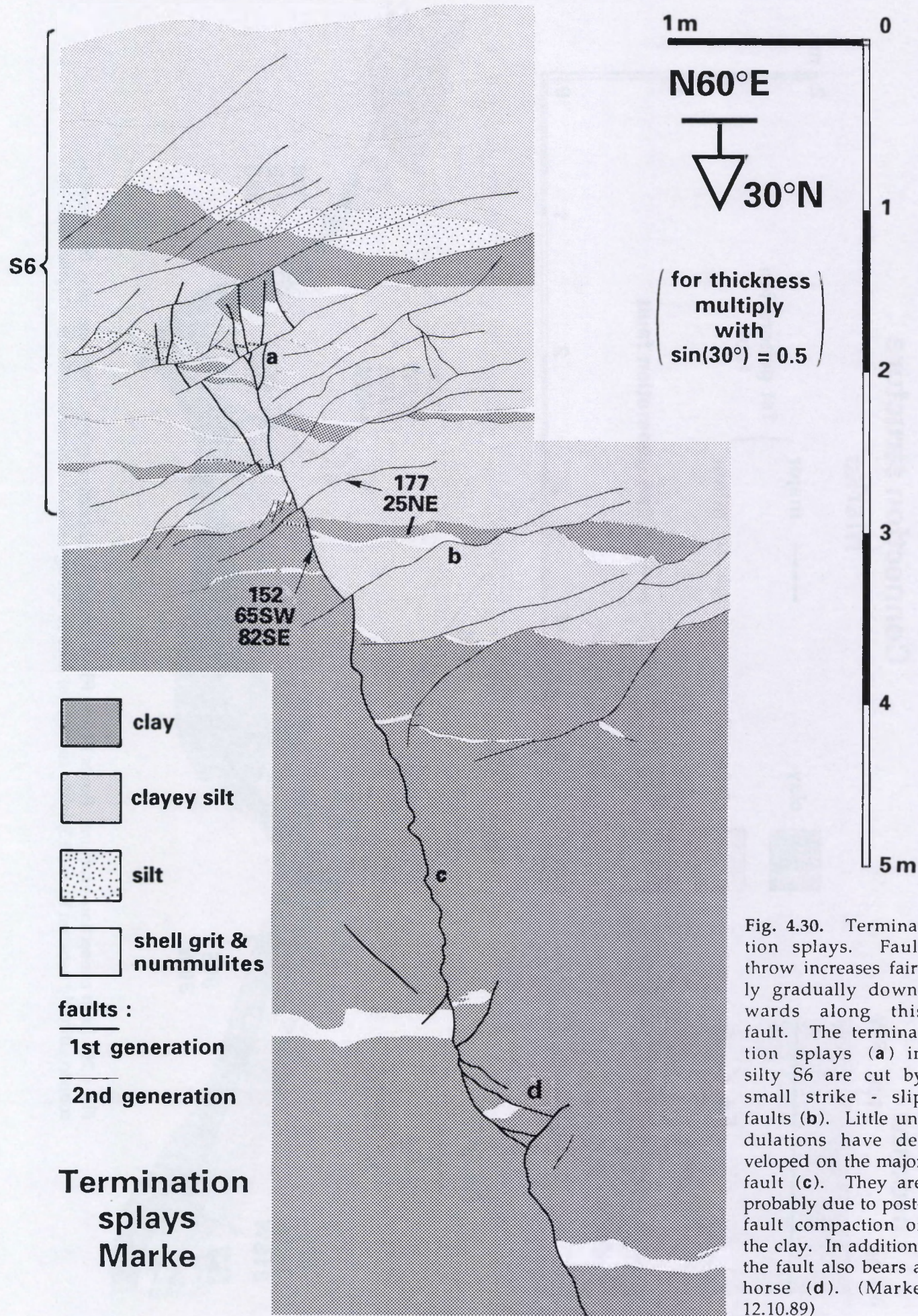


Fig. 4.30. Termination splays. Fault throw increases fairly gradually downwards along this fault. The termination splays (a) in silty S6 are cut by small strike - slip faults (b). Little undulations have developed on the major fault (c). They are probably due to post-fault compaction of the clay. In addition, the fault also bears a horse (d). (Marke 12.10.89)

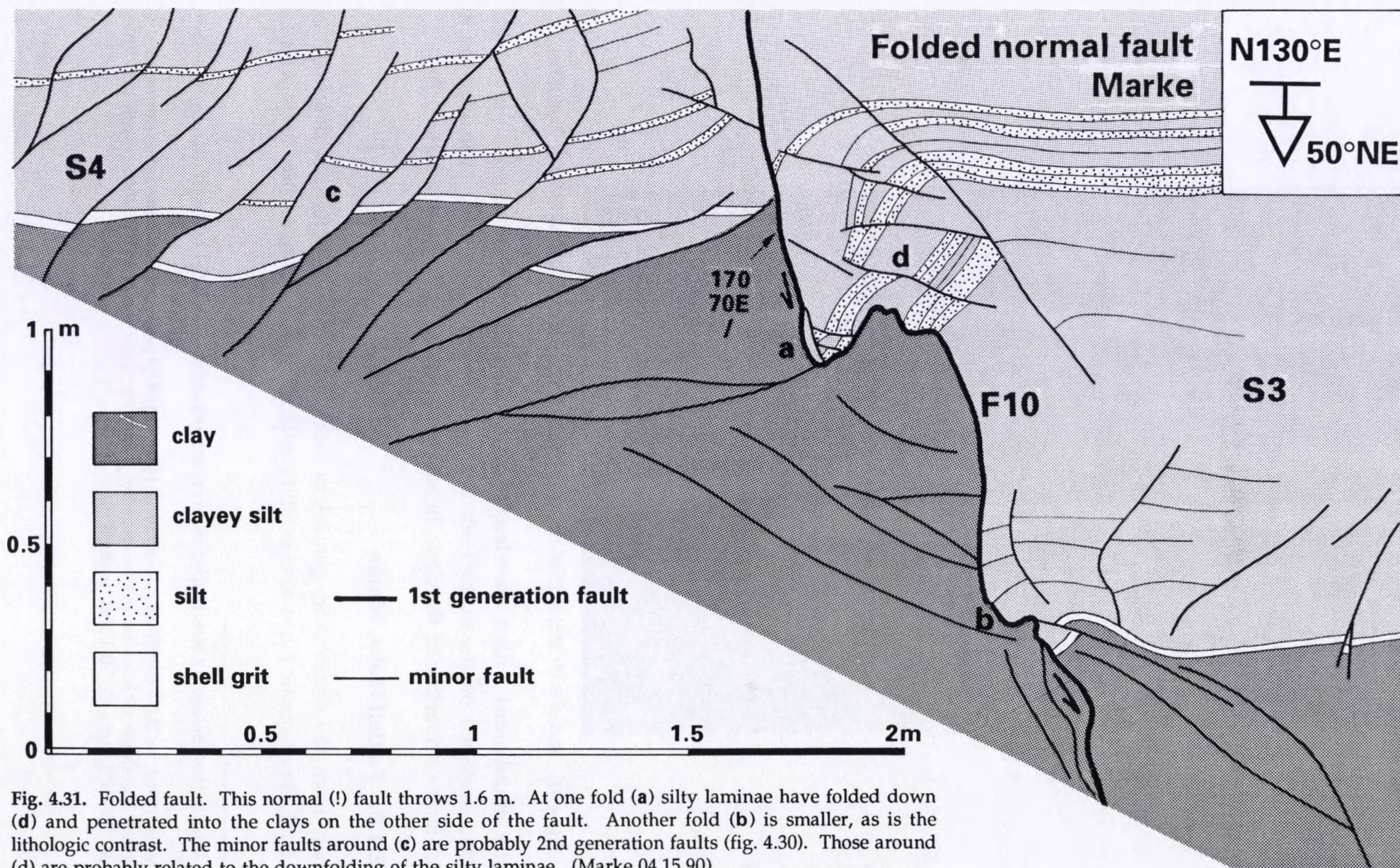


Fig. 4.31. Folded fault. This normal (!) fault throws 1.6 m. At one fold (**a**) silty laminae have folded down (**d**) and penetrated into the clays on the other side of the fault. Another fold (**b**) is smaller, as is the lithologic contrast. The minor faults around (**c**) are probably 2nd generation faults (fig. 4.30). Those around (**d**) are probably related to the downfolding of the silty laminae. (Marke 04.15.90)



Fig. 4.32. Folded fault at S side of clay pit, with exploitation slope below (Marke 04.15.90).

Little undulations with a wavelength of 10-20 cm and an amplitude of a few cm have developed on the major fault in this section (c). They are probably due to post-fault compaction of the clay. In addition, the fault also bears a *horse*¹ (d).

4.2.1.8. Folded faults, Marke

Apart from the decametric, gentle², vertical and lateral undulations described in §4.2.1.3, clay tectonic faults also exhibit localized open to close vertical folds with an

¹ A *horse* in this context is a lens shaped mass of rock bounded on all sides by faults (Ramsay & Huber, 1987).

² Fleuty (1964, in AGI (1980) and Ramsay & Huber (1987)) recommended the following names to describe the shape of folds on the basis of the interlimb angle : gentle (180°-120°), open (120°-70°), close (70°-30°), tight (30°-0°) and isoclinal (0°).

Horse on folded fault, Marke

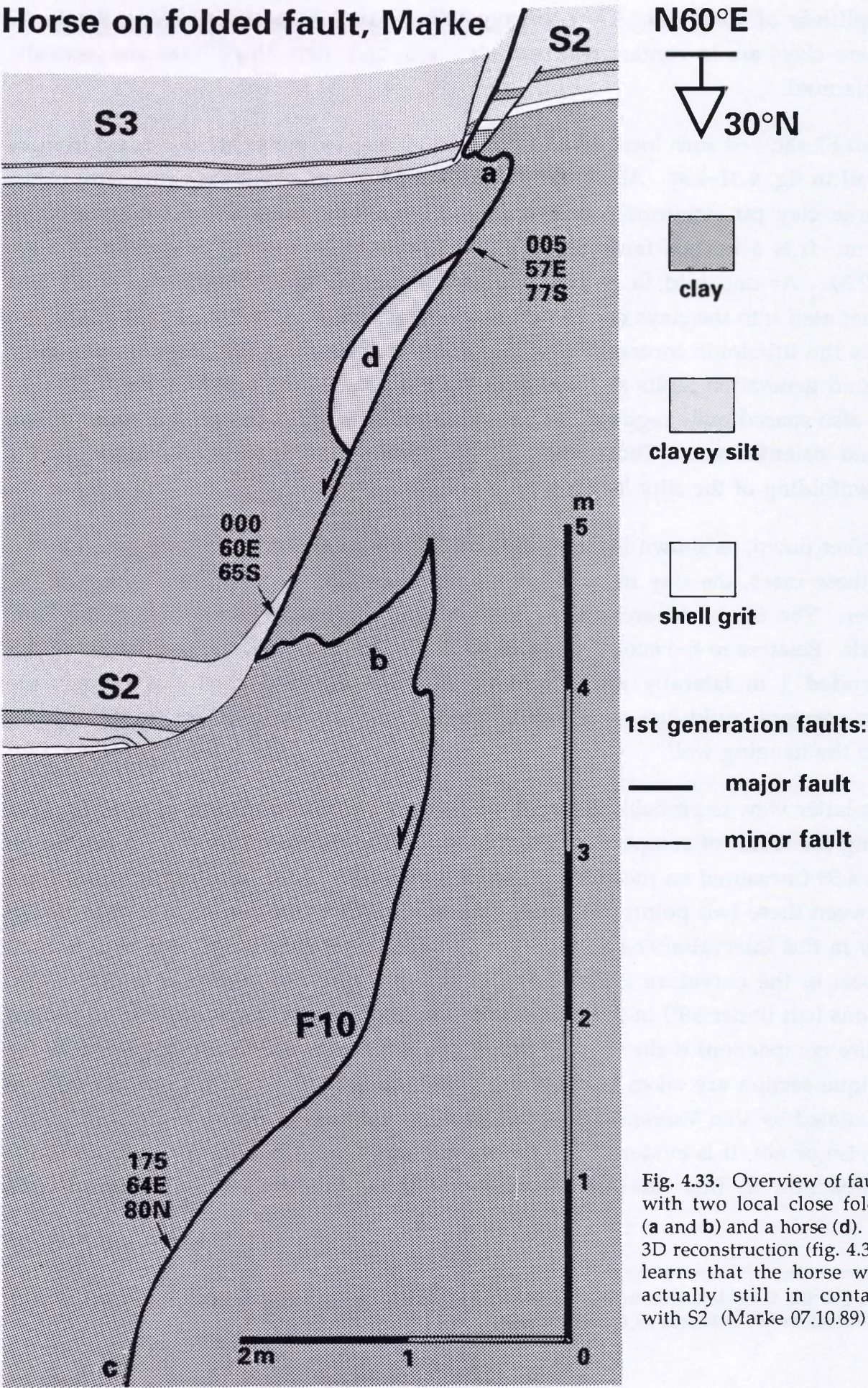


Fig. 4.33. Overview of fault with two local close folds (a and b) and a horse (d). A 3D reconstruction (fig. 4.35) learns that the horse was actually still in contact with S2 (Marke 07.10.89)

amplitude of 10-20 cm. They are typically related to positions along the faults where clays are in contact with silts or clays, and their hinge lines are generally horizontal.

Fault F2 showed such local folds in fig. 4.25. Other examples are described in more detail in fig. 4.31-4.34. All of these figures are sections along the same fault in the Marke clay pit, arbitrarily named F10¹. The throw along this fault amounts to 1.6 m. It is a normal fault, although it appears to be reverse in fig. 4.31-32 (see §4.2.3). At one fold (a in fig. 4.31) silty laminae have folded down (d) and penetrated into the clays on the other side of the fault. Another fold (b) is smaller, as is the lithologic contrast. The minor faults around (c) are probably the same second generation faults as those affecting the termination splays in fig. 4.30: they are also spaced quite regularly and closely, and have small throws and more or less equal orientations. Those around (d) however are probably related to the downfolding of the silty laminae.

Further down, as shown in fig. 4.33, fault F10 displays two more folds (at a and b). In these cases, the clay from one block seems to have flowed into the clay of the other. The tight fold around (b) is the largest one encountered during this field work. Relative to the cut-off point of S2 in the hanging wall, the clay under S2 has intruded 1 m laterally and 0.3 m up into the footwall clay. Of course, the displacement could just as well be described with the footwall above (b) sagging into the hanging wall.

The latter view is probably better in the light of the interpretation of these folds as being the result of compaction after faulting. The distance between (a) and (c) on fig. 4.33 (measured on the outcrop plane) is only 70% of the length of the fault trace between these two points. We may take this value as the compaction ratio of the clay in this interval after faulting. It may be a higher percentage (less compaction) if part of the curvature is attributed to possible gentle vertical and lateral undulations (cut under 30°) in the fault shape prior to folding. It may also be 5-10% less (more compaction) if the present dip of this fault (about 60°) and the skew in the oblique section are taken into account. This compaction ratio is equal to the one calculated by Van Vaerenbergh (1987; §1.3) on the basis of flattened tubular fossils. Precise or not, it is evident from these compaction ratio estimates that most of the compaction in this interval happened *after* the faulting. In other words, the

¹Just like the fault described in §4.2.1.7, this fault was documented at a different time than fig. 4.23, and therefore not indicated in the latter figure.

faulting happened when these clays were clearly undercompacted and much more plastic than they are today.

Considering

1. that the major faults are sparse relative to splays, minor and microfaults,
2. that the major faults accommodated most of the deformation in this outcrop,
3. the high plasticity at the moment of faulting
4. and the conclusions of Maltman (1987; §1.2),

we may also conjecture that the deformation rate was high in such plastic clays.

4.2.1.9. Horses, Marke

Fig. 4.33 also shows a horse (d) on F10. Its silty composition and position implies that it is a part of S2 that glided down along F10. This horse, about 1.4 m long in the outcrop plane and showing evidence of rotation and internal deformation, was specially prepared with alternatively vertical and horizontal cuts like in a flight of stairs (fig. 4.34), and perpendicular to the strike of the main fault. In contrast to the outcrop plane, these are true textbook sections that greatly facilitate interpretation (fig. 4.35-36). The strike of laminae and faults can be read directly from them, and the true dip is easily constructed on a Wulff net (inset in fig. 4.36). The orientation of the laminae for instance was not measured in the field, but it can be verified to be around N140°E, 29°NE(= 23°E in the vertical EW sections).

Fig. 4.35 is a detailed overview¹ of the horse (a) and other features on the major fault. Apart from the close folds above (b), small horizontal undulations can also be tracked in this figure. The clay under the close fold proved to be stained black. A 3D reconstruction learns that the upper branch line of the horse projects above the vertical plane V3 and the base of S3 in the hanging wall. Contrary to what might be concluded from fig. 4.33, the horse was therefore still in contact with S2, the silty layer of which it is probably a piece.

The bedding orientation (fig. 4.36) indicates a rotation of the material in the horse around a horizontal axis, with a component of rotation parallel to the major fault strike and with the expected sense, but also with a component perpendicular to the strike. Faults (a) and (b) form a conjugate set with an internal angle of around 83° in the horse. The axis of this conjugate set almost coincides with the bedding plane, which indicates that these faults are closely related to the rotational defor-

¹The reader is invited to reconstruct the outcrop in 3D with a copy of fig. 4.35bis.

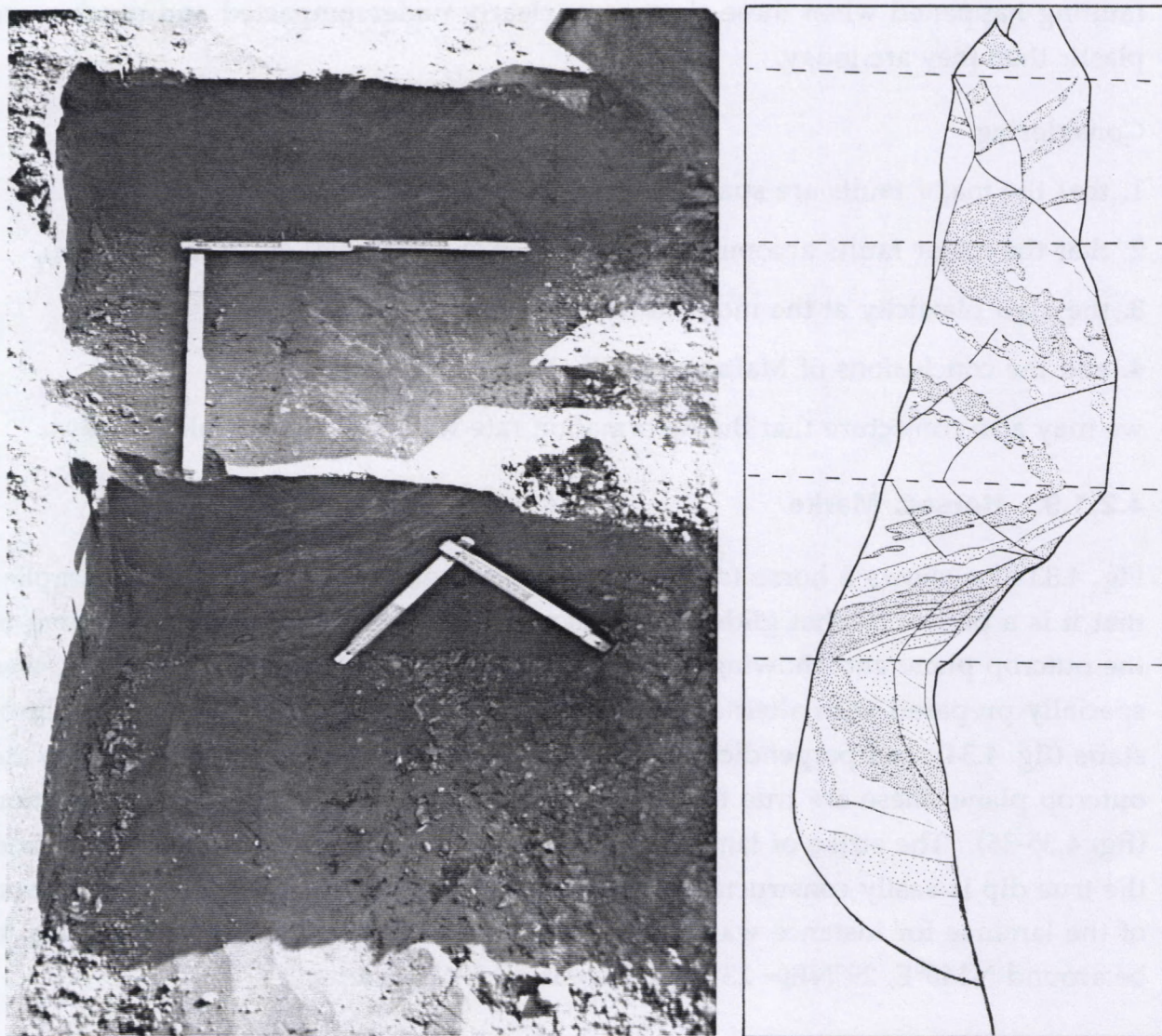
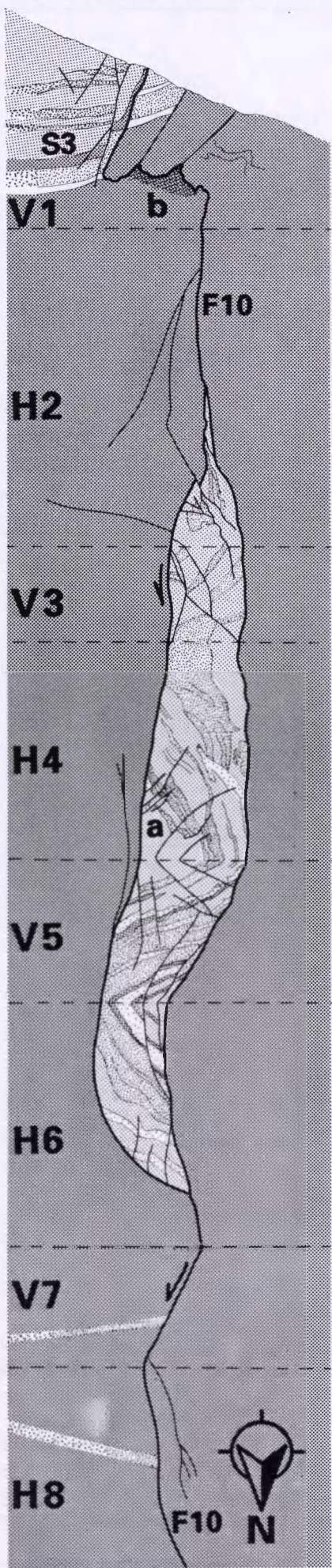


Fig. 4.34. Rotated and deformed horse from fig. 4.33, cut along successive vertical and horizontal sections perpendicular to the main fault strike, to aid interpretation. Interpretation on the right (legend as in fig. 4.35; Marke 05.10.89).

mation of the horse material. The southern end of the horse (c) is more disorderly deformed.

Four horses observed in the Marke clay pit have been 'normalized' to the same dimensions and orientation and brought together in a scheme (fig. 4.37). We remind that the bedding orientation drawn within the horses is an apparent orientation along a section sloping 30° . Interpreting this as a rotation along a horizontal axis parallel with the main fault strike, rotation of bedding in the horses may vary between apparently opposite to fault displacement (a and d), over no rotation (b) to a rotation as expected (c). However, bedding orientation in the horse where they were measured (c and fig. 4.34-36) also indicate a component of rotation



Horse on folded fault Marke

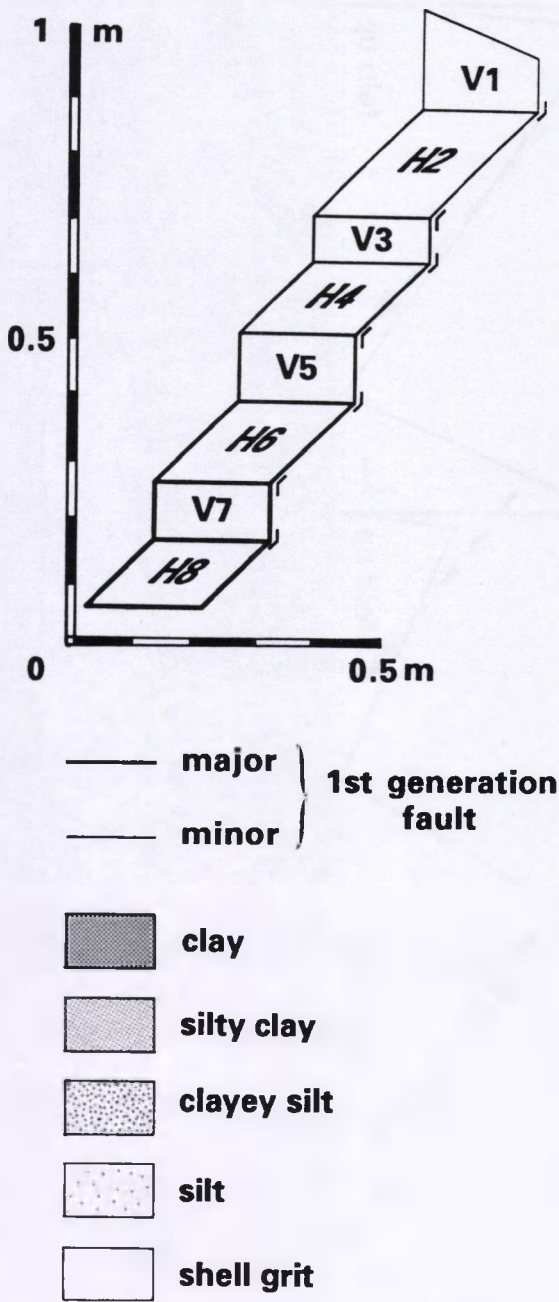


Fig. 4.35. Horse (a) on a locally (b) folded fault. Note the small undulations along the strike of major fault F10, and the rotated beds and conjugate faults within the horse. (Marke 05.10.89)

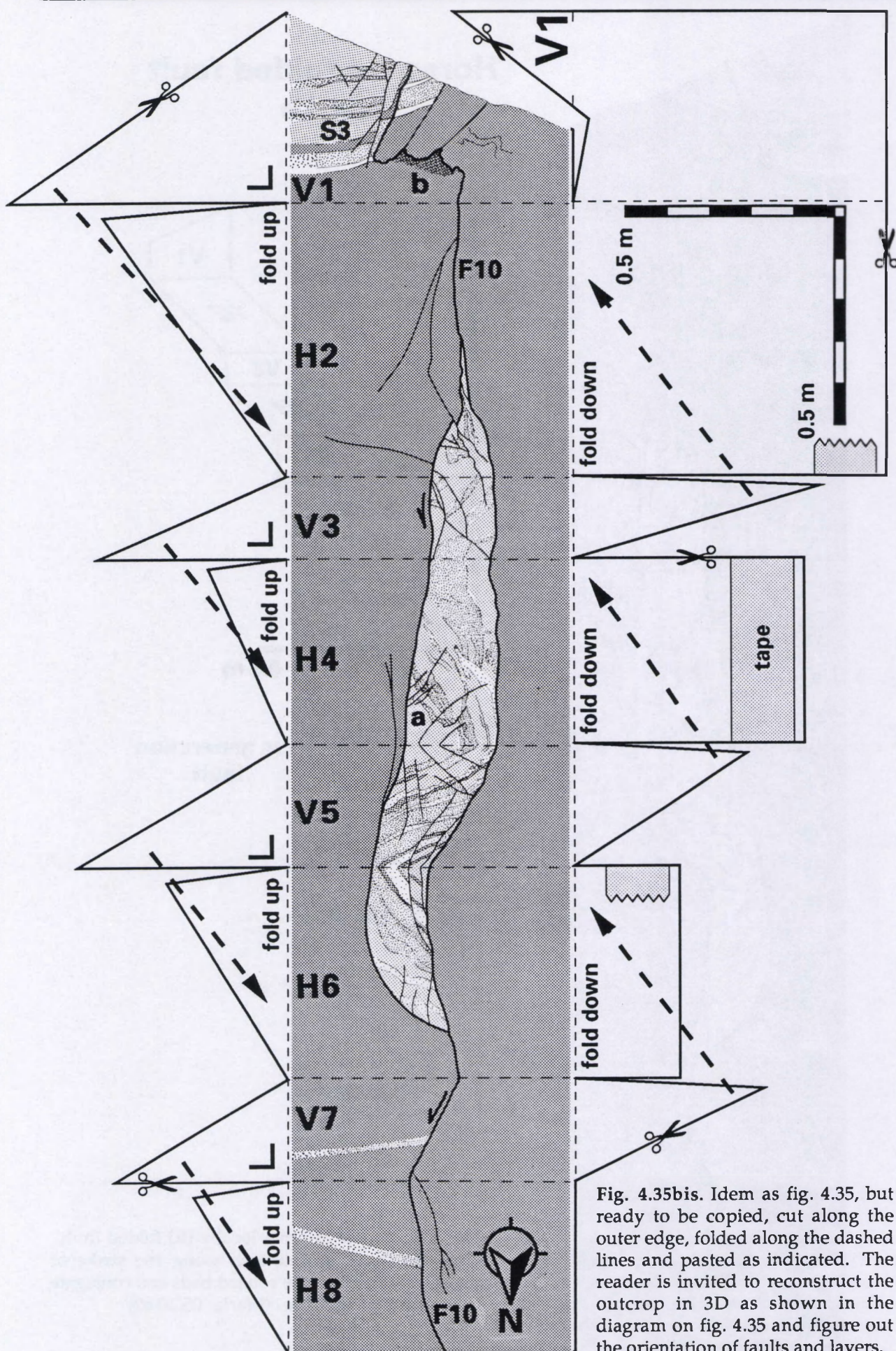


Fig. 4.35bis. Idem as fig. 4.35, but ready to be copied, cut along the outer edge, folded along the dashed lines and pasted as indicated. The reader is invited to reconstruct the outcrop in 3D as shown in the diagram on fig. 4.35 and figure out the orientation of faults and layers.

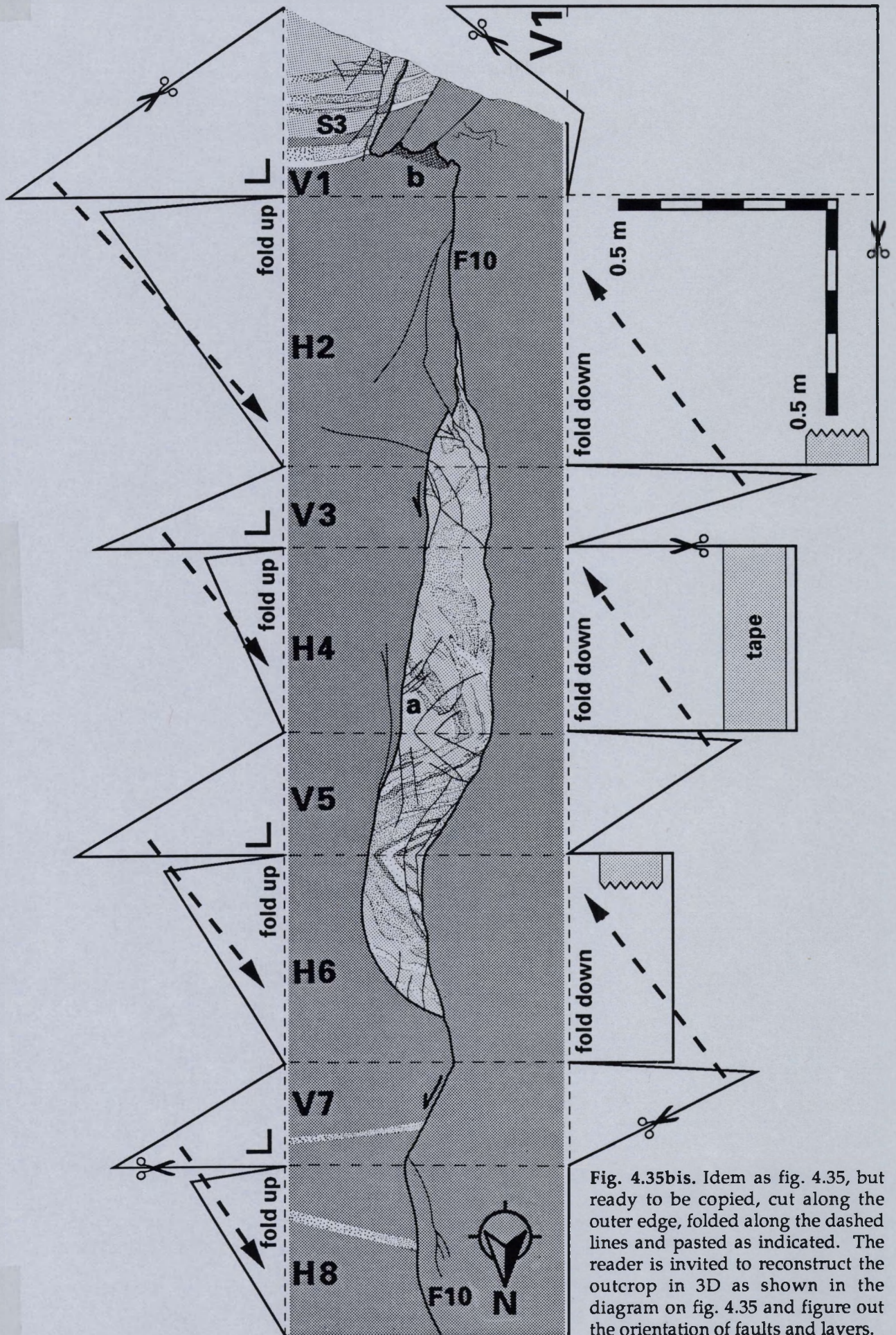
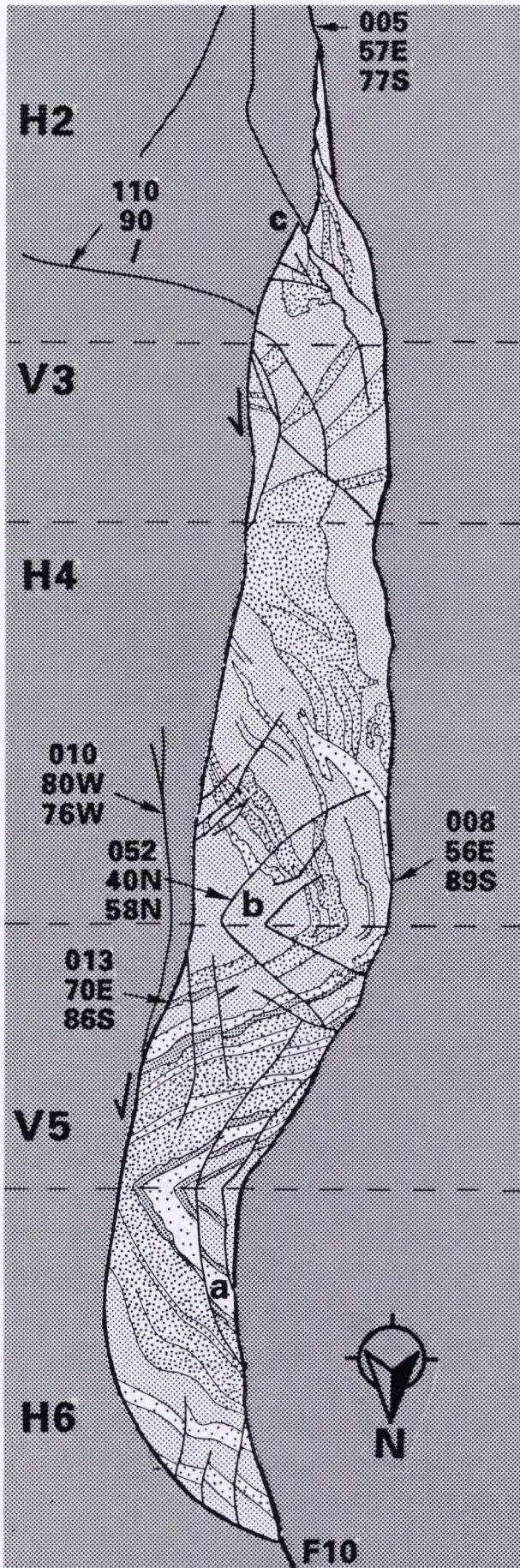
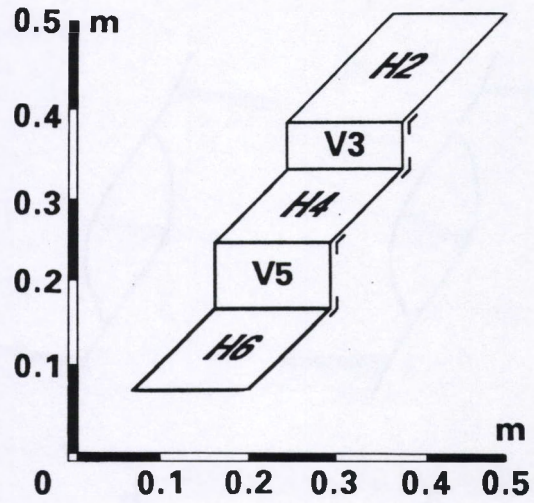


Fig. 4.35bis. Idem as fig. 4.35, but ready to be copied, cut along the outer edge, folded along the dashed lines and pasted as indicated. The reader is invited to reconstruct the outcrop in 3D as shown in the diagram on fig. 4.35 and figure out the orientation of faults and layers.



Horse Marke



— major } 1st generation
— minor } fault

clay clayey silt
silty clay silt

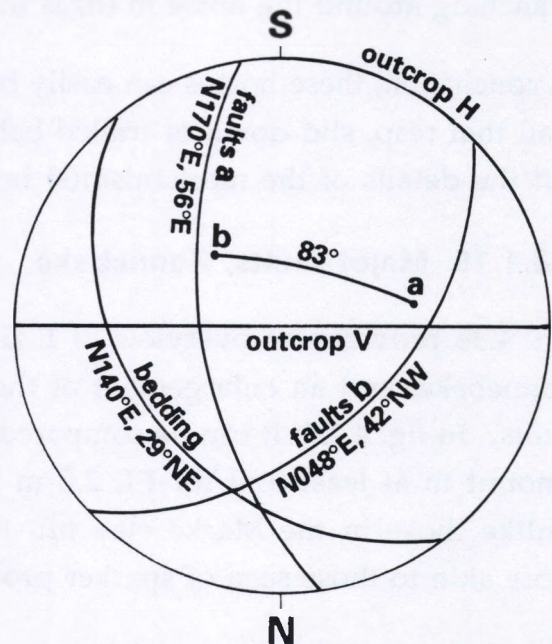


Fig. 4.36. Horse on major fault F10, with Wulff net (LH) showing the average orientation of rotated bedding and fault sets *a* and *b*. These are clearly conjugate faults. The southern end of the horse (*c*) is more disorderly deformed. (Marke 05.10.89)

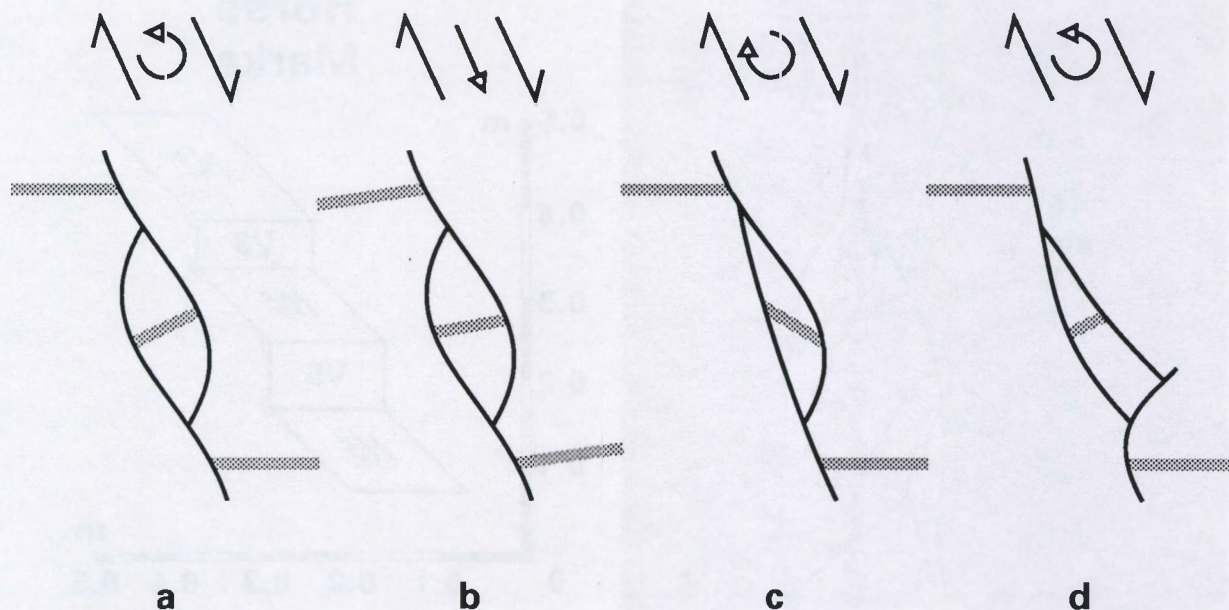


Fig. 4.37. Scheme of some clay tectonic horses observed in the Marke clay pit. Black lines are faults, grey ones indicate a marker horizon. Horse **a** is from fault F2 in fig. 4.24, horse **b** from fault F1 in fig. 4.25, horse **c** from fault F10 in fig. 4.34-36 and horse **d** from the main fault in fig. 4.30.

around a horizontal axis perpendicular to the main fault strike. It may be that the southern part of the horse simply got stuck or slipped slower due to lateral differences of friction. To complicate interpretation even more, the type of fault branching 'above' and 'below' horses appears to vary as well (fig. 4.37). Fault branching around the horse in (d) is most peculiar.

In conclusion, these horses can easily be interpreted as a part of the foot or hanging wall that resp. slid down or trailed behind for some part of the fault displacement, but the details of the mechanism(s) involved remain elusive.

4.2.1.10. Major faults, Zonnebeke

Fig. 4.38 provides an overview of E side of the eastern "Van Biervliet" clay pit in Zonnebeke, and an enlargement of the two parts of this slope with major normal faults. In fig. 4.23b it can be compared with the outcrop in Marke. Vertical throws amount to at least 5 m for F1, 2.5 m for F2, 5 m for F3, and at least 2 m for F4. Unlike those in the Marke clay pit, these faults are isolated, and they are even more akin to those seen of sparker profiles. Their orientations vary widely.

Clastic dykes with a black gauge were observed on both sides of F1 (§4.2.1.12). F2 and F4 also cut the base of the Quaternary mantle, indicating a Quaternary reactivation that added some throw along these faults (§4.2.4).

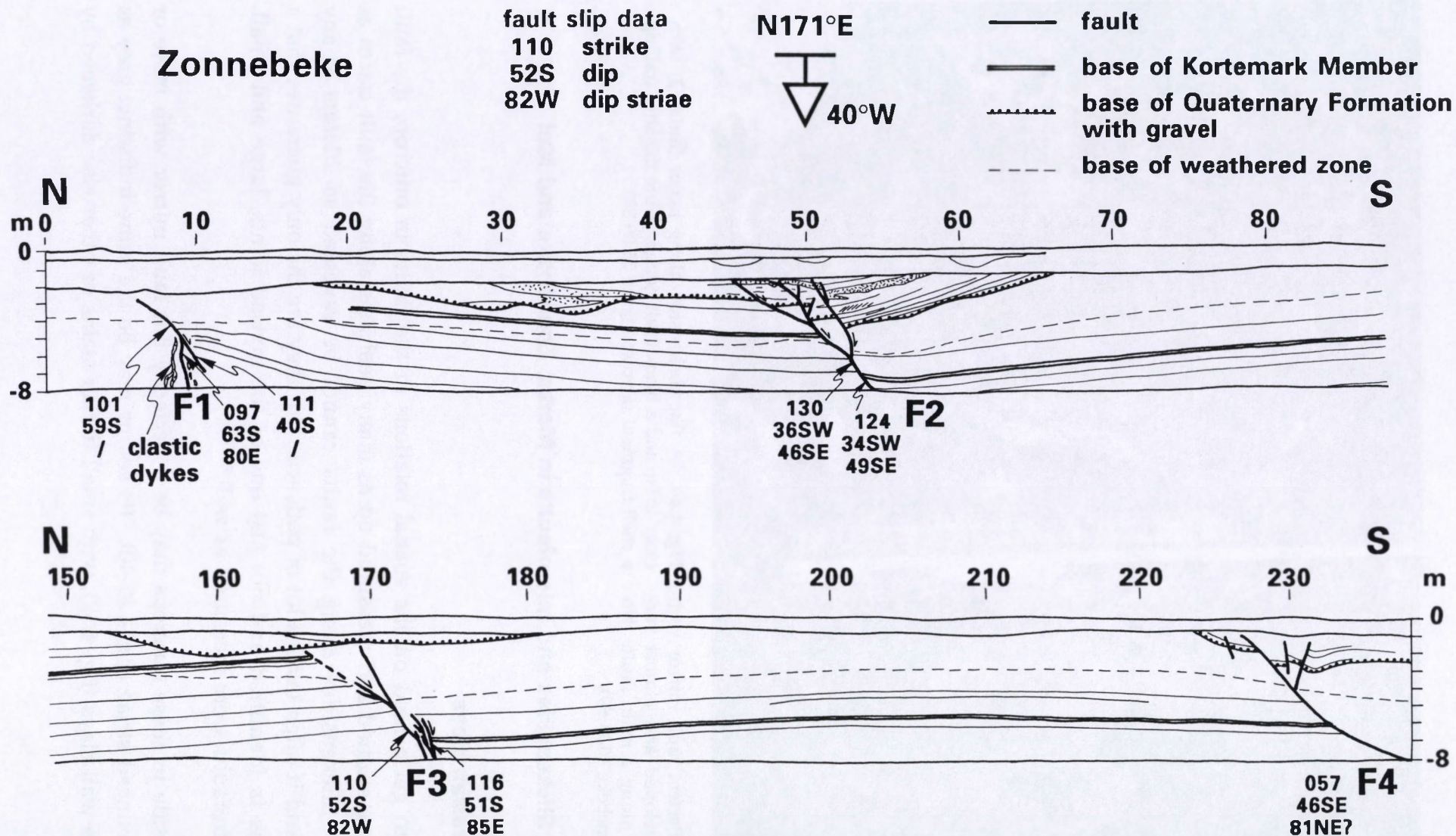


Fig. 4.38. Two parts of E side of the “Van Biervliet” clay pit in Zonnebeke, with faults (overview in fig. 4.23b). Selected orientation data and arbitrary names annotated at four major faults. Note the clastic dykes on both sides of F1, the reactivation of F2 and F4 during the Quaternary, and another ‘reverse’ splay fault at F4 (Zonnebeke 20.05.91).



Fig. 4.39. Perfect fault mirror with weakly developed and almost vertical striae, along a main fault. No gouge. (Zonnebeke 16.11.89).



Fig. 4.40. A flat slickenside along major fault F2, with clear striae and a black fault gouge. Note the stria trailing a shell fragment (arrow; Marke 25.09.89).

4.2.1.11. Slickensides and microfaults in Marke, Zonnebeke and Mol

Ypresian clays

In order to get a hold on the spatial relations of the faults in outcrop, the fault planes were studied and measured on as many positions along the fault traces as possible. Slickensides along the faults cannot be revealed *ad libitum* at any position, and it often takes a lot of patience. But they are the only guarantee that a fault plane is identified and not just one of the myriad joints, large and small. Many microfaults were measured as well.

A slickenside in these outcrops may be a perfectly flat fault mirror with more or less pronounced striae (fig. 4.39-40). Its colour may be the same indistinct grey as that of the wall clays (fig. 4.39), with small darker stains or otherwise darkened by



Fig. 4.41. Flat slickenside with striae in two directions (Marke 04.10.89).



Fig. 4.42. Undulating slickenside, affected by perpendicular shearing (Marke 04.10.89).

the shearing, reorientation and compaction of clay particles along the fault plane, or black by the presence of a gouge (fig. 4.40). Several slickensides displayed two intersecting sets of striae (fig. 4.41) indicating relative movement of blocks in successively different directions along the same fault. The steps in the slickenside of fig. 4.42 are reminiscent of the Riedel¹-type splays observed by Petit and Laville (1987) in hydroplastically² faulted, incompletely lithified sands in the High Atlas Mountains (Morocco). In this case however, the steps are the result of later shearing perpendicular to this fault plane. The undulations on slickenside may be due to this shearing and deformation by compaction. They may also have been present already at the time of faulting.

¹A *Riedel shear* is a slip surface which develops during the early stage of shearing. Such shears are typically arranged en-echelon, one set oriented at an angle of 10-15° to the direction of relative movement and the underlying shear surface, and a second set oriented 75-80° to this direction (AGI, 1980; Ramsay & Huber, 1987).

²*Hydroplasticity* is plasticity resulting from the presence of pore water and absorbed water films in a sediment, so that it yields easily to changes of stress (AGI, 1980; see also §1.2).



Fig. 4.43. Curved microfault with downwards diverging striae (Marke 19.10.89).

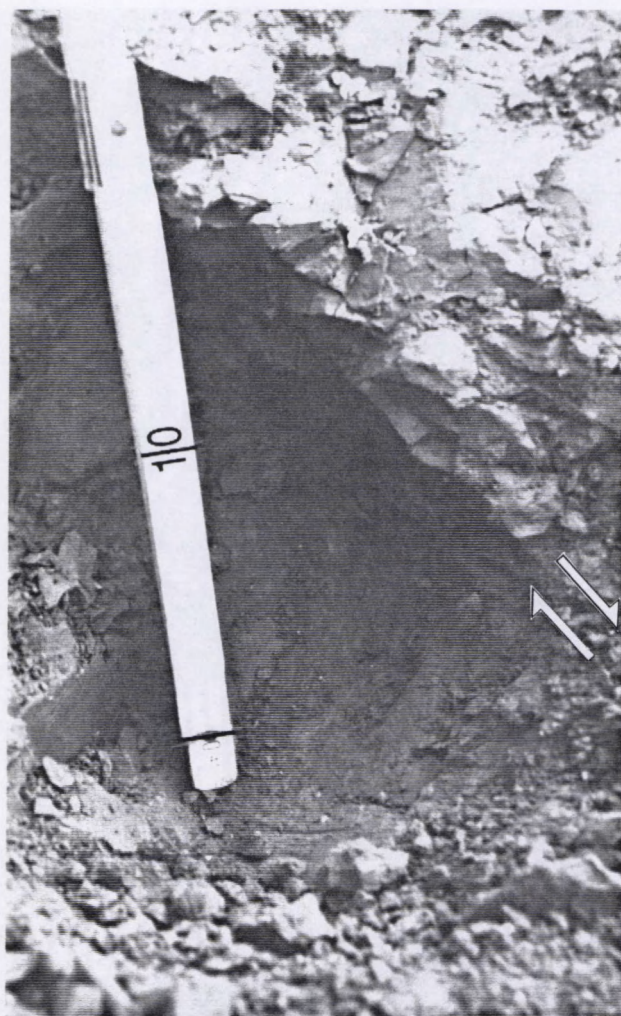


Fig. 4.44. Riedel splay in the footwall of a major fault (Marke 15.10.89).

The isolated microfault in fig. 4.43 is typical for many such faults, and comparable to the hydroplastic microfaults described in detail by Guiraud and Séguret (1987) in the Soria basin (northern Spain). The downwards diverging striae on this microfault indicate that the fault plane was curved when the displacement took place. Because the associated slip vectors diverge around a vertical axis on the same fault plane, a vertically oriented principal stress can be induced directly (see also §4.2.2).

Some microfaults are related with major faults as Riedel shears. In hard rock, Riedel shears are straight slip planes (e.g. Petit & Laville, 1987), but in clays they become listric due to plastic deformation in the shear zone (Morgenstern & Tchalenko, 1967; Maltman, 1987). For example, the Riedel splay in fig. 4.44 has a horizontal axis of curvature parallel with the main fault. The listric splay diverges downwards from the main fault into the footwall. It thereby indicates vertical and normal relative movement along the main fault, ascertained by striae. According

to Maltman (1987) such listric Riedel splays can take up a large part of the shear along the main fault.

Rupelian clay

No faults have been reported in outcrops of Rupelian clay in northern Flanders, except for one detected around the clay diapir and modelled in §4.1.3. No slickensides have been observed either, except in a test tunnel at a depth of about 200 m under the Nuclear Research Centre (SCK) in Mol (Belgium; fig. 1.1). The slickensides there are almost identical in appearance to those seen along some of the main faults in Marke, and without a (black) gouge. There are two possible explanations. One explanation relates the slickensides to the regional extension accompanying the still active Rhine Graben. The most southwestern fault parallel to this graben that has been mapped by Demyttenaere (Demyttenaere & Laga, 1988) passes several kilometres W of Mol. Another explanation is that the larger burial depth and consequently larger overburden than e.g. in the Antwerp area may have induced deformations in Rupelian clays similar to those in Ypresian clays. Systematic measurements of slickensides would rule out one explanation or the other (§4.2.2). Careful stratigraphic analysis would reveal the amount of throw and hence give an idea of the extension of these faults. Such a study falls outside the scope of this thesis, however.

4.2.1.12. Clastic dykes, Marke and Zonnebeke

Clastic dykes filled with a black gouge traverse the bedding of Ypresian clays and silts at least in the Moen Member (Marke) and the Aalbeke Member (Zonnebeke). They have been observed in close juxtaposition with major clay tectonic faults. The clastic dykes in fig. 4.45 were observed next to F1 in fig. 4.38 (Zonnebeke), and those in fig. 4.46 next to F2 in fig. 4.27 (Marke). In fig. 4.45a, the clastic dyke seems to have a diffuse connection with fault F2, one of the major faults with a black fault gouge.

Slickensides have been observed along some of the clastic dykes in Marke, indicating some shearing that is also visible by bed displacements of a few cm. Those in fig. 4.45a and 4.46 show no macroscopic evidence of shearing at all. None of the clastic dykes is flat. They are generally curved, possibly folded by later compaction, and branch in a complex way. They are invariably cut by later faults (fig. 4.27 and 4.46) and their emplacement should therefore be ascribed to an early phase of deformation. Their thickness is rarely larger than 1cm, but it locally reaches 2-3cm.

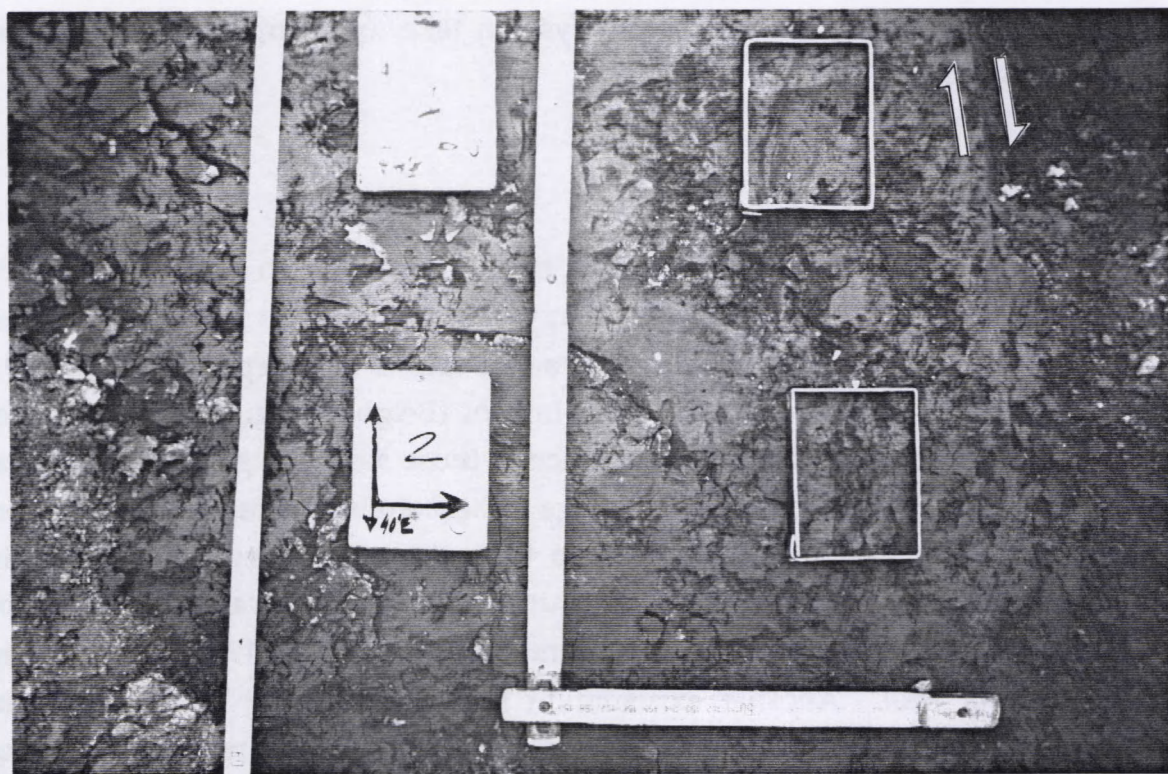


Fig. 4.45. Box samples on black clastic dyke, next to major fault F1 (Zonnebeke 05.06.90).

The literature on clastic dykes abounds. Charles Darwin (1851, p. 423) saw some in tuffs during his travels in Patagonia in 1833, and called them 'pseudo-dykes'. Shrock (1948) reviewed the early literature and Allan (1982) the more recent publications. A clastic dyke is a type of sedimentary dyke, a relatively new and more general name. The American Geological Institute (1980) gave a full definition of a sedimentary dyke: "a tabular mass of sedimentary material that cuts across the structure or bedding of pre-existing rock in the manner of an igneous dyke. It is formed by the filling of a crack or fissure from below, above, or laterally, by forcible injection or intrusion of sediments under abnormal pressure (as by gas pressure or by the weight of overlying rocks, or by earthquakes), or from above by simple infilling". Sedimentary dykes thought to be formed by the latter process are also known as Neptunian dyke or sedimentary vein. Those thought to arise from forcible injection or intrusion are variably known as injection dykes, sandstone dykes, pebble dykes or clastic dykes. The latter name is the most neutral and by far the most popular one.

The AGI definition succinctly raises the question of origin. Considering that the clastic dykes traverse large sections of Ypresian clays and the later deformation, it is clear that they cannot be interpreted as sedimentary veins. Revealing the driving force behind the injection of the black gouge would provide an answer to the question of upwards fluid movement raised in our working hypothesis (§1.4.4) and

thereby greatly improve our understanding of the early history of these Ypresian clays. A number of undisturbed and oriented box samples and many disturbed tube samples were taken for this purpose (fig. 4.45-46), and subjected to diverse analyses (§4.3).

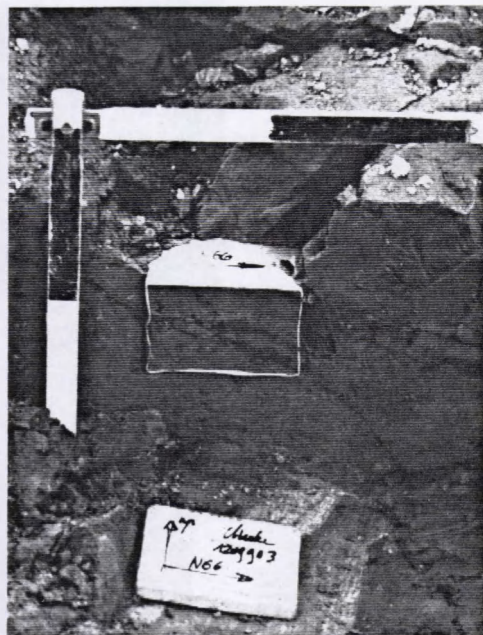
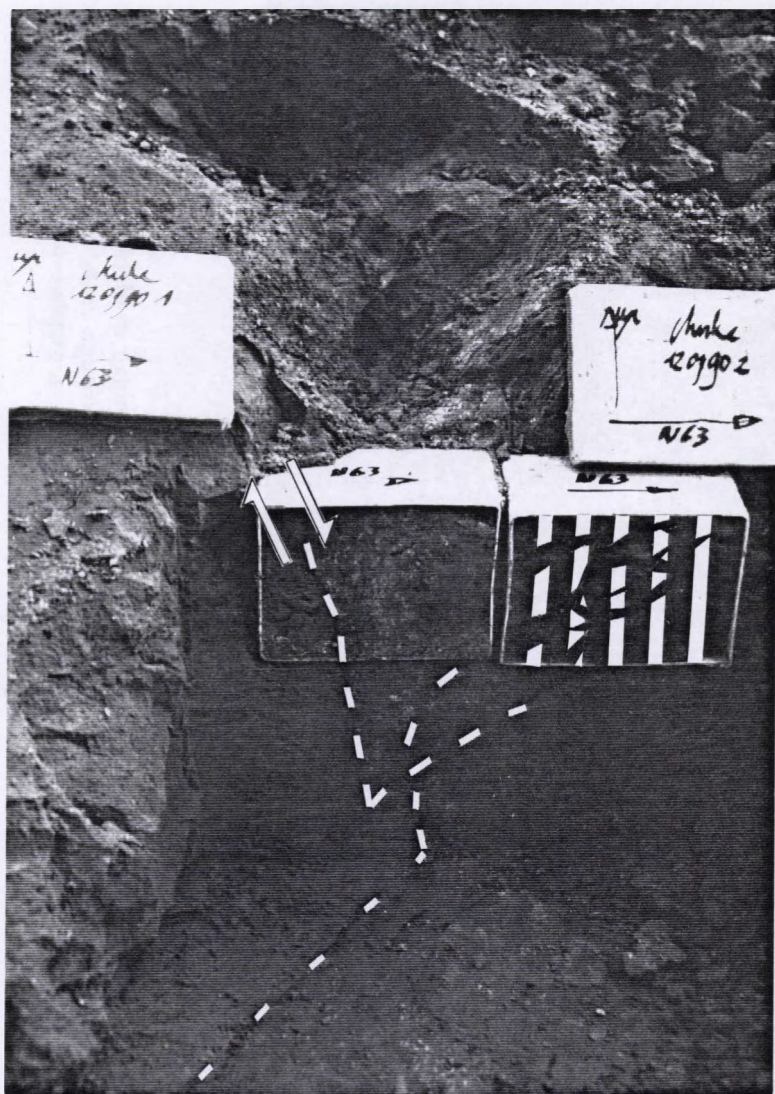


Fig. 4.46a(left). Box sample 120990/1 on a downfolded shell grit and nummulitic lamina and across F2 with a thin black gouge, and box sample 120990/2 on an irregular clastic dyke, also with a black gouge, that has a diffuse connection with the fault gouge (Marke 12.09.90; see fig. 4.65).

Fig. 4.46b(top). Box sample 120990/3 on a branching clastic dyke with black gouge, close to F2 (Marke 12.09.90)

4.2.1.13. Faults in Egem Member, Meulebeke

The photographs in fig. 4.47 constitute a panoramic view on part of the Egem Member in the "Ostyn" clay pit in Meulebeke. This is the uppermost of two exploitation faces, exposing over a length of almost 100 m about 8 m of the Egem Member and cryoturbated (convoluted) Quaternary sands of up to 1 m thickness. At the S end of this slope, there is a superposition of (from bottom to top) 1 m of

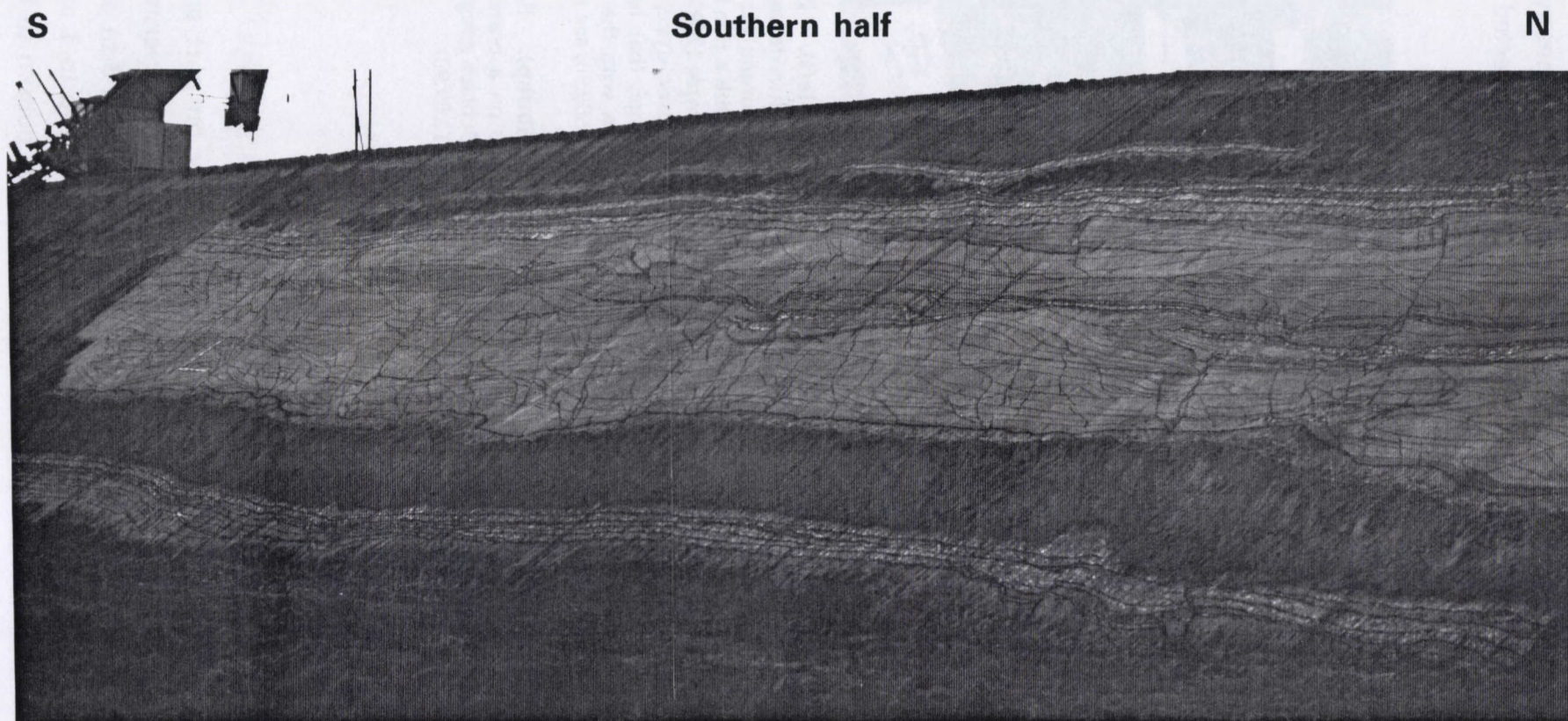
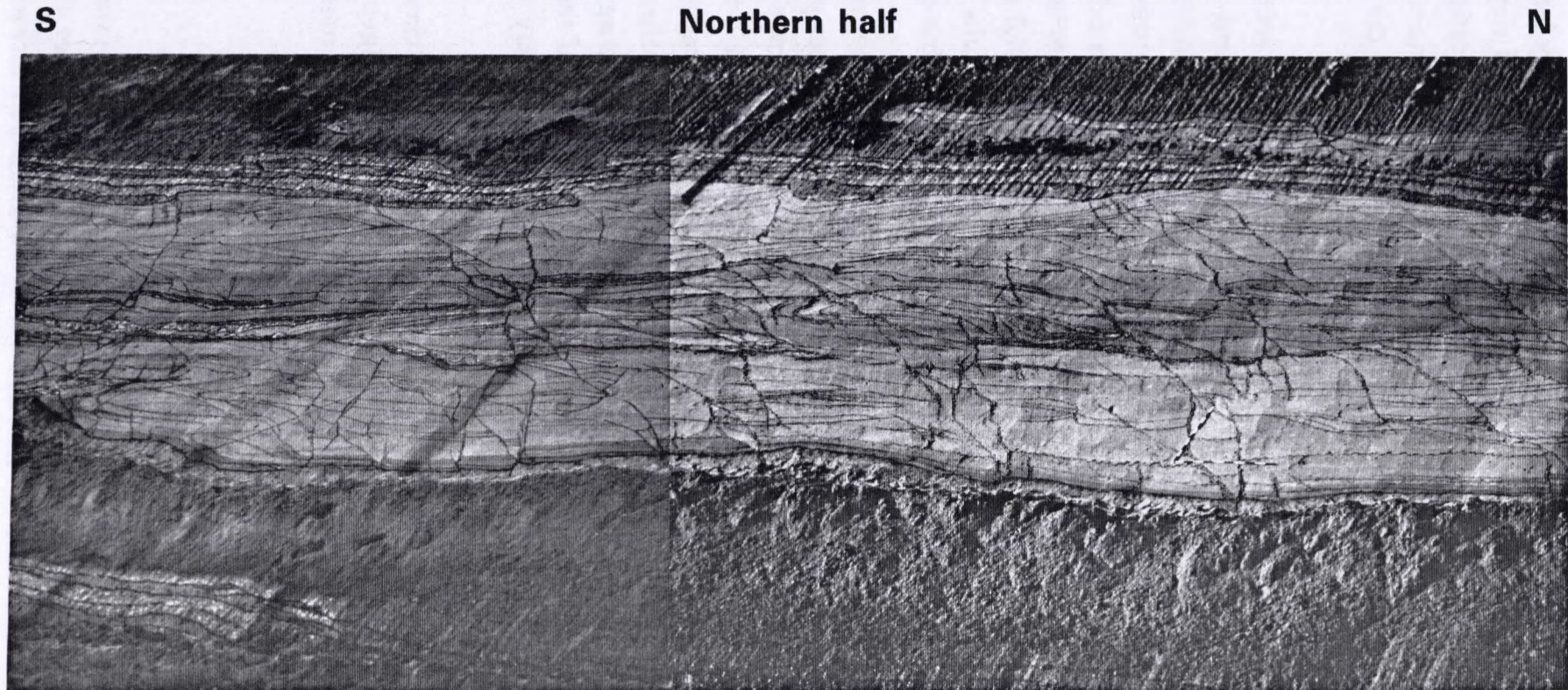


Fig. 4.47. (this and next page) Two overlapping parts of panoramic view on Egem Member in Meulebeke clay pit. View more or less along the strike of the small (strike slip?) faults that affected the fine sandy, trough cross-bedded layer. Notice that faults branch away from the sand-clay contacts into the sand, and reach largest apparent displacements (up to 0,25 cm) in the



middle of the sandy layer. Isolated faults and folds on the sand-clay contact accommodate the displacement of entire fault fans. Height of slope is 9 m, thickness of prepared sand layer is 3 m, length of prepared outcrop is about 65 m. Compare 450 m² of prepared outcrop with unprepared part (top left); 1 m³ of sand scraped down per 10 m. (Meulebeke, 24-28.10.89)

cross-bedded grey sand, 0.5 m of laminated and alternating sands and clays, 1.5 m of brown clay, 3 m of fine yellowish, cross-bedded sands with clayey lenses in some of the sets in the middle of this layer, and another 2 m of laminated clays and silts. A monocline with an apparent width of 40 m introduced a stratigraphic height difference of 1 m between the ends, so that the lower sands remain hidden below the platform at the N end. One end is visible at the extreme S of the panorama, the other one left of the centre of the N half.

Small faults traverse the fine sandy layer in the middle of the section. They are organized in fans that branch upwards from the lower clay-sand contact. They reach a maximum apparent displacement (up to 0.25 m) in the middle of the sandy layer. Isolated faults and folds (even recumbent ones) on the sand-clay contact accommodate the displacement of entire fault fans. There are much less faults at the S end, i.e. S of the monocline. It is hard to measure their orientations, but they are generally N020-040°E. Fig. 4.47 is a view more or less parallel to the strike of the faults. Slickensides were not found in the sands, so the faults may be either strike-slip or normal, though they often appear to be reverse in this outcrop.

Because no major clay tectonic faults have been observed in the underlying silty clay of the Kortemark Member, it is obvious from the above description that these small faults are not related with clay tectonics. The monocline may do so, but the timing of these faults suggests otherwise. As explained in §4.2.1.2, the faults were interpreted by tracing interruptions of bedding as well as of alteration patterns that apparently stained the sands *before* the faulting. The rust coloured alteration patterns may be attributed to the action of permeating, oxidizing groundwater, which probably did not happen before the late-Tertiary uplift of these strata. On these assumptions, the faults are probably more recent than clay tectonic deformation.

While these faults turned out to bear little if any relation with clay tectonics and were not investigated further for that reason, it was on the Egem sands in the Meulebeke clay pit that we developed the experience and techniques to reveal and document those other subtle faults, in Ypresian clays.

4.2.2. Palaeostress analysis

In our working hypothesis we proposed that the driving force system behind clay tectonic deformation resides in a gravitational instability rather than a tectonic stress. We have provided purely structural evidence in §4.1 already, but conclu-

sive evidence of a gravitational palaeostress can only be ascertained by a numerical stress inversion (§4.2.2.1) of fault slip data. Precisely this kind of data had hitherto not been collected. Experience and field techniques developed during our field-work allowed to do so on the numerous slickensides that were systematically uncovered and measured. The resulting palaeostress information is given and interpreted in §4.2.2.2.

4.2.2.1. Stress inversion method

In general (Angelier, 1989), the local determination of palaeostresses is based on graphical and numerical analyses of fault slip data. These data include fault plane orientations as well as directions and senses of slips. Such data may be processed regardless of the origin of faults, neoformed or inherited (fig. 4.48). However,

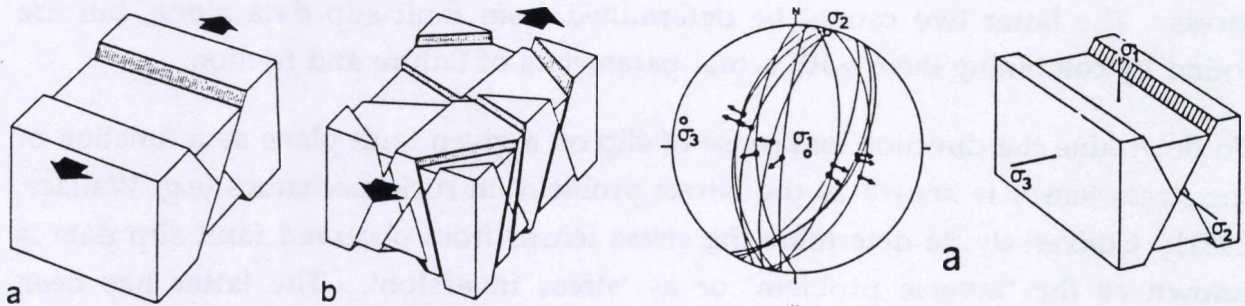


Fig. 4.48. Extension (arrows) can produce normal conjugate faults (a), but also cause reactivation of inherited faults with an orientation favourable to normal displacement (b). (from Angelier, 1989)

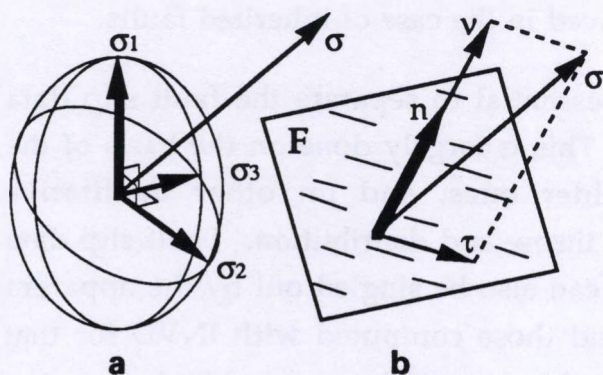


Fig. 4.50. Stress ellipsoid (a) with mutually perpendicular principal stresses ($\|\vec{\sigma}_1\| \geq \|\vec{\sigma}_2\| \geq \|\vec{\sigma}_3\|$) and resulting slip on a fault plane F (b) with normal \vec{n} . The stress $\vec{\sigma}$ exercised on F is decomposed in a normal stress \vec{v} and a tangential stress or shear $\vec{\tau}$. $\vec{\tau}$ results in slip along F and possibly in striae parallel to $\vec{\tau}$. (after Angelier, 1989)

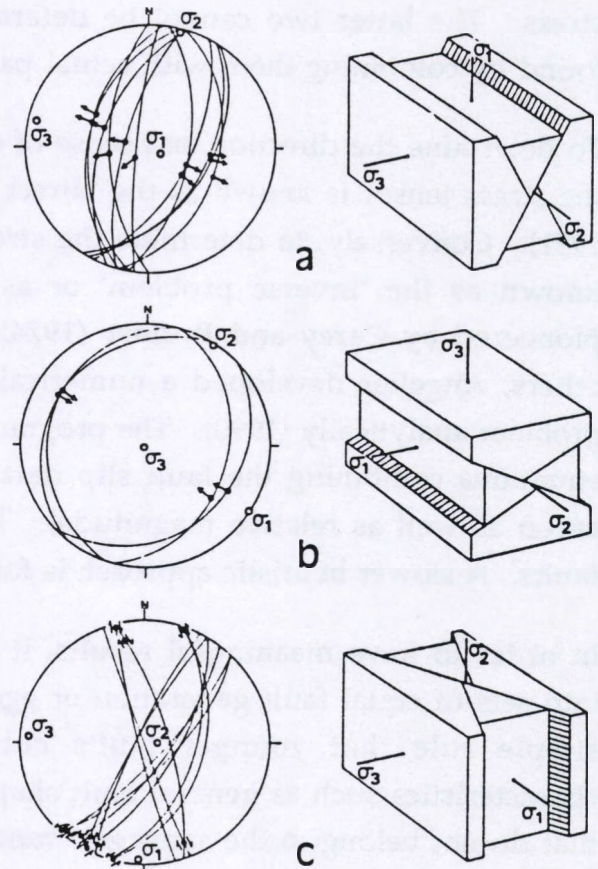


Fig. 4.49. Common conjugate fault systems. On the left, fault planes and striae in a Schmidt projections (lower hemisphere) after a few real examples. On the right, simplified corresponding block diagrams. Normal faults (a) due to extension, reverse faults (b) due to compression with vertical minimal principle stress, and (c) due to compression in one horizontal direction (σ_1) or extension in the other (σ_3). (from Angelier, 1989)

identification of neoformed faults (including the common conjugate systems) brings additional constraints, resulting in possibilities to get more information and to carry out rapid preliminary analyses (fig. 4.49).

Because data consist of orientation and senses, not magnitudes, the results are obtained in terms of reduced stress tensors (fig. 4.50). These consist of the orientations of the three principal stress axes $\vec{\sigma}_1$, $\vec{\sigma}_2$ and $\vec{\sigma}_3$, and the ratio Φ of principal stress differences, with $\Phi = (\sigma_2 - \sigma_3) / (\sigma_1 - \sigma_3)$. Note that $\vec{\sigma}_1$ designates the maximum compressional stress and $\vec{\sigma}_3$ the minimum stress ($\sigma_1 \geq \sigma_2 \geq \sigma_3$); Φ values thus range from 0 to 1. The orientation of the stress ellipsoid depends on three independent variables, while its shape and size depend on three other independent variables: Φ (defined above), a positive scale factor and some isotropic stress. The latter two cannot be determined from fault slip data alone, but are found by combining them with actual parameters of failure and friction.

To determine the direction and sense of slip on a given fault plane as a function of the stress tensor is known as the 'direct problem' in rock mechanics (e.g. Wallace, 1951). Conversely, to determine the stress tensor from observed fault slip data is known as the 'inverse problem' or as 'stress inversion'. The latter has been pioneered by Carey and Brunier (1974). Building on their work and of several others, Angelier developed a numerical method ('INVD') that solves the inverse problem analytically (1990). The program minimizes a system of four least squares equations combining the fault slip data with a variable shear stress (with orientation as well as relative magnitude). This approach works best with neoformed faults. A slower heuristic approach is followed in the case of inherited faults.

In order to have meaningful results, it is essential to separate the fault slip data into sets of equal fault generation or age. This is largely done on the basis of the simple rule that younger faults cut older ones, and on other qualitative characteristics such as general fault shape, throw and distribution. Fault slip data that do not belong to the same generation can also be singled out by the apparent incompatibility of observed slip vectors and those computed with INVD for that generation. It should again be noted that such a powerful numerical tool cannot be applied blindfold to just any set of numbers, without a critical evaluation of both data and results.

4.2.2.2. Palaeostress information, Marke

Sara Vandycke of the Université Pierre et Marie Curie, Paris and Faculté Polytechnique de Mons (Belgium) helped to gather fault slip data in the Marke clay

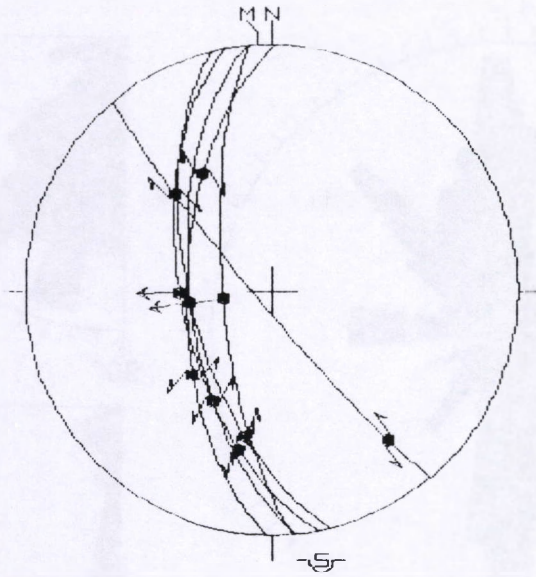


Fig. 4.51. Cyclographic projection of clastic dykes along F2 in Marke (10 fault slip data; Schmidt net, lower hemisphere; circles indicate slip vector for normal (one arrow) and sinistral or dextral strike-slip displacement (two arrows)). The limited slip with widely varying orientation along the clastic dykes is probably posterior to their emplacement. (Sara Vandycke, pers. comm.)

pit and she also did the data treatment with INVD. Four sets of fractures are distinguished here: the clastic dykes along major fault F2, (clay tectonic) large and small normal faults, a post-compaction system of conjugate strike-slip faults and a network of joints (fractures without striae).

The *clastic dykes* along major fault F2 have the same N-S strike (fig. 4.51) as this fault, but an opposite dip (fig. 4.27). Although conjugate dykes were not measured, the N-S strike is compatible with an E-W extension, thus already apparent in the earliest phase of clay tectonics. We remind that the limited slip in widely varying directions along the clastic dykes probably happened after their emplacement. Because fault F2 is lined with a black gouge that occasionally merges with the clastic dykes and because it has splays that cut them, F2 may be interpreted as a clastic dyke that later acted as a major clay tectonic fault plane.

The faults that have been assigned a *clay tectonic* origin are mostly normal and have widely dispersed strikes around a NNE-SSW trend (fig. 4.52). Out of 129 fault slip data, 55 were used for a stress inversion computation. They are plotted in a cyclographic projection in fig. 4.53a, and fig. 4.53b visualizes the derived palaeo-stress, which was essentially a vertical compression ($\sigma_1 \gg \sigma_2 = \sigma_3$, $\Phi \approx 0$) and corresponds with gravitational stress and pure compaction. This set weakly indicates a regional NW-SE extension. Another set of 37 fault slip data was gathered in the zone of major faults F1 to F4 in Marke and was treated separately (fig. 4.54). A

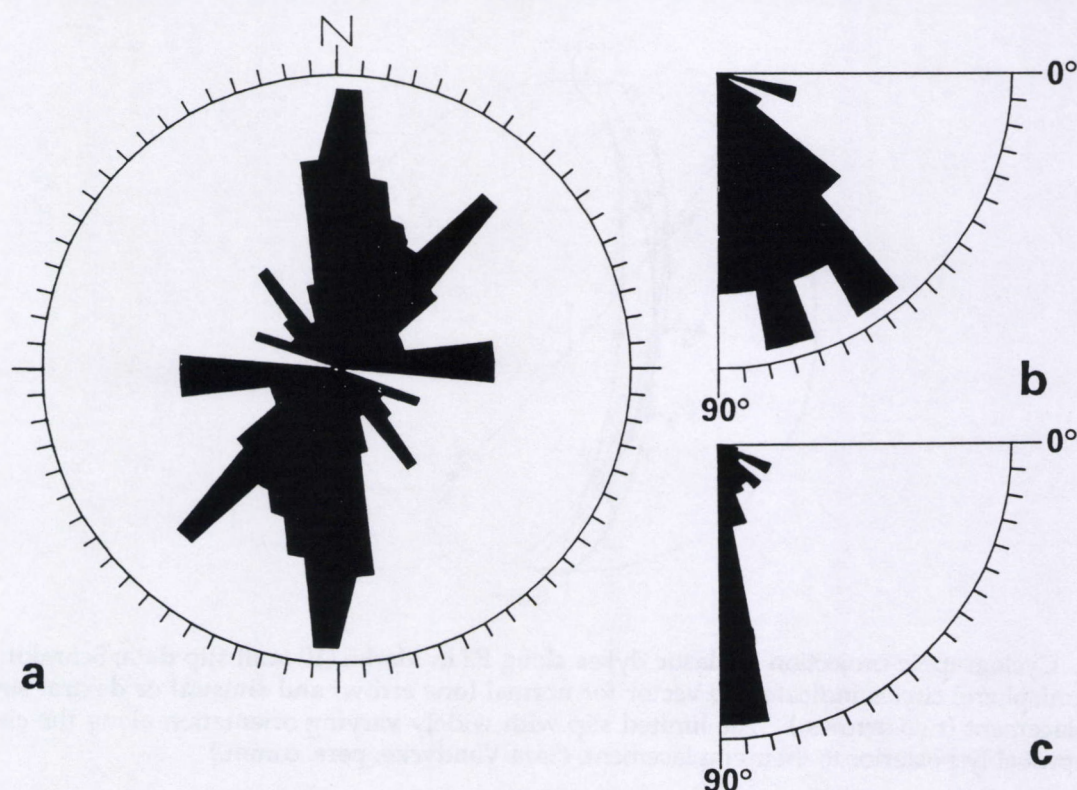


Fig. 4.52. Geometry of clay tectonic faults in Marke (129 fault slip data). Rose diagrams of strikes (a), dips (b) and slip inclinations (c) show predominance of normal faults. (Sara Vandycke, pers. comm.)

predominantly vertical compression is also computed from this set, with a weak indication of a regional extension almost perpendicular to that of the other set.

We conclude that the deformation interpreted as clay tectonic faulting has been largely driven by the action of gravity, but it may have been triggered or weakly influenced by regional E-W extension. This conclusion is identical to the one reached independently from the interpretation of clay tectonic structures in the North Hinder zone (§4.1.2), about 100 km NW of Marke. The coincidence of both conclusions seems to emphasize their truly regional applicability. The table below summarizes the numerical results of stress inversions with data from Marke.

Data set	σ_1	σ_2	σ_3	Φ	Tectonic regime
Clay tectonic faults, set 1 (55 fault slip data)	091° 85°	220° 03°	310° 04°	0.2	NW-SE extension (weak)
Clay tectonic faults, set 2 (37 fault slip data)	315° 81°	152° 08°	62° 03°	0.2	NE-SW extension (weak)
Strike-slip faults (12 fault slip data)	058° 13°	268° 75°	149° 07°	0.5	NW-SE extension/ NE-SW compression

Guiraud and Séguret (1987) came to a similar conclusion for the penecontemporaneous hydroplastic faults affecting fluvio-deltaic clays in the Soria Basin (N Spain).

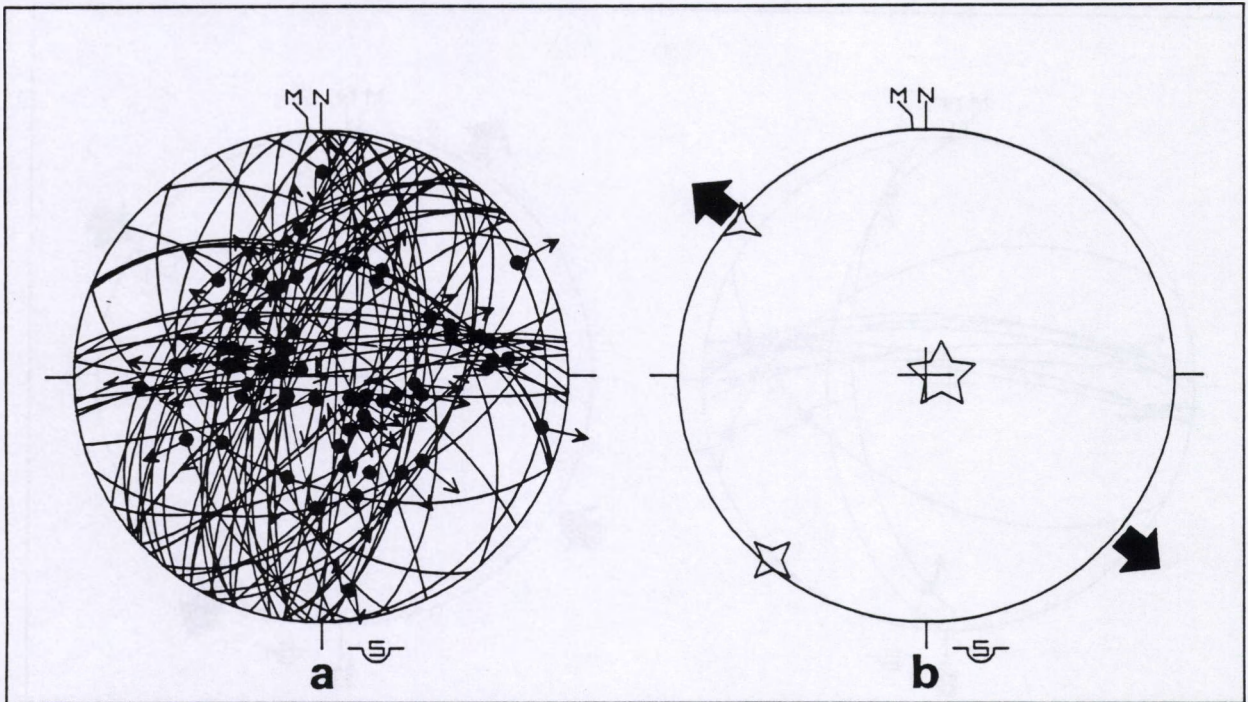


Fig. 4.53. Clay tectonic faults (a) and derived palaeostress (b) in Marke. Cyclographic projection of 55 fault slip data (Schmidt net, lower hemisphere). Projection of principal axes of computed palaeostress (stars with 5, 4 and 3 tips correspond to resp. σ_1 , σ_2 and σ_3 ; heavy arrows indicate direction of extension). The larger five-tipped star indicates that the vertical σ_1 is much larger than σ_2 and σ_3 , and that the orientation of the latter two axes is not reliable. (Sara Vandycke, pers. comm.)

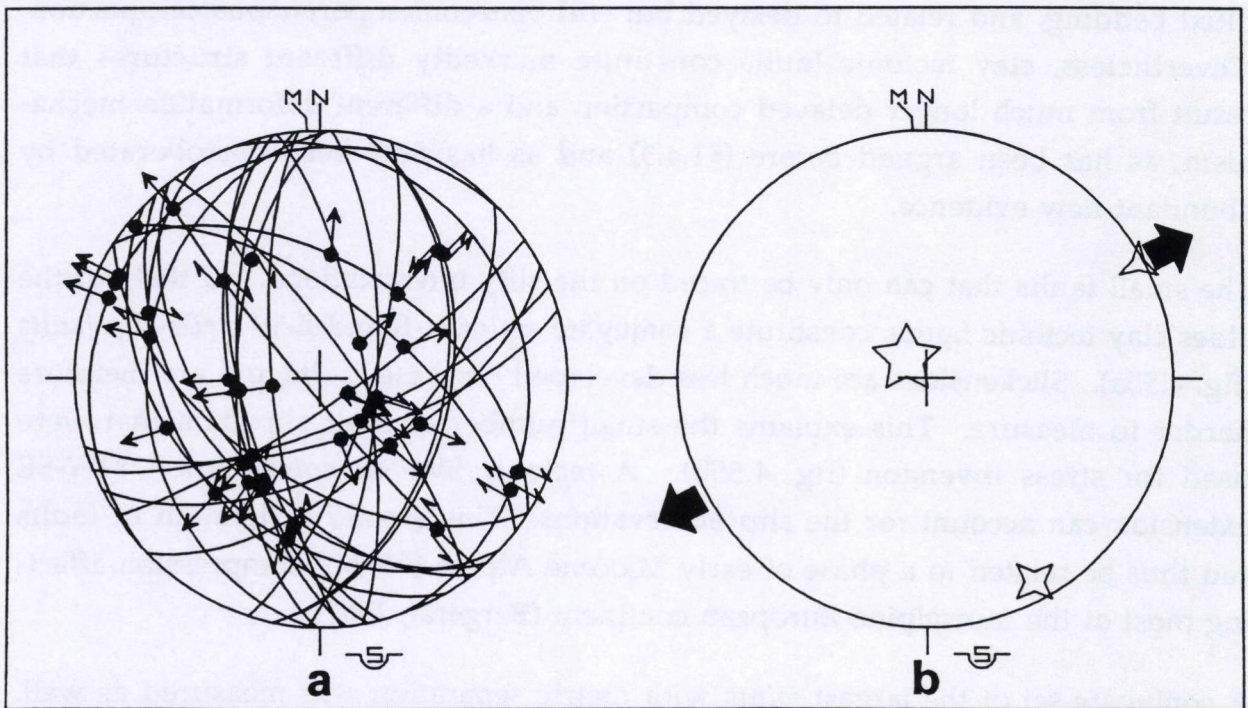


Fig. 4.54. Clay tectonic faults (a) and derived palaeostress (b) in Marke. Cyclographic projection of 37 fault slip data in the outcrop zone of faults F1 to F4 (same remarks as for fig. 4.53). Vertical compression is again predominant, but direction of computed extension is perpendicular to that in fig. 4.53. The reliability of the extension direction is small because the dispersion of fault strikes is even larger than in the other set. (Sara Vandycke, pers. comm.)

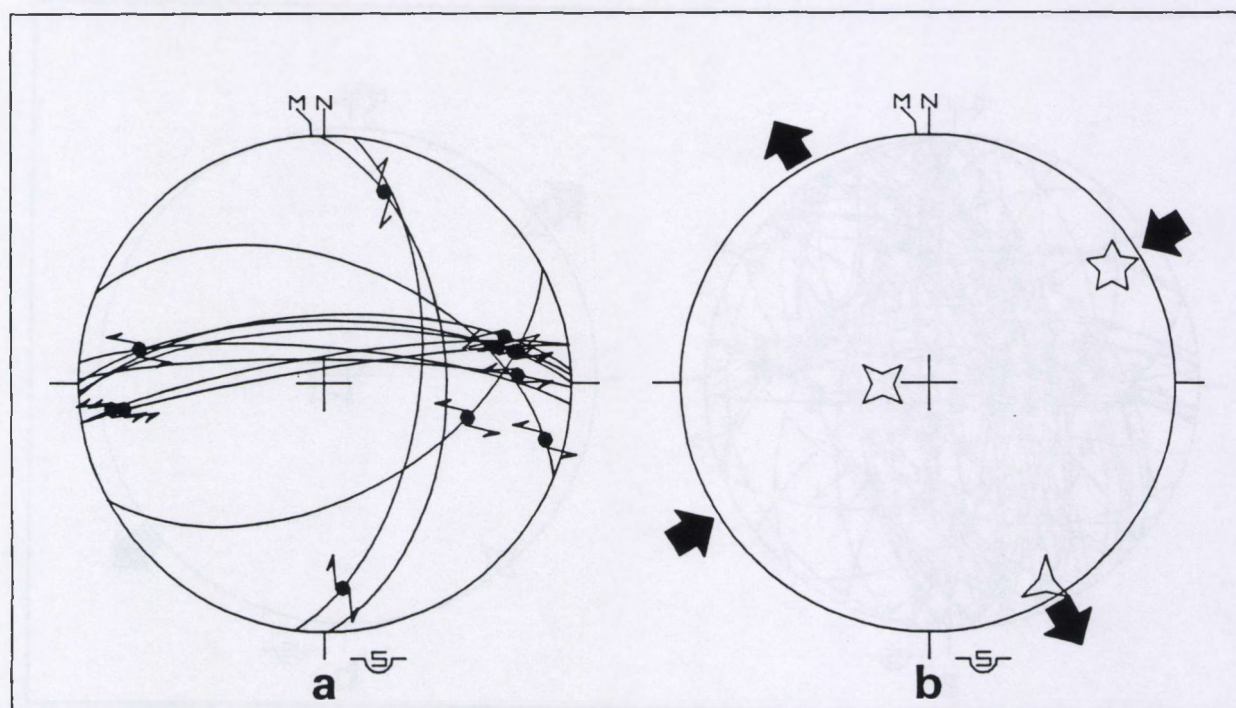


Fig. 4.55. Second generation strike slip faults (a) and derived palaeostress (b) in Marke. Cyclographic projection of 12 fault slip data (same remarks as for fig. 4.53). The conjugate faults can be explained by a tectonic SW-NE compression/NW-SE extension. (Sara Vandycke, pers. comm.)

They found a palaeostress consisting of compression purely perpendicular to the tilted bedding, and related to delayed but still penecontemporaneous compaction. Nevertheless, clay tectonic faults constitute markedly different structures that result from much longer delayed compaction and a different deformation mechanism, as has been argued before (§1.4.3) and as has now been corroborated by abundant new evidence.

The small faults that can only be traced on the silty intercalations and that cut the older clay tectonic faults, constitute a conjugate set of N-S and E-W *strike-slip faults* (fig. 4.55a). Slickensides are much less developed on these faults and are therefore harder to measure. This explains the small number of fault slip data that were used for stress inversion (fig. 4.55b). A tectonic SW-NE compression/NW-SE extension can account for the slip observations. This second generation of faults can thus be related to a phase of early Miocene Alpine SW-NE compression affecting most of the transalpine European continent (Bergerat, 1987).

A conjugate set of the largest *joints* with metric separation was measured as well. Only their geometry is represented in fig. 4.56, because the absence of slip and the consequent absence of measurable slickensides precludes stress inversion. The predominant E-W strike and steep dips can be explained by a regime of N-S extension.

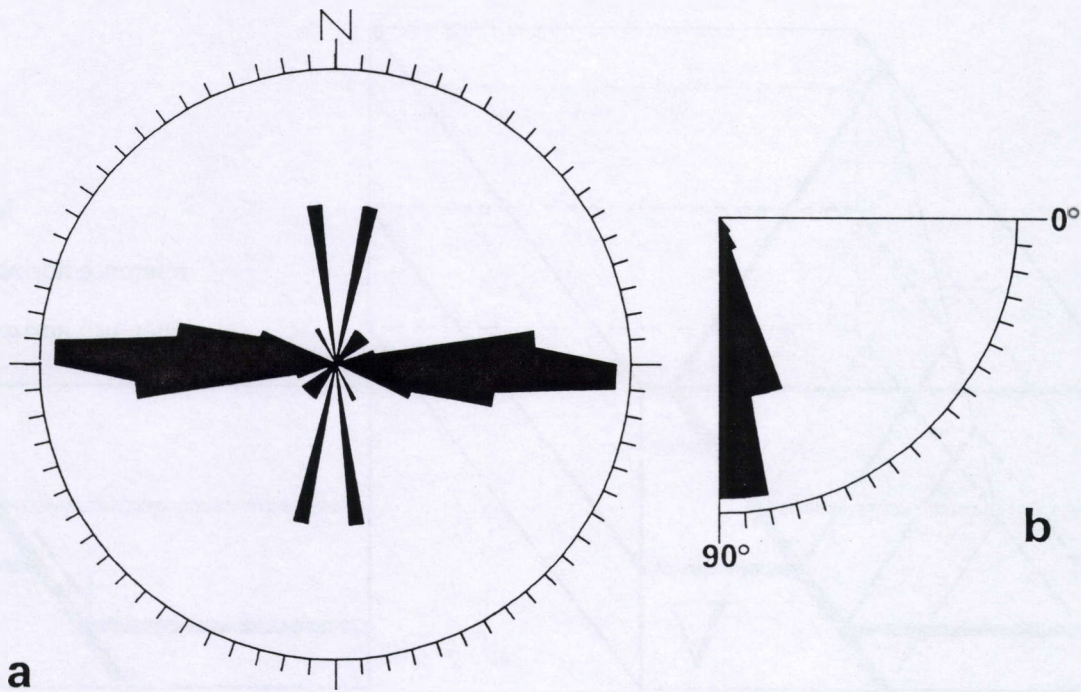


Fig. 4.56. Rose diagrams of strike (left) and dip (right) of joints in Marke. (S. Vandycke, pers. comm.)

Joints with the same orientation have been observed in a region up to 150 km away (Vandycke, 1992).

In conclusion, palaeostresses computed on the basis of fault slip data in the Marke clay pit corroborate and refine the proposed deformation history of the Ypresian clays.

4.2.3. 'Reverse' faults

Several authors (a.o. Steurbaut & Nolf, 1986; Van Vaerenbergh, 1987) noted 'reverse' faults in juxtaposition with 'normal' faults in the Ieper clay (e.g. fig. 1.13 and 1.15). Because clay tectonic faults are the result of a single deformation phase and stress field, this is energetically impossible (Mandl, 1988, p.11). What is wrong with these 'observations'?

Fig. 4.57b shows that normal fault on a sloping outcrop may appear to be reverse depending on outcrop orientation relative to fault strike. The folded normal fault in fig. 4.31 is a well documented example. Conversely, reverse faults may appear to be normal. Because sloping outcrops are deceptive, it is mandatory to *measure* all orientations. In addition, if such outcrops are interpreted and drawn for publication, it is better not to add arrows that indicated interpreted relative movement

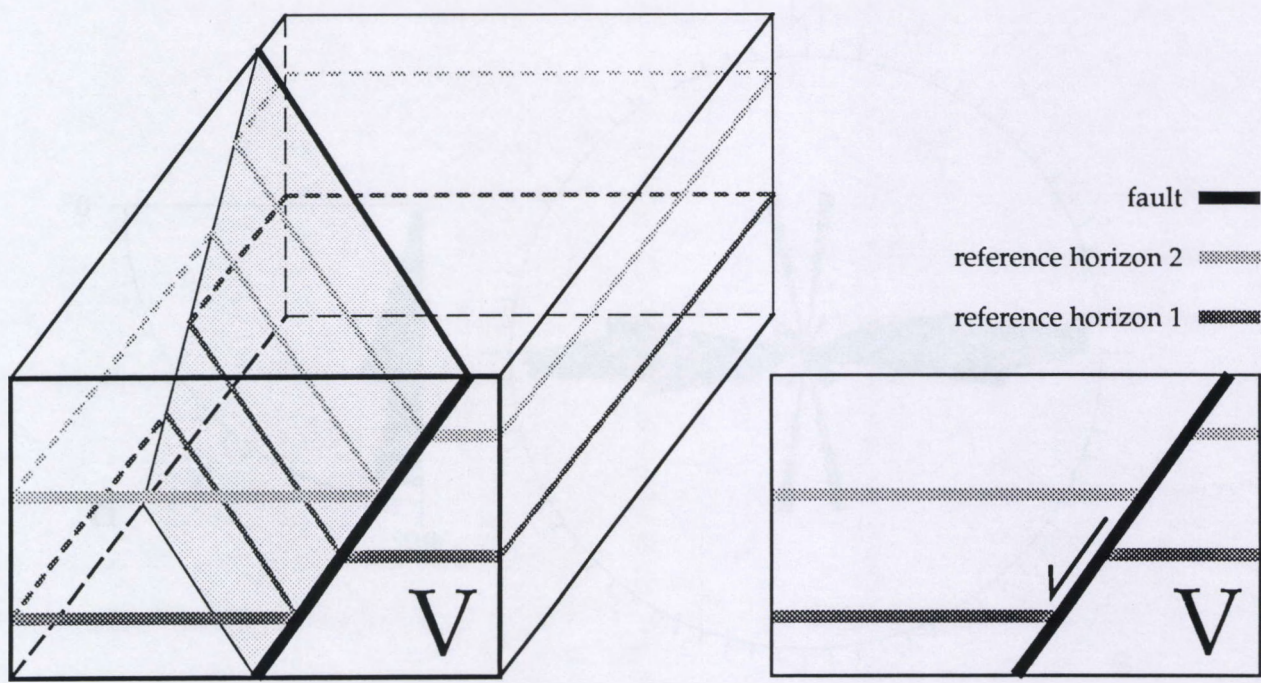


Fig. 4.57a. A normal fault on a vertical outcrop appears normal irrespective of outcrop orientation. The analogue is true for a reverse fault.

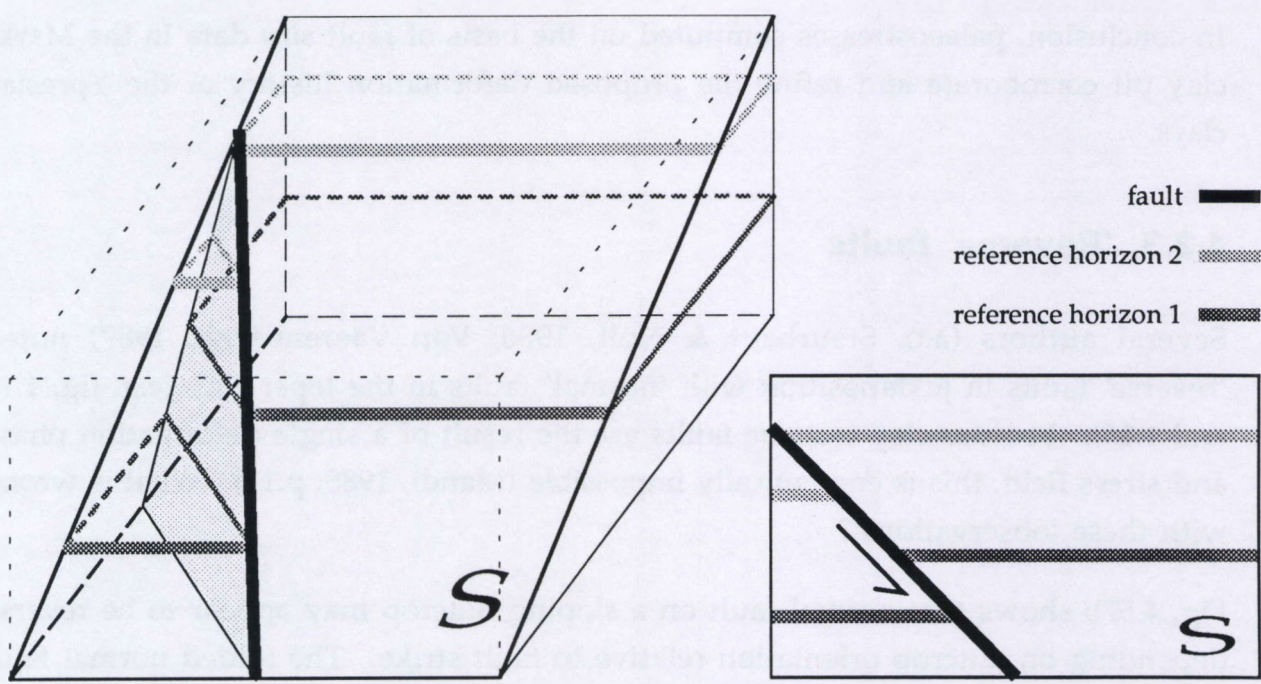


Fig. 4.57b. The same normal fault on a sloping outcrop may appear to be reverse, and *vice versa*, depending on outcrop orientation relative to fault strike. In case of a sloping outcrop, it is better not to draw arrows to indicate interpreted relative movement, because they may be either confusing or wrong. Because sloping outcrops are deceptive, it is mandatory to *measure* all orientations.

along a fault, because they may be either confusing or wrong. Not only should the strike of the outcrop be indicated, but also its dip.

These remarks seem to be self-evident, but even experienced structural geologists have been deceived by sloping outcrops. This is understandable. On the one hand, faults are much more common in hard rock. Hard rock can support steep to vertical outcrops, which are safer to interpret without measurements (fig. 4.57a). Faulted, unconsolidated sediments on the other hand cannot support steep slopes very long, and therefore tend to be excavated with slopes between 1:1 (45°) and 1:2 (26°).

Sloping or not, outcrops are most often arbitrary cross-sections that are not necessarily perpendicular to local faults and folds. Systematic measurements can lead directly to stress history reconstruction (§4.2.2) as well as prevent elementary misinterpretation.

4.2.4. Quaternary reactivation

In the Zonnebeke clay pit, two faults (F2 and F4 in fig. 4.38) show unmistakable evidence of reactivation. The Quaternary deposits, with their fine to coarse sands and gravel at the base, are faulted. Both F2 and F4 branch upwards at a depth of about two metres below the Quaternary-Tertiary contact. These splays are probably Quaternary neoformations and accommodate a normal throw of 1 m at F4 and 1.5 m at F2 (between c and d in fig. 4.58). Half of the throw in the Ypresian clays (3 m between a and b in fig. 4.58) is therefore due to the Quaternary reactivation of major fault F2. Part of the faulted Quaternary sands have been eroded away, so that younger, unfaulted sands (Q_{Zu}) rest unconformably on Q_{Zf} .

These and other aspects can be studied in the colour photographs of fig. 4.59. Notice how useful it can be to return to exactly the same site on a clayey outcrop, because different parts and layers stand out in different states of desiccation.

It remains to be investigated whether the base of the weathered zone is lower to the right (S) of F2 because of higher permeability in the silty Kortemark Member, or because the alteration reached its largest depth *before* the reactivation. This question requires more than cursory research, well outside the scope of this thesis.

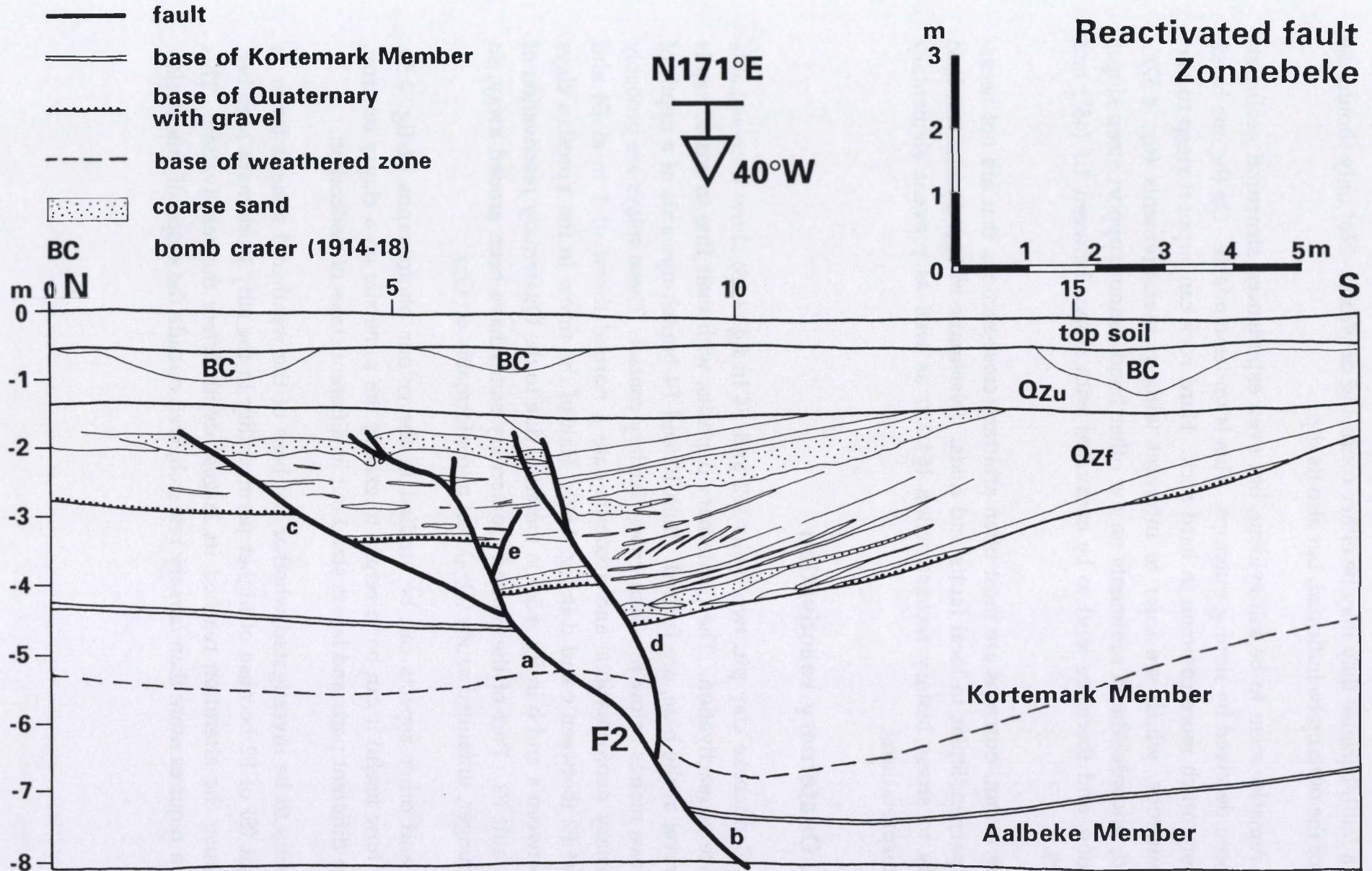


Fig. 4.58. Reactivated fault F2 in the eastern "Van Biervliet" clay pit in Zonnebeke. Interpreted linedrawing based on photographs like in fig. 4.59. Normal throw in Ypresian clays amounts to 3 m (between **a** and **b**), 1.5 m of which (between **c** and **d**) is due to the Quaternary reactivation. Notice seemingly reverse splay at **e**. The base of the weathered zone is lower to the right of F2. Unfaulted and faulted Quaternary sands (resp. QZu and QZf) are separated by an unconformity. Filled bomb craters from WW I are indicated as well (see fig. 4.59a).

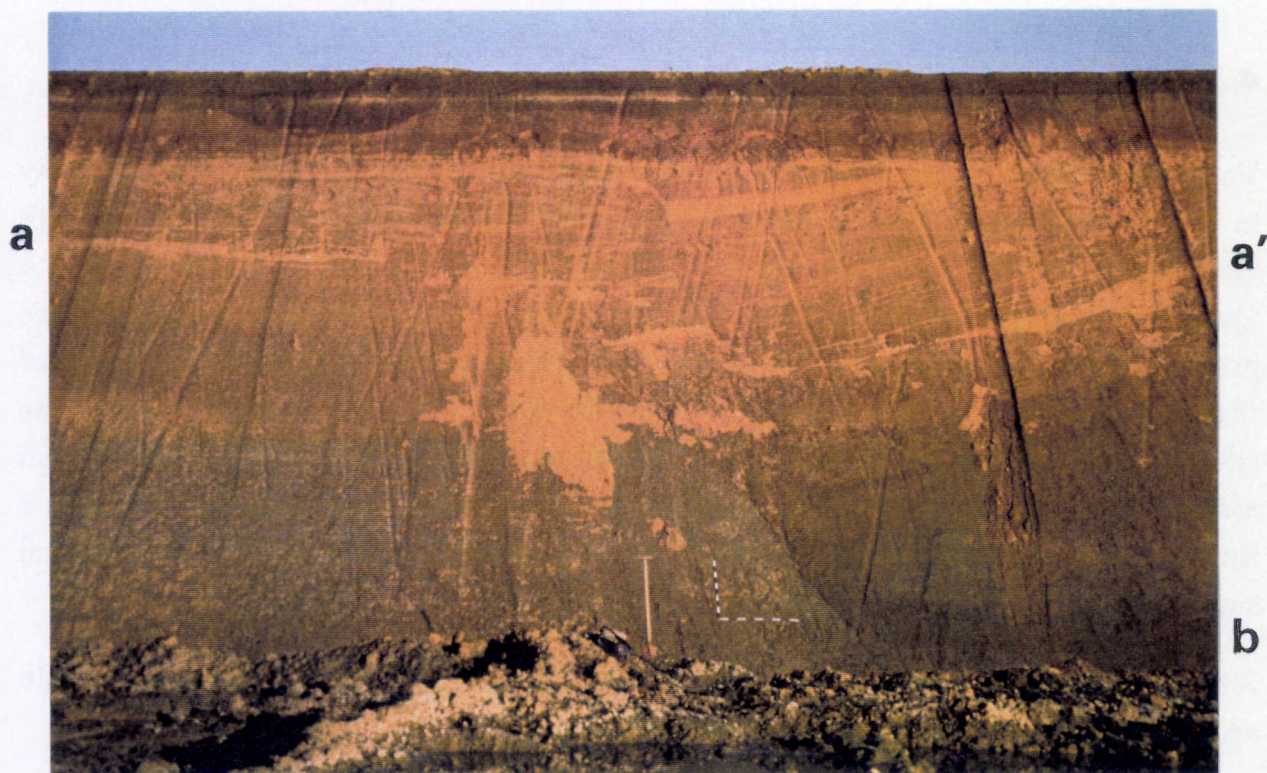


Fig. 4.59a. A clay tectonic fault reactivated during the Quaternary (eastern "Van Biervliet" clay pit, Zonnebeke). Compare with fig. 4.58 for an interpretation. Notice the faulted base of the Quaternary (lowest thin yellow band with white specks at pebbles, **a-a'**), the clear intra-Quaternary unconformity and the dark brown filled bomb craters. The top of the Aalbeke Member is visible on the right (dark brown, **b**), but not in the weathered zone on the left. (Zonnebeke, 16.11.89)

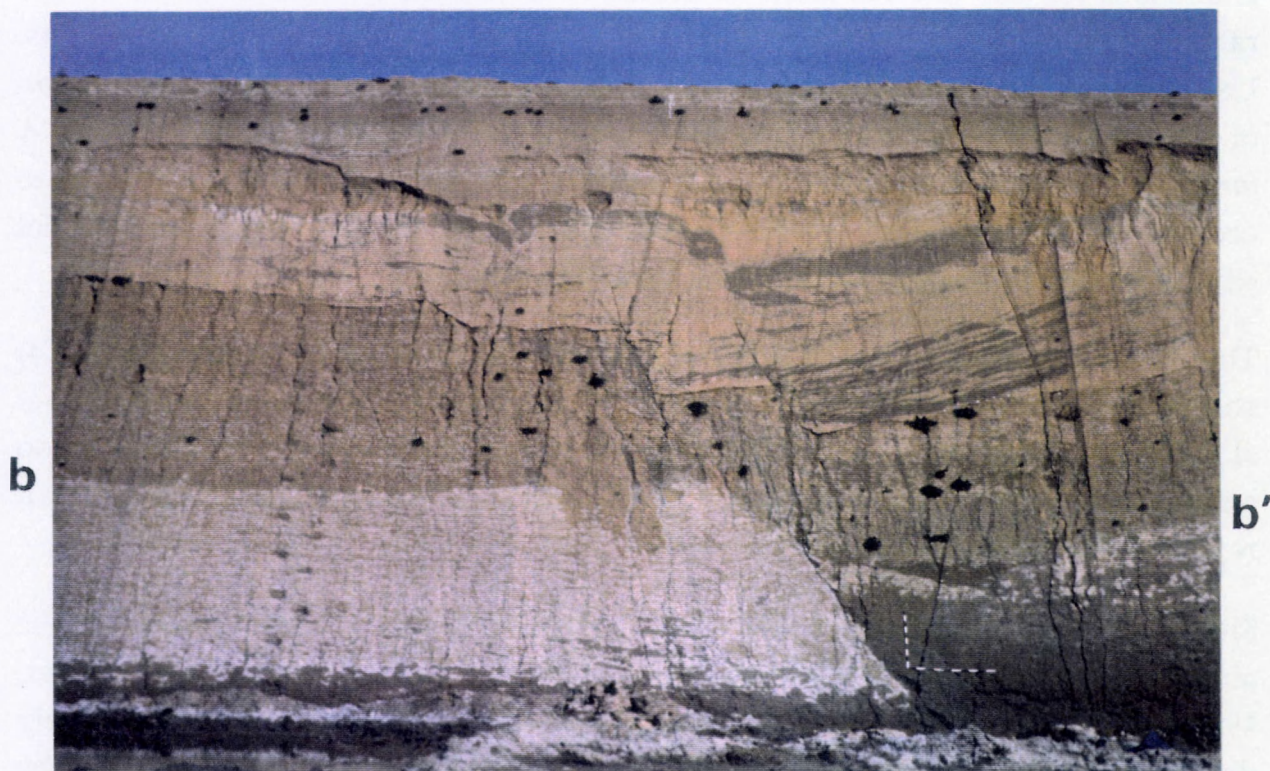


Fig. 4.59b. The same view four months later. The Tertiary-Quaternary contact can be sharply delineated, but the intra-Quaternary unconformity is not so clear. Other Quaternary sands stand out in this state of desiccation. The base (**b-b'**) of the weathered zone is now clearly visible. (Zonnebeke, 15.03.90)

4.2.5. Clay tectonic faults and slumping

Van Vaerenbergh (1987) studied a Quaternary slump in the Ypresian Aalbeke Clay in the "Kobbe" clay pit in Aalbeke, Belgium. This slump happened gradually, with Quaternary sediments filling up the trailing edge as the slump advanced into a Quaternary gully, also buried now. The result was a small (20 m long) buried listric growth fault. Not long after this author had investigated the internal geometry of the slump, the whole mass slipped out of the exploitation face, thus revealing the semi-circular outline of the fault. He conjectured that it was seeded by the partial reactivation of a pre-existing clay tectonic fault. We will argue here against such a link between Tertiary clay tectonic faults and slumps along natural or artificial slopes in the London/Ieper clay.

Firstly, the careful observations of Van Vaerenbergh (1987) simply do not contain any evidence of the supposedly pre-existing fault.

Secondly, the listric shape of the slip surface, both in a vertical and in a horizontal section, is typical for the many well studied slumps in the London/Ieper clay (Skempton, 1964; Skempton & La Rochelle, 1965; De Beer, 1979), but entirely anomalous for clay tectonic faults as described in this thesis. The latter are always rather straight in a horizontal plan, at least on the scale of the reported slumps. Listric splays exist, but it is improbable that the geometry, position and orientation of such a splay would be compatible with that of a candidate slump fault. *A fortiori*, it is even more unlikely that several such splays would be present to account for the frequently observed multiple slumps, with more or less parallel slip planes receding ever further away from the slope.

The Quaternary reactivation of clay tectonic faults in the Zonnebeke clay pit (§4.2.4) suggests that the faults may still be potential planes of failure (see also Henriët *et al.*, 1982), but from their geometry and size it is evident that they would only be so on a much larger scale and under much higher differential loads than in all reported slumps in these clays.

Slumps in the London/Ieper clays have been attributed to a coalescence of the abundant microfractures (Skempton, 1964; Skempton & La Rochelle, 1965; De Beer, 1979; §1.4.3). The shape, position and dimensions of the slip plane are largely determined by the height of the slope, humidity, and type of clay. Especially the 'Brown' London Clay, or the weathered upper part of the Ypresian clays in general, are sensitive to slumping because they are markedly more fissurated.

Our own observations confirm this commonly accepted view :

1. The steep head of slips in these clays is rough and faceted with many microfractures. It is only after a few metres towards the toe that the shear caused by the downsliding mass starts to smooth the slip plane. By then the dip of this surface is less than 45° , atypical for clay tectonic faults that generally dip between 45° and 85° (fig. 4.52).
2. A few slumps were observed in the course of field work in Marke. They started where the base of the overlying Quaternary sands reaches a local low. Phreatic ground water was seen to leak out of the sand in the lows and presumably wet the weathered clay before the slumping.

We conclude that there is no demonstrable link between clay tectonic faults and recent slumps along natural or artificial slopes in the London/Ieper clay.

4.2.6. Permeability issues

The study of clay tectonic faults raised a few questions concerning the vertical permeability of thick clayey sequences, relevant to hydrocarbon migration and to the management of dump sites.

Flat bottomed dump sites

Because of their very low permeability, walls of clay are used as vertical seals in dams. Abandoned clay pits with several metres of clay still in place are equally well fit to be used as dump sites for otherwise hazardous waste. Moreover, fractures do not open along the flat bottom of such a pit because there are no lateral stress differences. Anyone who tried to manually dig a small pit into the flat bottom can testify that the fracturation of these overconsolidated clays does not facilitate the hard labour because the fractures remain tightly closed. Moreover, the gouge along the clay tectonic faults and clastic dykes is clayey (§4.3.1) and likely to have equally low permeability, especially because of the strong clay particle reorientation along the faults (§4.3.5) and the fragmentation of the clastic dykes by later faulting (§4.2.1.12). Particle reorientation in the gouge by shearing along the faults may even introduce lateral seals in the silty horizons (Bouvier *et al.*, 1989). Consequently, if the microfractures did not pose a permeability problem until now (through artificial drainage and other safety measures), the rarer and entirely intraformational faults will not do so either.

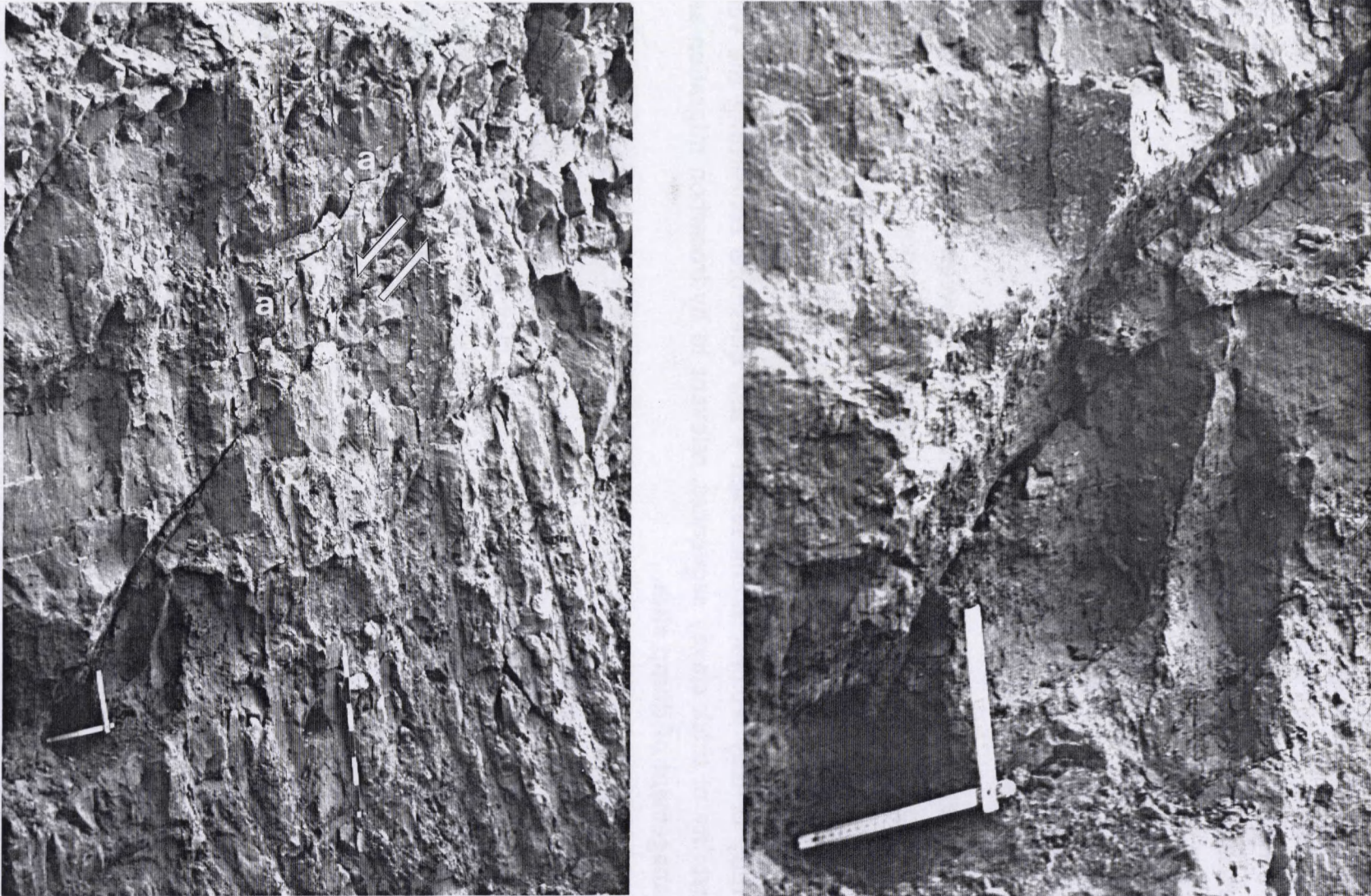


Fig. 4.60. Clay tectonic fault opened to a fissure. The fault (arrows) and some roughly parallel joints (e.g. *a-a'*) are opened up to 1 cm wide by stress differences along this almost vertical, 3 m high face at the foot of the exploitation slope. Close-up on the right. (Marke, 24.09.89)

Tunnels and steep slopes

Along tunnels and steep slopes in these clays large stress differences do cause the opening of fractures with favourable orientations. Fig. 4.60 shows an example in the Marke clay pit. A layer of calcareous clayey silt at the bottom of this pit (S1 in fig. 4.23c) is so stiff that it needs to be removed from below with a mobile excavator, resulting in an almost vertical face of up to 3 m high at the foot of the slope. The photographs show a clay tectonic fault with a throw of 1.5 m, dipping 60°E and striking 40° relative to the vertical clay face. The fault and some roughly parallel joints had locally become open fissures, up to 1 cm wide. Such a phenomenon was never observed along the gentle slope above. In regard of the stiffness of these clays and silts, these fissures may extend a considerable distance into the vertical face and may therefore serve as unexpected conduits.

Hydrocarbon migration

In petroleum geology, argillaceous petroleum source rocks often show evidence of fracturing, which is considered to be an important factor for the primary migration of hydrocarbons. Several authors consider over-pressuring of the enclosed pore fluids at great burial depths (3000–4000 m according to Tissot & Welte, 1984) as a major factor for the generation of microfractures. The London/Ieper clay, with a organic C content of only around 0.4% (§4.3.2) is not a potential source rock for hydrocarbons (Tissot & Welte, 1984), but many source rock formations (>0.5%OC) are argillaceous. Henriët *et al.* (1991) reasoned that source rocks having perhaps already undergone general fracturing at shallow depths may have reached the depths required for oil generation in a pre-fractured state. This would then have a bearing on the timing of the onset of primary migration, perhaps starting earlier than generally thought.

The results of the present study puts such a possibility into perspective:

1. Probably most of the microfractures in the outcrops of London/Ieper clays are due to the overconsolidation effect, as explained in §1.4.3. This effect is unlikely to occur or to be so prominent in the deeper parts of a basin, where most mobile hydrocarbons are generated.
2. Clay tectonic faults constitute only a sparse network of fractures (§4.2.1.5). Truly tectonic faults and joints have been shown to complicate that network, but most of the hydraulic microfracturing would still need to be accomplished at depth.

3. The presence of tectonic joints and (clay) tectonic faults in clayey cap rocks may well facilitate the formation of hydrocarbon dykelets and thus *secondary* migration out of overpressured hydrocarbon reservoirs (Mandl & Harkness, 1987).

Although this thesis work clarified the above-mentioned permeability issues, a more definite assessment can only follow from a more directed approach.

4.3. Microscopic and analytical evidence

In this section, we descend to the finest analytical scale, that of grain size and mineralogical composition (§4.3.1), chemical composition (§4.3.2), microfossil assemblages (§4.3.3), CT scans (§4.3.4) and thin sections (§4.3.5). In doing so, we address questions such as:

1. what is the composition and structure of the material in the clastic dykes?
2. in which senses is this black gouge different from the clays and silts into which it was placed?
3. where does the material come from?

These questions are important in the light of our main working hypothesis, which predicted that we should find evidence of intraformational and upward fluid injection along the clay tectonic faults. We remind from §4.2.1.12 that we sampled a clastic dyke that was not solicited by later displacements, as was ensured by the absence of throw in the silty laminations on either side of the clastic dyke (S3 in Marke, fig. 4.45). A nearby fault lined with the same black gouge was sampled as well for comparison. A clastic dyke in the Zonnebeke clay pit was only studied in thin section.

4.3.1. Grain size and clay-mineralogical composition

Dr. S. Geets and Mrs. N. Selen of the Universiteit Gent (Belgium) analysed the grain size distribution and clay minerals in the clastic dyke and in the wall clay.

Three suspensions of both the gouge and the wall clay were subjected to a centrifugal particle size distribution analyser (type HORIBA CAPA-300). This apparatus combines measurements of optical transmissivity vs. settling time with the Stokes law for spherical particles. All particles were smaller than 40 μm and

therefore within the optimal range for the CAPA-300. The results are summarized in the following table:

interval (μm)	40-20	20-10	10-5	5-2	2-1	1-0.5	0.5-0	median	silt (>4)	clay (<4)
Φ (appr.)	5	6	7	8	9	10	11			
gouge sample 1	0.0	3.5	8.9	10.3	16.8	26.1	32.5	0.78	14.3	85.7
gouge sample 2	1.0	4.1	9.3	10.7	18.6	24.3	30.0	0.89	13.7	86.3
gouge sample 3	0.0	3.8	7.7	7.9	17.7	24.7	35.0	0.76	14.7	85.3
gouge mean	0.3	3.8	8.6	9.6	17.7	25.0	32.5	0.81	14.2	85.8
wall clay sample 1	3.6	5.9	9.0	9.2	16.0	26.6	27.4	0.88	20.8	79.2
wall clay sample 2	4.2	6.6	9.5	8.2	14.1	23.4	31.5	0.85	22.8	77.2
wall clay sample 3	3.9	5.6	11.1	10.0	16.0	25.7	26.2	0.94	22.1	77.9
wall clay mean	3.9	6.0	9.9	9.1	15.4	25.2	28.4	0.89	21.9	78.1

This table learns that the wall clay from S3 (fig. 4.27) and the black gouge are both silty clays. The wall clay at this location is more silty than the gouge, which is anomalous for clastic dykes. In the reviews by Shrock (1948) and Allan (1982) clastic dykes were usually filled with material that is coarser grained than the wall rocks. Of course, this gouge is coarser than the clayey layers it penetrated as well.

Clay mineralogy data are based on standard X-ray diffractometry, in combination with glycolization for distinguishing smectites (i.e. swelling clays). The diffractograms showed strong and broad peaks related to smectites and a lesser sharp peak characteristic of illite. Both the clastic dyke material and the wall clays therefore largely consist of smectites and an amount of illite, without notable differences. This composition is typical of all Eocene and Palaeocene clays in this area (Mercier-Castiaux *et al.*, 1988). Oligocene to Pliocene clays contain more illite and a large amount of kaolinite (*ibidem*).

4.3.2. Chemical composition

Likely candidates that could account for the darker colour of the gouge were enrichments in Fe and Mn oxides and organic carbon.

Dr. S. Geets and Mrs. N. Selen of the Universiteit Gent (Belgium) analysed free Fe and Mn by dithionite extraction (Mehra & Jackson, 1960) and Atomic Absorption Spectrophotometry. After the addition of Na citrate and a NaHCO_3 buffer, solid $\text{Na}_2\text{S}_2\text{O}_4$ reduces the metal oxides so that they can be extracted. The solution is

analysed by AAS. This method does not reveal a difference between wall clay and gouge in their Fe or Mn²⁺ content:

	Fe	Mn ²⁺
gouge	0.6%	0.0035%
wall clay	0.6%	0.004%

The organogeochemical composition was analysed by Prof. D. Leythaeuser (now Universität Köln, Germany) and Dr. R. Schaefer (Forschungszentrum Jülich (KFA), Germany). Organic carbon contents of a number of airtightly sealed samples have been determined by a combustion method (LECO Carbon Analyzer IT 112) on thermovaporized sub-samples after treatment with hot 6N HCl. The accuracy of this method is 10% relative standard deviation at organic carbon levels as low as 0.1% (dry weight). Samples of gouge from the clastic dyke, the wall clay, and dark clay from a nearby lamina have been analysed, including several control measurements. The data are summarized in the table below.

		C-org	ethane	propane	n-butane	n-pentane	n-hexane	benzene	n-heptane	toluene
gouge (n=15)	mean	0.35	72.5	82.8	55.8	34.8	24.2	38.6	26.5	70.8
	s.dev.	0.05	29.6	28.6	18.4	11.3	14.4	41.3	40.9	95.9
	min.	0.27	11.7	24.9	18.0	13.5	10.4	12.1	4.7	15.1
	max.	0.44	115.7	131.8	90.6	56.1	68.6	136.9	170.9	354.4
wall clay (n=9)	mean	0.33	60.9	64.2	44.1	31.5	24.0	55.1	21.7	66.9
	s.dev.	0.05	24.8	20.9	14.3	9.6	8.1	33.9	10.1	39.1
	min.	0.24	34.6	39.3	26.0	18.4	10.9	9.2	6.0	14.6
	max.	0.44	105.6	97.4	64.7	43.0	35.0	106.9	37.2	123.4
dark clay (n=4)	mean	0.47	51.9	75.6	52.0	42.2	30.1	37.6	24.2	53.4
	s.dev.	0.10	13.1	19.2	18.2	21.6	22.9	38.0	22.4	51.2
	min.	0.33	42.5	49.7	39.5	22.4	15.0	12.9	11.3	20.3
	max.	0.55	70.4	93.7	75.2	72.6	64.2	94.2	57.7	129.6

Fig. 4.61. Concentrations of organic carbon in % dry weight, and of n-alkanes C₂-C₇, benzene and toluene in ppb dry weight; n is number of analyses. (Dr. R. Schaefer, pers. comm.)

There is no apparent enrichment of organic carbon in the gouge relative to the wall clay, and the concentrations are low. The highest concentrations have been measured in a nearby dark clayey lamina (“organic vein”, Steurbaut, 1987), but they remain rather low even here. The kerogen, i.e. the type of organic matter in

relation with hydrocarbon potential, has been characterized with Rock-Eval analyses (Espitalié *et al.*, 1977; Prof. D. Leythaeuser, pers. comm.) that measure the oxygen concentration and the temperature at maximum pyrolysis. In all of the samples, the organic matter can be characterized as type III kerogen, i.e. organic matter derived from higher land plant vegetation and/or oxidized during sedimentation and early diagenesis. In other words, not only are the concentrations measured in these samples too low, but the kerogen is also too poor to consider these Ypresian clays as potential source rocks for hydrocarbons (Tissot & Welte, 1984).

In order to see whether gouge and wall clay differ in their light hydrocarbon (C₂-C₉) fingerprints (fig. 4.61), many subsamples of one gram were analysed by hydrogen stripping in the flow system of a capillary gas chromatograph (Schaefer *et al.*, 1978). Sub-nanogram per gram (ppb) quantities can be determined with this method. Unexpectedly high concentrations of alkanes (C₂-C₇) and of aromatic hydrocarbons (benzene and toluene) were found in all three types of sample, but the concentrations in subsamples varied widely without any apparent systematic coherence, even between control measurements on the same samples. This is especially noticeable in the concentrations of alkanes C₆-C₇, benzene and toluene, which varied between the maximum values and one tenth of them.

This apparent heterogeneity has been tentatively attributed to a combination of :

1. the long storage period of several months between sampling and analyses, without the prerequisite deep freezing. This is most likely to affect the distribution of the most volatile alkanes C₂-C₅ (Dr. R. Schaefer, pers. comm.);
2. a contamination of the exploitation slope with lubrication oil from the electrically driven excavator and/or with exhaust gasses and soot from nearby highway traffic, which would primarily influence the concentrations of alkanes C₆-C₇, benzene and toluene (Jo Verschuren, pers. comm.).

In order to distinguish original concentrations from possibly contaminated ones, new samples should be taken at different depths on the slope. Light hydrocarbons have a very low viscosity and evaporate easily, so that the concentration of contaminants should decrease with depth, while a reverse trend should be noticed for concentrations of original light HCs. A comparison of mean concentrations of the lightest alkanes (C₂-C₄) is likely to reflect proportions undistorted by contamination. From this point of view, the gouge does seem to stand out with the highest concentrations of ethane, propane and n-butane, against intermediate values in the dark clay and lowest ones in the wall clay.

<p>Gouge in clastic dyke (Marke, 12.09.90)</p> <p>Present <i>Dracodinium varielongitutum</i> <i>D. solidum</i> à <i>varielongitutum</i> (rare) <i>Phthanoperidinium echinatum</i> <i>Phthanoperidinium crenulatum</i> (some specimens) <i>Eatonicysta ursulae</i> (rare) <i>Thalassiphora delicata</i> (1 specimen) <i>Deflandrea oebisfeldensis</i> (rare)</p> <p>Absent <i>Homotryblium</i> spp. <i>Charlesdowniea clathrata-coleothrypta</i> <i>Polysphaeridium zoharyi</i> <i>Trigonopyxidia ginella</i> <i>Pseudomasia trinema</i></p> <p>Remarks: relatively abundant pyritized diatoms and sponge spiculae</p> <p>Interpretion: mixture of material from Zones 2 and 3, and small amounts from Zones 4 and 5</p>	<p>Wall clay (Marke, S3, 11.09.90)</p> <p>Present <i>Dracodinium varielongitutum</i> (rel. abundant) <i>Dracodinium solidum</i> <i>Homotryblium</i> sp. <i>Phthanoperidinium echinatum</i> <i>Eatonicysta ursulae</i></p> <p>Absent <i>Charlesdowniea clathrata-coleothrypta</i> <i>Polysphaeridium zoharyi</i> <i>Phthanoperidinium crenulatum</i> <i>Thalassiphora delicata</i></p> <p>Interpretion: top of Zone 5</p>
<p>Gouge on clay tectonic fault (Marke, 24.10.89)</p> <p>Present <i>Dracodinium varielongitutum</i> (less frequent than in wall clay) <i>Homotryblium</i> spp. (markedly less frequent than in wall clay) <i>Eatonicysta ursulae</i> <i>Phthanoperidinium echinatum</i> <i>Wetzeliiella</i> aff. <i>lobisca</i> <i>Thalassiphora delicata</i> <i>Kallosphaeridium brevibarbatum</i> <i>Phthanoperidinium crenulatum</i> <i>Areoligeraceae</i> sp. C</p> <p>Absent <i>Polysphaeridium zoharyi</i> <i>Charlesdowniea clathrata-coleothrypta</i> <i>Deflandrea oebisfeldensis</i> <i>Trigonopyxidia ginella</i> <i>Pseudomasia trinema</i></p> <p>Remarks: abundant pyritized diatoms and some sponge spiculae</p> <p>Interpretion: mixture of material predominantly from Zones 2 and 3</p>	<p>Wall clay (Marke, 27.10.89)</p> <p>Present <i>Dracodinium varielongitutum</i> <i>Homotryblium</i> spp. <i>Eatonicysta ursulae</i> <i>Phthanoperidinium echinatum</i> <i>Thalassiphora delicata</i> <i>Polysphaeridium zoharyi</i> <i>Dracodinium solidum</i> à <i>varielongituda</i> <i>Deflandrea oebisfeldensis</i> à <i>phosphoritica</i></p> <p>Absent <i>Charlesdowniea clathrata-coleothrypta</i> <i>Phthanoperidinium crenulatum</i></p> <p>Remarks: no pyritized microfossil fragments</p> <p>Interpretion: top of Zone 5</p>

Fig. 4.63. Significant organic-walled phytoplankton species present and absent in selected samples of clastic dyke gouge and clay tectonic fault gouge and respective adjacent wall clays in Marke clay pit, Belgium. (Dr. J. De Coninck, pers. comm.)

4.3.3. Microfossil dating

The most unambiguous way to reveal any vertical transport of the clastic dyke material, whether upwards, downwards or local expulsion, is by dating the gouge. We were fortunate that the Belgian Cenozoic has been studied in great detail by a number of micropalaeontologists. This is especially true of the Ypresian stratotype (Dupuis, De Coninck & Steurbaut, 1988). Dr. J. De Coninck of the Universiteit Gent (Belgium) investigated the organic-walled phytoplankton assemblages of the clastic dyke gouge and the S3 wall clay (Marke, 10-11.09.90), and the assemblages in the gouge along major clay tectonic fault F1 and the wall clay there (S?, Marke, 24-27.10.89). The material was correlated with a zonation proposed for the Ypresian stratotype (fig. 4.62; De Coninck, 1988).

The data of the De Coninck are given in fig. 4.63, and his interpretation follows below. The assemblage of the S3 wall clay next to the clastic dyke most probably correlates with the top of Zone 5, while that of the clastic dyke itself indicates that the gouge is a mixture of material from Zones 2 and 3, and small amounts of Zones 4 and 5. The assemblage of the wall clay next to the clay tectonic fault also probably correlates with the top of Zone 5, while that of the fault gouge indicates that it is a mixture of material predominantly from Zones 2 and 3. The abundant pyritized diatoms in both gouges are typical of the diatom bloom known from Palaeocene-Eocene transitional strata (Willems & Moorkens, 1988).

We conclude that the gouge material along both clastic dykes and clay tectonic faults in the Marke clay pit was injected upwards from 30-80 m below within the same clayey Formation. This new evidence strongly corroborates our main working hypothesis (§1.4.4), by which it was predicted.

4.3.4. CT scans

X-ray Computer Tomography is an imaging technique that revolutionized medical radiology by producing anatomical cross-sectional images of extraordinary accuracy and clinical detail (Wellington & Vinegar, 1987). In a CT scanner (*ibidem*; Mandl, 1988, p.91), an X-ray source moves on a circular track and emits a fan of rays which penetrate a thin (1-2 mm) slice of the object. The intensity of the transmitted rays is measured by an array of detectors positioned on a circular arc, and recorded for

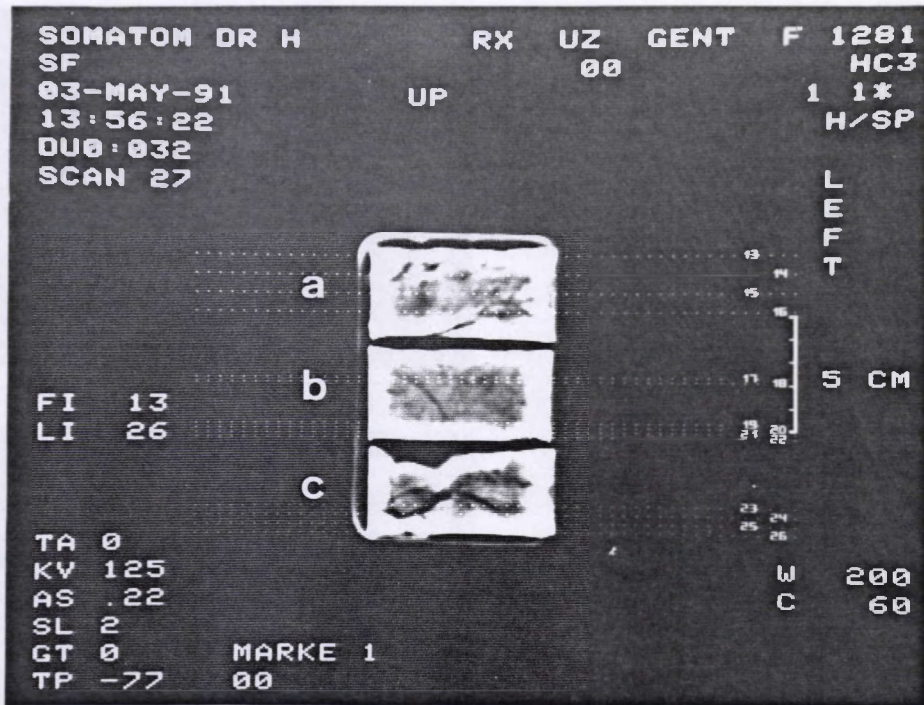


Fig. 4.64. Topogram (conventional X-ray image) of box samples from fig. 4.46, with indication of subsequent CT scans. **a** is sample 120990/3, **b** is sample 120990/2, **c** is sample 120990/1.

any position of the moving source. From these data the X-ray attenuation in any object element ($1\text{--}4\text{ mm}^3$) is calculated by a back-projection algorithm in the scanner's computer and the final image is generated for any cross-section of the object. Attenuation differences as small as 0.1 % can be measured in 3D and related to comparably small differences in density and atomic composition, without destroying the object.

The petrophysical applications of CT are numerous (Wellington & Vinegar, 1987), but we only used the University Hospital CT scanner (type SOMATOM DrH; courtesy of Prof. M. Kunnen and Dr. H. Lauwers, Radiology lab) to study the fractures in the oriented box samples of the Marke clay pit (fig. 4.46), before they were sliced to thin sections. Fig. 4.64 is a conventional X-ray image or *topogram* of the three box samples impregnated in a lump of polyester (rounded corners), and indicates the CT sections taken. Notice the different spacings for each box sample, chosen on the basis of expected structural complexity.

Fig. 4.65 gathers selected CT scans and the thin sections that were made to coincide with each other. These are all vertical sections more or less perpendicular to the strike of faults and clastic dykes shown in fig. 4.46. In the CT images, brighter areas stand for higher X-ray absorption and density. Voids (2) and cracks due to desiccation of the sample stand out most clearly. Some of the darker lines in the scans

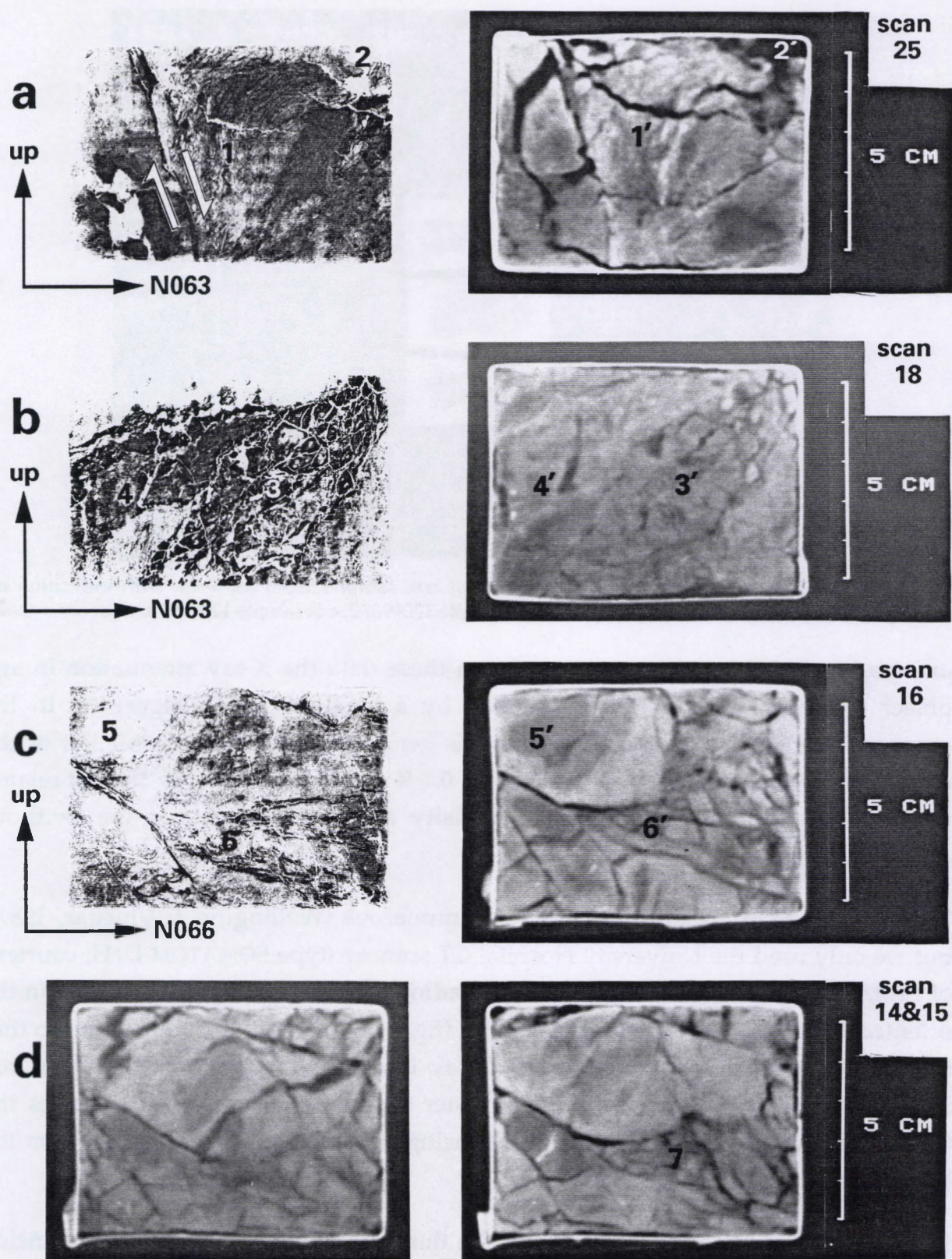


Fig. 4.65. CT scans (right) and thin sections (left) made to be almost coincident with each other and comparable with fig. 4.46. These are all vertical sections more or less perpendicular to the strike of faults and clastic dykes; enlargement is $\times 0.7$. Box sample 120990/1 (a) covers a major clay tectonic fault (arrows) and a downfolded nummulitic lamina (1). Voids (2) and cracks appear black on CT. Box sample 120990/2 (b) covers a thick (3 cm) clastic dyke with a typically breccious gouge (3). In box sample 120990/3 (c), the contrast between coherent wall clay (5) and the breccious gouge (6, 7) in a clastic dyke is more marked.

(e.g. below 6') can be attributed to worse packing in the gouge (Mandl, 1988). Other dark parts (e.g. at 5') indicate insufficient polyester impregnation of the sample, resulting in holes in the thin section (at 5).

Box sample 120990/1 (a) covers a major clay tectonic fault (arrows) and a nummulitic lamina (1). The downfolding of this lamina, highlighted by partial pyritization of the nummulites, is a rather odd reverse drag on this normal fault. This is perhaps a miniature version of those seen on seismic sections (fig. 2.10), and may also be explained by reverse shear along the fault when the clay was still undercompacted and very plastic, followed by normal collapse.

Box sample 120990/2 (b) covers an up to 3 cm thick clastic dyke with a typically breccious gouge (3). The dark zone around (4) that seems to join the clastic dyke is only partly brecciated. The other part is dark because it is more clayey. In box sample 120990/3 (c), the contrast between coherent wall clay (5) and the breccious gouge (6, 7) in a clastic dyke is more marked. The resolution in these low contrast CT images is about 1 mm, which is obviously worse than that of thin section photographs. However, closely spaced images, such as those in figs. 4.65c and d, can be generated easily. It is clear that CT is a fine, non-destructive technique to quickly get a 3D hold on complex and very small scale deformation. Thin sections can then be made at judiciously selected positions and orientations.

4.3.5. Thin sections

The microscopic structure and composition of the gouge in clastic dykes and along faults has been studied in thin sections. They have been prepared by impregnating undisturbed and oriented box samples from the clay pits in Marke and Zonnebeke (figs. 4.45 and 46) with polyester, slicing and grinding to 30 μm (Murphy, 1986). A Zeiss Axiophot with provisions for incident and fluorescent light (KFA-Jülich, Germany) was used to investigate organic matter and dark or opaque minerals, and a microscope of the Mineralogy Lab (Universiteit Gent) for other observations. We will first describe and interpret the microscopic structure of faults and clastic dykes and the texture of the gouge, and then search for an explanation of the gouge's dark colour.

Micromorphology

Part of a clastic dyke in the Zonnebeke clay pit was studied in its entirety by overlaying the thin section with a grid, copied on transparent plastic, and drawing

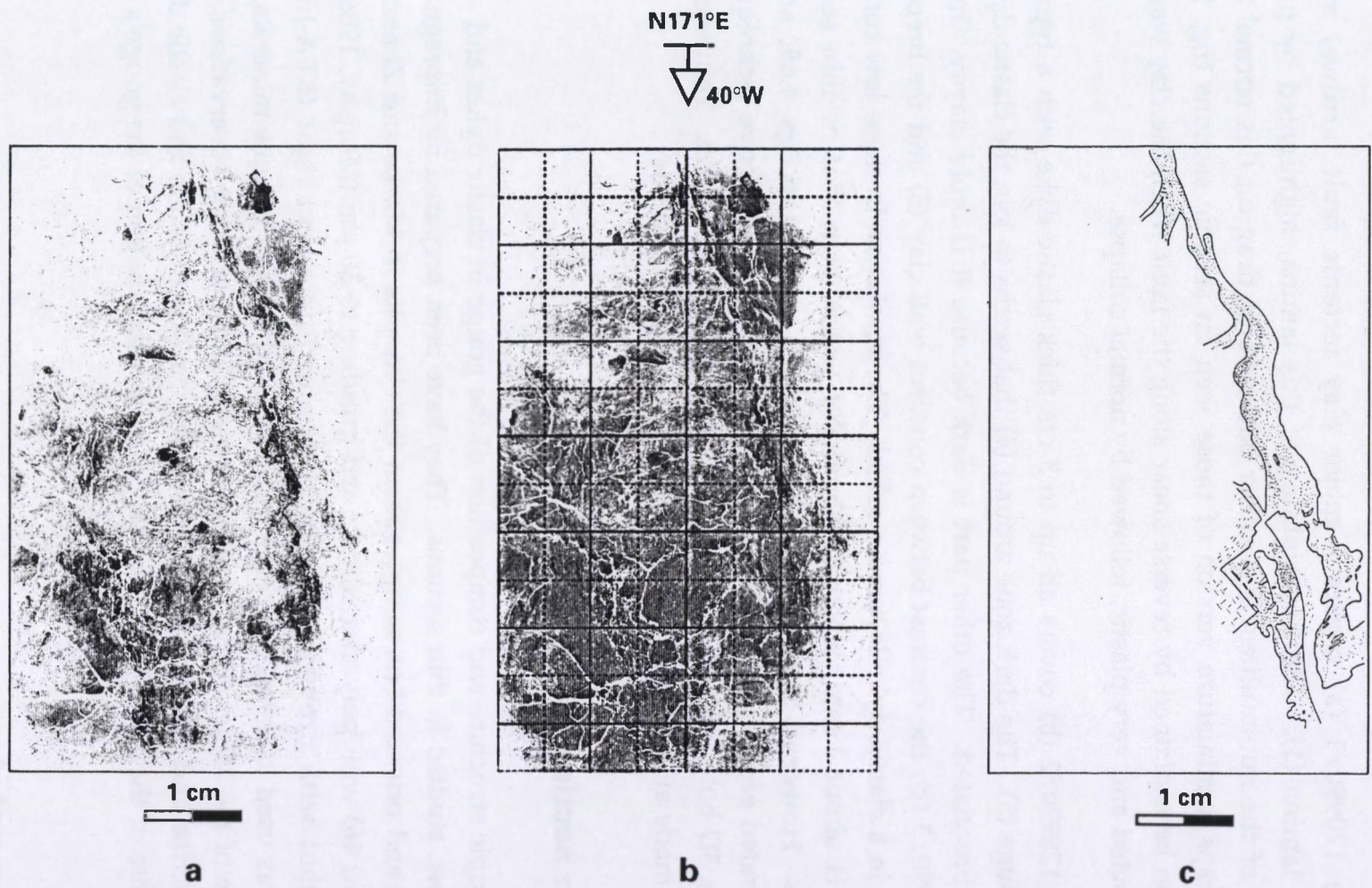
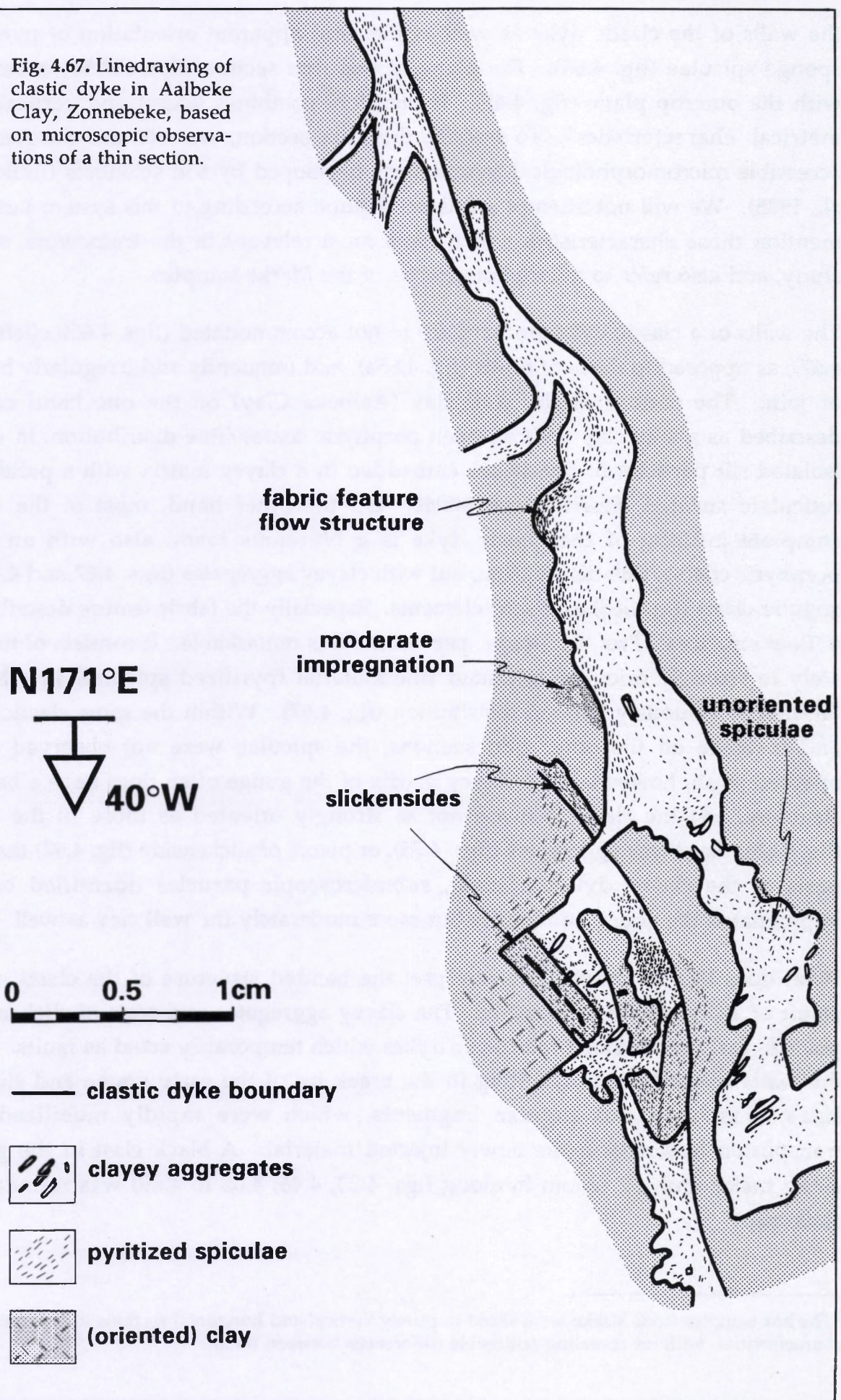


Fig. 4.66. Clastic dyke in a box sample from the Zonnebeke clay pit (fig. 4.45). **a** is a photocopy of a thin section; in **b** it is overlain with a grid (0.5 cm maze width) so that the overall structure as well as the details of this clastic dyke could be drawn accurately (**c** and fig. 4.67).

Fig. 4.67. Linedrawing of clastic dyke in Aalbeke Clay, Zonnebeke, based on microscopic observations of a thin section.



the walls of the clastic dyke as well as the local apparent orientation of pyritized sponge spiculae (fig. 4.66). The plane of this thin section dips 40° W, coincident with the outcrop plane (fig. 4.45). It therefore combines lateral and vertical geometrical characteristics¹. To *describe* this thin section, we will use the rich and accessible micromorphological terminology developed by soil scientists (Bullock *et al.*, 1985). We will not attempt a full description according to this system but only mention those characteristics which seem most relevant in the framework of this study, and also refer to microphotographs of the Marke samples.

The walls of a clastic dyke are partially to not accommodated (figs. 4.65b,c(left) and 4.67), as opposed to those of faults (fig. 4.65a), and frequently and irregularly branch or join. The texture of the wall clay (Aalbeke Clay) on the one hand can be described as a silty clay with an open porphyric coarse/fine distribution, in which isolated silt particles of quartz are embedded in a clayey matrix with a parallel or reticulate striated birefringence fabric. On the other hand, most of the dense complete infilling of the clastic dyke is a breccious loam, also with an open porphyric coarse/fine distribution, but with clayey aggregates (figs. 4.67 and 4.75) or angular clasts (fig. 4.68) as macro-elements. Especially the fabric feature described as a 'flow structure' (Prof. G. Stoops, pers. comm.) is remarkable. It consists of moderately to strongly oriented columnar fine material (pyritized spiculae) in a linear, fan-like or sinuously banded distribution (fig. 4.67). Within the same clastic dyke and in those on the other thin sections, the spiculae were not observed to be oriented at all, however. The clayey matrix of the gouge often does have a banded structure, but the clays in it are not as strongly oriented as those in the clasts (fig. 4.68), the clayey aggregates (figs. 4.75), or pieces of slickenside (fig. 4.67) that line parts of the clastic dykes. Lastly, submicroscopic particles (identified below) impregnated the gouge and locally but more moderately the wall clay as well.

What does this all mean? We *interpret* the banded structure of the clasts as the result of a first phase of injection. The clayey aggregates and rests of slickensides point to early shear along the clastic dykes which temporarily acted as faults. Then the walls opened again, resulting in the break up of the early gouge and slickensides to isolated and angular fragments, which were rapidly mobilized and transported upwards in the newly injected material. A black clast in the gouge along major fault F2 (zoom in along figs. 4.23, 4.46, 4.65 to 4.69) was rounded by shearing.

¹The box samples from Marke were sliced in purely vertical and horizontal sections to separate these characteristics, without revealing noticeable differences between them.

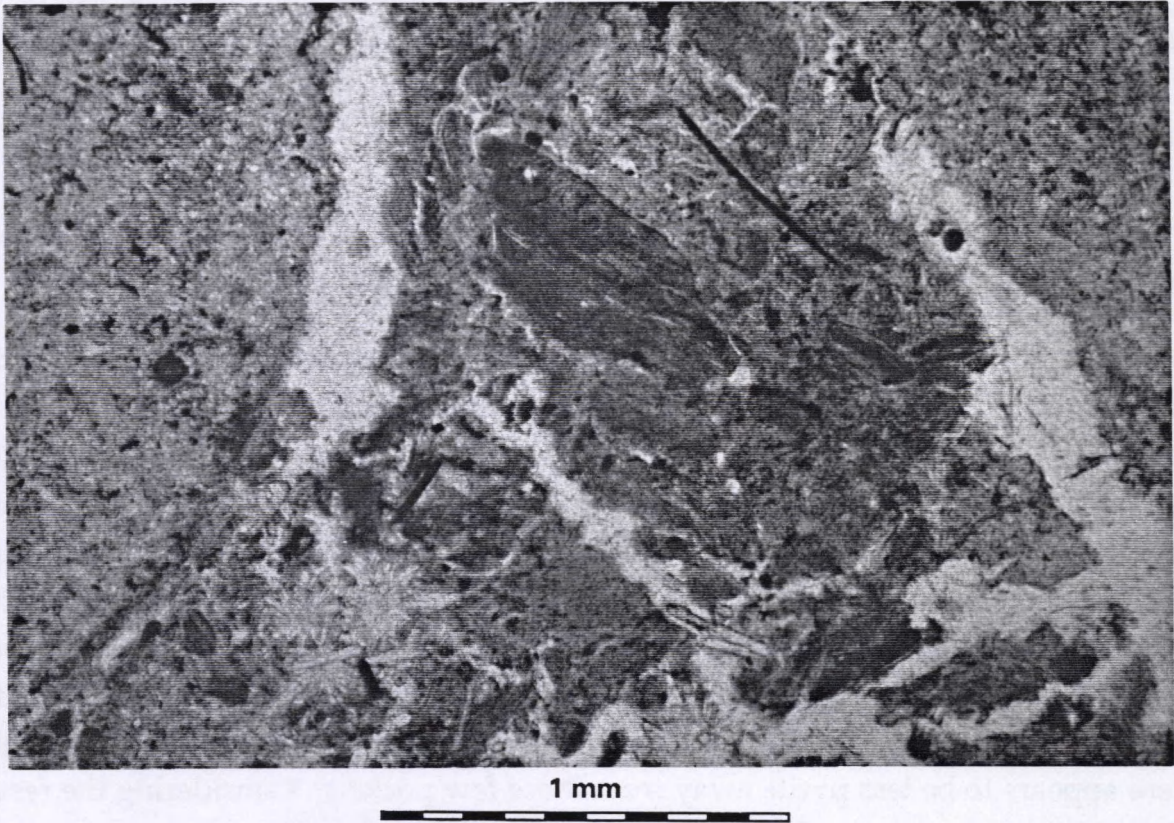


Fig. 4.68. Breccious texture of gouge in clastic dyke (Marke): angular clasts with a banded structure in a clayey matrix. Wall clay in upper left and right corners (transmitted light).

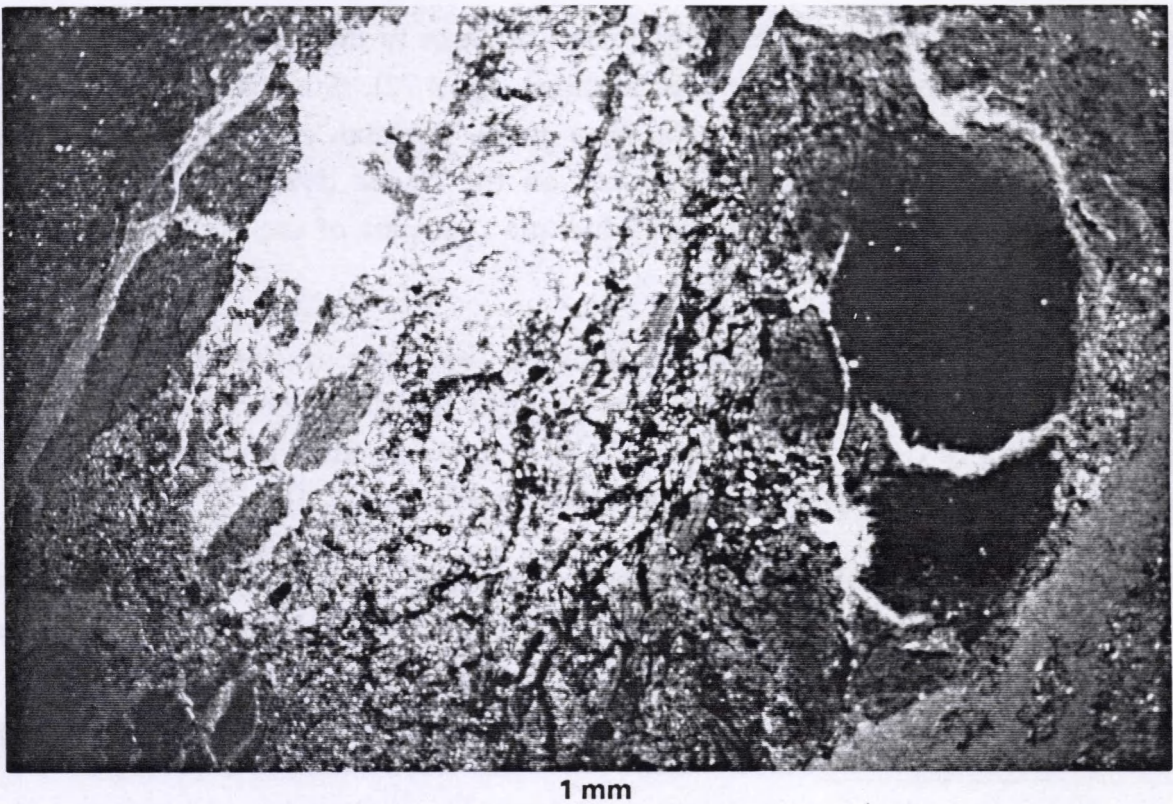


Fig. 4.69. Clast (dark patch on the right) rounded by shearing along a fault (F3, Marke), lined with strongly oriented clay particles occupying most of the photograph (transmitted light).

Based solely on microscopic evidence, the short history interpreted above fits perfectly into our main working hypothesis (§1.4.4) and even further refines it.

The gouge's dark colour

The following observations relate to the search for an explanation of the dark colour of the gouge in clastic dykes and along some of the clay tectonic faults.

At one time, a higher concentration of microcrystalline pyrite was also suspected of causing the darker to black colour of the gouge in outcrop. Isolated lenticular pockets of pyrite on the contact surface between gouge and wall clay strengthened this suspicion (fig. 4.70). A systematic inspection of thin sections however revealed microcrystalline pyrite with a *framboidal*¹ texture characteristic of a bacterial origin (fig. 4.71), pyritized sponge spiculae (fig. 4.72) and partly pyritized nummulites (the latter concentrated in laminations), all fairly homogeneously and sparsely distributed throughout gouge and wall clay. Except for a few pockets in one thin section, there seems to be no visible pyrite enrichment in the fault gauge. Actually, there appears to be less pyrite away from those few pockets. Considering the results of the chemical analyses that showed no difference in Fe concentration, the distribution of pyrite was not quantified microscopically.

Interestingly, the concentration of pyritized diatoms in the gouge is so large locally that they are prominent even in thin sections (fig. 4.72). Such an abundance points directly to the diatoms' origin at the base of the Ypresian clay (§4.3.3). Given that this is also the case for the thin section on the clastic dyke near the top of the Aalbeke Clay in Zonnebeke, we can conclude that part of the gouge material was injected upwards as much as 100 m.

As indicated by the organochemical analyses, the concentration of organic matter in the gouge is rather low and cannot account for the dark colour either. Low concentrations of both opaque minerals and organic matter are also evident from fig. 4.73, a photograph chosen to show at least some of it.

The only visible non-structural difference between the wall clay and the gouge resides the level of oxidation. The clay in the fault gauge is black largely because of thick clouds of dark, non-opaque, non-fluorescing particles, only resolvable at the largest microscopic magnification, with an orange metallic lustre in incident light,

¹A *framboid* is a microscopic aggregate of pyrite grains in argillaceous rock, often in spheroidal clusters resembling raspberries. It is linked with the presence of organic materials; sulfide crystals fill chambers or cells in bacteria. (AGI, 1980)



Fig. 4.70. Pocket (arrow) of pyrite microcrystals along a black clastic dyke (a-a'; Marke, 11.09.90).

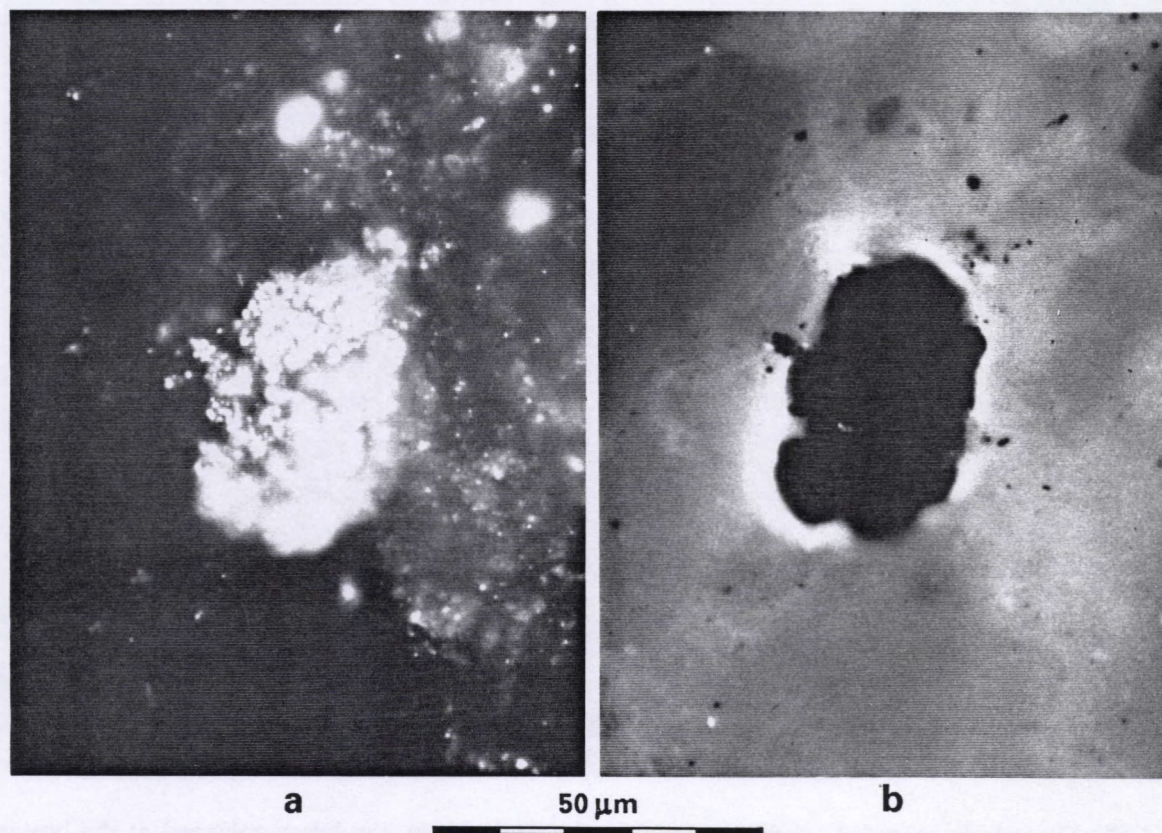


Fig. 4.71. Pyrite framboid, glistening in incident light (a), still surrounded by the bacteria's cell wall, shining in fluorescent light (b), in wall clay next to clastic dyke, Marke.

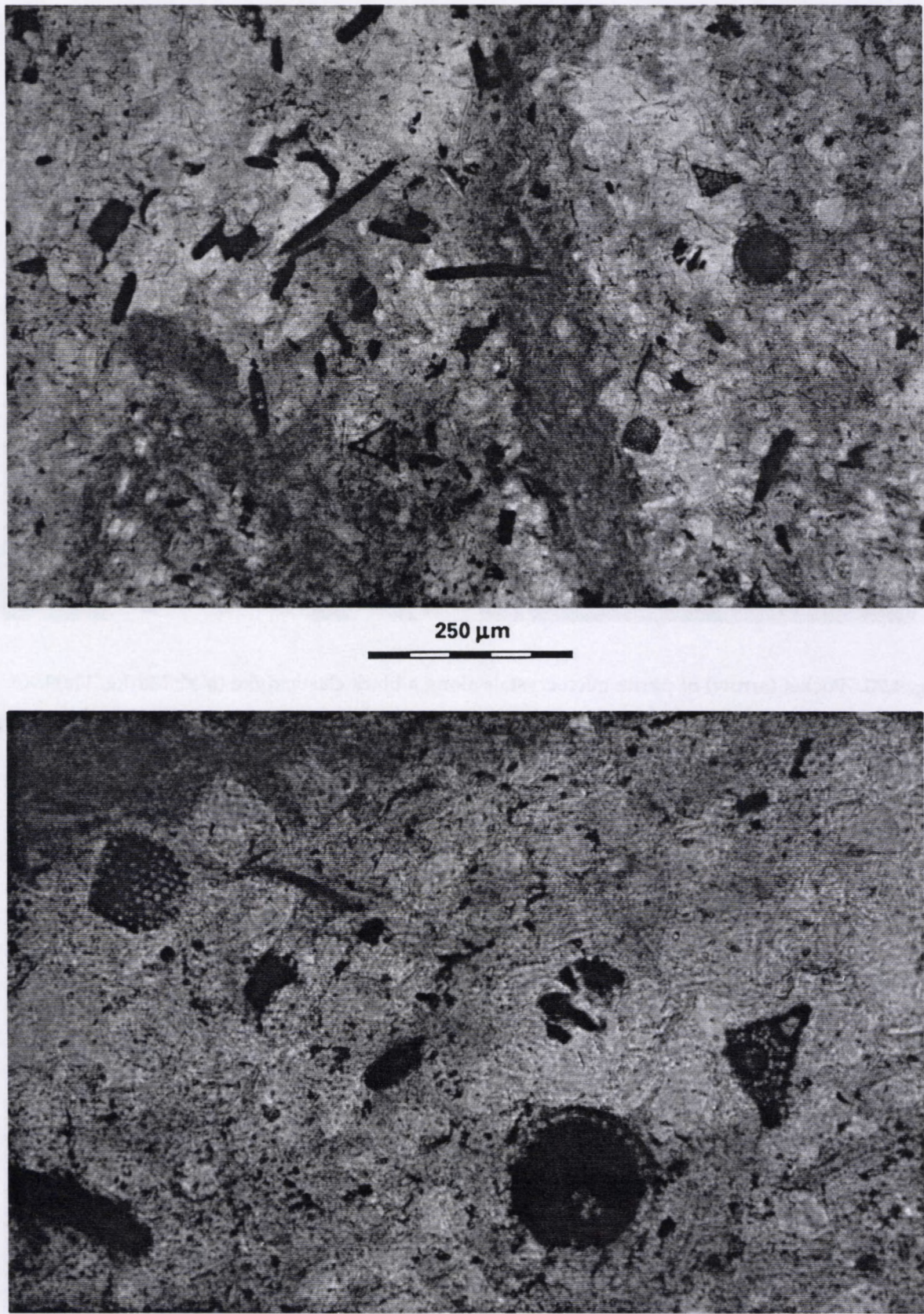


Fig. 4.72. Disorderly oriented sponge spiculae and diatoms (top, the latter enlarged at the bottom; both transmitted light) in a clastic dyke, Marke. Diatoms are only this abundant at the base of the Ypresian clay, about 80 m below the site of this sample.

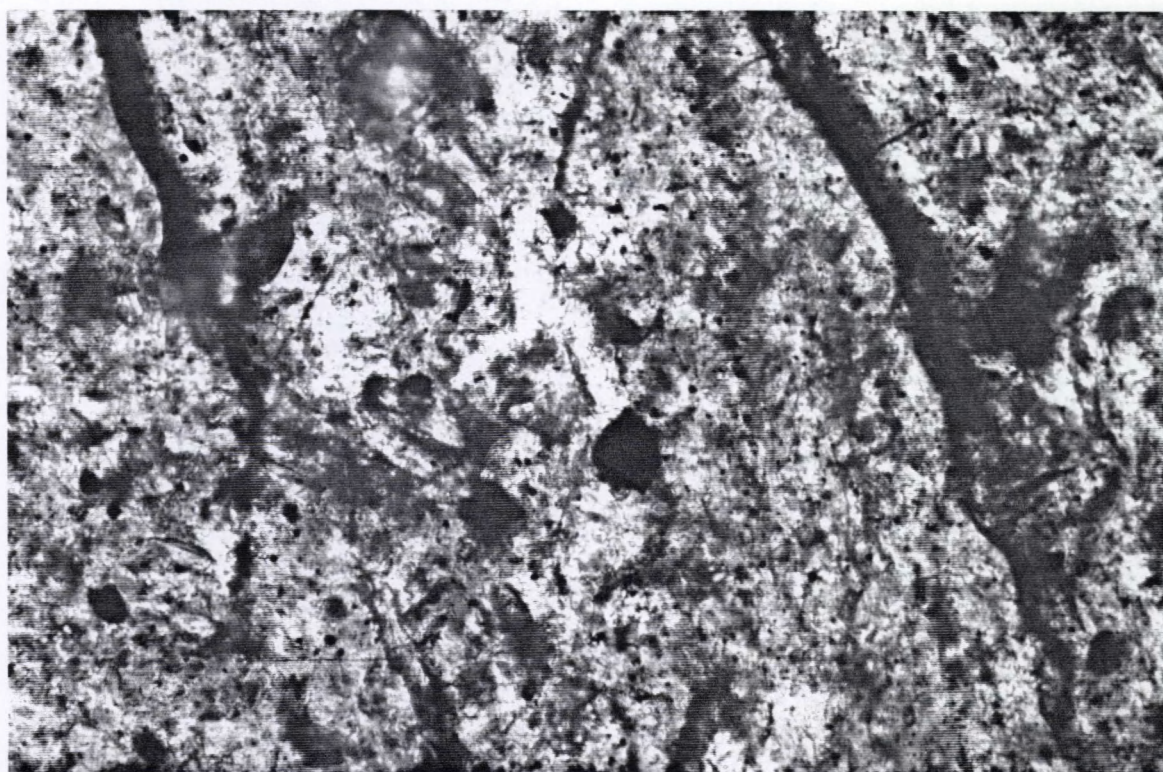
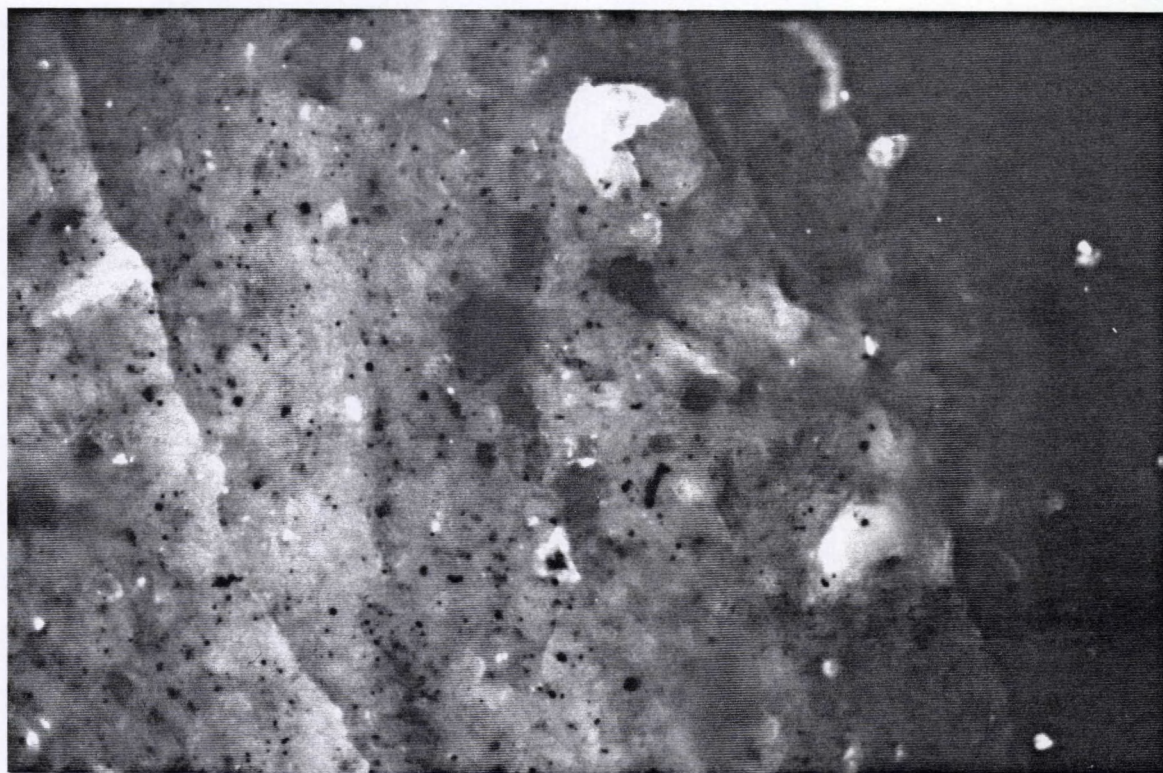
50 μm 50 μm

Fig. 4.73. More or less typical view of a fault gouge in Marke, with few opaque particles (black in transmitted (top) and in fluorescent light (bottom)) or organic particles (transparent in transmitted light and shining in fluorescent light).

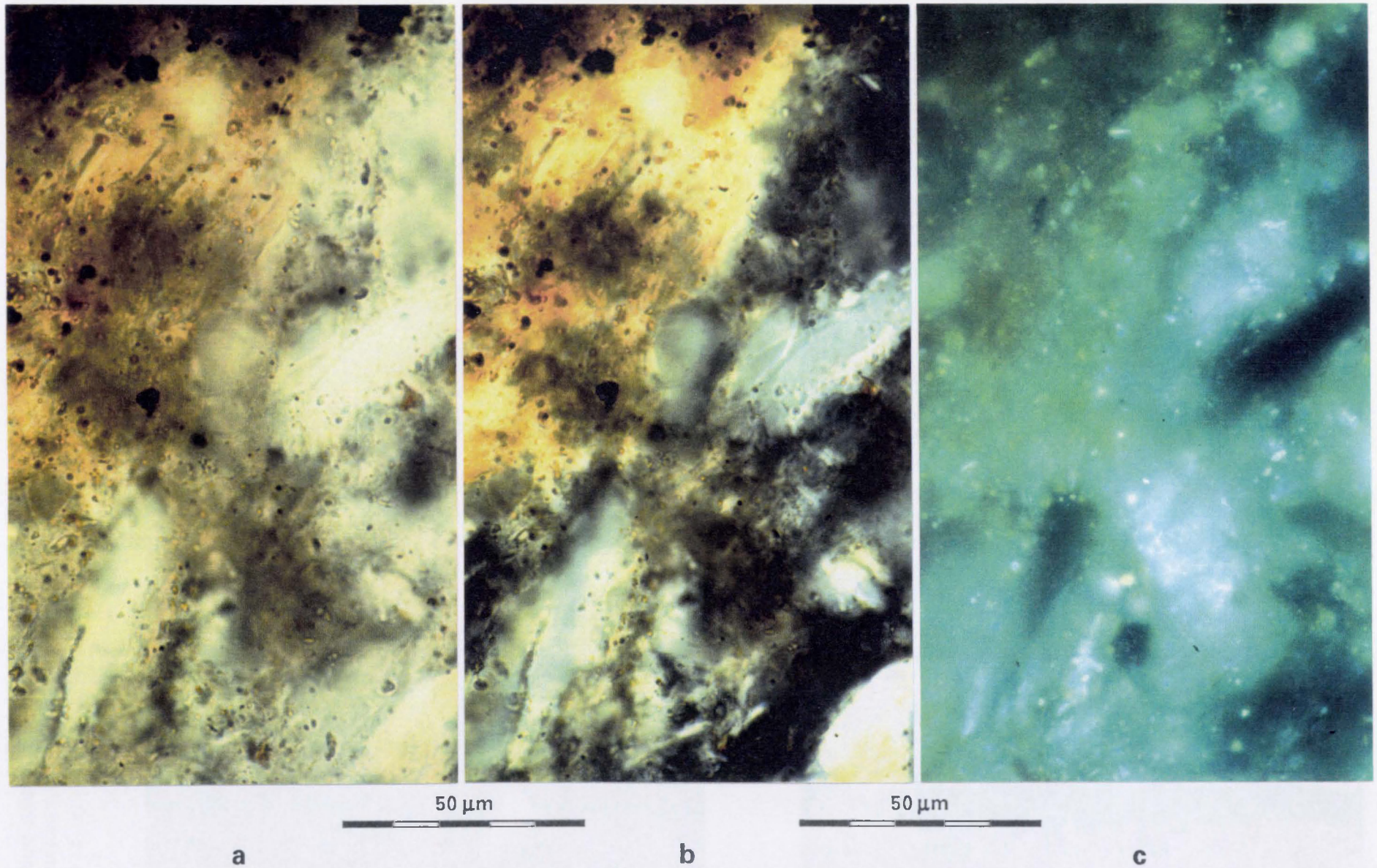
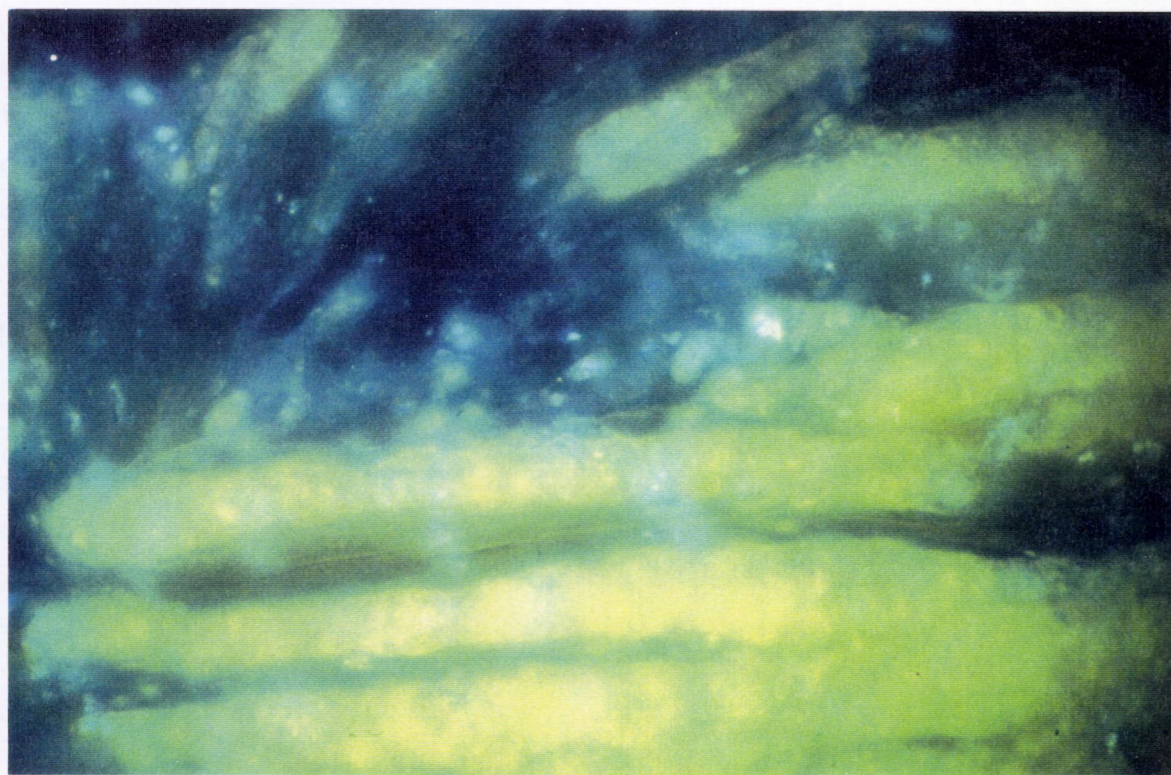


Fig. 4.74. Contact between clastic dyke (upper left corners) and wall clay (lower right corners), Marke, in transmitted (a), cross polarized (b) and incident light (c). Clays in the gouge are darker (a) and more strongly oriented (b) than in the wall clay, and impregnated by particles with an orange lustre (c).



50 μm



50 μm

Fig. 4.75. Uneven distribution of Fe-hydroxide particles (dark but non-opaque in cross polarized light (top) and with orange lustre in incident light (bottom)) in a clayey aggregate with strong internal orientation of clay particles; in clastic dyke, Marke.

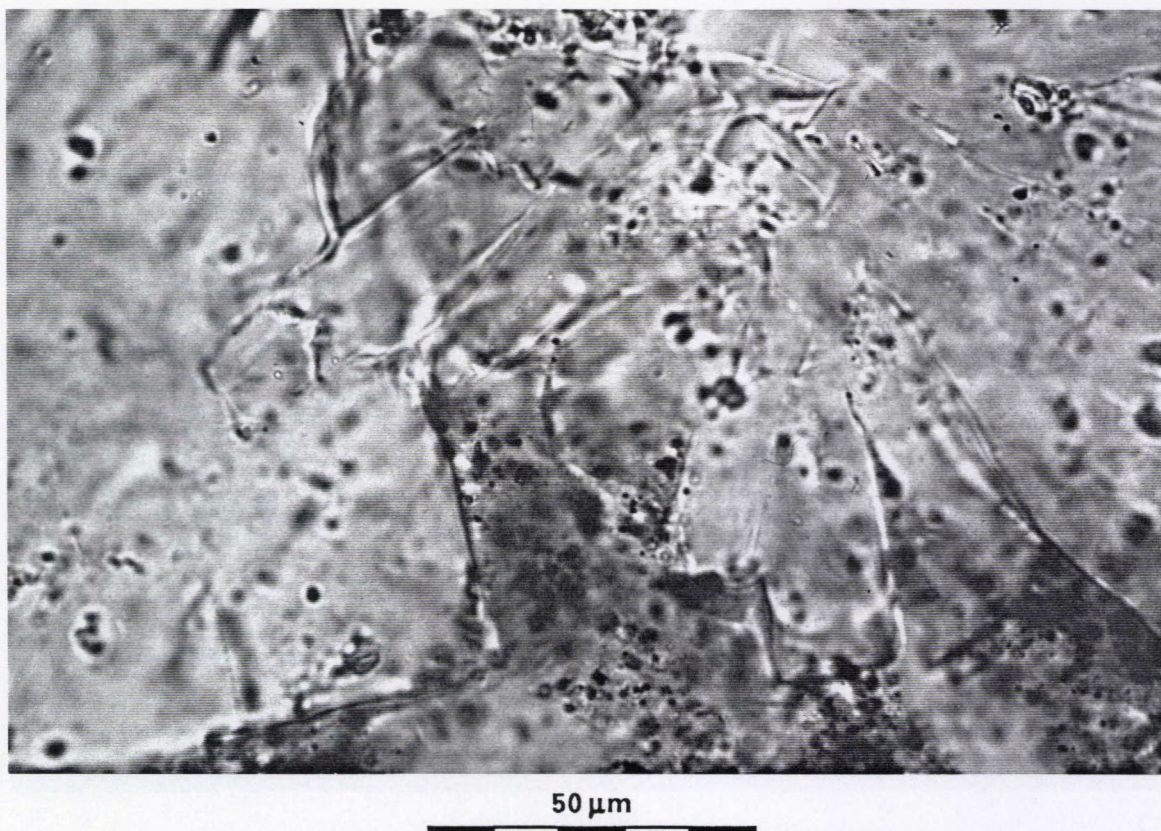


Fig. 4.76. Sulfate salt (thenardite?) microcrystalline aggregate with intergrowth; in clastic dyke, Marke.

and identified by Dr. R. Littke (KFA-Jülich, Germany; pers. comm.) as a Fe-hydroxide (figs. 4.74-75). These particles are fairly homogeneously distributed in the gouge matrix (fig. 4.74, upper left corners), but unevenly impregnated in the clayey aggregates (fig. 4.75) and almost entirely absent in the wall clay, even where it is in immediate contact with the gouge (fig. 4.74, lower right corners).

Such an interpretation of the darker colour can be coupled to the sulfate crystals (fig. 4.76; thenardite or Na_2SO_4 according to F. Mees, Universiteit Gent, pers. comm.) frequently observed in the gouge. These sulfates and Fe-hydroxides may have resulted from the oxidation of microcrystalline pyrite. The wall clay was hardly affected by the oxidation, because Fe-hydroxide particles are rare outside the gouge and because the cell wall around the framboidal pyrite in fig. 4.71 is still intact. Why the fluids ejected along the clastic dykes were oxidizing or at least carrying these Fe-hydroxide particles is an unanswered question.

5. Conclusions

In this final chapter we gather all conclusions reached during this thesis work and formulate a new synthesis, an updated story of clay tectonic deformation in Palaeogene clayey sequences in Belgium.

5.1. Conclusions proper

Conclusions related to the seismic method:

1. We have shown that a dense network of 2D sections can go a long way in small scale 3D modelling. A network of perpendicularly intersecting profiles with a constant maze width can unambiguously reveal linear structures with a length and spacing of at least twice the maze width. Such a network has been equalled to pseudo-3D coverage in this thesis. Information on smaller or denser features may be spatially aliased, that is, small faults may appear as part of larger ones.
2. It is possible to scale down the whole 3D seismic acquisition and processing methodology to the geotechnical world of very small structures. SEISCAT is a very high resolution, water born 3D seismic reflection acquisition system up to this task.
3. Both such 3D and pseudo-3D seismics with decimetre resolution vertically, critically depend on very precise dynamic positioning. In addition, high position accuracy requires exact synchronization of positioning and acquisition, and short offsets.

Conclusions related to digitization of curves and to data redundancy:

4. The precision of manual digitization of curves depends on the operator, curve complexity and the quality of the digitizer tablet, in that order.
5. The mean distance between two digitized versions of a sufficiently long part of a typical curve can be expected to be a stable and dependable measure of an operators digitization precision at a certain level of curve complexity. Hence, this measure should and can be calculated routinely at the start of each digitizer session.

6. The manual digitization procedure as proposed in §3.5.1.3 ensures both storage efficiency and data quality.
7. A new curve simplification algorithm reliably and objectively removes insignificant vertices from a polygonal line in 3D, below any given level of detail. It is based on a simple but sufficiently effective concept of maximum local significance, and scans the original segmented curve sequentially, so that it is also efficient in processing time.
8. Curve simplification can be used to reduce data redundancy before permanent storage and at the start of surface modelling, without a loss of significant information.

Conclusions related to computer aided 3D surface modelling:

9. We defined 3D surface modelling as a process of integrated objective mapping, geological interpretation and 3D visual inspection. We demonstrated that if these three tools are thoroughly integrated into an interactive computer program that provides immediate visual feedback, they not only allow to map structural data that are next to impossible to hand-contour, but also become an exacting instrument to quantify an evolving 3D geological image of the subsurface.
10. In order to reach a 3D understanding of the relative clay tectonic block deformations and displacements and to replace a manually drawn, qualitative map of the fault pattern by a quantitative model of both a typical horizon and the system of fault scarps on the basis of a network comprising 20+40 seismic sections with a total of about 1000 fault cuts, and infested with vertical and horizontal mis-ties, there was a clear need for the numerical assistance of a powerful 3D surface modelling tool. The Geofox program is such a tool. The many different applications outside the domain of this thesis bear testimony to Geofox' versatility.
11. The new 3D surface modelling method implemented in Geofox supports the 3D surface modelling process with repeated cycles consisting of three stages. Alternately, the user *adapts* the *triangulation* so that it better reflects his/her interpretation, and *grids* it to see smooth but possibly faulted contours and to *inspect* the on-going interpretation *in 3D*.
12. Any change in the correlation of fault cuts implicitly changes the faulted surface. We therefore envisaged to interactively model surface discontinuities as part of a generally smooth surface, not separately. Basically, this entailed a

direct interaction with data points, their *known* connections (the 2D shape along a profile) or the correlation of fault cuts and other features, which are *interpreted* connections. The latter determine the 3D shape of a geological surface. A network of triangular connections between the data points is therefore the most logical data structure to interact with directly and to create the surface model efficiently.

13. A new *hybrid triangulation/grid modelling method* combines the straightforwardness of triangular modelling with the advantages of regular grids. It incorporates a new gridding technique, with which a grid can directly inherit the shape of the underlying triangulation, together with interpreted discontinuities, but without the need for explicit digitization of scarp or fault traces. After iterative smoothing with splines in variable tension, the resulting grid can be partially smooth and partially discontinuous.
14. Sophisticated 3D computer graphics is not merely an eye-catching fancy after all the 'serious' work is finished. As an integrated part of 3D surface modelling and mapping it reveals the smallest detail as well as any remaining flaw in its 3D context, and therefore helps to improve overall quality.
15. It is possible to construct a gridded stratigraphic framework semi-automatically if the seismic or well data are still accessible after gridding of the separate surfaces. Whether this automatic framework makes sense or not depends on the interpretation and precise positioning of those data.
16. The results of computer aided interpretation and mapping not only depend on the capabilities of the software, but also on those of the interpreter. This is also true for Geofox. The user should know the data and possible errors or imprecisions, as well as the available software procedures and their sensitivity to changes in control parameters. (A tutorial in the Manual, on-line help, and Chapter 3 of this thesis should suffice as guidance, if read.)

Conclusions related to new geological evidence:

17. It was already known from 2D seismic data that the kind of clay diapirism seen under and close to the river Scheldt in Rupelian clays is closely related to the Tertiary-Quaternary unconformity. In a 3D model, the superposition of Scheldt gully and diapir is remarkable, and it may indicate that the origin of the diapir resides in differential decompaction.
18. The normal and concave sag fault in the North Hinder area cuts through all of the Meso-Cenozoic cover, and does not change shape in the basement. We

interpret the deformation as the result of E-W extension, possibly of Oligocene age.

19. The main northward direction of clay tectonic faults in the North Hinder area is roughly parallel to the nearby sag fault that cuts the basement and all Tertiary strata. The Ypresian clay there also shows a slight irregular undulation superposed on the slight regional NE dip. Clay tectonic faults are not very straight in a horizontal plan, and some are markedly concave towards the downthrown side. The faults are arranged in a graben-like setting in the antiform domain and in a horst-like setting in the synform domain, while blocks on fold limbs dip towards the trough line. This kind of clay tectonic deformation points to a purely vertical and gravitationally driven movement of material. In view of the general direction, the deformations may have been triggered tectonically.
20. Gravity sliding can be ruled out entirely as deformation driving force system for clay tectonics in this area.
21. We described a host of hitherto unreported structures in clay, including termination splays, a listric splay, a horizontal fault with two slip vectors, a horse and its internal structure and folded faults. Especially the latter indicate sudden failure of undercompacted plastic clay, followed by plastic deformation during later compaction.
22. Numerical palaeostress inversion revealed that the oldest stress regime was almost purely vertical compression. A weak indication of E-W extension was regarded as unreliable, but it happens to be fairly compatible with that seen in the North Sea and with a phase of extension that affected a large part of the European continent during the Rupelian. The second generation of faults can be related to a phase of Miocene Alpine NE-SW compression.
23. In close relation to some of the clay tectonic faults, clastic dykes traverse the Ieper clay. The more intense deformation and faulting of clastic dykes indicates that they generally preceded clay tectonic faults. They are filled with a black, breccious gouge of angular clayey clasts, which are rounded by shearing if they occur along dykes that also acted as faults.
24. In a clay pit in Marke (Belgium), the dinoflagellates in a clastic dyke are from between 30 and 50 m below the stratigraphic level of both wall clays. Abundant pyritized diatoms have been injected from the base of the clayey formation. Part of the gouge material in the Zonnebeke clay pit may have risen as much as 100 m relative to the wall clays.

25. Clays *can* temporarily behave viscously and undergo gravitation driven deformation by the development of undulations on a Rayleigh-Taylor instability due to undercompaction.
26. The Ypresian Formation and most notably its silty intercalations were also affected by late Tertiary tectonic SW-NE compression/NW-SE extension.
27. Some clay tectonic faults have been reactivated during the Quaternary.

Conclusions related to hydrocarbon migration along pre-existing fractures in clays:

28. Probably most of the microfractures in the outcrops of London/Ieper clays are due to the overconsolidation effect. This effect is unlikely to occur or to be so prominent in the deeper parts of a basin, where most mobile hydrocarbons are generated.
29. Clay tectonic faults constitute only a sparse network of fractures. Truly tectonic faults and joints have been shown to complicate that network, but most of the hydraulic microfracturing that precedes *primary* migration would still need to be accomplished at depth.
30. The presence of tectonic joints and (clay) tectonic faults in clayey cap rocks may well facilitate the formation of hydrocarbon dykelets and thus *secondary* migration out of overpressured hydrocarbon reservoirs.

Conclusions related to geologic tools:

31. 3D surface modelling with Geofox has enabled us to gain geological insight, and allowed us to weed between multiple hypotheses and look at 2D profiles with new eyes. Geofox is a powerful tool (and nothing more than that) in the hands of knowledgeable geologists.
32. With an adequately sharpened spade (cfr. fig. 4.18b), outcrops of microfractured and seemingly homogeneous clays can be cleaned up perfectly, revealing the minutest sedimentary and deformation structures, and allowing judicious sampling. The most efficient tool to do the same in silts and sands is a new type of sand scraper (cfr. fig. 4.20).
33. Also in contrast to preceding field work, it was possible to gather a sufficiently large number of 3D slip measurements to unveil the spatial relations of clay tectonic faults in outcrop, to calculate the determinant palaeostresses, and to unmask "reverse" faults.
34. A normal fault on a sloping outcrop may appear to be reverse, and *vice versa*, depending on outcrop orientation relative to fault strike. In case of a sloping

outcrop, it is better not to draw arrows to indicate interpreted relative movement, because they may be either confusing or wrong. Because sloping outcrops are deceptive, it is mandatory to *measure* all orientations, including that of the outcrop.

Conclusions related to the geotechnical behaviour of Ypresian clay:

35. Slumping of slopes in Ypresian clay is caused by the opening and wetting of microfractures, and is rarely, if ever, related to local clay tectonic faults. Slumps are most likely where a slope cuts the deepest parts of the undulating top of the clay, because that is where phreatic water in the overlying sediments collects.
36. Excavations for tunnels and steep slopes cause stress differences that lead to the opening of microfractures as well as some of the local clay tectonic faults. Depending on relative orientations, opening of the latter may extend deeply into the clay face. Clay tectonic faults may present a non-negligible permeability problem in such circumstances, because the well- or overconsolidated clay is so stiff that such fissures do not easily close by plastic deformation.
37. Along the flat bottom of dump sites there are no such stress differences, and the clay tectonic faults are therefore just as unlikely to be open fractures as the microfractures. Moreover, the beds on either side of clay tectonic faults are sealed by shearing of clays, and the gouge along both the clay tectonic faults and in clastic dykes is clayey. Both faults and clastic dykes therefore have low vertical permeability and even act as lateral seals of the silty compartments into which the formation is divided by faulting. Therefore, if the microfractures did not pose a permeability problem until now (through artificial drainage and other safety measures), the rarer and entirely intraformational faults will not do so either.

5.2. A new synthesis

We can now also present a new synthesis of clay tectonics and an updated deformation history of Palaeogene clays in Belgium, as compared with our working hypothesis in §1.4.4.

Between 54 and 50 My ago, the Ypresian clays were probably deposited as loose, high-porosity, water-logged muds. As sedimentation progressed and the thickness of the clay deposits increased, pore space gradually decreased through the expulsion of pore water. Pore fluids left the lower reaches of the formation upwards under

continuous clayey deposition. A normal compaction gradient was established, providing a downward seal.

Silty intercalations formed penecontemporaneous load casts and water escape structures with decimetric dimensions.

About 50 My ago, clay sedimentation ceased and gave way to the deposition of Ypresian fine grained and dense sands. Fast drainage through the permeable sand cover could have induced a compaction in the clay from the top down, in addition to the compaction from the bottom up.

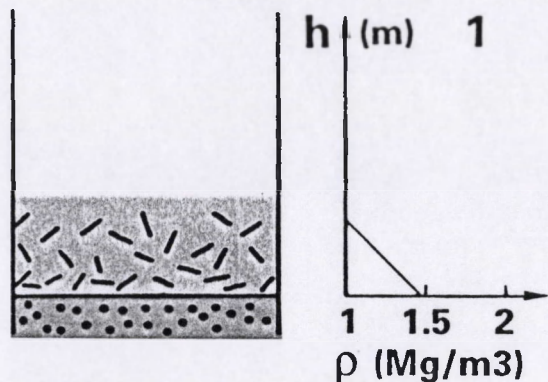
As a result, the clay may have sealed itself both at the bottom and at the top. Such a situation has two related consequences:

1. As water has a low compressibility, the sealed part of the clay will have remained undercompacted for a time and had a lower density than its overburden of compacted clays and sands. This density inversion is gravitationally unstable.
2. As soon as drainage was impeded in some part of the clay body, continued sedimentation meant that the locked pore water became overpressured. The resulting decrease in effective normal stress acting on the interparticle contacts decreased the shear strength of the sediment, and at the shallow depths involved here perhaps even down to the point of liquefaction;

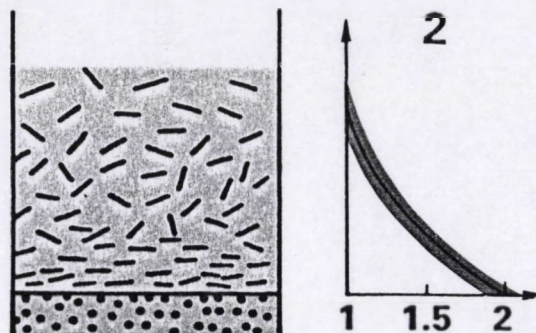
At this point, shallow overpressuring provides both a driving force system (1.) and a mechanism (2.) for deformation. Jointly, they may be regarded as main agents in the development of clay tectonic deformations like those observed in the Ypresian clay, and especially of the clay waves. The gravitational instability probably acted as the motor, which drove the sediment flow, while the overpressurized pore water acted as a lubricant, decreasing the shear resistance at the level of the grain contacts down to the point of general liquefaction.

The wave shape observed fits a model of deformation of an interface between two viscous fluids with different densities and viscosities, with the denser fluid resting on the lighter one. Such a model is known in fluid dynamics as a Rayleigh-Taylor instability. It predicts that the interface between a high-density upper layer and an underlying layer with lower density (and possibly lower viscosity) develops a sinusoidal instability that may evolve into a pattern of regularly spaced upwellings of the lower-density fluid into the denser layer. This is also possible in the case of a

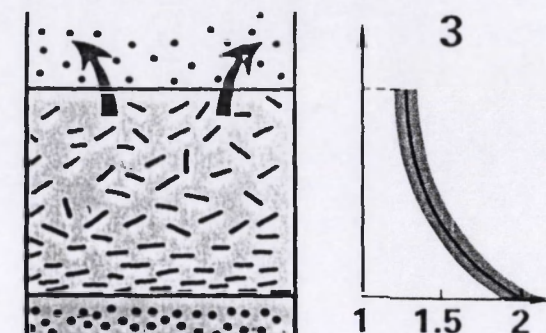
Genetic Model for Clay Diagenetic Deformation



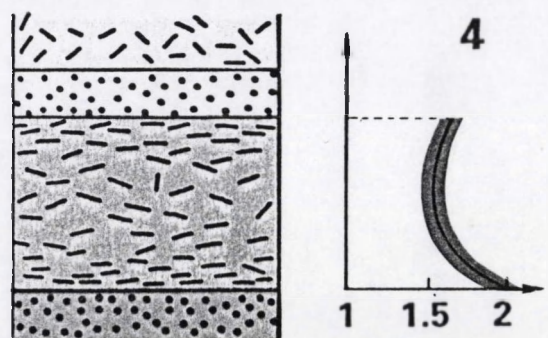
START OF DEPOSITION OF YPRESIAN CLAY ON THANETIAN SAND, 54.2 Ma



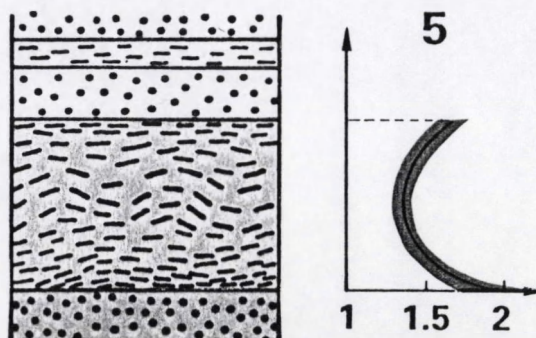
NORMAL COMPACTION IN YPRESIAN CLAY



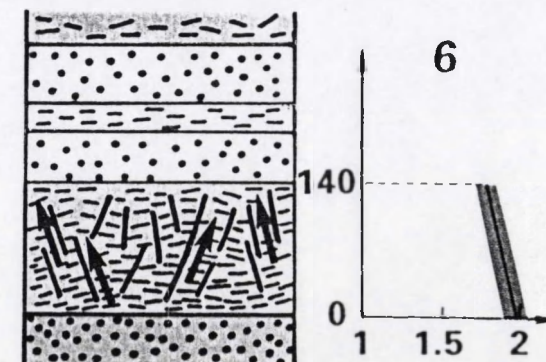
START OF DEPOSITION OF YPRESIAN SAND, 50 Ma



SELF-SEALING OF THE CLAY, GENERATING UNDERCOMPACTION AND DENSITY INVERSION



OVERPRESSURING LEADS TO GENERAL LIQUEFACTION, RAYLEIGH-TAYLOR INSTABILITY, AND VISCOUS DEVELOPMENT OF UNDULATIONS



TECTONIC TRIGGERING ± 35 Ma, PERVASIVE FAULTING, OVERPRESSURE RELAXATION BY UPWARD FLUID INJECTION, COLLAPSE AND COMPACTION

probably rather continuous density profile in the shallowly buried but undercompacted Ypresian clay.

Overpressure in shallow horizons is however intrinsically transitory. It has its origin in the delayed compaction of a clay body and disappears when conditions of hydrostatic pressure in the pore fluid are restored, either by slow seepage or by fracturing of the permeability barriers. The fracturing of the clay beds could have taken place both by hydrofracturing and by local fault developments, induced by the buoyant force of the upwelling clay wave crests.

The folded and faulted clastic dykes may be attributed to hydrofracturing prior to most of the faulting. Clastic dykes have acted as conduits for upward fluid movement, probably out of the Formation, and possibly several times. It is not clear why the black gouge testifies to oxidizing conditions in a clayey sequence that has always known reducing conditions.

The growth of undulations by viscous deformation of undercompacted parts probably induced stresses in the less undercompacted upper and lower parts of the clayey formation. Most of the resulting plastic strain was concentrated in narrow shear zones, partly seeded by clastic dykes, that developed into clay tectonic faults. Overlying horizons underwent faulting and tilting while progressively sagging into the initially undercompacted zone and thus destroying most of the initial wave shape. The relict wave shapes observed on the Belgian continental shelf have probably been 'frozen' by local regimes of pore water relaxation (faster, slower?) which differed from those governing the compaction over the major part of the continental shelf.

The faulting may have been *triggered* tectonically, as the strongly (North Hinder area) to questionably (Marke clay pit) preferential orientation of clay tectonic faults suggests. The regional Oligocene E-W extension is a likely candidate, and that would date clay tectonic deformation much later (± 35 My ago) and a bit deeper (supplementary Lutetian to Oligocene overburden) than originally suggested. However, the faulting has primarily been *driven* by the gravitational collapse of growing anticlines, as faults show orientations and sag directions closely related with the anticlines. The wide scattering of (micro)fault strikes in the Marke clay pit also fit with entirely vertical gravitational collapse.

During the compaction of the whole formation to a normal gradient, faults and clastic dykes were more or less intensely folded.

The Ypresian clay was also affected by possibly Miocene NE-SW compression, noticeable in silty intercalations.

During the Quaternary, valley incision resulted in diapiric upwellings in both Ypresian and Rupelian clays, and some of the clay tectonic faults were reactivated.

5.3. General conclusions

1. The very high resolution 3D and pseudo-3D methods explained here open up a vast domain of 3D analysis of sedimentary structures and fracturation patterns;
2. Geofox implements a new, interactive, hybrid triangulation-gridding surface modelling method, takes some of the pain out of mapping densely but normally faulted horizons, digitized along seismic sections, and is sufficiently versatile for many different applications;
3. Thick argillaceous shelf sequences in tectonically quiet settings can be generally faulted and fractured, with fluids escaping from undercompacted compartments, at a very early stage of burial (a few hundred m);
4. A more than intuitive grasp on this complex deformation required that 3D measurements replaced qualitative (and sometimes deceiving) 2D descriptions, that the phenomenon was studied on all relevant scales, i.e. roughly from kilometres to micrometres, and that diverse disciplines, such as reflection seismics, computer modelling, field work, palaeostress inversion, granulometry, mineralogy, (organo-)chemical analysis, biochronology and micromorphological analysis, were integrated into a single 3D approach.

Addendum : Geofox manual

(version 21.02.1992)

0.	Preparation of data for Geofox (RCMG Seismostrat only)	301
1.	Getting_Started.....	302
2.	Geofox tutorial.....	305
3.	Editing data files.....	312
4.	File formats (in map mode panel).....	312
5.	Frame->	313
6.	Grids	314
7.	Legend (in 'Main panel').....	323
8.	Mode_cycle (in 'Main_panel').....	328
9.	Mouse	331
10.	Move_points+triangles	332
11.	Print_Screen	333
12.	Scale	333
13.	Screen.....	334
14.	Shortcuts	337
15.	Shot_data.....	338
16.	Stop_it.....	339
17.	Triangles (in 'Main panel').....	339
18.	XYZ_lines (in Main_panel).....	344
19.	XYZ_points (in Main_panel).....	346

0. Preparation of data for Geofox (RCMG Seismostrat only)

0.1. Efficient digitization on NCR

1. In RCMG directory, run 'digitpreci.sh'. This shellscript starts an "ex" session; enter 'set term=wyse50' and 'vi' to start "vi"; enter 'a' to go in append mode and digitize a couple of representative lines, while pressing the 0-button. You should digitize your lines as if they were joined. The total length of your lines (one pass) should be more than 0.5 m. Digitize them a second time, pressing another cursor button. Leave "vi" with 'ZZ' and wait for the automatic calculation of your digitizing precision in mm. This is stored in file DIRPROFDIG/precision;
2. Digitize and print all you profiles in the usual way;
3. Transfer (copy or move) them all to DIRPROFDIG/TO-BE-FILTERED;
4. Run shellscript 'digprofchk.sh' to check the format of these files. You can filter digitization noise (details smaller than your digitizing precision) by using a filter factor = 1. If you don't want storage efficiency, use a filter factor < 0.001. Checked (and filtered) files are in DIRPROFDIG/FILTERED, ready to be transferred to Sparc.

0.2. Preliminary on Sparc

It is assumed that the files contain digitized data that have been checked by plotting profiles with software on NCR.

1. Decompress the relevant fix files in PROFILES / FIX
2. in RCMG / PROFILES / DIG2TIME / XYZ_LINES_FRESH, delete previous work (*Select all, cut.really delete OR Select all, cut.move to clipboard*, go to relevant folder in stock, and *Paste*) or put in RCMG / XYZ_LINES

0.3. Filtering

3. in RCMG / DIRPROFDIG / SURVEYNAME
select the profiles you want to transfer in Geofox
Copy
4. in RCMG / PROFILES / JUST_PREPARED_FOR / TO BE FILTERED
Paste
5. in JUST_PREPARED_FOR, begin the filter operations

do PREPARE.SH, double click, then *yes*

6. in JUST_PREPARED_FOR / TO_BE_FILTERED eliminate your profiles
select all, cut.really delete

0.4. Conversion

7. in JUST_PREPARED_FOR / FILTERED
select all, deselect the profiles which are not yours, cut.move to clipboard
8. in PROFILES / DIG2TIME / TO BE CONVERTED
paste
9. in DIG 2 TIME, do the conversion
do CONVERT.SH, *yes*
Answer the following questions
'CANAME' : survey name
'Different central meridian' : usually, it's not necessary to answer *yes*
'Are all these parameters correct ?' : Check the values of each parameter
'offset' = distance in meter between positioning antenna and hydrophones
answer what you want to Quality, it doesn't matter (for now)!
10. in DIG2TIME / TO BE CONVERTED
really delete all your files
11. in DIG2TIME / CONVERTED
really delete all your files (there is no program to work with these files yet)
12. treated files are now in RCMG / PROFILES / DIG2TIME / XYZ_LINES_FRESH
13. if you want to use files from different surveys in Geofox, go back to § 3.
14. you can concatenate the data in order to see all the reflectors on one picture in Geofox. In that case, read §15, in the other, go to §16 directly
15. on the bureau, open CONSOLE and go in the directory
RCMG / PROFILES / DIG2TIME / XYZ_LINES
Then for example, if you want to put together AA.1.line and AB.3.line in a file named FIRSTTRY.line
do CAT AA.1 AB.3 > FIRSTTRY_line
16. Run Geofox (see 2.0).

1. Getting_Started

Geofox is a 2D and 3D geological surface modeling and visualisation programme, and runs on all Sun workstations using SunView.

Conceived and written by Mark Verschuren
N.F.W.O. research assistant
R.C.M.G., University of Gent
Krijgslaan 281-S8, B-9000 GENT, BELGIUM
Tel 091/64 45 95
Fax 091/64 49 97

1.1. Some basic interaction

Geofox is a SunView application, and therefore has many aspects in common with other Sun applications. Moreover it also runs under the OpenWindows environment, which has a slightly different 'look and feel'. The user is expected to be familiar with both, as well as with a little bit of UNIX, and to be able to work with the SunView Organizer OR the OpenWindows FileManager. Geofox can be started either by typing **Geofox &** in a command window, or by double-clicking-left on its icon in the FileManager/Organizer.

When Geofox is started, a start panel asks for your name and the name of your current project. Enter them and click-left on **Done** button. The screen becomes largely occupied with the Geofox 'window' and some subwindows. A window is part of the screen that is bounded by a frame, a double thin line that becomes filled up when the cursor is moved into the window. A window has to be selected this way in order to allow interaction with its contents.

As the mouse is moved in the window, the 'About Geofox' panel shows up. This panel actually is an example of the numerous 'alert pop-ups' that have been built in to signal unexpected conditions. Alert pop-ups are removed by clicking left on one of their buttons.

The main window is smaller than the 'canvas', the area onto which everything is drawn, and through which the user interacts with the objects shown. The scrollbars along the left and bottom edge of the frame, show with the help of medium grey 'bubbles' which part of the canvas is visible through the window. Just like with this text window's scrollbar, click left in the scrollbar to scroll down, click right to scroll up, and click middle to centre the visible portion at the cursor location. Click left or right on the square arrow boxes to scroll one line at a time in text windows.

1.2. Help_on-> (in Frame_menu)

Drag right to browse through all available help items, and click right to select one of them. A window pops up with the contents of the relevant file in the help directory. As you gain experience, feel free to create new help files in the help directory, or edit existing ones, in order to help other users.

Some help file conventions

- preferably, the name of a help file corresponds to the name of a button or a menu_item. It might also inform on a general aspect that can be grasped in one word, such as 'Shortcuts' or 'Mouse';
- the name of the help file is repeated on its first line, with an indication where the relevant button or menu_item can be found;
- '->' are used to subdivide the help text into parts that pertain to the constitutive elements of a menu or popup;
- words between ' refer to other help files or options;
- a menu_item that brings a popup window, ends with '...';
- 'Grids.Interpolate...' is an example of format 'Button_name.Menu_item_name', where Button is a button in the 'Main_panel'.

1.3. Main_panel... (in Geofox frame menu)

Selecting this item pops up the main control panel. Every button in this panel has a menu that allows to manipulate the objects described by the button names.

Get more help on :

- > 'Mode_cycle' to toggle between map and 3D mode;
- > 'XYZpoints' to read and manipulate (x,y,z) points;
- > 'Shot data' for shotpoint data (number, time, x, y, z) and CDP's;
- > 'XYZ lines' for points structured in lines, such as reflector lines and contours. May contain isolated points;
- > 'Triangles' for triangulation and interactive surface modeling;
- > 'Grids' for interpolation, smoothing and manipulation of up to 5 stacked gridded surfaces;
- > 'Legend' for all kinds of general output settings (contour interval, line thickness,...);
- > 'Screen' for screen actions and colour table settings.

2. Geofox tutorial

Tutorial conventions

- Unix commands to be typed in a command window are in **bold**
- Geofox menu commands are in *italics* with first the name of a button in the "Main panel ...", followed by the relevant menu item, and separated by dots
- panel entries are in *outline*
- ⬢ ("meta" key) stands for a keyboard accelerator of a Geofox menu command. The cursor should be in the "canvas", and not on one of the panels or borders, to use a command accelerator.

2.1. Getting started

1. click left on the Geofox executable in the File Manager (in /home/tuser/geofox), or **cd** to geofox directory in a command window and type **Geofox &**;
2. read the message that appears when you move the cursor, and follow its guidance to get started. The on-line help explains the significance of all bells and wistles. This tutorial teaches how to use them to do major tasks;

2.2. Panel diagrams of entire profiles

1. **cat** all or a selection of reflectors in /home/tuser/rcmg/xyz_lines together in a new file, ending with ".line". E.g. for all main reflectors R* of a given survey AB: **cd /rcmg/xyz_lines; cp topoAB.line profilesAB.line; cat R* >> profilesAB.line; (cat internals >> profilesABall.line);**
2. in Geofox, type filename (without the .line extension, e.g. profilesAB) in the map_panel. Check whether Dirname is the current rcmg data directory;
3. **do XYZ_lines.Read.Depth.All;**
4. change contour interval with *Legend.Set...* Use *Legend.Show colourscale* and *Legend.Hide colourscale* repeatedly to find a good contour interval for the current

colour table (see *Help on.Screen.colour table* to get info on other available colour tables with more or less contour colours). Click left on **Done** to hide a panel;

5. do *XYZ_lines.View.All*, and start to look at (selected sectors of) the network at different scales in map mode, or from different angles in 3D mode. To change scale in map mode, drag and release scale slider; to select a sector, click left on one corner of sector of interest and drag-left to enclose the sector with a box; to deselect sector origin, click-middle; to go to 3D mode, click-left on *mode_cycle* (left of *menu_buttons* in *main_panel*) and drag slider(s) to change viewpoint and *Screen.Redraw on.Canvas* (or $\diamond r$) or set **AutoRedraw ON** and experiment; to go back to map mode, click-left on *mode_cycle* again (everything is redrawn within last selected sector); to focus 3D projection on a particular part of the network, select it in map mode and click on *mode_cycle* to redraw around new focus in 3D. For panel diagrams it is mandatory to view from a very large distance and a field of view of 1° . This telescopic viewpoint largely removes perspective distortion, and ensures that partial drawings can be glued together. See *Help on.Editing data files* if something appears to be wrong with the data points.

6. to print on Versatec :

6.1. set *contourcolour* to Off in *Legend.Set...*;

6.2. select *Legend.Show legend* (change title in *Legend.Set...*) and put info block and arrows (in 3D mode) with $\diamond i$ and $\diamond a$ at an interesting position in the canvas;

6.3. do *Screen.Redraw.Versatec*;

7. to combine with digitized bathymetry :

7.1. redraw in 3D so that the network looks understandable, and select *XYZ_lines.Filter...*;

7.2. select in 3D;

7.3. do **Filter lines**, and change **Weeding tolerance** (in m for X,Y and m or ms for Z) so that **Ratio filtered/unfiltered** is less than .33;

7.4. do *XYZ_lines.View filtered* and redraw with $\diamond r$ to compare filtered and unfiltered version (unfiltered is redrawn in black, filtered in colour). Change **Weeding tolerance** until the **Ratio** is as small as possible for a filtered version of acceptable quality. A **Ratio** of 0.25 is largely sufficient in most cases;

7.5. do *XYZ_lines.Save*;

- 7.6. for digitized bathymetry, do as in §3 and §4 to get a good triangulation;
- 7.7. with name of bathymetry, e.g. "bathy", in map_panel, do *Triangles.Read.Depth*;
- 7.8. select *Points.Change scale...*;
- 7.9. mark only in Z direction, set scale factor to 2 and do *Multiply* to get Two Way Depth, set scale factor to 1.5 (m/ms) and do *Divide* to get Two Way Time in ms;
- 7.10. add "ms" to name of bathymetry, e.g. "bathyms", and save with *Triangles.Save*;
- 7.11. select a sector and *Grids.Interpolate...* a nice grid on "bathyms";
- 7.12. type filename of profiles, e.g. "profilesAB", in map_panel, do *XYZ_lines.Read.Depth.Filtered*;
- 7.13. do *Legend.Set...* and set *contourcolour* of xyz lines to Off, perhaps also *linethickness* to 2, and do *XYZ_lines.View all*;
- 7.12. in *Legend.Set...*, set *One range* for to each grid, and select a *Contour*, tick and label interval and line divisions/interval appropriate for bathymetry;
- 7.13. do *Grids.View...* and Draw/redraw in map or 3D mode;
- 7.14. select *Legend.Show colourscale*, and put the colourscale with ϕ_c at a good place on the canvas;
- 7.15. redraw on Versatec;

2.3. Maps and 3D pictures of individual reflectors

1. see to it that reflector.line is in rcmg/xyz_lines;
2. in Geofox, type filename (without the .line extension, e.g. R1.1) in the map_panel. Make sure directory name is padname of rcmg data directory;
3. do *XYZ_lines.Read.Depth.All*;
4. change contour interval with *Legend.Set..* (see also §1.4);

5. do `XYZ_lines.View all`, and start to look at (selected sectors of) the reflector at different scales in map mode, or from different angles in 3D mode. Find an appropriate exaggeration of height. See *Help on Editing data files* if something appears to be wrong with the data points;
6. go to 3D mode and redraw with an inclination of 45°;
7. select `XYZ_lines.Filter...`;
8. select in 3D, and change the **Exaggeration of Z** to the one used in 3D mode;
9. next go to §4. 3D surface modelling;

2.4. Maps and 3D pictures of digitized contours

1. put all relevant files (that have been plotted successfully as background lines with software on NCR) in 2xy/ and do `cd 2xy; concatenate, e.g. cat bathy*.line >> BATHY.line; rm bathy*.line`;
2. do `geoxy filename central_meridian`, e.g. `geoxy BATHY.line -27`;
3. move `bathy.line` to `rcmg/xyz_lines`;
4. in Geofox, type filename (without the .line extension, e.g. BATHY) in the map_panel;
5. do `XYZ_lines.Read.Depth.All`;
6. change contour interval with `Legend.Set..` (see also §1.4);
7. do `XYZ_lines.View all`, and start to look at (selected sectors of) the contours at different scales in map mode, or from different angles in 3D mode. See *Help on Editing data files* if something appears to be wrong with the data points;
8. to print on Versatec :
 - 8.1. set **contourcolour** to Off in `Legend.Set...`;
 - 8.2. select `Legend.Show legend` (change title in `Legend.Set...`);
 - 8.3. do `Screen.Redraw.Versatec` ;
9. go to map mode;

10. select *XYZ_lines.Filter...*;
11. select from (constant z-) contours;
12. next go to §4. 3D surface modelling;

2.5. 3D surface modelling

1. do *XYZ_lines.Filter..* and *Filter lines*, and change *Weeding tolerance* (in meter) so that *Ratio filtered/unfiltered* is less then .33;
2. do *XYZ_lines.View Filtered* and redraw with $\diamond r$ to compare filtered and unfiltered version (unfiltered is redrawn in black, filtered in colour). Change *Weeding tolerance* until the *Ratio* is as small as possible for a filtered version of acceptable quality. A *Ratio* of .10 is largely sufficient for most reflectors, except for e.g. a bathymetry with lots of sandwaves, or a densely faulted reflector. For digitized contours, *Ratio* should be higher, around .20;
3. do *XYZ_lines.Save*;
4. do *XYZ_lines.Read.Depth.Filtered*;
5. in map mode, do *Triangles.Triangulate* and answer yes to first prompt, and yes or no to the second, depending on whether you are triangulating digitized contours or not;
6. do *Triangles.Contour Solid*, *Triangles.Contour.Lines* and *Triangles.View.All*;
7. do *Triangles.Narrow...* and *Eat Border* to hide narrow and therefore insignificant triangles around the border. This may take some time for triangulations of several thousand points. If Geofox eats too much, hit *Stop* key, do *Triangles.Make all visible*, increase *Narrowness*, and *Eat Border* again
8. modify the triangular surface model,

which is now an objective linear interpolation between data points, so that it better reflects your mental image of the surface, which may be more geo-logical, but necessarily less objective. You do this by *Triangles.Set Change ON* (or $\diamond 2$; notice different cursor) and by swapping the diagonal connections between data points (drag left over the diagonal connection you want to change), by hiding triangles in badly constrained areas of the surface (click middle to toggle between 'v'isible and

'hidden) and by selecting triangles that lie on faults or other scarps as fixed surface discontinuities (click right to toggle between 'visible and 'scarp). You can also modify the surface by changing the height of points : select *Points.Set Move ON* (or $\diamond 1$), click on the point you want to move to select it, and drag up or down. With *Legend.Shading...*, set *Phong illumination* to *On*, in order to have 3D-like interactive feedback (you will probably need to apply some vertical exaggeration (change it in 3D mode, but don't exaggerate too much)). If you want to go into detail, select a part of the triangulation and do $\diamond r$ (don't forget to leave the change mode with $\diamond 4$, before you select a sector). It is convenient to hit the F1 key to keep an eye on the actual line coherence along the profiles or contours. See also *Help on.Triangles* and *Help on.Move_points+triangles*, for more advanced interaction;

9. do $\diamond 4$ to leave any change mode, and do *Triangles.Save* to save the triangulation in a *reflectorname.tri* file in *rcmg/utm_z.tri*. This is an important file, because it stores your model, together with all your modelling work, for later use. (Don't hesitate to *Triangles.Save* now and then while you are modelling. If the system crashes for some reason, only your very latest work will then be lost : after restarting Geofox, type the *reflectorname* (without the *.tri* extension) in the *map_panel*, and do *Triangles.Read.Depth, Triangles.Contour.Solid, Triangles.Contour.Lines, Triangles.View.All, XYZ_lines.View all* and *Points.View Visible*, and go on modelling or whatever);

10. in map mode, with the triangulation visible, do *Grids.Set select ON* and select a sector that contains a part or all of the triangular surface model, and for which you want a gridded model with more or less smooth contours;

11. select *Grids.Interpolate...* and type the *reflectorname* next to *surface 1*;

12. do *Interpolate* to calculate a first shot at a smooth grid (with # of grid rows along largest side at only 50 and # of smoothing iterations at 5), and *Done*;

13. do *Grids.Set select OFF* and *Screen.Erase* and go to 3D mode;

14. select *Grids.View...*, and *Draw*. With automatic *redraw On*, change to an interesting viewpoint by dragging the viewpoint sliders to other values. When the new viewpoint looks interesting, select in *gridview_panel* *opaque, Grid as Solid*, and enlarge the E-W and N-S guides interval to anything more than the default 1m. Preferably with *Phong illumination On*, do $\diamond r$. Change back to *transparent*, to quickly find another viewpoint. Select *Legend.Show legend*, and

Or to put axes with labeled ticks around the grid. See also *Help on.Grids.View...*, *Help on.Legend.Set...* and *Help on.Legend.Shading...* for more fine-tuning;

15. still in 3D mode, do *Interpolate* again (for the same sector), but now with more # of grid rows along largest side (150-200 suffices in most cases) and more Max. # of smoothing iterations (20 is OK), and *Done*. See *Help on.Grids.Interpolate...* for more advanced use;

16. do Or in either map or 3D mode. The 3D view will show you all the details and flaws of the current surface model, so that you know what still needs to be done to the triangular surface model, or what other settings you need to change in *Grids.Interpolate....* Go back to §4.8, and keep on improving the model until it has converged to something you think is acceptably consistent both in its details and as a whole. Then apply the finishing touches by sparingly adding triangle vertices with *Triangles.Set VertexAdd ON* (or <>3). Move the cursor to places where an extra support point is needed, and click right ONCE (unwanted vertices cannot be removed, so be careful). Support points are marked with squares, and can be manipulated just like the true data points. You may want a support point to constrain interpolated smooth contours near the edges of triangulation, to model fault tips and branches, and to modify/update the triangulation with borehole data;

17. select *Legend.Show colourscale*, and put the colourscale with Oc at a good place on the canvas;

18. do *Screen.Redraw.Versatec* for a hardcopy in grey-shades, or hit PrSc key to save full colour screen in memory for later photography;

19. When you have modelled at least two surfaces in the same area, you can also AUTOMATICALLY build a stratigraphic framework with *Grids.Build Strat...* (read its *Help*). This function makes sure that all truncation and pinchout lines are just like you would like them to be, and that isopach maps are as expected, however complicated the stratigraphy may locally be, and even if the triangular surface models do not cover the respective surfaces exactly up to the truncation and pinchout lines, or if they occasionally extend a bit too far and into the cutoff surface. There are a few buts, though : garbage in, garbage out. Inspect your grids in 3D, transparent, and with *Thickness decrease* or *increase* (see *Help on.Grids.View...*) BEFORE a *Grids.Build Strat...* and see whether the grids have relative positions as expected. If not, you can't expect an acceptable stratigraphic framework or isopachs either until the triangular models are correct. If something is still wrong with the isopachs (negative thicknesses before *Build Strat*), you can

select **One range for all+isopach** in *Legend.Set...*, draw one of the triangulations on top of the isopach, Redraw both on a comfortable editing scale and move relevant parts of the triangulation up or down to get rid of the negative thicknesses.

3. Editing data files

When there is something wrong with your data points (points with meaningless heights, identical data points spotted during triangulation or linepieces longer than 10000 points spotted during line filtering), you need to change your data file manually. In map mode, zoom very closely in on a point where you want to change something. Locate the cursor on a point and do $\diamond p$ to print the current cursor position in the map_panel. Close all panels and the Geofox window apart from the map_panel, and open the data file in the Filemanager (if you don't see one, click right on OpenWindows background and select Programs.Filemanager). Select one of the coordinates in map_panel, hit 'Copy' button, move cursor into the data file window and hit 'Find' key to locate the data point in the file. Change its coordinates or its code, or delete it.

When you need to edit the data files, make sure that the file format (see Help on.File formats) is respected and especially that the codes around the edited points still make sense.

4. File formats (in map mode panel)

In map mode, a filename can be typed next to **File:** and a directory name next to **Dir:**. The filename is used to read data

- in dirname/utm_z/filename with *XYZpoints.Read*,
- in dirname/utm_z.tri/filename.tri with *Triangles.Read*,
- in dirname/shotpoints/filename with *Shot data.Read*,
- or in dirname/xyz_lines/filename.line with *XYZ lines.Read*.

These are all ASCII files, with a certain format and structure :

-> /utm_z files contain a list of (x, y, z) coordinates of individual points, with spaces between the real numbers;

-> /utm_z.tri files contain

- the number of triangles (nt) on the first line;

- 3 vertex indices and a character(v, s or h) on the nt following lines;
- the number of vertices (nv);
- 'x y z code(either 'v'isible or 'h'idden) kind (s r i o c, see further)' for nv

points.

-> /shotpoints files contain shotpoint records, each consisting of

- shotpoint number;
- timestamp in hhmmss;
- 'x y z' shotpoint coordinates.

-> /xyz_lines files contain lists of consecutive points on a line

EITHER (format 1, read only)

- starting with the number of points (np) that follow in the same line;
- list (can be only one) of these np 'x y z' points

OR (format 2, read only)

- "dig" in first record;
- the 'z' for the following points;
- list (can be only one) of 'x y' points

OR (format 3, read and write)

- "Saved" in first record;
- only 'x y z code kind' points. 'kind' is 's' for start, 'r' for relevant, 'i' for irrelevant (that is to say, at the moment, for this can be changed with 'XYZ lines.Filter...'), 'o'pen or 'c'losed end (the latter indicates that this end is connected with 's'tart). An xyz_lines file can be read with the first or second format, but will always be saved with the third format.

5. Frame->

(in Geofox frame menu (click right on Geofox label, in upper left corner))

This ones' pullright menu is the standard SunView frame menu, that allows you to close the Geofox frame into the Geofox icon or vice versa, or to Quit.

6. Grids

6.1. Grids.Set Select ON/OFF (in 'Grids'-button menu)

Select *Grids.Set select ON* to indicate that the sector that is selected next, should be used as grid sector. Do *Screen.Show* position and write down the selected sector limits if you want to make sure that you use the same grid sector every time you do another Geofox session. Upon the first such selection, the *Grids.Interpolate...* menu option will be activated. Do not forget to select *Grids.Set select OFF* in order to avoid inadvertent changes of grid sector during the current session.

6.2. Grids.Interpolate... (in 'Grids'-button menu)

Brings up a window that allows you to set several interpolation and smoothing parameters. From top to bottom :

-> # (= number) of surfaces :

An integer from 1 to 5, indicating the number of surfaces you want to visualize on top of each other. Grids are calculated within the currently selected sector in map-mode (interpolation can also be done while in 3D-mode however (see also 'Mode_cycle')).

-> names of surfaces :

Type names of files in the *utm_z/* directory. Type the name of the highest surface first.

-> # of grid rows along largest side :

Type an integer > 2. The number of grid rows along the shorter side is calculated with the ratio of the sides of the selected sector, so that the grid mazes are as nearly square as possible. All of the interpolation and smoothing consumes time proportional to the number of grid nodes.

-> Initialize with

- triangulation :

If there is a triangulation, saved as *utm_z.tri/*filename.tri, for one of the surfaces, it will be used to initialize the corresponding part of the grid, so that the grid initially coincides with the triangulation. Remaining nodes not covered by the

triangulation, are initialized with the minimum/average/maximum data node value so far. Best for topography with fixed sealevel or bathymetry with fixed shoreline level for rest of surface.

- triangulation + distance weighted averages :

For gridnodes covered by triangulation, idem as with triangulation only. For other ones, distance weighted averages are used. Best in most cases without a fixed level.

- distance weighted averages :

Slower. For every one out of 16 gridnodes, all points in utm_z/filename are scanned to collect the three closest neighbours. The search is not orientation sensitive. The node is then initialized with an inverse square distance weighted average of the three neighbours. Its 15 neighbours get the same value. The quality of such an initial grid is very low (even if it were explicitly calculated at each node), and should therefore be improved by least tension smoothing (see further). Only a few iterations suffice to yield an acceptable "first shot" surface. This initialisation is also rather slow, as all data points need to be scanned for the three neighbours of a lot of nodes. It is therefore advantageous to triangulate anyway, and save the unedited triangulation.

-> Max. # of smoothing iterations :

An integer that indicates how long you can afford to wait. The longer you can wait, the smoother the surface can be.

-> Smooth with

- | | | | |
|------------------------------------|---------------------------------|---|---|
| - 13 nodes (2 deep, with tension): | Stage 0 of iterative smoothing. | | |
| - 13 nodes (4 deep, with tension): | Stage 1 | " | " |
| - 33 nodes (4 deep, no tension): | Stage 2 | " | " |
| - 33 nodes (8 deep, no tension): | Stage 3 | " | " |
| - 33 nodes (16 deep, no tension): | Stage 4 | " | " |

Tension and curvature are iteratively reduced with modified versions of the Briggs (1974) and Smith & Wessel (1990) difference equations (Verschuren, 1992). When a non-0 stage is chosen, the smoothing phase passes also the lesser stages. After

every iteration, these difference equations yield a new value for each node, using a number (13 or 33) of neighbouring nodes in the following configurations.

Stage 0 and 1 :

```

      o
    o o o
  o o x o o
    o o o
      o
  
```

Stage 2, 3 and 4:

```

              o
              o
            o o o o o
            o o o o o
  o o o o o x o o o o
            o o o o o
            o o o o o
              o
              o
  
```

In stage 0 and 1, a simplified (isotropic) version of the Smith & Wessel difference equation with tension, for an internal, uncontrolled node, is applied. In stage 2, 3 and 4, an extended version of the classical Briggs least tension difference equation is used. It has been extended in order to speed up convergence to a smoother surface. Only uncontrolled nodes, i.e. away from scarp- or isolated observation nodes are affected in the latter 3 stages. In stage 1 and 3, the interval between affected neighbours is doubled, and in stage 4 even quadrupled, in order to extend the scope of the difference equations, and therefore also their smoothing power. Such a procedure is called 'successive grid refinement'. This is useful when the data density is low in comparison with the grid density, and even more so when the grid is initialized with distance weighted averages. Instead of a memory-expensive 'multiple grid strategy', a single grid 'scan reversion strategy' is applied in order to avoid smoothing asymmetries due to unidirectional scanning. Every other iteration step, the direction with which the grid is scanned, is reversed. Gridnodes at sealevel ($z = 0.0$) are never affected, so that the 'land' smoothly rises above the 'sea'.

-> Global tension :

A number between 0.0 (for least tension) and 1.0 (for maximum tension). In the last two stages ('2 and 4 deep, with tension'), the whole surface is smoothed with this global tension, except for the fixed nodes and a narrow zone around the scarps. A global tension of 0.0 works best in most cases. If the data were sampled on a relatively smooth surface with local peaks or troughs, a higher tension (>0.6) will avoid unwanted overshoots, and the peaks will be sharper.

-> Tension near fault scarps :

Again only in the last two stages, this tension is used at the nodes next to the fixed scarp nodes. Farther away, tension decreases toward the global tension over 3 nodes (stage 0) or over 6 nodes (stage 1).

-> Free edges with

- least tension extrapolation :

First, any initialisation artefacts along the edges are removed with two stages of leveling linear interpolation (see further). The surface is then smoothed and extrapolated beyond the data area with least tension, using 8 neighbouring edge- and internal nodes (see also Briggs, 1974). The edges may show large oscillations, so opt for early convergence detection (1/100 or 1/300).

- leveling linear interpolation :

In every iteration step, the new value for an edge node is simply the average of only three immediate neighbours. Local peaks or troughs that were introduced along the edges during the initialisation phase are completely leveled.

-> Convergence at 1/n of depth range :

After each of the smoothing iterations, the largest move of an individual node is compared with (epsilon =) 1/n of the z-range of the current grid. The grid is considered to be converged, when the largest move is smaller than epsilon. With a large epsilon (1/30), convergence can be detected very early, but the surface may not yet be as smooth as desirable. An epsilon = 1/1000 suffices in most cases. A larger epsilon (1/100 or 1/300), may result in an acceptable surface in less time. If there are close couples or dense clusters of highly variable points, least tension oscillations can be so large that a large epsilon is most sensible anyway. If you can spare all the time of the world to have a perfectly smooth, minimim tension surface, you can pick a tiny epsilon.

6.3. Grids.View... (in 'Grids'-button menu)

Brings up a window that allows you to set several 2D-grid viewing parameters. From top to bottom :

-> View :

Either as transparant nets or opaque surfaces.

- transparant :

This is the fastest way to project the grids, and therefore useful to find an interesting sector in map-mode, and a 3D viewpoint. Set the E-W/N-S guides interval (see further) to draw only those gridlines with approximately the chosen interval in XY units, and hence to speed up drawing even more.

- opaque :

In combination with 'Grid as Solid/Lines' (see further), either hidden surface or hidden line removal is applied to draw the grids. Shading in 3D-mode is possible only in 'opaque' mode.

-> E-W guides interval :

In XY units. Determines the distance between E-W gridlines in transparant mode, or between E-W guides in opaque mode.

-> N-S guides interval :

Analogous to E-W guides interval.

-> Shown surfaces :

Click-left on buttons to set selected interpolated surfaces On or Off. Is used in combination with 'Surfaces/CMP Coverage', left of the 'Draw' button.

-> Grid as :

- Solid :

Hidden surface removal. Both in map- and 3D-mode, each of the grid mazes is subdivided into 4 triangles, with their common vertex at the average height of the four corners. If one of the corners of a maze is markedly lower or higher than the other three, only 2 triangles are generated, with their common long side at the 'scarp'. Each of the triangles is subsequently colour contoured, line contoured (if 'Line contours' is On in the Legend Set.. popup), and shaded (if 'Phong shading' is On in the Legend Shading popup). In a 3D projection, grids, the mazes within the grids, and the triangles within the mazes, are always painted from the back to the front and from the outside inwards. With such a "Painter's algorithm", a facet drawn later is closer to the viewpoint, and may therefore naturally overpaint (parts of) facets that it hides for the viewer.

- Lines :

Hidden line removal, faster than hidden surface removal. This part of Geofox was originally written for a monochrome monitor. On such a monitor, a surface can only be shown by means of lines. The hidden line removal programme for regular grids with true perspective is considerably more complex than the hidden surface removal, that is only possible on multichrome monitors (preferably with an 8-bit frame buffer and therefore 256 shades or colours). Actually, the algorithm that was used for hidden surface removal is a simplified inversion of that for the hidden line removal. In order to get them in an 'occlusion compatible' order, the grids are mirrored and/or transposed. Facets are then drawn from the front to the back and from the inside outwards, exactly opposite to the Painter's order.

-> Linecolour On/Off :

If On, all gridlines are colour contoured. If Off, they are drawn in the fore- or background colour, depending on the status of the Fore/Background_cycle in the Legend Set.. window.

-> Thickness decrease/equal/increase :

If 'equal', all grids will be drawn with the linethickness in the Legend panel.

Otherwise, line thickness can be made to decrease/increase from youngest to oldest surface. This is true for up to 5 grids on the Versatec (thicknesses are 7, 5, 3, 1 and 0 (thin interrupted line). On screen, 4 or 5 grids are drawn with thicknesses 5, 5, 3, 3 and 1. So after Drawing the grids you want to see, you need to deselect some and Draw one or two grids again and on top of the rest (do not redraw) with linecolour Off and Thickness 'equal' (to 1). This feature is very helpful for deciphering stacks of grids BEFORE a Build Strat, so that you see what you can expect (garbage in, garbage out).

-> Guides On/Off :

Perspective guidelines not only help to understand a 3D image on complex structures in an 'at-first-glance' sense. They also allow quantitative interpretations in terms of orientation, distance, length and area. If Guides are On in transparant mode and/or map mode, gridlines are drawn every other E-W/N-S interval. In opaque and line mode, and linecolour Off, guidelines are twice as thick as normal gridlines. With linecolour Off, they are drawn with normal gridline thickness in

either fore- or background colour. In opaque and solid mode, perspective guidelines are drawn either with or without linecolour.

-> Cont.lines only On/Off :

If On, ONLY contourlines are drawn, either transparant or opaque ('hidden contour removal').

-> Fixed nodes Hide/Show :

Nodes that were fixed during the smoothing phase, i.e. scarp and isolated observation nodes, can be Shown or Hidden in transparant and/or map mode only.

-> Notriang nodes Hide/Show :

In opaque and/or map mode, parts of the surfaces that have not been initialized with a triangulation, can be either Shown or Hidden.

-> Isopach :

- On/Off : If On, isopach calculations are done on the fly, either between two selected surfaces, or between one calculated grid and a reference level (can be combined with Time/Depth conversion in 'Grids.Velocities...');

- below reference level : thickness below reference level;

- 'pos./ +/- / neg. diff.' : only those differences are shown, while the rest is flattened to zero thickness;

- AND/OR : isopach nodes are visible if they are determined by first surface AND/OR the other.

-> Surfaces/CMP coverage :

The surfaces shown are either grids stemming from those calculated with 'Grids.Interpolate...', or the CMP coverage, calculated with 'Shotpoints.Binning...'.

-> Draw button :

Click-left to draw with the current settings, on top of what was drawn before.

6.4. Grids.Build Strat... (in 'Grids'-button menu)

Brings up a window that allows you to build a stratigraphic framework starting with grids interpolated on triangulations. From top to bottom :

-> Build Stratigraphic Framework :

Does away with aimlessly floating parts of gridded sequence boundaries. Geofox can do so automatically and flawlessly, IF the following assumptions hold. Names of sequence boundaries should have been entered from young at the top to old at the bottom of the list in the *Grids.Interpolate...* panel. All sequence boundaries between top and bottom SB need to be entered, so that all sequences are fully bounded. Sequence boundaries are supposed to be known in an area bounded by (the visible part of) a triangulation of reflector data. Conversely, the 'v'isibly triangulated area is supposed to be bounded by truncations, baselaps and/or the survey boundary.

If the resulting isopach maps look odd, you may have problems with your surface models that can be solved by comparing and correcting respective triangulations. Do a *Screen.Erase*, do a new *Grids.Interpolate* without *Grids.Build Strat*, Draw the isopach map (with +/- differences) of a sequence, and look for negative thicknesses. If there are any, change to One range for all+isopach in *Legend.Set*, do a *Screen.Redraw*, read the triangulation of one of the sequence boundaries (put the correct name in the map_panel), do *Triangles.View.All* on top of the isopach map, and move vertices up or down for at least as much as the negative thicknesses underneath. When finished, do *Triangles.Save*, re-interpolated grids and check new isopach before you do *Grids.Build Strat* again.

-> Extend visibility :

- to that of youngest as well :

The visibility of surfaces will be extended to that of the youngest, so that below the area covered by the youngest surface, there remain no holes (due to lack of data) near truncation or baselap lines.

- but not to that of youngest :

May be necessary if youngest surface (e.g. topography) is a digitized map or based on another survey with an extension that is larger than that of the older surfaces.

6.5. Grids.Parametric model... (in 'Grids'-button menu)

This popup allows you to integrate structurally modeled and gridded interfaces, with values for a certain (geophysical) parameter pertaining to assumedly homogeneous layers between the interfaces, into a parametric (geophysical/geotechnical) model.

-> Parameter values between interfaces :

values of parameter between first and second interface ('P(1->2)'), and so on.

-> Parameter/unit name (length<9) :

name of parameter or units, to be written at the head of the colourscale. For this reason, the length of the name should be less than 9 characters.

-> Parametric model On/Off :

If On, grids selected in 'Grids.View...' are drawn in a colour corresponding with the parameter value below the interfaces, together with any combination of vertical side planes at the grid sector limits, yielding a 'solid' 3D effect.

-> Structural contours On/Off :

Since the colourscale is determined by the range of the parameter, and not by the structural z-range, the usual contour interval in 'Legend.Set...' is not available for structural contour lines. To the latter purpose, the tick and label interval along the z-axis are used, if Legend is ON.

6.6. Grids.Velocities... (in 'Grids'-button menu)

Some parameters to control time/depth conversion of up to four grids interpolated from two way time reflection data.

-> Interval Velocities :

down to first grid, between first and second ('V(1->2)') grid, and so on, are in units corresponding with the input reflection times (i.e. most often in m/ms or in m/s).

-> Waterlevel :

Either zero for ordinary sealevel, or non-zero for lake level at the moment of acquisition.

-> Time/Depth conversion On/Off :

When On, grids are time/depth converted on the fly, even in combination with isopach calculations (see also 'Grids.View...').

7. Legend (in 'Main panel')

Through this button's menu, all kinds of general settings, related to the objects shown, can be changed.

-> Set...:

Brings up the 'Legend.Set...' pop-up.

-> Show/Hide legend :

Show or hide map or projection information block, 3D arrows and colourscale. <Meta> i puts information block at the cursor location in the canvas. <Meta> a in 3D mode shows 3D arrows. The length of the vertical arrow is proportional to the exaggeration of height. Its length is equal to the length of the horizontal ones if the exaggeration of height is 10, since such an exaggeration is quite usual in geology. <Meta> c puts colourscale at the cursor position in the canvas (particularly handy on paper).

-> Show/Hide colourscale :

Show or hide the colourscale for the current array of points or grids. If the contour interval is too small, this can take quite a while and result in a overcrowded colourscale. In that case, interrupt drawing the colourscale with the 'Stop' key, increase the contour interval and try again.

-> Shading...:

Brings up the 'Legend.Shading...' pop-up.

7.1. Legend.Set... (in 'Legend'-button menu)

Click right on this menu item to pop up a window for all kinds of general settings that control the appearance of the objects shown.

-> Title :

Text (up to 40 characters and spaces) that is shown together with legend info ('Show legend' selected), so that the picture becomes more self-explaining.

-> Screendump :

Name of next screendump file. No blanks or special characters allowed (ordinary UNIX filename conventions). A unique timestamp is put in front of this name, in order to guard against overwriting previous screendumps, in case you don't change this name. You can always change the names of screendump files afterwards, as long as you leave the '.prsc(.Z)' at the end.

-> Contour interval :

In real z-value units, for colour and line contoured points, lines and surfaces.

-> One range for

- all objects :

One range of colour contours for all objects. Only one colourscale (see 'Legend.Show Colourscale') is used for all points, lines and surfaces. Most appropriate when the z-ranges of objects overlap;

- each grid :

Each grid is colour contoured with its own colour contour range. They all start with the same colour in the lowest interval.

- all+isopach :

Uses one range that encompasses isopach range and that of a triangulation, in order to compare the two and spot and correct negative thicknesses.

-> Colour step :

The colours of contour intervals are sampled from the current 'Screen.Colour_table'. In the colour tables, colours gradually grade into each other.

The colour step determines the sampling interval in the colour table for the colours of contour intervals. Increase the colour step to improve colour contrast between intervals. See *Help on.Screen.Colour* table.

-> Along Z-axis :

- tick interval :

In z-value units, the interval between ticks along the Z-axis of the 3D frame, that is projected together with the grid(s) when 'Legend.Show legend' has been selected. This is the structural line-contour interval when the 'Parametric model' in 'Grids.Parametric model...' is On.

- label interval :

Z-value numbers are printed next to the Z-axis, every so many tick marks. On the colourscale, numbers are printed every so many contour intervals.

-> Contourlines On/Off :

Show or hide contourlines on surfaces.

- line width : Standard thickness of contour lines in number of pixels.

- thin line interval : A thin contourline every so many intervals

- thick line interval : A thick contourline every so many intervals

- line divisions/interval : Number of extra line divisions per interval

- in FORE/BACKground colour : Contourlines in the same colour as text in the canvas (such as the legend) or the canvas background (see also 'Screen.Fore/Background').

-> Draw xyz-lines with :

- contourcolour On/Off.

- linethickness in pixels.

- visible ends On/Off : adds or leaves away dots at the ends of lines.

If *XYZ lines.View all* is combined with *XYZ lines.View filtered*, these settings are only used for the filtered lines, while the full lines are drawn with *Linewidth* (see above) in the foreground colour, in order to allow clear comparison.

-> Full scarp triangles/Scarp traces only

When you do *Triangles.View.Scarps*, all scarp triangles edges will be drawn by default. If you select Scarp traces only, triangle edges common to two triangles are identified. This may take a while. Subsequently, triangle edges within the scarp traces will not be drawn, so that they don't obscure the contours, which are often very close on scarps.

-> Triangle edge width

in pixels. Multiplied with 3 for scarp triangles.

-> Grid line width

in pixels. Applies to grid drawn as lines, or guidelines on solid grid.

-> 'Done' button

Click to hide the current settings.

7.2. Legend.Shading...

Click to pop-up Shading control window. Shading of triangular or gridded surfaces is calculated with Phong's illumination formula, which incorporates both the light source position and the 3D viewpoint.

Phong illumination calculates the intensity I of reflected light on a flat surface with normal vector N vector, and viewed along V vector, with the following formula (FOLEY & VAN DAM, 1984, Fundamentals of Interactive Computer Graphics, p.578) (name of parameters as in Shading pop-up, see further):

$$I = I_a k_a + \frac{I_p}{r+k} [k_d (\vec{L} \cdot \vec{N}) + k_s (\vec{R} \cdot \vec{V})^n]$$

It thus requires 9 parameter sliders to be set or changed by the user in the Shading pop-up. The looks of a surface is mostly determined by the exaggeration of height (set in the 3D mode pop-up), the light source orientation (bearing and inclination of L vector), k_s and n . Read the tips at the end of this Help file and experiment!

-> Phong illumination ON/OFF :

If the current (SCREEN.)Colour table holds 12x21, 8x31 or 256 shades, and the lighting is OFF, intervals are solidly coloured with up to resp. 12, 8 or 1 colour, that

are repeated along the colourscale as necessary. Start the System Colour Editor to grab and view the current colour table (only possible under SunView).

If the illumination is ON, the other shades of the same basic colours are used as well, in order to create a more realistic 3D impression of the surfaces. Structural details or flaws may be elicited without extra contour lines or an extra exaggeration of height.

-> LIGHT SOURCE

- distance (k in XY units) :

Distance between the point light source and the current (triangular) facet.

- bearing (L_a in deg, from N->E) and

- inclination (L_g in deg) of point light source.

- intensity (I_p) of light source :

Actually, the absolute intensity of the light source is unimportant, since the intensities of reflected light are automatically normalised. This avoids unneeded searching for an appropriate intensity level. In order to see any shades at all, I_p should simply be larger than I_a , the intensity of ambient light.

-> k_d = reflection coefficient for diffuse light :

When $k_d = 1$, the surface is a perfect diffuse, matte, dull reflector of light, so that the brightest parts have an average, saturated shade. The brightest parts are perpendicular to the direction of incident light.

-> k_s = reflection coefficient for specular light :

When $k_s = 1$, parts of the surface which have surface normals halfway between the direction of incident light and the viewing direction, completely reflect all (white) incident light IN THE DIRECTION OF the viewpoint. Those parts are therefore highlighted with 'specular' reflections.

-> n is proportional to the surface smoothness :

When n is infinity, the surface looks like a perfectly smooth reflector of light. Only those facets with surface normals (Nvector) exactly halfway between the direction of incident light (Lvector) and the viewing direction (Vvector) will show specular reflections. With smaller and smaller n 's, facets whose surface normals are

pointing further and further away from the halfway position, also reflect some specular light, while the maximum intensity always exactly at the halfway position, reflected along Rvector.

-> I_a = intensity of ambient light and

-> k_a = reflection coefficient for ambient light :

If some parts of the surface are shaded darker than you would like, more ambient light will improve on that. Don't overdo : strong ambient light hides any shading on a surface that reflects some ($0 < k_a < 1$) or all ($k_a = 1$) of ambient light.

Tips :

- for rough triangulations or grids, use low n ($0 < n < 3$) and/or low k_s ($k_s < 0.5$), or if still too rough, reduce vertical exaggeration;
- for dense, smooth grids, three interesting light source positions are :
 - viewpoint bearing -or+ 90 deg, with low to average inclination, high k_s ($k_s > 0.5$) and low n ($1 < n < 4$), so that 'soft' light shines from the 'left' or 'right';
 - viewpoint bearing + 180 deg, with viewpoint inclination, full k_s ($k_s = 1.0$) and average to large n (> 8);
 - light source coincident with view point, $k_s = 0$ and $k_d = 1$. If $k_s = 0$, diffuse reflection also uses undersaturated, whitish shades in order to create shades similar to the pseudo-shades of a projected fish net.
- for print on black&white Versatec : limit the number of colour intervals to 6 (4 is better) because the grey scale contrast is less than that with colours, take $k_s = k_d = 1.0$, reduce n and increase light source inclination (e.g. for a photograph, you may have chosen $n=10$ and $L_g=55$; for a Versatec print, this may become $n=3$ and $L_g=65$).

8. Mode_cycle (in 'Main_panel')

= first button in the main panel, with the little arrows. It offers the choice between drawing in map mode or 3D mode.

To select another mode : clicking left on the mode cycle cycles through possible modes, while clicking right on the mode cycle brings up a menu from which you can directly select the desired mode. Everything is automatically redrawn in the new mode. Hit the 'Stop' key to interrupt Redraw (see *Help on Stop_it*).

8.1. MAP MODE

This is the default mode when Geofox is started. In this mode, everything is projected onto a (horizontal) map, with a 'Scale' that can be adapted by dragging the scale_slider. In this mode only, a new sector can be selected by dragging left in the canvas. Click middle to undo selection. If Legend is ON in the legend menu, holding the meta-key (see help on 'Shortcuts') and hitting 'i' puts the scale and sector information at the current cursor position.

-> File :

Name of 'File' from which data are read when 'Read' is selected from any of the 'Main_panel' buttons (see also help on 'File').

-> New project/Add to project :

In order to focus properly on a number of objects that belong to a new project, Geofox automatically centres map and 3D projections on the first data that are read with 'New project' selected. As long as the user does not explicitly select another sector in map mode, it is assumed that other objects of the same project will be read and viewed in the same initial sector, so 'Add to project' is automatically selected for the rest of the objects. Similarly, the current range of z-values, the use of colour for contouring purposes and the z-focus of 3D projection is reinitialised when 'New project' is selected.

-> (xm,ym), (xM,yM):

Coordinates of lower left and upper right corners of currently visible and selected sector.

-> scale :

Current 'Scale'. The long box below it is the scale slider. See *Help on.Scale* (§11) for more details.

8.2. 3D MODE

In this mode, everything is projected in 3D. If Legend is ON in the legend menu, holding the meta-key and hitting 'i', puts the axis arrows and other information at the current cursor position.

-> Automatic Redraw Off/On :

don't/automatically redraw everything as soon as the setting of one of the sliders is changed.

-> Project upright/upside down :

allows you to project everything upside down. This can be useful for Isopach grids.

Distance, bearing and inclination determine viewpoint relative to the geometrical centre of the current objects of interest. When the legend is on (select *Legend.Show legend*), axis arrows show the current orientation. The length of the vertical arrow is proportional to the exaggeration of height. Its length is equal to the length of the horizontal ones if the exaggeration of height is 10, since such an exaggeration is quite usual in geology.

-> distance :

in (x, y, z) units, most often metres, allows you to change the distance of your viewpoint to the objects (i.e. something different from 'zooming in' (see further)).

-> bearing :

true bearing, in degrees, clockwise from N to E. So, dragging the slider to the right, moves the current front part of 3D objects to the right as well.

-> inclination :

inclination, in degrees. Choose a positive inclination to view from above.

-> exaggeration :

exaggeration of height, or more precisely, of the z-value. Used to blow up a feeble relief or deflate an excessively peaky one.

-> width of window :

in cm, width of the window through which you look at the objects. Used in connection with...

-> field of view :

in degrees, the field of view you have from behind the window. Allows you to truly zoom in and out on the objects, thereby changing the natural, default perspective. Geofox assumes that the user's eye is at 40cm from the screen, so that a natural perspective results from a window width of 25cm (= screen width for convenience) and a field of view of 45 degrees. You can have a fish-eye perspective with a large field of view, or an axonometric projection with no perspective foreshortening at all (or hardly so). For the latter, select a large distance first and then reduce the field of view to a few degrees.

9. Mouse

Apart from basic interaction with all the menus and panel items (text, toggles, cycles, sliders and buttons), the mouse is used to interact with (the pictures on) the canvas. See help on 'Getting_started' in order to learn basic interaction with SunView applications. This Help text is shown in a standard text window. It can be manipulated as with the System Text Editor.

9.1. Some Elementary Mouse Actions

- 'click left' = click left mouse button;
- 'drag middle' = click middle and move mouse while middle mouse button is down;

9.2. Specific Geofox Mouse Actions

In The Canvas (the Drawing Window)

- in Map mode :
 - drag left to select a sector;
 - click middle to forget the last selection origin, so that a new sector can be selected. The current selection sector remains active as long as you don't select a new one, indifferent of 'Screen.Redraw's, change of map mode to 3D and vice versa, redraws initiated by slider actions, or indeed any other action. This is important to know if you want to repeat or undo an action that was constrained by the last selected sector;

- click right on the canvas (the drawing window) to rotate the colour table with single steps. If you are using one of the colour tables with shades, it can be useful to activate the shading (see *Legend.Shading..*) and to select *Legend.Show colourscale*;

- shift click right to cycle back 8 steps in the colour table;

- <> i prints scale and sector information at the cursor position. See also *Help on.Legend.Show legend* and *Help on.Shortcuts*;

- with 'XYZpoints.Set Change visibility ON' :

- drag left around selected points to toggle their visibility from ON to OFF or vice versa;

- with 'XYZpoints.Set Move ON' :

- see *Help on 'Move_Points+Triangles'*;

- with 'Triangles.Set Change ON' :

- see *Help on 'Triangles'*;

- in 3D mode :

- <>a prints axis arrows at the cursor location.

- <>i prints title and viewpoint information at the cursor location.

See also *Help on.Legend.Set Legend ON* and *Help on.Shortcuts*;

10. Move_points+triangles

In map mode, individual or rows of points can be moved up or down along the Z-axis, together with all connected triangles. This allows you to judge the moves interactively. Obviously, you can only do so if there exists a triangulation in memory. So, either triangulate before you start moving, or read a saved triangulation.

To enable moving points and triangles, select 'Move ON' in XYZ_DATA-menu. Don't forget to select 'Move OFF' in the same menu as soon as you are finished.

-> To Select An Individual Point :

Click-left on point.

-> To Select A Row Of Points :

Add points to the first point (selected as above), by shift-clicking-left on the remaining points.

-> To Move An Individual Point Up Or Down :

Drag-left point up or down. Change along Z-axis is proportional to the number of pixels moved up or down.

-> To Move A Row Of Points Up Or Down:

Shift-drag-left one of the selected points up or down. Step along Z-axis is also proportional to the number of points selected.

11. Print_Screen

Hit the 'PrSc' button to dump the current framebuffer to file in your saved_screens/ directory. With the 'movie_slow', 'movie_average' and 'movie_fast' commands, you can cycle through all saved screens either as fast as possible, one every 10 seconds or one every 30 seconds.

For hardcopy on paper, do *Screen.Redraw.Versatec* (see also *Help on.Screen*, *Help on.Legend.Set.colourstep*, *Help on.Shading.Tips*).

12. Scale

Scale is only a meaningful concept in map mode. Cycling to this mode (with the 'Mode_cycle') on the main panel brings up a window that allows you to set the scale either explicitly or with the help of the scale-slider. A *Screen.Redraw* redraws everything within the currently selected sector, forgetting the previous scale. Hence, select the largest possible sector within the window, to Redraw at approximately the last scale.

Scale-slider :

This is an exponential slider, each step setting a scale that is a little smaller (drag-left to the left), or a little larger (drag-left to the right). Scales are rounded to the nearest 'nice' scale.

To Set Scale Explicitly :

Type desired scale in the scale parameter field, and shift-click-left on the scaleslider to Redraw at that scale.

To Change Scale of Point Coordinates Themselves :

see *Help on.XYZ_points.Change scale...*

13. Screen

-> Redraw

- screen :

Redraw everything in the current mode, without duplications and in a 'sensible' order, on the screen. Use shortcut $\diamond r$ (see *Help on.Shortcuts*);

- Versatec :

Redraws everything on Versatec 24" printer, in black and white. Colours are converted to shades of grey, so that the print looks like a black and white photograph of the canvas. Everything that fits on the canvas (an area quite a bit larger than the screen) will be printed at exactly the same scale. If you want to use these prints in a paper, report or whatever, see to it that it fits on an A3 on the canvas, so that you can reduce it to 66% to fit on an A4. The latter procedure makes the 200 dots/inch original look like a 300 dots/inch quality print. Do not forget to put a "colourscale" next to the picture (use $\diamond c$ with the colourscale ON; see *Help on.Shortcuts*). After printing, Geofox forgets the current map sector, so zoom out and redraw until you see your data, and zoom in on them again.

- Spectrum :

Idem, but produces a file of Versatec codes that is automatically compressed and sent to the NCR with uucp. On the NCR, the spdraw shellscript translates this file into a v9int.dat that is printed on the Spectrum. Since this Redraw is very time and space consuming, an alert asks whether you are sure to go ahead.

The conversion of RGB to CMY is as faithful as possible, but the Spectrum cannot be expected to produce pictures with vivid colours. Moreover, the viewpoint should be chosen so as to avoid hidden surfaces, since the Painters' algorithm for hidden surface removal does not work properly on the Spectrum. This clumsy Redraw should be avoided.

-> Show/Hide position :

Shows/hides a window with continuously updated (x, y) position of cursor, especially helpful while selecting a gridsector, to make sure you select the same sector as before. See also Help on Editing data files.

-> Erase :

Erases the screen and empties the redraw list.

-> Set clipper ON/OFF :

If the clipper is ON, lines and polygons will not be passed on to the SunView drawing routines, unless there is at least one vertex on the canvas. The extra tests add a negligible amount of time when everything fits on the screen, but save a lot of time and awkward effects when scale or distance are relatively small. Leaving it ON is safest.

-> Hide pop-ups :

Hides most of the pop-ups at once. Something convenient in between, but necessary before you Quit Geofox.

-> Cycle colours :

Rotates the current colour table five times, and gives an idea of the effect of using another part of the colour table (see further). Click right on the canvas (the

drawing window) to single-step rotate the colour table. Shift click right to cycle back 8 steps.

-> Original colours :

Restores the initial position of colours in the current colour table, e.g. after 'Cycle colours'.

-> Colour table :

Pick a different colour table for different purposes. Run the System Color Editor to grab and view the entire current colour table of a window, and to introduce personal changes.

- Screen colours :

A large range of 'pure' colours (without shades) for lots of different colour contours. Shading ON has no effect. The difference between successive colours is tiny, so that you may want to increase the colour contrast with a non-unity colour step in Legend.Set.. ;

- Spectrum colours :

This colour table is equivalent with the first, but has been optimized for the Spectrum, so that all colours can be differentiated. With a colour interval of 3, this is certainly the case;

- 12 colours x 21 shades :

This colour table and the following ones can be used either with Shading ON or OFF. The colours were chosen so that dark ones correspond to the deepest contour intervals, and so that the difference between any two successive colours is most nearly constant. With Shading OFF, 12 colours can be used for different colour contours. With Shading ON, all 21 shades of each colour is used to simulate different light reflection intensities. Colour step in Legend.Set... should be 1 or 2;

- 8 colours x 31 shades :

Equivalent with previous colour table, but with less and brighter colours and more gradual shades. Colour step in Legend.Set... should be 1 or 2;

- 256 grey shades :

256 shades of grey for 'metallic' surfaces, or for black and white publications.

- 256 grey levels :

256 levels of grey for surfaces with lots of contour intervals (no shading). Colour step in Legend.Set... should be quite large, between 15 and 30, to see some contrast.

-> Fore/Background :

Select another couple of fore- and background colour, without changing the rest of the colour table.

14. Shortcuts

In order to use shortcuts for common commands, you should move the cursor out of the pop-up panels, so that it appears as crosshairs (or another special cursor).

◊ stands for the 'meta' key, the key with the diamond shape on it, just next to the spacebar.

◊a in map mode, puts scale bar at cursor position;
in 3D mode, puts 3D arrows at cursor location.

◊i puts info block with viewpoint information (in 3D mode) or scale and sector information (in map mode) at the current cursor position.

◊c puts colourscale at cursor position.

◊h = *Screen.Hide pop-ups*.

◊l = *Legend.Set...*; brings up legend control pop-up.

◊p shows (x,y) coordinates of cursor position in map mode, and prints them in the map_panel.

◊r = *Screen.Redraw.Canvas*; redraws everything in a 'logical' manner.

◊s = *Legend.Shading...*; brings up shading control pop-up.

◊1 = *XYZpoints.Set Move ON/OFF* toggle.

◊2 = *Triangles.Set Change ON/OFF* toggle.

◊3 = *Triangles.Set VertexAdd ON/OFF* toggle.

◊4 = Sets any change mode OFF to allow areal selection.

F1 = *XYZlines.View all + XYZpoints.View visible*

'Stop' = Interrupt (re-)drawing.

'PrSc' = Print Screen

= dump current framebuffer to file (in your saved_screens/ directory)

15. Shot_data

Shot data are points that have a number, a shot time, and (x,y,z) coordinates.

-> Read:

In map-mode, write name of shot data file in File name field, and select either Read All or Read Constrained (within a selected sector) from the shot data menu.

-> View shotpoints:

does just that.

-> Set layout...:

pops up a window that allows you to set various source-receiver lay-out parameters.

-> View CMPs:

shows all Common Mid Points for each shotpoint.

-> Binning...:

pops up a window that allows you to set CMP binning parameters. The 'Bin's unit size' is the unit size of the bins (rather weedies) into which the CMP's are sorted. With 'X-units' and 'Y-units', bins can get other than square proportions. If the sector is not too large and you like pronounced bins in the output, set 'X-units' and 'Y-units' to at least '2'. Select a sector and click left on 'Start binning'. The actually used sector limits are feed back afterwards.

To View the CMP coverage grid, see *Help on Grids.View*.

16. Stop_it

Hit 'Stop' button to interrupt (re-)drawing, interpolation or any other calculation that takes a suspiciously long time. The cursor should rest in the canvas.

If you want to quit Geofox, choose 'Quit' from the frame menu.

If Geofox gets stuck for some reason (hitting 'Stop' doesn't help and you can't close its window), you will need to kill it from another terminal on the network. At RCMG Seismostrat, lit Eric's Mac, make sure that his Mac is connected with the Sparc on which you were running Geofox, start Versaterm from OnCue menu, login, do `ps`, read the PID of Geofox, and do `kill -9 PID`.

17. Triangles (in 'Main panel')

Triangles connect (x,y,z) data points in a triangulated network. This triangulation is used to model both a horizon and the normal faults that cut it, if there are data points that lie on both. It is also used to approximate a surface based on digitized contours. See also Verschuren, 1992, '3D modelling of a complex fault pattern on an entry level 2-D workstation'.

-> Read saved :

Only if you saved a triangulation for these XYZ data (points or lines) before (more precisely : if there exists a /home/rcmg/utm_z.tri/filename.tri for /home/rcmg/utm_z/filename).

-> Triangulate :

Constructs a new, convex Delaunay-triangulation with the current array of points, read as 'XYZpoints' or 'XYZ_lines'. The Akima (1978) algorithm is used to this purpose. A Delaunay-triangulation is unique, in that it maximizes the internal angles of all triangles, and connects pairs of points that are most closely neighbours. This automatic triangulation is geometrically sound, but may not conform to a geologists' idea of what the surface should look like.

Most often, the line coherence of the data points is reflected by their consecutive places in the input file, e.g. points along a profile or a contour. You are asked whether you want to force the triangulation with this coherence or not. Consecutive pairs of points that are really too far apart will not be connected.

If you are triangulating digitized contours, answer Yes to the second prompt in order to have narrow flat triangles along the contours cleaned up automatically and as much as possible.

You can improve or adapt the triangular surface model when *Triangles.Set Change ON* is selected (see further). As soon as the first change is made, this menu item is disabled as a safety measure. To delete all changes to the triangulation, read points a second time and retriangulate.

Sometimes, the triangulation routine alerts for identical data points. The position of these points are printed in the CONSOLE window, that you can see and open when you close the Geofox window. Open the relevant data file, select the x or y position in the CONSOLE, move the cursor into the data file window, and hit Find to see both points. Remove one of them and see to it that the codes make sense (see *Help on File formats*). Save the new version of your data file, open Geofox, read your file and try to triangulate again. You should Close but never Quit the CONSOLE window.

-> Save :

Saves the current triangulation together with all recent changes and the array of points that was used, in /utm_z.tri/filename.tri. The gridding and smoothing module uses only saved triangulations.

-> View->

- All : Show the outline of all triangles in the current triangulation;
- Visible : Show the 'visible' ones only (see further at 'Set Change ON/OFF');
- Hidden : Show the 'hidden' ones only;
- Scarp : Show 'scarp' triangles only.

-> Narrow... :

pops up a window that allows to remove triangles that are too narrow to be structurally meaningful or that are simply spoiling the look of the triangulation. This is certainly useful for most of the boundary triangles that are created by the automatic triangulation. The narrowness of a triangle is defined as the ratio of the longest base to the height of the triangle perpendicular to the longest base.

- Hide narrower :

Click left and Redraw to hide triangles that are narrower than the cut-off narrowness. The default cut-off narrowness of 50 is rather conservative, hiding only the extremely narrow boundary triangles. Most often, the cut-off narrowness needs to be decreased. If this is carried too far, significant internal triangles may be hidden as well. Increase cut-off narrowness and click left on...

- Show broader :

Click left and Redraw to show triangles that are broader than the cut-off narrowness.

- Eat border :

Eats away at the borders of the visible triangulation, by hiding all border triangles that are too narrow. Can be 'Stop'ped before its appetite is satisfied if it's eating too

much. In that case, do *Triangles.Make all visible*, increase *Narrowness* and *Eat Border* again.

- Done :

Hide this pop-up.

-> Make all visible :

Makes all triangles 'visible'. The 'scarp' triangles lose their significance.

-> Set Change ON/OFF :

Enables/disables the triangle editing mode. In this mode, the triangulation can be adapted so that it better reflects the geologists' interpretation of the spatial relations, the connections between the data. Triangles can be interactively changed from 'visible' to 'scarp' or 'hidden' and back. A side common to two triangles can be swapped. Common corner points can be moved up or down with *XYZpoints.Set Move ON* selected. See also *Help on.Move_points+triangles*. Put the triangle change mode OFF before doing anything else than a Redraw. Save the triangulation regularly as a precaution against unfortunate changes, and to register the most recent changes for the gridding module.

- To Toggle The Status Of A Triangle Between 'visible' And 'hidden' :

Click-middle on triangle. The triangle is hidden, not removed.

- To Hide Triangles Covered By A Sector :

Hold shift-key down and drag-middle to select a sector. At mouse button release, all triangles falling completely within the sector are 'hidden';

- To Make Triangles Covered By A Sector 'visible':

Hold shift- AND meta-key down, and drag-middle to select a sector. At button release, all triangles falling completely within the sector are made 'visible';

- To Toggle The Status Of A Triangle Between 'visible' And 'scarp' :

Click-right on triangle. A 'scarp' triangle is supposed to model a (part of a) scarp or fault in the otherwise smooth surface, and is drawn with heavier edges. When a

regular grid is interpolated starting with a triangular model of the surface, any discontinuity defined by 'scarp' triangles is honoured and not smoothed away;

- To Swap Common Triangle Edges :

Drag-left over the selected diagonal edge. The diagonal edge is swapped and the two triangles involved are redrawn as 'visible' with the current setting of contour interval, line thickness, colour and shading. Adapt these settings to improve the structural understanding of alternative swaps. Faults can be correlated between successive profiles with appropriate swaps. An attempt to swap a boundary edge, or an edge that is common to a couple of triangles that form a concave polygon is detected and results in an alert message.

- To Undo An Unappropriate Swap :

Either swap as usual, or hit the Undo key to undo the last swap.

-> Set VertexAdd ON/OFF :

Enables/disables the mode in which you can add vertices to the triangulation. With these additional control points, you apply the finishing touches to the triangulation. You may want a control point to constrain interpolated smooth contours near the edges of triangulation, to model fault tips, branches and crossings, and to modify/update the triangulation with borehole data.

- To Add a Vertex :

Carefully place the cursor at the required position, and click right. Support points are marked with squares, and can be manipulated just like true data points. Unwanted vertices cannot be removed, so be careful.

-> Contour solid :

Fills the 'visible' and 'scarp' triangles with solid colour contours, with or without shading. In 3D mode, an irregular triangulation may project in unpredictable ways, so that triangles may 'hide' each other in a wrong way. Grid the triangular surface model with *Grids.Interpolate* and inspect in 3D with *Grids.View*.

-> Contour lines :

Draws only the contour lines on 'visible' and 'scarp' triangles, according to the settings in *Legend.Set...*

18. XYZ_lines (in Main_panel)

XYZ lines are (x,y,z) points with or without connectivity. They are read from file `/home/rcmg/xyz_lines/filename.line`, where filename is written in the map mode panel (see *Help on.Mode_cycle* and *.File*), or constructed through the connection of 'XYZ points'. Then they can be visualized and manipulated.

-> Read :

If the z-coordinates are stored as positive depths (applicable to most depth or time sections), read as *Depth*. You can either read *All* points, or only the significant ones of *Filtered* lines.

-> View all and View filtered :

Shows current array of XYZ points, connected through linear interpolation, either *All* of them, or only the significant ones on *filtered* lines. If they are both selected, *All* lines are redrawn in black, and *Filtered* lines in colour. Linethickness and colour can be changed in *Legend.Set....* Use *Screen.Fore/Background colour.white/black* and *XYZline colour ON* and *XYZlinethickness 3* for clearest impression. See *Help on.Editing data files* if something appears to be wrong with the data points.

-> Filter...:

shows a popup that allows you to filter the visually/structurally significant points out of a polygonal line that connects consecutive points with a linear interpolation. Such a reduction of information to its most relevant core, is useful to speed up everything from drawing, over triangulation to interactive surface modelling. See *Help on.XYZ_lines.Filter...* for explanation.

-> Save :

Saves the current xyz_lines as a list of points together with codes indicating whether a point is a 'start or ('open or 'closed) end, or ('ir)r'elevant, in `/xyz_lines/filename.line`. If you have read the current points with `XYZ_lines.Read.Depth(or Height).FILTERED`, Save creates a `/xyz_lines/filename.f.line` that contains only the relevant points.

XYZ_lines.Filter... (in XYZ_lines menu)

shows a popup that allows you to filter the visually/structurally significant points out of a polygonal line that connects consecutive points with a linear interpolation. Such a reduction of information to its most relevant core, is useful to speed up everything from drawing, over triangulation to interactive surface modelling.

-> Lines can be filtered

either in 2D (horizontally, from (constant z-)contours, or vertically, from 2D profiles) or in 3D, as is most applicable to reflector lines along contorted profiles. Filtering lines from contours is fastest, for this uses the (x, y) coordinates only. For lines from 2D profiles, the (x, y) coordinates are used to calculate the cumulative distance of a point along the line. This distance is combined with the exaggerated z-value to filter the line in 2D. The safest, most general, but 'slowest' option is to filter lines in 3D.

-> Weeding tolerance

in (x, y, z) units, the smallest local peak or trough of interest.

-> Exaggeration of Z

(only in 3D or from 2D profiles) exaggeration of z units relative to x and y units. Preferably, this should be equal to the exaggeration of height (see *Help on.Mode_cycle*) with which you prefer to study this object.

-> Filter lines

Click left to filter lines with the current settings. Having done so, the Ratio of filtered/unfiltered is updated to indicate filter effectiveness. Redraw to evaluate and compare the filtered with the unfiltered version (see *Help on.XYZlines.View.All/Filtered*). If there are more than 10000 points in a linepiece, you need to cut that linepiece in smaller pieces. Hit F1 key in map mode and zoom in on points where a break in the line doesn't matter, such as in curved parts of generally straight profiles. Put cursor on one of the points and do $\diamond p$ to put its coordinates in map_panel. Then see *Help on.Editing data files* and *Help on.File formats* to change data files.

19. XYZ_points (in Main_panel)

XYZ points are isolated (x,y,z) points. They are read from file /home/rcmg/utm_z/filename, where filename is written in the map mode panel (see *Help on.Mode_cycle* and *.File*). They can also be vertices of polygonal lines or of triangles.

-> Read :

You can either read *All* data points, or read *Constrained* within a sector, selected in map mode. If the z-coordinates are stored as positive depths, read as *Depth*.

-> View visible and View hidden :

Shows current array of points, but only the Visible or Hidden ones (see *Change Visibility ON/OFF* below). $\diamond p$ shows the coordinates of a point under the cursor (see *Help on.Shortcuts*). See *Help on.Editing data files* if something appears to be wrong with the data points.

-> Set Change visibility ON/OFF :

In map mode, sets the point-visibility-change mode ON or OFF. If this mode is ON, the visibility of selected points can be toggled from visible to hidden and back. Drag left around one or more points to toggle; hold shift key down to hide all selected points; hold shift and meta key down to make all selected points visible. A *Screen.Redraw* with XYZ points.View visible shows the result.

-> Make all visible :

does just that.

-> Set Move ON/OFF :

This item is only enabled when the program has read or calculated a triangulation for the current points. In map mode, selecting this item sets the point-move mode on or off. In point-move mode, you can move points and connected triangles up or down along the Z-axis (see also *Help on .Move_points+triangles*).

-> Connect... :

Shows a popup that allows to connect consecutive points that are closer than a slider-selected distance apart, into lines. If the last point of a line is sufficiently close to the starting point, the line is closed and will be drawn as a loop. If all points come from (digitized) contours, select and on the same z-level instead of

regardless of z-level. The latter setting allows to form any conceivable line in 3D. Click left on button to **Connect** consecutive points with the current settings. Having done so, the XYZpoints can be viewed and manipulated as 'XYZ lines'. For instance, select *XYZ lines.View* or *Redraw* to evaluate the current connections.

-> Change scale... :

Shows a control panel to change the scale of X, Y and/or Z coordinates. For instance, when XY units are in cm on a digitized map with heights in m, they should be multiplied with the map scale, divided by 100, and used as such. Mark in X and Y direction, fill in the scale factor which you want to **Multiply** all points with, or **Divide** by.

If a bathymetry in m needs to be converted into ms TWT, mark in Z direction only, set the scale factor to 2, **Multiply**, then set scale factor to 1.5 and **Divide**. *Save* the newly scaled points for future work.

-> Exact move... :

Shows a control panel to move selected or all points in a controlled way. Fill in the **Offset E/W**, **Offset N/S** and **Move up/down** that are to be **Added** to, or **Subtracted** from x, y, and z coordinates respectively, and that of either **All points** or **Selected points only**.

If **Selected points only** is chosen, all points within the current selection sector will be affected. Therefore, you need to drag a selection box carefully around only those points that you really intend to move together. Draw points/lines/triangles over the current picture, in order to evaluate the last move. If you do not alter the offsets or the selection sector (see *Help on.Mouse*), you can then undo that last move exactly by clicking on the other button. If you select **Individual points**, you need to select points in the same way as is explained in *Help on.Move_Points+Triangles*. As long as you do not start to select a new (list of) point(s), and *Individual points* is selected, the (x,y,z) moves will be applied to the same points.

References

- AGI (1982) *see* AMERICAN GEOLOGICAL INSTITUTE (1980)
- AKIMA, H. (1978a) - A method of bivariate interpolation and smooth surface fitting for irregularly distributed data points. *Association for Computing Machinery, Transactions on Mathematical Software*, 4 (2), 148-159.
- AKIMA, H. (1978b) - Algorithm 526 Bivariate interpolation and smooth surface fitting for irregularly distributed data points. *Association for Computing Machinery, Transactions on Mathematical Software*, 4 (2), 160-164.
- ALLAN, J.R.L (1982) - Sedimentary structures, their character and physical basis. *Developments in Sedimentology*, 30 B, Elsevier, Amsterdam. 663 pp.
- AMERICAN GEOLOGICAL INSTITUTE (1980) - *Glossary of Geology*. BATES, R.L. & JACKSON, J.A. (eds.). 2nd ed., American Geological Institute, Falls Church, Virginia, USA. 751 pp.
- ANDERSON, D.P. (1982) - Hidden line elimination in projected grid surfaces. *Association for Computing Machinery, Transactions on Graphics*, 1 (4), 274-288.
- ANGELIER, J. (1989) - Tectonique cassante et neotectonique. *Annales Soc. Géol. Belg.*, 112 (2), 283-307.
- ANGELIER, J. (1990) - Inversion of field data in fault tectonics to obtain the regional stress-III. A new rapid direct inversion method by analytical means. *Geophys. J. Int.*, 103, 363-376.
- ARMITAGE, D.L. (1990) - Advances in surface modeling techniques. *Geobyte*, 5 (5), 15-16.
- ASADA, H. & BRADY, M. (1986) - The Curvature Primal Sketch. *IEEE Trans. Pattern Analysis and Machine Intelligence*, 8 (1), 2-14.
- ATKINSON, J.H. & BRANSBY, P.L. (1978) - *The mechanics of soils : an introduction to critical state soil mechanics*. McGraw Hill, London
- BANKS, R. (1990) - Modeling geological and geophysical surfaces. *Geobyte*, 5 (5), 20-23.
- BARNETT, J.A.M., MORTIMER, J., RIPPON, J.H., WALSH, J.J. & WATTERSON, J. (1987) - Displacement geometry in the volume containing a single normal fault. *Amer.Ass.Petrol.Geol. Bulletin*, 71, 925-937.
- BENTLEY, J. (1986) - *Programming Pearls*. Addison-Wesley Publ. Co., Reading, Massachusetts. 195 pp.
- BERGERAT, F. (1987) - Stress fields in the European platform at the time of Africa-Eurasia collision. *Tectonics*, 6 (2), 99-132.
- BERGERAT, F. (1987) - Paléo-champs de contrainte tertiaires dans la plate-forme européenne au front de l'orogène alpin. *Bull. Soc. Géol. France*, T III (8), 611-620.
- BERRY, F.G. (1979) - Late Quaternary scour-hollows and related features in central London. *Quarterly Journal of Engineering Geology*, 12, 9-29.
- BOLONDI, G., ROCCA, F. & ZANOLETTI, S. (1976) - Automatic contouring of faulted subsurfaces. *Geophysics*, 41 (6), 1377-1393.
- BOUVIER, J.D., KAARS-SIJPESTEIJN, C.H., KLUESNER, D.F., ONYEJEKWE, C.C. & VAN DER PAL, R.C. (1989) - Three-dimensional seismic interpretation and fault sealing investigations, Nun River Field, Nigeria. *Amer.Ass.Petrol.Geol. Bulletin*, 73, 1397-1414.
- BRASSEL, K.E. & REIF, D. (1979) - A procedure to generate Thiessen polygons. *Geographical Analysis*, 11 (3), 289-303.

- BREDE, E.C. & THOMAS, S.W. (1986) - Interactive fault mapping: a case study. *The Leading Edge*, 5 (9), 46-50.
- BRIGGS, I.C. (1974) - Machine contouring using minimum curvature. *Geophysics*, 39 (1), 39-48.
- BRODZIKOWSKI, K., GOTOWALA, R., KASZA, L. & VAN LOON, A.J. (1987) - The Kleszczow Graben (central Poland) : reconstruction of the deformational history and inventory of the resulting soft-sediment deformational structures. In: JONES, M.E. & PRESTON, R.M.F. (eds.), *Deformation of Sediments and Sedimentary Rocks. Geological Society Special Publication*, 26, 241-254.
- BROWN, A.R. (1986) - Interpretation of three-dimensional seismic data. *AAPG Memoir*, 42, AAPG, Tulsa, USA. 194 pp.
- BROWN, A.R., DAHM, C.G. & GRAEBNER, R.J. (1981) - A stratigraphic case history using three-dimensional seismic data in the Gulf of Thailand. *Geophysical Prospecting*, 29 (3), 327-349.
- BUKOVICS, C. & NOOTEBOOM, J.J. (1990) - Combining techniques in integrated 3D land, shallow water and deep channel seismic acquisition. *First Break*, 8 (10), 375-382.
- BULLOCK, P., FEDOROFF, N., JONGERIUS, A., STOOPS, G. & TURSINA, T. (1985) - *Handbook for Soil Thin Section Description*. Waine Research, Albrighton, England. 152 pp.
- C.E.E.D. COMMITTEE (1986) - CEED II : Mapping Systems Compared, Evaluated. *Geobyte*, 1 (3), 25-40.
- CAREY, E. & BRUNIER, B. (1974) - Analyse théorique et numérique d'un modèle mécanique élémentaire appliqué à l'étude d'une population de failles. *C. R. Acad. Sci. Paris*, 179-D, 891-894.
- CLINE, A.K. & RENKA, R.L. (1984) - A storage-efficient method for construction of a Thiessen triangulation. *Rocky Mountain Journal of Mathematics*, 14 (1), 119-139.
- CORSMIT, J., VERSTEEG, W.H., BROUWER, J.H. & HELBIG, K. (1988) - High resolution 3D reflection seismics on a tidal flat: acquisition, processing and interpretation. *First Break*, 6 (1), 9-23.
- CRANS, W. & MANDL, G. (1980) - On the theory of growth faulting part II(a) : genesis of the 'unit'. *Journal of Petroleum Geology*, 3 (2), 209-236.
- CRANS, W., MANDL, G. & HAREMBOURE, J. (1980) - On the theory of growth faulting : a geomechanical delta model based on gravity sliding. *Journal of Petroleum Geology*, 2 (3), 265-307.
- CROMLEY, R.G. & CAMPBELL, G.M. (1990) - A geometrically efficient bandwidth line simplification algorithm. In: *Proceedings of the 4th Int. Symp. on Spatial Data Handling*, Vol. 1, 77-84.
- DALLEY, R.M., GEVERS, E.C.A., STAMPFLI, G.M., DAVIES, D.J., GASTALDI, C.N., RUIJTENBERG, P.A. & VERMEER, G.J.O. (1989) - Dip and azimuth displays for 3D seismic interpretation. *First Break*, 7 (3), 86-95.
- DARWIN, C. (1851) - *On the structure and distribution of Coral Reefs; also Geological observations on the Volcanic Islands and parts of South America, visited during the voyage of HMS Beagle, 1832-1835*. The Minerva Library of Famous Books (s.d.), Ward, Lock & Bowden, Ltd., London. 549 pp.
- DE BATIST, M. (1989) - *Seismostratigrafie en structuur van het Paleogeen in de Zuidelijke Noordzee*. Unpublished Ph.D. thesis, Rijksuniversiteit Gent. 107 pp.
- DE BEER, E. (1979) - Historiek van the kanaal Leie-Ieper - Eigenschappen en gedragingen van de Ieperiaanse klei. *Tijdschrift Openbare Werken België*, 4-5-6, 91 pp.
- DE CONINCK, J. (1988) - Ypresian organic-walled phytoplankton in the Belgian basin and adjacent areas. In: DUPUIS, C., DE CONINCK, J. & STEURBAUT, E. (eds.), *The Ypresian Stratotype. Bull. Soc. belge Géol.*, 97 (3-4), 287-319.
- DEMYTTENAERE, R. & LAGA, P. (1988) - Breuken- en isohypsenkaarten van het Belgische gedeelte van de Roerdal slenk. *Professional Paper*, Nr. 234, Ministerie van Economische Zaken, Brussel. Bijlagen 1 tot 9.
- DENVER, L.E. & PHILLIPS, D.C. (1990) - Stratigraphic Geocellular Modeling. *Geobyte*, 5 (1), 45-47.

- DOUGLAS, D. & PEUCKER, T. (1973) - Algorithms for the reduction of the number of points required to represent a digitized line or its caricature. *The Canadian Cartographer*, 10, 112-122.
- DUPUIS, C., DE CONINCK, J. & STEURBAUT, E. (eds.) (1988) - The Ypresian stratotype. *Bull. Soc. belge Géologie*, 97 (3-4), 229-481.
- EL ABBASS, T., JALLOULI, C., ALBOUY, Y. & DIAMENT, M. (1990) - A comparison of surface fitting algorithms for geophysical data. *Terra Nova*, 2, 467-475.
- FERTL, W.H. (1976) - *Abnormal formation pressures, implications to exploration, drilling, and production of oil and gas resources. Developments in Petroleum Science*, 2, Elsevier, Amsterdam. 382 pp.
- FLEUTY, M.J. (1964) - The description of folds. *Proceedings of the Geologic Association of London*, 75, 461-492.
- FLYNN, J.J. (1990) - 3-D computing geosciences update. *Geobyte*, 5 (2), 30-36.
- FOLEY, J.D. & VAN DAM, A. (1982) - *Fundamentals of Interactive Computer Graphics*. Addison-Wesley, Reading, Mass. 664 pp.
- FOLEY, J.D., VAN DAM, A., FEINER, S.K. & HUGHES, J.F. (1990) - *Computer Graphics : Principles and Practice*, 2nd ed., Addison-Wesley Publishing Company, Reading, Mass. 1174 pp.
- FOOKES, P.G. & PARRISH, D.G. (1969) - Observations on small-scale structural discontinuities in the London Clay and their relationship to regional geology. *Quarterly Journal of Engineering Geology*, 1, 217-240.
- FRIED, C.C. & LEONARD, J.E. (1990) - Petroleum 3-D models come in many flavors. *Geobyte*, 5 (1), 27-30.
- GANGLOFF, P. & PISSART, A. (1983) - Evolution géomorphologique et paises minérales près de Kuujuaq (Fort Chimo, Québec). *Bull. Soc. Géogr. Liège*, 19, 119-132 (cited in Pissart, 1987).
- GREEN, W.R. (1991) - Exploration with a Computer : Geoscience Data Analysis Applications. *Computer Methods in the Geosciences*, 9, Pergamon Press, Oxford. 225 pp.
- GREGORY, C.H. (1844) - On railway cuttings and embankments; with an account of some slips in the London Clay on the line of the London and Croydon Railway. *Min. Proc. Instn civ. Engrs*, 3, 135-145, 148 (cited in Skempton *et al.*, 1969).
- GUIRAUD, M. & SÉGURET, M. (1987) - Soft-sediment microfaulting related to compaction within the fluvio-deltaic infill to the Soria strike-slip basin (northern Spain). In: JONES, M.E. & PRESTON, R.M.F. (eds.), *Deformation of Sediments and Sedimentary Rocks*. Geological Society Special Publication, 26, 123-136.
- HAAS, A.G. & VIALIX, J.R. (1976) - Krigeage applied to geophysics: The answer to the problem of estimates and contouring. *Geophysical Prospecting*, 24, 49-69.
- HAQ, B.U., HARDENBOL, J. & VAIL, P.R. (1987) - Chronology of fluctuating sea levels since the Triassic. *Science*, 235, 1156-1167.
- HAQ, B.U., HARDENBOL, J. & VAIL, P.R. (1988) - Mesozoic and Cenozoic chronostratigraphy and cycles of sea-level change. In: WILGUS, C.K. ET AL. (eds.), *Sea-level change : an integrated approach*. Society of Economic Paleontologists and Mineralogists Special Publication, 42, 71-108.
- HARRINGTON, S. (1983) - *Computer Graphics: a programming approach*. Mc Graw-Hill, Singapore. 448 pp.
- HEARN, E.D. (1987) - Digitizers for data entry (Reprinted from November 1986 issue of BYTE magazine). *Geobyte*, 2 (2), 46-50.
- HELDENS, PH. (1983) - *Een seismische studie van de Klei van Boom en de Klei van Ieper*. Unpublished Ph.D. thesis, Rijksuniversiteit Gent. 237 pp.
- HELLER, M. (1990) - Triangulation algorithms for adaptive terrain modeling. In: *Proceedings of the 4th Int. Symp. on Spatial Data Handling*, 1, 163-174.

- HENRIET, J.P., D'OLIER, B., AUFFRET, J.P. & ANDERSEN, H.L. (1982) - Seismic tracking of geological hazards related to clay tectonics in the Southern Bight of the North Sea. In: *Symposium Engineering in Marine Environment, Royal Society of Flemish Engineers (KVIV), Brugge*. 1.5-1.15.
- HENRIET, J.P. & DE BATIST, M. (1989) - The faulted zone of North Hinder (Southern North Sea). *Annales Soc. Géol. Belg.*, 112 (2), 313.
- HENRIET, J.P., DE BATIST, M., VAN VAERENBERGH, W. & VERSCHUREN, M. (1988) - Seismic facies and clay tectonic features of the Ypresian Clay in the southern North Sea. In: DUPUIS, C., DECONINCK, J. & STEURBAUT, E. (eds.), *The Ypresian Stratotype*. Bull. Soc. belge Géol., 97 (3/4), 457-472.
- HENRIET, J.P., DE BATIST, M. & VERSCHUREN, M. (1991) - Early fracturing of Paleogene clays, southernmost North Sea: relevance to mechanisms of primary hydrocarbon migration. In: SPENCER, A.M. (ed.), *Generation, accumulation and production of Europe's hydrocarbons*. Special Publication of the European Association of Petroleum Geoscientists, 1, Oxford University Press, Oxford. 217-227.
- HENRIET, J.P. & HELDENS, P. (1982) - *Rapport Seismisch Onderzoek voor Pre-Metrolijn naar Linkeroever*. Unpublished Technical Report, Rijksuniversiteit Gent. 35 pp.
- HENRIET, J.P., MONJOIE, A. & SCHROEDER, C. (1986) - Shallow seismic investigations in engineering practice in Belgium. *First Break*, 4 (5), 29-37.
- HENRIET, J.P., VERSCHUREN, M. & VERSTEEG, W. (1992) - Very high resolution 3D reflection seismic imaging of small scale structural deformations. *First Break*, 10 (3), 81-88.
- HOVLAND, M. & JUDD, A.G. (1988) - *Seabed pockmarks and seepages*. Graham & Trotman (Kluwer), London. 293 pp.
- INDELICATO, G.J. & MOORE, G.C. (1986) - Seismic mis-tie adjustment procedure (SMAP) using a minimax-minisum strategy. *Geophysics*, 51 (3), 673-678.
- JAEGER, J.C. (1969) - *Elasticity, fracture and flow : with engineering and geological applications*. 3rd ed., Methuen, London. 268 pp.
- JENNINGS, J.S. (1989) - The contribution of geophysics to the oil and gas industry in the 1990s. *First Break*, 7 (5), 185-193.
- JONES, M.E. & PRESTON, R.M.F. (eds.) (1987) - *Deformation of Sediments and Sedimentary Rocks*. Blackwell Scientific Publications, Oxford. 350 pp.
- JONES, T.A., HAMILTON, D.E. & JOHNSON, C.R. (1986) - *Contouring Geologic Surfaces with the Computer*. *Computer Methods in the Geosciences*, 4, Van Nostrand Reinhold, New York. 314 pp.
- KLEIN, H., PFLUG, R. & RAMSHORN, CH. (1989) - Shaded Perspective Views by Computer. *Geobyte*, 4 (4), 16-24.
- KNUTH, D.E. (1973) - *The Art of Computer Programming: Fundamental Algorithms*. 2nd ed., Vol. 1, Addison-Wesley Publ. Co., Reading, Massachusetts.
- KUROZOMI, Y. & DAVIS, W.A. (1982) - Polygonal Approximation by the Minimax Method. *Computer Graphics and Image Processing*, 19, 248-264.
- LAGA, P. (1966) - Kleidiapir in de uitgraving van de spoorwegtunnel van de E3-weg op de rechteroever te Antwerpen. *Het Ingenieursblad*, 35, 552-553.
- LAMBE, T.W. & WHITMAN R.V. (1969) - *Soil Mechanics*. (2nd ed. (SI version) in 1979), John Wiley & Sons, New York. 553 pp.
- LASSETER, T.J. (1990) - IREX, an interactive 3D reservoir modeling system. *Geobyte*, 5 (1), 48-49.
- LASSETER, T.J. (1992) - An interactive 3D modeling system for integrated interpretation in hydrocarbon reservoir exploration and production. In: PFLUG, R. & HARBAUGH, J. (eds.), *Three-dimensional computer graphics in modeling geologic structures and simulating geologic processes*. *Lecture Notes in Earth Sciences*, 41, 189-198.

- LAWSON, C.L. (1977) - Software for C1 Surface Interpolation. In: RICE, J.R. (ed.), *Mathematical Software*. III, Academic Press, New York. 161-194.
- LEONARD, J.E. (1986) - Special CEED II Preview : The event and the problem sets. *Geobyte*, 1 (2), 14-20.
- LINSTER, J.M. (1975) - *Bijdrage tot de kennis van het zogenaamde Paniseliaan op het kaartblad Moeskroen-Zwevegem*. Unpublished licentiate thesis, Rijksuniversiteit Gent. 68 pp.
- MAGARA, K. (1978) - Compaction and fluid migration, practical petroleum geology. *Developments in Petroleum Science*, 9, Elsevier, Amsterdam. 319 pp.
- MALTMAN, A. (1977) - Some microstructures of experimentally deformed argillaceous sediments. *Tectonophysics*, 39, 417-436.
- MALTMAN, A. (1982) - Experimentally deformed clay. In: BORRADAILLE, G.J., BAYLY, M.B. & POWELL, C.M.C. (eds.), *Atlas of Deformational and Metamorphic Rock Fabrics*. Springer Verlag, Berlin. 426-433.
- MALTMAN, A. (1987) - Shear zones in argillaceous sediments - an experimental study. In: JONES, M.E. & PRESTON, R.M.F. (eds.), *Deformation of Sediments and Sedimentary Rocks*. Geological Society Special Publication, 26, 77-87.
- MANDL, G. (1988) - *Mechanics of tectonic faulting*. Elsevier, Amsterdam. 407 pp.
- MANDL, G. & HARKNESS, R.M. (1987) - Hydrocarbon migration by hydraulic fracturing. In: JONES, M.E. & PRESTON, R.M.F. (eds.), *Deformation of Sediments and Sedimentary Rocks*. Geological Society Special Publication, 26, 39-53.
- MANIN, A., BOUCQUAERT, F., REGNAUDIN, J., REGNAULT, A. & THEVENOT, A. (1988) - Recent developments in source and streamer positioning. *First Break*, 6 (6), 183-188.
- MARÉCHAL, R. (1992) - A new lithostratigraphic scale for the Palaeogene of Belgium. In: *Proceedings of 3rd Regional Meeting of RCNPS-RCNNS*. Bull. Soc. belge Géol., in press.
- MASLYN, M. (1987) - Gridding Advisor: an expert system for selecting gridding algorithms. *Geobyte*, 2 (4), 42-43.
- MEHRA, O.P. & JACKSON, M.L. (1960) - Iron oxide removal from soils and clays by a dithionite-citrate system, buffered with sodium bicarbonate. *Clays and Clay Minerals*, 7, 317-327.
- MERCIER-CASTIAUX, M., CHAMLEY, H. & DUPUIS, C. (1988) - La sédimentation argileuse tertiaire dans le bassin belge et ses approches occidentales. *Ann. Soc. Géol. Nord*, 107, 139-154.
- MOKHTARIAN, F. & MACKWORTH, A. (1986) - Scale-based description and recognition of planar curves and two-dimensional shapes. *IEEE Trans. Pattern Analysis and Machine Intelligence*, 8 (1), 34-43.
- MORGENSTERN, N.R. & TCHALENKO, J.S. (1967) - Microscopic structures in kaolin subjected to direct shear. *Géotechnique*, 17, 309-328.
- MURPHY, C.P. (1986) - Thin Section preparation of Soils and Sediments. AB Academic Publishers, 149 pp.
- NEWMAN, P. (1989) - *Short offset 3D marine seismic applications*. Simon-Horizon Ltd. 4 pp.
- O'BRIEN, C.F. (1989) - On: "Seismic contouring: A unique skill" by PAUL M. TUCKER (*Geophysics*, 53, 741-749, June 1988). *Geophysics*, 54, 1651-1653.
- OLEA, R.A. (1975) - *Optimum mapping techniques using regionalized variable theory*. Kansas Geological Survey, Lawrence, Kansas. 137 pp.
- OLIVEROS, R.B. (1989) - Correcting 2-D seismic mis-ties. *Geobyte*, 4 (2), 43-48.
- OWEN, G. (1987) - Deformation processes in unconsolidated sands. In: JONES, M.E. & PRESTON, R.M.F. (eds.), *Deformation of Sediments and Sedimentary Rocks*. Geological Society Special Publication, 26, 11-24.

- PARADIS, A. (1990) - Three-dimensional computer mapping. In: PFLUG, R. & BITZER, K (eds.), *Three-dimensional Computer Graphics in Modeling Geologic Structures and Simulating Geologic Processes*. *Freiburger geowissenschaftliche Beiträge*, 2, 53-58.
- PARADIS, A. & BELCHER, B. (1990) - Interactive Volume Modeling. *Geobyte*, 5 (1), 42-44.
- PARKES, G. & HATTON, L. (1987) - Towards a systematic understanding of the effects of velocity model errors on depth and time migration of seismic data. *First Break*, 5 (4), 121-132.
- PEDERSEN, S.A.S. (1987) - Comparative studies of gravity tectonics in Quaternary sediments and sedimentary rocks related to fold belts. In: JONES, M.E. & PRESTON, R.M.F. (eds.), *Deformation of Sediments and Sedimentary Rocks*. *Geological Society Special Publication*, 26, 165-180.
- PEIKERT, E.W. (1969) - Developments at the man-machine interface. In: MERRIAM, D.F. (ed.), *Computer applications in the earth sciences*. Plenum Press, New York-London. 1-11.
- PETIT, J.P. & LAVILLE, E. (1987) - Morphology and microstructures of hydroplastic slickensides in sandstone. In: JONES, M.E. & PRESTON, R.M.F. (eds.), *Deformation of Sediments and Sedimentary Rocks*. *Geological Society Special Publication*, 26, 107-121.
- PFLUG, R. (1992) - Three-dimensional computer graphics in geology. In: PFLUG, R. & HARBAUGH, J. (eds.), *Three-dimensional computer graphics in modeling geologic structures and simulating geologic processes*. *Lecture Notes in Earth Sciences*, 41, xiii-xiv.
- PFLUG, R., KLEIN, H., RAMSHORN, CH., GENTER, M. (1990) - Modeling and visualizing geologic structures. In: PFLUG, R. & BITZER, K (eds.), *Three-dimensional Computer Graphics in Modeling Geologic Structures and Simulating Geologic Processes*. *Freiburger geowissenschaftliche Beiträge*, 2, 68-69.
- PFLUG, R., KLEIN, H., RAMSHORN, CH., GENTER, M. & STÄRK, A. (1992) - 3-D visualization of geologic structures and processes. In: PFLUG, R. & HARBAUGH, J. (eds.), *Three-dimensional computer graphics in modeling geologic structures and simulating geologic processes*. *Lecture Notes in Earth Sciences*, 41, 29-39.
- PISSART, A. (1987) - *Géomorphologie periglaciaire*. Rijksuniversiteit Gent, Gent. 135 pp.
- POTTER, P.E. & PETTIJOHN, F.J. (1977) - *Paleocurrents and basin analysis*. 2nd ed., Springer-Verlag, Berlin. 425 pp.
- POUZET, J. (1980) - Estimation of a surface with known discontinuities for automatic contouring purposes. *Mathematical Geology*, 12 (6), 559-575.
- PREUSSER, A. (1984) - Computing contours by successive solution of quintic polynomial equations. *Association for Computing Machinery, Transactions on Mathematical Software*, 10 (4), 463-472.
- PREUSSER, A. (1984) - Algorithm 626 TRICP: a contour plot program for triangular meshes. *Association for Computing Machinery, Transactions on Mathematical Software*, 10 (4), 473-475.
- PRICE, N.J. (1966) - *Fault and joint development in brittle and semi-brittle rock*. Pergamon Press, Oxford. 176 pp.
- PRIGOGINE, I. & STENGERS, I. (1989) - *Tussen tijd en eeuwigheid*. Bert Bakker, Amsterdam. 269 pp.
- RAMBERG, H. (1972) - Theoretical models of density stratification and diapirism in the earth. *Journal of Geophysical Research*, 77 (5), 877-889.
- RAMSAY, J.G. & HUBER, M.I. (1987) - *The Techniques of Modern Structural Geology*. Vol. 2: *Folds and Fractures*, Academic Press, London. 700 pp.
- SABIN, M. (1986) - A survey of contouring methods. *Computer Graphics Forum*, 5, 325-340.
- SAFAR, M.H. (1985) - On the lateral resolution achieved by Kirchhoff migration. *Geophysics*, 50 (7), 1091-1099.
- SCHAEFER, R.G., WEINER, B. & LEYTHAEUSER, D. (1978) - Determination of sub-nanogram per gram quantities of light hydrocarbons (C₂-C₉) in rock samples by hydrogen stripping in the flow system of a capillary gas chromatograph. *Analytical chemistry*, 50, 1848-1854.

- SCHITTEKAT, J., HENRIET, J.P. & VANDENBERGHE, N. (1983) - Geology and geotechnique of the Scheldt surge barrier. Characteristics of an overconsolidated clay. In: *8th Intern. Harbour Congress, Royal Society of Flemish Engineers (KVIV), Antwerp*. 1.121-1.134.
- SCHUMM, S.A. (1991) - *To interpret the Earth : ten ways to be wrong*. Cambridge University Press, Cambridge. 133 pp.
- SEDGEWICK, R. (1983) - *Algorithms*. Addison-Wesley Publ. Co., Reading, Massachusetts.
- SHERIFF, R.E. & GELDART, L.P. (1982) - *Exploration seismology*. Vol. 1 : *History, theory, and data acquisition*, Cambridge University Press, Cambridge. 252 pp.
- SHERIFF, R.E. & GELDART, L.P. (1982b) - *Exploration seismology*. Vol. 2 : *Data-processing and interpretation*, Cambridge University Press, Cambridge. 221 pp.
- SHROCK, R.R. (1948) - *Sequence in layered rocks*. McGraw-Hill Book Co., New York. 507 pp.
- SIDES, E.J. (1990) - Geological modelling of a faulted stratiform massive sulphide orebody (Neves-Corvo, Portugal). In: PFLUG, R. & BITZER, K (EDS.), *Three-dimensional Computer Graphics in Modeling Geologic Structures and Simulating Geologic Processes*. *Freiburger geowissenschaftliche Beiträge*, 2, 93-94.
- SIDES, E.J. (1992) - Modelling of geological discontinuities for reserve estimation purposes at Neves-Corvo, Portugal. In: PFLUG, R. & HARBAUGH, J. (eds.), *Three-dimensional Computer Graphics in Modeling Geologic Structures and Simulating Geologic Processes*. *Lecture Notes in Earth Sciences*, 41, 213-228.
- SKEMPTON, A.W. & LA ROCHELLE, P. (1965) - The Bradwell slip : a short-term failure in London Clay. *Géotechnique*, 15, 221-242.
- SKEMPTON, A.W., SCHUSTER, R.L. & PETLEY, D.J. (1969) - Joints and fissures in the London Clay at Wraysbury and Edgware. *Géotechnique*, 19 (2), 205-217.
- SKLANSKY, J. & GONZALES, V. (1979) - Fast polygonal approximation of digitized curves. *IEEE Trans. Pattern Recognition*, 12, 327-331.
- SMITH, W.H.F. & WESSEL, P. (1990) - Gridding with continuous curvature in tension. *Geophysics*, 55, 293-305.
- SPIEGEL, M.R. (1975) - *Schaum's Outline of Probability and Statistics*. McGraw-Hill Book Co., New York. 372 pp.
- SRIVASTAVA, R.M. & MALLET, J.L (1990) - *Triangulation of faulted surfaces*. In: PFLUG, R. & BITZER, K (eds.), *Three-dimensional Computer Graphics in Modeling Geologic Structures and Simulating Geologic Processes*. *Freiburger geowissenschaftliche Beiträge*, 2, 100-102.
- STEURBAUT, E. (1988) - The Ypresian in the Belgian Basin. In: *Centenary Field Guide to the Tertiary*. *Bull. Soc. belg. Géol.*, 96 (4), 339-351.
- STEURBAUT, E. (1988) - New Early and Middle Eocene calcareous-nannoplankton events and correlations in middle to high latitudes of the northern hemisphere. *Newsl. Stratigr.*, 18 (2), 99-115.
- STEURBAUT, E. & NOLF, D. (1986) - Revision of Ypresian stratigraphy of Belgium and northwestern France. *Meded. Werkgr. Tert. Kwart. Geol.*, 23 (4), 115-172.
- SUN MICROSYSTEMS (1988) - *SunView Programmer's Guide*. Sun Microsystems, Mountain View, CA. 457 pp.
- TEARPOCK, D.J. & BISCHKE, R.E. (1991) - *Applied subsurface geological mapping*. Prentice-Hall, London. 648 pp.
- TERZAGHI, K. (1961) - Discussion on : Skempton, A.W. "Horizontal stresses in an overconsolidated Eocene clay". *Proc. 5th Int. Conf. Soil Mech., Paris*, 3, 144-145 (cited in SKEMPTON & LA ROCHELLE, 1965).
- TISSOT, B.P. & WELTE, D.H. (1984) - *Petroleum formation and occurrence*. Springer-Verlag, Berlin. 699 pp.

- TRABANT, P. K. (1984) - *Applied high-resolution geophysical methods*. International Human Resources Development Corporation, Boston. 265 pp.
- TUCKER, P.M. (1988) - Seismic contouring: A unique skill. *Geophysics*, **53**, 741-749.
- TUCKER, V. (1989) - Ambiguities in stereopsis. *Nature*, **337**, 605.
- TURCOTTE, D.L. & SCHUBERT, G. (1982) - *Geodynamics : applications of continuum physics to geological problems*. John Wiley & Sons, New York. 450 pp.
- VAIL, P.R., MITCHUM, R.M. & THOMPSON S.III (1977) - Seismic stratigraphy and global changes of sea level, Part 4: Global cycles of relative changes of sea level. In: C.E. PAYTON (ed.), *Seismic Stratigraphy - applications to hydrocarbon exploration*. Memoirs of the American Association of Petroleum Geologists, **26**, Tulsa. 83-97
- VAN DE WALLE, L. (1988) - *Ontwerp van een gegevensbank voor het seismisch netwerk van het Belgisch Kontinentaal Plat*. Unpublished licentiate's thesis, Labo voor Aardkunde, Rijksuniversiteit Gent. 147 pp.
- VAN VAERENBERG, W. (1987) - *Struktuurgeologische studie van de Ieperse klei*. Unpublished licentiate thesis, Rijksuniversiteit Gent. 136 pp.
- VANDENBERGHE, N., LAGA, P., HERMAN, J. & BOUCKAERT, J. (1990) - Lithological description of the Knokke well. In: LAGA, P. & VANDENBERGHE, N., *The Knokke well (11E/138)*. Mém. Expl. Cartes Géologique et Minières de la Belgique, **29**, 9-17.
- VANDENBERGHE, N. & VAN ECHELHOEL, E. (1987) - Field guide to the Rupelian stratotype. *Bull. Soc. belge Géol.*, **96** (4), 325-337.
- VANDYCKE, S. (1992) - *Tectonique cassante et paléo-contraintes dans les formations crétacées du Nord-Ouest européen*. Ph.D. thesis, Université Pierre et Marie Curie, Paris VI. 178 pp.
- VERCOUTERE, C. (1987) - *Vorbereidende studie tot het opstellen van een seismisch snelheidsmodel voor het Belgisch continentaal plat*. Unpublished licentiate's thesis, Labo voor Aardkunde, Rijksuniversiteit Gent. 129 pp.
- VERSCHUREN, M. (1985) - *Interpretatie en driedimensionele (3-D) voorstelling van reflektieseismische opnamen van een paleoreliëf op het Tertiair substraat in de Belgische Noordzeesektor*. Unpublished licentiate's thesis, Labo voor Aardkunde, Rijksuniversiteit Gent, Gent. 93 pp.
- VERSCHUREN, M. (1990) - 3-D modeling of a complex fault pattern on an entry level 2-D workstation (extended abstract). In: PFLUG, R. & BITZER, K. (eds.), *Three-dimensional computer graphics in modeling geologic structures and simulating geologic processes*. Freiburger Geowissenschaftliche Beiträge, **2**, 111-113.
- VERSCHUREN, M. (1992) - 3-D modeling of a complex fault pattern on an entry level 2-D workstation. In: PFLUG, R. & HARBAUGH, J. (eds.), *Three-dimensional computer graphics in modeling geologic structures and simulating geologic processes*. Lecture Notes in Earth Sciences, **41**, 83-88.
- VERSCHUREN, M. & HENRIET, J-P. (1989) - Three-dimensional analysis of sediment deformations in the offshore environment. *Communications de la Comité belge de Géologie de l'ingénieur*, **II.11-19**.
- VINKEN, R. (comp.) (1988) - The Northwest European Tertiary Basin. Results of the IGCP Project No 124. *Geologisches Jahrbuch*, **A 100**, 508 pp.
- VLERICK, R. (1982) - *Biostratigrafie van het Onder-Eoceen te Heestert (West-Vlaanderen)*. Datering op basis van mikrofossielen met organische wand. Unpublished licentiate thesis, Rijksuniversiteit Gent. 32 pp.
- WALLACE, R.E. (1951) - Geometry of shearing stress and relation to faulting. *Journal of Geology*, **59**, 118-130.
- WALTON, G.G. (1972) - Three-dimensional seismic method. *Geophysics*, **37** (3), 417-430.
- WARD, J.R. & PHILLIPS, M.J. (1987) - Digitizer technology : performance characteristics and the effects on the user interface. *IEEE Trans. Computer Graphics and Applications*, **4**, 31-44.

- WARD, W.H., MARSLAND, A. & SAMUELS, S.G. (1965) - Properties of the London Clay at the Ashford Common shaft : in situ and undrained strength tests. *Géotechnique*, **15**, 321-344.
- WARTEL, S. (1980) - The Tertiary and Quaternary subbottom of the Schelde estuary near Antwerpen (Belgium). *Geologie en Mijnbouw*, **59** (3), 233-240.
- WATSON, D.F. & PHILIP, G.M. (1984) - Systematic Triangulations. *Computer Vision, Graphics, and Image Processing*, **26**, 217-223.
- WATSON, D.F. & PHILIP, G.M. (1987) - Neighborhood-Based Interpolation. *Geobyte*, **2** (2), 12-16.
- WELLINGTON, S.L. & VINEGAR, H.J. (1987) - X-ray computerized tomography. *Journal of Petroleum Technology*, **39**, 885-898.
- WILLEMS, W. & MOORKENS, T. (1988) - The Ypresian stage in the Belgian basin. In: DUPUIS, C., DE CONINCK, J. & STEURBAUT, E. (eds.), *The Ypresian Stratotype*. *Bull. Soc. belge Géol.*, **97** (3-4), 231-249.
- WILLIAMS, C.M. (1978) - An efficient algorithm for the piecewise linear approximation of planar curves. *Computer Graphics and Image Processing*, **8**, 286-293.
- ZIEGLER, P.A. (1982) - *Geological Atlas of Western and Central Europe*. Shell Internationale Petroleum Maatschappij B.V. 130pp.+40 encl.
- ZORASTER, S. & EBISCH, K. (1990) - Incorporating fault geometry into geologic horizon models. *Geobyte*, **5** (2), 30-36.

Index

- 3D computer graphics 92; 98
- 3D facies analysis 221
- 3D mental image 90; 98
- 3D modelling 92; 96
- 3D seismic acquisition 49
- Aalbeke 15; 17; 209; 280
- Aalbeke (loc.) 264
- accuracy 66; 105
- ALGOL 113
- algorithm 91
- aliasing 53
- ASCII 126
- axonometric projection 176
- bin size 81
- boomer 70
- clastic dyke 39; 247; 255; 268; 269
- clay mineralogy 269
- clay tectonics 13
- colourmap 124
- compaction 18
 - ratio 25; 236
- consolidation 18
- contamination 271
- contouring 90; 91; 134
- control points 96
- convergence 167
- correlation 96
 - hypotheses 90; 98
- CT 274
- curvature 155
- curve simplification 111; 127
- data
 - honouring 95; 100
 - reduction 127
 - redundancy 92; 103; 104
 - significant 114
 - structure 127; 130
- Decca 64
- deformation
 - mechanism 20
 - rate 24; 237
- Delaunay triangulation 130
- deposition rate 25
- detail 93; 105
- device coordinates 103; 118
- diapir 43; 201
- diatom 274; 282
- difference equation 155; 157
- digitization 93; 103
 - precision 106
- distance 106
- dot pattern 187
- driving force system 20
- dump sites 265
- effective stress 23
- efficiency (diverse contexts) 90; 103; 104; 105; 120; 130; 163; 167; 220
- Egem 17; 212; 249
- event (on interactive computer) 124
- fault 18
 - aliasing 101
 - bifurcation 96; 141
 - correlation 53; 86; 98; 101; 137
 - cut 85
 - folded 234
 - gap 96; 137
 - intersection 226
 - listric 229
 - pick 101
 - reverse 36; 259
 - sag 194
 - slip data 224
 - tip 98; 141
 - traces 96
- fissure 18; 36
- fix lines 67; 94; 118
- flow structure 280
- fluidization 22
- fold
 - shapes 234
- fracture 18
- framboid 282

- Fresnel zone 56
- gouge 32; 247; 268; 282
- GPS 65
- grain size distribution 268
- graphical user interface 124
- gravitational body force 23
- gridding 99; 146
- growth fault 42
- hardcopy 187
- hidden line removal 177
- hidden surface removal 179
- high-resolution 56
- horse 234; 237
- hydraulic fracturing 21; 38
- hydrocarbon data 270
- hydrofracturing 21; 38
- hydroplasticity 245
- Ieper clay 15; 17; 25
- illite 269
- imprecisions 93; 104; 105
- increment mode 104
- interactive 91
- interpolation 95; 96
- interpretative ambiguities 86
- interrogator 60
- "inverse drag" 30; 75; 201; 277
- isochore 169
- isopach 169
- joint 18; 36
- kerogen 270
- Kortemark 17; 25; 212
- Kortrijk Formation 15; 17; 25
- kriging 146
- lanes 64
- Lauwe 15; 35
- line mode 104
- liquefaction 22
- liquidization 22
- lithification 18
- load casts 229
- Marke 15; 35; 209; 224; 247; 268
- Meulebeke 15; 209; 249
- mflops 102
- microfault 37; 244
- microfossil 274
- microfracture (see fracture) 36
- micromorphology 277
- migration
 - primary 267
 - secondary 268
- mips 102
- mis-ties 94; 137
- mispositioning 94
- modelling 91
- Moen 17; 209
- Mol 15; 247
- monocline 198
- navigation 67
- network density 53
- North Hinder zone 194
- notifier 124
- O(N) notation 108
- organic carbon 270
- organic vein 270
- organogeochemical composition 270
- outcrop rendering 221
- overconsolidation 18
- overpressure 41
- overshoots 160
- oxidation 288
- palaeostress 253
- penecontemporaneous faulting 39
- permeability 265
- perspective projection 176
- photography
 - outcrop 221
 - screen image 187
- pinger 61
- pingo 44
- pitfalls of contouring 96
- pixel 99
- plastic deformation 24
- pockmark 44
- point mode 104
- POLARTRACK 67
- pollution control 265
- polygonal approximation 112
- positioning 56; 58; 74
- precision 66; 93; 105
- pseudo-3D 53; 55

- pseudo-range 64
- range-range 62
- Rayleigh-Taylor instability 23; 41
- reactivation 261
- resolution 56; 105
- responder 61
- reverse drag 277
- Riedel 245; 246
- Rupelian clay 15; 17; 247
- sag 194
- sampling 53; 104
- scale 53; 55; 105; 112
- sedimentary dyke 248
- SEISCAT 71
- seismic reflection methods 48
- Selective Availability 65
- sensitivity 22
- shear
 - strength 18
 - stress 24
- significant vertex 114
- singular points 55; 96
- slickenside 24; 36; 244; 280
- slumping 264
- smectite 269
- soft-sediment deformation 20
- source rock 19; 271
- spade 214; 216
- sparker 70
- spatial aliasing 53
- splay 226
 - connection 229
 - listric 229
 - termination 229
- spline 150; 167
- stacking 87
- stratigraphic framework 169; 292
- stress inversion 254
- striae 36
- subroutine 99
- SunView 122
- Syledis 64; 94
- synchronization 67
- tectonic deformation phases 27
- tension 155; 160
- thin clastic dyke 226
- thin sections 277
- thixotropy 22
- time-depth conversion 118
- topogram 275
- Toran 64
- transponder 61; 62
- triangulation 100; 119; 130
- trigger of deformation 22
- Trisponder 64
- trivia on contours 104
- tunnels 267
- visual quantitative feedback 95; 96
- visualization 172
- waste disposal 19; 265
- watergun 68
- weeding tolerance 114; 128
- window
 - management system 122
 - manager 122
 - system 122
- working hypotheses 39
- workstation 99; 102
- world coordinates 103; 118
- X-ray Computer Tomography 274
- yield strength 20
- Zonnebeke 15; 36; 209; 242; 247; 261

